Volume 2: Nanostructures through Chemistry

A Specialist Periodical Report

Nanoscience

Volume 2: Nanostructures through Chemistry

A Review of Recent Literature

Editor
P.J. Thomas, *Bangor University, UK*
Paul O'Brien, , *UK*

Authors
Osman M. Bakr, *King Abdullah University of Science and Technology (KAUST), Saudi Arabia*
Mrinmoyee Basu, *Indian Institute of Technology, Delhi, India*
Cyrille Boyer, *University of New South Wales, Sydney, Australia*
Serena A. Corr, *University of Glasgow, UK*
Alexander E. Dunn, *University of New South Wales, Sydney, Australia*
Douglas J. Dunn, *University of New South Wales, Sydney, Australia*
Ashok K. Ganguli, *Institute of Nano Science and Technology Habitat Centre, Mohali, India*
Aparna Ganguly, *Indian Institute of Technology, Delhi, India*
Valerie A. Gerard, *Trinity College Dublin, Ireland*
Yurii K. Gun'ko, *Trinity College Dublin, Ireland*
G.U. Kulkarni, *Jawaharlal Nehru Centre for Advanced Scientific Research, Bangalore, India*
Gonghu Li, *University of New Hampshire, Durham, UK*
Jin Li, *Nanjing University of Science and Technology, China*
May Lim, *University of New South Wales, Sydney, Australia*
Xiaoheng Liu, *Nanjing University of Science and Technology, China*
Michael E. Louis, *University of New Hampshire, Durham, UK*
Mohammad Azad Malik, , *UK*
Angela S. Pereira, *University of Aveiro, Portugal*
B. Radha, *Northwestern University, Evanston, U.S.A.*
Karthik Ramasamy, *University of Alabama, U.S.A.*
Neerish Revaprasadu, *University of Zululand, South Africa*
Nguyễn Thi Kim Thanh, *University College London, UK*
Tito Trindade, *University of Aveiro, Portugal*
Xiaxi Yao, *Nanjing University of Science and Technology, China*
Jian Zhang, *Nanjing University of Science and Technology, China*

RSC Publishing

ISBN: 978-1-84973-582-7
DOI: 10.1039/9781849734844
ISSN: 2049-3541

A catalogue record for this book is available from the British Library

Published by The Royal Society of Chemistry,
Thomas Graham House, Science Park, Milton Road,
Cambridge CB4 0WF, UK

Registered Charity Number 207890

For further information see our web site at www.rsc.org

Preface

DOI: 10.1039/9781849737623-FP005

Welcome to the second RSC SPR on Nanoscience. Research in Nanoscience attracts interests from nearly all science disciplines and continues to be at the forefront worldwide efforts. The sheer scale of outputs makes gaining a meaning perspective of developments challenging for both new comers as well as seasoned researchers.

We have sought to provide a clear viewpoint of developments with specific emphasis on the past twelve months by highlighting key research themes, providing country specific perspective as well as focusing on materials. Chapters in this volume cover photocatalysts for water-splitting, design and synthesis of materials for solar energy generation and drug delivery, China and India specific perspectives on developments in nanoscience, nanolithography. Further, insight is provided by essays focusing on materials: ZnO, Ag, Au and metal oxides. We hope you enjoy reading the book.

Paul O'Brien (Manchester)
P. John Thomas (Bangor)

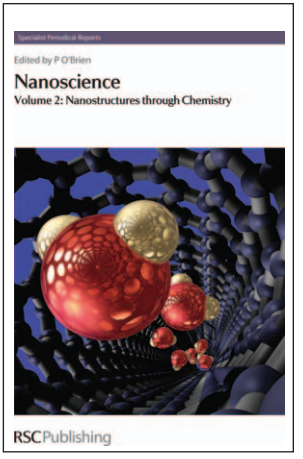

Cover

The cover image shows a model of molecules of water being channelled through a single-walled carbon nanotube.

Gold and silver nanostructures of controlled shape

Valerie A. Gerard and Yurii K. Gun'ko*
DOI: 10.1039/9781849737623-00001

Plasmonic properties of metallic nanoparicles are strongly dependent on the size and shape of these nanomaterials. Therefore significant efforts have been directed towards controlling the synthesis of new shaped and anisotropic metal nanostructures. This review presents some recent years advances in the production and potential applications of shape-controlled gold and silver nanostructures and their assemblies. Many interesting synthetic routes have been developed for a very wide variety of particle morphologies. These include: seed-mediated aqueous synthesis of gold nanoparticles of defined shape; preparation of 1D gold and silver nanostructures (*e.g.* nanowires); photo-chemical synthesis of silver nanostructures; synthesis of anisotropic gold nanostructures using galvanic replacement; preparation of silver nanostructures by cluster aggregation and some other. We also consider and discuss some recent advances in production and uses of gold and silver based nanoparticle assemblies. One of the point of interest is the fabrication of tailor-made nanostructures for specific applications. SERS is presented as an example for it benefits immensely from optimisation of plasmon resonance through shape-control. Over last few years there also were significant advances in the development of novel chiral plasmonic nanostructures. It is expected that these new chiral nanomaterials could find a range of potential applications in new plasmonic devices and chiral sensing.

1 Introduction

Gold and silver nanoparticles have been widely investigated for their unique optical and electronic properties enabling potential applications in biological sensing,[1–5] catalysis,[6–9] drug delivery[10,11] energy harvesting[12] and optoelectronics[13] amongst others. Their small sizes enable them to achieve electronic confinement, which combined to their metallic nature results in unique properties. In bulk metals, the valence and conduction bands are not separated by any energy gap, a property responsible for their high conductivity but also for the appearance of surface plasmons. These are the collective oscillation of electrons that occur in a metal subjected to an external electromagnetic field. At the interface of the metal with a dielectric medium, surface plasmons can arise from interaction with light and propagate as an evanescent wave, or polariton, along the surface until the energy is dissipated through absorption by the metal or scattering. In the case of metal nanoparticles the surface area is so large that all plasmons can be seen as polaritons as opposed to the free plasmons occurring in bulk metal.

With nanoparticles being much smaller than the wavelength of visible light, it can be considered that all the electrons confined in a given nanoparticle are subjected to the same field at any given time; this is referred to as

Trinity College Dublin, Ireland. E-mail: IGOUNKO@tcd.ie

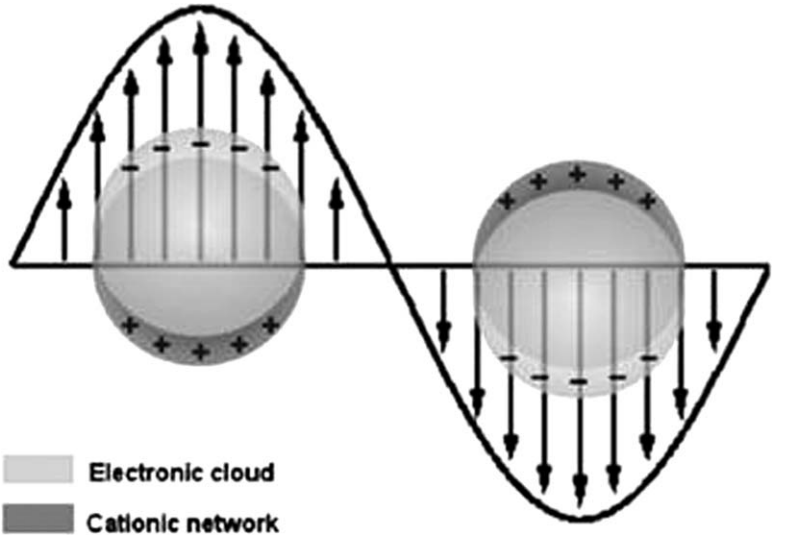

Fig. 1 Schematic representation of electronic cloud displacements in nanoparticles under the effect of an electromagnetic wave.[14] Reproduced with permission from Ref. 14.

the quasi-static hypothesis. Displacement of the electron cloud by the electric field results in the creation of surface charges as represented in Fig. 1. The electrons can thus be assimilated to an oscillator which may be described by the Maxwell equations. Consequently, conditions may be found for which the electron cloud can resonate.

That collective oscillation of electrons creates a strong enhancement of the electromagnetic field in the vicinity of the nanoparticles upon photo-excitation. This in turn is the basis for many applications. It has been successfully employed to enhance Raman signals in Surface Enhanced Raman Spectroscopy (SERS). Raman spectroscopy is a characterisation technique based on the inelastic scattering of photons by certain molecules. The photon sets the material into vibration and is scattered with a different frequency, or energy, and that shift is measured. SERS arises from the presence of metal nanoparticles on the substrate. The SPR-induced enhancement of the electromagnetic field in the vicinity of the surface strongly enhances the vibrational modes. A charge-transfer complex may also be formed between the surface and the analyte molecule, with electronic transitions in the visible range. It should be noted that the SERS effect does not occur on smooth surfaces, but only on rough, nanoparticulate ones. Although initially developed with spherical nanoparticles, SERS has been proven to be influenced by the particle size and shape.[15,16] The optimal signal enhancement is obtained with the appropriate combination of analyte and nanoparticle.[17] Furthermore, there is a growing interest for gold nanoparticles in the fields of drug delivery and biological imaging. They are indeed a biologically inert material which also provides opportunities for functionalization as well as plasmonic imaging.[18–20] They can also be triggered by an external stimulus to release their cargo or produce heat.[11]

Since the position and intensity of SPR are sensitively dependent on the size and shape of the metallic nanoparticle, most efforts have been directed

towards controlling the synthesis of new shaped and anisotropic metal nanostructures. This review will present some recent years advances in the production and potential applications of shape-controlled gold and silver nanostructures and their assemblies.

2 Recent developments in the synthesis gold and silver nanostructures of controlled shape

Nanospheres, nanoplates, nanoprisms, nano-cubes, nanooctohedra, nano-pyramids, nanorods and nanowires are some examples of the shapes that have been produced from gold. In the colloidal synthetic route, it is generally accepted that ligands play a crucial role in directing the growth by preferentially binding to one crystal face or another. More control has recently been gained by investigating the influence of other parameters. Also, other synthetic routes such as electrochemical growth and layer-by-layer template synthesis have been developed further.

2.1 Seed-mediated aqueous synthesis of gold nanoparticles of defined shape

Most shapes of gold nanostructures can be obtained *via* the reduction of a gold salt in the presence of an appropriate surfactant. A variety of geometrically complex high-index faceted structures, such as bipyramids,[21,22] rhombic dodecahedra,[21] concave cubes,[23–26] or tetrahexahedra,[27] have all been prepared using a cetyltrimethylammonium halide surfactant but with the finely tuned addition of halides or silver ions. The role of the additives has recently been elucitaded, thus allowing for more controlled syntheses.

Initially, the effect of silver ions on gold nanoparticle growth was investigated by using their concentration as the only varying parameter leading to the selective formation of octahedra with $\langle 111 \rangle$ facets, rhombic dodecahedra with $\langle 110 \rangle$ facets, truncated ditetragonal prisms with $\langle 310 \rangle$ facets, and concave cubes with $\langle 720 \rangle$ facets, as illustrated in Fig. 2.[28]

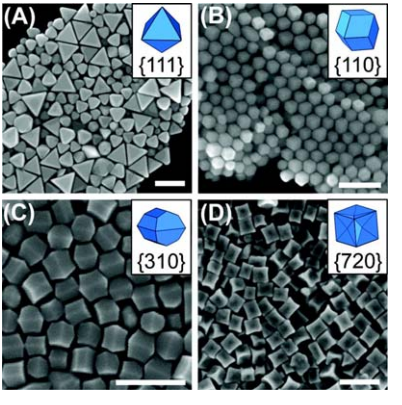

Fig. 2 SEM images of (A) octahedra, (B) rhombic dodecahedra, (C) truncated ditetragonal prisms, and (D) concave cubes synthesized from reaction solutions containing Ag^{+}/Au^{3+} ratios of 1 : 500, 1 : 50, 1 : 12.5, and 1 : 5, respectively. Scale bars: 200 nm. Note that the octahedra form concomitantly with $\langle 111 \rangle$-faceted twinned truncated bitetrahedra, which are larger in size. Reproduced with permission from Personick *et al.*[28]

Gold seeds were produced through the reduction of $HAuCl_4$ by $NaBH_4$ in presence of cethyltrimethylammonium chloride (CTAC). They were subsequently added to a growth solution containing CTAC, $HAuCl_4$, ascorbic acid, $AgNO_3$ and HCl. The resulting four particle types obtained from four different Ag : Au ratios were characterised by X-ray photoelectron spectroscopy (XPS) and inductively coupled plasma atomic emission spectroscopy (ICP-AES) in order to evaluate the amount of silver present on the surfaces. Silver coverage was found to increase in the following order: octahedra < rhombic dodecahedra < truncated ditetragonal prisms < concave cubes, which corresponded to increasing energy of the facets exposed (determined by HRTEM). The authors concluded that under-potential deposition (UPD) was the mechanistic cause for this differentiation. UPD is a phenomenon by which silver can be reduced at the gold surface even though its potential is less negative than the Nernst potential, and results in the deposition of an atomic layer or sub-layer of silver. UPD occurs preferentially on most reactive, high energy facets, thus slowing down their growth and stabilising them in the final structure. Higher energy facets also require a larger amount of silver atoms to be fully stabilised. Shape differentiation lies in the competition between gold and silver deposition; until the facet is fully covered by silver, the latter may be displaced by gold and redeposit on a lower-energy facet.

The same research group subsequently investigated the role of halides in the seed-mediated synthesis in the absence of silver ions.[29] Halides have been known to form complexes with gold ions thus dropping their reduction potential, and to bind to gold surfaces, inhibiting their growth. The two combined effects result in a decrease of the reaction rate which was quantitatively measured by monitoring the particle growth with ICP-AES. The reduction potential of the complexes decreases in the order $[AuCl_2] > [AuBr_2] > [AuI_2]$, and the binding strength of the halides to an Au particle surface increases in the order $Cl^- < Br^- < I^-$. Therefore, the rate of reaction can be tuned by using a chloride containing surfactant (CTAC) which will allow fast growth and adding a larger halide to slow it down. By doing so, more thermodynamically favourable, lower-energy faceted nanoparticles were formed. For instance, the addition of NaBr to a CTAC based synthesis resulted in $<100>$-faceted cubes rather than high-index faceted trisoctahedra.

In presence of silver ions as well as traces of halides, the formation of Au-X complex competes with that of Ag-X. The affinity for silver decreases in the order: $Cl^- > Br^- > I^-$. Therefore, a better silver coverage of high energy gold facets can be obtained by adding bromide or iodide to a CTAC-directed reaction, at constant silver concentration. This means that kinetically-favoured, high index faceted particles were obtained with lower concentration of silver than in the absence of halide additive. At high halide concentration however, the strong binding of bromide or iodide to the gold surface was found to block the silver deposition and thereby to inhibit the formation of high index-faceted particles. These findings are summarised in Fig. 3.

Although most syntheses of anisotropic nanoparticles are accepted to rely on the preferential binding of surfactants to some crystal faces,[30] it has been

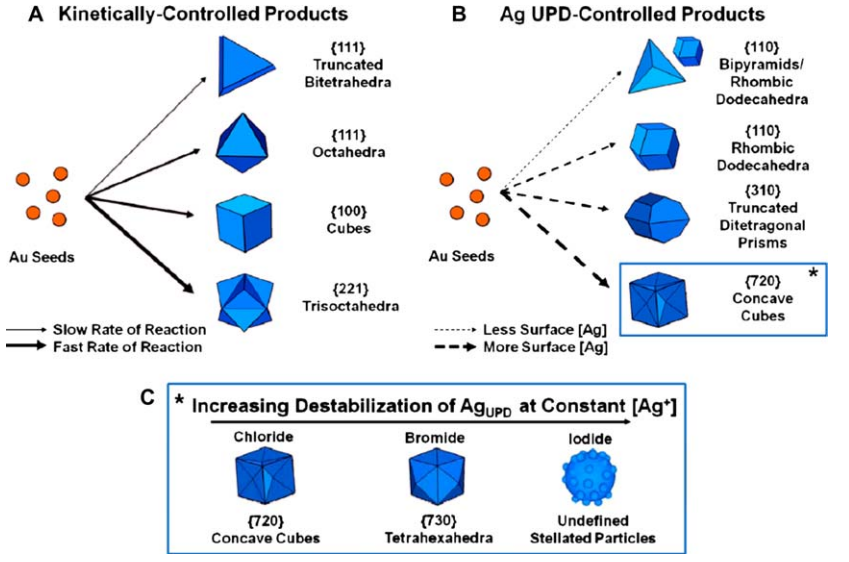

Fig. 3 Scheme illustrating how halides and silver ions can be used to direct the growth of gold seeds down different growth pathways to yield different shaped products: (A) kinetically controlled products in the absence of silver ions; (B) Ag underpotential deposition-controlled products where the interactions of silver with the particle surface dictate product shape; (C) effect of varying the stability of the Ag UPD layer with high concentrations of chloride, bromide, or iodide in the growth solution, yielding concave cubes, tetrahexahedra, and stellated particles, respectively. Reproduced with permission from Langille *et al.*[29]

difficult to produce a clear proof of such adsorption. Burgess and co-workers provided such evidence owing to electrochemical monitoring of Au^{3+} reduction by sodium borohydride in presence of 4-dimethylaminopyridine (DMAP).[31] They observed that the shape of the final nanoparticles depended strongly on the incubation time of $AuCl_4$ with DMAP prior to injection of $NaBH_4$, varying from spherical, to rod-like, to multipodal. Measurements of the differential capacity of the reaction solution indicated a double role played by DMAP. Initially, DMAP reduces Au(III) to Au(I) while forming a complex. Sodium borohydride cannot reduce Au(I) as fast as Au(III), which allows for seeds to grow more slowly and to adopt a lower energy twin structure. Simultaneously, DMAP molecules preferentially bind to high energy facets, thus directing the growth in the $\langle 111 \rangle$ direction. The final shape of the particles finally depends on the degree of twinning that what achieved in the seeding step. Fig. 4 summarises the proposed mechanism.[31] Once again, slowing down the kinetics of the reaction appeared to be the key to control the shape and anisotropy.

2.2 Synthesis of 1D gold and silver nanostructures

One-dimensional (1D) objects exhibit two distinct axes with an aspect ratio higher than 5. Such structures are typically referred to as nanorods if their aspect ratio is comprised between 5 and 25, and nanowires above 25. Many different methods have been developed in order to anisotropically confine the highly symmetrical fcc structure of gold and silver. Some of the approaches involve the physical directional growth using hard templates such

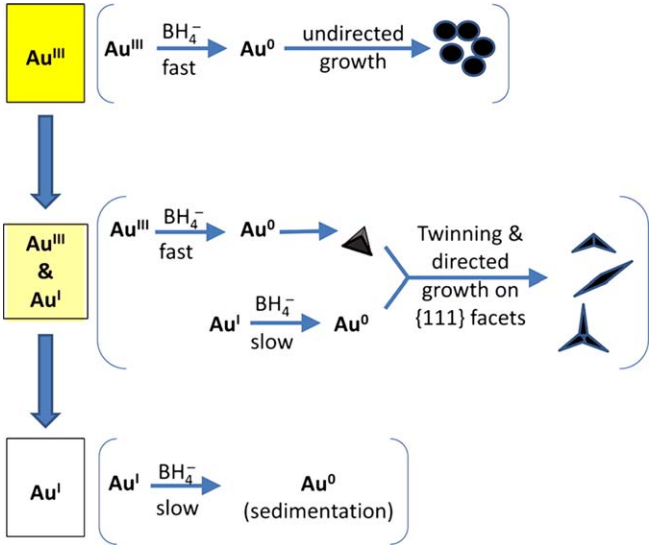

Fig. 4 Mechanistic scheme for the preparation of various sizes and shapes of DMAP stabilized anisotropic gold metal nanoparticles. Reproduced with permission from Burgess *et al.*[31]

as porous alumina.[32] Others employ the colloidal route, a seed-mediated synthesis where the 1D growth is induced and maintained by surface-capping agents. Most common directing surfactants are cetyl trimethylammonium bromide (CTAB)[33] and polyvinylpyrrolidone (PVP).[34]

In both cases investigations revealed a similar mechanism of nanowire growth. The synthesis starts the same way as that of silver nanoprisms with the formation of small seeds. These seeds are then grown into larger metal nanoparticles through Ostwald ripening. This is a crucial step as it allows for the seeds to adopt the crystal structure that is necessary for one-dimensional growth: beyond a critical size, around 8 nm, a multiply twinned structure becomes energetically more favourable as opposed to the mostly monocrystalline structure described above.[34] The resulting nanoparticles exhibit five twin plane boundaries, five triangular $\langle 111 \rangle$ faces at each end, and five $\langle 100 \rangle$ faces which will become the side faces of the nanowires[35] as illustrated on Fig. 5. Appropriate stabilisers, CTAB or PVP, preferentially bind to the more reactive $\langle 100 \rangle$ faces and block the growth from those faces. Simultaneously, the exposed twin planes are the highest energy sites and therefore attract silver atoms which deposit on the seeds. Once the elongation has been initiated, the stabilisation of side faces allows for rapid growth of the nanowires.

More recently the use of density functional theory enabled to demonstrate the role of PVP in the shape-selective synthesis of Ag nanostructures. It was shown that at the segment level, PVP binds more strongly to Ag(100) than Ag(111) because of a surface-sensitive balance between direct binding and van der Waals attraction. This work enabled to identify differences between small-molecule and polymeric structure-directing agents and to spot several physicochemical elements that likely contribute to efforts to synthesize silver nanostructures with well defined sizes and shapes.[36]

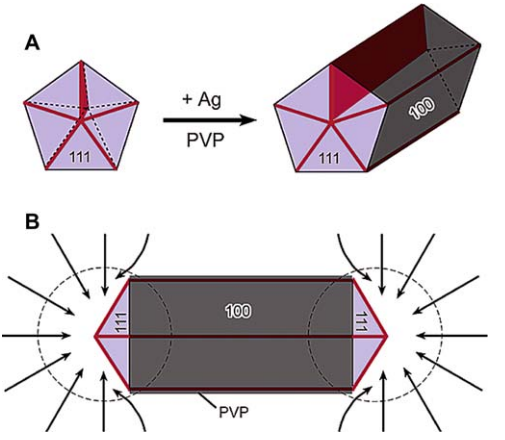

Fig. 5 Schematic illustration of the mechanism proposed to account for the growth of silver nanowires with pentagonal cross sections: (A) Evolution of a nanorod from a multiply twinned nanoparticle of silver under the confinement of five twin planes and with the assistance of PVP. (B) Schematic model illustrating the diffusion of silver atoms toward the two ends of a nanorod, with the side surfaces completely passivated by PVP. Reproduced with permission from Sun *et al.*[34]

Gold 1D nanostructures have been synthesised for many years using a seed-mediated colloidal route similar to that described in the section 2.1. Typically, cethyltrimethylammonium bromide (CTAB) directs the growth of nanowires in a multi-step process where gold ions are added sequentially.[33] The presence of silver ions has been known to produce nanorods. Further addition of copper (II) ions were found to improve the quality and uniformity of nanorods produced with this method.[37] The mechanism of action of Cu^{2+} was elucidated by monitoring the reaction by spectrophotometry. Cu^{2+} ions were proven to catalyse the etching of gold seeds by oxygen, thus forming smaller, more reactive seeds with a narrower size distribution. The subsequent nanorod growth was accelerated and kinetic control was annihilated. Furthermore, copper ions also etched the end-cap of the final nanorods from the typical dog-bone shape into the more stable round morphology. Recently however, unusual wavy gold nanowires were synthesised *via* a seedless, one-step method.[38] First, a CTAB-Au complex was formed, and Au(III) was reduced to Au(I) by the addition of ascorbic acid. The addition of NaOH then enhanced the reducing power of ascorbic acid to complete the reduction into Au(0). By imaging the contents of the reaction mixture by TEM at various time points, the authors showed that the nanowires grew by coalescence of spherical nanoparticles into rods, and of the rods into wires. Diffusion of gold atoms along the formed nanowires smoothed the surfaces, but kinks remained where rods had fused.

In the case of silver nanowires and nanorods, the colloidal route is referred to as the polyol method, due to the use of ethylene glycol (EG) both as the solvent and reducing agent, and PVP as a growth-directing stabiliser. The reaction is normally carried out at 150 °C. As mentioned above, the presence of adequate seeds is crucial in order to induce a faster silver reduction at the twin planes boundaries. The mechanism was further asserted by monitoring the formation of seeds and nanowires by UV-visible

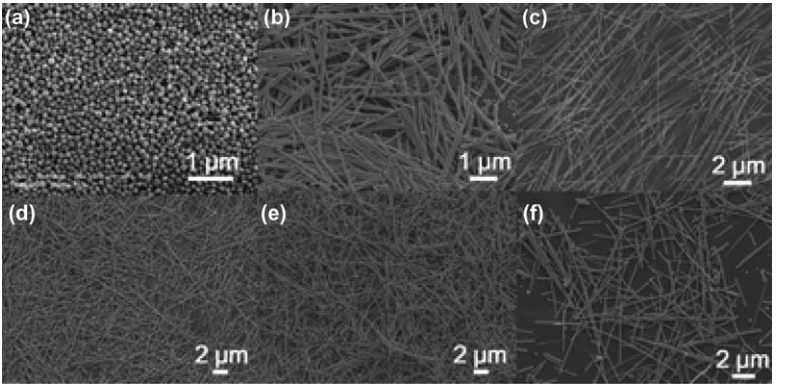

Fig. 6 SEM images of as-prepared silver nanowires with different aspect ratios under different concentrations of chloride ions, (a) without the addition of chloride ions; (b) $C_{Cl^-} = 0.1$ mM; (c) $C_{Cl^-} = 0.2$ mM; (d) $C_{Cl^-} = 0.4$ mM; (e) $C_{Cl^-} = 0.8$ mM; (f) $C_{Cl^-} = 2$ mM. $T = 160\,^{\circ}C$, $C_{AgNO_3} = 0.15$ M, $V_{EG} = 40$ ml. Reproduced with permission from Hu *et al.*[39]

absorption spectroscopy and TEM. It was thus demonstrated that fine monocrystalline silver particles were initially formed upon addition of silver nitrate to the ethylene glycol solution. In order to obtain multiply-twinned seeds, it is necessary to expose the solution to ambient light for 5 min. Ethlene glycol is weakly reducing at room temperature, but photo-induced reduction is more efficient. As the seeds grow, the twinned structure becomes more thermodynamically preferable. Not letting the seeds grow or etching them down to fine monocrystals resulted in the formation of nanocubes as previously reported.[26,30] It was also noted that technical grade ethylene glycol contains traces of chloride which catalyse the reduction.[25] The influence of chloride was confirmed by another group who added various amounts of NaCl to the reaction.[39] They observed an improvement in nanowire uniformity and aspect ratio, up to the point where the formation of AgCl solid overwhelmed the nanowire growth as seen in Fig. 6.

2.3 Photo-chemical synthesis of silver nanostructures

The strong plasmonic property of silver nanostructures and its dependence on size and shape has been exploited in the past to trigger and control the growth of nanoprisms or triangular bipyramids through dipole and quadrupole plasmon excitation.[22,40,41] Recently, Mirkin and co-workers have extended the photo-chemical method to the production of silver nanorods.[42] First, monodisperse spherical – pentagonal twinned – seed nanoparticles from an aqueous solution containing $AgNO_3$, bis(p-sulfonatophenyl)-phenylphosphine dihydrate dipotassium salt (BSPP), trisodium citrate, and sodium hydroxide irradiated with 254 nm light. This twin structure was, again, crucial in order to form nanorods rather than nanoprisms in the next step. The seeds were added to an aqueous growth solution containing $AgNO_3$ and sodium citrate which was in turn irradiated for 24 h with tuned light between 600 and 750 nm. Such excitation wavelength is very much red-shifted from the plasmon resonance of the seed particles. This means that only a small amount of light can be absorbed by the seeds and therefore the plasmon-mediated reduction of silver ions is

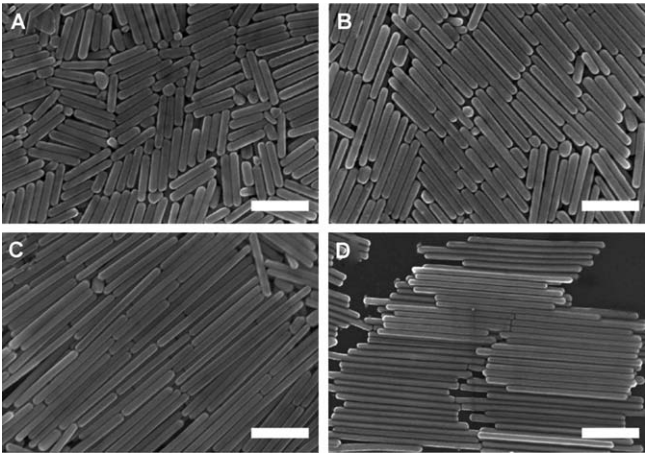

Fig. 7 SEM images of the stacks of silver nanorods (scale bars: 400 nm) generated with the bandpass filter centered at (A) 600 ± 20, (B) 650 ± 20, (C) 700 ± 20, and (D) 750 ± 20 nm. Reproduced with permission from Zhang *et al.*[42]

slow. In such kinetically-controlled conditions, reduction occurs almost exclusively at twin-plane boundaries for they are the most reactive. Consequently, initial growth from penta-twin seeds rather than plane-twin or monocrystalline is promoted, and reduction on nanorods continues at the tips rather than the sides. Increasing the wavelength from 600 to 750 nm slows the reaction further, favours growth from the tips even more, and produces nanorods with higher aspects ratios, as pictured in Fig. 7.

A similar photochemical method was used to produce decahedral silver nanoparticles with edge length around 45 nm.[43] They were synthesised by the irradiation at 460 nm of an aqueous solution of silver nitrate and trisodium citrate. The main mechanistic difference with the plasmon-mediated synthesis of nanorods is the formation of seeds *in situ*. The first step of the process is therefore a photo-assisted citrate reduction. There are initially no silver particles to excite, so the seeds are formed owing to the reducing ability of citrate enhanced by light. Once the seeds are formed, plasmon-mediated growth dominates. Monitoring of the reaction by UV-visible absorption spectroscopy and TEM suggested that decahedral particles arose from the gradual growth of individual penta-twin seeds as illustrated by Fig. 8.

2.4 Synthesis of anisotropic gold nanostructures in organic medium using galvanic replacement

Gold nanoparticles, spherical or anisotropic, have been synthesised in organic solvents using oleylamine as a capping agent for many years.[7,44] Recently however, a new galvanic platinum-assisted synthesis of nanostars and nanomultipods was reported (Fig. 9).[45] Such structures are particularly interesting because they are energetically unfavourable, therefore their synthesis required to ensure the reaction is kinetically controlled. Unlike the strategy presented in the section 2.1, where multipodal structures were obtained by decreasing the reaction rate and capping the high energy

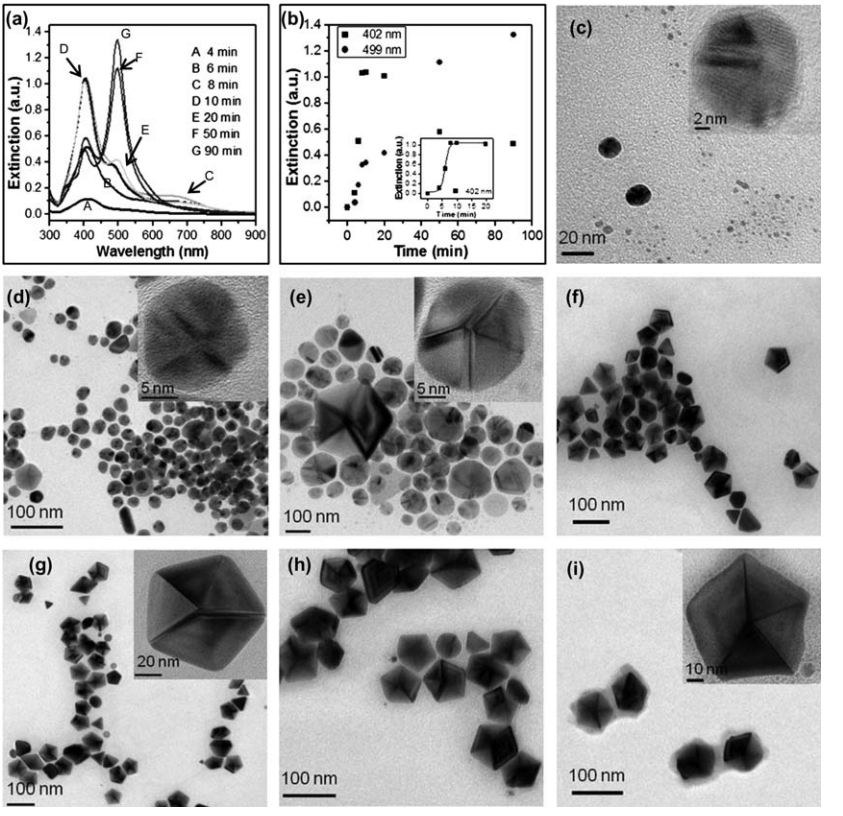

Fig. 8 Photoassisted citrate reduction of silver colloids. (a) The spectra of silver colloids synthesized at various reaction times. (b) The temporal evolution of SPR bands at 402 and 499 nm with the inserted plot showing the change of the intensity of the peak at 402 nm in the early stage. TEM images of the silver colloids synthesized at (c) 6, (d) 10, (e) 20, (f) 50, (g) 90 min, (h) 9 h, and (i) 16 h. Reproduced with permission from Yang *et al.*[43]

facets,[31] here the process is an overgrowth of twinned seeds induced by an excess of adatoms and a fast rate of reaction.[45] In these conditions, the adatoms do not have time to diffuse and adopt a thermodynamically stable position. AuCl and $Na_2PtCl_4 \cdot X\ H_2O$ were used as sources of Au(I) and Pt(II) respectively, and oleylamine was the reducing agent. Structural analysis through TEM imaging suggested that oleylamine was not responsible for the final shape. The use of Au(I) rather than Au(III) however was found crucial because of the stoichiometry of the two redox reactions below:

$$Pt_{(s)} + 2Au^{+} \rightarrow Pt^{2+} + 2Au_{(s)} \quad (1)$$

$$3Pt_{(s)} + 2Au^{3+} \rightarrow 3Pt^{2+} + 2Au_{(s)} \quad (2)$$

The postulated mechanism was as follows: Pt(II) is reduced *in situ* and is oxidised back by galvanic replacement with Au(I). This results in fast generation of Au adatoms deposited onto the seeds, and consequent overgrowth. Importantly to notice that the end product does not contain any

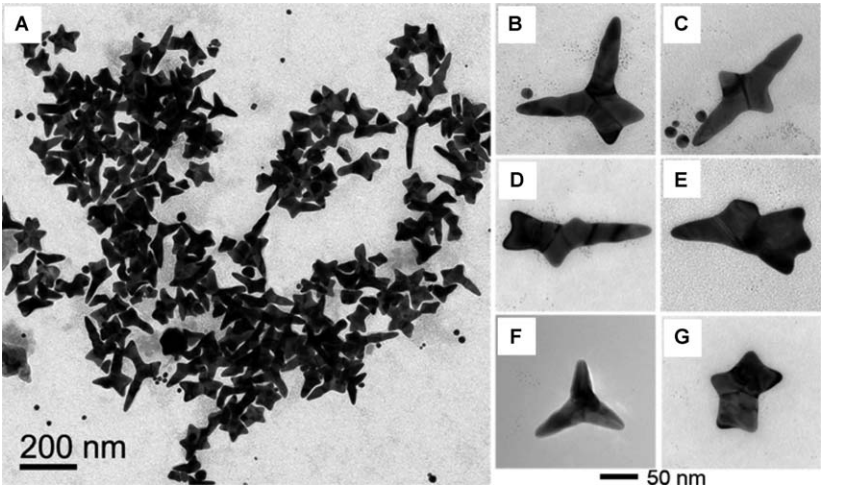

Fig. 9 TEM images of branched Au nanocrystals. (A) Low magnification TEM image highlighting the variety of branched nanocrystals achieved. (B–G) Higher magnification TEM images that reveal the internal twin structures giving rise to the various branched nanocrystals. The particles in (B) and (C) are singly twinned, (D) and (E) doubly twinned, and (F) and (G) multiply twinned. Reproduced with permission from Ortiz *et al.*[45]

platinum, as determined by EDX. When Au(III) precursor is used, the galvanic replacement reaction required three time platinum atoms. It is thus much slower and produces spherical nanoparticles.

2.5 Formation of new silver nanostructures by cluster aggregation

Silver nanostructures, especially nanoprisms, have been produced through an aqueous seed-mediated route similar to that described for gold nanostructures. They have relied on the twin nature of the seeds, and facet stabilisation with ligands, commonly citrate.[46,47] Kitaev and co-workers recently described a different route to silver nanoprisms based on the coalescence of thiol-protected silver nanoclusters upon addition of a base.[48] The anisotropic growth was due to the high reactivity of twin planes which directed coalescence laterally. This was a somewhat complicated procedure compared to the seed-mediated one.[46] Nonetheless, this provided a starting point for more complex and interesting structures, so-called nanoflowers.[49] The addition of chloride in high concentration alters the growth of nanoprisms. Chloride ions bind to silver, forming insoluble AgCl, and block further deposition of silver. Only the most reactive sites, namely those where the curvature is the highest, are still able to grow. Fig. 10 summarises the mechanism and displays SEM images of the various morphologies obtained with different chloride concentrations.[49]

Silver nanoflowers exhibit multiple facets and nanosized asperities which make them potentially excellent SERS substrates. Indeed, SERS probing with 5,5′-dithiobis(2-nitrobenzoic acid) (DTNBA) revealed enhancement factors up to 4.6×10^8. Plasma cleaning was however required in order to remove the thiol stabilisers. SERS was tested on nanoflower thin film as well as in dispersion, thus suggesting that enhancement arose from individual

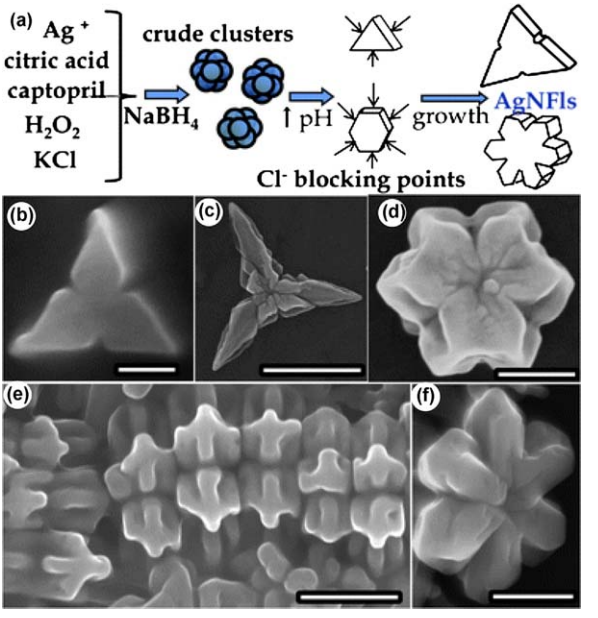

Fig. 10 (a) Schematics of AgNFl formation and representative SEM images illustrating restricted growth due to halide selective blocking in triangular, D_{3h}, (b and c) and hexagonal, D_{6h}, (d–f) AgNFl morphologies. Scale bars are (b) 100 nm; (c) 1 μm; (d–f) 300 nm. Reproduced with permission from Cathcart *et al.*[49]

particles.[49] Fig. 11 shows the enhancement factors induced by various morphologies of nanoflowers.

3 Recent advances in production and uses of gold and silver nanoparticle assemblies

Depending on their interactions, anisotropically shaped nanoparticles can serve as building blocks for self-assembled materials suitable for many applications, including solar cells, computer chips, SERS, sensing and many more.[48,50–54] Therefore there is an increased interest in development of new approaches for the preparation of metal nanoparticle assemblies. Recently Mirkin *et al*. reported that the modification of the properties of surface-confined ligands in nanoparticle systems can be achieved through the introduction of particle shape anisotropy. The researchers have demonstrated that triangular gold nanoprisms, densely functionalized with oligonucleotide ligands, hybridize to complementary particles with an affinity that is several million times higher than that of spherical nanoparticle conjugates functionalized with the same amount of DNA. These results have implications in the field of anisotropic nanoparticle assembly and can be used to govern the self-organization of nanostructures into new and complex architectures.[55] In overall building plasmonic nanostructures using DNA deserved a lot of attention because of the unique base-pairing rules and structural features of DNA that can be used to programme and precisely control the assembly of plasmonic nanostructures.[56]

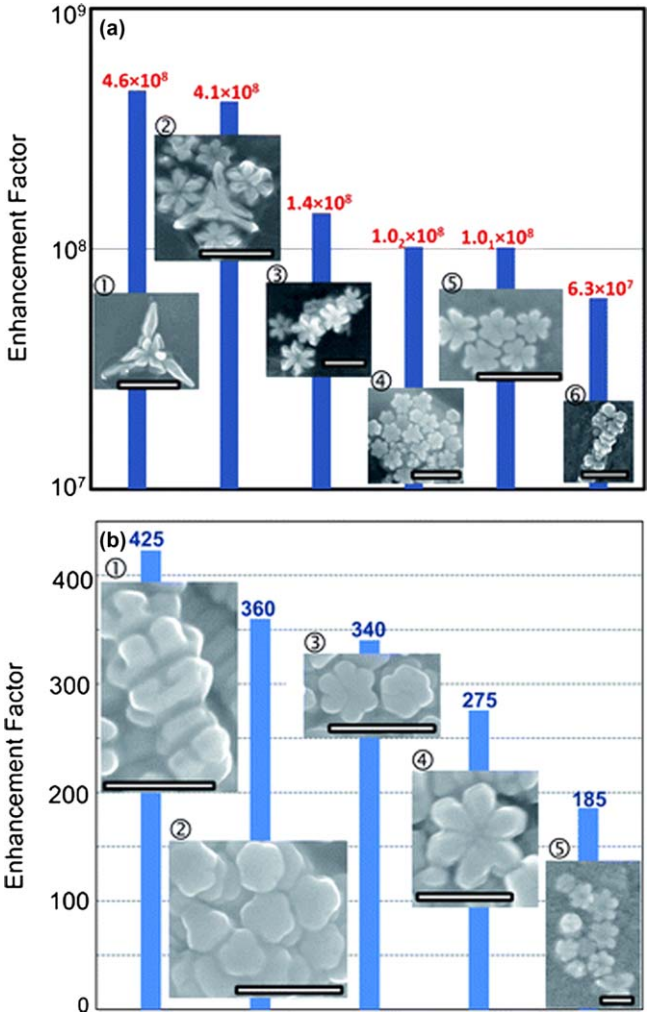

Fig. 11 Bar graphs of Raman enhancement factors measured for several AgNFl samples (corresponding SEM images are shown next to the bars) measured in (a) solid films after plasma treatment. Scale bars are 500 nm for (1), (2), (4), (5) and (6); and 250 nm for (3); (b) aqueous phase of AgNFl dispersions after plasma treatment and re-dispersion. Scale bars are 200 nm for (1) and (5) 1 and 250 nm for (2), (3), and (4). The largest enhancement factor of 4.6×10^8 in (a) corresponds to measured intensities of 6500 ± 150 counts for DTNBA coverage of 3.2×10^{-14} mol cm^{-2} (200 mW laser power and 10 s measurement time). The largest enhancement factor of 425 in (b) corresponds to measured intensities of 280 ± 10 counts for DTNBA concentration in solution of 0.5 mM (200 mW laser power and 10 s measurement time). Reproduced with permission from Cathcart *et al.*[49]

In this section we will focus only on some recent developments of gold and silver nanoparticle assemblies for SERC and creation of chiral nanostructures.

3.1 Plasmonic nanoarrays for SERS

Some applications of metal nanoparticles, especially Surface Enhanced Raman Spectroscopy (SERS) require the particles to be assembled. SERS arises from the presence of metal nanoparticles on the substrate. Surface

Plasmon Resonance (SPR) causes a large enhancement of the electromagnetic field in the vicinity of the surface and strongly enhances the vibrational modes. A charge-transfer complex may also be formed between the surface and the analyte molecule, with electronic transitions in the visible range. It should be noted that SERS effect does not occur on smooth surfaces, but only on rough, nanoparticulate ones. One major difficulty in producing SERS substrates is to reproducibly create electromagnetic hot spots with the same geometry in order to ensure a constant enhancement factor. Highly organised packing of nanoparticles thus appears to be very attractive for this application.

Nanorods have been shown to be very useful for SERS as they act like nanoantennae.[57] The tip-to-tip coupling of nanorod dimers concentrates the near-field and induces a very high enhancement factor. Liz-Marzan and co-workers demonstrated that self-assembled 3D supercrystals of highly organised gold nanorods exhibited the antenna effect and made possible the sensitive detection of prions from complex biological media.[58] Their nanorods spontaneously crystallised when the aqueous solution was slowly dried in air, due to the capillary attraction forces between them. They formed islands of 1 μm diameter and 15 vertically standing nanorod layers high. The distance between two neighbour nanorods was around 3 nm, due to the CTAB ligands, an optimal distance for hot spot generation. As illustrated by Fig. 12, the nanorod supercrystal islands exhibited homogeneous field enhancement and better enhancement factor than other arrangements of nanorods such as fractal aggregates. Their SERS applicability was tested with the quantitative detection of benzenethiol (BT).

In order to gain more control over the vertical self-assembly of nanorods, another group performed the crystallisation on a nanopatterned substrate composed of hydrophobic silica and islands of hydrophilic gold.[53] The substrate was dipped into a nanorod solution which was left to evaporate slowly, as shown in Fig. 13. The solution concentration could be varied to adjust the degree of packing, and a temperature above 45 °C ensured that the rods were confined to the energetically more favoured gold surfaces. SEM and small-angle X-ray scattering (SAXS) analyses determined that the nanorods assembles in hcp ordering, provided the concentration was high enough. The as-produced SERS substrates demonstrated excellent signal enhancement.

Another geometry that has been recently explored is concentric rings, where the antenna effect was also found to occur. Initially such patterns were fabricated by electron beam lithography (EBL).[59] Gold cylinders were patterned into a circular concentric arrangement to combine dimer coupling with the concentric plasmonic effect. The method was however limited by the interparticle distance maintained at 25 nm. For optimal hot-spot field enhancement, the spacing should be below 10 nm. This issue was circumvented by using a bottom-up fabrication approach, based on the observation that anodized aluminium oxide (AAO) templates exhibited large areas of round-shaped cavities. Spin-coating of polystyrene-block-polymethylmethacrylate (PS-*b*-PMMA) onto the pore created lamellar domains of alternating PS and PMMA. Silver was finally deposited by thermal evaporation, selectively on PS rather than PMMA, thus forming

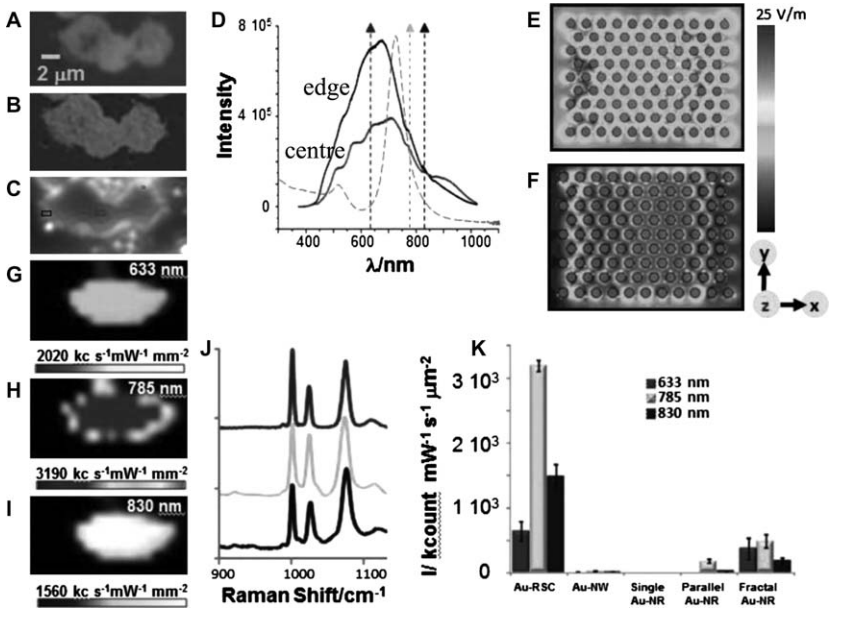

Fig. 12 Optical properties of the nanorod supercrystals. (A–C) Optical, SEM, and dark-field images of an NR supercrystal, respectively, after plasma-etching removal of surfactant coating of the NRs. (D) Localized surface plasmon resonance bands of the rods in solution (gray) and within a supercrystal, either at the center or at the edges. Dotted arrows indicate the excitation laser lines used for SERS. (E and F) Electric field enhancement maps calculated for the top part of a three layer rod-stacked supercrystal (E) and for the same location in a single monolayer (F). (G–J) SERS intensity maps at 1,072 cm^{-1} (BT ring breathing) corresponding to the supercrystal in A, for BT as excited with a 633 (G), 785 (H), and 830 nm (I) laser lines, representative SERS spectra for each laser being presented in J. (K) Comparison of the SERS intensities at 1,072 cm^{-1} provided by a gold rod supercrystal (Au-RSC) film with common SERS substrates, including aggregated ultralong nanowires (Au-NW), single rods, parallel and fractally aggregated gold NRs (Single Au-NR, Parallel Au-NR, and Fractal Au-NR, respectively). The intensity is the result of averaging over 50 different randomly distributed spots in the supercrystal and those corresponding to maximum intensity for the rest of substrates. Reproduced with permission from Alvarez-Puebla *et al.*[58]

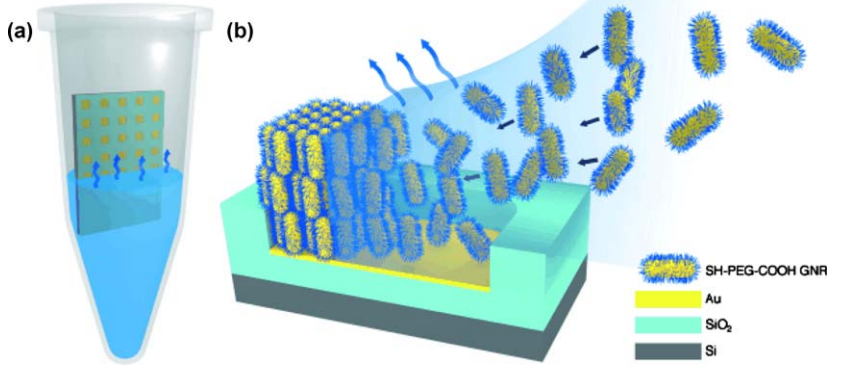

Fig. 13 a) Illustration of the experimental setup. The micropatterned substrate is placed in the center of an Eppendorf tube and immersed in a concentrated colloidal solution of GNRs. The substrate is left to dry under isothermal conditions. b) Schematic representation of the formation of standing arrays of GNRs on a template upon solvent evaporation. Reproduced with permission from Thai *et al.*[53]

concentric silver rings made up of individual silver nanoparticles of about 10 nm in diameter.[60] The ring spacing could be tuned by varying the molecular weight of PS-*b*-PMMA, which resulted in an order of magnitude improvement of the enhancement factor when the gap decreased from 25 to 12 nm as shown in Fig. 14.

3.2 Chiral assemblies of plasmonic nanostructures

Growing attention has been given to forming chiral assemblies of nanoparticles for potential sensing applications, such as plasmonic rulers.[2,61,62] Plasmonic hot spots have been theoretically expected to strongly enhance circular dichroism (CD) of chiral molecules in their vicinity,[63] and that of nanoparticle chiral assemblies.[64] It was recently shown experimentally that enhancement of CD from peptides or DNA fragments by gold nanoparticles was directly dependent on the aggregation of said nanoparticles, and therefore on the generation of plasmonic hot-spots.[65,66]

Another latest interesting experimental realization of a chiral system with a strong plasmon-related optical activity was reported by Qi and colleagues (Fig. 15).[67] The authors employed nematic porous silica films with embedded silver NPs and observed characteristic plasmonic structures in the

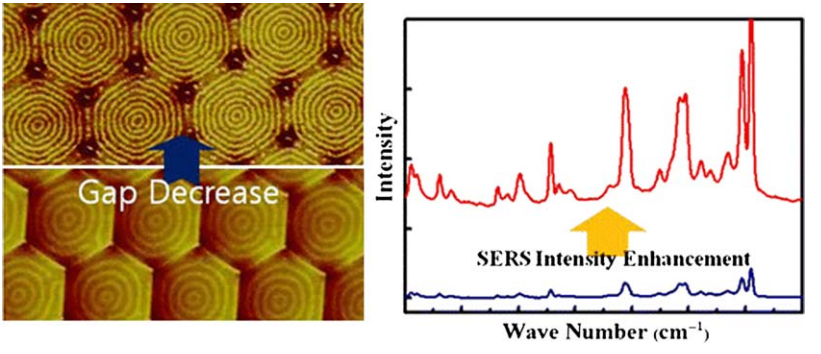

Fig. 14 AFM images of arrays of concentric gold nanorings with two different ring gap, and the corresponding SERS spectra showing significant enhancement. Reproduced with permission from Bae *et al.*[60]

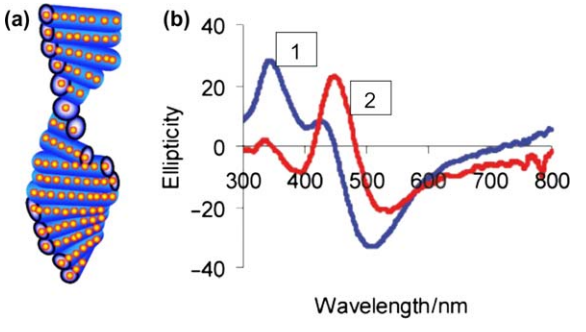

Fig. 15 a) A model of nematic porous silica films with embedded interacting Ag NPs. b) CD spectra taken from this system before (blue online) and after (red online) soaking with water. Reproduced with permission from Qi *et al.*[67]

visible spectral range (Fig. 15).[67] The CD spectra in this study exhibited positive and negative bands that are quite typical of the CD mechanism based on the plasmon-plasmon Coulomb interaction between metal NPs.[64] One can see similar bisignate structures in calculated CD spectra of NP complexes of various geometries, including the related helical geometry.

Following similar approaches, two papers[62,68] reported Au-nanorod assemblies demonstrating plasmonic CD responses with the characteristic bisignate shapes. According to the interpretation,[62,68] these CD responses come from the plasmon-plasmon interaction between nanorods. The first report[62] concerns a nanorod structure assembled with twisted fibers, whereas the second paper[68] utilizes soft bio-molecules for a templated assembly. In contrast to spherical-NP assemblies, nanorod complexes have an additional type of disorder, a namely an orientational disorder. In experimental realizations, the control of orientations of nanorods in an assembly can be an extra challenge. The second paper[68] also demonstrated an interesting effect of flipping of the plasmonic CD pattern using a chemical method. According to the interpretation of Wang and co-workers,[68] the controlling molecules added to the solution create changes in the geometry of the assembly and, in particular, these molecules can cause a change in the pitch of the helical nanorod assembly. This variation of a pitch may result in a flipping of the plasmonic CD spectrum. This flipping effect was supported qualitatively by the theoretical modelling.[69] In the theoretical calculations for the helical plasmonic complexes, one can see the effect of inversion of a CD spectrum when a helical complex becomes stretched or compressed.[69] The observed sensitivity of the plasmonic CD spectrum to the geometry of a complex assembled with the help of a biomolecular template suggests interesting possibilities in bio-sensing applications.

Unique helical assemblies of spherical nanoparticles were also generated by an elegant DNA origami approach.[70] DNA origami 24-helix bundles were decorated with helically arranged attachment sites for 10 nm gold nanoparticles as presented in Fig. 16.

The gold nanoparticle helices exhibited strong CD with the bisignate shape characteristic of helical structures. The role of plasmons in the phenomenon was again emphasised when the authors grew shells of gold, silver, or gold-silver alloy around the initial gold nanoparticles, while the overall helix remained the same. As the particles became larger, CD intensity increased and shifted to longer wavelength, as does the absorption spectrum. The addition of silver had the double effect of increasing the CD intensity and shifting it to the blue. This is relatable to the plasmon resonance of silver being stronger than that of gold, and blue-shifted. These results are presented in Fig. 17. This research demonstrates that it is possible to finely tune the optical activity of a metal nanoparticle assembly.

In other experiments, phosphorothioate-modified oligonucleotides were immobilized on gold nanoparticles and gold nanorings which then exhibited a plasmon-induced CD in the 500–700 nm region (Fig. 18).[65] However, the strong CD response was only observed when the conjugated particles were partially aggregated. The reversibility of the phenomenon upon de-aggregation and aggregation suggested that the density of plasmonic particles around the chiral species and possibly the distance between them

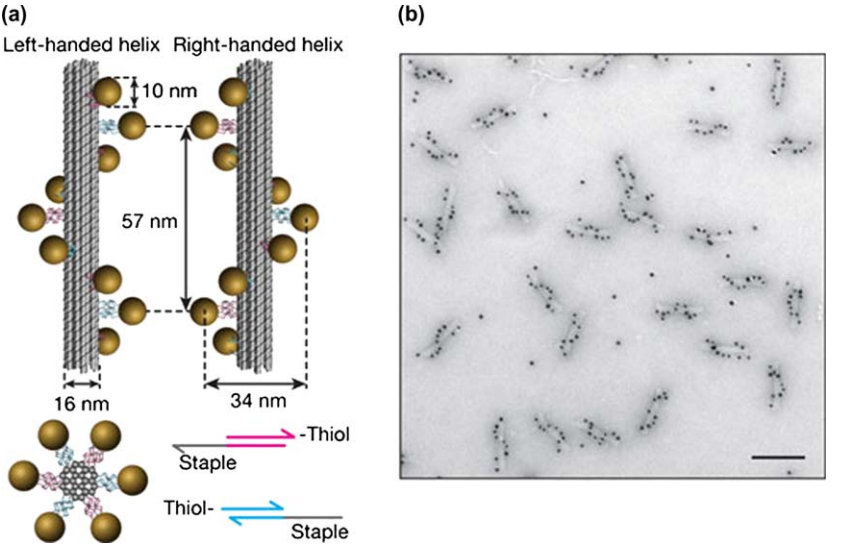

Fig. 16 Assembly of DNA origami gold nanoparticle helices. a, Left- and right-handed nanohelices (diameter 34 nm, helical pitch 57 nm) are formed by nine gold nanoparticles each of diameter 10 nm that are attached to the surface of DNA origami 24-helix bundles (each of diameter 16 nm). Each attachment site consists of three 15-nucleotide-long single-stranded extensions of staple oligonucleotides. Gold nanoparticles carry multiple thiol-modified DNA strands, which are complementary to these staple extensions. Nanoparticles and 24-helix bundles are mixed for assembly and the resulting constructs are gel-purified. b, TEM image of assembled left-handed gold nanohelices (scale bar, 100 nm). Analysis of the TEM data yields a 98% success rate for directed attachment of nanoparticles. Reproduced with permission from Kuzyk *et al.*[70]

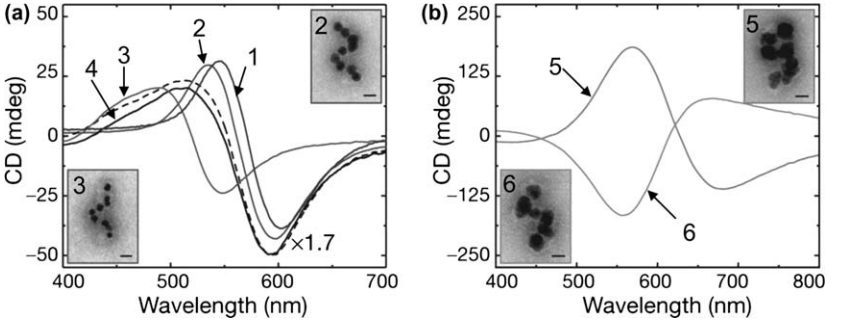

Fig. 17 a) A pronounced blueshift of the peak position in the CD response was achieved by depositing several nanometres of silver on gold nanoparticles of diameter 10 nm. Growth of silver + gold alloy shells gives rise to an intermediate blueshift (spectrum 2 of left-handed gold-core/silver + gold-shell helices). Mixing of solutions that contain nanohelices of various metal compositions results in a superposition of individual CD responses (spectrum 4): a 2 : 3 mixture of gold-core/silver-shell (spectrum 3) and gold-core/silver + gold-shell (spectrum 2) exhibits CD close to the predicted superposition (dashed black line; black curves were rescaled by a factor of 1.7 for presentation purposes). b) Excessive metal deposition leads to the merging of nanoparticles and further enhancement of the CD signal for the left-handed (spectrum 5) and right-handed (spectrum 6) gold-core/silver-shell helices. The corresponding molar CD in the visible spectrum is huge with a strength of about 108 M^{-1} cm^{-1}. The CD spectra were recorded at concentrations of nanohelices of 0.4 nM in a and 40pM in b. The insets in a and b show TEM images of left-handed (frames 2, 3 and 5) and right-handed (frame 6) nanohelices (scale bars, 20 nm). Reproduced with permission from Kuzyk *et al.*[70]

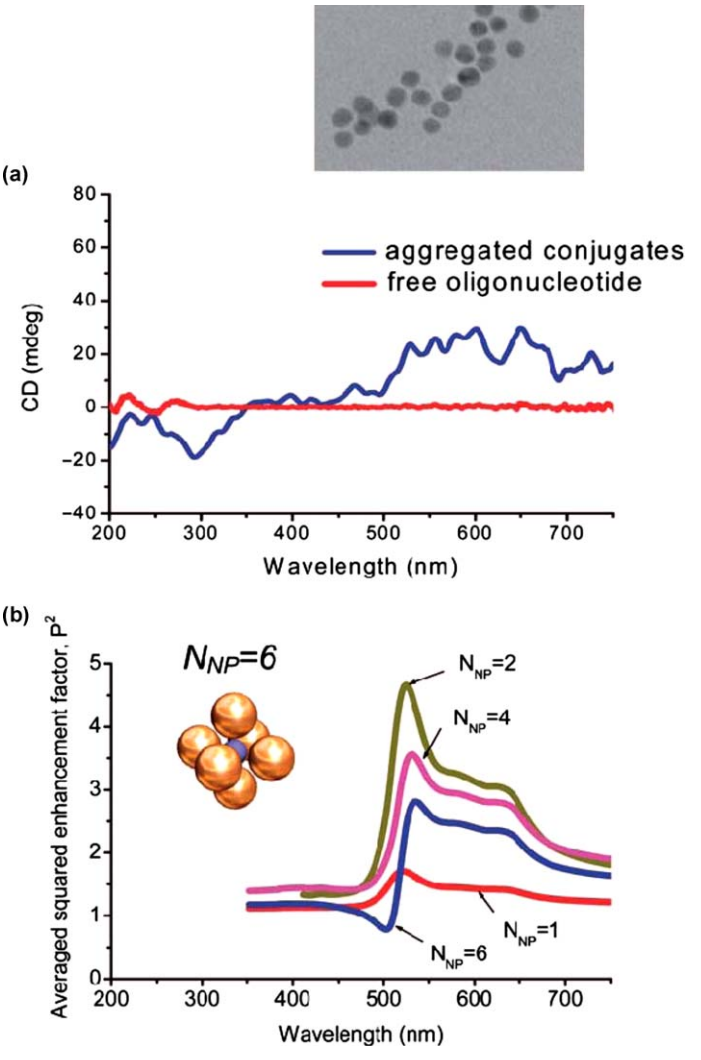

Fig. 18 a) CD spectra measured by Gerard and co-workers for oligonucleotides alone and for aggregates of 10 nm Au NPs conjugated with oligonucleotides. Inset: TEM image of oligonucleotide-conjugated gold nanoparticles. b) Calculated averaged plasmonic enhancement factors for the plasmonic hot spot in the center of an assembly of Au nanoparticles. Inset: Geometry of one particular complex with NNP the plasmonic hot spot is located in the center of the system indicated as a blue sphere.[71] Reproduced with permission from Govorov *et al.*[71]

were key elements in the generation of plasmon-induced CD. This observation is consistent with the Coulomb hot-spot mechanism since plasmonic hot spots will appear in both gold nanoparticles and nanorings systems.

Importantly, this mechanism creates CD lines in a wavelength region where an attached chiral molecule has not its own absorption.

4 Concluding remarks

The field of plasmonic nanostructures has been extensively researched for many years. Surface plasmon resonance has proved to be a unique asset of

these materials. It is the basis for many applications, as well as a characterisation tool and in some cases it also plays a role in syntheses themselves.

This review highlighted the general trends in gold and silver nanostructures of controlled shape and anisotropy that have emerged recently. Synthetic routes have been found for a very wide variety of particle morphologies. Efforts are now focused on elucidating the mechanisms involved in the nanostructure formation and growth processes. This knowledge should provide more control over the processes as well as insight into understanding of fundamental physico-chemical phenomena.

Recent discoveries of shape related effects on metal nanocrystal binding forces and DNA based assesmbling techniques also open up new horizons for constructing novel useful architectures from nanoparticle building blocks.[50,55,56,70]

The other point of interest is the fabrication of tailor-made nanostructures for specific applications. SERS is presented as an example for it benefits immensely from optimisation of plasmon resonance through shape-control.

Finally, over last years there were significant advances in the development of novel chiral plasmonic nanostructures. We believe that these new chiral nanomaterials could find a range of potential applications in new plasmonic devices and chiral sensing.

References

1 H. Zhong, X. Lei, X. Hun and S. S. Zhang, *Chem. Comm.*, 2009, 6958–6960.
2 Y.-w. Jun, S. Sheikholeslami, D. R. Hostetter, C. Tajon, C. S. Craik and A. P. Alivisatos, *Proceedings of the National Academy of Sciences*, 2009, **106**, 17735–17740.
3 J. J. Storhoff, R. Elghanian, C. A. Mirkin, R. C. Mucic and R. L. Letsinger, *J. Am. Chem. Soc.*, 1998, **120**, 1959–1964.
4 N. Liu, M. L. Tang, M. Hentschel, H. Giessen and A. P. Alivisatos, *Nature Materials*, 2011, **10**, 631–636.
5 N. Verellen, P. Van Dorpe, C. J. Huang, K. Lodewijks, G. A. E. Vandenbosch, L. Lagae and V. V. Moshchalkov, *Nano Letters*, 2011, **11**, 391–397.
6 M. Zahmakiran and S. Ozkar, *Nanoscale*, 2011, **3**, 3462–3481.
7 M. B. Mohamed, K. M. AbouZeid, V. Abdelsayed, A. A. Aljarash and M. S. El-Shall, *ACS Nano*, 2010, **4**, 2766–2772.
8 Z. Jurasekova, C. Domingo, J. V. Garcia-Ramos and S. Sanchez-Cortes, *Journal of Raman Spectroscopy*, 2012, **43**, 1913–1919.
9 E. Gross, J. H. C. Liu, F. D. Toste and G. A. Somorjai, *Nature Chemistry*, 2012, **4**, 947–952.
10 P. Ghosh, G. Han, M. De, C. K. Kim and V. M. Rotello, *Advanced Drug Delivery Reviews*, 2008, **60**, 1307–1315.
11 J. H. Park, G. von Maltzahn, L. L. Ong, A. Centrone, T. A. Hatton, E. Ruoslahti, S. N. Bhatia and M. J. Sailor, *Advanced materials (Deerfield Beach, Fla.)*, 2010, **22**, 880–885.
12 S. Linic, P. Christopher and D. B. Ingram, *Nature Materials*, 2011, **10**, 911–921.
13 F. McKenzie and D. Graham, *Chem. Comm.*, 2009, 5757–5759.
14 A. Moores and F. Goettmann, *New Journal of Chemistry*, 2006, **30**, 1121–1132.
15 S. E. J. Bell and N. M. S. Sirimuthu, *Chem. Soc. Rev.*, 2008, **37**, 1012–1024.
16 R. Boyack and E. C. Le Ru, *Phys. Chem. Chem. Phy.*, 2009, **11**, 7398–7405.

17 Z. Wang, S. Zong, W. Li, C. Wang, S. Xu, H. Chen and Y. Cui, *J. Am. Chem. Soc.*, 2012, **134**, 2993–3000.
18 L. A. Austin, B. Kang, C.-W. Yen and M. A. El-Sayed, *J. Am. Chem. Soc.*, 2011, **133**, 17594–17597.
19 H. Cang, A. Labno, C. Lu, X. Yin, M. Liu, C. Gladden, Y. Liu and X. Zhang, *Nature*, 2011, **469**, 385–+.
20 R. de la Rica and M. M. Stevens, *Nature Nanotechnology*, 2012, **7**, 821–824.
21 M. L. Personick, M. R. Langille, J. Zhang, N. Harris, G. C. Schatz and C. A. Mirkin, *J. Am. Chem. Soc.*, 2011, **133**, 6170–6173.
22 J. Zhang, S. Li, J. Wu, G. C. Schatz and C. A. Mirkin, *Angewandte Chemie International Edition*, 2009, **48**, 7787–7791.
23 J. Zhang, M. R. Langille, M. L. Personick, K. Zhang, S. Li and C. A. Mirkin, *J. Am. Chem. Soc.*, 2010, **132**, 14012–14014.
24 S. Mazzucco, N. Geuquet, J. Ye, O. Stephan, W. Van Roy, P. Van Dorpe, L. Henrard and M. Kociak, *Nano Letters*, 2012, **12**, 1288–1294.
25 S. Chang, K. Chen, Q. Hua, Y. Ma and W. Huang, *J. Phys. Chem. C*, 2011, **115**, 7979–7986.
26 S. H. Im, Y. T. Lee, B. Wiley and Y. Xia, *Angewandte Chemie International Edition*, 2005, **44**, 2154–2157.
27 T. Ming, W. Feng, Q. Tang, F. Wang, L. Sun, J. Wang and C. Yan, *J. Am. Chem. Soc.*, 2009, **131**, 16350–16351.
28 M. L. Personick, M. R. Langille, J. Zhang and C. A. Mirkin, *Nano Lett*, 2011, **11**, 3394–3398.
29 M. R. Langille, M. L. Personick, J. Zhang and C. A. Mirkin, *J. Am. Chem. Soc.*, 2012, **134**, 14542–14554.
30 Y. Sun and Y. Xia, *Science*, 2002, **298**, 2176–2179.
31 B. R. Danger, D. Fan, J. P. Vivek and I. J. Burgess, *ACS Nano*, 2012, **6**, 11018–11026.
32 J. Choi, G. Sauer, K. Nielsch, R. B. Wehrspohn and U. Gösele, *Chemistry of Materials*, 2003, **15**, 776–779.
33 C. J. Murphy, A. M. Gole, S. E. Hunyadi and C. J. Orendorff, *Inorganic Chemistry*, 2006, **45**, 7544–7554.
34 Y. Sun, B. Mayers, T. Herricks and Y. Xia, *Nano Letters*, 2003, **3**, 955–960.
35 C. J. Johnson, E. Dujardin, S. A. Davis, C. J. Murphy and S. Mann, *J. Mat. Chem.*, 2002, **12**, 1765–1770.
36 W. A. Al-Saidi, H. J. Feng and K. A. Fichthorn, *Nano Letters*, 2012, **12**, 997–1001.
37 T. Wen, Z. Hu, W. Liu, H. Zhang, S. Hou, X. Hu and X. Wu, *Langmuir*, 2012, **28**, 17517–17523.
38 C. Zhu, H.-C. Peng, J. Zeng, J. Liu, Z. Gu and Y. Xia, *J. Am. Chem. Soc.*, 2012, **134**, 20234–20237.
39 M. Hu, J. Gao, Y. Dong, S. Yang and R. K. Y. Li, *RSC Advances*, 2012, **2**, 2055–2060.
40 R. C. Jin, Y. W. Cao, C. A. Mirkin, K. L. Kelly, G. C. Schatz and J. G. Zheng, *Science*, 2001, **294**, 1901–1903.
41 R. Jin, Y. Charles Cao, E. Hao, G. S. Metraux, G. C. Schatz and C. A. Mirkin, *Nature*, 2003, **425**, 487–490.
42 J. Zhang, M. R. Langille and C. A. Mirkin, *Nano Letters*, 2011, **11**, 2495–2498.
43 L.-C. Yang, Y.-S. Lai, C.-M. Tsai, Y.-T. Kong, C.-I. Lee and C.-L. Huang, *J. Phys. Chem. C*, 2012, **116**, 24292–24300.
44 H. Hiramatsu and F. E. Osterloh, *Chemistry of Materials*, 2004, **16**, 2509–2511.
45 N. Ortiz and S. E. Skrabalak, *Crystal Growth & Design*, 2011, **11**, 3545–3550.

46 D. Aherne, D. M. Ledwith, M. Gara and J. M. Kelly, *Advanced Functional Materials*, 2008, **18**, 2005–2016.
47 G. S. Métraux and C. A. Mirkin, *Advanced Materials (Deerfield Beach, Fla.)*, 2005, **17**, 412–415.
48 N. Cathcart and V. Kitaev, *ACS Nano*, 2011, **5**, 7411–7425.
49 N. Cathcart and V. Kitaev, *Nanoscale*, 2012, **4**, 6981–6989.
50 S. C. Glotzer, *Nature*, 2012, **481**, 450–452.
51 O. Rabin, *Nature Nanotechnology*, 2012, **7**, 419–420.
52 B. Gao, G. Arya and A. R. Tao, *Nature Nanotechnology*, 2012, **7**, 433–437.
53 T. Thai, Y. Zheng, S. H. Ng, S. Mudie, M. Altissimo and U. Bach, *Angewandte Chemie International Edition*, 2012, **51**, 8732–8735.
54 O. Benson, *Nature*, 2011, **480**, 193–199.
55 M. R. Jones, R. J. Macfarlane, A. E. Prigodich, P. C. Patel and C. A. Mirkin, *J. Am. Chem. Soc.*, 2011, **133**, 18865–18869.
56 S. J. Tan, M. J. Campolongo, D. Luo and W. Cheng, *Nature Nanotechnology*, 2011, **6**, 268–276.
57 J. Aizpurua, G. W. Bryant, L. J. Richter, F. J. García de Abajo, B. K. Kelley and T. Mallouk, *Physical Review B*, 2005, **71**, 235420.
58 R. A. Alvarez-Puebla, A. Agarwal, P. Manna, B. P. Khanal, P. Aldeanueva-Potel, E. Carbó-Argibay, N. Pazos-Pérez, L. Vigderman, E. R. Zubarev, N. A. Kotov and L. M. Liz-Marzán, *Proceedings of the National Academy of Sciences*, 2011, **108**, 8157–8161.
59 A. J. Pasquale, B. M. Reinhard and L. Dal Negro, *ACS Nano*, 2012, **6**, 4341–4348.
60 D. Bae, W. J. Cho, G. Jeon, J. Byun and J. K. Kim, *J. Phys. Chem. C*, 2012, **116**, 26523–26528.
61 A. J. Mastroianni, S. A. Claridge and A. P. Alivisatos, *J. Am. Chem. Soc.*, 2009, **131**, 8455–8459.
62 A. Guerrero-Martínez, B. Auguié, J. L. Alonso-Gómez, Z. Džolić, S. Gómez-Graña, M. Žinić, M. M. Cid and L. M. Liz-Marzán, *Angewandte Chemie*, 2011, **123**, 5613–5617.
63 A. O. Govorov, Z. Fan, P. Hernandez, J. M. Slocik and R. R. Naik, *Nano Letters*, 2010, **10**, 1374–1382.
64 Z. Fan and A. O. Govorov, *Nano Letters*, 2010, **10**, 2580–2587.
65 V. A. Gerard, Y. K. Gun'ko, E. Defrancq and A. O. Govorov, *Chem. Comm.*, 2011, **47**, 7383–7385.
66 J. M. Slocik, A. O. Govorov and R. R. Naik, *Nano Letters*, 2011, **11**, 701–705.
67 H. Qi, K. E. Shopsowitz, W. Y. Hamad and M. J. MacLachlan, *J. Am. Chem. Soc.*, 2011, **133**, 3728–3731.
68 R.-Y. Wang, H. Wang, X. Wu, Y. Ji, P. Wang, Y. Qu and T.-S. Chung, *Soft Matter*, 2011.
69 Z. Fan and A. O. Govorov, *J. Phys. Chem. C*, 2011, **115**, 13254–13261.
70 A. Kuzyk, R. Schreiber, Z. Fan, G. Pardatscher, E.-M. Roller, A. Hogele, F. C. Simmel, A. O. Govorov and T. Liedl, *Nature*, 2012, **483**, 311–314.
71 A. O. Govorov, Y. K. Gun'ko, J. M. Slocik, V. A. Gerard, Z. Y. Fan and R. R. Naik, *J. Mat. Chem.*, 2011, **21**, 16806–16818.

Nanomaterials for solar energy

Neerish Revaprasadu,[a] Osman M. Bakr,[b] Karthik Ramasamy[c] and Mohammad Azad Malik*[d]

DOI: 10.1039/9781849737623-00023

Nanostructured metal chalcogenides of the elements copper, iron, tin, lead and cadmium have attracted interest in their use as colloidal nanocrystal inks for solar cells. Some of these materials have the advantages of being available in abundance and having low toxicity. Developing methods for the combination of the elements to produce binary, ternary and quaternary compounds has dominated research in the field. This chapter will provide the most recent developments (from year 2012 onwards) for the synthesis and use of colloidal nanocrystal inks for solar cell applications.

1 Introduction

There has been a concerted effort by scientific community and society at large to find affordable, efficient, low-carbon and sustainable energy solutions that will make a larger contribution to the current energy basket. Solar energy is the largest potential source of renewable energy, however, this technology only meets *ca*. 0.1% of the world's energy demand. Silicon based technology dominates the photovoltaics market. The so called 1st generation solar cells based on crystalline and polycrystalline silicon are firmly established due in part to a mature silicon industry and relatively high conversion efficiencies. However, the high cost of silicon solar cells, due to the requirement of near perfect single crystal substrates has led to emergence of 2nd generation thin film solar cells based on II-VI semiconductors, copper indium gallium selenide (CIGS) and CdTe. The toxic nature of cadmium, relative scarcity of indium and gallium has driven researchers to find alternative materials which have band gap tuneability across the solar spectrum and comparable conversion efficiencies. These materials are being employed in 3rd generation solar cells such as organic photovoltaics, quantum dot/dye sensitized solar cells and organic-inorganic hybrid solar cells. The control of dimensionality and morphology has emerged as an important parameter that will enhance the functional behaviour of these materials.

Metal chalcogenide semiconductor nanocrystals have been identified as an important class of materials for nonlinear optical devices and photovoltaic solar cells. Compared with the traditional physical deposition

[a]*Department of Chemistry, University of Zululand, Private Bag X 1001, Kwa-Dlangezwa, 3886, South Africa. E-mail: RevaprasaduN@unizulu.ac.za*
[b]*Division of Physical Sciences and Engineering, Solar and Photovoltaics Engineering Center, King Abdullah University of Science and Technology (KAUST), Thuwal 23955-6900, Saudi Arabia. E-mail: osman.bakr@kaust.edu.sa*
[c]*Center for Materials for Information Technology, The University of Alabama, Tuscaloosa, Alabama, 35487, USA. E-mail: kramasamy@mint.ua.edu*
[d]*School of Chemistry, The University of Manchester, Oxford Road, Manchester, M13 9PL(UK). *E-mail: azad.malik@manchester.ac.uk*

techniques, the application of suitable inorganic colloidal nanocrystal inks to produce high efficiency solar cells and the lower fabrication cost makes the solution route more attractive. Recent advances include the development of materials in unique combinations and compositions that promise to deliver high efficiencies at lower costs. An example is kesterite based $Cu_2ZnSn(S,Se)_4$ (CZTSSE) thin film solar cells in which indium and gallium are replaced by readily available copper and zinc.[1] This chapter covers the most recent advances in the synthesis of nanocrystals that have potential in solar cell applications.

2 Ternary and quaternary materials

Ternary and quaternary metal chalcogenide nanoparticles (NPs) have great importance for environmental friendly, low-cost, and higher efficiency solar cells. $CuIn_xGa_{1-x}Sy Se_{1-y}$ (CIGSSe) is one of the most efficient and stable thin-film semiconductors for use in photovoltaic applications known today. However, the limited availabilities of indium and gallium from the minerals hinder its sustainability and large scale production of CIGSSe thin film solar cells. Nanocrystals of Cu_2ZnSnS_4 (CZTS) and Cu_2FeSnS_4 (CFTS) appear to be promising for use as efficient thin film solar cells for enhancing light absorption and lower cost solar cells due to their earth abundance, high light absorption coefficiency and band gap tunability by varying the compositions.

2.1 Copper indium-gallium sulfide/selenides (CIGS/CIGSe)

The research on chalcopyrite based solar cells have has been focused on the development of low-cost processes for the preparation of Cu $(InGa)Se_2$ (CIGS) films. They have been particularly fascinating due to their high conversion efficiency, reliability, high absorption coefficient ($>10^5\,cm^{-1}$), direct band gap and stability against photo-degradation. CIGS has gained a reputation as the thin film solar cell technology with the highest efficiencies (20.3%). CIGS thin films have been deposited using various techniques including co-evaporation, sputtering, pyrolysis, electro deposition, rapid thermal process, and selenization of sequentially stacked precursors. Despite the high efficiency of state-of the-art CIGS solar cells, the high production cost of conventional vacuum-based processes, *i.e.,* a multi-stage co-evaporation and a two-step process of sputtering and selenization is considered to be a main obstacle to the widespread use of CIGS thin films solar cells. Furthermore, the vacuum based technologies are difficult to scale up the solar cells. Hence, research is currently focused on the development of scalable low cost, non-vacuum based techniques. In this regard, many efforts have been made to develop alternative deposition techniques for thin film CIGS solar cells using non-vacuum coating processes. based on their inherent advantages such as the use of less expensive vacuum equipment, less energy intensive deposition and much better material utilization. Electro-deposition is one of the promising non-vacuum techniques for the fabrication of chalcopyrite CIGS thin films. In contrast, nanoparticles can be used as a nanoparticle ink that is coated on a substrate to yield a low-cost solar cell. These inks can be applied by fast high throughput, non-vacuum and continuous roll to roll coating or printing methods.

Mousavi *et al.*[2] improved the synthesis of Cu(In,Ga)Se_2 (CIGS) nanoparticles by a wet chemical method originally carried out by Chun *et al.*[3] by increasing the reaction temperature to increase the solubility of the source materials. This method does not involve vacuum or a separate selenization process. The experiments were carried out under different conditions to investigate the effects of temperature, source materials, and growth conditions on the phase and particle size of the material. In a typical experiment 2 mmol of the copper, 1 mmol of indium, 1 mmol of gallium source materials, and 4 mmol of selenium powder in ethylenediamine were loaded in a Teflon container. The mixture was vigorously stirred for 12 h and then put in a stainless steel pressure vessel used as an autoclave chamber. The reactions were carried out between 190 and 230 °C at the heating rate of 5 K/min, and the final temperature was maintained for 36 h for each sample. After that, the product was washed several times with ethanol and distilled water, and finally dried at 80 °C for 12 h under vacuum. The product was obtained as black powder which was redispersed in ethanol for characterisation. X-ray diffraction patterns showed the formation of a tetragonal CIGS structure as the main phase (size 20–80 nm) with the purity more than 99% obtained by energy-dispersive X-ray spectroscopy (EDX). The band gap was determined to be about 1.44 eV, which corresponds to an acceptable wavelength region for absorber layers in solar cells.

CIGS thin films were fabricated using precursor nanoparticle-ink and sintering technology.[4] The precursor used quaternary compound composition ratios of $Cu/(In + Ga) = 0.95$, $Ga/(In + Ga) = 0.39$, and $Se/(Cu + In + Ga) = 0.75$, respectively. The quaternary-alloy powders were mixed with appropriate solvents at an initial stoichiometric ratio of $Cu/(In + Ga) = 0.95$, $Ga/(In + Ga) = 0.39$, and $Se/(Cu + In + Ga) = 0.75$, respectively, and then ground into nanoscale-size particles by using a rotary ball milling technique to obtain the required ink in order to prepare the precursor films. Next, the ink for manufacturing the CIGS precursor films was obtained by mixing the quaternary-alloy compounds of 100 g CIGS with a 500 ml of propanol and zirconium beads; each zirconium bead (*i.e.* diameter of 0.5 mm and mass of 100 g) was mixed in a ball mill for grinding. After 4 h of coarse grinding, the zirconium beads were replaced with smaller beads (diameter, 0.1 mm); however, the total mass was maintained. An hour later, 50 mL of propylene glycol and 10 mL of diethanolamine were added to the ball mill and ground continuously for an hour to obtain the required ink. Closely examining scanning electron microscope (SEM) photographs of the agglomerated CIGS powder revealed an average grain size smaller than 100 nm (Fig. 1). Also, anhydrous ethanol was used with a solvent (propanol, propylene glycol, diethanolamine) to wash out the CIGS nanoparticle, and the alcohol was removed by placing CIGS nanoparticles in a vacuum environment and then held at a temperature of 80 °C, the required dry CIGS nanoparticles were obtained. Moreover, a precursor mixture solution was prepared by dissolving appropriate amounts of CIGS (20 g) in propanol (45 mL), followed by adding triethylenetetramine (2.0 mL) and polyvinylidenefluoride (PVdF, 1.0 g) to dimethylformamide solution (32 mL) following condensation of the mixture solution at 50 °C under reduced pressure, a viscous paste with rheological properties deemed

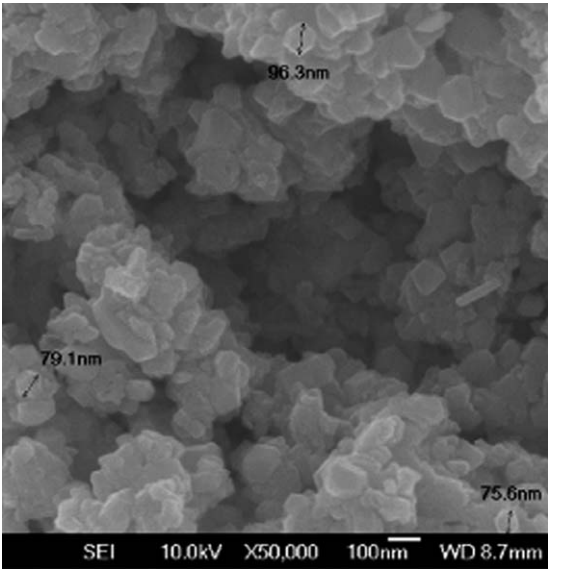

Fig. 1 Scanning electron microscope (SEM) images of the agglomerated CIGS powder showing an average grain size smaller than 100 nm.[4]

appropriate for doctor blade coating was prepared. Analytical results indicate that the CIGS absorption layer prepared with a nanoparticle-ink polymer, through sintering, has a chalcopyrite structure. Analysis of a performance of the obtained solar cell under standard air mass 1.5 global illumination revealed a conversion efficiency of 2.392%.

The same workers also used binary-alloy powders of In_2Se_3, Ga_2Se_3, and CuSe to prepare CIGS thin films.[5] The commercially available binary-alloy powders of In_2Se_3,Ga_2Se_3, and CuSe (whose sizes are around 74 μm) were used in the initial stoichiometric ratio of 39% CuSe, 45% In_2Se_3, and 16% Ga_2Se_3, in appropriate solvents and then ground into nanoscale by using a ball mill to obtain the required ink for preparing the precursor films. The ink was printed onto a Mo/soda lime glass substrate and baked at a low temperature to remove solvents to forma dry precursor.

Next, the required absorption layer of $CuIn_{0.7}Ga_{0.3}Se_{2.0}$ used in solar cells was obtained by thermally treating the precursor through means of rapid sintering to reduce the weight loss of the Se components. The ink was fabricated by a ball milling procedure and the size of the agglomerated copper–indium–gallium–diselenide powder after milling was less than 100 nm. Crystallographic, morphological, stoichiometric, and photovoltaic properties of the films were characterized by sintering the precursor copper–indium–gallium–diselenide samples with different holding times in a non-vacuum environment without selenization. Analytical results indicate that the copper–indium–gallium–diselenide absorption layer prepared with a holding time of 7.5 min has a chalcopyrite structure and favourable compositions. The obtained compositions of the sample are $Cu_{0.976}In_{0.811}Ga_{0.277}Se_{1.935}$, and the ratios of Ga/(In + Ga) and Cu/(In + Ga) are 0.254 and 0.896, respectively.

Mitzi *et al*. reported that Sb-doping can substantially enhance the grain growth in CIGS thin films fabricated through hydrazine based processing.[6,7] Following this work, Xiang *et al*. demonstrated that Sb diffusion across the film thickness during annealing at elevated temperature can improve the mass transfer in CIGS thin films prepared by sputtering.[8] Recently Xiang *et al*. investigated the effect of Sb on the formation of Cu-Se binary phases, important intermediates in the formation pathway of CIGS thin films.[9] The solvothermal reaction of $CuCl_2$ with Se gave Cu_3SbSe_3 in presence of Sb, which was determined to be a mobile phase at high temperatures in the DSC analysis indicating the promotional role of this species. They also investigated the effect of Sb on the synthesis of CIGS nanoparticles. In a typical synthesis of CIGS nanoparticles, a mixture of selenium powder (0.204 g, 2.58 mmol) and $SbCl_3$ (0.022 g, 0.096 mmol) were suspended in 5 mL ethylenediamine in a 20 ml Teflon lined autoclave, followed by an ultrasonic treatment for 5 min. A separate solution of $CuCl_2 \cdot 2H_2O$ (0.164 g, 0.96 mmol), $InCl_3$ (0.192 g, 0.868 mmol), and $Ga(acac)_3$ (0.068 g, 0.186 mmol) was prepared in in 5 mL deionized water. This solution was added to the suspension of $SbCl_3$ and Se in the Teflon autoclave. An additional 6 mL of ethylenediamine was then added to make the volume of the mixture to 16 mL. The autoclave was sealed and sonicated for 15 min. A parallel experiment was carried out under similar conditions without using Sb dopant. The two sealed autoclaves were moved into an oven, and the temperature in the oven was raised from room temperature to 200 °C and maintained for 12 h. The oven was cooled to room temperature and the precipitates in the autoclaves were collected by centrifugation, washed six times with the mixed solvent of ethanol and deionized water. The powders were dried in a vacuum drying oven at 60 °C temperature for 4 h. To determine the effect of Sb on the formation kinetics of CIGS nanocrystals, a similar solvothermal procedure with same amount of reactants and solvents were also carried to prepare samples with and without Sb for reaction time of 12 h, 24 h and 48 h separately. The presence of Sb into the solvothermal reactions of $CuCl_2$, $InCl_3$, $Ga(acac)_3$, and Se at 200 °C significantly promoted reaction rate to form single phase chalcopyrite CIGS nanocrystals within 12 h, while similar reactions without Sb produced CIGS with Cu_2Se impurities even after 48 h.

Layer-by-layer (LbL) processes can be used to fabricate precisely tailored thin film on various types of substrates, both rigid and flexible. This nanoassembly does not require sophisticated laboratory facilities or precise process control, thus yields a cost-effective thin film manufacturing process. In LbL nanoassembly, positive and negatively charged species are sequentially deposited on a substrate *via* alternate dipping. Hemati *et al*. prepared nanoassembly of CIGS nanoparticles linked with polymers.[10] CIGS nanoparticles were synthesized by heating copper chloride, indium chloride, gallium chloride, and selenium in oleylamine and were dispersed in water (Fig. 2). Their desired surface charges were obtained through pH regulation and by coating the particles with polystyrene sulfonate (PSS). Increasing the pH of the nanoparticle dispersion reduced the zeta-potential from +61mV at pH 7 to −51mV at pH 10.5. Coating the CIGS nanoparticles with PSS (CIGS-PSS) produced a stable dispersion in water with −56.9 mV zeta-potential. Thin films of oppositely charged CIGS nanoparticles

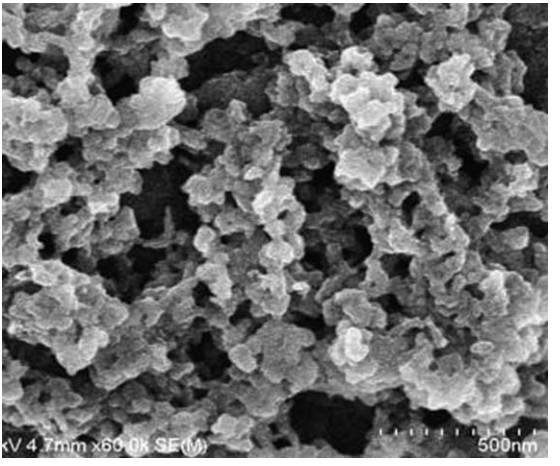

Fig. 2 SEM image of CIGS nanoparticles synthesised by heating copper chloride, indium chloride, gallium chloride, and selenium in oleylamine and were dispersed in water.[10]

(CIGS/CIGS), CIGS nanoparticles and PSS (CIGS/PSS), and PSS-coated CIGS nanoparticles and polyethylenimine (CIGS-PSS/PEI) were prepared. Film thickness and resistivity of each bilayer of the films were measured, and photoelectric properties of the films were studied for solar cell applications. Solar cell devices fabricated with a 219 nm CIGS film, when illuminated by 50W light-source, produced 0.7 V open circuit voltage and 0.3 mA/cm^2 short circuit current density.

2.2 Copper iron sulfide ($CuFeS_2$)

Chalcopyrite (CH–$CuFeS_2$) structure consists of Cu^{1+} and Fe^{3+} at alternate tetrahedral sites of a cubic close packed sulfur network in the tetrahedral symmetry.[11] Nagarajan *et al.*[12] reported solution based synthesis of wurtzite and chalcopyrite polymorphs of $CuFeS_2$ by reacting a Cu(I) thiourea complex $(Cu_4(tu)_9](NO_3)_4]4H_2O)$ (tu = thiourea) with $Fe_2(SO_4)_3$ and $FeCl_3$ in ethylene glycol respectively. The reaction of copper complex with $Fe_2(SO_4)_3$ produced WZ-$CuFeS_2$ nanoparticles with a flower-like morphology (Fig. 3) and an average diameter of 0.8 to 1.0 μm. The mapping from the Field Emission-Scanning Electron Microscopy (FE-SEM) shows that Cu, Fe and S elements are homogeneously distributed within the particles. The ratio of Cu : Fe : S obtained from the EDX analysis was found to be 1.16 : 1 : 1.80. The reaction of copper complex $(Cu_4(tu)_9](NO_3)_4] \cdot 4H_2O)$ with $FeCl_3$ produced tetragonal $CuFeS_2$ nanoparticles. The average crystallite size has been estimated to be 10 nm by the Scherrer analysis. A flower-like morphology similar to the wurtzite phase comprising of plate shaped petals has been noticed for CH–$CuFeS_2$ in its FESEM images. EDX analysis confirmed the presence of Cu, Fe and S with a ratio of 1.25 : 1.08 : 1.70.

Chalcopyrite $CuFeS_2$ nanocrystals with a diameter of 6.4 nm were synthesized using oleic acid and dodecanethiol as capping agents (optimized ratio is 1 : 2).[13] Sodium diethyldithiocarbamate in hot-injection was used as a sulfur source for an immediate reaction at 180 °C. For a typical reaction 0.085 g of $CuCl_2$ and 0.081 g of $FeCl_3$ were mixed with 12 mL oleic acid

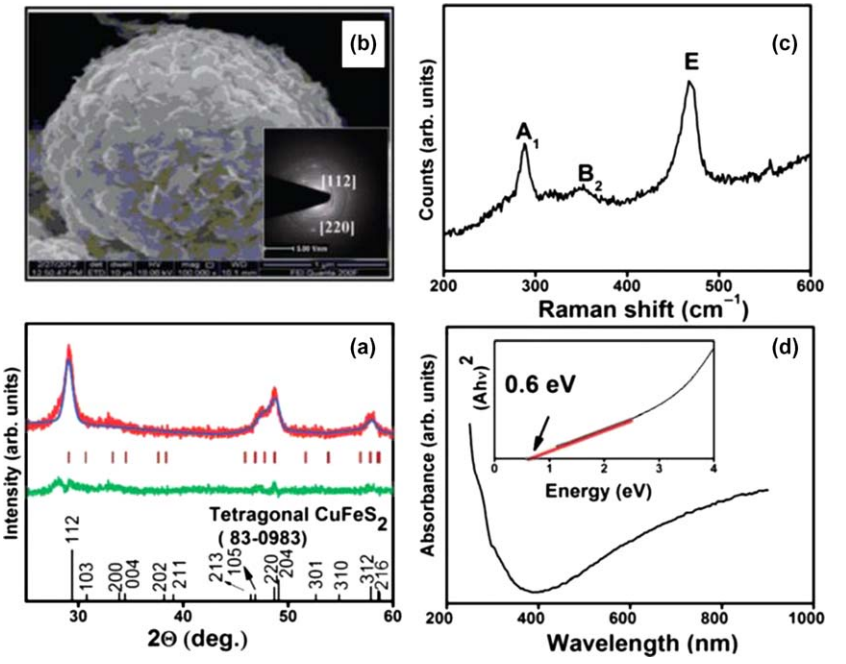

Fig. 3 (a) Rietveld fit of the p-XRD pattern along with the JCPDS file of CH–$CuFeS_2$ (observed, calculated (profile matching), and difference profiles are given as red, blue, and green lines (online), respectively), (b) FE-SEM image with the SAED pattern in the inset, (c) room temperature Raman spectrum, (d) UV-Visible absorption spectrum of the product obtained from the reaction of $[Cu_4(tu)_9](NO_3)_4$ with $FeCl_3$ in ethylene glycol for 1.5 h under refluxing conditions. The inset in (d) shows the plot of energy (eV) vs. $(Ahv)^2$ of the optical absorption data. Reproduced from ref. 12 with permission from the Royal Society of Chemistry.

(OA) and 18 mL n-dodecanethiol (DT) in a three neck 100 ml round bottom flask. The flask was heated at 140 °C under N_2 while stirring until reactants were completely dissolved. After that 6 mL of 0.2 M sodium diethyldithiocarbamate trihydrate ($NaS_2CN(C_2H_5)_2 \cdot 3H_2O$) in DT suspension was injected into the solution and quickly raised the temperature to 180 °C and maintained it for 15 min. After 15 minutes the reaction was quenched by immersing the flask in a cold water bath. The product was separated by centrifugation and washed with toluene/methanol twice and once with toluene/acetone to remove any impurities. The p-XRD pattern corresponds to the chalcopyrite phase of $CuFeS_2$ (JCPDS 37-0471). The size of $CuFeS_2$ nanoparticles calculated from Debye–Sherrer formula was 6.9 nm. EDX analysis gives formulae of $CuFe_{0.99}S_{2.08}$ and $CuFe_{0.97}S_{1.89}$, respectively. Both of them are close to the stoichiometric proportion of chalcopyrite $CuFeS_2$. The TEM studies show uniform nanocrystals with an average size of 6.4 ± 0.5 nm. The electrical conductivity and thermal conductivity of $CuFeS_2$ nanoparticles have been investigated between 300 K and 500 K with comparisons to bulk chalcopyrite. The electrical conductivity of $CuFeS_2$ nanoparticles increases from 87.4 Sm^{-1} at 300 K to 326.5 Sm^{-1} at 500 K. The comparison of thermoelectric properties with those of bulk chalcopyrite material shows a significant increase in the power factor with a major reduction of thermal conductivity.

Garje *et al.*[14] prepared chalcopyrite ($CuFeS_2$) nanocrystallites from single-source precursors, CuL_2 and $Cu(LH)_2Cl_2$ (where LH = monoacetylferrocene thiosemicarbazone) by pyrolysis and solvothermal decomposition methods. The $CuFeS_2$ nanocrystallites obtained from the pyrolysis of CuL_2 and $Cu(LH)_2Cl_2$ have a cubic phase and rod-like morphology. These crystallites have diameters of about 18 and 15 nm and lengths of about 195–390 and 100–145 nm, respectively. However, $CuFeS_2$ nanoparticles prepared by solvothermal route from CuL_2 and $Cu(LH)_2Cl_2$, in ethylene glycol possess spherical shapes with an average grain size of 16 and 11 nm, respectively.

Aup-Ngoen *et al.*[15] synthesized copper iron sulfide ($CuFeS_2$) nanoparticles by a 300 W cyclic microwave radiation, exposing onto ethylene glycol containing $Cu(CH_3COO)_2$, $FeCl_3$ $6H_2O$ or $FeCl_2 \cdot 4H_2O$ and L-cysteine biomolecules. Tetragonal chalcopyrite $CuFeS_2$ nanoparticles were identified by p-XRD, FE-SEM and TEM.

2.3 Cu_2MSnS_4 ($M = Co^{2+}$, Fe^{2+}, Ni^{2+}, Mn^{2+})

The nanocrystals of quaternary semiconductor Cu_2MSnS_4 ($M = Co^{2+}$, Fe^{2+}, Ni^{2+}, Mn^{2+}) have been synthesized *via* a solvothermal method.[16] The spherical morphology was observed for Cu_2FeSnS_4 and Cu_2CoSnS_4 whereas Cu_2NiSnS_4 and Cu_2MnSnS_4 shows a nail-like and a rod-like morphology. All these four types of nanocrystals exhibit significantly different magnetic properties. Ferromagnetic behaviour was shown by Cu_2FeSnS_4 and Cu_2CoSnS_4 nanocrystals. The Cu_2MnSnS_4 and Cu_2NiSnS_4 nanorods exhibit superparamagnetic behavior at low temperature. The band gaps for all these nanocrystals are in the range of 1.2–1.5 eV, indicating a high potential application in low-cost thin film solar cells. For a typical reaction in a 50 mL conical flask, 1.0 mmol CuCl, 0.5 mmol $SnCl_2 \cdot 2H_2O$, and 0.5 mmol $Co(NO_3)$ $2.6H_2O$ (0.5 mmol $FeCl_2 \cdot 4H_2O$, 0.5 mmol $Ni(NO_3)2 \cdot 6H_2O$, or 0.5 mmol $MnCl_2 \cdot 4H_2O$) were dissolved in 8.0 mL hexylamine by ultrasound. In another 50 mL conical flask 12.0 mL of hexylamine was loaded and then slowly dropped 1.0 mL carbon disulfide and 1.0 mL 3-mercaptopropionic acid into the conical flask in an ice-water bath. The two solutions from both flasks were mixed, and 1.0 ml 3-mercaptopropionic acid was added to the solution and the contents stirred for 12 h. The solution was then transferred into a 30 mL Teflon lined stainless steel autoclave and put into an oven at 180 °C for 2 h. The autoclave was cooled to room temperature followed by the addition of 30 mL of methanol for the precipitation of the nanocrystals. The nanocrystals were isolated by centrifugation and re-dispersed in chloroform for TEM and XRD analysis.

A simple, rapid and non-aqueous scaled-up microwave route was introduced for the synthesis of uniform quaternary Cu_2FeSnS_4 (CFTS) nanotubes by using benzyl alcohol as the microwave absorbing solvent.[17] These nanotubes have 400–800 nm outer diameter an100–200 nm thickness. The facile microwave non-aqueous synthesis method based on a series of designed experiments. The possible mechanism for the formation of the copper-indium-tin sulfide (CITS) nanotubes was proposed, which was governed by the *in situ* generated self-sacrificial Cu(Tu)Cl nanorods.

The CFTS nanotubes had a strong absorption in the visible region with a bandgap of 1.71 eV suitable for photovoltaic applications.

Liu *et al.*[18] reported the quaternary tetragonal Cu_2FeSnS_4 nanocrystals synthesized by a simple hot-injection method. A solution of elemental sulfur was injecting in oleylamine (OA) into an oleylamine solution containing 1.5 mmol copper(II) acetylacetonate ($Cu(acac)_2$), 0.5 mmol iron(II) acetylacetonate ($Fe(acac)_2$), and 0.75 mmol of tin(II) chloride ($SnCl_2$) at 280 °C. The TEM images of nanocrystals (Fig. 4) show triangular and round shaped Cu_2FeSnS_4 nanocrystals with an average diameter of 13.2 ± 1.1 nm. The band gap of the tetragonal Cu_2FeSnS_4 nanocrystals obtained was measured as 1.28 ± 0.02 eV. The preliminary photoelectrochemical characterizations of the Cu_2FeSnS_4 films indicate p-type conductivity and the values of the photocurrent density for this system are in the range of 11 and 13 mA cm^{-2}. These nanocrystals can be easily dispersed in relatively low toxic solvents and well fabricated into Cu_2FeSnS_4 films by drop-casting. The film thus obtained has a clear and stable photoelectrochemical response. The studies show that Cu_2FeSnS_4 has potential application in the solar cell devices.

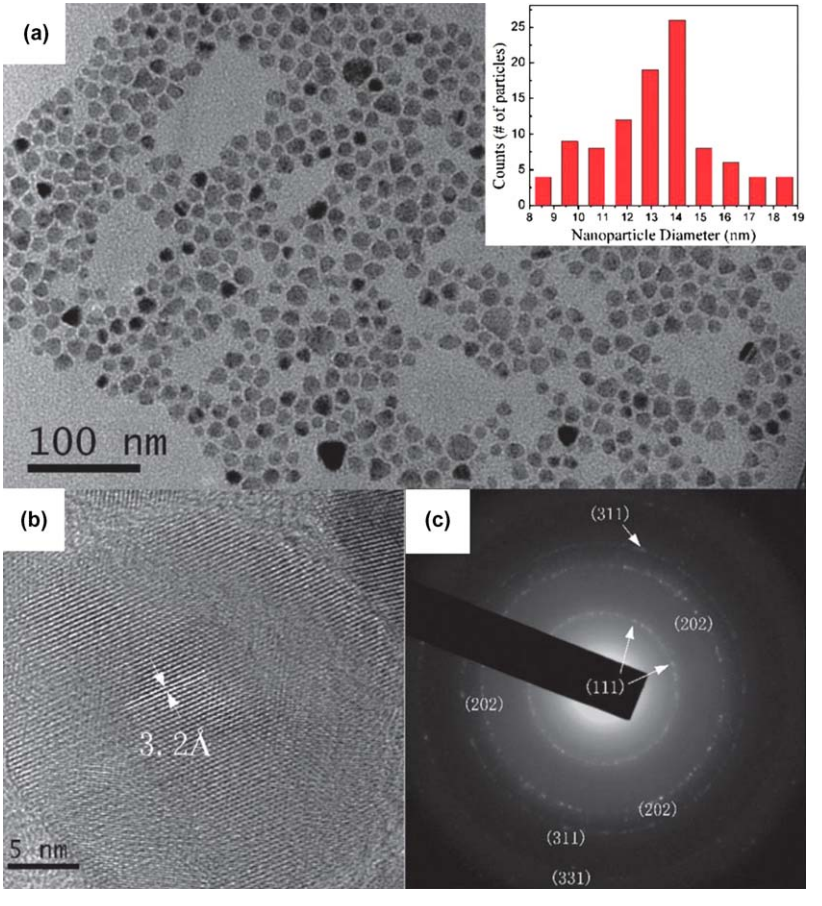

Fig. 4 (a) Low resolution TEM image of Cu_2FeSnS_4 nanocrystals. (b) High resolution TEM image showing interplanar spacing of 3.2 Å. (c) The SAED pattern indexed to Cu_2FeSnS_4 Reproduced from ref. 18 with permission from the Royal Society of Chemistry.

Gupta *et al.*[19] synthesised Cu_2FeSnS_4 (CFTS) nanocrystals with tunable crystal phase using a solution-based method. For the synthesis of CFTS nanocrystals with the wurtzite structure, 1 mmol $Cu(acac)_2$, 0.5 mmol $Fe(acac)_3$ and 0.5 mmol $SnCl_4 \cdot 5H_2O$ were mixed with 10 mL oleylamine (OA). The solution was heated up to 150 °C. A mixture of 1-dodecanethiol (1-DDT) and *tert*-dodecanethiol (t-DDT) was quickly injected into the above solution and the temperature was increased to 210 °C. This temperature was maintained for 30 min. A similar procedure was used for the synthesis of phase-pure zinc blende CFTS nanocrystals at 310 °C, using a mixture of 8 mL 1-octadecene (ODE) and 2 mL oleic acid (OA) as solvent. The TEM analysis shows that the wurtzite-phase CFTS nanocrystals synthesized in OLA have oblate spheroids shape morphology with an average size of 20 ± 2 nm (Fig. 5a). The HRTEM image of nanocrystal (Fig. 5b) shows lattice fringes corresponds to the (002) planes of wurtzite. Energy-Dispersive X-ray Spectroscopy (EDX) analysis shows Cu/Fe/Sn/S compositions (%) of 26.43 : 12.35 : 12.12 : 49.10 and 26.34 : 12.42 : 11.38 : 49.86 for the wurtzite and zinc blende CFTS nanocrystals, respectively. These values are close to the desired 2 : 1 : 1 : 4 ratio. Both wurtzite and zinc blende phases exhibit strong absorption at visible wavelengths with band gap values around 1.5 eV, which makes them attractive for photovoltaic applications.

Multicomponent chalcogenide $Cu_2(Fe_xZn_{1-x})SnS_4$ nanocrystals were synthesized by a solution method.[20] In a typical reaction oleylamine was used as both solvent and capping agent for the nanocrystals. Sulfur powder was dissolved in oleylamine ultrasonically used as the sulfur source. For metal source $Cu(acac)_2$, $Fe(acac)_2$, $Zn(acac)_2$ and $SnCl_2$ were used.

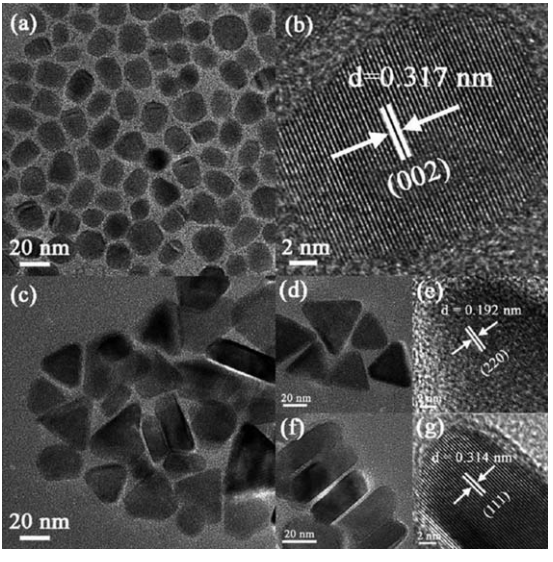

Fig. 5 (a) TEM and (b) HRTEM images of wurtzite CFTS nanocrystals. (c) TEM image of zinc blende CFTS nanocrystals. (d) TEM and (e) HRTEM images of zinc blende CFTS from top-view; (f) and (g) corresponding side-view images. Reproduced from ref. 19 with permission from the Royal Society of Chemistry.

All experiments were performed by utilizing a Schlenk line and air free techniques. In a 50 mL three-neck round bottom flask 10 mL oleylamine, 1.5 mmol $Cu(acac)_2$, 0.75 mmol $Zn(acac)_2$, 0.25 mmol $Fe(acac)_2$ and 0.75 mmol $SnCl_2$ were heated to 130 °C under vacuum and degassed. The reaction temperature was increased to 180 °C and maintained until the reaction mixture turned brown; and then the temperature was further raised to 270 °C. At this stage 3 mL of the sulfur source was rapidly injected into the mixture with rapid stirring. The mixture immediately turned dark brown, indicating the formation of nuclei. The reaction temperature was maintained for 30 min and then the mixture was cooled down to 60 °C. Addition of 5 mL of toluene and 25 mL ethanol gave precipitation which were centrifuged and re-dispersed in toluene for further characterization. Thin films for various characterizations were deposited by drop casting nanocrystals dispersed in toluene. Thin films used for photoelectrochemical characterization were annealed under argon gas at 350 °C for 1 hour.

Ricardo *et al.*[21] reported high energy ball milling method to obtain $Cu_2(Zn,Fe)SnS_4$ powders for solar inks production. The starting materials for CZ/FTS precursor was Cu powder (<75 mm, 99%), Zn powder (purum, 99%), Fe fine powder (99%), Sn powder (puriss, 99%) and Sulfur flakes (purum, 99.5%) and Ethanol (99.8%). For ink production, a-terpineol (96%) was used. The precursor powders were then annealed under Argon flux at 550 °C for 2 h with the presence of sulfur atmosphere to promote complete formation of a CZ/FTS powder. Ink solutions were prepared and deposited on glass substrates by spin coating using a rotational speed of 800 rpm for 60 s. Substitution of zinc by iron, either as an effect of contamination from the milling vials and/or as an addition in controlled quantity, was studied by structural p-XRD and SEM-EDX techniques. XPS measurements provided further information on the oxidation state of iron, whereas *in situ* high temperature synchrotron radiation XRD was used to follow the evolution of the system, and in particular the transformation of iron from the starting metallic condition to the alloying in the final kesterite powders.

2.4 Copper Zinc Tin Sulphide (CZTS)

Cu_2ZnSnS_4 (CZTS) is a p-type semiconductor with direct bandgap of about 1.5 eV and high absorption co-efficient of the order of 10^4 cm^{-1}, is one of the most promising thin film absorber material for photovoltiacs. It is made of comparatively non-toxic elements which are abundant in nature hence making it a relatively cheap material for solar cells. It has two structures stannite and kesterite which differ only on the arrangements of Cu and Zn atoms in the two structures. However, CZTS usually appears in kesterite phase as it is thermodynamically more stable than the stannite type. An economically attractive way of producing CZTS layers with required stoichiometry and crystal phase is to chemically synthesize CZTS nanocrystals (NC), and deposit thin films using an ink based on this nanomaterial.

Zhou *et al.*[22] synthesised pure phase metastable wurtzite Cu_2ZnSnS_4 (CZTS) nanocrystals with different shapes by a one-pot method using different capping agents. In a typical experiment, 10 mL of dodecanthiol

(DDT), 0.5 mL of olylamine (OA), 0.1 mmol of $Sn(acac)_4$ (53 mg) (acac = acetylacetonate), 0.1 mmol of $Zn(acac)_2$ (28 mg), and 0.2 mmol of $Cu(acac)_2$ (56 mg) were heated to 220 °C in an oil bath and held for 4 h. After being cooled to room temperature, the CZTS nanoparticles were separated by precipitation with the addition of excess ethanol and then collected by centrifugation at 9500 rpm for 4 min. The supernatant was decanted, while the precipitates were dispersed in the hexane and further purified by ethanol precipitation several times. Final products were obtained and dried in a vacuum oven overnight at room temperature for further characterizations. The effect of the amount of OA, reaction temperature, reaction time, and concentration of precursors on the morphology, size, and monodispersity of nanoparticles were investigated. The major factor effecting the formation of wurtzite CZTS rather than kesterite CZTS was found to be the DDT. The use of pure DDT resulted in the formation of two coexisting CZTS phases (wurtzite, unstable and stable kesterite CZTS) whereas a mixture of DDT with some OA gave only metastable wurtzite CZTS. It was believed that OA adjusted the chemical environment and prevented the phase transition from metastable wurtzite to stable kesterite CZTS. Time-dependent experiments showed the final CZTS morphology evolved from spherical through rhombus-like intermediate shape to rice-like pure wurtzite CZTS nanoparticles (Fig. 6). On the basis of the detailed time-dependent shape and elemental composition evolutions, a possible asynchronous doping growth and formation mechanism was also proposed. The UV/Vis absorption spectra revealed that the pure wurtzite CZTS NCs had an absorption in the visible wavelength range, indicating its potential application as a solar absorber. Meanwhile, the I–V curve showed that the pure wurtzite form favored the generation of photoinduced carrier and electronic transmission.

Syntheses of CZTS require a good control over synthesis parameters to get the desired stoichiometry. The ideal stoichiometry of CZTS corresponds to the ratios of Cu/(Zn + Sn) and Zn/Sn equal to one but earlier work suggested that CZTS stoichiometry with slightly Cu poor and Zn-rich shows good optoelectronic properties and the better device efficiency. Therefore, by tuning the chemical composition of CZTS nanoparticles, it is possible to achieve improved optoelectronic properties suitable for photovoltaic applications. Pal *et al.* synthesised phase-pure, highly crystalline CZTS nanoparticles with controlled Cu/(Zn + Sn) ratio through a solution-based solvothermal process.[23] In a typical synthesis, the required quantities of copper(II) chloride dihydrate, zinc(II) acetate and tin(IV) chloride pentahydrate were added into 50 mL of ethylene diamine (ED) and the mixture was subjected to an alternate cycle of magnetic stirring (4 min) and ultra-sonication(1 min) during 20 min in order to facilitate the complex formation between ED and Cu^{+2}, Zn^{+2} and Sn^{+4} ions. Subsequently 0.5 M of sulfur powder was dissolved into the above mixture under vigorous magnetic stirring. The thick green colored solution was then transferred into a stainless steel autoclave with a Teflon liner. The sealed autoclave was maintained at 180 °C for 15 h and allowed to cool to room temperature naturally.

The precipitate was collected by centrifugation at 9000 rpm for 15 min, washed several times by ethanol and air-dried. Three CZTS samples

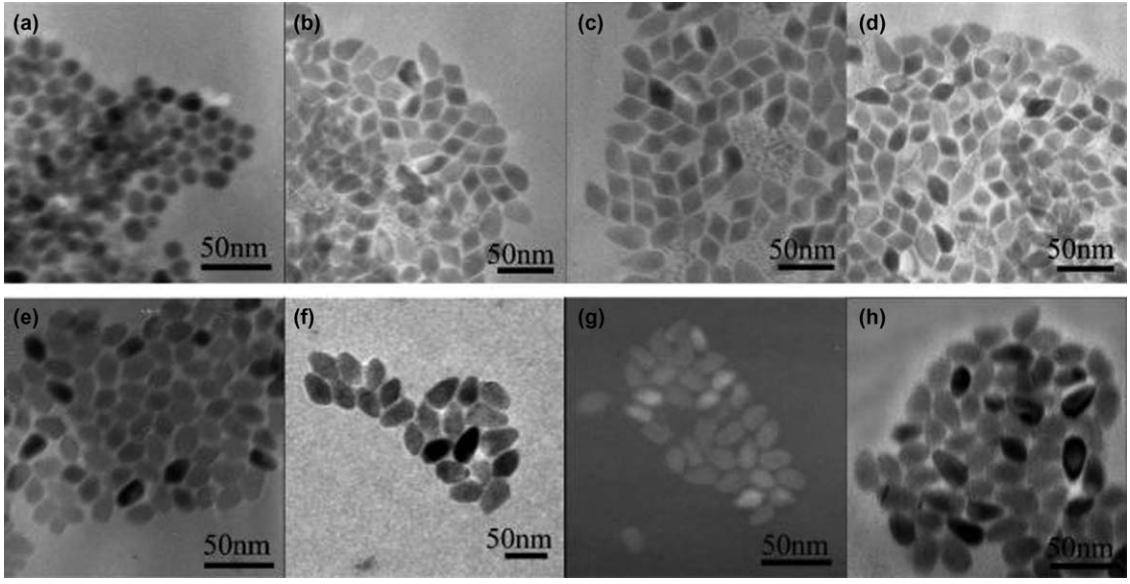

Fig. 6 TEM images of the CZTS products synthesized at different reaction times: (a) 30 min, (b) 40 min, (c) 50 min, (d) 1 h, (e) 2 h, (f) 4 h, (g) 8 h, and (h) 24 h, respectively.[22]

denoted as CZTS-1, CZTS-2 and CZTS-3 were prepared by varying the concentrations of Cu and Zn salts. They tried to control the atomic ratios of Cu/(Zn + Sn) and Zn/Sn near to 0.85 and 1.25 respectively by varying the metal salt concentrations in the precursor solution. The material properties were investigated in order to identify the most appropriate initial precursor concentrations to obtain stoichiometric CZTS NPs.

Li *et al*. fabricated photovoltaic devices with a heterojunction made with layers of CZTS nanoparticles and a fullerene derivative, [6,6]-phenyl-C61-butyric acid methyl ester (PCBM).[24] The CZTS nanoparticles were synthesised by dissolving 1 mM $CuCl_2 \cdot 2H_2O$, 0.5 mM $ZnCl_2 \cdot 2H_2O$, and 2 mM of sulfur in 20 mL of OA. The mixed solution was degassed for 15 min at room temperature and 0.06 mL of anhydrous $SnCl_4$ (0.5 mM) was then injected into the reaction mixture. The reaction temperature was increased to 120 °C followed by further degassing for 30 min. Finally the temperature of the solution was raised to 180 °C and maintained for 1 h. The reaction was stopped by lowering the temperature to 80 °C and injecting 5 mL of toluene into the product. The solution was stirred for 5 more minutes to improve size distribution of the particles. The nanoparticles were precipitated by adding 2-propanol to the solution and separated by centrifuging the solution at 8000 rpm. The precipitation and separation processes were repeated twice. Finally a dispersed solution of nanoparticles in toluene (15 mg mL^{-1}) was prepared. A solution of pyridine in acetonitrile at 30% volume ratio was also prepared. For deposition of each layer, the following 4 steps (each of 15 s duration) were followed: (i) 5 drops of oleylamine-capped CZTS solution were spun on an ITO substrate, (ii) 5 drops of pyridine solution were spun on the nanoparticle layer to exchange the ligands, (iii) 6 drops of anhydrous acetonitrile were spun to remove the excess pyridine, and (iv) 6 drops of anhydrous toluene were spun to clean the surface for deposition of the next layer. Each step was carried out with an interval of 30 s to dry the surface. The steps were repeated to achieve CZTS films of 3, 5 and 7 layers having a thickness of 36, 58, and 82 nm, respectively. Thickness of the films was measured by recording the depth profile of an intentional scratch on the films through atomic force microscopy. On top of the CZTS, a fullerene derivative, namely, [6,6]-phenyl-C61-butyric acid methyl ester (PCBM) has been spun from chlorobenzene solution (20 mg mL^{-1}) at 2500 rpm. To complete the device fabrication process, Ca (10 nm) followed by Al (100 nm) were thermally evaporated under vacuum (B10^{-6} Torr) as strips orthogonal to ITO electrodes. The area of the devices was 2 × 2 mm. Optical absorption spectra of CZTS–PCBM heterolayer, CZTS, and PCBM thin-films were measured (Fig. 7).

The CZTS–PCBM heterostructure formed a hybrid pn-junction suitable for dissociation of photogenerated excitons. Inter dot spacing in CZTS thin-films has been reduced by pyridine-treatment replacing long-chain oleylamine surfactants of the nanocrystals through an exchange reaction. This facilitated carrier transport through the CZTS nanoparticle film. From C–V characteristics, the width of the depletion region and carrier density at the junction were determined which showed the potential for solar cell applications. CZTS layers were deposited using various ratios of copper(II)

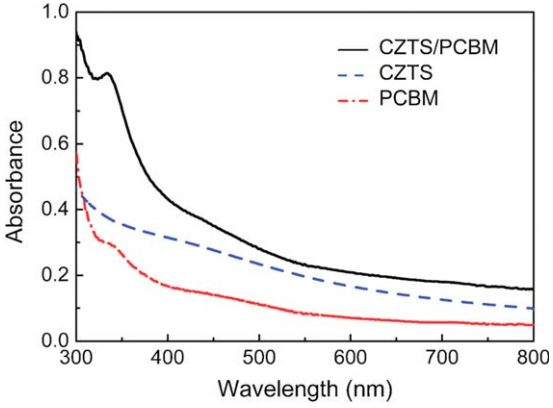

Fig. 7 Optical absorption spectra of CZTS–PCBM heterolayer, CZTS, and PCBM thin-films. Reproduced from ref. 24 with permission from the Royal Society of Chemistry.

dibenzyldithiocarbamate, zinc(II) dibenzyldithiocarbamate, and tin(IV) dibenzyldithiocarbamate (all synthesised from sodium salt, which was prepared by the reaction of dibenzylamine, carbon disulfide and sodium salt) dissolved either in pyridine or chloroform.[25] Dibenzyldithiocarbamates were chosen due to their lower thermal stability and lower volatility compared to dialkylcarbamates. The amount of zinc precursor was set to 1 equiv using a concentration of 0.025 mol L^{-1}. The solution was drop coated onto the glass substrates, which had been cleaned in an ultrasonic water bath followed by an ultrasonic isopropanol bath each for 20 min. The coated substrates were annealed at temperatures of 350 °C for 30 min in a tube furnace under nitrogen atmosphere. After the heating step the substrates were cooled down to room temperature under nitrogen atmosphere. UV/vis measurements were carried out on the coated substrates without further treatment. However, for XRD-measurements, TEM/EDX investigations, SEM studies and Raman spectroscopy analysis the CZTS layer was scraped off the substrates to obtain the metal sulfide powder. X-ray diffraction measurements show that a precursor solution containing an excess of the zinc precursor, compared to the Cu and Sn precursors, has to be used to obtain CZTS films without secondary phases. Thus, the prepared films are Zn-rich, which is beneficial for solar cell applications. Raman as well as X-ray photoelectron spectroscopy studies confirm the formation of CTZS. No clear evidence for free ZnS has been found. Electron microscopy shows agglomerates of 10 nm-sized crystallites forming spherical particles with a diameter between 50 nm and 400 nm (Fig. 8). The prepared films possess high optical absorption ($>10^4$ cm^{-1}) and an optical band gap of approximately 1.6 eV.

Kheraj *et al.*[26] used binary sulfide precursors (CuS, ZnS and SnS) to synthesise large CZTS particles. They used amounts in atomic stoichiometric proportion and sealed in a quartz ampoule at a base pressure of 10-5 mbar. Three samples, S1, S2 and S3 were prepared by adding 0%, 10% and 20% excess sulphur respectively, in the raw mixture in ampoules. The ampoules were heated in electrical furnace from room temperature to 670 K at the rate of 4 K/min and then up to 1030 K at the rate of 2 K/min, where it

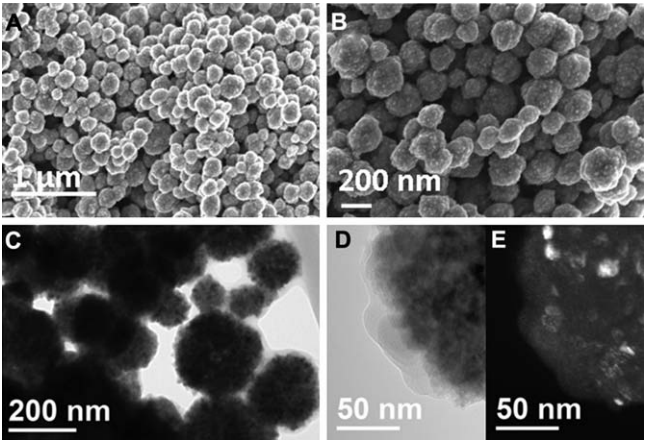

Fig. 8 SEM-images of the CZTS layer with different magnifications (A,B), a TEM micrograph of the sample (C) and a bright field (D) as well as a dark field (E) TEM image of a single agglomerate indicating that the layers consist of spherical particles (diameter up to approx. 200 nm) and smaller crystallites with diameters of about 10 nm.[25]

was kept for 24 hours to ensure homogenous crystallization. It was cooled down up to 670 K at the rate of 4 K/min and then up to room temperature naturally. The solid ingot was then powdered by mechanical grinding to a mean particle size of 40 to 60 µm.

Shin *et al.*[27] synthesised CZTS by microwave using 40 mL of certain concentration of Cu(OAc), 40 mL 0.1 M Zn(OAc) and 40 mL 0.1 M $SnCl_2$. Subsequently, 40 mL of a 0.2 M thioacetamide solution was added and the pH was adjusted to seven by adding an ammonia (NH_4OH) solution with constant magnetic stirring for 10 min at room temperature. When the copper concentration of precursor solutions was varied from 0.01 to 0.25 M, the color of precursor solution changed from a transparent to a brown–green. The precursor solution was irradiated with microwave energy using a commercial microwave oven (KR-B200B, Daewoo, Korea) at 700 W for 10 min. After 6 min, the precursor solution was boiled and the color changed from brown–green to dark-blue. The reacted solution was then cooled to room temperature in an air. The powder formed in the solution was separated from the precursor solution by centrifugation at 3000 rpm for 10 min and this process was repeated three times. Finally, the precursor powder was dried in a vacuum oven at 60 °C for 8 h. The dried precursor powders were sequentially sulfurized using a tubular furnace system in an atmosphere of the mixed N_2 (95%) + H_2S (5%) at 550 °C for 1 h. They investigated the effect of different Cu concentration from 0.01 to 0.025 M on the structural, morphological, compositional, chemical and optical properties of CZTS nanoparticles. X-ray diffraction patterns, X-ray photoelectron spectroscopy and transmission electron microscopy results showed that the precursor powder contains several broad peaks that could not be assigned to CZTS, ZnS, $Cu_{2-x}S$, Sn_2S_3 and Cu_2SnS_3. However, the sulfurized NPs showed both kesterite CZTS and copper and tin based secondary phases except for that formed at copper concentration of 0.02 M. Inductively coupled plasma (ICP) results showed that the presence of copper in the

sulfurized CZTS NPs increased with increasing copper concentration from 16.57 to 32.94% while zinc and tin in the sulfurized CZTS NPs decreased with increasing copper concentration. UV–Vis spectroscopy results showed that the absorption coefficient of the sulfurized NPs was over 10^4 cm^{-1} in the visible region and band gap energy of the sulfurized CZTS NPs decreased from 1.65 to 1.28 eV with increasing copper concentration.

A route for the fabrication of surfactant-free, solvent-redispersible CZTS nanoparticles has been reported by Zaberca *et al.*[28] They used a simple sulfide source which acts as a complexing agent inhibiting crystallite growth, a surface additive providing redispersion in low ionic strength polar solvents and a transient ligand easily replaced by a carbon-free surface additive. This multifunctional use of the sulfide source was achieved through a fine tuning of $((Cu^{2+})_a(Zn^{2+})_b(Sn^{4+})_c\,(Tu)_d(OH^-)_e)^{t+}$, Tu = thiourea) oligomers, leading after temperature polycondensation and S^{2-} exchange to highly concentrated ($c > 100$ g l^{-1}),stable, ethanolic CZTS dispersions. Polycondensation reactions at 200 °C were performed in ethylene glycol, ethanol and isopropanol using $CuCl_2 \cdot 2H_2O$, $SnCl_4 \cdot 5H_2O$ and $ZnCl_2$ as metallic salts and respectively thiourea and tetra methyl ammonium hydroxide (TMaOH) as sulfide and OH^- sources. $CuCl_2$ was used due to its better solubility as compared to CuCl.

In a typical experiment, CZTS (Cu : Zn : Sn : S : OH) D (2.0 : 1.3 : 1.1 : 10 : 2.0) were synthesised by mixing 1.73 g $SnCl_4 : 5H_2O$ (4.95 mmol), 0.8 g$ZnCl_2$ (5.85 mmol) and 1.534 g $CuCl_2 : 2H_2O$ (9 mmol) in 200 mL of ethylene glycol under stirring at room temperature. After complete dissolution of the metallic salts, 3.42 g $CS(NH_2)_2$ (45 mmol) are incorporated into the solution. After stirring for 10 min at room temperature, 3.645 mL TMaOH 25% (9 mmol) is poured into the mixture then stirred for about 30 min and finally diluted to 300 mL by ethylene glycol. The resulting solution is loaded into a 1000 mL Teflon-lined steel autoclave and transferred into an oven preheated to the desired temperature. The autoclave is maintained at 200 °C for 16 h and then cooled to room temperature naturally. Samples are subsequently washed three times with deionized water, then finally with ethanol. The as-prepared material is finally collected by centrifugation and dried at room temperature. Production of small crystallite size was promoted by achieving high supersaturation conditions through the addition of ascorbic acid, when employing non-reductive solvents such as ethanol or isopropanol. Various compositions of reaction mixtures close to the stoichiometric composition were investigated.

High energy ball milling was used to obtain $Cu_2(Zn,Fe)SnS_4$ powders for the preparation of solarinks.[21,29] Cu powder (< 75 mm, 99%), Zn powder (purum, 99%), Fe fine powder (99%), Sn powder (puriss, 99%) and Sulfur flakes were used for milling. Recently Akhavan *et al.*[30] reviewed the synthesis and the use of CIGS and CZTS materials in PV devices.

2.5 Lead sulfide

The morphology of nanoparticles have an influence on their performance in hybrid polymer/nanoparticle solar cells.[31] Morphologies such as nanorods, tetrapods and hyperbranched nanoparticles usually are more difficult to synthesize reproducibly since additional steps maybe involved in their

synthetic methodology. However, they can potentially improve the electron hopping and charge transport in hybrid polymer/nanoparticle solar cells. Another important factor in nanoparticle synthesis is the presence of the stabilizing ligands. The ligands are insulating and provide a barrier to charge transport. In many instances ligand exchange is a common method used to replace long chain ligands with volatile shorter ligands, such as pyridine, which may be subsequently removed by heating. It is the use of various stabilizing ligands that allow the growth of particles with different shapes. Therefore research groups are constantly seeking new methodologies to synthesize particles with varying morphologies.

Salavati-Niasari and co-workers have developed a hydrothermal route to PbS nanoparticles in the form of cubes, star shapes and dendrites.[32–34] The PbS nanocubes were synthesized using [*bis*(salicylate)lead(II)] and L-cystein at an initial temperature of 180 °C .[32] In a typical experiment different molar ratios of the [*bis*(salicylate)lead(II)] and L-cystein were dissolved in a 100 mL distilled water under heating and stirring. After 20 minutes the solution was sealed into a Teflon lined stainless steel autoclave and heated to 180 °C for 3–24 h in an electric oven. After heating the autoclave was cooled to room temperature, the reaction products were then washed with distilled water and absolute ethanol several times to remove the by-products, followed by drying in an oven at 60 °C for 12 h. Molar ratios of 1 : 1 and 1 : 2 [*bis*(salicylate)lead(II)] to L-cystein gave the best formed cubic structures from the SEM measurements. The authors have also reported the preparation of PbS nanocrystals with varying morphologies using the same route. $Pb(NO_3)_2$ was reacted thioglycolic acid (TGA) at a relatively low temperature.[33] By varying the reaction temperature PbS particles in the form of star shaped dendrites were observed. The PbS nanodendrites had three dimensional structure consisting of a trunk, four symmetric arms and four rows of branches. Each branch is parallel to each other and perpendicular to the trunk. The arm also contains small particles in the 50–100 nm size range. The effects of the Pb^{2+} to TGA mole ratio in the starting solution on the morphology were investigated. The authors used the same route to synthesize PbS nanostructures with star-like and dendritic morphologies.[34] The hydrothermal reaction of lead (II) salicylate and thiourea was carried out at 160 °C for 3–20 hours. They also investigated the effects of the mole ratio of thiourea to lead precursor, reaction time and pH on the morphology of the PbS. Mighri and co-workers used a methanolic lead acetate-thiourea complex (PbAc-Tu) complex *via* various precipitation techniques based on the decomposition of the methanolic PbAc-Tu complex.[35] The chemical bath deposition (CBD) technique produced spherical PbS particles with an intricate network of flakes (Fig. 9a). The size of the particles is around 1.5–1.7 μm. The sonochemical bath deposition (SCBD) technique gave particles either cubic or spherical with sizes of 0.19–0.21 μm (Fig. 9**)**. The smaller sizes of the particles were attributed to the ultrasonic effect which causes the particles to break under ultrasonic frequency thereby producing smaller well shaped particles. The two capping groups used fat room temperature for the thermal decomposition were poly(vinyl-pyrrolidone) (PVP) and oleylamine (OA). The microwave assisted chemical bath deposition (MACVD) produced layers of thin flakes

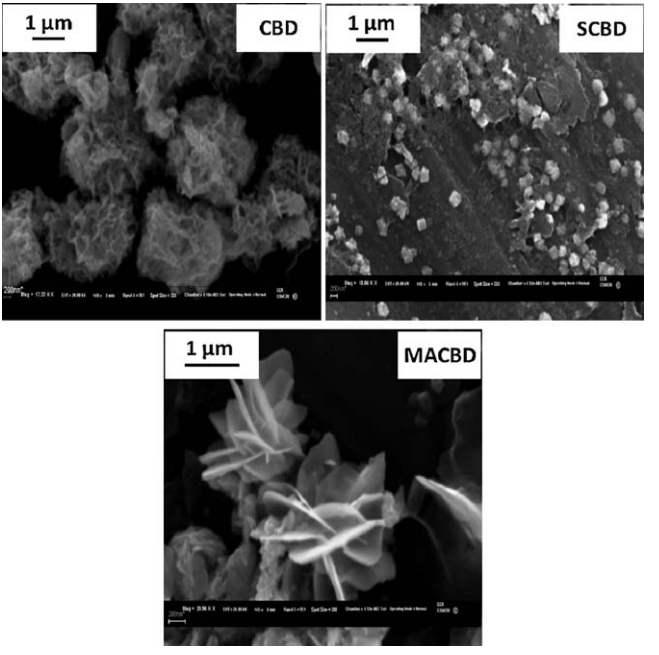

Fig. 9 Scanning electron micrographs of PbS particles produced *via* CBD, SCBD and MACBD techniques.[35]

with particle sizes varying from 0.5 to 1.5 µm (Fig. 9c). Using the capping assisted chemical bath deposition (CACBD) technique for PVP the PbAc-TU complex decomposed at room temperature to produce PbS nanoparticles. For OA the PbAc-TU complex decomposed thermally to give PbS nanoparticles.

The variation in decomposition routes lead to differences in size and particle shape. The use of $Pb(CH_3COO)_2 \cdot H_2O$ and CH_3CSNH_2 in ethylene glycol by the sonochemical method was also reported.[36]

Wang *et al*. synthesized PbS nanoparticles in oleic acid and a paraffin liquid mixture using a green approach. The PbS particles were then functionalized with a silica and polyethylene glycol (PEG) phospholipid dual-layer coating for biomedical applications.[37] Octadecene was replaced with paraffin and the authors argued that the liquid paraffin is more cost effective, environmentally friendly and chemically stable in the atmosphere than octadecene.

The PbS particles obtained had an average size of 3 nm with a cubic rocksalt structure. Wang and co-workers[38] reported the synthesis of single-crystalline hexagonal nanoplates and microspheres *via* a two phase method. Carbon disulfide (CS_2) was used as the sulfur source and a reaction medium and N′N-dimethylformamide (DMF) or dimethyl sulfoxide (DMSO) as the other reaction medium. The influence of the reaction parameters such as lead and solvent on the morphologies of the PbS were investigated. When $Pb(NO_3)_2$ was used in DMF uniform PbS cubes were obtained. Replacing the DMF with DMSO produced PbS microspheres with diameters of 2–4 µm. The high resolution TEM image showed that the spheres were made up of primary cubes 5–100 nm in diameter.

Semiconductor nanoparticles have been considered as building-blocks for the fabrication of large and ordered nanostructures that have new collective properties. There has been many reports recently of the self-assembly PbS nanoparticles into 2D arrays and superlattices. Kotov and co-workers investigated the self-assembly of nanostructures using star-like PbS superstructures as an example.[39] They found that the complexity of the particle geometry is related to several switches in self-assembly patterns (Fig. 10). They identified five stages in the formation of the PbS hyperbranched stars (1) nucleation of PbS nanoparticles with an average diameter of 31 nm; (2) assembly into 100–500 nm octahedral mesocrystals, (3) assembly into 1000–2500 nm hyperbranched stars; (4) assembly into six arm rods and finally (5) deconstruction into rods and cuboctahedral nanoparticles (Fig. 10). Simon and co-workers studied the structural ordering within the 3D PbS-organic colloidal superlattice.[40] The overall structure is closely related to the model depicting hard spheres with a large anistropic core and a relatively thin shell of organic molecules. They developed atomistic models that described the structure of the colloidal superlattice in reasonable agreement with experimental data. The PbS-colloidal superlattice system reported was classified as mesocrystals. The particles were truncated

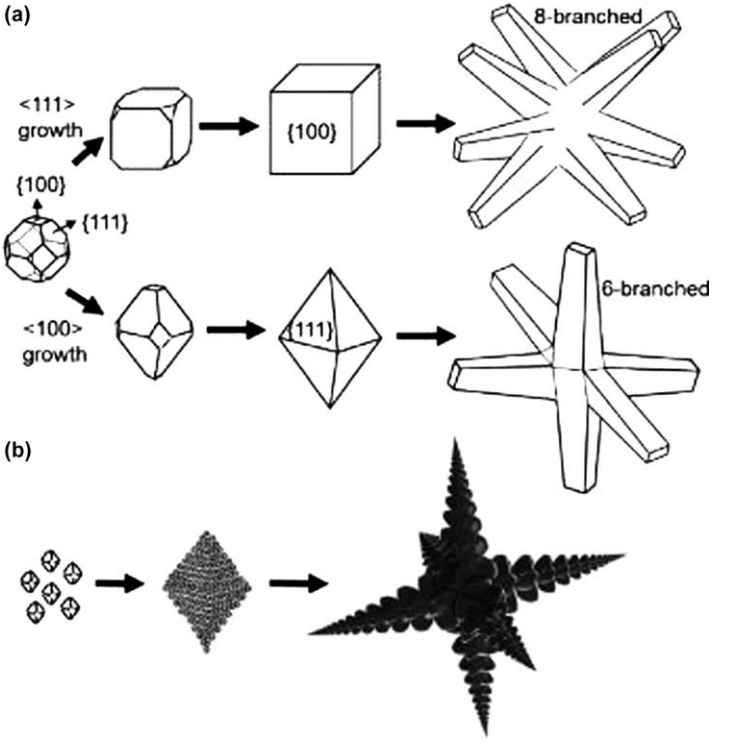

Fig. 10 (a) Growth of truncated octahedral seeds containing six {100} and eight {111} crystallographic faces into(first row) cubic and eight-branched crystals and (second row) octahedral and six-branched crystals. (b) Schematics of the nanoparticle assembly leading initially to octahedral mesocrystals (superparticles) and later to hierarchical hyperbranched superstructure. Reproduced from ref. 39 with permission from The American Chemical Society.

octahedrally shaped PbS nanocrystals stabilized by organic molecules which assemble into an *fcc* superlattice. Sticolli *et al*. studied near infrared emission from monomodal and bimodal PbS nanocrystal superlattices.[41] The PbS nanoparticles were classified by variation of synthetic parameters as those with a narrow monomodal size distribution (MSD) or alternatively a bimodal size distribution (BSD) characterized by two well defined and highly monodispersed populations.

The nanocystals were self-assembled onto a suitable substrate by the use of a solvent evaporation procedure resulting in a well-defined geometry depending on the PbS size and size ratio. The spectroscopic properties of the particles in solution and in the superlattice were investigated by steady state and time resolved photoluminescence measurements. The optical results confirm the occurrence of a Förster resonant energy transfer (FRET) mechanism between closed-packed neighbouring PbS nanocrystals.

Golan and co-workers developed a method for the directed assembly of oriented PbS nanocrystal arrays whereby the orientation of the nanocrystals is not determined by particle ordering.[42] They used the crystallization of the unbound alkylamine (either octadecylamine or hexadecylamine) to define the PbS nanocrystal spatial ordering and crystallographic orientation. The alkylamine surfactant molecules crystallize into lamellar sheets which function as a substrate.

The synthesis of PbS heterostructures have also gained some attention recently. Fang *et al*. reported the synthesis of PbS-Au heterodimer with the Au nanoparticles grown on the tips of PbS nanooctohedrons in ethylene glycol.[43] The surfactant, oleylamine plays a role in the formation of the PbS octahedrons. The charge transition at the interface between PbS and Au was observed by Uv-vis absorption spectroscopy. PbS nanoparticles with a cuboctahedral geometry were modeled based on HRTEM images of obtained from thin films deposited *via* the pulse electrodeposition technique.[44] The films were deposited on transparent conducting substrates and consisted of nanoparticles in the 2–20 nm size range. Using the atomic resolution images an atomic model with cuboctohedral morphology was proposed. A very good example of colloidal nanoheterostructures was demonstrated by the synthesis of PbTe-PbS Core shell nanoparticles (Fig. 11).[45] The particles had a narrow size distribution with good compositional control. The PbTe@PbS core-shell nanoparticles were used as building blocks for the bottom-up production of PbTe-PbS nanocomposites with tuned composition. The nanocomposites were characterized by higher electrical conductivities and lower thermal than the parent PbTe and PbS nanomaterials. The higher thermoelectric figures make them useful as functional materials in many potential applications.

PbS nanowires have been grown by the solution-liquid-solid growth using lead (II) diethyldithiocarbamate, $Pb(S_2CNEt_2)_2$ as a single-source precursor.[46] By optimizing reaction parameters such as coordinating/non-cordinating solvent, temperature and amount of Bi catalyst, nanowires crystalline, straight nanowires with smooth surfaces were grown. They also extended the work to compositionally tunable ternary $PbSeS_{1-1x}$ ($x = 0.23$, 0.39, 0.49, 0.68 and 0.90) nanowires.

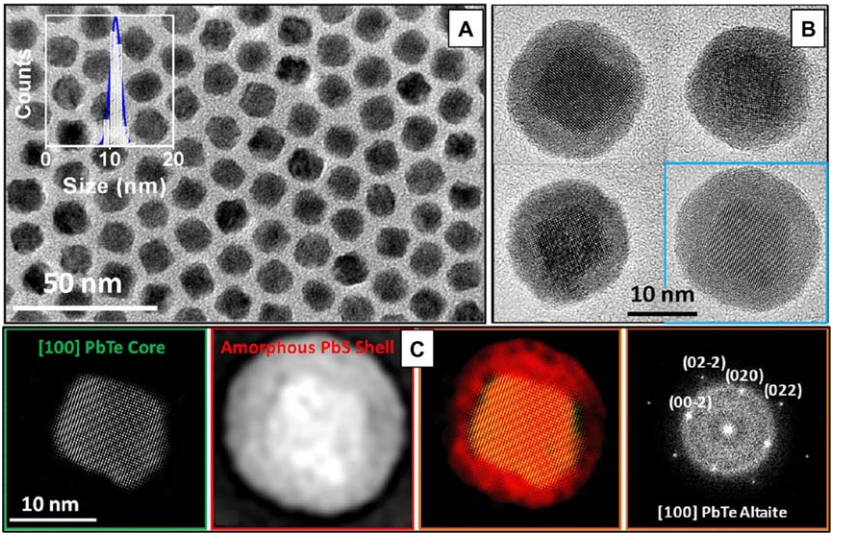

Fig. 11 (A) TEM micrograph of (PbTe)0.25@(PbS)0.75 coreshell nanoparticles having amorphous PbS shells. Inset displays the histogram of the particle size distribution. (B) HRTEM micrograph of a few (PbTe)0.25@(PbS)0.75 core-shell nanoparticles. (C) Power spectrum analysis of a (PbTe)0.25@(PbS)0.75 nanoparticle and PbTe and PbS crystallographic color maps. Reproduced from ref. 45 with permission from the American Chemical Society.

2.6 Tin sulfide

Rath and co-workers developed a novel colloidal synthesis of SnS nanoparticles.[47] They reacted $SnCl_2$ with triethanolamine and sodium sulfide in ethylene glycol. The particles were spherical in shape with an average diameter of 4 nm. The absorbance of the materials was in the Vis/NIR region. The optical absorption spectrum was confirmed by photothermal deflection spectroscopy (PDS) which gave a band gap of 1.6 eV. SnS nanoparticles have also been synthesized by reacting tin chloride ($SnCl_2$) and sodium sulfide (Na_2S) under ultrasound irradiation at room temperature.[48] The ultrasound technique was chosen because of it's advantages of easier composition control, low toxicity, better homogeneity, low temperature, lower cost and high yield. A study of the optical properties of the resultant SnS particles showed an absorption band edge shifted towards to a lower wavelength, with the direct band gap estimated at 1.74 eV. This measured band gap was in good agreement with the results of theoretical calculations of exciton energy based on the Hartree-Fock approximation. The SEM and TEM studies confirmed the spherical morphology of the particles. Chaki *et al*. synthesized SnS particles *via* a wet chemical route.[49] The SnS particles were assembled into pellets by hydraulic pressing. The electrical transport properties of the pellets were then studied. The dc resistivity-temperature curve showed that the dc resistivity decreases with increase in temperature thereby confirming the semiconducting behaviour of the particles. The photocatalytic properties of SnS_2 nanoparticles synthesized *via* a hydrothermal route were also studied.[50] The synthetic procedure involved the hydrothermal reaction between $SnCl_4 \cdot 5H_2O$ and thiourea ina 5 vol% Triton® aqueous solution. The results from the

degradation of formic acid in an aqueous solution demonstrate that the material has high visible lightphotocatalytic activity.

A hydrazine hydrate assisted diethylene glycol solution based synthesis of SnS was recently reported.[51] Diethylene glycol (DEG) is a polar solvent with less toxicity, low cost, relatively high boiling point and shows good dissolvability to many metal inorganic salts. Tin dichloride ($SnCl_2 \cdot 2H_2O$) was used as the tin source and thioacetamide as the sulphur source.

The hydrazine hydrate promotes the decomposition of the thioacetamide, thereby producing adequate HS^- ions resulting in the supersaturation of SnS which is needed for nucleation. At all reaction temperatures of 120, 140 and 180 °C. Nearly spherically shaped particles were obtained, with the particle size increasing with temperature.

SnS hollow nanoparticles were prepared by a two- step method by a combination of laser ablation and chemical etching (Fig. 12).[52] In the first step, laser ablation of a Sn target was carried out in an ethanol solution of thioacetamide forming Sn@SnS core-shell nanoparticles. Chemical etching was then done to remove the Sn cores. In the initial step, core shell particles with an average size of 40 nm were obtained. The XRD pattern revealed two phases, a tetragonal Sn and orthorhombic SnS. In the second step, chemical etching with dilute HCl produced spherical particles with sizes similar to the core-shell particles. The authors postulated that the SnS particles with a hollow structure should possess unique properties that could be used in various applications.

Yue *et al.* reported the synthesis of SnS homojunction nanowires on an aluminium foil substrate through Au catalyzed chemical vapour deposition technique.[53] The SEM images show the SnS nanowires with a tapered structure. The SnS nanowires form arrays with lengths in the range of 10 μm. The XRD results confirm the crystalline nature of the films with growth along the [101] plane. The application of the SnS nanowires in a solar cell was demonstrated. The study showed that the SnS nanowires have excellent potential for use in homojunction solar cells. The advantage is that the nanowires can be directly incorporated into the device structure in a simple fabrication procedure.

Honma and co-workers modified Graphene oxide nanosheets with Sn ions to form SnS_2 decorated graphene nanosheet (GNS) electrode materials.[54] The preparation of the SnS_2/GNS nanocomposites involved three steps. In the first

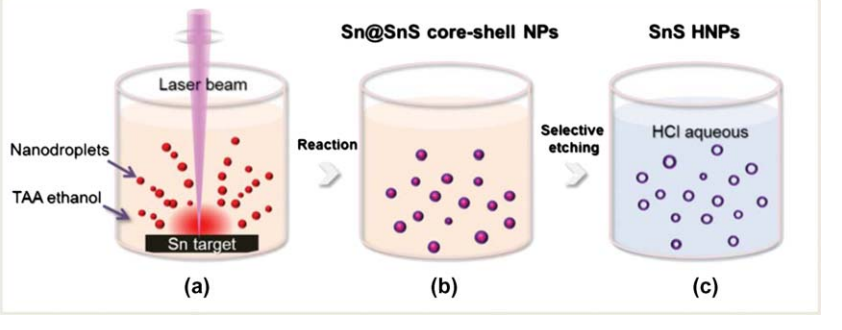

Fig. 12 Schematic formation of SnS HNPs by combining laser ablation and chemical etching. Reproduced from ref. 52 with permission from the Royal Society of Chemistry.

step the Sn ions were anchored on the graphene sheets through the functional group on the graphene oxide surface at very dilute conditions. This was followed by the addition of L(+) ascorbic acid to partly reduce the unutilized functional groups. In the final step thiourea was added as a sulfur source and subjected to hydrothermal conditions for SnS_2 formation. The XRD of the SnS_2/GnS composites reveal the presence of SnO_2 impurities, which are formed during the solution phase synthesis. However the diffraction pattern of the composites after the hydrothermal treatment displays no peaks assigned to SnO_2, an indication that the SnS_2 and SnO_2 are completely reduced to SnS. The TEM results of the show the presence of ultrafine SnS_2 nanoparticles distributed on the GnS surface. The average particle size of the SnS_2 is estimated between 2 and 3 nm in diameter. The Li-ion storage capacity of the nanocomposites was demonstrated to be much higher than its theoretical capacity. Graphene-SnS_2 were also prepared *via* a solvothermal method.[55] The SEM and TEM studies showed a homogenous distribution of SnS_2 particles on the graphene sheets. Electrochemical tests were carried out on the nanocomposites to determine their function as lithium-ion battery anode materials. The capacity and cyclic performance of the nanocomposites increased with increase in the amount of SnS_2 in the nanocomposites. This improvement in properties of the graphene/SnS_2 nanocomposite compared to pure SnS_2 was attributed to the synergistic effects between graphene sheets and SnS_2.

2.7 Iron sulfide

Iron sulfides have attracted renewed interest in recent years for solar cell applications owing to their suitable band gap, remarkable absorption coefficient, non-toxicity, and large abundance in the earth's crust. The use of nanodimensional iron sulfides as solar-ink has been considered one of the methods for the fabrication of solar cells in recent years. Accordingly, a number of methods have been developed in 2012 for the synthesis of iron sulfides nanocrystals in various shapes and sizes. Macpherson and Stoldt reported the synthesis of pyrite iron sulfide nanocubes by reacting $FeCl_2$ and elemental sulfur in alkylamines.[56]

In a detailed synthesis, $FeCl_2$, hexadecylamine and sulfur were heated to 250 °C under argon atmosphere for 3 h for the formation of nuclei. Once nucleation of the reaction was completed, the reaction vessel was cooled to room temperature to freeze the reaction. A portion of $FeCl_2$, sulfur and oleylamine were added to the reaction vessel and reheated to 200 °C for 9 h. This process was repeated for the complete growth of pyrite nanocrystals. The nanocrytsals obtained by this method after initial heating at 250 °C, are random oblate shaped, whereas cubes with large size distribution were obtained after the first stage of growth at 200 °C. However, the size distribution of the nanocubes was improved after the second stage growth. Figure 13 shows TEM images of FeS_2 nanocrystals obtained at different growth stages. The final FeS_2 nanocubes isolated by this method had a lateral size of 37 ± 11 nm. Absorption measurements of the nanocubes obtained at final stage of synthesis showed an indirect band gap around 1.1 eV along with two excitonic transitions at 1.9 eV and 3.0 eV.

Continuing the development of synthetic methods for pyrite FeS_2 nanocrystals, Korgel *et al.* reported the synthesis of FeS_2 nanocrystals.[57]

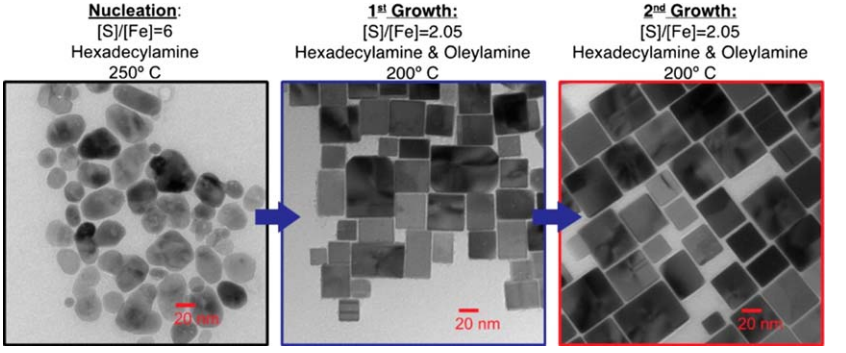

Fig. 13 TEM images of FeS_2 nanocrystals obtained at different growth stages. Reprinted with permission from Macpherson and Stoldt.,[56] Copyright © 2012 American Chemical Society.

$FeCl_2$ was heated to 220 °C along with octadecylamine, to this heated reaction mixture, elemental sulfur dispersed in diphenyl ether was injected and the resulting mixture was maintained at 220 °C for 3 h. FeS_2 nanocrystals synthesized by this method were 14.8 ± 3.6 nm in size (d), which were showed absorption band gap around 1.0 eV. The as synthesized nanocrystals were free from any secondary phases which were confirmed by Raman measurement. In order to substantiate the postulation made by number of researchers on the solar energy conversion properties of FeS_2, four different solar cell structures have been fabricated using FeS_2 nanocrystals synthesized using this method. The solar cell architectures fabricated in this study include Schottky junction, heterojunction, hybrid organic/nanocrystals device and typical p-n junction with CdS. Disappointingly, none of the device structures showed appreciable solar energy conversion efficiency. Nevertheless, these findings do not discourage the exploration of FeS_2 based solar cells, since the method of solar cell fabrication is crucially important to get a workable device. Morrish *et al.*, prepared FeS_2 through plasma assisted sulfurization of Fe_2O_3 nanorods.[58] For this, ~150 nm sized Fe_2O_3 nanorods were prepared by chemical bath deposition using $FeCl_3$ and $NaNO_3$ on FTO glass plates, which were further annealed at 550 °C for 20 min in air. Fe_2O_3 nanorods were converted to FeS_2 by sulfurization using a mixture of 10% H_2S : 90% Ar gas. FeS_2 prepared by this method contained both marcasite and pyrite phases, which was confirmed by Raman measurement. The authors reported that the prolonged sulfurization of F_2O_3 nanorods has reduced the presence of marcasite phase. However, the complete eradication of marcasite phase was not achievable by this method. The band gap of FeS_2 obtained by this method was 1.2 eV (direct). Xu *et al.* reported the synthesis of carbon coated FeS nanosheets.[59] For the synthesis, 1-dodecanthiol was injected into a vessel containing $Fe(acac)_3$ and oleylamine at 150 °C and then the reaction mixture was maintained at 220 °C for 20 min. After isolation of the reaction mixture, samples were annealed at 400 °C for 2 h under argon atmosphere to form carbon coated FeS. The isolated nanostructure was found to be troilite FeS phase with sheet morphology. The carbon coated FeS nanostructures as anode material for Li-ion batteries, and they have found these carbon coated FeS nanostructures to show 233 mAh/g specific capacity during the 100th cycle. Beal *et al.* reported the synthesis of $Fe_{1-x}S$

and Fe_3S_4 nanocrystals.[60] Reaction with $Fe(acac)_2$ and elemental sulfur in oleylamine at 200 °C for 4 h produced extremely thin sheets of Fe_3S_4. The same reaction above 300 °C for 30 min produced 70 nm $Fe_{1-x}S$ nanocrystals with hexagonal plate and prism morphologies. Magnetic measurement on Fe_3S_4 nanocrystals showed saturation magnetization value of 14.7 $Am^2\ kg^{-1}$ and a coercivity of 14 kA m^{-1}, whereas $Fe_{1-x}S$ showed 4.9 $Am^2\ kg^{-1}$ and a coercivity value of 110 kA m^{-1} at room temperature.

2.8 Copper sulfide

Copper sulfide is one of the solar cell materials, composed of earth abundant and non-toxic elements. Notably, copper sulfide exists in variable stoichiometries, which make it an interesting material for fundamental studies in addition to its photocatalytic and solar cell applications. The synthesis of hollow nanostructured materials has been interest for many synthetic chemists in recent years owing to their synthetic challenges. Xiong and Zeng reported the synthesis of multishelled copper sulfide hollow spheres.[61] In an interesting method, polyvinylpyrrolidone (PVP) coated Cu_2O spheres were initially synthesized by polyol method and then these Cu_2O nanospheres were ion-exchanged using thiourea and sodium sulfide for multishelled Cu_2S hollow spheres. Figure 14 shows TEM images of multi-shelled Cu_2S hollow spheres. The optical band gap of single, double and triple-shelled Cu_2S hollow spheres varied from 2.10 eV to1.49 eV and to 1.42 eV upon increasing the diameter of the spheres. Synthesis of

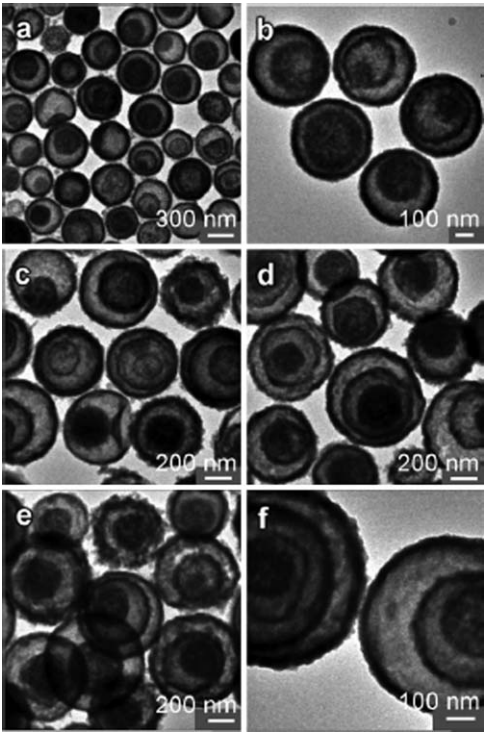

Fig. 14 TEM images of multishelled Cu_2S hollow spheres. Reprinted with permission from Xiong and Zeng.[61] Copyright 2012 John Wiley & Sons.

hierarchical hollow spheres of CuS at the interface of water and oil have been reported.[62,63] For this, thioacetamide dissolved in water and copper naphthenate dissolved in dimethylbenzene were allowed to react at the interface for 24 h at room temperature. The interfacial reaction produced amorphous hollow spheres. These amorphous spheres were autoclaved in ethanol at 60 °C for 96 h to yield hierarchical CuS hollow spheres.

Sun *et al*. reported the synthesis of polyhedral 26-facet hollow cages of Cu_7S_4 by the sacrificial template method.[64] Cu_2O template particles containing 26-facets were synthesized by reducing $Cu(CH_3COO)_2$ using glucose. These templates were then reacted with Na_2S at room temperature for the formation of Cu_2O/Cu_7S_4 core/shell particles. Cu_2O core was selectively removed using ammonia. SEM images of the hollow cages showed that the cages are in polyhedral structure, which contained rectangle, triangle and square shells. In continuation to the synthesis of caged copper sulfides, Vinokurov *et al*. reported the synthesis of hybrid Ru-Cu_2S nanostructures with morphologies of cages and nanonets.[65]

Hybrid nanostructures are beneficial for solar cell applications for better electron-hole separation. Ru-Cu_2S hybrid structures were synthesized by injecting $Ru(acac)_3$ in octylether into a vessel containing Cu_2S seeds in octadecylamine at 205 °C. The caged structures were sensitive to reaction temperature; those were only obtained at 205 °C. While, the same reaction at 210 °C and 220 °C yielded string-like and nano-net like structures of Ru respectively. Han *et al*. reported the synthesis of heteronanostructures of $Cu_{1.94}S$-ZnS, $Cu_{1.94}S$-ZnS-$Cu_{1.94}S$ and $Cu_{1.94}S$-ZnS-$Cu_{1.94}S$-ZnS-$Cu_{1.94}S$.[66] These heteronanostructures were synthesized by following a one-pot colloidal method using CuI and diethyldithiocarbamate complex of zinc in oleylamine. Heterostructures with morphologies of screw, dumbbell and sandwich-like were obtained by controlling the molar ratio of CuI and zinc complex. Figure 15 shows STEM-EDS elemental mapping of the dumbbell-like $Cu_{1.94}S$-ZnS-$Cu_{1.94}S$ heteronanostructure.

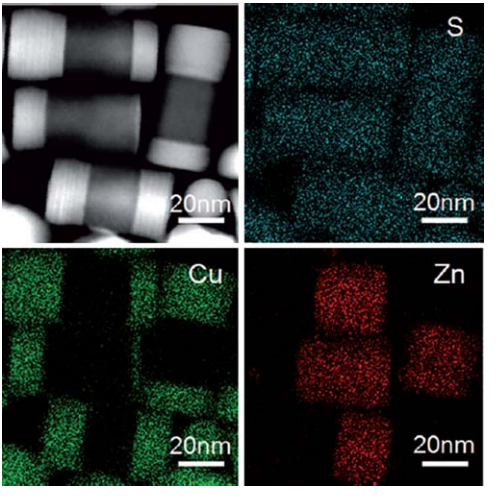

Fig. 15 STEM-EDX elemental mapping images of $Cu_{1.94}S$-ZnS-$Cu_{1.94}S$ heteronanostructures. Reprinted with permission from Han *et al*.[66] Copyright 2012 John Wiley & Sons.

Hierarchical CuS nanostructures by two-phase thermal method using ionic liquids have been synthesized.[67] The copper cupferronate and ionic liquid $[C_8min][BF_4]$ were kept in an autoclave at 150 °C for 10 h along with thiourea. The product isolated after 10 h was a dark green powder, which had a flower like morphology. The morphology of these structured varied from flower-like to nanodisks, dendrites and to irregular shapes when the reaction was carried out using different ionic liquids. Another two-phase synthesis was reported for the synthesis Cu_2S nanocrystals.[68] Dodecanethiol in toluene and copper sulphate in water were kept in a vessel and heated to 190 °C with a pressure of 220 ± 10 psi using microwave reactor. The Cu_2S obtained by this method were 7 nm spherical nanocrystals.

The use of single source precursors for the synthesis of copper sulfide nanocrystals is very well reported. Accordingly, copper complexes of alkylxanthates, mercaptobenzothiazole, thiobenzoates, dithiocarbamates and dithiolates were synthesized and used for the synthesis of copper sulfides with various morphologies. Abdelhady *et al.* used 1,1,5,5-tetra-isopropyl-2-thiobiuret complex of copper as a single source precursor for the synthesis of copper sulfide nanocrystals in a continuous flow method.[69] In this method, oleylamine solution copper complex was passed through microcapillary tube at different temperatures with a residence time of 4.2 s. Spherical Cu_7S_4 nanocrystals with 6.7 ± 1.6 nm, 10.8 ± 1.9 nm and 11.4 ± 2.4 nm were obtained at 170 °C, 200 °C and 230 °C respectively. Another single source precursor method for the synthesis of copper sulfide nanocrystals was reported.[70] In this method a copper complex of S-methyl dithiocarbazate was thermolysed in different high boiling solvents such as ethylene glycol, ethylenediamine, hydrazine hydrate and hexamethylenediamine at different temperatures. Depending on the solvents and temperatures, the morphologies of the nanoparticles varied from spherical to hexagonal disks and to rods. Sobhani *et al.* reported the use of [*bis*(thiosemicarbazide)copper(II)] chloride as single source precursor for the synthesis of copper sulfide nanoparticles by the hydrothermal method.[71] CuS nanoparticles obtained by this method are 20–50 nm in size with irregular shapes.

Du *et al.* reported the synthesis of ultrathin hexagonal nanosheets of copper sulfides by low temperature colloidal method.[72] In their method, elemental sulfur dissolved in an octylamine and oleylamine mixture was injected into a vessel containing CuCl in oleylamine and octylamine at 95 °C. The resulting reaction mixture was kept at 95 °C for 18 h, which produced a dark solution. The sample isolated by this method was the covellite CuS phase, which had nanosheet morphology with a thickness of 3.5 nm. Optical measurements of these CuS nanosheets showed an absorption peak at 465 nm and emission peaks at 418 and 445 nm. Further, these CuS nanosheets were used as an electrode material for Li-ion battery application, which showed discharge capacity of 642 m Ah/g after the 360th cycle. The authors have extended the synthetic method for the preparation of ultrathin nanostructures of other metal sulfides such as ZnS, Bi_2S_3 and Sb_2S_3. Hsu *et al.* reported the observation of localized surface plasmon resonance (LSPR) from $Cu_{2-x}S$ nanodisks.[73] For this study, $Cu_{2-x}S$ nanodisks were synthesized by thermolysing copper alkanethiolate

precursor in nitrogen atmosphere and air at temperatures between 190 and 200 °C. The aspect ratios of the nanodisks were 3.87 ± 0.25 and 4.65 ± 0.29 synthesized in air and nitrogen atmospheres respectively. Optical measurements of these nanodisks showed a LSPR peak in the near infrared region around 1800 nm corresponding to the out-of-plane LSPR mode. The observed LSPR peak was blue shifted when the aspect ratio of the nanodisks was increased. Ku *et al*. showed copper sulfide nanoparticles can be used as a photoacoustic contrast agent for deep tissue imaging.[74] For this purpose CuS nanoparticles were synthesised by an aqueous method using $CuCl_2$, sodium citrate and sodium sulfide at 90 °C. These nanoparticles had an average size of 11 ± 3 nm, which showed an absorption maximum at 990 nm. Imaging studies using these nanoparticles employing Nd : YAG laser at a wavelength of 1064 nm excitation showed CuS visualized CuS nanoparticles in mouse brain and rat lymph nodes.

2.9 Bismuth sulfide

Bismuth sulfide is a direct band gap semiconducting material that has a band gap around 1.3 eV. The use of bismuth sulfide nanostructures for solar cell applications has been considered in recent years. A few studies on bismuth sulfide nanocrystals synthesis with different morphologies have been reported in 2012. Hu *et al*. reported the synthesis of planar network of bismuth sulfide nanorods by a simple hydrothermal process.[75] The synthesis was carried out in a Teflon-lined autoclave containing bismuth nitrate and 1-pyrrolidine dithiocarboxylic acid ammonium salt in water at 170 °C for 8 h. SEM and TEM images of nanocrystals isolated from the reaction carried out after 8 h showed grid-shaped network of nanofabrics which was composed of 10–40 nm (*d*) nanorods. TEM images of samples obtained from experiments carried out for 2 and 4 h showed the presence of spherical nanoparticles, which is evident that the nanorods network may be formed through the oriented attachment of spherical nanoparticles. UV-Vis absorption spectra of sample isolated after 4h showed absorption peak centered at 679 nm.

Microwave synthesis of Bi_2S_3 nanostructures has been reported recently.[76] The synthesis involved microwave irradiation of $Bi(NO_3)_3 \cdot 5H_2O$ and thioglycolic acid in ethylene glycol. Nanocrystals with petal-like, flower like and urchin like structures were obtained depending on microwave power and bismuth to sulfur ratio. A solar cell constructed using these bismuth sulfide nanostructures as p-type semiconductor along with PbS nanoparticles (n-type) by a doctor blading method showed photovoltaic effect, but the solar cell parameters extracted from I-V measurement were not significant. Further to use of bismuth sulfide nanostructures for solar cell application, Liao *et al*. fabricated polymer/inorganic hybrid solar cell using P_3HT and Bi_2S_3 nanorods.[77] For this, Bi_2S_3 nanorods were prepared by injecting sulfur in olelylamine into a vessel containing bismuth chloride and oleylamine at 170 °C for 20 min. The isolated nanorods had 37.2 nm length and 6.1 nm width. These nanorods had a band gap of about 1.4 eV with conduction and valence bands of -3.8 eV and -5.2 eV respectively. For fabrication of polymer/inorganic hybrid solar cell, these Bi_2S_3 nanorods were blended with poly(3-hexylthiophene) (P3HT) in 1 : 1 ratio, which was spin coated on top of the PEDOT : PSS layer. J-V measurements on this

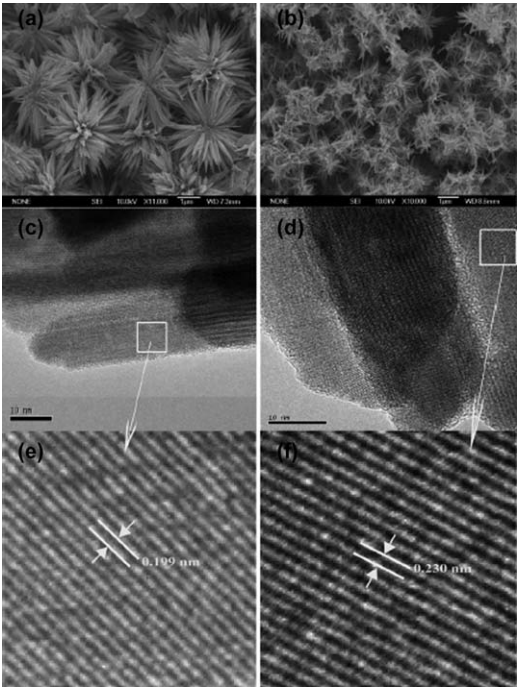

Fig. 16 SEM images for (a) Bi_2S_3-130 and (b) Bi_2S_3-211 samples. (c)–(f) are the HRTEM images of Bi_2S_3 products. Reprinted with permission from Zhang *et al.*[78] Copyright 2012 Royal Society of Chemistry.

solar cell showed current density of 0.230 mA cm^{-2} and open circuit voltage of 0.60 V. In an interesting study to find out the facet dependent activity of bismuth sulfide as low-cost counter-electrode for dye-sensitized solar cells (DSSC), synthesis of flower like Bi_2S_3 nanostructures with dominantly exposed facets of (130) and (211) have been reported.[78]

For this purpose, Bi_2S_3 nanostructures were synthesized by hydrothermal process using $Bi_2(NO_3)_3$, dithiocarbamide and polyvinylpyrolidone (PVP) in a Teflon-lined autoclave at 150 °C for 24h. SEM and TEM images of flower like structures obtained by this hydrothermal method are shown in Fig. 16. DSSC cell constructed using these nanostructures showed 3.5 % and 1.9 % efficiency from Bi_2S_3 with (130) and (211) facets respectively. The surface energy of these nanostructures with different facets was calculated and it was found that the (130) facet has more surface energy than (221), (211) and (040) facets.

2.10 Cadmium telluride

CdTe, a II-VI semiconductor with a narrow direct band gap (ca. 1.5 eV) has been identified as a material with applications in photovoltaic devices. The efficiency of CdS/CdTe thin film solar cells has not reached its true potential, however considerable work is being done to improve its efficiency by the use of nanosized CdTe particles. Some techniques have been designed to deposit ultra-thin, uniform layers of CdTe on various substrates while

others involve the synthesis of CdTe nanowires and quantum dots that are uniform in size and assembly.

Kim *et al*. grew epitaxial (001) CdTe on a (001) Si substrate by metal organic chemical vapour deposition (MOCVD).[79] A GaAs buffer layer was used between the CdTe and Si substrates which determined the single or poly-crystalline nature of the films. By use of a thin buffer layer of GaAs, a thin CdTe was epitaxially grown. The laser ablation technique was used to deposit CdTe thin films on glass substrates at room temperature.[80] CdTe powder was used as a target with growth time of 10 minutes The EDS measurements indicate an excess of Te, suggesting *p*-type conductivity, making them useful in photovoltaic applications. The wavelength of the laser had no marked effect on the structure, composition and optical properties of the films. Amin and co-workers used the magnetron sputtering technique to deposit high quality CdTe thin films.[81] The films were post treated with $CdCl_2$ by dipping or spin coating techniques. The optimum temperature was 390–420 °C for the cadmium chloride treatment resulting in 1.5–2.0 μm films. These high temperatures reduced the dislocation densities, structural defects and increased the crystallinity and grain size.

The sputtering approach was also used to prepare well aligned CdTe nanowires with different crystallographic phases.[82] Wurtzite or zinc blende CdTe was obtained by changing the growth temperature and deposition rate. Under high deposition temperature and low deposition rate zinc blende CdTe nanowires were obtained. When the substrate temperature is decreased and deposition rate increased the wurtzite phase is observed. The SEM images show that the nanowires have uniform perpendicular growth with an average length of 2.4 μm. The TEM images also show that the nanowires have an ordered array structure with no surface defects. The authors used a Gibbs free energy nucleation model to explain the formation of the different crystal phases under the growth conditions.

The synthesis of CdTe nanowires have also been reported using the closed space sublimation (CSS) method.[83] The CSS approach has been previously used for CdTe thin film deposition since it has the advantages of simplicity, high growth rate, easy scalability and high transport efficiency. A nano-sized Au droplet acted as a catalyst in the vapour-liquid solid (VLS) growth mechanism. The effects of varying the temperature gradient and growth time were investigated. They found that growth times of 5, 15 and 30 minutes produced CdTe nanowires. An increase in the temperature gradient resulted in the formation of microwires and sphere-shaped microstructures. The preparation of CdTe nanowires is an important development in solar cell research as they are known to improve the efficiency of CdTe-based solar cells due to the shorter travel of carriers.

Kraft *et al*. used very low temperatures (190–300 °C) using an advanced physical vapour deposition (PVD) process to deposit CdTe layers which were then processed to solar cells.[84] Higher deposition temperature gave larger grains, with smoother compact structures for temperatures between 200 and 300 °C. At temperatures of 180 and 190 °C non-uniform grains were observed. At 300 °C conversion efficiencies of up to 11.7% were obtained. Ding *et al*. reported a novel non-organometallic phosphine-free synthesis of CdTe nanoparticles.[85] They prepared the phosphine-free Te precursor by

passing H_2Te directly into oleylamine in 1-octadecene at room temperature forming the oleylammonium telluride salt. The Te^{2-} from the salt then reacts with the Cd precursor. The authors argue that the route does not require any air sensitive and expensive materials and employs relatively low temperatures. Thioglycolic acid (TGA) is a commonly used capping group for water-soluble CdTe nanoparticles. Zhang *et al*. reported the synthesis of TGA capped water soluble CdTe nanoparticles using K_2TeO_3 as the Te source and $NaBH_4$ as the reducing agent.[86] $NaBH_4$ has two roles, the first is to rapidly reduce Te^{4+} to Te^{2-} and the second to provide a protective surrounding to avoid the oxidation of Te^{2-} during the nanoparticle growth. They also found that under certain pH there is partial hydrolysis of the TGA releasing the S^{2-}, resulting in the formation of CdS on the surface of the CdTe. The extra CdS shell passivates the surface trap states and enhances the PL quantum yield. Josh and co-workers also reported increased quantum yields for TGA capped CdTe quantum dots that were irradiated.[87] They attributed this increase in quantum yields with low doses of radiation to the formation of the CdS shell after the TGA dissociates into sulphur ions. Water soluble CdTe with high emission properties synthesized *via* a hydrothermal route were also reported by Kim *et al*.[88] They used *N*-acetyl-L-cysteine thiol ligand instead of TGA as the capping group. They found that the pH of the precursor solutions play an important role in the monodispersity of the particles, with the best quality particles obtained at pH 5. Prolonged reaction times gave the higest PL quantum yields. This was attributed to the formation of the CdS shell on the CdTe. Revaprasadu and co-workers synthesized cysteine and triethanolamine capped CdTe nanoparticles have been synthesized using a simple aqueous solution based method.[89] Tellurium was reduced in solution by $NaBH_4$ in water to produce Te^{2-} ions, followed by the simultaneous addition of an aqueoussolution of cadmium chloride or other cadmium source (acetate, carbonate and nitrate) and solution of L-cysteine ethyl ester hydrochloride or triethanolamine. The effect of capping agent on the size, structure and morphology of the as-synthesized nanoparticles was investigated.

3 Conclusions

In recent years there has been an exponential growth in research into chalcogenide-based materials that have potential in solar cell applications. The use of earth abundant and non-toxic elements to form compound semiconductor nanoparticles has become an important focus in this area. There have been many advances in the control of particle size, shape and processing of nanomaterials to form uniform assemblies as thin films for solar cells.

References

1 D. B. Mitzi, O. Gunawan, T. K. Todorov, K. Wang and S. Guha, *Sol. Energy. Mat. Sol. C*, 2011, **95**, 1421.
2 S. H. Mousavi, T. S. Müller and P. W. de Oliveira, *J. Colloid Interf. Sci.*, 2012, **382**, 48.
3 Y.-G. Chun, K. H. Kim and K. H. Yoon, *Thin Solid Films*, 2005, **46**, 480–481.

4 C. P. Liu and C. L. Chuang, *Sol Energy*, 2012, **86**, 2795.
5 C. P. Liu and C. L. Chuang, *Powder Technol*, 2012, **229**, 78.
6 M. Yuan, D. B. Mitzi, W. Liu, A. J. Kellock, S. J. Chey and V. R. Deline, *Chem. Mater.*, 2010, **22**, 285.
7 M. Yuan, D. B. Mitzi, O. Gunawan, A. J. Kellock, S. J. Chey and V. R. Deline, *Thin Solid Films*, 2010, **519**, 852.
8 S. Zhang, L. Wu, R. Yue, Z. Yan, H. Zhan and Y. Xiang, *Thin Solid Films*, 2013, **527**, 137.
9 Y. Xiang, X. Zhang and S. Zhang, *J. Solid State Chem.*, DOI: 10.1016/j.jssc.2013.06.012.
10 A. Hemati, S. Shrestha, M. Agarwal and K. Varahramyan, *J. Nano Mat*, 2012, Article ID 512409, 6 pages, DOI: 10.1155/2012/512409.
11 (a) V. Raghavan, *J. Phase Equilib. Diffus.*, 2004, **25**, 450; (b) P. B. Barton Jr., *Econ. Geol.*, 1973, **68**, 455; (c) S. R. Hall and Y. M. Stewart, *Acta Crystallogr., Sect. B*, 1973, **29**, 579.
12 P. Kumar, S. Uma and R. Nagarajan, *Chem. Commun.*, 2013, **49**, 7316.
13 D. Liang, R. Ma, S. Jiao, G. Pang and S. Feng, *Nanoscale*, 2012, **4**, 6265.
14 S. D. Disale and S. S. Garje, *Appl. Organometal. Chem.*, 2009, **23**, 492.
15 K. A. Ngoen, T. Thongtemb, S. Thongtema and A. Phuruangrat, *Mater. Lett.*, 2013, **101**, 9.
16 Y. Cui, R. Deng, G. Wang and D. Pan, *J. Mater. Chem.*, 2012, **22**, 23136.
17 L. Ai and J. Jiang, *Nanotechnology*, 2012, **23**, 495601.
18 C. Yan, C. Huang, J. Yang, F. Liu, J. Liu, Y. Lai, J. Lib and Y. Liua, *Chem. Commun.*, 2012, **48**, 2603.
19 X. Zhang, N. Bao, K. Ramasamy, Y. Hsiang, A. Wang, Y. Wang, B. Linb and A. Gupta, *Chem. Commun.*, 2012, **48**, 4956.
20 C. Huang, Y. Chan, F. Liu, D. Tang, J. Yang, Y. Lai, J. Liac and Y. Liua, *J. Mater. Chem. A*, 2013, **1**, 5402.
21 C. L. Azanza Ricardo, M. S. Su'ait, M. Müller and P. Scardi, *J. Power Sources*, 2013, **230**, 70.
22 M. Pal, N. R. Mathews, R. Silva Gonzalez and X. Mathew, *Thin Solid Films*, 2013, **535**, 78.
23 M. Li, W.-H. Zhou, J. Guo, Y.-L. Zhou, Z.-L. Hou, J. Jiao, Z.-J. Zhou, Z.-L. Du and S.-X. Wu, *J. Phys. Chem. C*, 2012, **116**, 26507.
24 S. K. Saha, A. Guchhait and A. J. Pal, *Phys. Chem. Chem. Phys.*, 2012, **14**, 8090.
25 M. Edler, T. Rath, A. Schenk, A. Fischereder, W. Haas, M. Edler, B. Chernev, B. Kunert, F. Hofer, R. Resel and G. Trimmel, *Mater. Chem. Phys.*, 2012, **136**, 582.
26 K. K. Patel, D. V. Shah and V. Kheraj, *Solid State Physics*, Proceedings of the 57th DAE Solid State Symposium 2012, 2013, **1512**, 185.
27 S. W. Shin, J. H. Han, C. Y. Park, S.-R. Kim, Y. C. Park, G. L. Agawane, A. V. Moholkar, J. H. Yun, C. H. Jeong, J. Y. Lee and J. H. Kim, *J. Alloy Compd.*, 2012, **541**, 192.
28 O. Zaberca1, F. Oftinger, J. Y. Chane-Ching, L. Datas, A. Lafond, P. Puech, A. Balocchi, D. Lagarde and X. Marie, *Nanotechnology*, 2012, **23**, 185402.
29 Q. Chen, S. Cheng, S. Zhuang and X. Dou, *Thin Solid Films*, 2012, **520**, 6256–6261.
30 V. A. Akhavan, B. W. Goodfellow, M. G. Panthani, C. Steinhagen, T. B. Harvey, C. J. Stolle and B. A. Korgel, *J. Solid State Chem.*, 2012, **189**, 2.
31 B. R. Saunders, *J Colloid Interf. Sci.*, 2012, **369**, 1.
32 H. Emadi and M. Salavati-Niasari, *Superlattice Microst.*, 2013, **54**, 118.
33 M. Salavati-Niasari, D. Ghanbari and M. R. Loghman-Estarki, *Polyhedron*, 2012, **35**, 149.

34 M. Salavati-Niasari and Davood Ghanbari, *Particuology*, 2012, **10**, 628.
35 J. D. Patela, F. Mighria, A. Ajji and T. K. Chaudhuri, *Mater. Chem. Phys.*, 2012, **132**, 747.
36 A. Phuruangrat, S. Thongtem, T. Thongtem and B. Kuntalue, *Dig. J. Nanomater. Bios.*, 2012, **7**(4), 1413.
37 D. Wang, J. Qian, F. Cai, S. He, S. Han and Y. Mu, *Nanotechnology*, 2012, **23**, 245701.
38 Q. Han, F. Jin, W. Yang, D. Sun and X. Wang, *Mater. Lett.*, 2012, **69**, 10.
39 A. Querejeta-Fernandez, J. C. Hernandez-Garrido, H. Yang, Y. Zhou, A. Varela, M. Parras, J. J. Calvino-Gamez, J. M. Gonzalez-Calbet, P. F. Green and N. A. Kotov, *ACS Nano*, 2012, **6**(5), 3800.
40 P. Simon, E. Rosseeva, I. A. Baburin, L. Liebscher, S. G. Hickey, R. Cardoso-Gil, A. Eychmller, R. Kniep and W. Carrillo-Cabrera, *Angrew Chem. Int. Ed.*, 2012, **51**, 10776.
41 M. Corricelli, F. Enrichi, D. Altamura, L. De Caro, C. Giannini, A. Falqui, A. Agostiano, M. L. Curri and M. Striccoli, *J. Phys. Chem. C*, 2012, **116**, 6143.
42 A. Rabkin, N. Belman, J. Israelachvili and Y. Golan, *Langmuir*, 2012, **28**, 15119.
43 Z. Fang, X. Wang, Q. Wang, C. Wang, F. Fan and X. Liu, *Micro. Nano Lett.*, 2012, **7**(2), 101.
44 N. R. Mathews, C. Ángeles–Chávez, M. A. Cortés-Jácome and J. A. Toledo Antonio, *Electrochim Acta*, 2013, **99**, 76.
45 M. Ibanez, R. Zamani, S. Gorsse, J. Fan, S. Ortega, D. Cadavid, J. R. Morante, J. Arbiol and A. Cabot, *ACS Nano*, 2013, **7**(3), 2573.
46 A. C. Onicha, N. Petchsang, T. H. Kosel and M. Kuno, *ACS Nano*, 2012, **6**(3), 2833.
47 C. Prastania, M. Nanub, D. E. Nanub, J. K. Ratha and R. E. I. Schroppa, *Mater. Sci. and Eng. B*, 2013, **178**, 656.
48 Y. Azizian-Kalandaragh, A. Khodayari, Z. Zeng, C. S. Garoufalis, S. Baskoutas and L. C. Gontard, *J. Nanopart. Res.*, 2013, **15**, 1388.
49 S. H. Chaki, M. P. Deshpande, M. D. Chaudhary, J. P. Tailor, K. S. Mahato, *AIP Conference Proceedings*, 2013, **1512**, 966.
50 R. Lucena, F. Fresno and J. C. Conesa, *Appl. Catal. A-Gen*, 2012, **100**, 102112.
51 L. Ren, Z. Jin, S. Cai, J. Yang and Z. Hong, *Cryst. Res. Technol*, 2012, **47**(4), 461.
52 M. Sun, J. Yang, T. Lin and X. Du, *RSC Adv.*, 2012, **2**, 7824.
53 G. Yue, Y. Lin, X. Wen, L. Wang and D. Peng, *J. Mater. Chem.*, 2012, **22**, 16437.
54 M. Sathish, S. Mitani, T. Tomai and I. Honma, *J. Phys. Chem. C*, 2012, **116**, 12475.
55 C. Shen, L. Ma, M. Zheng, B. Zhao, D. Qiu, L. Pan, J. Cao and Y. Shi, *J. Solid State Electr.*, 2012, **16**, 1999.
56 H. A. Macpherson and C. R. Stoldt, *ACS Nano*, 2012, **6**, 8940.
57 C. Steinhagen, T. B. Harvey, C. J. Stolle, J. Harris and B. A. Korgel, *J. Phys. Chem. Lett.*, 2012, **3**, 2352.
58 R. Morrish, R. Silverstein and C. A. Wolden, *J. Am. Chem. Soc.*, 2012, **134**, 17854.
59 C. Xu, Y. Zeng, X. Rui, N. Xiao, J. Zhu, W. Zhang, J. Chen, W. Liu, H. Tan, H. H. Hng and Q. Yan, *ACS Nano*, 2012, **6**, 4713.
60 J. H. L. Beal, P. G. Etchegoin and R. D. Tilley, *J. Solid. State. Chem*, 2012, **189**, 57.
61 S. Xiong and H. C. Zeng, *Angew. Chem. Int. Ed.*, 2012, **51**, 949.
62 D. Jiang, W. Hu, H. Wang, B. Shen and Y. Deng, *Chem. Eng. J*, 2012, **189–190**, 443.

63 D. Jiang, W. Hu, H. Wang, B. Shen and Y. Deng, *J. Mater. Sci.*, 2012, **47**, 4972.
64 S. Sun, D. Deng, C. Kong, X. Song and Z. Yang, *Dalton Trans.*, 2012, **41**, 3214.
65 K. Vinourov, J. E. Macdonald and U. Banin, *Chem. Mater.*, 2012, **24**, 1822.
66 S. K. Han, M. Gong, H.-B Yao, Z.-M. Wang and S.-H. Yu, *Angew. Chem. Int. Ed.*, 2012, **51**, 6365.
67 K. Yao, W. Lu, X. Li and J. Wang, *J. Solid. State. Chem.*, 2012, **196**, 557.
68 Y. Wang, X. Ai, D. Miller, P. Rice, T. Topuria, L. Krupp, A. Kellock and Q. Song, *Cryst. Eng. Comm.*, 2012, **14**, 7560.
69 A. L. Abdelhady, M. A. Mailk and P. O'Brien, *Mater. Sci. Semiconductor Process*, 2012, **15**, 218.
70 P. Bera and S. I. Seok, *Solid State Sci.*, 2012, **14**, 1126.
71 A. Sobhani, M. Salavati-Niasari and S. M. Hosseinpour-Mashkani, *J. Clust. Sci.*, 2012, **23**, 1143.
72 Y. Du, Z. Yin, J. Zhu, X. Hunag, X.-J. Wu, Z. Zeng, Q. Yan and H. Zhang, *Nat.Commun.*, DOI: 10.1038/ncomms2181.
73 S.-W. Hsu, W. Bryks and A. R. Tao, *Chem. Mater.*, 2012, **24**, 3765.
74 G. Ku, M. Zhou, S. Song, Q. Huang, J. Hazle and C. Li, *ACS Nano.*, 2012, **6**, 7489.
75 P. Hu and Y. Cao, *Cryst. Eng. Commun.*, 2012, **14**, 7694.
76 M. Yousefi, M. Sabet, M. Salavati-Niasari and H. Emadi, *J. Clust Sci.*, 2012, **23**, 511.
77 H.-C. Liao, M.-C. Wu, M.-H. Jao, C.-M. Chuang, Y.-F. Chen and W.-F. Su, *Cryst. Eng. Comm.*, 2012, **14**, 3645.
78 H. Zhnag, L. Yang, Z. Liu, M. Ge, Z. Zhou, W. Chen, Q. Li and L. Liu, *J. Mater. Chem.*, 2012, **22**, 18572.
79 K. C. Kim, S. H. Baek, W. C. Choi, H.J. Kim, J. D. Song and J. S. Kim, *Mater. Lett*, 2012, **87**, 141.
80 F. De Moure-Flores, J .G. Quinones-Galvan, A. Guillen-Cervantes, J. Santoyo-Salazar, A. Hernandez-Hernandez, G. Contreras-Puente, M. de la, L. Olvera and M. Melendez-Lira, *Mater. Lett*, 2013, **92**, 94.
81 M. A. Islam, Q. Huda, M. S. Hossain, M. M. Aliyu, M. R. Karim, T. Razykov, K Sopian and N. Amin, *Curr. Appl. Phys.*, 2013, **13**(2), 115.
82 B. Luo, Y. Deng, Y. Wang, M. Tan, L. Cao and W. Zhu, *Cryst Eng Comm*, 2012, **14**, 7922.
83 G. Yang, Y. Jung, S. Chun, D. Kim and J. Kim, *Thin Solid Films*, 2013, Article in press.
84 C. Kraft, C. Heisler, A. Harpf, M. Brückner, H. Metzner and W. Wesch, *Thin Solid Films*, 2012, **522**, 145.
85 C. Xu, A. Kong, H. Ding and Y. Shan, *Mater. Lett*, 2012, **82**, 45.
86 S. Wu, J. Dou, J. Zhang and S. Zhang, *J. Mater. Chem*, 2012, **22**, 14573.
87 P. S. Chethan, M. P. Joshi, S. R. Mohan, T. S. Dhami, J. Khatei, K. S. Koteshwar Rao, L. M. Kukreja and S. Ganesh, *Adv. Mater. Lett.*, 2013, **4**(6), 454.
88 H. Bu, H. Kikunaga, K. Shimura, K. Takahasi, T. Taniguchi and D. Kim, *Phys. Chem. Chem. Phys*, 2013, **15**, 2903.
89 N. Mntungwa, V. S. R. Pullabhotla and N. Revaprasadu, *Colloids Surface B*, 2013, **101**, 450.

Direct write nanolithography

B. Radha[a] and G.U. Kulkarni*[b]
DOI: 10.1039/9781849737623-00058

The article presents comprehensive literature on 'direct write' lithography methods for patterning nanomaterials. The resist or the direct-write 'ink', is an important ingredient of any lithography technique, and is made to play an active role in direct writing thereby tailoring the properties of the end product, while reducing the number of process steps. Direct writing also enables a good control on the composition and morphology of the nanomaterial in pattern, be it a nonstoichiometric inorganic compound, an organic material or a biomolecule. The survey includes e-beam lithography, soft and nano imprint lithography, laser based lithography as well as scanning probe lithography. A brief outlook at the end provides future course of lithography techniques in general and direct writing in particular.

1 Introduction

Lithography processes are inevitable; while the microelectronics industry relies heavily on patterning materials in devices employing lithography processes, the latter are assuming importance in microfluidics and energy devices as well.[1] In all known lithography processes, there is always a compromise between the resolution and the throughput.[2] The resolution of a lithography technique, going with the convention, refers to the smallest pitch with which features can be patterned while its throughput is the area patterned per unit time (sec). For instance, news-paper printing has a very high throughput, but a poor resolution of $\sim$10–20 μm, which suffices for casual reading (see the plot in Fig. 1).[3] On the other hand, scanning tunneling microscopy (STM) represented on the same plot operates down to atomic resolution, but with a very low throughput.

To arrive at a practical compromise between throughput and resolution, is to resort to direct write techniques,[4] where the number of lithography process steps is minimized. Conventional lithography techniques involve multiple process steps[5] which are usually cumbersome, time consuming and cost-prohibitive when applied to high resolution large area patterning. There are crucial steps such as metal etching and lift-off, where there is a high probability of contaminating the patterned material with the external agents. In "direct-write" lithography, the process steps such as development, etching and lift-off are avoided, thus making the process flow much simpler. In this context, there is an increasing emphasis on processable single source precursors, which can directly lead to the desired materials.[6–8] The chemistry of single source precursors is rich[9] and well-studied;[10] if applied in the context of direct-write inks, it would make an enormous

[a]*Department of Materials Science and Engineering, Northwestern University, 2145 Sheridan Road, Evanston, IL 60208, USA*
[b]*Chemistry and Physics of Materials Unit and DST Unit on Nanoscience, Jawaharlal Nehru Centre for Advanced Scientific Research, Jakkur P.O., Bangalore 560 064, India.*
**E-mail: kulkarni@jncasr.ac.in*

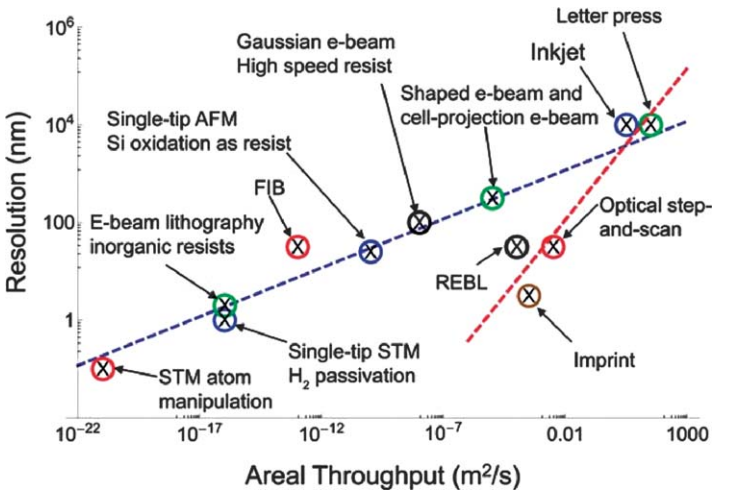

Fig. 1 Resolution versus areal throughput for various lithography techniques. Reprinted with permission from The Royal Society of Chemistry.[3]

impact. Thus, direct writing using suitable inks has become popular in many beam based techniques (electron beam,[11–16] focused ion beam,[17–19] laser lithography[20–22]). Recently, direct methods have been explored for large area patterning techniques such as soft lithography[14,23–26] and nano-imprinting[27–29] as well. Single source precursors which can be made to flow into narrow microchannels of a mold are highly desirable for these techniques.

1.1 Direct write lithography

Specifically, direct write lithography techniques aim at the following:

a. Site specific synthesis of nanomaterials: Currently, the emphasis in nanomaterials research is shifting from discovery to production. Taking a concoction of nanomaterials in a bottle to the processing steps of manipulating and placing them in circuits is rather a challenge. Various aspects in this regard namely alignment, registration, and interconnection of nanomaterials with multiple functionalities in circuits, calls for a paradigm shift away from conventional approaches of present day fabrication. Direct-write technologies aim at resolving these issues. Instead of using conventional polymeric/organic resists for patterning, followed by a pattern transfer to the nanomaterial, metal-organic resists can be used as direct write inks for lithography. This potentially implies on-site synthesis, which calls for materials design and synthetic routes, which are compatible with lithography processes.

b. Minimum number of process steps: Direct write lithography aims at cutting down number of process steps as well as avoiding unwanted species from processing. This leads to integration of chemical recipes with device fabrication for producing patterned functional materials.

c. Feature size reduction: Miniaturization being an important direction for many applications, direct-write lithography aims at an in-built engineering of feature size reduction, aided by the precise control of functional material content in direct write inks.

d. Enhanced lithography efficiency and high throughput: Metal-organic based direct write precursor materials can also be useful in improving the efficiency of the lithography process itself. For instance, in beam based patterning techniques, metal-organic precursors provide enhanced beam scattering and thus reduce the amount of beam energy required for patterning by many folds (*vide infra*), thus increasing the process efficiency.

1.2 Direct write 'ink'

A direct-write precursor 'ink' is a single source precursor, with all the ingredients that are required in the product film, incorporated into one precursor. General properties of such an ink are as below.

a. Processability: The ink should possess reasonable solubility in common solvents. It should form smooth films upon coating a few drops of solution on to a surface.

b. Ease of synthesis: Synthesis of Single source precursor should not be limited by poor yields of product. The synthesis route of a direct write precursor ink should have the scope to scale up with reliable chemical yields.

c. Post lithography treatment: After a lithography process, simple processing steps should lead to functional materials from single source precursors. Curing the precursor by radiation or heat, preferably at moderate temperatures to lead to the final product is a viable goal. Residual carbon and other impurities in the end-product are to be kept minimal.

d. Precursor chemistry: Ability of a single source precursor ink to form various materials by merely tuning the thermolysis conditions is an additional asset for it to be a direct-write ink.

e. Adaptability: A direct-write ink should be amenable to processing with the existing lithography techniques, not demanding for sophisticated modifications or improvements. And the ink itself should be stable to withstand the processing conditions.

2 Direct write 'inks' for various lithography techniques

We discuss the direct write material inks in the context of various lithography techniques. Although the name implies direct writing of a material, it is used in a broader sense and many of the techniques that fall into this category do not simply involve writing of a material. To illustrate the difference between conventional and direct write lithography methods, two techniques are taken as examples and the process steps are shown in Fig. 2 in brief. E-beam lithography involves direct writing of electron beam onto precursor thin films whereas molding/imprinting involves the use of ''direct'' precursor ink solutions in the process flow.

2.1 Direct write electron-beam lithography

Electron beam lithography (EBL) is a high-resolution (sub-20 nm) direct write technique using electrons for patterning. It is a serial technique, which can pattern fine features with high density.[30] Conventionally, polymeric compositions such as poly(methylmethacrylate) (PMMA), ZEP (Zeon Corp) *etc*., are used as resists for EBL.[31] An e-beam resist is sensitive to e-beam and undergoes either faster dissolution or remains insoluble in a

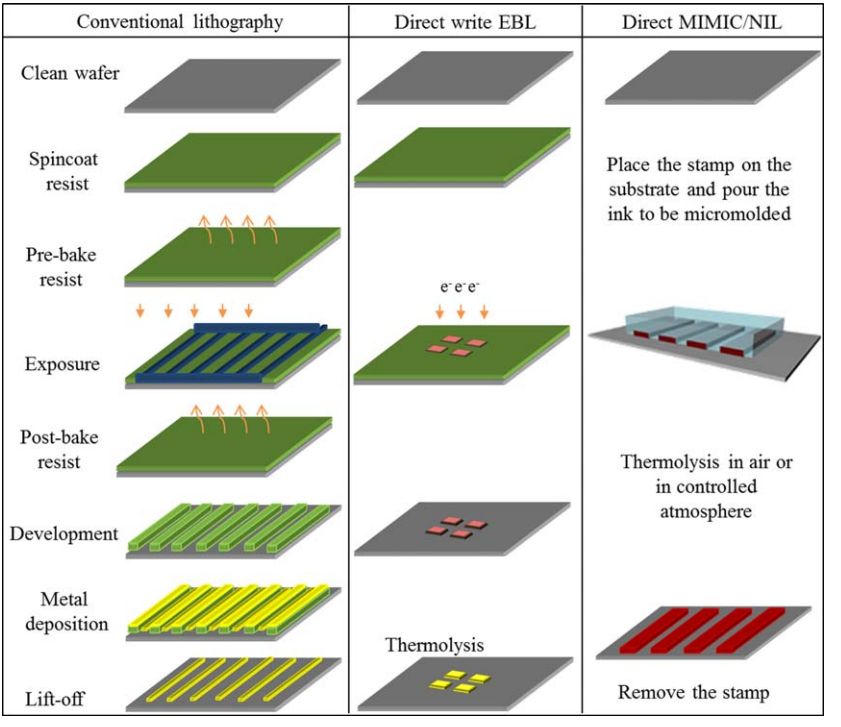

Fig. 2 Conventional lithography versus direct-write lithography methods. In conventional lithography, resist coating is followed by hardening and exposure to create patterns after development. The patterns are transferred to desired material by lift-off or etching. In direct-write lithography, patterns are directly created onto the desired material.

solvent (called as developer) after exposure. For instance, if the regions exposed to the e–beam remained on the substrate after development, it is a negative–tone resist behavior. The number of electrons dosed per unit area of the resist (expressed as $\mu C.cm^{-2}$), to achieve the desired chemical response in the resist is called the electron dose.[32] The optimum dose refers to the dose at which the measured line-width after development, is equal to the designated line-width.

For an e-beam resist, the characteristic properties are its contrast and sensitivity. Contrast curves (also called as response curves) can be obtained by plotting the thickness remaining after the development process versus the e-dose (Fig. 3) and these curves are used for determining the contrast and sensitivity of the resist. The sensitivity is defined as the critical dose required for removal (positive) or retention (negative) of half the thickness of the resist film. Resist sensitivity increases with increasing molecular weight. The sensitivity of a resist can be obtained from its contrast curve. Further, the resolution achievable with a resist is defined in terms of its contrast parameter, γ: the higher the contrast, the higher the resolution. For a negative resist,

$$\gamma = \frac{1}{\log\left(\frac{d_0}{d_i}\right)} \tag{1}$$

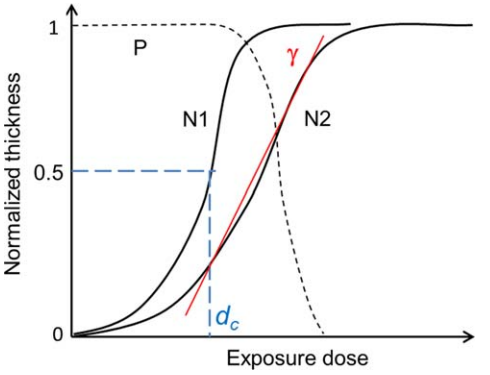

Fig. 3 Schematic of a typical contrast curve of a resist. P stands for positive tone resist (dotted line) and N stands for negative tone (solid lines). Sensitivity (d_c) is the dose required for dissolution (positive) or retention (negative) of half of the resist film thickness. Contrast (γ) is derived from slope of the dose curve. Thus, N1 and N2 are high contrast and low contrast negative resists.

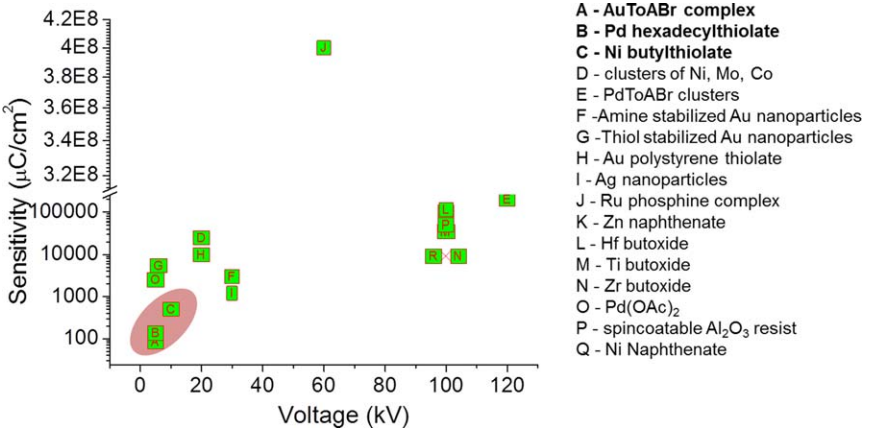

Fig. 4 A plot of sensitivity versus voltage for various direct-write resists.

where d_0 is the dose required to retain 100% of the resist material and d_i is the minimum dose at which resist action just begins. An ideal e-beam resist should have both a high contrast and a high sensitivity. But in general, an increase in one of these parameters leads to a decrease in the other. A high sensitivity will provide a high throughput (*e.g.* reduction of the writing time), but leads to a shallower slope for the contrast curve, hence a lower contrast.

In order to improve the resolution, instead of polymeric resists, small molecule resists such as organic SAMs have been tried out.[33–35] But the drawback of molecular resists is the high-dosage required, typically few mC/cm^2 to few hundreds of mC/cm^2. A better alternative is to employ direct-write resists which have the desired functional component in the resist itself. Various metal salts and metal complexes have been studied in this regard, as shown in Fig. 4 with the specific references included in Table 1. As

Table 1 Comprehensive survey of various inorganic direct write e-beam resists. Please note the list is not exhaustive.

S. No.	System	Precursor	Sensitivity (Dosage)	kV	Ref.
A.	Au	Au-ToABr	83 $\mu C/cm^2$	5	13, 36
B.	Pd	Pd hexadecyl thiolate	135 $\mu C/cm^2$	5	11
C.	Ni	Ni butylthiolate	500 $\mu C/cm^2$	10	15
D.	Clusters of Ni, Mo and Co	Polyferrocenyl Containing Pendant Organo-Ni, Mo, Co Clusters	25 mC/cm^2	20	37
E.	Pd and Pd/Pt nanostructures	Pd-ToABr clusters	0.2 C/cm^2	120	38
F.	Au	Amine stabilized Au nanoparticles	3 mC/cm^2	30	39
G.	Au	Thiol stabilized Au nanoparticles	7 mC/cm^2	6	40
H.	Au	Au polystyrene thiolate	9.8 mC/cm^2	20	41
I.	Ag	Ag nanoparticles	1.2 mC/cm^2	30	42
J.	Ru	$[Ru_6C(CO)_{15}Ph_2PC_2PPh_2]_n$	400000 mC/cm^2	60	43
K.	ZnO	Zn naphthenate	15 mC/cm^2	100	44
L.	HfO_2	Hf butoxide	115 mC/cm^2	100	45
M.	TiO_2	Ti butoxide	35 mC/cm^2	100	46
N.	ZrO_2	Zirconium butoxide	9 mC/cm^2	100	47
O.	Pd	$Pd(OAc)_2$	2500 $\mu C/cm^2$	5	48
P.	Al_2O_3	Spin-coatable Al_2O_3 resist	50 mC/cm^2	100	49
Q.	Ni	Ni Naphthenate	9 mC/cm^2	100	50

is clear from the plot, most direct write resists exhibit high sensitivity and require low voltages. With the right choice of the metal-organic complex, one can achieve improved process flow with a minimal e-dosage.

A metal-organic complex may behave superior when compared to the performance of the organic ligand alone. For instance, alkanethiol molecular layers need a large amount of e-dosage (typically, 500–800 $\mu C/cm^2$),[33–35] whereas metal alkanethiolates need minimal dose such as a few hundred $\mu C/cm^2$ for resist action.[11,15] Tetraoctylammonium bromide (ToABr) complexed metal anions[13] are other examples, which are detailed below. ToABr itself acts as a negative tone e-beam resist (schematic in Fig. 5a). When spin coated, it forms smooth films, with an average roughness of $\sim$1.5 nm (Fig. 5b). At 5 kV, patterning was done with varying e-dosages, followed by development in toluene for 5 s. Figure 5c shows a pattern of ToABr on Si, with the corresponding EDS maps for C K, Br K and N K levels shown in Fig. 5d–f. The pattern is primarily composed of carbon as the resist is an organic molecule. The response curves obtained by exposing $10 \times 10\,\mu m^2$ square areas on a film of thickness $\sim$200 nm are shown in Fig. 5g (unpublished work from authors). Following development in toluene, optical profilometric measurements were done to determine the thickness of the patterned regions. From the plot in Fig. 5g obtained with developed film, the sensitivity of the ToABr resist was found to be 65 mC/cm^2, which is comparable to commercial polymeric resists. The measured contrast value for ToABr resist is 0.36. Arbitrary shapes such as squares, lines, concentric circles can be easily written onto ToABr (Fig. 5h–k). Further, large area

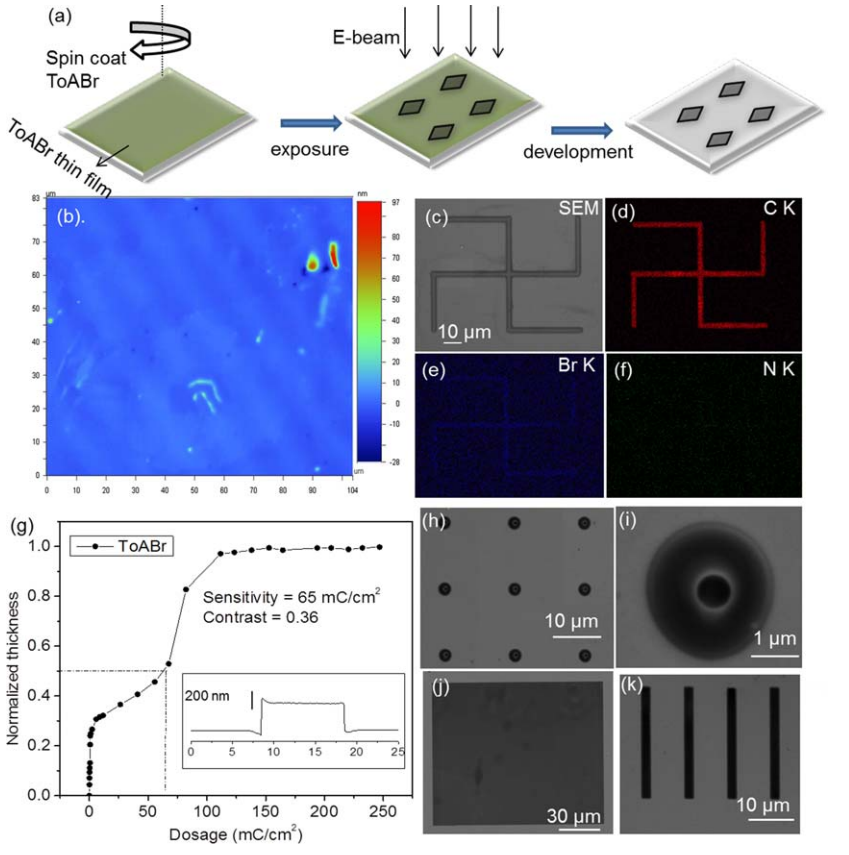

Fig. 5 ToABr e-beam resist: (a) Schematic of EBL using ToABr direct-write resist - spin-coating, EBL and development. (b) optical profilometric image showing the smoothness of a ToABr film. (c) SEM image showing a '*swastik*' pattern in ToABr and (d-f) C K, Br K and N K EDS maps. The C/Br/N elemental ratio is 80 : 11 : 3 for the patterned region whereas the initial composition of the unexposed ToABr resist ($N^+(C_8H_{17})_4Br$) is 70.4 : 14.5 : 2.5 (g) Variation in the film thickness (after development) normalized with respect to initial thickness, versus the e-dose (beam energy, 5 kV). Inset shows the *z*-profile of a patterned region (e-dosage, 150 $mC \cdot cm^{-2}$) obtained from optical profilometric measurement. (h-k) palettes showing various patterns of ToABr e-resist. (j) A large area pattern of ToABr (e-dosage 50 mC/cm^2) (Unpublished work from the authors).

patterning is feasible employing low e-dosages; a patterned area of dimensions 120 × 140 μm^2 is shown in Fig. 5j.

ToABr has an additional important property that metal anions can be linked with it.[13,51] Indeed, ToABr is widely used as a phase transfer agent; through electrostatic interaction,[52] it can hold the negatively charged ions and transfer them from aqueous to the organic phase.[53] Importantly, the ligand ToABr makes the metal highly processable.[13] For instance, $(AuCl_4)^-$ anions phase transferred using ToABr, *i.e.*, $N^+AuCl_4^-$ $(C_8H_{17})_4Br$ (termed as Au-ToABr) can act as an e-beam resist[36] with much better sensitivity (Fig. 6). Not only Au, but various other metal-ToABr complexes such as of Pt, Pd, Cu, Ag *etc.*, can be utilized as direct write resists.[13] Importantly, with this method, not only direct patterning of various metals is possible, but also, the dosage required for patterning can be much lower (as compared to

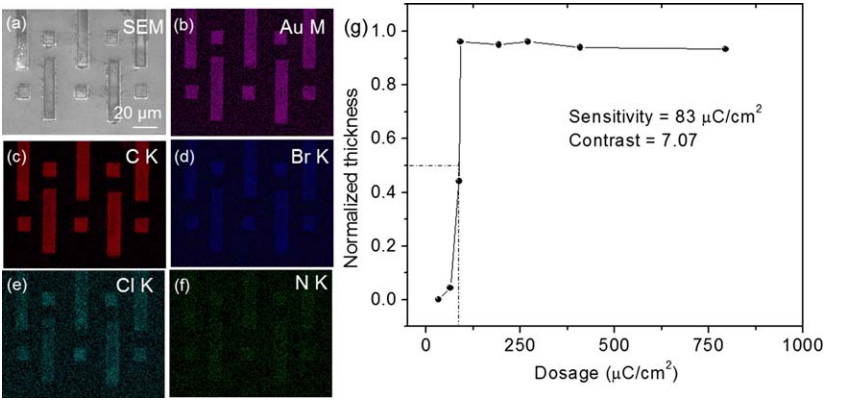

Fig. 6 (a) SEM image of patterned Au–ToABr e–resist and (b–f) the corresponding EDS maps. (g) Variation in the film thickness (after development) of Au–ToABr normalized with respect to initial thickness, versus the e–dose (beam energy, 5 kV). Adapted with permission from Wiley-VCH.[36]

ToABr itself). For example, Au-ToABr ($AuCl_4^-$ anions complexed with ToABr) is a negative-tone resist with sensitivity (Fig. 6g) several hundred times better compared to that in the absence of the metal ion (see Fig. 5g). EDS images of a typical patterned region of Au-ToABr (shown in Fig. 6b–f), as expected, indicate the presence of C, Br, Cl along with that of Au in the designated areas, demonstrating the direct patternability of the precursor.

Increasing the metal content in the metal-organic resist can lead to better yield of the metal and thus contiguous patterned structures after thermolysis. In this regard, direct write resists with higher metal content than M-ToABr, are metal alkanethiolates (25–40 at% as against 5–20 at% in the former). As noted earlier, alkanethiols themselves have been used as positive and negative resists, but metal alkanethiolates in contrast act as negative resists, importantly with much lower dosage.[11,15] Pd alkanethiolate has been studied successfully in this regard to produce high resolution contiguous features down to 30 nm resolution.[11]

Direct writing with metal-organics is not limited to metal end-products. One can achieve a desired composition to lead to semiconductors as well as dielectrics in the final patterns by fine-tuning the post-thermolysis conditions after development (Fig. 7). For instance, Pd alkanethiolate resist can lead to Pd metal or Pd sulfide or Pd oxide, based on thermolysis atmosphere.[14] With metal-ToABr complexes, metals, oxides, nitrides, sulfides have been obtained by appropriate thermolysis temperature and atmosphere.[13]

2.2 Direct micromolding

While EBL is a high-resolution technique, an inherent limitation is its serial nature. For large scale patterning, parallel lithography techniques are sought after and thus low-cost soft lithographic techniques attract wide attention in this regard. Among the set of various soft-lithographic techniques, micromolding is a versatile technique for patterning with

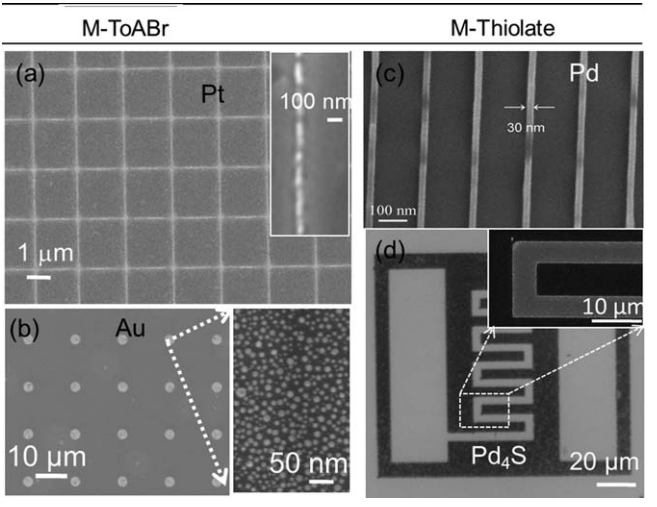

Fig. 7 SEM images of (a) Pt nanolines (b) Au dots produced by direct write EBL of PtToABr and AuToABr respectively, followed by thermolysis. (c) SEM image of Pd line produced by Pdhexadecanethiolate EBL and post-thermolysis. (d) Optical image of Pd_4S pattern produced by changing the thermolysis atmosphere to produce a sulphide after the pattern was made by direct-EBL. Adapted with permission from The American Chemical Society,[11,13] and Wiley-VCH.[14]

direct-write precursor inks, as it is ideal for depositing precursor solutions in continuous networked channels. It is important to note that the final conversion of metal-organic precursor to functional materials involves loss of organics and thus shrinkage of patterns. Therefore, techniques such as contact printing per se, which are ideal for making molecular monolayers, are not quite suitable for patterning direct-write precursors if the end product after thermolysis is required to be contiguous for further applications.

Important criterion for a direct write precursor to qualify as a suitable ink for micromolding is its ability to flow inside microchannels. Poor dispersions clog the channels and do not yield good patterns. This criterion has been met by few inks, which can reasonably be micromolded well. One of the early efforts of using direct write inks for direct micromolding was Pt carbonyl cluster compound (Fig. 8a–c).[23] Later on, metal thiolates[54,55] and metal phosphines,[25] MToABr complexes[13] were also explored. After the precursor solutions have been molded, a post treatment step such as thermolysis yields the desired metal pattern. Further, miniaturization to nanochannels during direct micromolding, has been reported as efficient method for achieving smaller features (Fig. 8d and e).[54] Employing a sol gel–block copolymer solution, mesostructured silica was patterned on Si surfaces for use as waveguides (Fig. 8f and g).[56] In this case, after filling the microchannels with block copolymer precursor solution, gelation occurred within a few hours. An increased cross-linking and association of the silica network can be realized by leaving the mold and the substrate undisturbed for several hours. The pump-probe experiments of thus patterned mesostructures were performed by shining a frequency-doubled neodymiun–yttrium-aluminum-garnet (Nd-YAG) laser with 532 nm

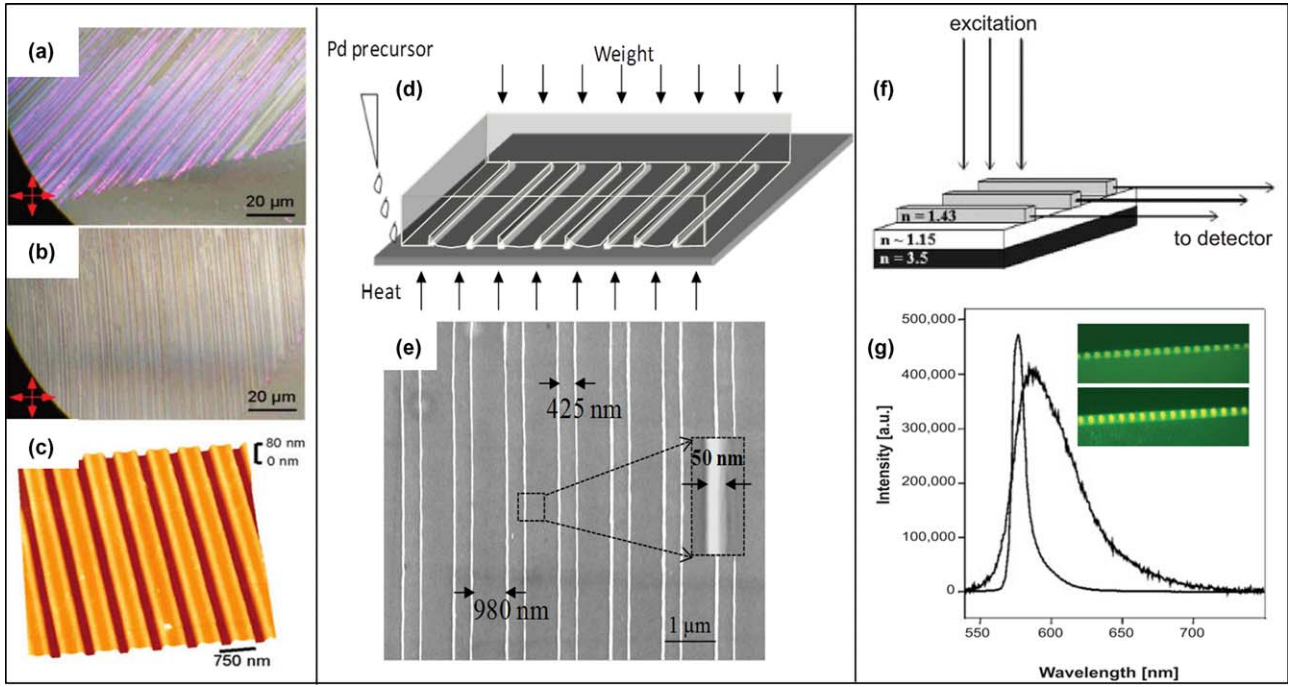

Fig. 8 Optical micrographs of micrometric stripes fabricated on glass by MIMIC using platinum carbonyl solutions under nitrogen, with crossed polars, (a) rotated $\sim 30^{\circ}$ and (b) parallel with respect to the polars, and (c) corresponding AFM image. (d) Modified micromolding method illustrated by schematic showing the collapse of nanochannels. (e) SEM image of the nanowires formed by confining the Pd alkanethiolate single source precursor 'ink' into nanochannels, followed by thermolysis. (g) Emission spectra collected normal to the excitation beam (schematic in (f)) along the waveguide (mesostructured silica) axis at two different pump power densities (0.8 kW cm^{-2} and 42 kW cm^{-2}). In the insets are shown the optical images of the axial output beams recorded with a CCD camera below (top image) and above (bottom image) the threshold power density. Adapted with permission from The American Chemical Society,[23] Wiley-VCH[54] and The American Association for the Advancement of Science.[56]

wavelength followed by detection of the axial emission from the end of the waveguides. Only a broad photoluminescence emission was observed at low pumping intensities, whereas above threshold, amplified spontaneous emission was observed, as indicated by the sharp emission peak.[56]

Patterned sol-gel precursors leading to lead zirconate titanate (PZT) nanostructures were made by direct micromolding with slight modification.[57] The technique employed was termed as soft contact imprint lithography (SCIL) and nanotransfer molding (NTM) which is schematically depicted in Fig. 9. After patterning and annealing, the sol-gel precursor patterns were converted to crystalline PZT.

As a variant, imprinting by soft stamps is also useful in direct patterning. While SCIL depicted above employs direct write ink for imprinting, one can also imprint directly onto a desired functional material as shown below. Microscale patterns were made onto a bulk chalcogenide glass (As_3S_7),[58] for use in photonic crystals (Fig. 10).

2.3 Direct nanoimprint lithography

Although soft lithography is a viable technique for parallel patterning, the limitation is the inability to scale up to industry requirements. Thus, soft lithography remains as a popular technique for academic research and for researching the patterning ability of new material inks. The next step in this direction is nanoimprint lithography (NIL), which utilizes hard stamp made of Si, quartz, Ni *etc*., for imprinting thin films of materials under pressure.[59] Forming smooth films by spin coating is thus an essential criterion for an ink to be imprintable.[60] During imprinting under pressure and temperature, the ink flows into the nanochannels of the mold. Upon cooling, the mold is removed leaving behind the replicate patterns of precursor ink on substrate. Thus ability to flow easily in narrow channels, at reasonable temperature, is another criterion for the ink.

Using a mold of desired structures, gratings, dots or other complicated 2D structures can be imprinted onto single source precursors. Thermally curable direct-write inks which comprise of polymer radical initiator along with a metal precursor had been conceived as sol-gel precursors for direct imprinting.[61,62] Following this, metal methacrylates in the presence of cross-linker such as ethylene glycol dimethacrylate were formulated for thermal nanoimprinting.[29] While imprinting, heat induces free-radical polymerization and traps the metal precursor in the imprinted nanopatterns. The formulation was later extended for UV-curable photopolymerization, amenable for step and flash imprint lithography by the aid of acrylate-based formulation containing allyl-functionalized metal-complex.[63] The metal content in such formulations is quite low[64] and the organic residues left behind impede the quality of the functional material obtained. A solution for this problem is to have a direct-write precursor ink, which by itself is imprintable without polymer additives. Only known direct-write ink till date, which satisfies the criterion of imprintability without a polymer additive is Pd benzylthiolate.[27] It is a metal-organic complex with a melting temperature of 120 °C, which can be used directly for imprinting. The protocol for direct imprinting is quite simple. Analogous to polymer imprinting, where the polymer is taken *via* glass

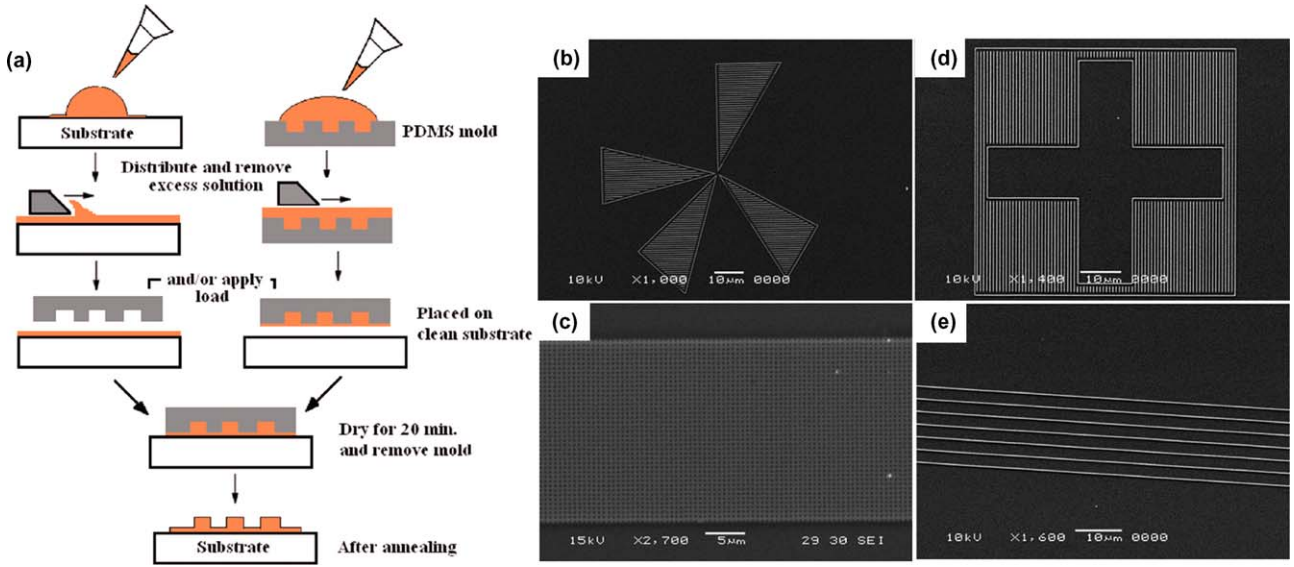

Fig. 9 (a) Schematic illustration of soft confocal imprint lithography and nanotransfer molding. SEM images of PZT patterns by (b,c) SCIL and (d,e) NTM on Si substrates after annealing at 650 °C in air. Reproduced with permission from The American Chemical Society.[57]

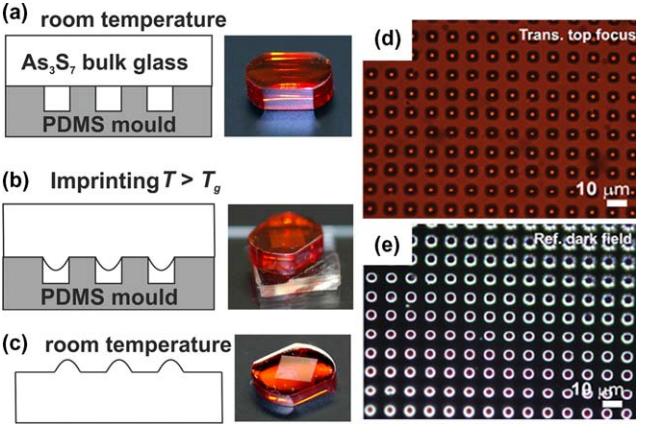

Fig. 10 Cross-sectional sketches and photographs of (a) a PDMS mould and a sample of polished As_3S_7 bulk glass; (b) the imprinting process, and (c) an imprinted pattern on the glass surface. (d) Transmission and (e) dark-field optical micrographs of the 'lens-array' imprinted into the surface of the As_3S_7 bulk glass. Adapted with permission from The Optical Society.[58]

transition T_g to soften the polymer and increase its flow, a metal-organic complex can have a melting or softening temperature. Along with imprinting surface structures, metal-organic complexes can be used for hierarchical and 3D imprinting as well (Fig. 11). After imprinting, the patterns can be subject to thermolysis to yield the desired material structures. Loss of organics leads to shrinkage of patterns laterally as well as vertically. Size reduction of the precursor patterns after thermolysis is an additional advantage to push the resolution of the functional material while maintaining areal throughput. The resolution achievable by size reduction is quite remarkable and is below that of obtainable with conventional NIL.

Semi-transparent silver nanoparticle gratings have been directly imprinted onto polyimide substrates. The polymeric precursor is composed of silver citrate, ethylene glycol and citric acid (Fig. 12). A two-step imprinting process was employed for imprinting and hardening the imprinted polymeric precursor. After imprinting and the removal of stamp, thermal annealing was employed to get rid of the organics. A sandwiched electroluminescent device was demonstrated utilizing such imprinted Ag gratings.

In general, the imprinting processes leads to a scum layer connecting the patterned features. One can engineer the film thickness such that the capillary forces are enough to get rid of the scum layer, but it limits the thickness and the depth as well as the pitch of the features which can be patterned. In order to alleviate this, if the mold is made with a low-surface energy, chemically resistant fluoropolymer, it eliminates the formation of a residual interconnecting film or the scum layer (Fig. 13).[65] This technique is called as particle replication in nonwetting templates (PRINT) and has been widely used for the patterning and synthesis of a variety of biomaterials with control over size, shape and composition.[66]

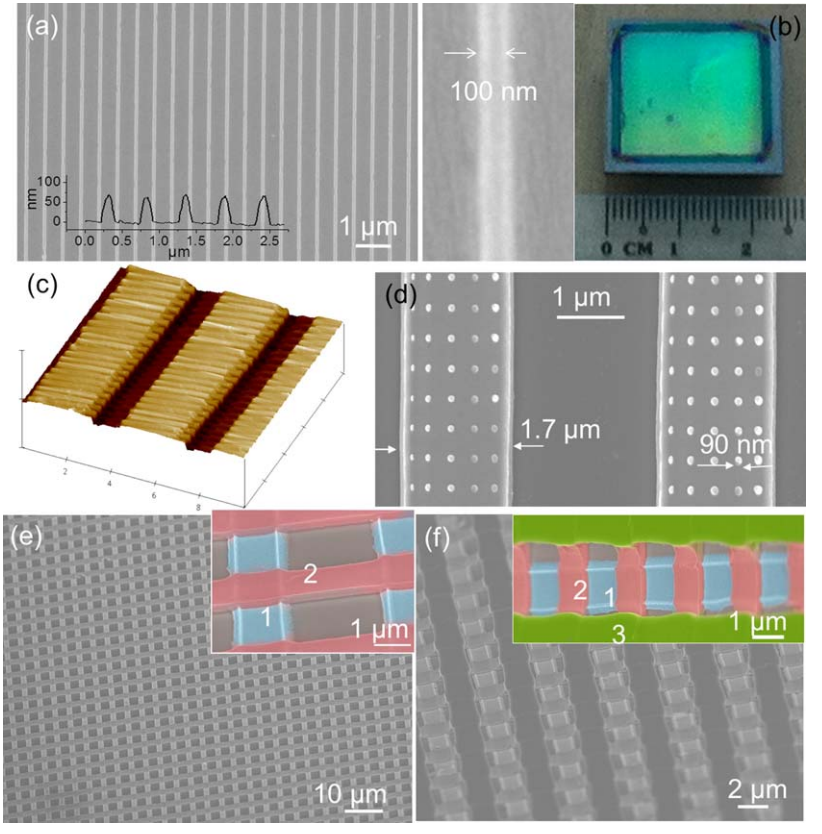

Fig. 11 (a) Direct nanoimprinting of 100 nm wide Pd nanowires, with magnified view shown alongside. (b) Digital photograph of a typical imprinted sample, showing the patterning yield and uniformity. Hierarchical direct patterning of (c) grating-over-grating and (d) dot-over-grating structures. Stacked structures of (e) two-layer and (f) three-layer gratings by direct NIL. Adapted with permission from Nature Publishing Group.[27]

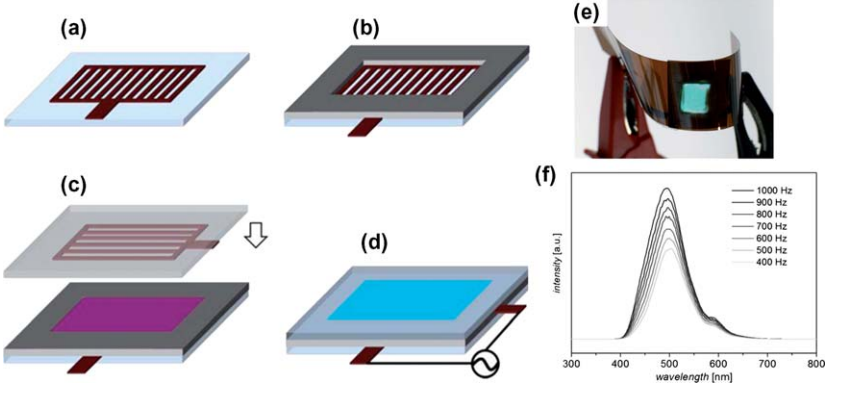

Fig. 12 (a) Illustration of the manufacturing process for an EL device based on two patterned silver electrodes: substrate coating and patterning (a), mounting of a dielectric separator (b), phosphor deposition followed by covering with the second electrode (c) and AC excitation of the blue emitting phosphor (d). (e) Imprinted silver luminescent device and (f) luminescent spectra of the device (applied voltage, 350 V). Adapted with permission from The Royal Society of Chemistry.[28]

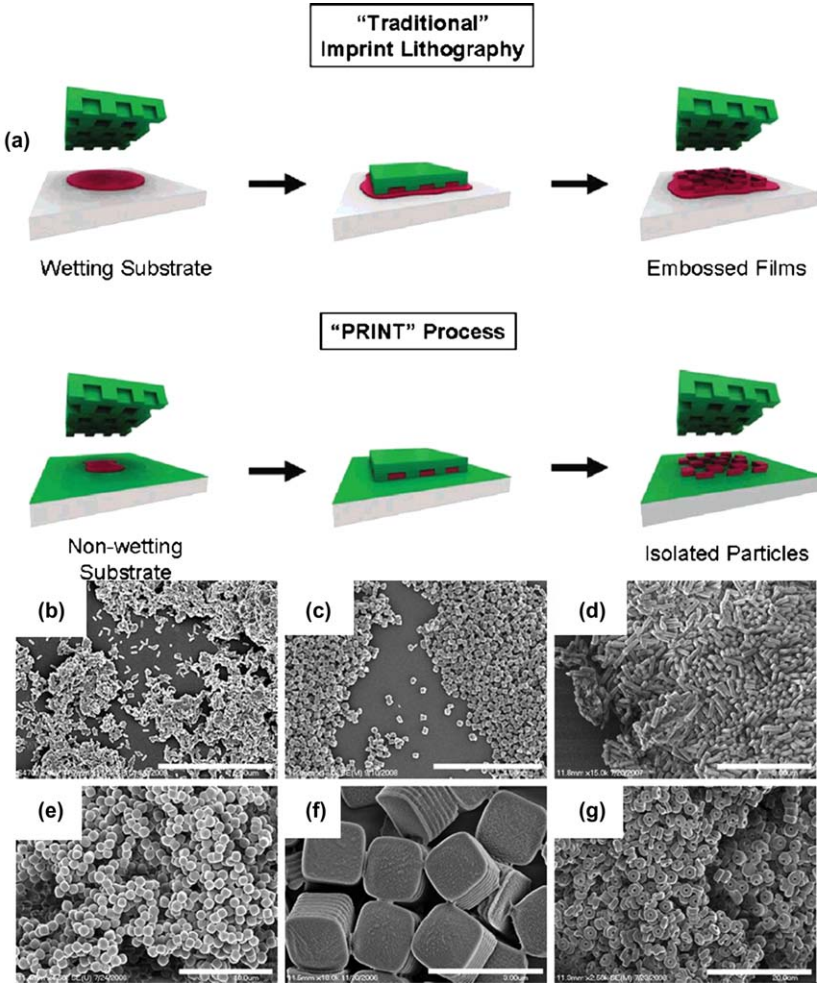

Fig. 13 (a) Illustration of the PRINT process compared to traditional imprint lithography in which the affinity of the liquid precursor for the surface results in a scum layer. In PRINT, the nonwetting nature of fluorinated materials and surfaces (shown in green) confines the liquid precursor inside the features of the mold, allowing for the generation of isolated particles. (b–g) PLGA nano- and microparticles fabricated by the PRINT process. (b) 80 nm × 320 nm cylinders, (c) 200 nm × 200 nm cylinders, (d) 200 nm × 600 nm cylinders, (e) 1 μm sphere approximates, (f) 2 μm cubes with ridges, and (g) 3 μm particles with center fenestrations. Scale bars: (b) 5 μm, (c) 4 μm, (d) 3 μm, (e) 10 μm, (f) 3 μm, and (g) 20 μm. Adapted with permission from The American Chemical Society.[65,66]

2.4 Laser writing of direct write inks

Direct laser writing is a useful technique for writing complex structures and especially for 3D structures such as wood-pile, log-pile *etc*., useful for photonics.[67] Conventionally, photo-polymerizable materials are used in direct laser writing. Post-electroless or chemical deposition of metals or semiconductors is done onto the polymeric 3D structures, for applications such as visible photonics.[68,69] Instead of polymeric materials, laser writing on metal-organic precursors has been tried out by complexing metal ions with polymerizable alkoxide radicals. An oxide resist of TiO_2 has been

successfully used as direct laser write resist (Fig. 14).[70] Photopolymerization and simultaneous photoreduction has also been employed leading to metal nanoparticle-polymer composite patterns. Using this method, Au reduced in SU-8 polymer matrix has been produced.[22]

On the other hand, thin films of functional materials can be directly exposed to laser beams for 3D structuring. In this way, a chalcogenide film of As_2S_3 has been successfully cast into a photonic structure[71] as shown in Fig. 15. Likewise a nanoparticle thin film exposed to pulsed laser beam has been employed to make Ag patterns onto rigid and flexible substrates (Fig. 16).[21]

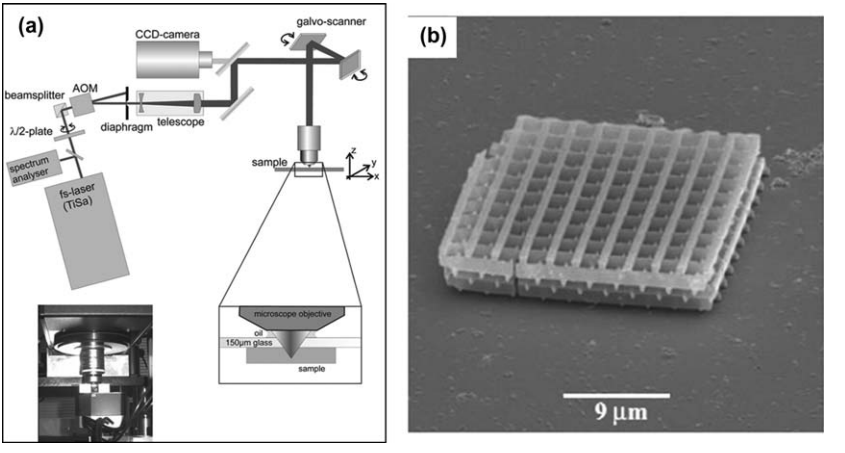

Fig. 14 Direct laser 3D writing – (a) schematic diagram and photograph of the experimental setup used for 3D structuring using a femtosecond laser. The enlarged area shows the position of sample face to face with the microscope objective. (b) SEM images of 3D structures fabricated in the spin-coatable TiO_2 resist. The periodicity of the structure is 3.5 μm with the distance between single layers being 1.2 μm. The crack in the patterned structure originated from drying and shrinkage of very thick resist on the substrate. Reproduced with permission from Wiley-VCH.[70]

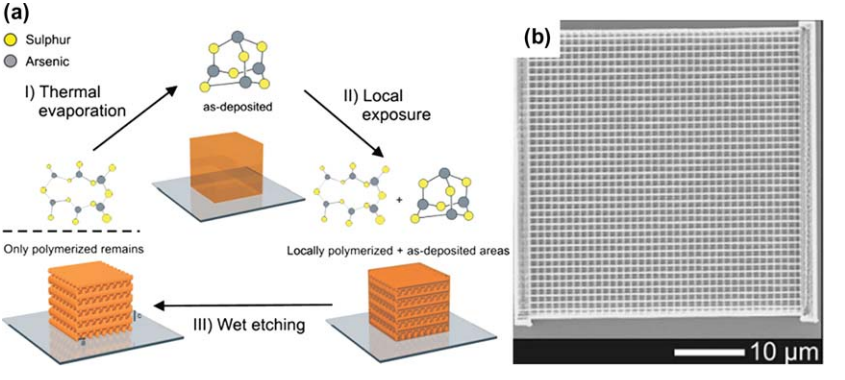

Fig. 15 (a) Schematic of fabrication steps: I) Thermal evaporation of glassy As_2S_3 as a thin film of molecular glass composed of As_4S_6 cage molecules. II) DLW locally exposes the material, initiating a topotactic ring-opening polymerization back into the glassy As_2S_3. III) Removal of the unexposed molecular glass by means of wet etching reveals the 3D photonic crystal. (b) Top view of a woodpile with a 40 μm × 40 μm footprint and twelve layers. Reproduced with permission from Wiley-VCH.[71]

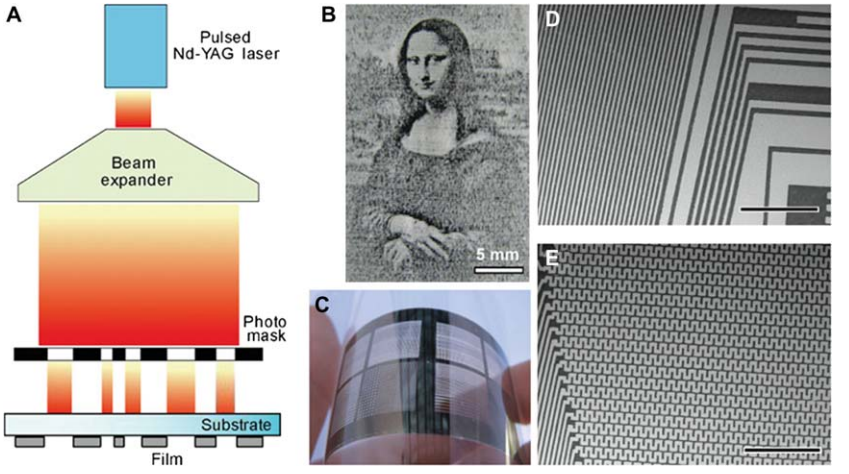

Fig. 16 Ag films patterned by direct exposure to a pulsed Nd : YAG laser. (a) Schematic of the patterning process. (b) Photographic image of the "Mona Lisa" patterned on a glass substrate. (c) Image of the patterns formed on a transparency sheet. (d) Scanning electron microscopic (SEM) image of a film patterned on glass substrate. (e) SEM image of a pattern on polyimide. Scale bars are 500 μm. Reproduced with permission from Wiley-VCH.[21]

2.5 Direct scanning probe lithography

Scanning probe lithography (SPL) is a promising method for nanopatterning utilizing an atomic force microscopy (AFM) tip for writing patterns. It makes use of the probe tip - surface interaction, which is confined to the nanoscale, due to which high-resolution patterning at the nanoscale can be realized. Numerous AFM-based lithographic techniques have been developed in the last two decades. Dip-pen nanolithography (DPN) pioneered by Mirkin and coworkers is a popular technique for materials transfer. In DPN, the tip is used as a nanoscale pen to directly deposit a variety of ink materials onto the substrate to define a functional structure.[72,73] In this direct-write lithographic technique, an AFM tip coated with a molecular ink to be deposited. This ink is transferred from the tip to a substrate through the water meniscus that forms at the tip-sample junction under ambient conditions. DPN, is applicable to immobilize a large diversity of organic molecules, and in particular biomolecules, for constructions of (bio) functional surface arrays.[74] Unlike beam-based techniques, DPN is a particularly useful technique for direct-writing of biomolecules and proteins as it does not denature them.[75,76] Thiol-modified oligonucleotide arrays have been patterned on metal and insulator surfaces by DPN.[77] Stem cell differentiation studies have been carried out by utilizing fibronectin immobilized onto DPN patterns of mercapto-hexadecanoic acid.[78]

DPN technique is amenable for on-site reactions and synthesis of functional materials as well. A Au ink was formulated such that it undergoes surface reduction upon deposition by DPN leading to Au nanostructures.[79] DPN is not a merely a patterning technique but has the capability to induce reactions on site such as heterogenous catalysis.[80] Reactive DPN process has been demonstrated employing thioacetamide

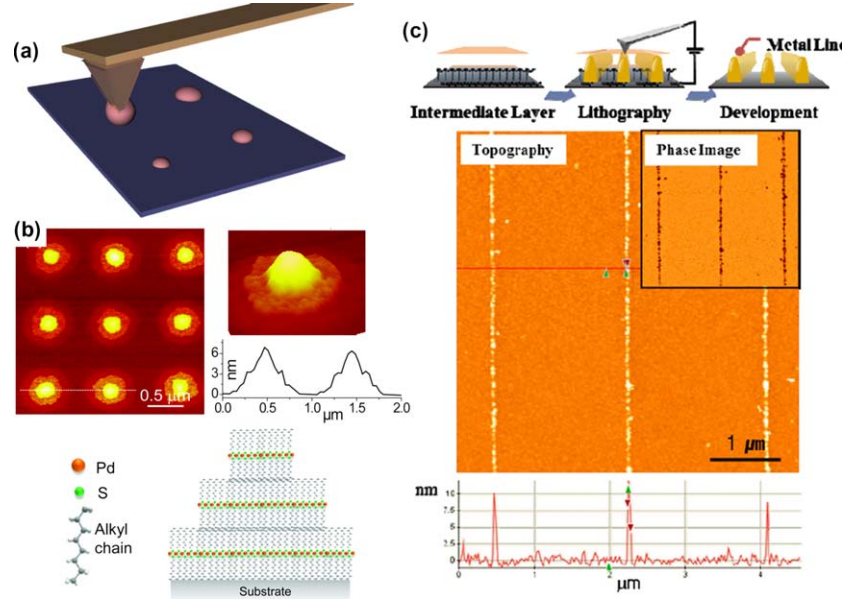

Fig. 17 (a) Schematic of the deposition of molecular layers by DPN. (b) AFM topography images of three layer pattern with z-profile. The schematic arrangement of Pd octylthiolate lamellae is shown below. (c) Fabrication scheme of direct AFM lithography with topographic images and profiles of the copper lines after lithography shown below. Reproduced with permission from The American Chemical Society[83] and Institute of Physics.[87]

and cadmium acetate to write CdS features.[81] Another formulation of direct DPN ink was to use a block copolymer (PVP-b-PEO) to deliver metal salts in the form of a molecular nanoreactors, which can be annealed to form sub-5 nm sized nanoparticle arrays.[82] Metal-organics described in section 2.1–2.3 can also be employed as direct DPN inks and an example of such patterning is shown in Fig. 17. Layer-by-layer patterning of Pd octylthiolate features was feasible by DPN due to the fine control it offers over the rate of deposition of molecules.[83] Nanoparticle inks can also be directly written as nanoscale features by DPN by suitable surface modifications.[84]

Another variant of SPL is local anodic oxidation (LAO), which is widely used for the fabrication of nanosized oxide structures.[85] It is based on direct oxidation of the sample surface by negative voltage applied to the AFM tip with respect to the sample. The process utilizes the presence of a water bridge created between the sample and the tip.[86] For local electric field larger than the critical value, 10^9 V/m or (1 V/nm),[86] the water molecules split into H^+ and OH^- ions. OH^- ions are transported to the positively biased sample surface in the direction of the electric field, which react with the surface atoms and form oxides. LAO method can be applied to various metallic, semiconducting, or insulators samples. The bias voltage, substrate, separation between tip and sample surface, duration, and ambient humidity- all have significant effect on the oxidation. Although primarily discovered process was oxidation, this can be employed for direct writing of

materials from precursor films. Direct AFM lithography[87] has been attempted by applying negative sample bias on a metal precursor film such as copper acetate to lead to patterned Cu lines. An intermediate self-assembled monolayer of n-tridecylamine hydrochloride, coated below the metal precursor layer improves the resolution of the obtained Cu features (Fig. 17).[87] Conductive molecular resists containing metal anions have also been explored for direct metal fabrication by biased-SPL. An example of such a study utilizes polystyrene sulfonate containing $Cu(NO_3)_2$ which can be reduced to Cu metal locally by applying a negative bias.[88] Electrochemical nanopatterning can be induced by the tip, wherein the terminal functional groups of a molecular layer can be modified by bias.[89] Such modifications have been used to template deposition of a second layer of nanomaterials by electrostatic,[90] covalent[89] or wetting[91] driven interactions. Importantly, scanning probe lithography is not limited in terms of throughput, as the 2D arrays comprising millions of tips made of Si_3N_4,[92] Si[93,94] as well as polymer[95] are available.

2.6 Nozzle printing of direct write inks

Printing technology has been pushed in terms of achievable resolution and thus it finds a niche as micropatterning technique.[96] Ink-jet printing has been employed widely with nanoparticle inks.[96,97] After printing, nanoparticles can be sintered in the following step for obtaining contiguous structures. In order to further improve the resolution of the printing, nozzle printing with sub-100 nm diameter nozzles has been developed.[98] For obtaining fine patterns with decent line-edge roughness, the inks have to be nanoparticulate dispersions. Omnidirectional printing of Ag nanoparticles in polymer ink has been demonstrated which can produce spanning and meandering structures (Fig. 18).[98] Ink formulations should possess enough viscosity and should not clog the nozzles. Instead of nanoparticle inks, metal-organic complexes have also been tried out.[99] Silver complexes have been successful for nanopatterning and there is a lot of scope to improve the printable materials and try library of direct-write inks. This is an emerging technique and thus new direct write inks are expected to play an important role.

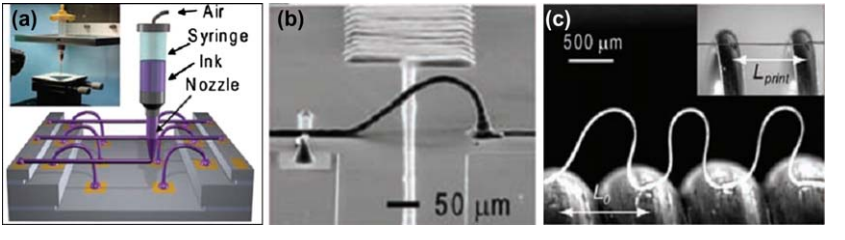

Fig. 18 Omnidirectional printing: (a) Schematic diagram illustrating omnidirectional printing and optical image of apparatus used (inset). (b) A silver interconnect arch printed over an electrode junction (top left) and on a gold contact pad (80 by 80 μm). (c) Optical image of stretchable silver arches printed onto a spring. Reproduced with permission from The American Association for the Advancement of Science.[98]

3 Conclusions and outlook

Here the term, direct write has been defined in a broader sense to refer to depositing the desired ink in micro or nano patterns, which with a simple post treatment such as thermolysis or curing in air, yields the end product. The latter is, in a way, programmed in the direct-write 'ink' to lead to, say, a nonstoichiometric inorganic compound. Direct writing has thus evolved to generate many functional nanomaterials including organic materials or biomolecules. With traditional lithography process flow using polymeric resists, it is difficult to encompass many functional and active materials which are produced usually under harsh deposition conditions not amenable to polymeric resists. Direct-write techniques will surely play a major role in realizing the patterned structures of complex materials (for *e.g.*, binary/ternary oxides, supramolecules, sensitive biomaterials or some other complex inorganic compounds), that are incompatible with traditional lithography processes. Direct write is, in principle, extendable to any lithography process. In this article, literature examples on e-beam lithography, soft and nanoimprint lithography, laser based lithography as well as scanning probe lithography have been dealt with. As sophisticated device fabrication requires congregation of functional materials in micro/nanopatterns, the role of lithography is insurmountable; it is likely that hybrid processes involving more than one lithography technique may be employed routinely. With the advent of direct write recipes, material patterning in the future will see a new horizon.

References

1 M. Madou, *Fundamentals of Microfabrication: The Science of Miniaturization*, CRC Press, United States of America, 2002.
2 R. Luttge, *J. Phys. D: Appl. Phys.*, 2009, **42**, 123001.
3 J. A. Liddle and G. M. Gallatin, *Nanoscale*, 2011, **3**, 2679.
4 D. B. Chrisey, *Science*, 2000, **289**, 879.
5 G. L. T. Chiu and J. M. Shaw, *IBM J. Res. Dev.*, 1997, **41**, 3.
6 K. L. Choy, *Prog. Mater. Sci.*, 2003, **48**, 57.
7 B. D. Fahlman, *Curr. Org. Chem.*, 2006, **10**, 1021.
8 A. A. Sagade, B. Radha and G. U. Kulkarni, *Sensor Actuat B: Chem*, 2010, **149**, 345.
9 M. Afzaal, M. A. Malik and P. O'Brien, *J. Mater. Chem.*, 2010, **20**, 4031.
10 F. F. Lange, *Science*, 1996, **273**, 903.
11 T. Bhuvana and G. U. Kulkarni, *ACS Nano*, 2008, **2**, 457.
12 M. K. Corbierre, J. Beerens and R. B. Lennox, *Chem. Mater.*, 2005, **17**, 5774.
13 B. Radha, S. Kiruthika and G. U. Kulkarni, *J. Amer. Chem. Soc.*, 2011, **133**, 12706.
14 B. Radha and G. U. Kulkarni, *Adv. Func. Mater.*, 2010, **20**, 879.
15 K. D. M. Rao, T. Bhuvana, B. Radha, N. Kurra, N. S. Vidhyadhiraja and G. U. Kulkarni, *J. Phys. Chem. C*, 2011, **115**, 10462.
16 N. Jiang, G. G. Hembree, J. C. H. Spence, J. Qiu, F. J. G. de Abajo and J. Silcox, *App. Phys. Lett.*, 2003, **83**, 551.
17 D. S. Kong, J. S. Varsanik, S. Griffith and J. M. Jacobson, The 48th International Conference on Electron, *Ion, and Photon Beam Technology and Nanofabrication, San Diego, California (USA)*, 2004.
18 S. Reyntjens and R. Puers, *J. Micromech. Microeng.*, 2000, **10**, 181.

19 G. M. Shedd, H. Lezec, A. D. Dubner and J. Melngailis, *App. Phys. Lett.*, 1986, **49**, 1584.
20 S. Riedel, P. Leiderer, E. Scheer and J. Boneberg, *Acta Phys. Pol. A*, 2012, **121**, 385.
21 H. Shin, H. Kim, H. Lee, H. Yoo, J. Kim, H. Kim and M. Lee, *Adv. Mater.*, 2008, **20**, 3457.
22 S. Shukla, X. Vidal, E. P. Furlani, M. T. Swihart, K.-T. Kim, Y.-K. Yoon, A. Urbas and P. N. Prasad, *ACS Nano*, 2011, **5**, 1947.
23 P. Greco, M. Cavallini, P. Stoliar, S. D. Quiroga, S. Dutta, S. Zacchini, M. C. Iapalucci, V. Morandi, S. Milita, P. G. Merli and F. Biscarini, *J. Amer. Chem. Soc.*, 2008, **130**, 1177.
24 G. U. Kulkarni and B. Radha, *Nanoscale*, 2010, **2**, 2035.
25 B. Radha and G. Kulkarni, *Nano Res.*, 2010, **3**, 537.
26 B. Radha, A. A. Sagade and G. U. Kulkarni, *ACS Appl. Mater. Interf.*, 2011, **3**, 2173.
27 B. Radha, S. H. Lim, M. S. M. Saifullah and G. U. Kulkarni, *Sci. Rep.*, 2013, **3**, 1078.
28 B. Schumm, F. M. Wisser, G. Mondin, F. Hippauf, J. Fritsch, J. Grothe and S. Kaskel, *J. Mater. Chem. C*, 2013, **1**, 638.
29 L. Su Hui, M. S. M. Saifullah, H. Hazrat, L. Wei Wei and L. Hong Yee, *Nanotechnol.*, 2010, **21**, 285303.
30 A. E. Grigorescu and C. W. Hagen, *Nanotechnol.*, 2009, **20**, 292001.
31 K. Koshelev, M. A. Mohammad, T. Fito, K. L. Westra, S. K. Dew and M. Stepanova, *J. Vac. Sci. Technol. B*, 2011, **29**, 06F306.
32 M. Hatzakis, *J. Electrochem. Soc.*, 1969, **116**, 1033.
33 D. W. Carr, M. J. Lercel, C. S. Whelan, H. G. Craighead, K. Seshadri and D. L. Allara, *J. Vac. Sci. Technol. A*, 1997, **15**, 1446.
34 S. O. Koswatta, A. D. Scott, S. Bhattacharya, D. B. Janes, The 4th IEEE Conference on Nanotechnology, 2004.
35 P. M. St. John and H. G. Craighead, *J. Vac. Sci. Technol. B*, 1996, **14**, 69.
36 B. Radha and G. U. Kulkarni, *Adv. Func. Mater.*, 2012, **22**, 2837.
37 W. Y. Chan, S. B. Clendenning, A. Berenbaum, A. J. Lough, S. Aouba, H. E. Ruda and I. Manners, *J. Amer. Chem. Soc.*, 2005, **127**, 1765.
38 M. T. Reetz, M. Winter, G. Dumpich, J. Lohau and S. Friedrichowski, *J. Amer. Chem. Soc.*, 1997, **119**, 4539.
39 K.-C. Kim, I.-B. Lee, D.-J. Kang and S. Maeng, *Etri J.*, 2007, **29**, 814.
40 X. M. Lin, R. Parthasarathy and H. M. Jaeger, *App. Phys. Lett.*, 2001, **78**, 1915.
41 M. K. Corbierre, J. Beerens and R. B. Lennox, *Chem. Mater.*, 2005, **17**, 5774.
42 T. Bhuvana, C. Subramaniam, T. Pradeep and G. U. Kulkarni, *J. Phys. Chem. C*, 2009, **113**, 7038.
43 B. F. G. Johnson, K. M. Sanderson, D. S. Shephard, D. Ozkaya, W. Zhou, H. Ahmed, M. D. R. Thomas, L. Gladden and M. Mantle, *Chem. Comm.*, 2000, **0**, 1317.
44 M. S. M. Saifullah, K. R. V. Subramanian, D. J. Kang, D. Anderson, W. T. S. Huck, G. A. C. Jones and M. E. Welland, *Adv. Mater.*, 2005, **17**, 1757.
45 M. S. M. Saifullah, M. Z. R. Khan, D. G. Hasko, E. S. P. Leong, X. L. Neo, E. T. L. Goh, D. Anderson, G. A. C. Jones and M. E. Welland, *J. Vac. Sci. Technol. B*, 2010, **28**, 90.
46 M. S. M. Saifullah, K. R. V. Subramanian, E. Tapley, D.-J. Kang, M. E. Welland and M. Butler, *Nano Lett.*, 2003, **3**, 1587.
47 K. R. V. Subramanian, M. S. M. Saifullah, E. Tapley, K. Dae-Joon, M. E. Welland and M. Butler, *Nanotechnol.*, 2004, **15**, 158.
48 T. J. Stark, T. M. Mayer, D. P. Griffis and P. E. Russell, *J. Vac. Sci. Technol. B*, 1991, **9**, 3475.

49 M. S. M. Saifullah, H. Namatsu, T. Yamaguchi, K. Yamazaki and K. Kurihara, *Proc. SPIE.*, 1999, **3678**, 633.
50 M. Nedelcu, M. S. M. Saifullah, D. G. Hasko, A. Jang, D. Anderson, W. T. S. Huck, G. A. C. Jones, M. E. Welland, D. J. Kang and U. Steiner, *Adv. Func. Mater.*, 2010, **20**, 2317.
51 M. Brust, M. Walker, D. Bethell, D. J. Schiffrin and R. Whyman, *J. Chem. Soc., Chem. Commun.*, 1994, **0**, 801–802.
52 V. V. Belova, A. I. Khol'kin and T. I. Zhidkova, *Theor. Found. Chem. Eng.*, 2007, **41**, 743.
53 Y. J. Park and D. J. Fray, *J. Hazard. Mater.*, 2009, **164**, 1152.
54 B. Radha and G. U. Kulkarni, *Small*, 2009, **5**, 2271.
55 B. Radha, A. A. Sagade, R. Gupta and G. U. Kulkarni, *J. Nanosci. Nanotech.*, 2011, **11**, 152.
56 P. Yang, G. Wirnsberger, H. C. Huang, S. R. Cordero, M. D. McGehee, B. Scott, T. Deng, G. M. Whitesides, B. F. Chmelka, S. K. Buratto and G. D. Stucky, *Science*, 2000, **287**, 465.
57 S. U. Khan, O. F. Göbel, D. H. A. Blank and J. E. ten Elshof, *ACS Appl. Mater. Interf.*, 2009, **1**, 2250.
58 J. Orava, T. Kohoutek, A. L. Greer and H. Fudouzi, *Opt. Mater. Express*, 2011, **1**, 796.
59 S. Y. Chou, P. R. Krauss and P. J. Renstrom, *Science*, 1996, **272**, 85.
60 H. Schift, *J. Vac. Sci. Technol., B*, 2008, **26**, 458.
61 M. Li, H. Tan, L. Chen, J. Wang and S. Y. Chou, *J. Vac. Sci. Technol., B*, 2003, **21**, 660.
62 J. Barbé, A. F. Thomson, E.-C. Wang, K. McIntosh and K. Catchpole, *Prog. Photovolt. Res. Appl.*, 2012, **20**, 143.
63 R. Ganesan, J. Dumond, M. S. M. Saifullah, S. H. Lim, H. Hussain and H. Y. Low, *ACS Nano*, 2012, **6**, 1494.
64 R. Ganesan, S. H. Lim, M. S. M. Saifullah, H. Hussain, J. X. Q. Kwok, R. L. X. Tse, H. A. P. Bo and H. Y. Low, *J. Mater. Chem.*, 2011, **21**, 4484.
65 J. P. Rolland, B. W. Maynor, L. E. Euliss, A. E. Exner, G. M. Denison and J. M. DeSimone, *J. Amer. Chem. Soc.*, 2005, **127**, 10096.
66 E. M. Enlow, J. C. Luft, M. E. Napier and J. M. DeSimone, *Nano Lett.*, 2011, **11**, 808.
67 I. Sakellari, E. Kabouraki, D. Gray, C. Fotakis, A. Pikulin, N. Bityurin, M. Vamvakaki and M. Farsari, Proc. SPIE 8456, Nanophotonic Materials IX, 84560E, San Diego, California, USA, 2012.
68 A. Radke, T. Gissibl, T. Klotzbücher, P. V. Braun and H. Giessen, *Adv. Mater.*, 2011, **23**, 3018.
69 S. C. Wu, F. J. Hou, P. C. J.-. Jian, M. S. Tsai, M. C. Chen, L. S. Li, J. Y. Huang and S. Y. Lin, *J. Phys. Conf. Ser.*, 2007, **61**, 1261.
70 S. Passinger, M. S. M. Saifullah, C. Reinhardt, K. R. V. Subramanian, B. N. Chichkov and M. E. Welland, *Adv. Mater.*, 2007, **19**, 1218.
71 S. Wong, M. Deubel, F. Pérez-Willard, S. John, G. A. Ozin, M. Wegener and G. von Freymann, *Adv. Mater.*, 2006, **18**, 265.
72 H. Zhang, Z. Li and C. A. Mirkin, *Adv. Mater.*, 2002, **14**, 1472.
73 X. N. Xie, H. J. Chung, C. H. Sow and A. T. S. Wee, *Mat. Sci. Eng. R*, 2006, **54**, 1.
74 C.-C. Wu, D. N. Reinhoudt, C. Otto, V. Subramaniam and A. H. Velders, *Small*, 2011, **7**, 989.
75 K. Salaita, Y. Wang and C. A. Mirkin, *Nature Nanotechnol.*, 2007, **2**, 145.
76 D. L. Wilson, R. Martin, S. Hong, M. Cronin-Golomb, C. A. Mirkin and D. L. Kaplan, *Proc. Nat. Acad. Sci. USA*, 2001, **98**, 13660.

77 L. M. Demers, D. S. Ginger, S.-J. Park, Z. Li, S.-W. Chung and C. A. Mirkin, *Science*, 2002, **296**, 1836.
78 L. R. Giam, M. D. Massich, L. Hao, L. Shin Wong, C. C. Mader and C. A. Mirkin, *Proc. Nat. Acad. Sci. USA*, 2012, **109**, 4377.
79 B. W. Maynor, Y. Li and J. Liu, *Langmuir*, 2001, **17**, 2575.
80 W. F. Paxton, J. M. Spruell and J. F. Stoddart, *J. Amer. Chem. Soc.*, 2009, **131**, 6692.
81 L. Ding, Y. Li, H. Chu, X. Li and J. Liu, *J. Phys. Chem. B*, 2005, **109**, 22337.
82 J. Chai, F. Huo, Z. Zheng, L. R. Giam, W. Shim and C. A. Mirkin, *Proc. Nat. Acad. Sci. USA*, 2010, **107**, 20202.
83 B. Radha, G. Liu, D. J. Eichelsdoerfer, G. U. Kulkarni and C. A. Mirkin, *ACS Nano*, 2013, **7**, 2602.
84 W. M. Wang, R. M. Stoltenberg, S. Liu and Z. Bao, *ACS Nano*, 2008, **2**, 2135.
85 A. Fuhrer, A. Dorn, S. Lüscher, T. Heinzel, K. Ensslin, W. Wegscheider and M. Bichler, *Superlattices Microst.*, 2002, **31**, 19.
86 R. Garcia, M. Calleja and H. Rohrer, *J. Appl. Phys.*, 1999, **86**, 1898.
87 G. Kwon, H. Chu, J. Yoo, H. Kim, C. Han, C. Chung, J. Lee and H. Lee, *Nanotechnol.*, 2012, **23**, 185307.
88 C. Haena, G. Kwon, Y. Jae Beom, S. Yibin and H. Lee, 10th IEEE Conference on Nanotechnology, *Seoul*, 2010, 410.
89 R. Maoz, E. Frydman, S. R. Cohen and J. Sagiv, *Adv. Mater.*, 2000, **12**, 725.
90 S. Liu, R. Maoz and J. Sagiv, *Nano Lett.*, 2004, **4**, 845.
91 D. Chowdhury, R. Maoz and J. Sagiv, *Nano Lett.*, 2007, **7**, 1770.
92 K. Salaita, Y. Wang, J. Fragala, R. A. Vega, C. Liu and C. A. Mirkin, *Angew. Chem. Int. Ed.*, 2006, **45**, 7220.
93 W. Shim, A. B. Braunschweig, X. Liao, J. Chai, J. K. Lim, G. Zheng and C. A. Mirkin, *Nature*, 2011, **469**, 516.
94 D. J. Eichelsdoerfer, K. A. Brown, R. Boya, W. Shim and C. A. Mirkin, *Nano Lett.*, 2013, **13**, 664.
95 F. Huo, Z. Zheng, G. Zheng, L. R. Giam, H. Zhang and C. A. Mirkin, *Science*, 2008, **321**, 1658.
96 B. Michel, A. Bernard, A. Bietsch, E. Delamarche, M. Geissler, D. Juncker, H. Kind, J. P. Renault, H. Rothuizen, H. Schmid, P. Schmidt-Winkel, R. Stutz and H. Wolf, *IBM J. Res. Dev.*, 2001, **45**, 697.
97 G. C. Jensen, C. E. Krause, G. A. Sotzing and J. F. Rusling, *Phys. Chem. Chem. Phys.*, 2011, **13**, 4888.
98 B. Y. Ahn, E. B. Duoss, M. J. Motala, X. Guo, S.-I. Park, Y. Xiong, J. Yoon, R. G. Nuzzo, J. A. Rogers and J. A. Lewis, *Science*, 2009, **323**, 1590.
99 S. B. Walker and J. A. Lewis, *J. Amer. Chem. Soc.*, 2012, **134**, 1419.

Nanostructured photocatalysts for solar water-splitting

Michael E. Louis and Gonghu Li*
DOI: 10.1039/9781849737623-00081

Solar water-splitting is a feasible approach to convert and store solar energy in the form of chemical energy. Nanostructured materials possess particularly interesting characteristics that are desired for photocatalytic applications. By tuning the structures of photoactive materials at the nanoscale, it is possible to optimize the properties of such materials in photocatalysis. In this chapter we summarize literature research published in the years of 2011 and 2012 on nanostructured water-splitting photocatalysts. Different photocatalytic systems are discussed, including titanium dioxide, various other metal oxides and non-oxide semiconductors, composite materials as well as the photoelectrochemical cells. This chapter focuses on new developments in the field regarding how structural modifications at the nanoscale alter the properties of different photocatalytic systems.

1 Introduction

Solar fuel production by water-splitting has become of increasing interest as the worldwide demand for energy has drastically increased over the past few decades.[1–5] There is a lack of inexpensive and robust photocatalysts for efficient solar water-splitting. The use of wide bandgap semiconductors featuring innovative nanostructures represents one promising solution to this challenge. Semiconductors are attractive photocatalysts in solar water-splitting as they tend to be inexpensive, chemically and photochemically stable. Semiconductor photocatalysis starts with the formation of photoexcited electron-hole pairs which then diffuse to the photocatalyst surface to participate in relevant redox reactions.[6–7] While semiconductors have been of intense interest in the past few decades, these materials do have major limitations, including low efficiency in photocatalysis due to bulk recombination of electron-hole pairs and short charge diffusion distances of photoexcited charge carriers. Some semiconductors with band gaps greater than 3.1 eV often require UV light ($\lambda < 400$ nm) for activation. Accordingly, decreasing charge recombination, increasing charge diffusion distances and modifying the band gaps of these semiconducting materials has been the focus of recent research on solar water-splitting using semiconductor photocatalysts.

Titanium dioxide (TiO_2) is the most extensively studied semiconductor in water-splitting photocatalysis. It has been of specific interest due to its low toxicity, low cost, and high photostability. The band gap of TiO_2 is well aligned with the redox potentials for water-splitting. Other semiconductor systems have been studied in solar water-splitting, including metal oxides (ZnO, WO_3, and Fe_2O_3), non-oxide based semiconductors (ZnS, CdS, and GaN),

Department of Chemistry and Materials Science Program, University of New Hampshire, Durham, NH 03824, United States. E-mail: gonghu.li@unh.edu

various coupled combinations of these materials, as well as the photoelectrochemical cells. This chapter summarizes research in the literature on nanostructured semiconductors as photocatalysts for water-splitting reported in the years of 2011 and 2012. The focus of this chapter is on how nanostructures affect the performance of semiconductors in photocatalytic water-splitting. Although this chapter is entitled "nanostructured photocatalysts for solar water-splitting", many examples discussed here used sacrificial electron donors for hydrogen production, largely because of the difficulty to carry out multi-electron water oxidation on semiconductor surfaces.

2 Titanium dioxide-based photocatalysts

The principles of TiO_2 photocatalysis are well known.[8–10] Upon photoexcitation of TiO_2 materials, electrons are pumped from the valence band into the conduction band, leaving behind positively charged holes in the valence band. The band gap of bare TiO_2 is suitable to carry out water-splitting as the conduction band is more negative than the potential for hydrogen production by proton reduction while the valence band is more positive than the potential for water oxidation. Two forms of TiO_2, anatase and rutile, are often used in photocatalysis which have band gaps of 3.2 and 3.0 eV respectively. With such large band gaps one drawback of TiO_2 materials is their inability to absorb visible light ($\lambda > 400$ nm) which makes up the majority of the solar spectrum.

This section discusses some examples of recent studies that address limitations associated with TiO_2 photocatalysis, namely the requirement for UV irradiation due to wide band gaps and low photocatalytic efficiency due to bulk charge recombination. For example, the band gap of TiO_2 can be decreased by nitrogen doping which effectively extends the absorption edge of TiO_2 into the visible light region.[11] Surface modification using metal nanoparticles has been shown to effectively improve charge separation and subsequently enhance efficiency in TiO_2 photocatalysis.[12–17] The morphology of TiO_2 materials can be optimized to achieve improved photocatalytic activities.[18–21] It should be noted that structural or surface modifications may not necessarily serve well for all purposes. For example, introducing cationic and anonic dopants into TiO_2 has shown to increase light absorption in the visible portion of the solar spectrum but tends to decrease the life times of photogenerated electron-hole pairs.[22–25]

2.1 Black hydrogenated TiO_2

Hydrogenation is an effective treatment to improve visible light photoresponse of TiO_2 nanocrystals.[26–29] In a study by Mao and co-workers, a hydrogenation treatment was carried out by heating TiO_2 nanocrystals to 200 °C in an atmosphere of hydrogen for 5 days.[27] This modification was accompanied by a dramatic change in color to a black material. The significant enhancement in visible light photoresponse was explained by the presence of disordered surface layers as a result of the hydrogenation treatment.[27] This modification also led to an increase in photocatalytic hydrogen production in the presence of a sacrificial donor. In water-splitting tests, the black TiO_2 was loaded with platinum and irradiated in a

aqueous solution containing methanol, which served as a sacrificial electron donor.[27] The platinized black TiO_2 gave a hydrogen production rate of approximately 10 mmol h^{-1} g^{-1}. In comparison, platinized TiO_2 without hydrogenation treatment showed no activity under the same conditions.[27]

Zheng and co-workers prepared surface hydrogenated anatase TiO_2 from protonated titanate nanotubes.[28] As expected, the surface hydrogenation treatment led to enhanced photoresponse in the visible light region (Fig. 1a).[28] Through combined experimental and theoretical studies, the researchers revealed the presence of Ti-H and O-H bond on the surface of resulting TiO_2 nanowire-microspheres (Fig. 1, c-f).[28] The presence of Ti-H bonds contributed to the stabilization of surface disorder induced by the hydrogenation treatment. The TiO_2 nanowire-microspheres demonstrated enhanced activity in H_2 production under visible light irradiation.[28] The researchers attributed the enhancement in photocatalytic activity to efficient charge separation, which was induced by the surface Ti-H bonds and the 1-D nanowire structure.[28]

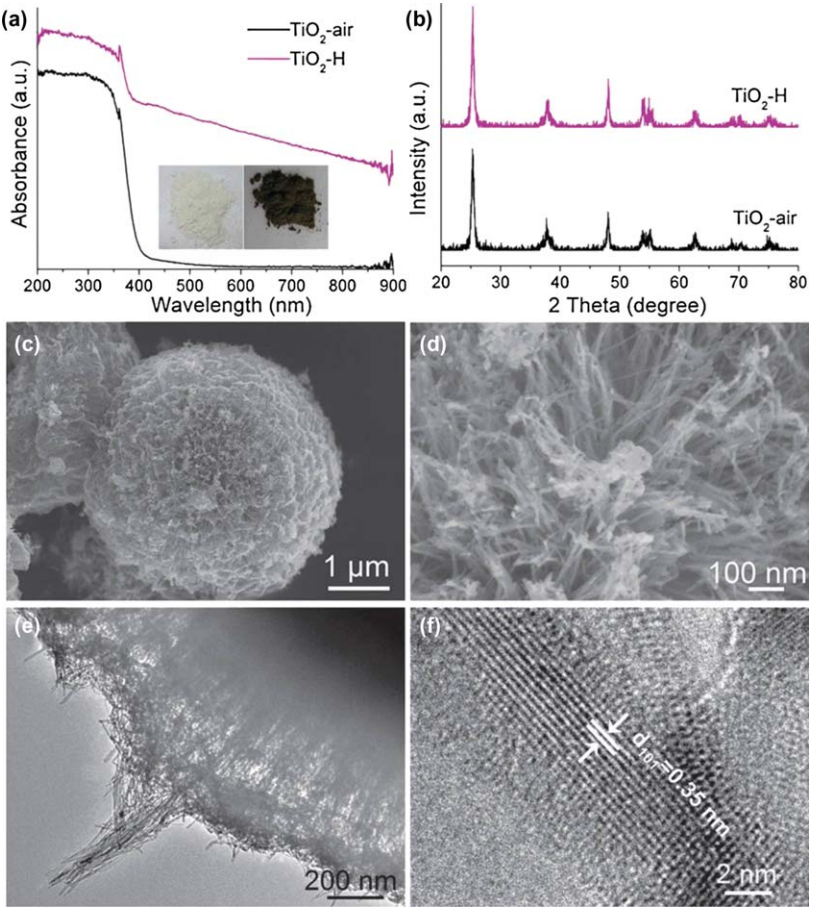

Fig. 1 Optical spectra (a) and XRD patterns (b) of TiO_2–H and TiO_2–air microspheres; (c,d) SEM (c, d) and HRTEM (e, f) images of TiO_2–H nanowire-microspheres. Reproduced from Ref. 28 with permission from The Royal Society of Chemistry.

2.2 Nitrogen doped TiO_2

Other modifications for increasing visible light absorption include doping with non-metal atoms such as nitrogen.[23,30–31] Doping with non-metal atoms decreases the band gap of semiconductors and leads to the formation of defect sites which could enhance charge separation. In comparison, metal dopant atoms are potential sites for charge recombination which is detrimental to photocatalysis. Rayalu and co-workers examined how different dopant concentration effected the change in the band gap of mesoporous TiO_2 as well as photocatalytic activity in hydrogen production.[23] The researchers introduced nitrogen into the TiO_2 framework during a templating synthesis using biopolymer chitosan which contains glucoseamine and actyl glucoseamine.[23] By varying the ratio of TiO_2 to the nitrogen-containing template, the researchers were able to control the dopant concentration.[23] The 1 : 1 TiO_2-to-template ratio led to an optimal dopant concentration and the most effective photocatalyst in hydrogen production from a solution of ethanol.[23]

Liu and co-workers also investigated nitrogen doping as an effective approach to decrease the band gap of TiO_2 materials.[30] The researchers' approach, however, differed from the method by Rayalu and co-workers in that they focused on increasing the ease with which nitrogen could be introduced into the TiO_2 framework. The researchers started with boron doped TiO_2 microspheres and achieved nitrogen doping by heating the boron-doped TiO_2 in the presence of ammonia (Fig. 2a).[30] The synthesized material has substantially enhanced photoresponse in the visible light region

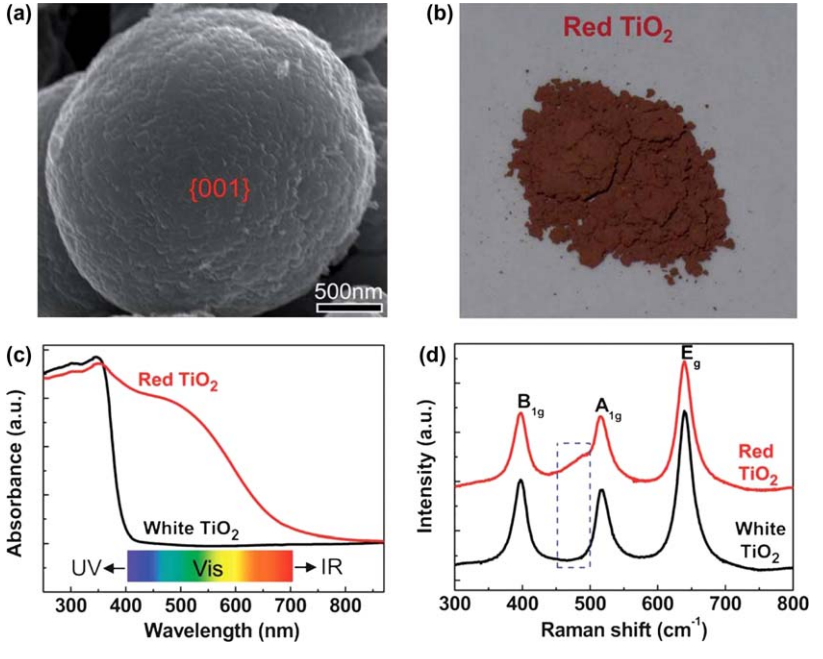

Fig. 2 (a) An SEM image of TiO_2 microsphere, (b) a picture of red TiO_2 material, (c) Optical spectra of red TiO_2 and unmodified TiO_2, and (d) Raman spectra of red TiO_2 and unmodified TiO_2. Reproduced from Ref. 30 with permission from The Royal Society of Chemistry.

(Fig. 2c), having a surface band gap energy of 1.94 eV and a core band gap energy of 3.22 eV.[30] This band gap gradient in the TiO_2 microspheres allows for more significant visible light absorption. The production of both hydrogen and oxygen were detected when the microspheres were put on to an electrode and used in a photoelectrochemical water-splitting cell.[30]

2.3 Plasmonic metal nanoparticles on TiO_2

The presence of noble metal nanoparticles on TiO_2 surface can significantly enhance the photocatalytic ability of TiO_2 materials.[21,32] Tsai and co-workers prepared a plasmonic photocatalyst by loading gold nanoparticles on TiO_2 for use in solar water-splitting.[16] The presence of plasmonic Au nanoparticles on TiO_2 was clearly seen in microscopic images and further confirmed by the presence of a surface plasmon resonance peak at 563.8 nm in its optical spectrum (Fig. 3). The researchers found that the production of hydrogen was minimal when pure TiO_2 was irradiated with UV light, significant hydrogen production was observed on Au/TiO_2.[16] Surface Au nanoparticles contributed to the excellent activity of Au/TiO_2 by acting as electron sinks for improved charge separation and active sites for hydrogen production. Furthermore, the surface plasmon resonance phenomenon of Au provided extra electromagnetic field, which also contributed to the enhancement of H_2 production.[16]

Garcia and co-workers studied the mechanism of charge separation in Au/TiO_2 photocatalysts.[14] The researchers probed the effect of activation of the TiO_2 photocatalyst or excitation of surface gold nanoparticles. The activation of TiO_2 was done by using UV light ($\lambda < 382$ nm) while the gold nanoparticles were photoexcited under visible light irradiation ($\lambda \sim 532$ nm).[14] Under UV light, photoexcited electrons in the TiO_2 conduction band were injected into the surface gold nanoparticles for hydrogen production, while positively charged holes remained in the valence band of TiO_2 and were quenched by a sacrificial electron donor.[14] When the material was irradiated using visible light ($\lambda \sim 532$ nm), the gold plasmon band was photoexcited, generating electron-hole pairs in Au nanoparticles (Fig. 4). Photoexcited electrons in the gold nanoparticles were injected into the conduction band of TiO_2 and holes remained in the gold nanoparticles. Subsequent photocatalytic processes occurred on surfaces of both TiO_2 and Au nanoparticles in the presence of sacrificial agents (Fig. 4).[14]

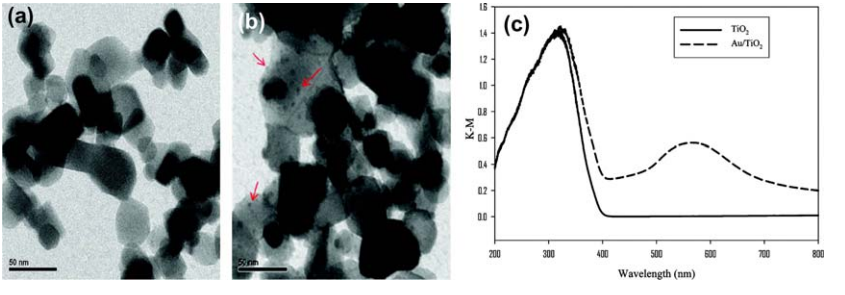

Fig. 3 TEM micrographs of (a) TiO_2 and (b) 3.0 wt% Au on TiO_2. Optical spectra of the two samples are shown in (c). Reproduced from Ref. 16 with permission from The American Chemical Society.

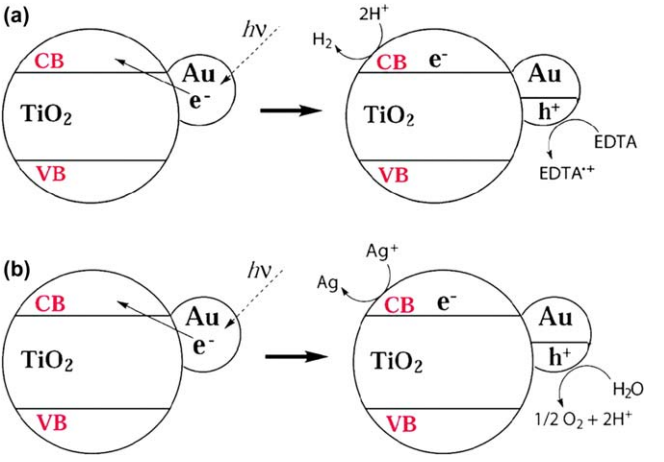

Fig. 4 Schematics of photocatalytic processes on Au/TiO_2 upon excitation of the gold surface plasmon band for (a) hydrogen production and (b) water oxidation. Reproduced from Ref. 14 with permission from The American Chemical Society.

2.4 Morphology optimization of TiO_2

Enhanced charge separation and hindered charge recombination can be achieved by controlling the morphology of TiO_2 materials. Pan and co-workers investigated the photocatalytic activity of different facets of anatase in hydrogen production.[33] The relative reactivity of anatase facets follows this trend, $001 < 101 < 010$.[33] Based on this work, Pan and co-workers synthesized hollow anatase single crystals and mesocrystals with dominant 101 facets (Fig. 5).[18] The hollow single crystals demonstrated much higher photocatalytic activity than solid anatase TiO_2 materials.[18] The enhanced activity of the hollow crystals was associated with the presence of abundant 101 facet, shortened charge diffusion length and higher surface area of the hollow material.[18] In particular, the different reactivity of various facets was attributed to the numbers of uncoordinated surface Ti atoms present on the facets. The researchers further demonstrated that the hollow single crystals behaved differently than hollow mesocrystals in photocatalytic hydrogen production or oxygen evolution in the presence of sacrificial agents.[18]

Tubular nanostructures have been examined in photocatalytic water-splitting.[34] Wei and co-workers synthesized TiO_2 nanotube arrays with different geometric parameters, including wall thickness, inner diameter and porosity (Fig. 6a).[19] The TiO_2 nanotubes were tested in photoelectrochemical water-splitting where the photoconversion efficiency was monitored as a function of the geometric parameters. The optimal photoelectrochemical efficiency was achieved for an inner diameter of 48 nm, while the photoelectrochemical efficiency increased monotonously with porosity of the nanotube arrays (Fig. 6b).[19] No clear correlation between wall thickness and photoelectrochemical efficiency was found. In general, nanotube arrays with thinner walls exhibited better photoelectrochemical efficiency due to facile charge separation.[19]

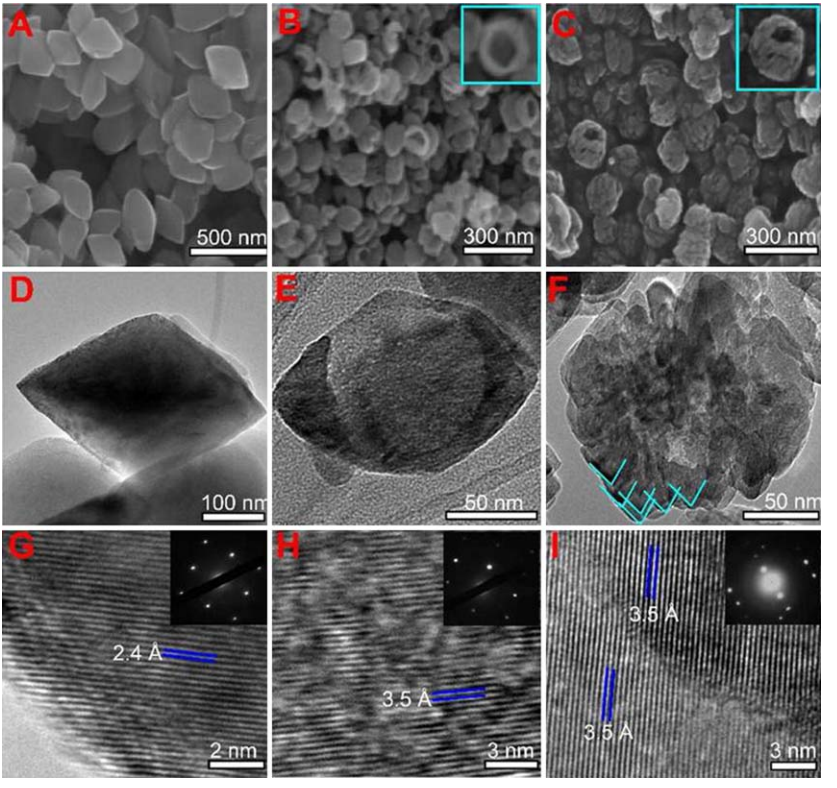

Fig. 5 SEM, TEM and HRTEM images of (A, D, G) solid anatase, (B, E, H) hollow anatase, and (C, F, I) hollow anatase mesocrystals with 101 facets. Reproduced from Ref. 18 with permission from The American Chemical Society.

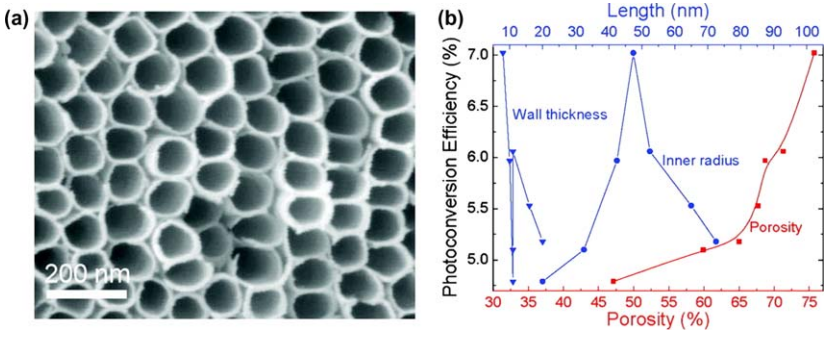

Fig. 6 (a) An SEM image of TiO_2 nanotube arrays; (b) photoconversion efficiency as a function of nanotube wall thickness, inner radius and porosity. Reproduced from Ref. 19 with permission from The American Chemical Society.

3 Other metal oxide photocatalysts

Many non-titanium based metal oxides have displayed photocatalytic activity in water-splitting and artificial photosynthesis. Semiconductors including WO_3,[35–44] ZnO,[45–51] and Fe_2O_3[52–56] have been of particular interest in recent research. Some of these materials have narrower band gaps than

Table 1 Selected semiconductors studied in photocatalytic water-splitting during the years of 2011 and 2012.

Semiconductor	E_{bg} (eV)[a]	Light Sources[b]	Sacrificial Agents	Reported Efficiency[c]	References
WO_3	2.5–2.8	Vis (>400)	EtOH/MeOH	42%	35, 37, 39, 41
S-WO_3	2.0	UV/Vis (300–400/500)	SO_4^{2-}	–	57
$RuO_2/PtO_x/WO_3$	2.7	Vis (>420)	–	14.4%	58
α-Fe_2O_3	2.05	UV (300–400)	MeOH/Formic acid/Oxalic acid	3.76	52
Pt/Fe_3O_4	2.7	–	–	–	55
ZnO	3.34	–	–	–	46
GaN-ZnO	2.6–2.7	Vis (418)	–	5.1%	51, 49
CuO-ZnO	3.37	UV	MeOH	–	48
$SrTiO_3$	3.2	UV/Vis	–	–	59–60
$Rh/SrTiO_3$	2.3	Vis (420)	–	0.18%	61, 62, 63
NiO-$SrTiO_3$	3.2	UV/Vis	–	0.041%	64
$CsTaWO_6$	3.8	Vis	–	–	65–66
$PbTiO_3$	2.75	>300	MeOH	–	67
$GaFeO_3$	2.7	>395	None	0.3%	68
CdS	2.3	Vis (>400)	EtOH	16.6%	69–70
C_3N_4	2.7	Vis (>420)	TEOA	0.1%	71–74
$Zn_xCd_{x-1}S$	2.4	Vis (>420)	S^{2-}/SO_3^{2-}	30.4%	75–77
ZnS	3.66	Vis (>400)	S^{2-}/SO_3^{2-}	–	78, 79
$NaTaO_3$	–	UV (>200)	–	–	80, 81
$SrNbO_2N$	1.8	Vis (>400)	SO_4^{2-}	47%	82
Ta_3N_5	2.05	UV/Vis (300–800)	–	–	83

[a]E_{bg}: band gap in eV.
[b]Wavelength in nm specified in parentheses where available.
[c]Efficiency was defined differently in individual studies.

TiO_2 and are able to harness more visible light of the solar spectrum. Table 1 lists some representative results from the literature using non-TiO_2 metal oxides in photocatalysis.

Hematite (α-Fe_2O_3) has been of particular interest in water-splitting as it has similar properties to TiO_2. For instance, hematite is inexpensive and non-toxic. It does however have a smaller band gap energy in comparison to TiO_2, making it a more attractive choice as a visible-light photocatalyst.[56] Although hematite can absorb visible light and photoexcited holes in its valence band are capable of oxidizing water into oxygen, the conduction band of hematite is slightly too positive to reduce water into hydrogen.[56] Structural modifications to hematite could open up the possibility of shifting band edges and eventually making it a suitable photocatalyst for water-splitting. Rayalu and co-workers synthesized ferrite nanoparticles for use in photocatalytic water-splitting.[55] The synthesized nanoparticles had an average diameter of $\sim$12.42 nm and a measured band gap of 2.7 eV which is greater than that of bulk hematite.[55] The synthesized ferrite nanoparticles exhibited improved activity in photocatalytic water-splitting because of enhanced charge separation.[55]

Coupling with another semiconductor or other nanomaterials could significantly enhance the efficiency of hematite as a water-splitting photocatalyst.[53,84,85] Wang and co-workers have developed an approach to solve the problem of short diffusion distances in hematite by creating a nanonet structure which provides both a high surface area to carry out water-splitting catalysis.[53] The researchers coated a $TiSi_2$ nanonet with a thin layer of hematite to efficiently separate photoexcited electrons and holes by conducting the electrons through the core of the nanonet. Such a structure allows for efficient diffusion of holes to the surface of the hematite to carry out water oxidation.[53] The same group also deposited hematite on vertically aligned Si nanowires to for a dual-absorber system (Fig. 7, left).[84] In the dual-absorber system, Si nanowires absorb photons in the range between 600 nm and 1100 nm, which are transparent to Fe_2O_3, and convert the photons into additional photovoltage needed for photoelectrochemical water-splitting by hematite.[84] The dual-absorber system successfully resolved a major limitation of hematite as a photocatalyst for solar water-splitting, which concerns the conduction band being too positive for high-efficiency water-splitting.[84]

Similarly, tungsten oxide has a band gap of 2.8 eV with a valence band at an energy low enough to oxidize water but the position of its conduction band falls just short of the reduction potential for hydrogen production.[86] In order to shift the conduction band to an appropriate energy to carry out

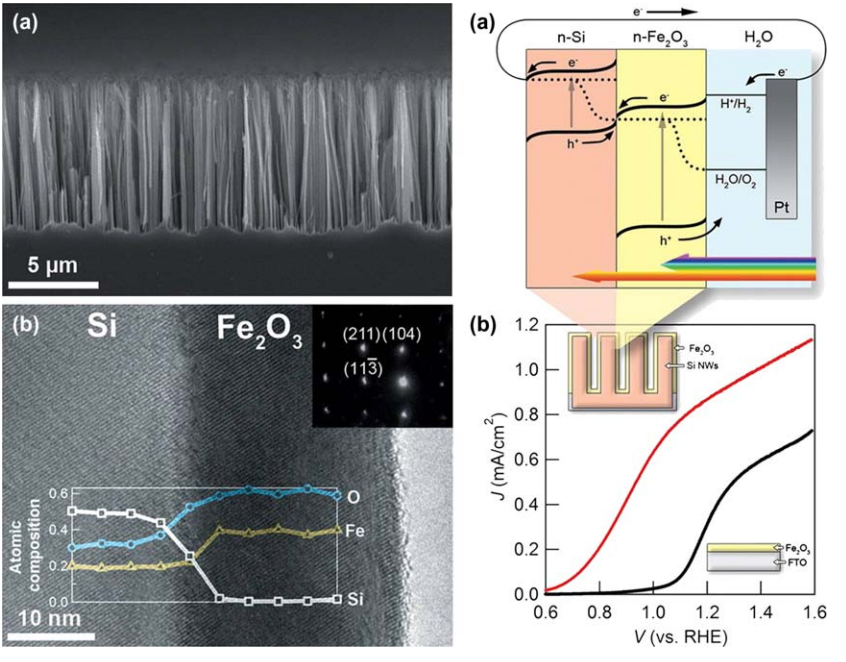

Fig. 7 Left: (a) an SEM image of Si nanowires and (b) a TEM image showing the crystalline quality of the Fe_2O_3 film grown on Si nanowires; Right: (a) energy band schematics of the Fe_2O_3/Si nanowire system and (b) J–V plots under simulated solar illumination in 1.0 M NaOH aqueous electrolyte for the Fe_2O_3/Si nanowire system (top - red online) and Fe_2O_3 on a planar fluorine-doped tin oxide conducting glass (black). Reproduced from Ref. 84 with permission from The American Chemical Society.

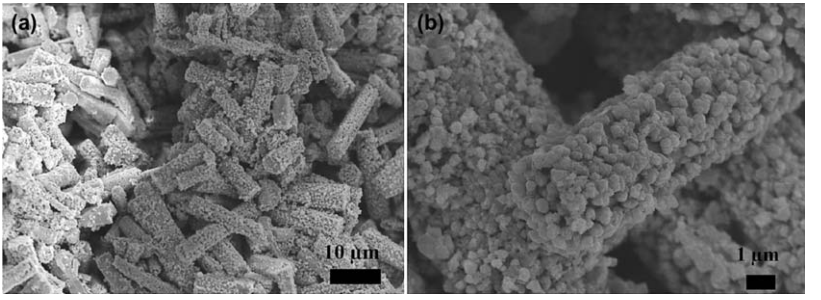

Fig. 8 SEM images of the hierarchical ZnO-CuO composite at different magnifications. Reproduced from Ref. 48 with permission from Elsevier.

hydrogen production, various modifications have been examined such as doping[57] and forming composites with co-catalysts.[58] Chen and co-workers synthesized sulfur-doped WO_3 with significantly lower band gap (2.0 eV) than that of undoped WO_3 (2.8 eV). This significant reduction in the band gap energy further extends the absorption range of WO_3 into the visible light region.[40] The doped photocatalyst demonstrated higher activity than the undoped material in solar water-splitting.[40]

Zinc oxide has received much attention in recent research as a photocatalyst for solar water-splitting. Pure ZnO has a band gap energy of 3.34 eV,[46] making it inactive under visible light. Furthermore, the photocatalytic activity of ZnO-based materials is generally poor in comparison to TiO_2 materials. Photocatalytic performance of ZnO materials could be improved by coupling with other materials. In a recent study, Sun and co-workers synthesized ''corn-like'' nanostructures of CuO-ZnO (Fig. 8), which demonstrated enhanced surface area and improved efficiency in solar water-splitting.[48] The researchers suggested that the ''core-like'' nanostructures improved the photostability of ZnO and that photogenerated charge carriers are better separated in the composite material.[48]

4 Other semiconductor photocatalysts

Similar to oxide-based semiconductors, some non-oxide semiconducting materials have smaller band gaps than the bench mark TiO_2, making them more attractive for visible-light photocatalysis (see Table 1 for some examples). But non-oxide semiconductor photocatalysts often suffer from drawbacks including poor band positioning relative to the redox potentials for water-splitting as well as poor stability under photochemical conditions. Cadmium sulfide (CdS) has been employed as a water-splitting photocatalyst and has been further modified in various ways to enhance its photocatalytic properties.[69,70,87–94] As a photocatalytic material, CdS undergoes photocorrosion when used in splitting water as the oxidation potentials for cadmium are more negative than the potential of photochemically generated holes in the valence band.[69] This results in the degradation of CdS and the formation of Cd^{2+} ions. Numerous efforts have been made to decrease the degradation of CdS materials by coupling with other semiconductors.[69,87–89,91,92,94] By creating coupled systems, the lifetime of photogenerated charge carriers (holes and electrons) can be

extended, and the band gap can be tuned to become suitable for water-splitting.[94]

Carbon nitride (C_3N_4) materials have investigated as photocatalysts for water-splitting in recent studies.[72–74,95–99] Carbon nitride differs from many of the photocatalytic systems in current research due to the fact that it is an organic based semiconducting material. Ogale and co-workers synthesized nanocomposite materials consisting of multi-walled carbon nanotubes (MWCNTs) and graphitic carbon nitride (g-C_3N_4, Fig. 9).[72] The presence of MWCNTs significantly increased the photocatalytic activity of g-C_3N_4 in hydrogen production.[72] The researchers attributed the enhancement in photocatalytic activity to increased charge transfer ability originated from the unique tubular morphology.[72]

A variety of composite materials have been investigated in photocatalytic water-splitting. By tuning the composition and nanostructures, composite photocatalysts could have properly spaced band gaps for solar water-splitting. Specifically, $NaTaO_3$[80,81] and $SrNbO_2N$[82] have been studied recently. Maeda and co-workers investigated $SrNbO_2N$ as a photocatalyst for water-splitting as it has a band gap of 1.8 eV.[82] The $SrNbO_2N$ photocatalyst was able to oxidize water in the absence of an external potential, making it the only material with a band gap less than 2.0 eV capable of splitting water photochemically. Hong and co-workers studied $NaTaO_3$ as a photocatalyst for hydrogen production.[81] The researchers found that the presence of $Mo_3S_4^{4+}$ as a co-catalyst for $NaTaO_3$ resulted in a 28-fold increase in hydrogen production rate over bare $NaTaO_3$.[81] The optimal loading of the co-catalyst was found to be 8% by weight at pH 2.[81]

5 The photoelectrochemical approach

Photoelectrochemical cells are complete artificial photosynthetic systems for water-splitting. Application of a bias voltage to the electrodes in a photoelectrochemical cell has the ability to improve photoexcited charge separation and achieve sequential electron transfer needed for water-splitting that involves multi-electron processes. Semiconductors, particularly TiO_2 nanomaterials, have been widely employed in photoelectrochemical studies. Other semiconductors, including hematite and silicon, have been incorporated in photoelectrochemical cells for water-splitting.[53,84,85,100–107] Shao and coworkers studied photoelectrochemical water-splitting using TiO_2 nanotube arrays as the photoanode and a Pt/C carbon paper as the photocathode.[108] The photoelectrochemical cell was constructed by separating the anode and cathode with an asbestos membrane. Under light irradiation, production of hydrogen and oxygen gases was detected above a KOH solution in the presence of an applied bias of 0.6 V.[108] Experimental results indicated that the well-ordered nanotubular array layer was necessary for achieving high conversion efficiency in the photoelectrochemical cell.[108]

Wang and co-workers investigated hydrogen-treated TiO_2 nanowires in photoelectrochemical water-splitting.[29] The hydrogenated TiO_2 nanowires were prepared by thermally annealing pristine rutile TiO_2 nanowires in hydrogen atmosphere (Fig. 10). In comparison to untreated TiO_2 samples,

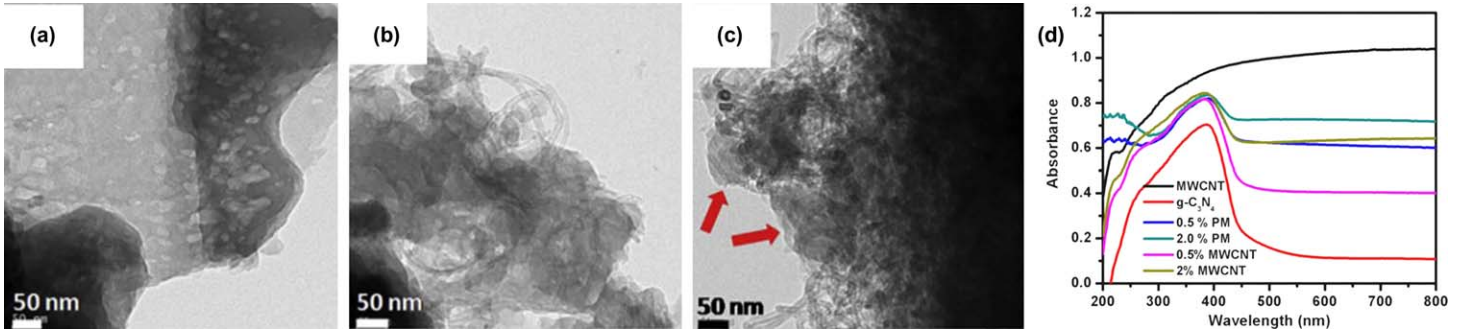

Fig. 9 TEM images of (a) g-C_3N_4, (b) 0.5% MWCNT/g-C_3N_4, (c) 2% MWCNT/(a) g-C_3N_4, and (d) optical spectra of C_3N_4 and its composites with MWCNTs. Reproduced from Ref. 72 with permission from Elsevier.

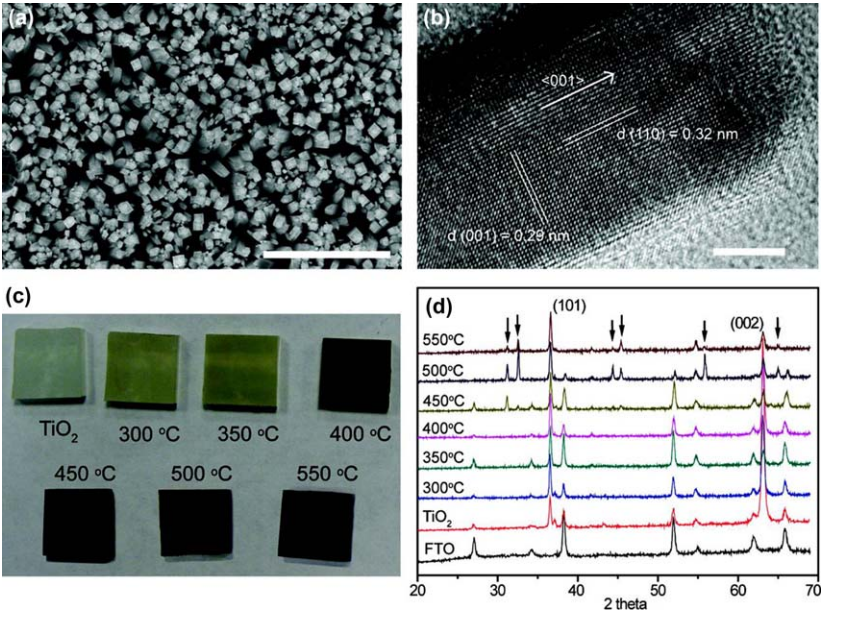

Fig. 10 (a) An SEM image of vertically aligned TiO_2 nanowire arrays, (b) an TEM image of a single TiO_2 nanowire, (c) digital pictures and (d) XRD spectra of pristine TiO_2 and hydrogenated TiO_2 nanowires annealed at various temperatures. Reproduced from Ref. 29 with permission from The American Chemical Society.

the hydrogenated nanowires showed efficient charge separation and transportation, and as a result, substantially enhanced photocurrent.[29] A solar-to-hydrogen efficiency of $\sim$1.1% was obtained under the experimental conditions employed in the study. A high density of oxygen vacancies, which served as electron donors in water-splitting, was created in the TiO_2 nanowires upon hydrogen treatment.[29]

6 Conclusions

With so many different approaches to creating a system capable of splitting water using only solar light, the field is making strong advances toward this overall goal. Of the systems which are currently under investigation many of them show promise but most of the systems have significant drawbacks. Titanium dioxide systems face the issue of poor utilization of the entire solar spectrum, being only capable of harvesting UV light due to its large band gap. Oxide-based materials such as hematite can have smaller band gaps but their band edge potentials are not always properly aligned with the redox potentials of water-splitting. These materials also have issues with charge separation, charge diffusion and photostability. In order to address the issues with many semiconducting materials, approaches such as cationic and anionic doping, surface functionalization with metal nanoparticles, as well as morphology controlled systems have been attempted as to increase the efficiencies of these systems. In addition to these approaches research on novel materials such as $NaTaO_3$ and $SrNbO_2N$ have been studied. Many approaches have proven useful in creating efficient photocatalytic systems.

Although the field is far from developing a system which would be able to scale up and provide clean energy and solve the current global energy crisis, ongoing research in the field is providing insight as to which materials may be promising as a viable solution to this global issue.

References

1 Y. Tachibana, L. Vayssieres and J. R. Durrant, *Nat. Photonics*, 2012, **6**, 511–518.
2 F. E. Osterloh and B. A. Parkinson, *MRS Bull.*, 2011, **36**, 17–22.
3 M. G. Walter, E. L. Warren, J. R. McKone, S. W. Boettcher, Q. Mi, E. A. Santori and N. S. Lewis, *Chem. Rev.*, 2010, **110**, 6446–6473.
4 K. Maeda and K. Domen, *J. Phys. Chem. Lett.*, 2010, **1**, 2655–2661.
5 A. Kudo and Y. Miseki, *Chem. Soc. Rev.*, 2009, **38**, 253–278.
6 P. V. Kamat, *Chem. Rev.*, 1993, **93**, 267–300.
7 M. Matsuoka, M. Kitano, M. Takeuchi, K. Tsujimaru, M. Anpo and J. M. Thomas, *Catalysis Today*, 2007, **122**, 51–61.
8 A. L. Linsebigler, G. Q. Lu and J. T. Yates, *Chem. Rev.*, 1995, **95**, 735–758.
9 O. Carp, C. L. Huisman and A. Reller, *Prog. Solid State Chem.*, 2004, **32**, 33–177.
10 M. Anpo, *Bull. Chem. Soc. Jpn.*, 2004, **77**, 1427–1442.
11 R. Asahi, T. Morikawa, T. Ohwaki, K. Aoki and Y. Taga, *Science*, 2001, **293**, 269–271.
12 H. J. Yun, H. Lee, N. D. Kim, D. M. Lee, S. Yu and J. Yi, *ACS Nano*, 2011, **5**, 4084–4090.
13 S. Onsuratoom, S. Chavadej and T. Sreethawong, *Int. J. Hydrogen Energy*, 2011, **36**, 5246–5261.
14 C. Gomes Silva, R. Juarez, T. Marino, R. Molinari and H. Garcia, *J. Am. Chem. Soc.*, 2011, **133**, 595–602.
15 Z. Liu, W. Hou, P. Pavaskar, M. Aykol and S. B. Cronin, *Nano Lett*, 2011, **11**, 1111–1116.
16 J.-J Chen, J. C. S. Wu, P. C. Wu and D. P. Tsai, *J. Phys. Chem. C*, 2011, **115**, 210–216.
17 X.-W. Wang, G. Liu, L.-Z. Wang, J. Pan, G.-Q. Lu and H.-M. Cheng, *J. Mater. Chem.*, 2011, **21**, 869–873.
18 W. Jiao, L. Wang, G. Liu, G. Q. Lu and H.-M. Cheng, *ACS Catal*, 2012, **2**, 1854–1859.
19 S. Liang, J. He, Z. Sun, Q. Liu, Y. Jiang, H. Cheng, B. He, Z. Xie and S. Wei, *J. Phys. Chem. C*, 2012, **116**, 9049–9053.
20 Y. Jun, J. H. Park and M. G. Kang, *Chem. Commun.*, 2012, **48**, 6456–6471.
21 G. Li and K. A. Gray, *Chem. Phys.*, 2007, **339**, 173–187.
22 R. Dholam, N. Patel and A. Miotello, *Int. J. Hydrogen Energy*, 2011, **36**, 6519–6528.
23 M. M. Joshi, P. A. Mangrulkar, S. N. Tijare, P. S. Padole, D. V. Parwate, N. K. Labhsetwar and S. S. Rayalu, *Int. J. Hydrogen Energy*, 2012, **37**, 10457–10461.
24 L. Jing, J. Zhou, J. R. Durrant, J. Tang, D. Liu and H. Fu, *Energy Environ. Sci.*, 2012, **5**, 6552–6558.
25 X. Ma, Y. Wu, Y.-H. Lu, J. Xu, Y.-J. Wang and Y.-F. Zhu, *J. Phys. Chem. C*, 2011, **115**, 16963–16969.
26 Y. H. Hu, *Angew. Chem., Int. Ed.*, 2012, **51**, 12410–12412.
27 X. Chen, L. Liu, P. Y. Yu and S. S. Mao, *Science*, 2011, **331**, 746–750.

28 Z. Zheng, B. Huang, J. Lu, Z. Wang, X. Qin, X. Zhang, Y. Dai and M.-H. Whangbo, *Chemical Communications*, 2012, **48**, 5733–5735.
29 G. Wang, H. Wang, Y. Ling, Y. Tang, X. Yang, R. C. Fitzmorris, C. Wang, J. Z. Zhang and Y. Li, *Nano Letters*, 2011, **11**, 3026–3033.
30 G. Liu, L.-C Yin, J. Wang, P. Niu, C. Zhen, Y. Xie and H.-M. Cheng, *Energy Environ. Sci.*, 2012, **5**, 9603–9610.
31 J. Tang, A. J. Cowan, J. R. Durrant and D. R. Klug, *J. Phys. Chem. C*, 2011, **115**, 3143–3150.
32 P. V. Kamat, *Pure Appl. Chem.*, 2002, **74**, 1693–1706.
33 J. Pan, G. Liu, G. Q. Lu and H.-M. Cheng, *Angew. Chem. Int. Ed.*, 2011, **50**, 2133–2137.
34 G. K. Mor, O. K. Varghese, M. Paulose, K. Shankar and C. A. Grimes, *Sol. Energy Mater. Sol. Cells*, 2006, **90**, 2011–2075.
35 F. M. Pesci, A. J. Cowan, B. D. Alexander, J. R. Durrant and D. R. Klug, *The Journal of Physical Chemistry Letters*, 2011, **2**, 1900–1903.
36 F. Wang, C. Di Valentin and G. Pacchioni, *J. Phys. Chem. C*, 2012, **116**, 8901–8909.
37 W. Zhao, Z. Wang, X. Shen, J. Li, C. Xu and Z. Gan, *Int. J. Hydrogen Energy*, 2011, **37**, 908–915.
38 R. Abe, M. Higashi and K. Domen, *ChemSusChem.*, 2011, **4**, 228–237.
39 A. Tacca, L. Meda, G. Marra, A. Savoini, S. Caramori, V. Cristino, C. A. Bignozzi, V. G. Pedro, P. P. Boix, S. Gimenez and J. Bisquert, *ChemPhysChem.*, 2012, **13**, 3025–3034.
40 W. Li, J. Li, X. Wang and Q. Chen, *Appl. Surf. Sci.*, 2012, **263**, 157–162.
41 W. Wei, S. Shaw, K. Lee and P. Schmuki, *Chem.–Eur. J.*, 2012, **18**, 14622–14626.
42 J. Guo, Y. Li, S. Zhu, Z. Chen, Q. Liu, D. Zhang, W.-J. Moon and D.-M. Song, *RSC Adv.*, 2012, **2**, 1356–1363.
43 S. S. K. Ma, K. Maeda, R. Abe and K. Domen, *Energy Environ. Sci.*, 2012, **5**, 8390–8397.
44 R. Liu, Y. Lin, L.-Y. Chou, S. W. Sheehan, W. He, F. Zhang, H. J. M. Hou and D. Wang, *Angew. Chem., Int. Ed.*, 2011, **50**, 499–502.
45 D. K. Kanan and E. A. Carter, *J. Phys. Chem. C*, 2012, **116**, 9876–9887.
46 Y. H. Lu, S. P. Russo and Y. P. Feng, *Phys. Chem. Chem. Phys.*, 2011, **13**, 15973–15976.
47 G.-L. Chai, C.-S. Lin and W.-D. Cheng, *J. Mater. Chem.*, 2011, **21**, 17071–17076.
48 Z. Liu, H. Bai, S. Xu and D. D. Sun, *Int. J. Hydrogen Energy*, 2011, **36**, 13473–13480.
49 T. Ohno, L. Bai, T. Hisatomi, K. Maeda and K. Domen, *J. Am. Chem. Soc.*, 2012, **134**, 8254–8259.
50 Y.-G. Lin, Y.-K. Hsu, Y.-C. Chen, S.-B. Wang, J. T. Miller, L.-C. Chen and K.-H. Chen, *Energy Environ. Sci.*, 2012, **5**, 8917–8922.
51 F. Dionigi, P. C. K. Vesborg, T. Pedersen, O. Hansen, S. Dahl, A. Xiong, K. Maeda, K. Domen and I. Chorkendorff, *J. Catal.*, 2012, **292**, 26–31.
52 A. J. Cowan, C. J. Barnett, S. R. Pendlebury, M. Barroso, K. Sivula, M. Gratzel, J. R. Durrant and D. R. Klug, *J. Am. Chem. Soc.*, 2011, **133**, 10134–10140.
53 Y. Lin, G. Yuan, S. Sheehan, S. Zhou and D. Wang, *Energy Environ. Sci.*, 2011, **4**, 4862–4869.
54 Z. Huang, Y. Lin, X. Xiang, W. Rodriguez-Cordoba, K. J. McDonald, K. S. Hagen, K.-S. Choi, B. S. Brunschwig, D. G. Musaev, C. L. Hill, D. Wang and T. Lian, *Energy Environ. Sci.*, 2012, **5**, 8923–8926.

55 P. A. Mangrulkar, V. Polshettiwar, N. K. Labhsetwar, R. S. Varma and S. S. Rayalu, *Nanoscale*, 2012, **4**, 5202–5209.
56 M. J. Katz, S. C. Riha, N. C. Jeong, A. B. F. Martinson, O. K. Farha and J. T. Hupp, *Coord. Chem. Rev.*, 2012, **256**, 2521–2529.
57 Y. Zhao, S. Zhang, B. Li, H. Yan, S. He, L. Tian, W. Shi, J. Ma, M. Wei, D. G. Evans and X. Duan, *Chem.–Eur. J.*, 2011, **17**, 13175–13181.
58 Y. Ohsaki, N. Masaki, T. Kitamura, Y. Wada, T. Okamoto, T. Sekino, K. Niihara and S. Yanagida, *Phys. Chem. Chem. Phys.*, 2005, **7**, 4157–4163.
59 T. K. Townsend, N. D. Browning and F. E. Osterloh, *ACS Nano*, 2012, **6**, 7420–7426.
60 S. Hara and H. Irie, *Applied Catalysis, B: Environmental*, 2012, **115–116**, 330–335.
61 K. Iwashina and A. Kudo, *J. Am. Chem. Soc.*, 2011, **133**, 13272–13275.
62 S. Kawasaki, K. Nakatsuji, J. Yoshinobu, F. Komori, R. Takahashi, M. Lippmaa, K. Mase and A. Kudo, *Appl. Phys. Lett.*, 2012, **101**, 033910/1–033910/4.
63 S. Kawasaki, K. Akagi, K. Nakatsuji, S. Yamamoto, I. Matsuda, Y. Harada, J. Yoshinobu, F. Komori, R. Takahashi, M. Lippmaa, C. Sakai, H. Niwa, M. Oshima, K. Iwashina and A. Kudo, *J. Phys. Chem. C*, 2012, **116**, 24445–24448.
64 T. K. Townsend, N. D. Browning and F. E. Osterloh, *Energy Environ. Sci.*, 2012, **5**, 9543–9550.
65 A. Mukherji, R. Marschall, A. Tanksale, C. Sun, S. C. Smith, G. Q. Lu and L. Wang, *Adv. Funct. Mater.*, 2011, **21**, 126–132.
66 R. Marschall, A. Mukherji, A. Tanksale, C. Sun, S. C. Smith, L. Wang and G. Q. Lu, *J. Mater. Chem.*, 2011, **21**, 8871–8879.
67 D. Arney, T. Watkins and P. A. Maggard, *J. Am. Ceram. Soc.*, 2011, **94**, 1483–1489.
68 P. Dhanasekaran and N. M. Gupta, *Int. J. Hydrogen Energy*, 2012, **37**, 4897–4907.
69 R. Peng, D. Zhao, J. Baltrusaitis, C.-M. Wu and R. T. Koodali, *RSC Adv*, 2012, **2**, 5754–5767.
70 C. Li, J. Yuan, B. Han and W. Shangguan, *Int. J. Hydrogen Energy*, 2011, **36**, 4271–4279.
71 S. Xu, A. J. Du, J. Liu, J. Ng and D. D. Sun, *Int. J. Hydrogen Energy*, 2011, **36**, 6560–6568.
72 A. Suryawanshi, P. Dhanasekaran, D. Mhamane, S. Kelkar, S. Patil, N. Gupta and S. Ogale, *Int. J. Hydrogen Energy*, 2012, **37**, 9584–9589.
73 J. Zhang, M. Grzelczak, Y. Hou, K. Maeda, K. Domen, X. Fu, M. Antonietti and X. Wang, *Chem. Sci.*, 2012, **3**, 443–446.
74 X. Wang, S. Blechert and M. Antonietti, *ACS Catal*, 2012, **2**, 1596–1606.
75 Y. Wang, J. Wu, J. Zheng and R. Xu, *Catal. Sci. Technol.*, 2011, **1**, 940–947.
76 S. A. Macias-Sanchez, R. Nava, V. Hernandez-Morales, Y. J. Acosta-Silva, L. Gomez-Herrera, B. Pawelec, S. M. Al-Zahrani, R. M. Navarro and J. L. G. Fierro, *Int. J. Hydrogen Energy*, 2012, **37**, 9948–9958.
77 J. Lu, Y. Dai, M. Guo, W. Wei, Y. Ma, S. Han and B. Huang, *ChemPhysChem*, 2012, **13**, 147–154.
78 J. Zhang, J. Yu, Y. Zhang, Q. Li and J. R. Gong, *Nano Lett.*, 2011, **11**, 4774–4779.
79 Y. Yu, G. Chen, Q. Wang and Y. Li, *Energy Environ. Sci.*, 2011, **4**, 3652–3660.
80 T. Yokoi, J. Sakuma, K. Maeda, K. Domen, T. Tatsumi and J. N. Kondo, *Phys. Chem. Chem. Phys.*, 2011, **13**, 2563–2570.
81 S. W. Seo, S. Park, H.-Y. Jeong, S. H. Kim, U. Sim, C. W. Lee, K. T. Nam and K. S. Hong, *Chem. Commun.*, 2012, **48**, 10452–10454.

82 K. Maeda, M. Higashi, B. Siritanaratkul, R. Abe and K. Domen, *J. Am. Chem. Soc.*, 2011, **133**, 12334–12337.
83 Y. Kado, C.-Y. Lee, K. Lee, J. Mueller, M. Moll, E. Spiecker and P. Schmuki, *Chem. Commun.*, 2012, **48**, 8685–8687.
84 M. T. Mayer, C. Du and D. Wang, *J. Am. Chem. Soc.*, 2012, **134**, 12406–12409.
85 M. Zhang, Y. Lin, T. J. Mullen, W.-F. Lin, L.-D. Sun, C.-H. Yan, T. E. Patten, D. Wang and G.-Y. Liu, *J. Phys. Chem. Lett.*, 2012, **3**, 3188–3192.
86 J. Tang, A. J. Cowan, J. R. Durrant and D. R. Klug, *J. Phys. Chem. C*, 2011, **115**, 3143–3150.
87 J. Hou, Z. Wang, W. Kan, S. Jiao, H. Zhu and R. V. Kumar, *J. Mater. Chem.*, 2012, **22**, 7291–7299.
88 P. Gao, J. Liu, S. Lee, T. Zhang and D. D. Sun, *J. Mater. Chem*, 2012, **22**, 2292–2298.
89 Q. Li, B. Guo, J. Yu, J. Ran, B. Zhang, H. Yan and R. G. Jian, *J. Am. Chem. Soc.*, 2011, **133**, 10878–10884.
90 R. Sasikala, A. R. Shirole, V. Sudarsan, K. G. Girija, R. Rao, C. Sudakar and S. R. Bharadwaj, *J. Mater. Chem.*, 2011, **21**, 16566–16573.
91 Z. Khan, T. R. Chetia and M. Qureshi, *Nanoscale*, 2012, **4**, 3543–3550.
92 Z. Shen, G. Chen, Q. Wang, Y. Yu, C. Zhou and Y. Wang, *Nanoscale*, 2012, **4**, 2010–2017.
93 S. Zhang, Q. Chen, Y. Wang and L. Guo, *Int. J. Hydrogen Energy*, 2012, **37**, 13030–13036.
94 Y. Shemesh, J. E. MacDonald, G. Menagen and U. Banin, *Angew. Chem., Int. Ed.*, 2011, **50**, 1185–1189.
95 H. Pan, Y.-W. Zhang, V. B. Shenoy and H. Gao, *ACS Catal.*, 2011, **1**, 99–104.
96 Y. Cui, Z. Ding, X. Fu and X. Wang, *Angew. Chem., Int. Ed.*, 2012, **51**, 11814–11818.
97 J. Hong, X. Xia, Y. Wang and R. Xu, *J. Mater. Chem.*, 2012, **22**, 15006–15012.
98 G. Zhang, J. Zhang, M. Zhang and X. Wang, *J. Mater. Chem.*, 2012, **22**, 8083–8091.
99 Y.-G. Lin, Y.-K. Hsu, Y.-C. Chen, S.-B. Wang, J. T. Miller, L.-C. Chen and K.-H. Chen, *Energy Environ. Sci.*, 2012, **5**, 8917–8922.
100 X. Ao, X. Tong, D. S. Kim, L. Zhang, M. Knez, F. Mueller, S. He and V. Schmidt, *Appl. Phys. Lett.*, 2012, **101**, 111901/1–111901/4.
101 A. Braun, K. Sivula, D. K. Bora, J. Zhu, L. Zhang, M. Gratzel, J. Guo and E. C. Constable, *J. Phys. Chem. C*, 2012, **116**, 16870–16875.
102 M. T. Mayer, C. Du and D. Wang, *J. Am. Chem. Soc.*, 2012, **134**, 12406–12409.
103 I. Oh, J. Kye and S. Hwang, *Nano Lett.*, 2012, **12**, 298–302.
104 J. Oh, T. G. Deutsch, H.-C. Yuan and H. M. Branz, *Energy Environ. Sci.*, 2011, **4**, 1690–1694.
105 M. Shi, X. Pan, W. Qiu, D. Zheng, M. Xu and H. Chen, *Int. J. Hydrogen Energy*, 2011, **36**, 15153–15159.
106 F. Toor, T. G. Deutsch, J. W. Pankow, W. Nemeth, A. J. Nozik and H. M. Branz, *J. Phys. Chem. C*, 2012, **116**, 19262–19267.
107 T. Yang, H. Wang, X.-M. Ou, C.-S. Lee and X.-H. Zhang, *Adv. Mater.*, 2012, **24**, 6199–6203.
108 Y. Li, H. Yu, W. Song, G. Li, B. Yi and Z. Shao, *Int. J. Hydrogen Energy*, 2011, **36**, 14374–14380.

A perspective for photocatalytic materials chemistry in China

Jian Zhang, Xiaxi Yao, Jin Li and Xiaoheng Liu*
DOI: 10.1039/9781849737623-00098

Photocatalytic chemistry has received much attention as a potential solution to the worldwide energy shortage as well as for environmental protection. This article reviews the most recent progresses on photocatalytic research in China, including its specific applications in water splitting for hydrogen generation and photodegradation of pollutants. The review shows a survey of efforts to explore suitable materials (most in nanosized) and to optimize their energy band configurations for designing and fabrication of advanced photocatalysts.

1 Introduction

Since the 1970s, energy shortage and environmental pollution have presented major challenges to humanity. Over the past two decades, with the fast development of industrialization China also has met with these problems, which need to be solved to sustain development. Nowadays Chinese scientific researchers have raised the same awareness as global scientists'. In the photocatalytic research area, Chinese scientists are aiming at potential effective applications in water splitting for hydrogen generation and photodegradation of pollutants, and they are working at more than 100 laboratories in universities and other scientific research institutes. This paper reviews the most recent progress, and discusses chosen reports.

2 Photocatalytic water splitting for hydrogen generation

Hydrogen is regarded as a clean fuel for the next generation, because no harmful gases or green house gases are emitted after burning. Currently hydrogen is mainly produced by steam reforming of fossil fuels like natural gas. However, green house gases are emitted during hydrogen production. In order to avoid emission of green house gases, hydrogen production from water is the most desirable process, in which only oxygen is released as a by-product. Since the pioneering report by Fujishima and Honda on photoelectrochemical (PEC) water splitting on a TiO_2 electrode, the technology of semiconductor-based photocatalytic water splitting to produce hydrogen using solar energy has been considered as one of the most important approaches to solve the world energy crisis. During the past four decades, numerous active photocatalysts for water splitting have been synthesized and investigated over the world. Continuing breakthroughs have been made in the development of novel photocatalysts, especially during the past two decades.

Key Laboratory of Education Ministry for Soft Chemistry and Functional Materials, Nanjing University of Science and Technology, Nanjing 210094, China. E-mail: xhliu@mail.njust.edu.cn

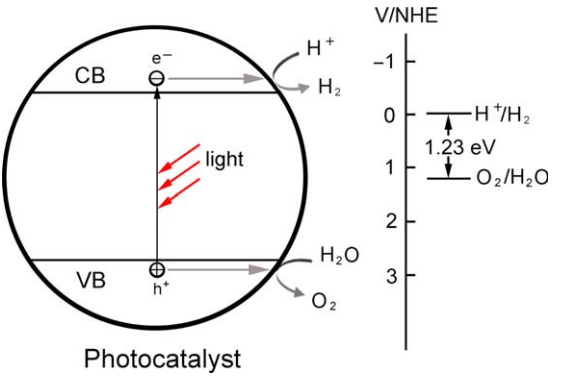

Fig. 1 Schematic illustration of basic mechanism of semiconductor-based photocatalyst.

A photocatalyst absorbs Ultraviolet (UV) and/or visible (Vis) light irradiation from sunlight or an artificial light source. After photoexcitation, the excited electrons and holes separate and migrate to the surface of photocatalyst. In the photocatalytic water splitting reaction, they act as reducing agent and oxidizing agent to produce hydrogen and oxygen, respectively. Figure 1 illustrates the basic principle of the photocatalytic system for water splitting. Water splitting for hydrogen and oxygen is an uphill reaction. It needs the standard Gibbs free energy change ΔG_0 of 237 kJ/mol or 1.23 eV. Therefore, the band gap energy of the photocatalyst should be more than 1.23 eV to achieve water splitting.

Up to now, photocatalysts for water splitting can be used for this purpose in two types of configuration: (i) particulate photocatalytic systems and (ii) PEC cells. Although the principle of particulate photocatalytic hydrogen production is similar to that of PEC hydrogen generation, the main difference between the two approaches lies in the location of the redox reactions. This review summarizes the recent development of particulate photocatalytic systems as well as PEC cells for hydrogen production from water.

2.1 Photocatalytic water splitting using semiconductor nanoparticles

TiO_2 is the first reported photocatalyst for water splitting under UV irradiation. Since then, enormous efforts have been devoted to the research of TiO_2 material. Recently, Yu and co-workers[1] reported that the $Cu(OH)_2$ cluster-modified TiO_2 ($Cu(OH)_2/TiO_2$) was active in photocatalytic hydrogen evolution from aqueous solutions containing ethylene glycol as sacrificial reagent under UV light even without the presence of Pt cocatalyst. The optimal $Cu(OH)_2$ loading content was found to be 0.29 mol%, giving an hydrogen production rate of 3418 μmol h^{-1} g^{-1} with a quantum efficiency (QE) of 13.9%, which exceeded the rate on pure TiO_2 by more than 205 times. As shown in Fig. 2, they found that the $Cu(OH)_2$ could be expected to act as a co-catalyst to reduce protons efficiently ($E^0_{H+/H2} = 0$ V *vs.* SHE, pH = 0) because the potential of $Cu(OH)_2/Cu$ is about -0.224 V (*vs.* SHE, pH = 0). Cui and co-authors[2] synthesized TiO_2/graphene sheets (GS) nanocomposites using a one-step hydrothermal method. Hydrogen evolution from water splitting, under UV-Vis light illumination was attributed

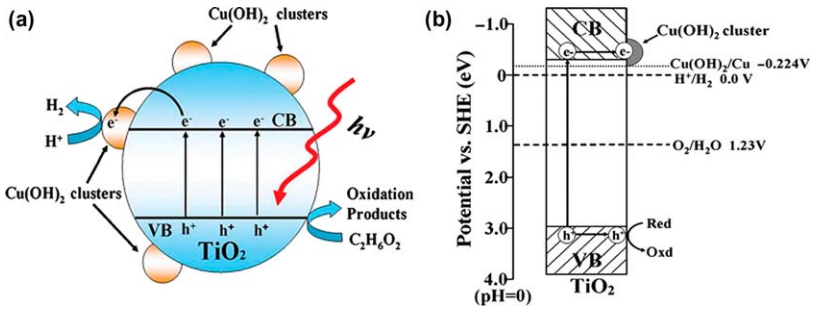

Fig. 2 (a) Schematic illustration for the charge transfer and separation in the $Cu(OH)_2$ cluster-modified TiO_2 system under UV irradiation. (b) Proposed mechanism for photocatalytic hydrogen production under UV light irradiation.[1]

to the excellent electron conductivity of GS and the chemical bonding between TiO_2 and GS. Ding *et al.*[3] found that the optimum mass ratio of GS to TiO_2 in the nanocomposites was 0.5 wt%.

The use of Zn-doped $SrTiO_3$ with perovskite structure as water-splitting photocatalysts was first reported in 2012 by Luo's group.[4] The photocatalytic mechanisms, examined using theoretical methods indicated that the substitutional doping of Zn ions could change the crystal and band structures and significantly promote carrier mobility of the catalysts, which resulted in good photocatalytic activities. Cheng and co-workers[5] developed a facile route using F^-/PO_4^{3-} as a morphology controlling co-mediator in one-pot synthesis of hollow anatase TiO_2 single crystals and mesocrystals with dominant reactive {101} facets. These hollow crystals showed a much superior photocatalytic activity in hydrogen and oxygen evolution from water splitting under UV-Vis irradiation. Recently, Lin and co-workers[6] designed a self-organized Pt@TiO_2 nanotube arrays (TNTAs) for solar water splitting with hydrogen evolution rate up to 495 μmol h^{-1} cm^{-2}. And the maximum photocurrent density and IPCE from the optimized Pt@TNTAs photoelectrode (Pt, ~1.57 wt%) were about 24.2 mA cm^{-1} and 87.9% at 350 nm, which was much higher than that of the pure nanotubes sample. Li's group[7] reported that Ga_2O_3 with tunable α-β phase junctions could stoichiometrically split water into hydrogen and oxygen with drastically enhanced activity over those with α or β phase structures alone. The enhanced photocatalytic performance was due to efficient charge separation and transfer across the α-β phase junction. As shown in Fig. 3, upon irradiation of Ga_2O_3 with α-β phase junctions, the photogenerated electrons tend to transfer from the α phase to the β phase, while the photogenerated holes transfered from the β phase to the α phase, driven by the potential difference caused by the differing band levels of α-Ga_2O_3 and β-Ga_2O_3. Chen's group[8] was the first to report the positive effect of the ordered surface structure (Sr-doped $NaTaO_3$) on the photocatalytic activity for water splitting.

During the last two years, many researches have been focused on the development of visible-light responsive photocatalysts, because UV light only accounts for about 4% of solar radiation energy, while visible light contributes about 43%. With a view to developing photocatalytic

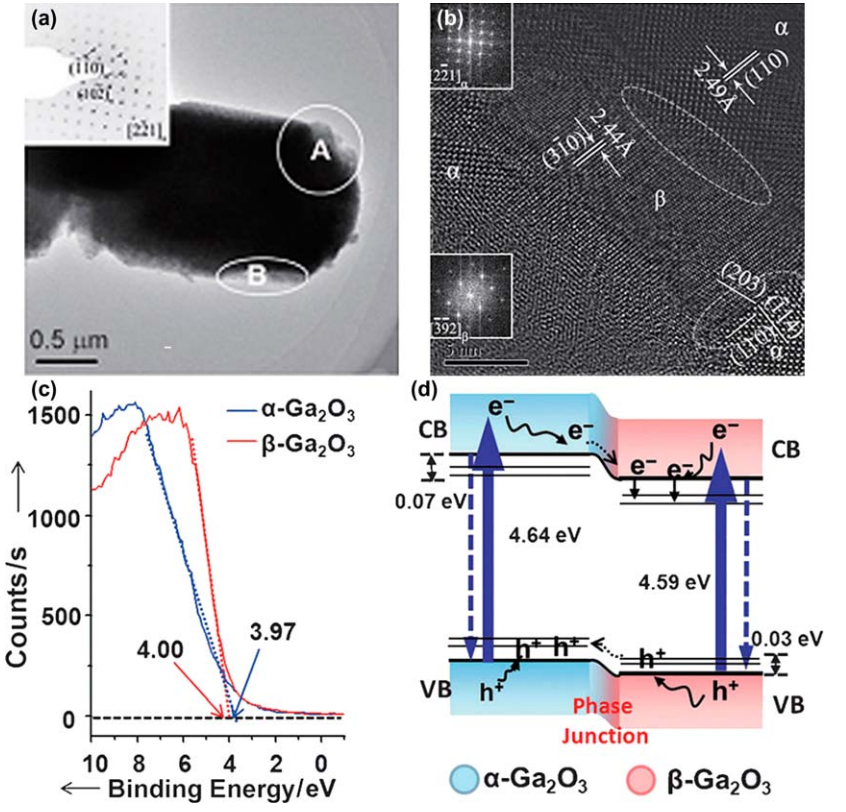

Fig. 3 (a) Low-magnification image of Ga_2O_3. (b) HRTEM image taken from area B in (a). (c) XPS valence band spectra of α-Ga_2O_3 and β-Ga_2O_3. (d) Illustration of charge transfer cross the α-β phase junction.[7]

applcations using visible-light irradiation, several common approaches have been adopted in order to make photocatalysts visible-light active for water splitting into hydrogen and/or oxygen: (1) cocatalyst loading; (2) metal and nonmetal ions doping; (3) semiconductor combinations; (4) dye sensitization to harvest visible light.

Transition metals, especially the noble metals, are widely used as effective cocatalysts for photocatalytic water splitting. Taking Pt as an example, when Pt is loaded onto the surface of the photocatalyst, the photogenerated electrons migrate to the surface of the photocatalyst and are entrapped by the noble metal cocatalyst, because the Fermi energy level of Pt is always lower than that of the semiconductor photocatalyst. Meanwhile, the photogenerated holes stay at the photocatalyst and migrate to its surface. This results in the efficient separation of the photogenerated electrons and holes. Subsequently, the separately localized electrons and holes become involved in their roles as the reducer and oxidizer, respectively, in the photocatalytic reaction. In summary, the role played by the cocatalysts dispersed on the surface of the photocatalysts is particularly important. By helping to promote charge separation, the cocatalysts improve the photocatalytic activity of the water splitting.

By using Ru and single-wall carbon nanotubes as cocatalysts, Long *et al.*[9] reported that $C_3N_3S_3$ polymer could significantly improve the ability to generate hydrogen from water under visible-light irradiation. Lv and co-workers[10] used Cu and graphene synergetically as cocatalyst to enhance the catalytic activity of TiO_2. They found that the synergetic effect between the Cu and graphene sheets as cocatalyst could efficiently accept and transport electrons from the excited semiconductor, suppress charge recombination, and thus provided much more active adsorption sites and photocatalytic reaction centers, which consequently enhanced the photocatalytic hydrogen production activity. By depositing the CoPi as the oxidation cocatalyst and Pt as the reduction cocatalyst on an yttrium-doped $BiVO_4$ ($Bi_{0.5}Y_{0.5}VO_4$), Li and co-workers[11] realized overall water splitting reaction and revealed the essential relations between photocatalysis and electrocatalysis in water splitting reaction. In contrast to the numerous reports using metal-containing material as a cocatalyst, the number of reports employing metal-free cocatalyst is still very scarce. Liu and co-workers[12] developed $B_2O_{3-x}N_x$ as a novel cocatalyst for photocatalytic water splitting. They proposed that B_2O_3 and its nitride are typically insulating so that the charge carrier transfer from WO_3 to $B_2O_{3-x}N_x$ nanocluster would not occur. However, the size of the $B_2O_{3-x}N_x$ nanocluster ranges from 2 to 5 nm, which should be thin enough to allow carrier tunnelling between WO_3 and the cluster for water oxidation as illustrated in Fig. 4.

One of the most effective ways to develop visible-light driven photocatalysts is to create impurity levels in the forbidden band through metal and nonmetal ion doping. Over the past two years, there have been numerous reports on the modification of wide band gap photocatalysts using metal and nonmetal ion doping to make them visible-light active. These include doped TiO_2,[13,14] doped $SrTiO_3$,[15] doped $BiVO_4$,[16] and doped ZnS.[17,18]

Recently, Cheng and co-workers[13] reported a heteroatom-modulated switching of photocatalytic reaction preference towards hydrogen or oxygen producing reaction from water splitting with boron contained anatase TiO_2 microspheres. This switching was sensitively controlled by creating a shell with an interstitial $B^{\sigma+}$ ($\sigma \leq 3$) gradient in the TiO_2 microsphere (Fig. 5). Fan's group[14] found the unusual enhancement of hydrogen

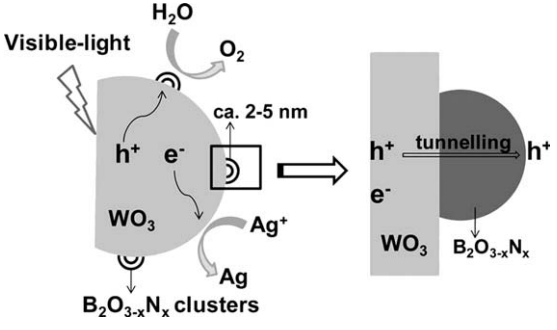

Fig. 4 Schematic of the bulk diffusion, surface separation and transfer processes of photoexcited electrons and holes in a $B_2O_{3-x}N_x@WO_3$ particle.[12]

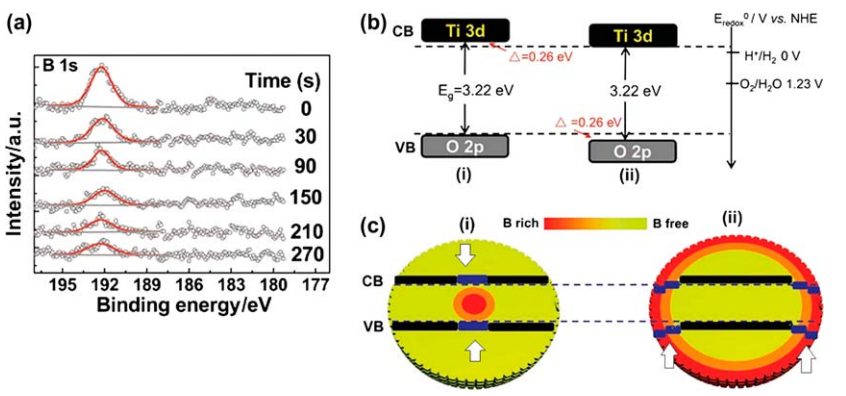

Fig. 5 (a) Argon ion sputtering dependent XPS spectra of B from the TiO_2 microspheres after thermal. (b) Surface band structure alignments of the TiO_2 microspheres. (c) The dependence of spatial electronic structures on the distribution of boron within the TiO_2 microspheres. The bands in the boron containing areas are highlighted by the arrows (blue online). i) TiO_2 microspheres with a boron-free shell and ii) TiO_2 microspheres with a boron-containing shell.[13]

evolution by Fe and Ni doped TiO_2 photocatalyst under visible-light irradiation. It should be noted that, using these abundant and cheap metal ion, the photocatalytic activities of the catalysts were estimated by detecting the hydrogen evolution rate from water, and the average maximum hydrogen evolution rate was 361.64 μmol h^{-1} using 5.0% Fe-4.0% Ni/TiO_2 catalyst under visible-light irradiation. It is worth mentioning that Li and co-workers[15] investigated the doping effects of different metal ions (Fe, Mn, Co) on the structural and photocatalytic properties of $SrTiO_3$ and $NaTaO_3$ photocatalysts. $BiVO_4$ was an excellent photocatalyst for producing oxygen. However, it was unable to reduce H_2O to H_2 because of the redox potential of its CB is lower than that of H_2O/H_2. Interestingly, Lei's group[16] synthesized series of solid solution photocatalysts $Bi_{1-x}Sm_xVO_4$ (BSV) by partial substitution of Sm^{3+} for Bi^{3+} in $BiVO_4$ and discovered that a synergistic effect existed between Bi^{3+} and Sm^{3+} in the above photocatalysts which enhanced the capability to split water into hydrogen and oxygen.

Although ZnS is a highly efficient photocatalyst for hydrogen evolution because of its high conduction band level, it is only active in the UV light region. Hence, it would be quite interesting to see if ZnS becomes visible-light responsive while maintaining its high hydrogen evolution activity following some modification. With this in view, a series of Cu-and Ni-doped ZnS photocatalysts were prepared by Zhang's group.[17] These samples showed excellent photocatalytic hydrogen evolution activity under visible-light irradiation without any noble metal loading owing to their high surface area (as high as 101.6 m^2 g^{-1}) and unique hierarchical structure. In addition, Chen and co-authors[18] developed a convenient method for constructing 2 dimension (D) anisotropic structures of ZnS-based materials (Fig. 6). They found that Cd and In co-doped ZnS photocatalysts also exhibited excellent photocatalytic activities under visible-light irradiation ($\lambda > 400$ nm). Similarly, a series of $Zn_{1-x}Cd_xS$ solid solutions with a nanoporous structure were successfully synthesized *via* a facile template-free method at room temperature by Xu and co-authors.[19] They found that the solid solutions

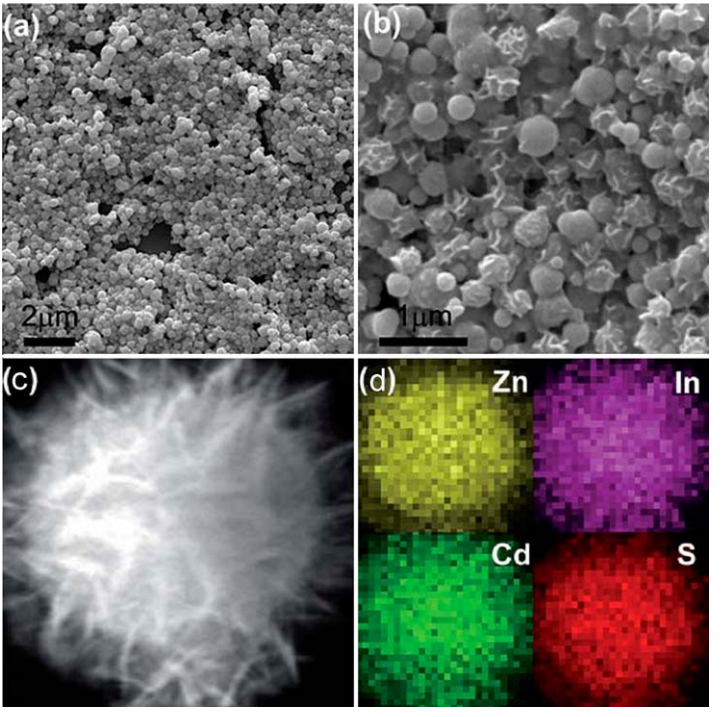

Fig. 6 (a) low-magnification FESEM image. (b) high-magnification FESEM image. (c) HAADF image of an individual microsphere of sample D and (d) the corresponding XEDS energy mapping of Zn (yellow online), In (purple online), Cd (green online) and S (red online).[18]

show efficient photocatalytic activity for hydrogen evolution from aqueous solutions containing S^{2-} and SO_3^{2-} as sacrificial reagents under visible-light irradiation without a Pt cocatalyst.

Unlike metal ion dopants, nonmetal ion dopants are less likely to form donor levels in the forbidden band but instead shift the valence band edge upward. This results in a narrowing of band gap. Specifically, Binary carbon nitrides (CNs), this cheap, easily available organic semiconductor was recently proposed as the basis for a new family of solar energy transducers, but also shows great promise in metal-free water splitting.

Wang and co-workers[20] first advanced the solution synthesis of CNs using cyanuric chloride and $NaNH_2$ with a pressurized hot or supercritical fluid technique that has been widely used for many chemical and material processes. They believed that this innovative assembly route in solution for nanostructured CNs at mild conditions would offer a new avenue to construct CN-based semiconductors in solution at low temperatures. The abundant-metal-based polyoxometalate complex $[Co_4(H_2O)_2(PW_9O_{34})_2]^{10-}$ supported on a mesoporous CNs scaffold has been established for the first time as a highly efficient water oxidation catalyst in an oxygen evolving anode surface by Yuan's group.[21] They believed that mesoporous CNs with its nitrogen functionalities acts as a stabilizing, conducting, and pore-size-controlling agent without addition of any external agent or surface modification of the wall structure. In addition, Chen *et al.*[22] synthesized graphitic

carbon nitride (g-C_3N_4) from urea. As a result, the hydrogen evolution rate was 47.23 μmol h^{-1}, which was nearly 4 times greater than that for g-C_3N_4 derived from cyanamide under visible-light irradiation ($\lambda > 420$ nm). Similarly, in the study of Long *et al.*,[9] a novel organic semiconductor photocatalyst mimicking natural light-harvesting antenna complexes in photosynthetic organisms, a disulfide (–S–S–) bridged $C_3N_3S_3$ polymer, was designed and developed to generate hydrogen from water under visible-light irradiation.

The semiconductor combination approach has been shown to be another effective method for improving photocatalytic activity through better photogenerated charge separation with a formation of a heterojunction structure.

As is well-known, CdS, which is a fascinating visible-light driven photocatalyst for hydrogen production, is very unstable toward photocorrosion, as a result of serious self-oxidation by the photogenerated holes in the valence band. To improve its photocatalytic activity and stability, CdS has been embedded in different kinds of inert matrices. Furthermore, owing to its superior electron mobility and high specific surface areas, graphene was considered to be a high performance support for photocatalysts. Based on the above description, Yu *et al.*[23] developed an CdS-Pt-graphene heterojunction, in which CdS, the electron-transfer medium graphene and Pt were all spatially fixed. This three-component system exhibited a high photocatalytic activity, far exceeding those of the two-component system. Under visible-light irradiation, electrons were excited from the VB to the CB of the CdS semiconductor and then likely transfered in one of three following ways: (1) to Pt deposited on the surface of CdS clusters; (2) to carbon atoms on the graphene sheets; (3) to Pt located on the graphene nanosheets. Eventually, the electrons reacted with the adsorbed H^+ ions to form H_2. The mechanism of the photocatalytic reaction proposed as illustrated in Fig. 7. Most recently, they developed a novel visible-light driven photocatalyst multiwalled carbon nanotube modified $Cd_{0.1}Zn_{0.9}S$ solid solution (CNT/$Cd_{0.1}Zn_{0.9}S$) by a simple

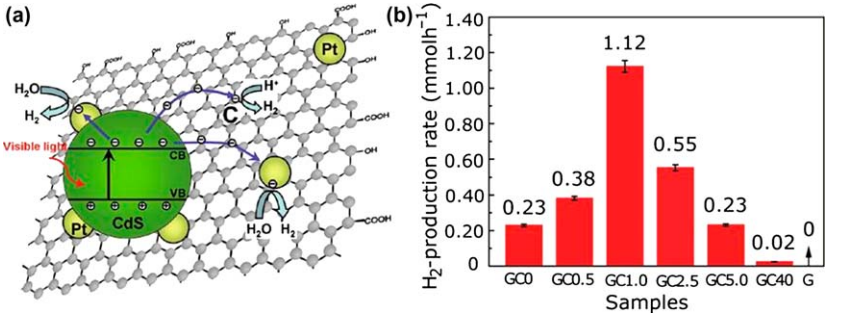

Fig. 7 (a) Schematic illustration of the charge separation and transfer in the graphene-CdS system under visible light. The photoexcited electrons transfer from the conduction band of semiconductor CdS not only to the located Pt, but also to the carbon atoms on the graphene sheets, which are accessible to protons that could readily transform to hydrogen. (b) Comparison of the visible-light photocatalytic activity of samples for the hydrogen production using 10 vol % lactic acid aqueous solution as a sacrificial reagent and 0.5 wt% Pt as a cocatalyst.[23]

hydrothermal method. The rate of hydrogen production was 1563.2 μmol h^{-1} $g^{-1}$with apparent QE of 7.9% at 420 nm even without any noble metal cocatalysts.[24] Meanwhile, CNT was replaced by reduced graphene oxide in above system, they found even more efficient photocatalytic activity.[25] In addition, a new efficient visible-light driven composite photocatalyst polypyrrole (PPy)/CdS was prepared by Chen's group.[26] It showed pretty good photoactivity in the absence of noble metals. In independent studies, Chen and co-authors[27] designed a ternary component ($CdS/ZnS/In_2S_3$) for efficient photocatalytic hydrogen production under artificial irradiation ($\lambda > 400$ nm). In such structures, the formed nanostructured heterojunction can lead to a more efficient electron transfer between metal sulfides. The improvement of visible-light adsorption, the transfer of photogenerated electrons and the unique nanostructure with CdS and ZnS nanocrystals were thought to be responsible for the highly efficient photocatalytic activity of the $CdS/ZnS/In_2S_3$ composite.

Using a simple hydrothermal and cation exchange processes, Yu's group[28] successfully synthesized CuS/ZnS porous nanosheet photocatalysts. Even without a Pt cocatalyst, the as-prepared CuS/ZnS porous nanosheets reached a high hydrogen production rate of 4147 μmol h^{-1} g^{-1} at CuS loading content of 2 mol% and an apparent QE of 20% at 420 nm. The charge transfer is shown by the blue bold arrow in Fig. 8. The potential of CuS/Cu_2S is about -0.5 V (*vs.* SHE, pH = 0), and the interfacial transition energy from the VB of ZnS to CuS/Cu_2S is determined to be 2.94 eV. Therefore, it was reasonable to assume that the absorption from ~350 to 450 nm could be ascribed to the direct interfacial charge transfer (IFCT) from the VB of ZnS to CuS. Shortly afterward, they developed a new composite material consisting of TiO_2 nanocrystals grown in the presence of a layered MoS_2/graphene hybrid as a high-performance photocatalyst for hydrogen evolution.[29] Even without a noble-metal cocatalyst, the TiO_2/MoS_2/graphene composite also reached a high hydrogen production rate of 165.3 μmol h^{-1} when the content of the MoS_2/graphene cocatalyst was 0.5 wt% and the content of graphene in this cocatalyst was 5.0 wt%, and the apparent QE reached 9.7% at 365 nm. This unusual photocatalytic activity arised from the positive synergetic effect between the MoS_2 and

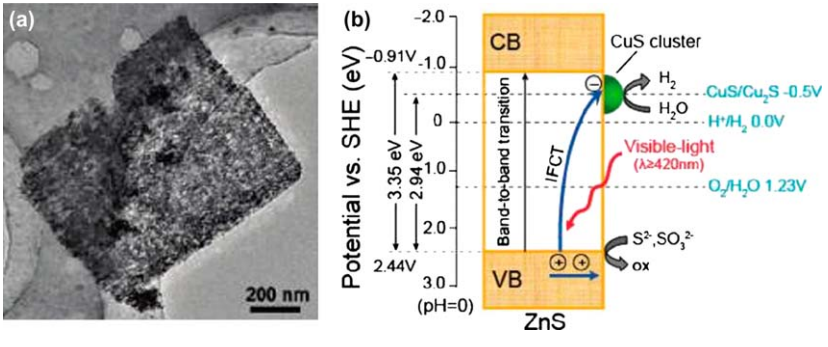

Fig. 8 (a) TEM of the sample. (b) Schematic illustration for visible light induced IFCT from the valence band of ZnS to the CuS clusters in CuS/ZnS system as the proposed mechanism for photocatalytic hydrogen production.[28]

graphene components in this hybrid cocatalyst, which served as an electron collector and a source of active adsorption sites, respectively.

Li and co-workers[30] successfully synthesized a visible-light driven WO_3/Ag-Bi based oxygen-evolution catalyst. The results showed that modifying Ag-Bi with WO_3 was effective in decreasing energy consumption. Moreover, the oxygen evolution rate increased from 21.42 μmol h^{-1} to 30.85 μmol h^{-1} and the Faradaic efficiency attained a value of 91.3 %, further confirming that the WO_3/Ag-Bi catalyst showed a better catalytic activity and that WO_3 played an important role in improving the performance of the Ag-Bi catalyst for oxygen evolution. Subsequently, hexagonal $ZnIn_2S_4$ photocatalysts with 3D-hierarchical persimmon-like shape have been successfully synthesized *via* an oleylamine-assisted solvothermal method by Qian's group.[31] In such structures, holes were three dimensionally confined to the $ZnIn_2S_4$, whereas the delocalized electrons were transferred to Pt. Therefore, the obtained 3D-hierarchical Pt-$ZnIn_2S_4$ could be a good candidate for hydrogen production with high and stable photocatalytic activity. The hydrogen production rate could reach 220.45 μmol h^{-1} and the QE was up to 13.16 %.

Similar to dye-sensitized solar cells, in which the charge injection from dye molecules into metal oxides is used for electricity generation, dye sensitization has been used to improve water splitting for hydrogen production as well as photoelectrochemical (PEC) reactions by increasing visible-light absorption and photoconversion. Photocatalytic systems for hydrogen generation typically consist of a photosensitizer, an electron relay, a sacrificial electron donor, and a catalyst. As shown in Fig. 9, when photosensitizer molecules absorb photon energy, they inject electrons into the conduction band of a semiconductor catalyst. The electrons are consumed by reduction of water at a catalytic nanoparticle to form hydrogen, while the oxidized sensitizer molecules are regenerated by accepting electrons from a donor molecule.

Many transition metal complexes such as polypyridine complexes, alizarine, phthalocyanine, and metalloporphyrins with metal centers including Ru (II), Pt (II), Co (II), Zn (II), and Cr (III) have also been widely used as sensitizers for wide band gap photocatalysts to improve their optical and photocatalytic properties for hydrogen evolution in the visible light

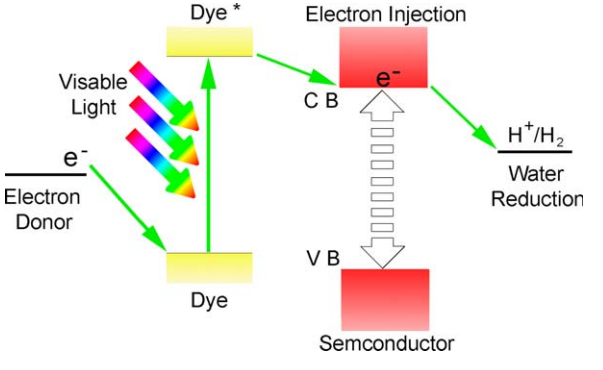

Fig. 9 Basic principle of dye-sensitized photocatalytic hydrogen production from water.

region. Moreover, metal-free dyes, such as porphine dyes, xanthene dyes, melocyanine dyes, and coumarin dyes, have also been investigated.

2.2 Photoelectrochemical (PEC) water splitting

Photoelectrochemical (PEC) water splitting is attractive due to its potential high efficiency, up to $>30\%$ in principle, environmental friendliness and low cost. In this section, we will focus on recent developments in the study of hydrogen production from water splitting using PEC cells based on semiconductor nanomaterials, with emphasis on new strategies developed to enhance PEC efficiency. Nanostructured materials offer unique advantages for potential PEC applications. First, nanoscale sizes are comparable to carrier scattering lengths, significantly reducing the scattering rate and increasing carrier collection efficiency. Second, the bandgap of nanomaterials can be tuned to absorb in a particular wavelength by varying size and, in principle, cover the whole solar spectrum. Third, nanomaterials have strong absorption coefficients due to an increase of oscillator strength, thereby enabling high conversion efficiency. Finally, bottom-up growth approaches, which use smaller components to produce larger and more complex structures, allow scalable synthesis of single crystal nanostructures on flexible substrates under mild conditions, leading to light weight and low cost. In addition, different strategies have been developed to enhance visible-light absorption (*e.g.*, doping, dye, or quantum dot sensitization and band structure engineering) as well as to enhance transport by reducing the density of trap states *via* surface modification, improving crystallinity, and using 1D array structures.

Although the principle of PEC hydrogen generation is relatively simple, the underlying fundamental processes are complex and still not well understood at the molecular level. A typical PEC device consists of a photoanode and cathode immersed in water containing some electrolyte. The photoanode is typically a semiconductor that absorbs light and generates excitons or electron-hole pairs. The electrons are transported to a metal cathode (*e.g.*, Pt), often aided by an external bias that can come from a solar cell or from the electrical grid. Hydrogen generation occurs at the cathode from the reduction of protons by the electrons. On the photoanode, the holes left behind oxidize water molecules into oxygen and protons.

Figure 10 illustrates the energy levels involved in a typical semiconductor photoanode. First of all, light absorption and charge carrier generation. Secondly, charge separation and transport in the solid and at the solid-liquid interface. Actually, charge transport depends strongly on the structural and morphological details of the photoanode. Associated with each step, there are undesired loss mechanisms such as recombination, trapping, slow reaction due to overpotential, and disrupted mass transport.

For ease of discussion, first of all, we will focus on photoelectrodes that are primarily based on single-component that do not require other materials as sensitizers or dopants. For example, nanostructured metal oxides semiconductor materials that have been studied for PEC cells include WO_3,[32] Cu_2O,[33] SnO,[34] and more commonly, TiO_2.[35–37]

Gan *et al.*[32] investigated the effects of crystal size on photoanode materials based on WO_3 in a PCE film system. In the PEC system, the smaller

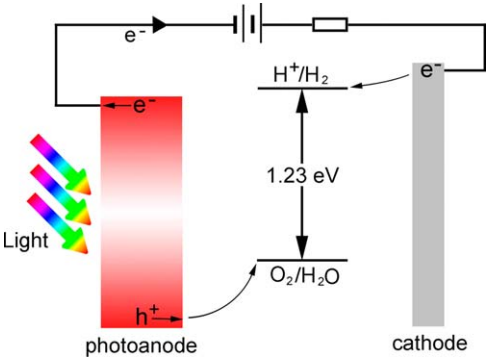

Fig. 10 Energy diagram of PEC components.

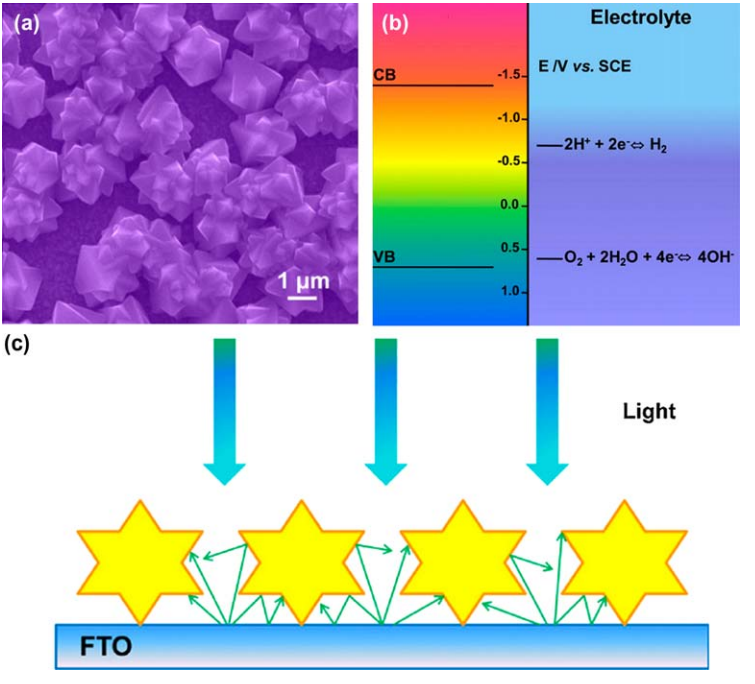

Fig. 11 (a) TEM images of the Cu_2O star. (b) Overview of the redox potentials for water splitting with respect to the Cu_2O band edges. (c) Schematic of hierarchically structured Cu_2O stars that can act as the 3D light-harvester.[33]

crystals performed better because of the reduced holes diffusion length. As an environmentally friendly p-type semiconductor material, Cu_2O with assembled 3D structures has been studied for PEC applications by Liu's group.[33] They found that the multi-faced structure could act as the light-scattering layer (shown in Fig. 11), which could significantly improve the photocurrent. As shown in figure above, the light passing through the free space between the Cu_2O stars might experience multiple scattering in the free space between the 3D structured Cu_2O stars and the F-doped SnO_2 coated glass (FTO) substrate, resulting in the enhancement of photocurrent.

Moreover, Tian and co-workers[34] presented a new photoelectrode material prepared from just coating tin halides on substrate of FTO or metal Ti to form SnO based film, which showed good photoanodic current under visible-light irradiation ($\lambda > 420$ nm).

The most extensively studied metal oxide system is TiO_2, which commonly exists in anatase (bulk bandgap 3.18 eV) and rutile (bulk bandgap 3.03 eV) phases. In general, UV illumination is needed, and the PEC efficiency is low, less than 1%, especially in the visible range. Recent efforts have focused more on 1D nanostructures that are expected to have better charge transport properties. Yan and co-authors[35] reported that an efficient and economical technology to produce hydrogen from solar energy by splitting water in a two-compartment PEC cell without any external applied voltage. Due to the excellent crystallization and the maintenance of tubular structures, TiO_2 nanotubes annealed at 450 °C exhibited the highest photoconversion efficiency of 4.49% and maximum hydrogen production rate of 122 μmol h^{-1} cm^{-2}.

Actually, compared to 0D nanostructures, 1D nanostructures, such as nanorods and nanotubes, are expected to exhibit improved transport properties. Specifically, nanorods should improve the transport of charge carriers and thus reduce the recombination losses at grain boundaries due to vectorial, or directional, charge transport along the long axis. Furthermore, the small diameter of nanorods can minimize the distance for holes to diffuse to the semiconductor/electrolyte interface. Based on the above analysis, Liu's group[36] prepared highly ordered TiO_2 nanotube arrays with tuned inner diameter (40 ~ 145 nm), wall thickness (8 ~ 20 nm), and fixed tube length (10 μm) by anodization of Ti foil in different ethylene glycol electrolyte. The PEC measurements showed that all samples present photoconversion efficiently around 7%, comparable with the state-of-the-art results (Fig. 12). At the same time, they suggested that large porosity could benefit the photoconversion efficiency from two aspects. First, the large surface areas ensure a much shorter path toward wall surface than the holes diffusion length. Second, a larger inner space of nanotube is important to accelerate the ion migration in the tube and overcome the kinetic bottleneck. Similarly, a film of rutile TiO_2 pillars with well-developed facets

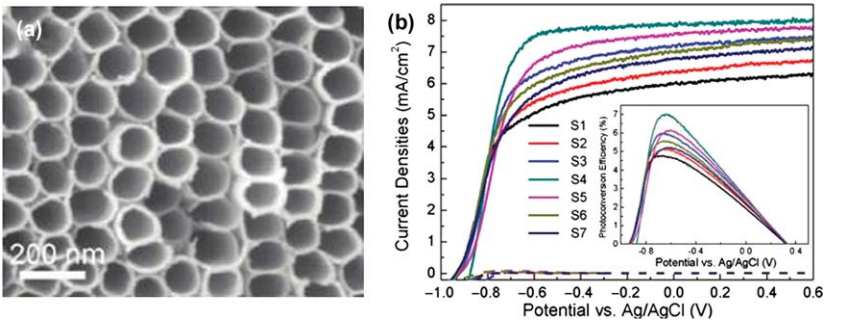

Fig. 12 (a) FESEM images of a nanotube arrays sample (top surface). (b) Photocurrent density (in 1 M KOH solution) *vs.* measured potential, under a UV light illumination (280–400 nm, 100 mW cm^{-2}).[36]

was developed as an efficient photoelectrode for water splitting by Liu *et al*.[37] They pointed out that due to the exposed high-energy facets as active sites for water oxidation and the extended light absorption range by 23 nm, the electrode exhibited a much higher activity in photoelectrolysis of water compared to conventional anatase nanotube array electrode.

Doping is well known to be an effective way to alter the optical and electronic properties of semiconductors for PEC applications. When doped with metal ions such as Sn, metal oxide TiO_2 showed much higher efficiency PEC activities, attributed to decreased effective bandgap or intra-bandgap states that result in visible-light absorption. This research was reported by Zheng and co-workers.[38] Yu *et al*.[39] synthesized Ni-doped Fe_2O_3 thin films by electrodeposition and discovered that the optimum at 8% Ni doping may balance these competing effects most effectively. Nonmetal ion doping also has been demonstrated in other metal oxide such as ZnO. Vertically aligned single-crystal ZnO nanorod arrays with nanotetrapods were synthesized by Yang's group.[40] After N-doping, they found that the photocurrent density enjoyed an even more dramatic enhancement to 0.99 mA cm^{-2} at $+0.31$ V *vs*. Ag/AgCl.

2.3 Summary and prospects

Photocatalytic hydrogen production from water is an attractive reaction, since it has a potential of converting solar energy and renewable resources into the chemical potential of the storable hydrogen. As reviewed, various attempts had been done to achieve the efficient hydrogen evolution, such as development of various photocatalysts and cocatalysts, metal and nonmetal doping of photocatalyst, combination of photocatalyst, sensitization of photocatalyst, optimization of reaction conditions and so on. However, from the point of view of industrialization and commercialization, many challenges remain in the areas of materials science and engineering.

3 Photocatalytic decomposition of aqueous pollutants

3.1 Fundamentalsof photocatalytic degradation

With industrialization and population growth, the environmental contamination caused by organic pollutants is becoming an overwhelming problem all over the world. Water is one of the most important natural resources and necessary for human daily life. Unfortunately, 50% of the population are exposed to polluted water sources in developing countries.[41] Purification of polluted water is becoming a problem to be solved urgently. It has been suggested that heterogeneous photocatalysis of polluted water is a very promising way to alleviate the increasingly serious water resources crisis.[42–44] When a semiconductor photocatalyst absorbs a photon with energy equal to or greater than its band-gap, the electrons transfer form the valence band to the conduction band and the holes stay in the valence band. Then the electrons and holes migrate randomly to the surface of the photocatalyst and are trapped by the defects or other absorbed molecule to generate active redox species. The electrons and holes also can recombine in the bulk or on the surface to release the heat (Fig. 13).[45]

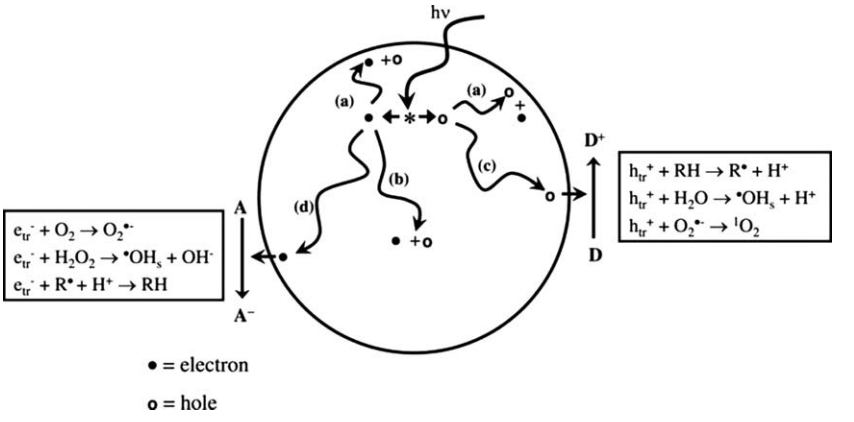

Fig. 13 Processes occurring on semiconductor particle after light excitation.[45]

The semiconductor TiO_2 has proven to be an excellent photocatalyst on which many organic substrates have been shown to be oxdatively degraded and ultimately mineralized completely under UV irradiation. The mechanism of photocatalysis can be described as follows in the view of TiO_2 semiconductor:

$$TiO_2 + h\nu \rightarrow TiO_2(e_{CB}^- + h_{VB}^+) \quad (1)$$

$$O_2 + e_{CB}^- \rightarrow O_2^{\bullet-} \quad (2)$$

$$H_2O + h_{vB}^+ \rightarrow {}^\bullet OH + H^+ \quad (3)$$

$$R{-}H + {}^\bullet OH \rightarrow R^\bullet + H_2O \quad (4)$$

$$\begin{aligned} &R{-}H(R^\bullet) + (O_2, O_2^{\bullet-}, {}^\bullet OH) \quad \text{intermediates} \\ &\rightarrow\rightarrow CO_2 + H_2O + \text{Inorganic species} \end{aligned} \quad (5)$$

The active oxygen species $O_2^{\bullet-}$ or $^\bullet OH$ radicals have been implicated in the degradation of various organic compounds. The photocatalytic process was shown in Fig. 14A. However, the electrons can only be photoexcited from the valence band to the conduction band of TiO_2 under UV light irradiation. The quantum efficiency is very low due to the limited absorption of solar light. It is worth noting that J. Zhao *et al.* proposed a new strategy to extend the photo-response of a semiconductor with a wide band gap to the visible region. That is, the adsorbed dyes or other color species harvest the visible light to be excited while the semiconductor does not absorb light directly. Then, the dyes on the excited state can inject the electrons into the conduction band of the semiconductor to form conduction band electrons (Fig. 14B).[42,46] This process extends the photo-response of wide-band-gap semiconductors such as TiO_2 from the UV to the visible region, and opens a unique route to use visible light from the sun light.

3.2 Visible-light-induced photocatalysis

Up to now, titanium dioxide has been investigated most extensively among various photocatalysts since Fujishima and Honda discovered the

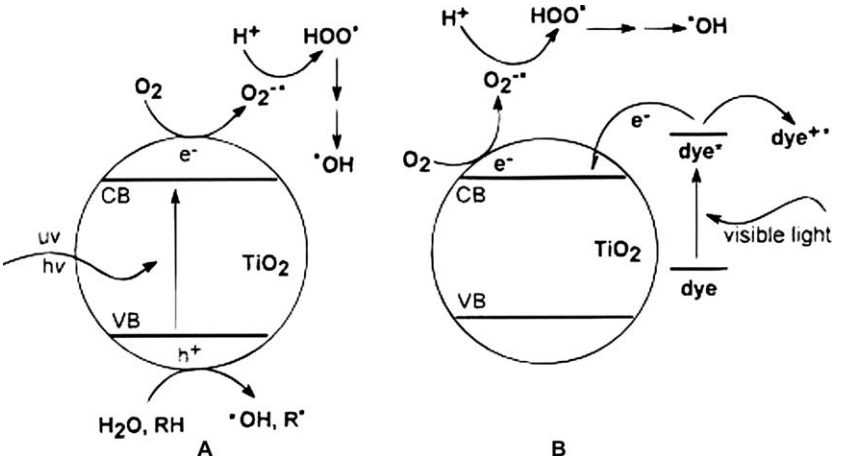

Fig. 14 Comparison of the photocatalytic mechanism for UV irradiation of TiO_2 particles (A) with the self-photosensitized pathway under visible light illumination (B).[46]

photocatalytic splitting of water on TiO_2 electrodes in1972 owing to its favorable properties such as non-toxicity, chemical inertness and high stability under light irradiation.[47] However, the relatively wide band gap unfortunately makes titanium dioxide only respond to ultraviolet irradiation, which accounts for 4% of the incoming solar energy. In recent years, great interests have been focused on the development of novel photocatalysts with visible light response, owing to the fact that visible light takes up about 43% of the solar spectrum. Therefore, this section mainly introduces a serial of novel photocatalysts that has attracted much attention recently.

Iron oxides as a semiconductor show great promise in view of being naturally abundant and environmentally benign. Hematite (α-Fe_2O_3) is the most thermodynamically stable semiconductor ($Eg = 2.1–2.2\,eV$) that can absorb visible light, that is, a substantial fraction of the solar spectrum. X. Zhou and co-workers investigated visible-light-induced photodegradation of model dye rhodamine B (RhB) in the presence of hydrogen peroxide (H_2O_2) over hematite architectures, namely 1D nanorods, 2D nanoplates, and 3D nanocubes with different basal planes (Fig. 15).[48] They take the first study to investigate heterogeneous photo-Fenton catalysis by nanocatalysts with well-defined architectures. All the as-prepared samples exhibited the photocatalytic activity for RhB photodegradation under visible-light illumination ($\lambda > 420\,nm$), and the nanorods sample showed the highest photocatalytic activity. Table 1 lists the physicochemical properties of α-Fe_2O_3 nanoplates, nanocubes, and nanorods. In addition, the surface atomic and electronic structures were carefully investigated. The results suggested that the line shape and the width of the band structure are almost identical. However, the samples with particular morphologies own the different dominant facets. For α-Fe_2O_3, oxygen and iron of termination layers coexist on the (001) facet, which limits the fraction of surface low-coordinate iron cations on the (001) facet. On the other hand, both (012) and (110) facets display ridge-and-valley topography, which can expose a greater number of low-coordinate surface iron cations than the (001)

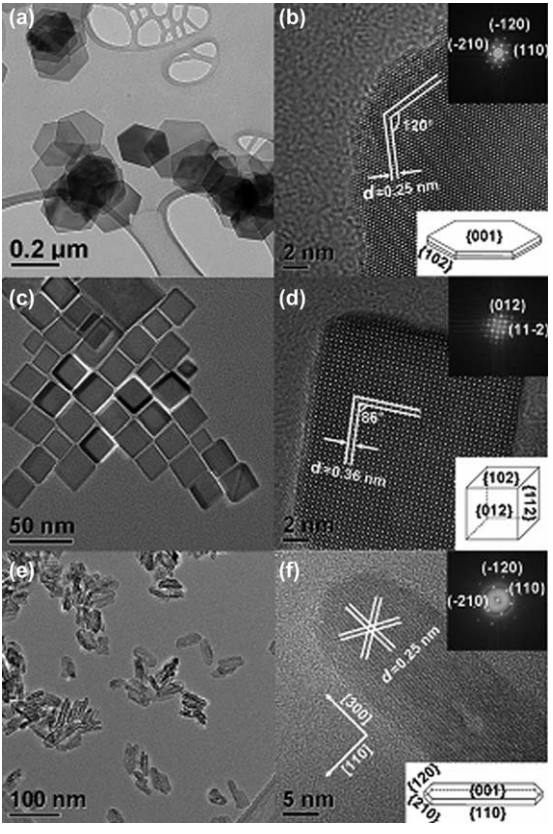

Fig. 15 Representative morphologies and structures of α-Fe_2O_3 architectures. a) TEM image and b) HRTEM image of 2D α-Fe_2O_3 nanoplates. Insets: FFT pattern and drawing of a plate. c) TEM image and d) HRTEM image of 3D α-Fe_2O_3 nanocubes. Insets: FFT pattern and drawing of a cube. e) TEM image and f) HRTEM image of 1D α-Fe_2O_3 nanorods. Insets: FFT pattern and drawing of a rod.[48]

Table 1 Physicochemical properties of α-Fe_2O_3 nanoplates, nanocubes, and nanorods.[48]

Sample	Length [nm]	Width [nm]	Heigh [nm]	SSA [m^2g^{-1}]	Dominant facets	Reaction rate constants k [$\times 10^{-3}min^{-1}$]	Normalized rate constants k_s [c] [$10^{-4}min^{-1}Lm^{-2}$]
nanoplates	–	208.5 ± 27.3	14.6 ± 2.6	30.1 ± 4.1	{001}	4.38 ± 0.35	7.28 ± 1.14
nanocubes	22.0 ± 3.2	22.0 ± 3.2	22.0 + 3.2	51.8 ± 8.0	{012}	28.20 ± 1.70	27.2 ± 4.5
nanorods	40.3 ± 8.7	10.9 ± 5.0	5.0 ± 1.2	119.8 ± 23.3	{001}{110}	73.26 ± 4.96	30.6 ± 6.3

facet. Combined with the observed photoreactivity differences, the reactivity trend can be rationalized as exposed facets in the order (110) > (012) ≫ (001). This work offers a promising new strategy for engineering practical photocatalysts for waste water treatment based on heterogeneous photo-Fenton oxidation.

WO_3 is an important visible-light-responsive photocatalyst and has been widely used in the photocatalytic degradation of organic pollutants.[49–51] G. Li *et al*. reported the synthesis of well-defined WO_3

hollow spheres with multiple-shells, and the as-synthesized multiple-shell WO_3 hollow spheres with high surface area exhibit greatly enhanced activity in the visible-light photocatalytic degradation of organic contaminants due to the their large specific surface areas and special internal structure (Fig. 16). In addition, the WO_3 hollow sphere photocatalyst shows high stability for efficient recycle at least five times.[49] D. Zhang reported the WO_3 nanocrystals with tunable percentage of (001) facet exposure by hydrothermal reaction using BF_4^- as the guiding agent.[50] The photocatalytic activity was enhanced efficiently through large percentage exposure of high energy (001) facet in terms of the photodegradation of Rhodamine B (RhB) under visible-light irradiation.

In addition to WO_3, Fe_2O_3, metal sulfides, silver orthophosphate and halides have received great attention due to their relatively good performance as photocatalysts for the degradation of pollutants.[52,53] Ag@AgCl has caused a considerable attention as a new visible light plasmonic photocatalyst because of the localized surface plasmon resonance (LSPR) of noble metal nanoparticles. J. Liao *et al.* reported the facile hydrothermal synthesis of heart-like Ag@AgCl with enhanced visible light photocatalytic performance.[54] The as-prepared Ag@AgCl photocatalyst had a uniform heart-like morphology. For comparison, the heart-like particles existing with cubic ones were referred to as mixed Ag@AgCl particles. The heart-like Ag@AgCl photocatalyst has a strong absorption in the visible light region due to the LSPR effect of Ag nanoparticles, while the AgCl particles showed the weak absorption peak in the visible range. The obtained heart-like Ag@AgCl photocatalyst exhibited the enhanced photocatalytic activity on the photodegradation of a model pollutant methyl orange (MO) under visible light irradiation ($\lambda > 420$ nm) compared with mixed sample of heart-like and cubic ones (Fig. 17).

Silver orthophosphate semiconductors also show strong response in visible light region. Recently, J. Ye *et al.* reported Ag_3PO_4 semiconductor that can harness visible light to oxidize water as well as decompose organic contaminants in aqueous solution.[52] Subsequently, many groups[55–57] devote to the research of the synthesis and the photocatalytic activity of Ag_3PO_4 semiconductor. W. Wang *et al.* prepared silver orthophosphate nanoparticles by a facile precipitation method and systematically studied in detail their properties with regard to adsorption, photocatalysis, and stability.[53] The Ag_3PO_4 sample shows a relatively higher photocatalytic activity than P25 and $TiO_{2-x}N_x$. 96% of RhB was photodegraded by the Ag_3PO_4 under visible-light irradiation for 14 min. Among all samples, Ag_3PO_4 in the 4th cycle exhibits the highest photocatalytic activity (Fig. 18a). The UV-vis spectra suggested that the absorbance increased in the visible-light region with increasing the recycle times. In addition, another absorption peak located at 452 nm appeared due to the surface plasmon resonance (SPR) produced by Ag nanoparticles (Fig. 18b). Further characterizations including XRD, XPS also convinced the formation of metallic silver. The direct SEM and TEM observation displays that the Ag nanoparticles and Ag film deposited on the surface of Ag_3PO_4 with increasing recycle times. Based on the above results, they proposed a possible mechanism that at the initial stage of photocatalytic reactions, part of Ag^+ on the

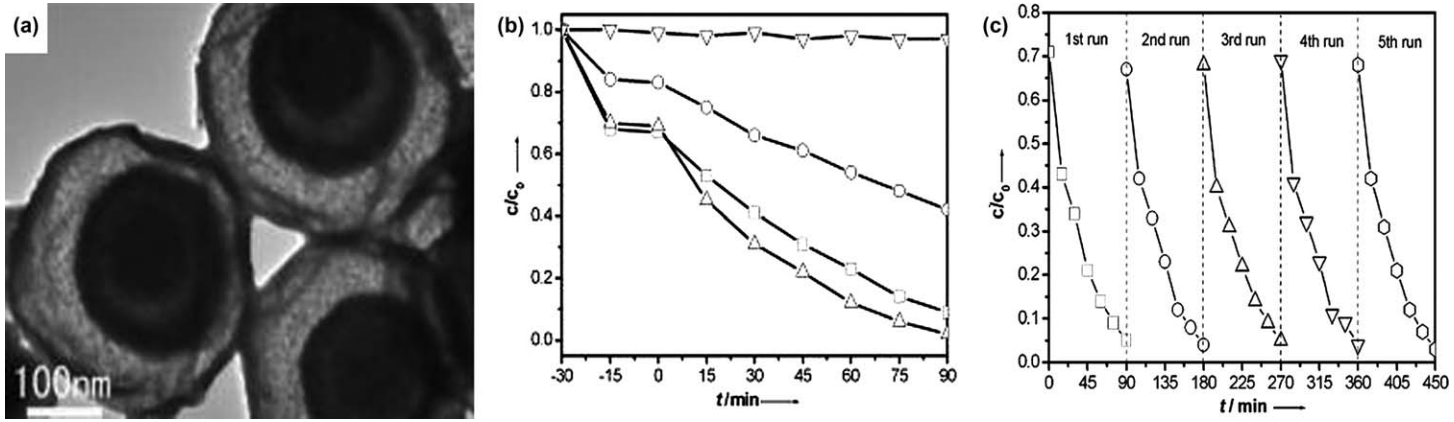

Fig. 16 (a) TEM image of multiple-shell WO_3 hollow spheres; (b) The contrast of photocatalytic degradation of RhB in the presence of the multiple-and single-shell WO_3 hollow spheres; ∇: no photocatalyst, ○: large single-shell hollow spheres, □: small single-shell hollow spheres, △: multiple-shell hollow spheres. (c) Recyclability of the photocatalytic decomposition of RhB with the multiple-shell WO_3 hollow spheres.[49]

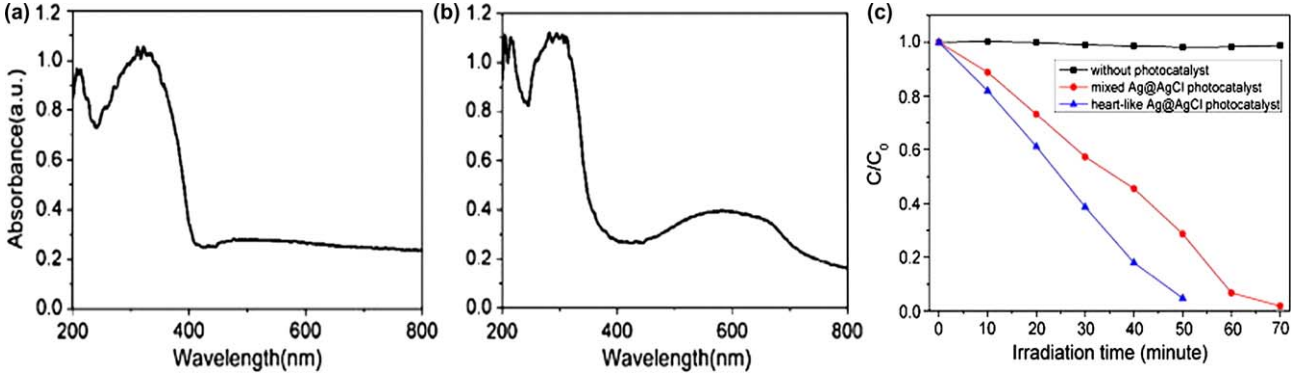

Fig. 17 The UV–vis spectra of heart-like AgCl particles (a) and Ag@AgCl particles (b). (c) Photocatalytic degradation rate of MO on different catalysts under visible light irradiation ($\lambda > 420$ nm).[54]

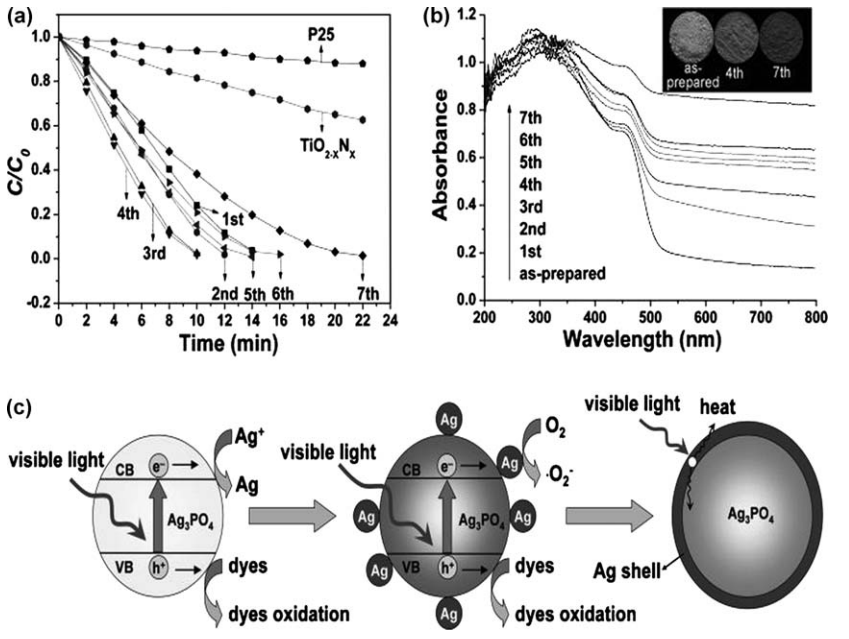

Fig. 18 (a) Photocatalytic activity of the Ag_3PO_4 sample at different recycle times as well as $TiO_{2-x}N_x$ and Degussa P25 for the decomposition of RhB; (b) UV/Vis spectra of Ag_3PO_4 samples at different recycle times. The inset shows photographs of the as-prepared sample and those in the 4th and 7th cycle; (c) Schematic diagram for photo-induced charge transfer, electron-hole separation, and the shielding effect of an Ag layer.[53]

surface of Ag_3PO_4 was reduced by photogenerated electrons to form metallic Ag. Then, the photoexcited electrons can migrate to Ag nanoparticles to accelerate the separation of electron-hole pairs, while holes accumulated at the valence band of Ag_3PO_4 can directly oxidize RhB into CO_2 and H_2O. However, more Ag nanoparticles deposited on the surface of Ag_3PO_4 formed a layer of Ag film, which shielded the light absorption and also inhibit the transfer of holes and hinder the contact of dye molecules with Ag_3PO_4. The photocatalytic activity decreased after the 4th cycle.

Novel photocatalytic materials have been widely explored for visible-light-driven photocatalysis. Some bismuth-containing complex oxides could be activated by visible light and mineralize organic pollutants, and have been a research focus in the field of photocatalysis.[41,58,59] Y. Sun *et al.* reported the synthesis of monoclinic $BiVO_4$ (m-$BiVO_4$) quantum tubes and ordered m-$BiVO_4$ quantum tubes-graphene nanocomposites.[41] The band structure, density of states (DOS) and optical absorption spectrum of m-$BiVO_4$ are calculated based on first-principles density functional theory, which shows the calculated band gap of 2.2 eV is fairly consistent with the experimental result obtained from the diffuse reflectance spectrum (Fig. 19). The as-prepared m-$BiVO_4$ showed the higher photocatalytic activity than P25 and bulk $BiVO_4$ by decolorization of rhodamine B (RhB), methylene blue (MB) and methyl orange (MO) under visible-light ($\lambda > 400$ nm) irradiation. Importantly, the ordered m-$BiVO_4$ quantum tubes-graphene nanocomposites exhibit the highest visible-light-driven photocatalytic activity due to the efficient photogenerated electrons transfer from the

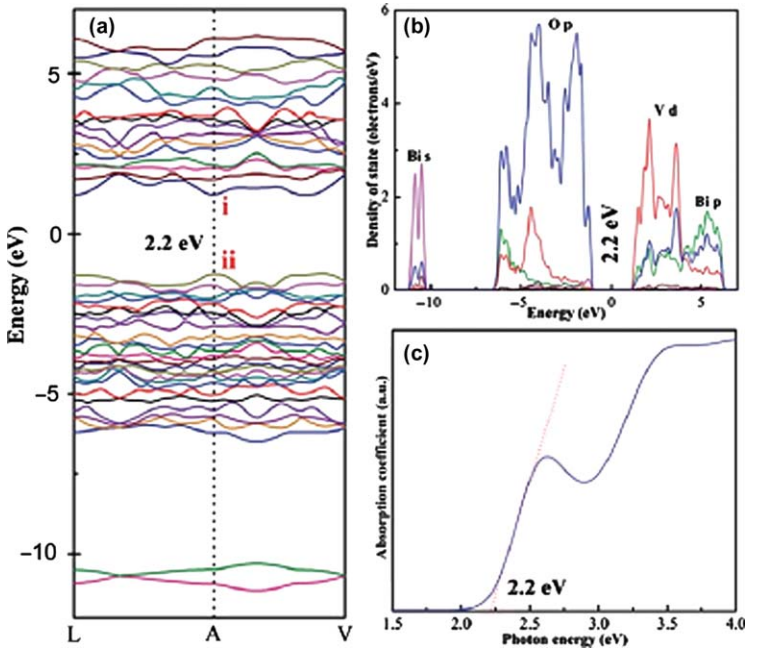

Fig. 19 Calculated (a) electronic band structure, (b) electronic density of states and (c) optical absorption spectrum of m-$BiVO_4$.[41]

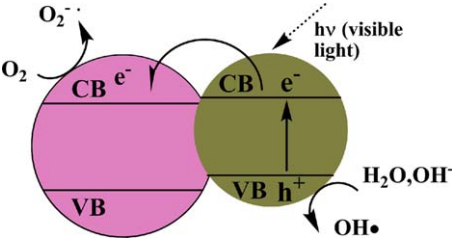

Fig. 20 Schematic illustration of charge transfer in semiconductor-semiconductor composites with a sensitization mechanism.

conduction band of m-$BiVO_4$ quantum tubes to the carbon atoms of grapheme sheets *via* a percolation mechanism.

3.3 Approaches to modifying the photocatalysts

The practical photocatalytic application of TiO_2 is limited due to its only absorption in the UV light region ($\lambda < 387$ nm) which accounts for 4% of the solar energy. Many efforts have been made to extend the light response to visible light including doping foreign elements into the lattices of TiO_2,[60–62] coupling with narrow band-gap semiconductors,[63–65] and surface sensitization.

Semiconductor-semiconductor composites. The composites of narrow band-gap semiconductor and wide band-gap semiconductor have been widely applied for the enhanced photocatalytic activity.[56,66–68] In the general mechanism (Fig. 20), the photogenerated electrons by visible-light

irradiation in a narrower band gap semiconductor with a higher conduction-band (CB) edge could migrate to a wider band gap semiconductor with a lower conduction-band edge, while the photogenerated holes stay in the narrower band gap semiconductor. This would facilitate electron-hole separation and prevent charge recombination, and improve the photocatalytic activity.[63]

Typically, CdS is a simple visible-light-driven photocatalyst but has the low activity and instability toward photocorrosion. It has been demonstrated that the combination of CdS with another wider band gap semiconductor is an effective strategy to improve the photocatalytic activity and stability of CdS.[69,70] For example, TiO_2@CdS and CdS@TiO_2 double-shelled hollow spheres (DHS) were successfully synthesized using SiO_2 nanospheres as sacrificial templates (Fig. 21a–c).[69] The samples displayed strong absorption in visible-light region (400–500 nm) compared to TiO_2 hollow spheres (Fig. 21d). The TiO_2@CdS DHS samples demonstrate the highest photocatalytic activity by degradation of RhB dye in water under visible light illumination ($\lambda > 400$ nm). This is attributed to the architecture structure for the interaction between CdS and TiO_2. The photogenerated electrons in the conduction band of CdS under visible light can quickly migrate to the conduction band of TiO_2, which promotes the separation of photogenerated electrons and holes.

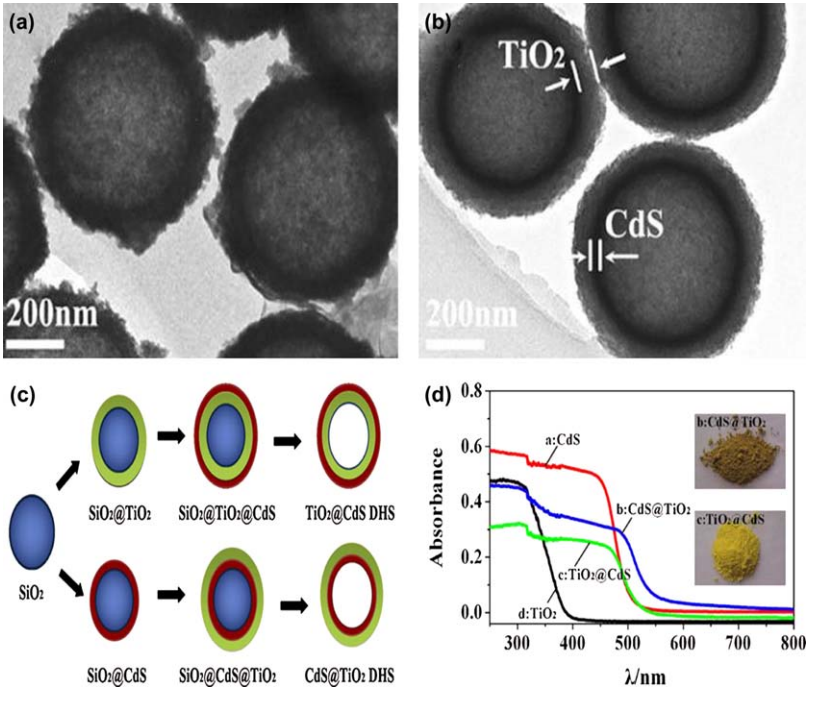

Fig. 21 (a) TEM image of TiO_2@CdS DHS, (b) TEM image of CdS@TiO_2 DHS; (c) Schematic diagram of the synthesis procedure of the double-shell hollow spheres (DHS). (d) UV–vis DRS spectra of CdS hollow spheres, CdS@TiO_2 DHS, TiO_2@CdS DHS, and TiO_2 hollow spheres.[69]

However, a similar sensitization mechanism can also be conducted. That is, the photogenerated holes by visible-light irradiation in a narrower band gap semiconductor with a lower valence-band edge could migrate to a wider band gap semiconductor with a higher valence-band (VB) edge, while the photogenerated electrons stay in the narrower band gap semiconductor. This would promote electron-hole separation and prevent charge recombination. For example, Bi_2WO_6 coupling with wide-band-gap TiO_2 semiconductor exhibited the enhanced photocatalytic degradation of RhB under visible-light.[64] Figure 22 showed the energy band matching and migration and separation of electron-hole pairs in the coupled Bi_2WO_6/TiO_2 photocatalyst. The VB level Bi_2WO_6 is lower by 0.353 V than that of TiO_2. In the process of photocatalysis, the electrons in the VB Bi_2WO_6 are excited to its CB under irradiation, and the holes in the VB of the Bi_2WO_6 can be transferred to that of TiO_2. The electrons on the surface of Bi_2WO_6 sheets and holes on the TiO_2 particles, respectively, can participate in photocatalytic reactions. Moreover, the coupled Bi_2WO_6/TiO_2 was stable during the repeated use.

Doping. Element doping is an efficient approach based on the formation of allowed electronic states within the gap between the conduction band and the valence band. The electronic transition between these states and the bands of the semiconductors requires less energy, compared to the band to band transition of the semiconductor. Thus, the electron transitions can be excited by visible light (Fig. 23).[42]

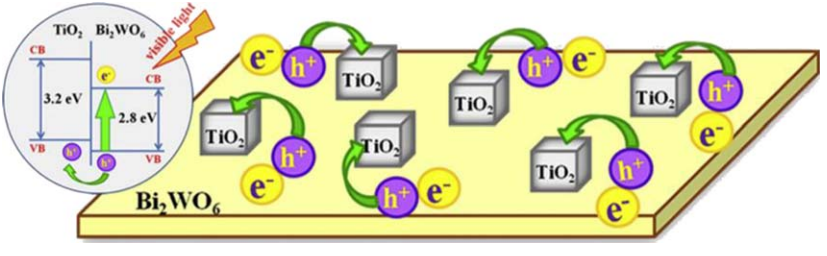

Fig. 22 Schematic diagram for energy band matching and migration and separation of electron-hole pairs in the coupled Bi_2WO_6 /TiO_2 photocatalyst.[64]

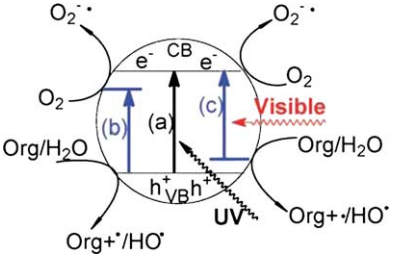

Fig. 23 Strategies to realize visible-light-induced degradation of organic pollutants on a semiconductor with a wide band gap. The band-band excitation of the pure semiconductor under UV irradiation (a); the bulk-doping to extend the photoresponse by forming electronic states just below the conduction band (b) or above the valence band (c).[42]

TiO_2 hollow microspheres codoped with N, Si were successfully prepared by a facile aerosol flow synthesis method.[71] The absorption edge shifted to longer wavelength of the porous N, Si codoped TiO_2 sample and a shoulder absorption band at 390–530 nm was clearly observed. The as-prepared N, Si codoped TiO_2 sample showed the enhanced photocatalytic activity on the degradation of salicylic acid under visible-light irradiation ($\lambda > 420$ nm). S. Wang *et al*. synthesized the anatase and rutile TiO_2 composite doped with Fe element by sol-gel technique.[72] The Fe doped TiO_2 sample induced an evident increase in absorption peak and a significant red-shift in absorption edge from 420 nm to 460 nm in UV-vis absorption spectrum. The 1.0at% Fe-doping TiO_2 with 20.64wt% rutile phase exhibited the higher degradation than that without Fe doping.

Combining with noble metal plasmonic photocatalyst. In recent years, the surface plasmon resonance (SPR) effect of noble metal (such as Ag, Au) nanoparticles on photocatalysis has attracted much attention. The frequency of the SPR can be spectrally tuned by changing the size, shape, and dielectric environment of the particles.[73,74] SPR can dramatically amplify the absorption of visible light and is therefore utilized to develop efficient visible-light-driven plasmonic photocatalysts.[75–78] For example, G. Wang synthesized mesoporous Au/TiO_2 nanocomposite microspheres for visible-light photocatalysis by using a microemulsion-based bottom-up self-assembly (EBS) process.[77] The as-prepared Au/TiO_2 nanocomposite exhibited a strong absorption in the visible-light region owing to the strong surface plasmon resonance (SPR) of Au nanoparticles (Fig. 24A), and the the mesoporous Au/TiO_2 microspheres showed advanced photocatalytic-degradation efficiency of AO7 under visible-light irradiation ($\lambda > 420$ nm) (Fig. 24B). The proposed rationalization was analyzed. As shown in Fig. 24C, Au nanoparticles were photoexcited under visible light and subsequently injected electrons into the conduction band of TiO_2 and the photogenerated holes stayed in the Au nanoparticles.

In addition, noble metal Ag nanoparticles also have the similar surface plasmon resonance. Nanocomposites of Ag/TiO_2 nanowires with enhanced photoelectrochemical performance have been reported.[79] The as-prepared nanocomposites exhibited significant responses in visible-light region from 500–600 nm and improved cathodic photocurrent responses under visible-light illumination, which is attributed to the local electric field enhancement of Plasmon resonance effect near the TiO_2 surface. Moreover, the Ag/TiO_2 nanowires showed photocatalytic activity on the degradation of methylene blue (MB) under visible-light irradiation based on the Ag plasmonic photocatalyst.

4 The degradation of air pollutants

Since human beings enter into the industrial era, the development of science and technology has brought huge spiritual and material wealth and created modernized style of human production and life. The rapid advancement of human civilization has provided us with the material world, but at the expense of environment. Environmental-contamination, which widely exists in air, water, soil, and food, has become a tremendous challenge. Especially,

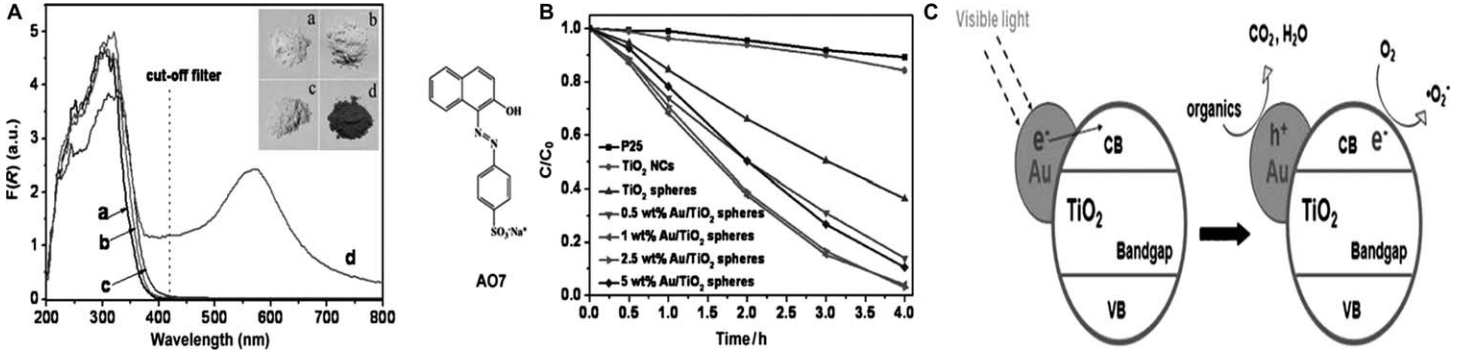

Fig. 24 A) UV/Vis absorption spectra plotted as the Kubelka-Munkfunction of the reflectance (R). Inset: photographs of the photocatalysts: a) P25, b) TiO_2 NCs, c) pure TiO_2 mesoporous spheres, and d) mesoporous Au/TiO_2 spheres (1wt%Au). The dashed vertical line indicates the cutoff wavelength of the filter used in the photocatalytic experiments. (B) Photodegradation of AO7 by P25 and by the as-synthesized mesopores. (C) Proposed rationalization of the photocatalytic activity of Au/TiO2 upon excitation of the Au surface Plasmon band.[77]

air pollution can have serious consequences for the health of human beings, and also severely affect natural ecosystems. However, pollution-control and environmental-restoration have never been simple because they require various collective manpower and material resources. Furthermore, with rapid economic development and intensive improvement of living standards worldwide, more and more energy is needed. Sooner or later we know it will come to this, and then increasing concern about an energy crisis has driven the efforts to find substitute energies due to the limited resources. Consequently, it is important to reduce air pollutants and convert air pollution into useful industrial materials or safe substances for human beings.

4.1 Photocatalytic reduction of CO_2

With the global expansion of industrial activities, global warming caused by a large-scale emission of greenhouse gases has gained increasing concern all over the world. As the most abundant greenhouse gas to induce global warming, atmospheric carbon dioxide (CO_2) concentration has been monotonically growing due to the combustion of hydrocarbon fuels, which has generated much concern. For the considerations of environment protection and the sustainable development of human society, it is highly desired to reduce the emission level of carbon dioxide, and to convert carbon dioxide into useful substances such as alternative fuels and raw materials for chemical industry. In view of worsening air pollution and global warming threats, it has been a worldwide topic to build a low carbon society. The reduction of CO_2 is a promising strategy to reduce CO_2 level in the atmosphere and in the meantime produce alternative fuels or a value-added product for industrial chemicals. Among various approaches for the transformation of CO_2, artificial photosynthesis, which employs the inexpensive semiconductor photocatalysts to convert the waste CO_2 into the reusable hydrocarbons (*e.g.* formaldehyde, formic acid, methanol, and methane) by means of solar energy at room temperature and ambient pressure, is undoubtedly one of the most sustainable among economical alternatives. This synthetic conversion can on the one hand reduces atmospheric CO_2 concentrations in the atmosphere, and on the other hand can provide the best solution to the energy shortage problem. Consequently, many research efforts have been made to develop efficient heterogeneous photocatalysts for the reduction of CO_2.

Zou's group has done many valuable and good studies in the conversion of CO_2. For example, an ultrathin, single-crystal WO_3 nanosheet of $\sim$4–5 nm in thickness, has been synthesized using a solid–liquid phase arc discharge route.[80] Size-quantization effects in this ultrathin nanostructure alter the WO_3 band gap to enable the nanosheet to exhibit enhanced performance for photocatalytic reduction of CO_2 to CH_4 in the presence of water in hydrocarbon fuels that do not exist in its bulk form (Fig. 25a). They also reported the high-yield production of ultrathin and uniform Bi_2WO_6 square nanoplates of $\sim$9.5 nm thickness corresponding to six repeating cell units in the presence of oleylamine.[81] The Bi_2WO_6 nanoplates showed great potential in the utilization of visible light energy to the highly efficient reduction of CO_2 into a renewable hydrocarbon fuel. Because the ultrathin geometry of the nanoplates not only promotes charge carriers to

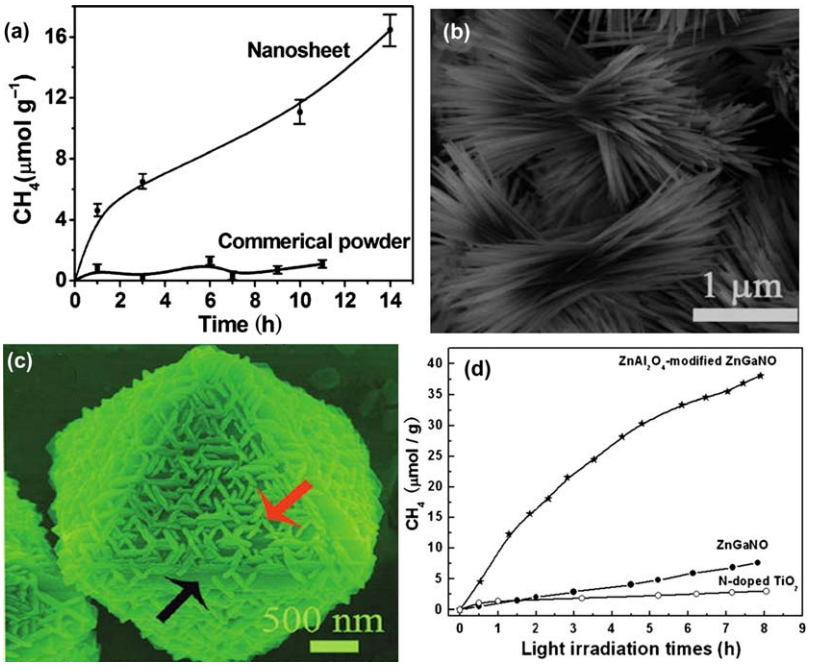

Fig. 25 (a) CH_4 generation over the WO_3 nanosheet and commercial powder as a function of visible light irradiation times ($\lambda > 420$ nm). (b) FE-SEM image of the sheaflike Zn_2GeO_4 superstructure. (c) From side view. The black arrow and red arrow mark the micro-octahedron and upstanding nanoplate, respectively. (d) CH_4 generation over the ZnGaNO, $ZnAl_2O_4$-modified ZnGaNO and N-doped TiO_2 as a function of irradiation time. All catalysts were modified by loading 0.5 wt% Pt as co-catalyst.

move rapidly from the interior to the surface to participate in the photoreduction reaction but also favor the improved separation of photogenerated electron and hole and a lower electron-hole recombination rate; meantime, the Bi_2WO_6 square nanoplate is proven to provide the well-defined {001} facet for two dominantly exposed surfaces, which is a prerequisite for the high level of photocatalytic activity of CO_2 fixation. Zinc orthogermanate (Zn_2GeO_4) is a chemically and thermally stable semiconductor, which is expected to be a good photocatalyst used in the photocatalytic overall water splitting, photoreduction of CO_2 and environmental purification. Single-crystalline hexagonal prism Zn_2GeO_4 nanorods with different aspect ratios have been prepared,[82] which exhibits improved photocatalytic activities photoreduction of CO_2 due to the less crystal defects, high specific surface area and beneficial microstructure on the catalyst's surface. Meantime, higher-order, Sheaf-like, hyperbranched Zn_2GeO_4 nanoarchitectures were successfully synthesized in a binary ethylenediamine(En)/water solvent system using a solvothermal route.[83] These Zn_2GeO_4 superstructures are composed of numerous closely packed nanorods (Fig. 25b). Nitridation of the resulting Zn_2GeO_4 superstructures under NH_3 flow produced a yellow $Zn_{1.7}GeN_{1.8}O$ solid solution that inherits the bundle shape, which allows photocatalytically converse CO_2 into hydrocarbon fuel (CH_4) in the presence of H_2O at ambient conditions under visible light irradiation. When loaded with co-catalysts, $Zn_{1.7}GeN_{1.8}O$ gives

high conversion rates of CO_2 into renewable hydrocarbon fuel (CH_4). A new copper (I) complex with the ability to bind to TiO_2 was synthesized.[84] Furthermore, they demonstrated that the copper (I) dye-sensitised TiO_2-based photocatalyst exhibits impressive effectiveness for the selective photoreduction of CO_2 to CH_4 under visible light. The superior performance of the copper complexes may be due to a modification of the key structural and electronic features that sustain efficient CO_2 reduction. The results may upgrade copper to the metal of choice in CO_2 reduction catalysts. Further detailed investigations are also needed to obtain an exact mechanistic understanding of the reaction process. We believe that these investigations would contribute significantly to the exploitation of new efficient light-harvesting complexes for the creation of sustainable artificial photosynthesis. A hexagonal nanoplate-textured octahedron Zn_2SnO_4 (Fig. 25c), abbreviated as nanoplate/micro-octahedrons, was synthesized with the assistance of L-tryptophan.[85] The generation of this unique architecture was found to undergo two consecutive nucleation processes. The unique nanoplate/micro-octahedron Zn_2SnO_4 was demonstrated to greatly promote the photocatalytic reduction of CO_2 into renewable hydrocarbon fuel (methane, CH_4) in the presence of water vapor. Considering light absorption by narrowing the band gap and gas capture by the mesostructure and basicity of material, an efficient artificial photosynthesis system was constructed based on a mesoporous $ZnAl_2O_4$-modified ZnGaNO photocatalyst, which showed a high photocatalytic activity for converting CO_2 to CH_4 under visible light irradiation (Fig. 25d).[86] The $ZnAl_2O_4$-modified mesoporous ZnGaNO photocatalyst was synthesized by a two-step reaction template route. the higher photocatalytic activity of the $ZnAl_2O_4$-modified mesoporous ZnGaNO toward reduction of CO_2 relative to that of the one without mesostructure and $ZnAl_2O_4$ modification can be attributed to the following three reasons: (1) Constructing the mesoporous structure improved the gas adsorption; (2) The $ZnAl_2O_4$ modification induces CO_2 chemistry absorption on the photocatalyst; (3) The high Zn content in the $ZnAl_2O_4$-modified ZnGaNO narrows the band gap and extends the light absorption.

Micro/mesoporous Zn_2GeO_4 with crystalline pore-walls was successfully synthesized *via* a simple ion exchange method at room temperature.[87] This structure showed enhanced activity in photoreduction of CO_2 in comparison with Zn_2GeO_4 prepared by a solid state reaction. This synthetic strategy is expected to be utilized in fabrications of unique micro/mesoporous structures of various semi-conductor functional materials with advanced properties. Mesoporous zinc germanium oxynitride was obtained by Zhang *et al.*,[88] which was synthesized by directly nitriding the microporous Zn_2GeO_4 at high temperature (800 °C) under an NH_3 atmosphere. The mesoporous structure was relatively stable under high temperature, which allowed optimally modulating the visible-light absorption and redox potentials. Moreover, optimal balance between effective visible-light absorption and adequate redox potentials as well as improved crystallinity is achieved through adjusting the nitridation time. It made this material improve activity in CO_2 photoreduction. Compared with the reference ZGON particles synthesized by a solid state reaction route and the commercial

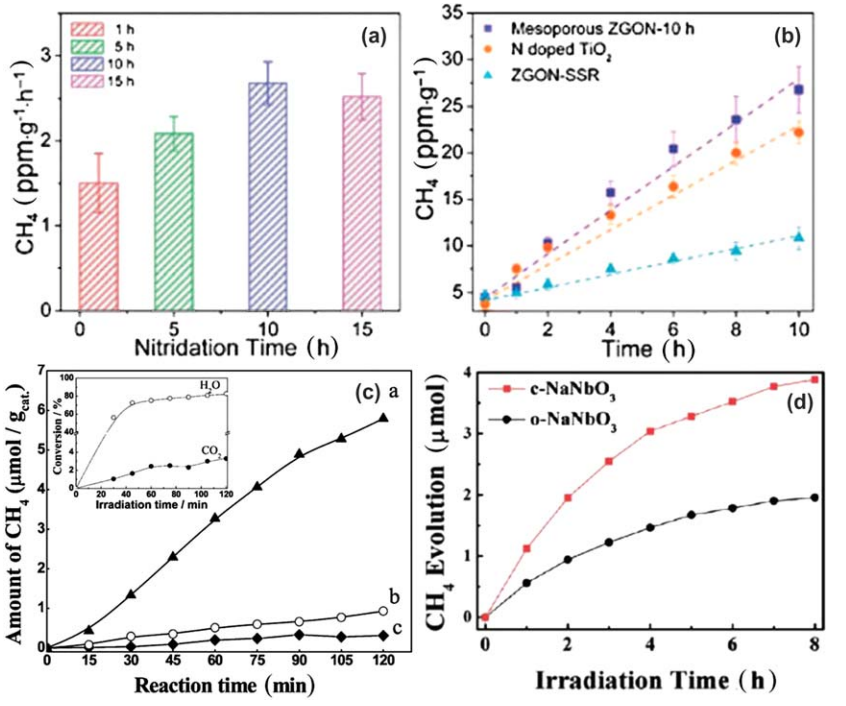

Fig. 26 (a) Average CH_4 evolution rates over mesoporous ZGON under visible light ($\lambda > 400$ nm, irradiation time: 10 h); (b) CH_4 evolution over mesoporous ZGON prepared at 10 h, N doped TiO_2, and ZGON prepared by SSR method. All samples are loaded with 1wt% Pt as co-catalyst ($\lambda > 400$ nm). (c) Photocatalytic reduction of CO_2 over (a) SiO_2–HNb_3O_8, (b) HNb_3O_8, and (c) Nb_2O_5. Pt (0.4 wt%) was loaded as cocatalyst for all the samples. Reaction conditions: catalyst, 0.1 g; H_2O/CO_2, 0.14; temperature, 60 ± 2 °C full Xe-arc irradiation; light intensity, 34.8 mW cm^{-2}. The inset shows the conversion of CO_2 and H_2O over SiO_2–HNb_3O_8. (d) CH_4 evolution in gas-phase reaction over c-$NaNbO_3$ and o-$NaNbO_3$ samples (with loading 0.5 wt% Pt).

N-doped TiO_2, the optimal mesoporous ZGON exhibited enhanced activity in CO_2 photoreduction under visible light (Fig. 26a–b). The results presented in this paper provide useful information for preparing other mesoporous oxynitrides and some new insight into the effect of a micro-structure in materials on gaseous chemical reactions. CO_2 photoreduction by gaseous water over silica-pillared lamellar niobic acid, *viz*. HNb_3O_8, was investigated in detail (Fig. 26c).[89] With layered structure, expanded interlayer distance, and stronger intercalation ability to water molecules, the silica pillared niobic acid showed much higher activity than the nonpillared niobic acid, Nb_2O_5, and TiO_2. Pt loading obvious promoted the activity for CO_2 photoreduction, and the optimum loading amount of Pt for SiO_2–HNb_3O_8 was 0.4 wt%. The SiO_2–HNb_3O_8 sample has unique intercalation behavior to water molecules through hydrogen bonding, and this contributed significantly to the activity of the sample. A uniform NiO/$InTaO_4$ layer was obtained on the top of pre-coated SiO_2 sublayer on the internal channels of the monolith.[90] The structure of monolith can significantly increase the amount of catalyst loading due to its multiple channels. The Optical fibers can effectively deliver light to illuminate the catalyst inside the

channels. By using mid-carve fibers, the deep-channel catalyst in the monolith was evenly illuminated. Vapor-phase CO_2 with H_2O was reduced to hydrocarbons by UV or visible-light in a steady-state flow mode. The maximum methanol conversion rate achieved was 0.16 mmol g^{-1} h^{-1} with visible-light. More importantly, the quantum efficiency was significantly improved indicating that photon energy was effectively utilized in the monolith reactor, compared with previous optical-fiber reactor. They demonstrated that the combination of optical fiber and monolith successfully enhanced a photoreaction, that is, the CO_2 photoreduction into fuel. Cheng *et al.*[91] present the synthesis of Bi_2WO_6 hollow microspheres (HMSs) by an anion exchange method, which involves the microscale Kirkendall effect from BiOBr microspheres as precursor under hydrothermal treatments. The as-prepared Bi_2WO_6 hollow microspheres, which possess large surface area and high CO_2 adsorption capacity, displayed efficient visible light CO_2 photocatalytic conversion into methanol in solution without any co-catalyst. This work illustrated a facile surfactant-free access to hierarchical inorganic materials with hollow interiors and may provide a generalized design strategy to achieve better photocatalytic efficiency of CO_2 conversion by microstructure modulation. Ever since the first report by Fujishima and Honda in 1972, TiO_2-based photocatalysts have attracted more and more attention owing to their potential applications in the fields of energy and environment.[92] Recently, Pan *et al.*[93] have directly synthesized single crystalline anatase TiO_2 rods with dominant reactive {010} facets by hydrothermally treating $Cs_{0.68}Ti_{1.83}O_4/H_{0.68}Ti_{1.83}O_4$ particles. The nanorods show a superior photocatalytic conversion of CO_2 into methane to the benchmark P25 nanocrystals. The excellent performance in converting CO_2 into CH_4 of the {010} dominant rods can be understood as the synergistic effects of both the unique surface atomic structure and higher CB minimum of {010}. Ce–TiO_2/SBA-15 catalysts were synthesized by Zhao *et al.*[94] Firstly, cerium-doped titanium oxide (Ce–TiO_2) nanoparticles were prepared by a simple sol–gel method. Subsequently, the as-synthesized Ce–TiO_2 nanoparticles were dispersed on SBA-15, mesoporous silica with one-dimensional pores, forming a Ce–TiO_2/SBA-15 nanocomposite. The nanocomposite materials were tested as photocatalysts to convert CO_2 and H_2O to value-added fuels under UV-vis illumination. Compared with unsupported Ce–TiO_2, Ce–TiO_2 supported on SBA-15 remarkably enhanced the CO_2 reduction rate, the results showed more than 100-fold enhancement in CO_2 photoreduction to CH_4, demonstrating the superior photocatalytic activity of the prepared Ce–TiO_2/SBA-15 nanocomposite materials. By contrast, amorphous silica as the substrate was much inferior to SBA-15. The superior catalytic activity may be related to the partially embedded Ce–TiO_2 nanoparticles in the ordered 1-D pores in SBA-15 that form synergies between the different components of the catalysts and enhance the diffusion and adsorption of CO_2.

Cubic and orthorhombic NaNbO3 were fabricated by Li *et al.*,[95] they investigated the effects of crystal structure and electronic structure on the photocatalytic activities in detail. The photocatalytic activities of the two phases of $NaNbO_3$ have been assessed by CO_2 photoreduction in gas phase. The results showed that the photocatalytic CO_2 reduction activities over cubic $NaNbO_3$ were nearly twice of those over orthorhombic $NaNbO_3$

(Fig. 26d). It should be mentioned that the c-$NaNbO_3$ shows a narrower band gap (3.29 eV) than the common o-$NaNbO_3$ (3.45 eV), theoretical calculation demonstrated that the band gap difference between the two phases of $NaNbO_3$ is caused by the variant octahedral ligand field. Furthermore, the high symmetry in c-$NaNbO_3$ results in its unique electronic structure that is beneficial for the electron excitation and transfer and thus contributes to its higher photocatalytic activity compared with o-$NaNbO_3$. The present work revealed that reforming the crystal structure of the perovskite semiconductor toward a higher symmetry can improve the photoelectron excitation and transfer. Thus, it offered a new idea to enhance the photocatalytic efficiency in other perovskite or multilayered perovskite photocatalysts. Feng *et al.*[96] displayed an easily implemented microwave-assisted solvothermal method for organic ligand free, rapid, *in situ* and uniform decoration of 1D long nanotube array walls with Pt nanoparticles. The Pt-nanoparticle/TiO_2 nanotube composite is shown to greatly promote the photocatalytic conversion of carbon dioxide and water vapor into methane, a behavior attributed to the homogeneous distribution of metal co-catalyst nanoparticles over the TiO_2 nanotube array surface providing a large number of active reduction sites. The novelty and flexibility of the technique, described herein, could prove effective for deposition within a variety of semiconductor nanoporous or nanotube material systems, with different metal, metal alloy or metal oxide nanoparticles, the resulting materials of which should have great use in catalysis, photocatalysis, photovoltaic, and photoelectrochemical applications and photoelectric conversion applications. An *et al.*[97] have proposed a facile and versatile glycerol-mediated route to prepare regular cube-tetrapod-like AgCl : Ag nanoparticles and AgBr : Ag nanoplates. The as-prepared AgX : Ag nanoparticles exhibited regular shapes, *i.e.*, cube-tetrapod-like AgCl : Ag nanoparticles and AgBr : Ag nanoplates. Compared with the pristine AgX, AgX : Ag nanocomposites displayed stronger absorption in the visible region due to the surface plasmon resonance of silver nanoparticles. Their band-gaps were determined on the basis of the UV-vis absorption spectra and the positions of their conduction bands were also estimated. The results demonstrated that the conduction edge potential of the obtained AgX : Ag is viable for the reduction of CO_2. For example, reduction of CO_2 under visible light irradiation with the assistance of the anisotropic AgX : Ag nanoparticles yields as much as 100 mmol methanol in the products. In addition, the AgX : Ag nanoparticles can maintain their structure and activity after 3 runs of reactions. Therefore, the high activity and stability of the as-prepared shaped AgX : Ag nanophotocatalysts mean they are promising materials for use in conversion of CO_2 to useful organic fuel.

4.2 Photocatalytic oxidation of CO

As a toxic gas, carbon monoxide (CO) forms widely in the utilization processes of fuel burning appliance, vehicles and in many industrial processes due to incomplete combustion. Meantime, carbon monoxide can cause oxygen deficiency. To prevent CO pollution, it is necessary to develop active and stable catalysts that enable CO to be completely oxidized at room temperature or below. Up to now, the catalytic oxidation of carbon

monoxide (CO) to carbon dioxide (CO_2) is one of the most effective methods to clean the exhaust from automobile and industries in order to avoid air pollution. Hence, the oxidation of carbon monoxide (CO) to carbon dioxide (CO_2) has attracted considerable research interest in recent years because the reaction has many industrial applications such as in catalytic conversion of automobile exhaust, fuel cells, cleaning air, lowering CO emissions from automobiles and industries, as well as removing CO from hydrogen gas fuel to avoid electrode poisoning.

Zhao *et al.*[98] have synthesized Au/FeOx–hydroxyapatite composite prepared by a simple deposition–precipitation, and investigated their catalytic performance for CO oxidation and sintering-resistant for calcination. The results showed that the as-obtained Au/FeO_x–hydroxyapatite composite possesses high activity for CO oxidation along with durability and strong stability. Hierarchical $LaFeO_3$ fibers were prepared by a sol–gel nanocasting method using a cotton cloth as the template.[99] Compared to the counterpart particles prepared by the conventional sol–gel method, the resulting $LaFeO_3$ fibers inherited the initial network morphology of the template very well and showed enhanced catalytic CO oxidation activity and satisfactory stability. Sun *et al.*[100] used a facile synthesis of ultrathin Co_3O_4 nanostructures by heating cobalt foils under atmospheric conditions. The obtained Co_3O_4 nanostructures were selectively exposing (111) planes composed of plenty of Co^{3+} cations. Exposing more Co^{3+} cations on the exposed planes is particularly important for improving their catalytic capacity, thus the specific rate of catalytic oxidation was enhanced about 40 times compared with that of Co_3O_4 nanostructures reported in the literature. As shown in Fig. 27a–c, different morphology of hematite (a-Fe_2O_3),[101] such as nanorods, nanotubes, and nanocubes, were synthesized *via* a hydrothermal process and subsequent calcination treatment, respectively. The nanorods showed higher catalytic activity than the nanotubes and the nanocubes for CO oxidation. It may be attributed to the highest occupancy of iron ions on the surface of the nanorods. Recently, hierarchical NiO flower-like microspheres with tunable porosity were prepared with a facile solvothermal method.[102] Three kinds of NiO microflowers (NiO-A, NiO-B, and NiO-C) with different porosity have been fabricated by tuning the concentration of nickel nitrate. These flower-like microspheres are constructed of densely packed irregular sheets and display a multi-peaks pore distribution in a wide range in both mesoporous and macroporous regions. These NiO spheres displayed a strong morphology dependant nature for CO oxidation catalysis. Compared to the reference sample of NiO (NiO-R) nanoparticles, these flower-like NiO micro-spheres possess a superior catalytic activity for CO oxidation (Fig. 27d–e). Qi *et al.*[103] have easily prepared uniform Au@CeO_2 core–shell submicrospheres, in which one Au nanoparticle core is coated with a shell composed of CeO_2 nanoparticles. When the Au@CeO_2 core–shell submicrospheres are used for catalytic oxidation of CO to CO_2, the full conversion temperature is decreased from over 300 °C to 155 °C with respect to the conventional supported Au–CeO_2 catalysts. Furthermore, the Au@CeO_2 core–shell submicrospheres show superior catalytic stability, and no deactivation occurs after 72 h reaction. CuO has attracted much attention owing to relative

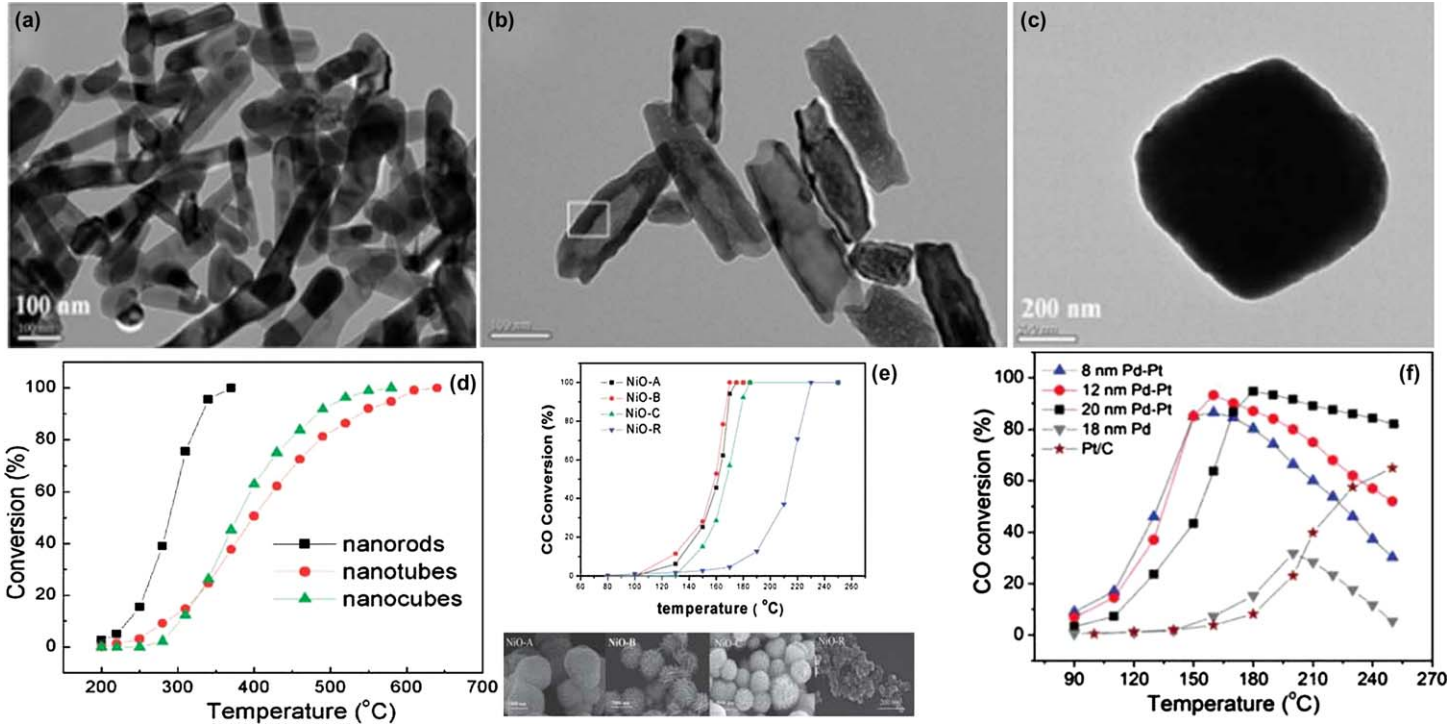

Fig. 27 (a) TEM image of a pile of nanorods. (b) TEM image of nanotubes. (c) TEM image of a nanocube. (d) CO oxidation as a function of temperature over a-Fe_2O_3 nanorods, nanotubes, and nanocubes at GHSV = 25500 $cm^3 g^{-1} h^{-1}$. (e) Catalytic activities of CO oxidation under different temperature for NiO-A, NiO-B, NiO-C and NiO-R, and the corresponding morphologies of the samples. (f) Catalytic activities of CO oxidation on Pd-Pt alloy nanocages of 8, 12, and 20 nm in size, Pd nanocubes of 18 nm in size, and the commercial Pt/C catalyst.

high efficiency and affordable price. Huang *et al.*[104] have synthesized various morphologies of CuO nanostructures with tuning by hetero-metal cations at room temperature. The morphologies of CuO can be engineered from nanosheets to nanoparticles with different length ratios. Furthermore, among all the synthesized CuO nanostructures, the fascinating colloidal mesoporous CuO quasi-monocrystalline nanosheets prepared at 25 °C with a thickness of *ca.* 10 nm and large specific surface area of 80.32 m^2g^{-1} is investigated intensively. These CuO nanosheets demonstrate a superior catalytic activity for CO oxidation, with features of high CO conversion efficiency (47.77 mmol CO $g^{-1}{}_{CuO}$ h^{-1} at 200 °C). Zhong *et al.*[105] have prepared poorly-crystallized CuO NRs grown directly from a sacrificial Cu foil *via* naturally-generated electrochemical corrosion, occurring in a liquid membrane self-constructing on the foil. The liquid membrane environment makes the CuO NRs grow at the gas–liquid interfaces and causes incomplete crystallization of the NRs, leading to large quantities of defect structures being generated in the resultant nanostructures, and these CuO NRs demonstrate a good catalytic activity for CO oxidation. It is reported that a noble metal (NM) can stabilize mono-layer-dispersed surface oxide phases with metastable nature. The formed ''oxide-on-metal'' inverse catalyst presents better catalytic performance than the NM because of the introduction of coordinatively unsaturated cations at the oxide–metal boundaries. Guo *et al.*[106] demonstrated that an ultrathin NM layer grown on a non-NM core could impose the same constraint on the supported oxide as the bulk NM. Cu@Pt core–shell nanoparticles (NPs) decorated with FeO patches use much less Pt but exhibit performance similar to that of Pt NPs covered with surface FeO patches in the catalytic oxidation of CO. The ''oxide-on-core@shell'' inverse catalyst system may open a new avenue for the design of advanced nanocatalysts with decreased usage of noble metals. Various well-defined Ni–Pt (111) model catalysts are constructed at atomic-level precision under ultra-high-vacuum conditions.[107] Subsequent studies of CO oxidation over the surfaces show that a sandwich surface (NiO_{1-x}/Pt/Ni/Pt(111)) consisting of both surface Ni oxide nanoislands and subsurface Ni atoms at a Pt(111) surface presents the highest reactivity. Among the supported Pt-Ni catalysts studied, the sandwich bimetallic catalysts demonstrate the highest activity to CO oxidation, where 100% CO conversion occurs near room temperature. Both surface science studies of model catalysts and catalytic reaction experiments on supported catalysts illustrate the synergetic effect of the surface and subsurface Ni species on the CO oxidation, in which the surface Ni oxide nanoislands activate O_2, producing atomic O species, while the subsurface Ni atoms further enhance the elementary reaction of CO oxidation with O. Zhang *et al.*[108] described a new method for the facile synthesis of Pd-Pt alloy nanocages with hollow interiors and porous walls by using Pd nanocubes as sacrificial templates. The size of Pd-Pt nanocages was found to have an impact on their catalytic performance. Specifically, reducing the size of the Pd-Pt nanocages could increase the conversion rate of CO (Fig. 27f).

4.3 Photocatalytic reduction of NO_x

Nitrogen oxides (NO_x), which are frequently emitted from mobile and stationary sources, have become a major source of air pollution.

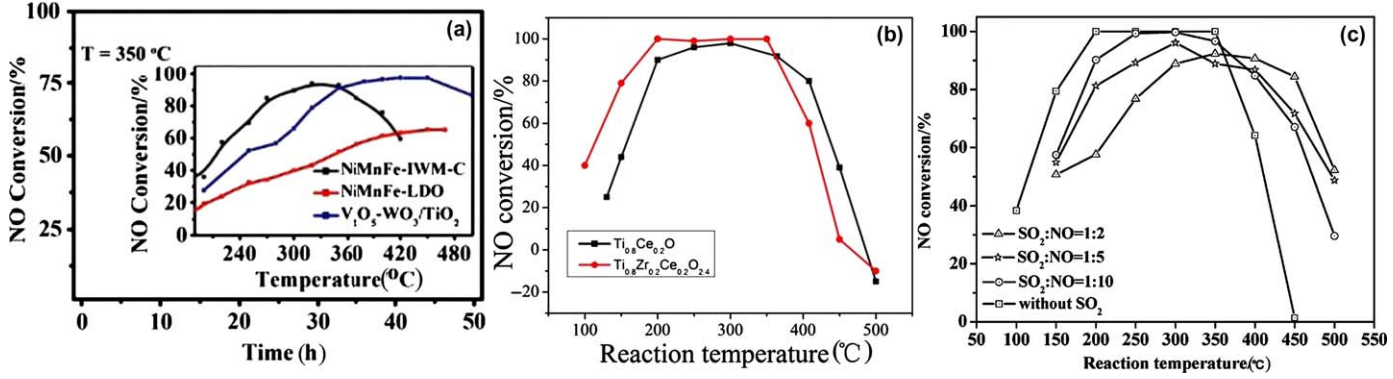

Fig. 28 (a) Activity evaluation (in) and stability tests (out) of the fabricated monolith catalysts. Reaction conditions: $[NO] = [NH_3] = 500$ ppm, $[O_2] = 3$ vol%, N_2 balance and GHSV = 20000 h^{-1}. (b) Effect of reaction temperature on NO conversions for NH_3-SCR of NO. (c) Catalytic activities for NH_3-SCR of NO over $Ti_{0.8}Zr_{0.2}Ce_{0.2}O_{2.4}$ catalysts both in the presence of SO_2 and without SO_2.

Disturbingly, they not only cause acid rain and photochemical smog but also induce the greenhouse effect. Currently, NO_x pollution is getting more and more serious to humans. Fortunately, many stringent emission regulations, rigorous emission control standards and growing environmental awareness are being imposed or raised to reduce the NO_x pollution. Thereby, highly efficient denitrification has become a very important and challenging research subject in the world. More recently, various alternative denitrification techniques, including selective non-catalytic reduction, selective catalytic reduction, electron beam irradiation, pulse corona plasma, carbon reduction, adsorption method, microwave method, microbiological method, plasma method, and so on, have been explored to remove NO_x from stationary sources. Among all the denitrification techniques, selective catalytic reduction has been recognized as the most promising approach for removing NO_x from coal-fired flue gas.

Li and coworkers[109] demonstrated a hydrothermal method to fabricate a novel class of monolithic NiMnFe mixed metal oxides *in situ* growing on iron wire meshes in cylindrical form (IWM-C), which showed high catalytic activity and $\sim$100% selectivity for N_2 for SCR of NO with NH_3 as shown in Fig. 28a. The catalyst showed uniform 3D flower-like nanoarrays with homogeneous distribution of the active components and good binding of the active material with the iron substrate, ideally allowing their catalytic properties to be maintained even under harsh reaction conditions. Shen *et al.*[110] have prepared zirconium-doped $Ti_{0.8}Ce_{0.2}O$ and tested in NH_3-SCR of NO. The results showed that zirconium additives not only dramatically improve the catalytic activity and N_2 selectivity, but also significantly enhance the anti-sulfur ability as shown in Fig. 28b and Fig. 28c.

References

1 J. Yu and J. Ran, *Energy Envion. Sci.*, 2011, **4**, 1364–1371.
2 X. Zhang, Y. Sun, X. Cui and Z. Jiang, *Int. J. Hydrogen Energy*, 2012, **37**, 811–815.
3 P. Cheng, Z. Yang, H. Wang, W. Cheng, M. Chen, W. Shangguan and G. Ding, *Int. J. Hydrogen Energy*, 2012, **37**, 2224–2230.
4 J. Z. L. Zhang, S. Luo, L. Leng, X. Luo, M. Zhang, Y. Luo and G. Guo, *Int. J. Hydrogen Energy*, 2012, **37**, 17068–17077.
5 W. Jian, L. Wang, G. Liu, G. Q. Lu and H. Cheng, *ACS Catal.*, 2012, **2**, 1854–1859.
6 Y. Lai, J. Gong and C. Lin, *Int. J. Hydrogen Energy*, 2012, **37**, 6438–6446.
7 X. Wang, Q. Xu, M. Li, S. Shen, X. Wang, Y. Wang, Z. Feng, J. Shi, H. Han and C. Li, *Angew. Chem. Int. Ed.*, 2012, **51**, 13089–13092.
8 J. Sun, G. Chen, J. Pei, R. Jin, Q. Wang and X. Guang, *J. Mater. Chem.*, 2012, **22**, 5609–5614.
9 Z. Zhang, J. Long, L. Yang, W. Chen, W. Dai, X. Fu and X. Wang, *Chem. Sci.*, 2011, **2**, 1826–1830.
10 X. Lv, S. Zhou, C. Zhang, H. Chang, Y. Chen and W. Fu, *J. Mater. Chem.*, 2012, **22**, 18542–18549.
11 D. Wang, R. Li, J. Zhou, J. Shi, J. Han, X. Zong and C. Li, *J. Phys. Chem. C*, 2012, **116**, 5082–5089.
12 Y. P. Xie, G. Liu, G. Q. Lu and H. M. Cheng, *Nanoscale*, 2012, **4**, 1267–1270.

13 G. Liu, J. Pan, L. Yin, J. T. Irvine, F. Li, J. Tan, P. Wormald and H. Cheng, *Adv. Funct. Mater.*, 2012, **22**, 3233–3238.
14 T. Sun, J. Fan, E. Liu, L. Liu, Y. Wang, H. Dai, Y. Yang, W. Hou, X. Hu and Z. Jiang, *Powder Technol.*, 2012, **228**, 210–218.
15 X. Zhou, J. Shi and C. Li, *J. Phys. Chem. C*, 2011, **115**, 8305–8311.
16 Q. Wang, N. An, W. Chen, R. Wang, F. Wang, Z. Lei and W. Shangguan, *Int. J. Hydrogen Energy*, 2012, **37**, 12886–12892.
17 Y. Lin, F. Zhang and D. Pan, *J. Mater. Chem.*, 2012, **22**, 22619–22623.
18 Y. Yu, G. Chen, Q. Wang and Y. Li, *Energy Envion. Sci.*, 2011, **4**, 3652–3660.
19 D. Wang, L. Wang and A. Wu, *Nanoscale*, 2012, **4**, 2046–2053.
20 Y. Cui, Z. Ding, X. Fu and X. Wang, *Angew. Chem. Int. Ed.*, 2012, **51**, 11814–11818.
21 J. Wu, L. Liao, W. Yan, Y. Xue, Y. Sun, X. Yan, Y. Chen and Y. Xie, *ChemSusChem*, 2012, **5**, 1207–1212.
22 J. Liu, Y. Zhang, L. Lu, G. Wu and W. Chen, *Chem. Commun.*, 2012, **48**, 8826–8828.
23 Q. Li, B. Guo, J. Yu, J. Ran, B. Zhang, H. Yan and J. R. Gong, *J. Am. Chem. Soc.*, 2011, **133**, 10878–10884.
24 J. Yu, B. Yang and B. Cheng, *Nanoscale*, 2012, **4**, 2670–2677.
25 J. Zhang, J. Yu, M. Jarniec and J. R. Gong, *Nano Lett.*, 2012, **12**, 4584–4589.
26 S. Zhang, Q. Chen, Y. Wang and L. Guo, *Int. J. Hydrogen Energy*, 2012, **37**, 13030–13036.
27 Z. Shen, G. Chen, Q. Wang, Y. Yu, C. Zhou and Y. Wang, *Nanoscale*, 2012, **4**, 2010–2017.
28 J. Zhang, J. Zhang, Y. Zhang, Q. Li and J. R. Gong, *Nano Lett.*, 2011, **11**, 4774–4779.
29 Q. Xiang, J. Yu and M. Jaroniec, *J. Am. Chem. Soc.*, 2012, **134**, 6575–6578.
30 Q. Zhan, Z. Yu, W. Yuan and J. Li, *Int. J. Hydrogen Energy*, 2012, **37**, 13249–13255.
31 J. Shen, J. Zai, Y. Yuan and X. Qian, *Int. J. Hydrogen Energy*, 2012, **37**, 16986–16993.
32 W. Zhao, Z. Wang, X. Shen, J. Li, C. Xu and Z. Gan., *Int. J. Hydrogen Energy*, 2012, **37**, 908–915.
33 Y. Mao, J. He, X. Sun, W. Li, X. Lu, J. Gan, Z. Liu, L. Gong, J. Chen, P. Liu and Y. Tong, *Electrochimica Acta*, 2012, **62**, 1–7.
34 M. Tian, W. Peng, B. Shang, W. Tao and Y. Xiao, *Int. J. Hydrogen Energy*, 2012, **37**, 12827–12832.
35 Y. Sun, K. Yan, G. Wang, W. Guo and T. Ma, *J. Phys. Chem. C*, 2011, **115**, 12844–12849.
36 S. Liang, J. He, Z. Sun, Q. Liu, Y. J. Hao, B. He, Z. Xie and S. Wei, *J. Phys. Chem. C*, 2012, **116**, 9049–9053.
37 C. Zhen, G. Liu and H. M. Cheng, *Nanoscale*, 2012, **4**, 3871–3874.
38 M. Xu, P. Da, H. Wu, D. Zhao and G. Zheng, *Nano Lett.*, 2012, **12**, 1503–1508.
39 Y. Liu, Y. Yu and W. D. Zhang, *Electrochimica Acta*, 2012, **59**, 121–127.
40 Y. Qiu, K. Yan, H. Deng and S. Yang, *Nano Lett.*, 2012, **12**, 407–413.
41 Y. Sun, B. Qu, Q. Liu, S. Gao, Z. Yan, W. Yan, B. Pan, S. Wei and Y. Xie, *Nanoscale.*, 2012, **4**, 3761–3767.
42 C. Chen, W. Ma and J. Zhao, *Chem. Soc. Rev.*, 2010, **39**, 4206–4219.
43 X. Wang, S. Li, H. Yu, J. Yu and S. Liu, *Chem. Eur. J.*, 2011, **17**, 7777–7780.
44 S. Sun, W. Wang and L. Zhang, *J. Mater. Chem.*, 2012, **22**, 19244–19249.
45 A. Fujishima, X. Zhang and D. A. Tryk, *Surf. Sci. Rep.*, 2008, **63**, 515–582.

46 T. Wu, G. Liu, J. Zhao, H. Hidaka and N. Serpone, *J. Phys. Chem. B.*, 1998, **102**, 5845–5851.
47 A. Fujishima and K. Honda, *Nature*, 1972, **238**, 37–39.
48 X. Zhou, J. Lan, G. Liu, K. Deng, Y. Yang, G. Nie, J. Yu and L. Zhi, *Angew. Chem. Int. Ed.*, 2012, **51**, 178–182.
49 G. Xi, Y. Yan, Q. Ma, J. Li, H. Yang, X. Lu and C. Wang, *Chem. Eur. J.*, 2012, **18**, 13949–13953.
50 D. Zhang, S. Wang, J. Zhu, H. Li and Y. Lu, *Appl. Catal. B: Environ.*, 2012, **123–124**, 398–404.
51 S. Wei, Y. Ma, Y. Chen, L. Liu, Y. Liu and Z. Shao, *J. Hazard. Mater.*, 2011, **194**, 243–249.
52 Z. Yi, J. Ye, N. Kikugawa, T. Kako, S. Ouyang, H. S. Williams, H. Yang, J. Cao, W. Luo, Z. Li, Y. Liu and R. Withers, *Nat. Mater.*, 2010, **9**, 559–564.
53 W. Wang, B. Cheng, J. Yu, G. Liu and W. Fan, *Chem. Asian J.*, 2012, **7**, 1902–1908.
54 J. Liao, K. Zhang, L. Wang, W. Wang, Y. Wang, J. Xiao and L. Yu, *Mater. Lett.*, 2012, **83**, 136–139.
55 H. Zhang, H. Huang, H. Ming, H. Li, L. Zhang, Y. Liu and Z. Kang, *J. Mater. Chem.*, 2012, **22**, 10501–10506.
56 W. Yao, B. Zhang, C. Huang, C. Ma, X Song and Q. Xu, *J. Mater. Chem.*, 2012, **22**, 4050–4055.
57 G. Li and L. Mao, *RSC Adv.*, 2012, **2**, 5108–5111.
58 X. Zhang, Y. Gong, X. Dong, X. Zhang, C. Ma and F. Shi, *Mater. Chem. Phys.*, 2012, **136**, 472–476.
59 H. Huang, H. Chen, Y. Xia, X. Tao, Y. Gan, X. Weng and W. Zhang, *J. Colloid Interf. Sci.*, 2012, **370**, 132–138.
60 Y. Niu, M. Xing, J. Zhang and B. Tian, *Catal. Today*, 2013, **201**, 159–166.
61 X. Zong, Z. Xing, H. Yu, Z. Chen, F. Tang, J. Zou, G. Q. Lu and L. Wang, *Chem. Commun.*, 2011, **47**, 11742–11744.
62 G. Liu, L. C. Yin, J. Wang, P. Niu, C. Zhen, Y. Xie and H. M. Cheng, *Energy Environ. Sci.*, 2012, **5**, 9603–9610.
63 W. Fan, Q. Zhang and Y. Wang, *Phys. Chem. Chem. Phys.*, 2013, **15**, 2632–2649.
64 J. Xu, W. Wang, S. Sun and L. Wang, *Appl. Catal. B: Environ.*, 2012, **111–112**, 126–132.
65 Y. Shen, F. Li, D. Liu, S. Li and L. Fan, *Sci. Adv. Mater.*, 2012, **4**, 1214–1219.
66 T. Lv, L. Pan, X. Liu and Z. Sun, *Electrochim. Acta.*, 2012, **83**, 216–220.
67 B. Li and Y. Wang, *J. Phys. Chem. Solids.*, 2011, **72**, 1165–1169.
68 Y. Huo, X. Yang, J. Zhu and H. Li, *Appl. Catal. B: Environ.*, 2011, **106**, 69–75.
69 H. L. Meng, C. Cui, H. L. Shen, D. Y. Liang, Y. Z. Xue, P. G. Li and W. H. Tang, *J. Alloy. Compd.*, 2012, **527**, 30–35.
70 D. Barpuzary, Z. Khan, N. Vinothkumar, M. De and M. Qureshi, *J. Phys. Chem. C*, 2012, **116**, 150–156.
71 Z. Ai, Z. Gao, K. Su, W. Ho and L. Zhang, *Catal. Commun.*, 2012, **29**, 189–193.
72 S. Wang, J. S. Lian, W. T. Zheng and Q. Jiang, *Appl. Surf. Sci.*, 2012, **263**, 260–265.
73 S. Linic, P. Christopher and D. B. Ingram, *Nat. Mater.*, 2010, **10**, 911–921.
74 X. Xia, J. Zeng, L. K. Oetjen, Q. Li and Y. Xia, *J. Am. Chem. Soc.*, 2012, **134**, 1793–1801.
75 Q. Xiang, J. Yu, B. Cheng and H. C. Ong, *Chem. Asian J.*, 2010, **5**, 1466–1474.
76 L. Jiang, G. Zhou, J. Mi and Z. Wu, *Catal. Commun.*, 2012, **24**, 48–51.
77 G. Wang, X. Wang, J. Liu and X. Sun, *Chem. Eur. J.*, 2012, **18**, 5361–5366.

78 Y. Wen, H. Ding and Y. Shan, *Nanoscale.*, 2011, **3**, 4411–4417.
79 H. Li, W. Lu, J. Tian, Y. Luo, A. M. Asiri, A. O. Al-Youbi and X. Sun, *Chem. Eur. J.*, 2012, **18**, 8508–8514.
80 X. Chen, Y. Zhou, Q. Liu, Z. Li, J. Liu and Z. Zou, *ACS Appl. Mater. Interfaces*, 2012, **4**, 3372–3377.
81 Y. Zhou, Z. Tian, Z. Zhao, Q. Liu, J. Kou, X. Chen, J. Gao, S. Yan and Z. Zou, *ACS Appl. Mater. Interfaces*, 2011, **3**, 3594–3601.
82 S. Yan, L. Wan, Z. Li and Z. Zou, *Chem. Commun.*, 2011, **47**, 5632–5634.
83 Q. Liu, Y. Zhou, Z. Tian, X. Chen, J. Gao and Z. Zou, *J. Mater. Chem.*, 2012, **22**, 2033–2038.
84 Y. Yuan, Z. Yu, J. Zhang and Z. Zou, *Dalton Trans.*, 2012, **41**, 9594–9597.
85 Z. Li, Y. Zhou, J. Zhang, W. Tu, Q. Liu, T. Yu and Z. Zou, *Cryst. Growth Des.*, 2012, **12**, 1476–1481.
86 H. Yan, N. Yu, Z. Wang, Z Li and Zou, *Chem. Commun.*, 2012, **48**, 1048–1050.
87 N. Zhang, S. Ouyang, P. Li, Y. Zhang, G. Xi, T. Kako and J. Ye, *Chem. Commun.*, 2011, **47**, 2041–2043.
88 N. Zhang, S. Ouyang, T. Kako and J. Ye, *Chem. Commun.*, 2012, **48**, 1269–1271.
89 X. Li, W. Li, Z. Zhuang, Y. Zhong, Q. Li and L. Wang, *J. Phys. Chem. C*, 2012, **116**, 16047–16053.
90 P. Liou, S. Chen, J. C. S. Wu, D. Liu, S. Mackintosh, M. M. Valer and R. Linforth, *Energy Environ. Sci.*, 2011, **4**, 1487–1494.
91 H. Cheng, B. Huang, Y. Liu, Z. Wang, X. Qin, X. Zhang and Y. Dai, *Chem. Commun.*, 2012, **48**, 9729–9731.
92 A. Fujishima and K. Honda, *Nature*, 1972, **238**, 37–41.
93 J. Pan, X. Wu, L. Wang, G. Liu, G. Q. Lu and H. Cheng, *Chem. Commun.*, 2011, **47**, 8361–8363.
94 C. Zhao, L. Liu, Q. Zhang, J. Wang and Y. Li, *Catal. Sci. Technol.*, 2012, **2**, 2558–2568.
95 P. Li, S. Ouyang, G. Xi, T. Kako and J. Ye, *J. Phys. Chem. C*, 2012, **116**, 7621–7628.
96 X. Feng, J. D. Sloppy, T. J. LaTempa, M. Paulose, S. Komarneni, N. Bao and C. A. Grimes, *J. Mater. Chem.*, 2011, **21**, 13429–13433.
97 C. An, J. Wang, W. Jiang, M. Zhang, X. Ming, S. Wang and Q. Zhang, *Nanoscale*, 2012, **4**, 5646–5650.
98 K. Zhao, B. Qiao, J. Wang, Y. Zhang and T. Zhang, *Chem. Commun.*, 2011, **47**, 1779–1781.
99 P. Li, X. Hu, L. Zhang, H. Dai and L. Zhang, *Nanoscale*, 2011, **3**, 974–976.
100 Y. Sun, P. Lv, J. Yang, L. He, J. Nie, X. Liu and Y. Li, *Chem. Commun.*, 2011, **47**, 11279–11281.
101 Q. Gao, X. Wang, J. Di, X. Wu and Y. Tao, *Catal. Sci. Technol.*, 2011, **1**, 574–577.
102 J. Xiao, B. Chen, X. Liang, R. Zhang and Y. Li, *Catal. Sci. Technol.*, 2011, **1**, 999–1005.
103 J. Qi, J. Chen, G. Li, S. Li, Y. Gao and Z. Tang, *Energy Environ. Sci.*, 2012, **5**, 8937–8941.
104 H. Huang, L. Zhang, K. Wu, Q. Yu, R. Chen, H. Yang, X. Peng and Z. Ye, *Nanoscale*, 2012, **4**, 7832–7841.
105 K. Zhong, J. Xue, Y. Mao, C. Wang, T. Zhai, P. Liu, X. Xia, H. Li and Y. Tong, *RSC Advances*, 2012, **2**, 11520–11528.
106 X. Guo, Q. Fu, Y. Ning, M. Wei, M. Li, S. Zhang, Z. Jiang and X. Bao, *J. Am. Chem. Soc.*, 2012, **134**, 12350–12353.

107 R. Mu, Q. Fu, H. Xu, H. Zhang, Y. Huang, Z. Jiang, S. Zhang, D. Tan and X. Bao, *J. Am. Chem. Soc.*, 2011, **133**, 1978–1986.
108 H. Zhang, M. Jin, H. Liu, J. Wang, M. J. Kim, D. Yang, Z. Xie, J. Liu and Y. Xia, *ACS Nano*, 2011, **5**, 8212–8222.
109 H. Li, D. Zhang, P. Maitarad, L. Shi, R. Gao, J. Zhang and W. Cao, *Chem. Commun.*, 2012, **48**, 10645–10647.
110 Y. Shen, Y. Ma and S. Zhu, *Catal. Sci. Technol.*, 2012, **2**, 589–599.

Nanoscience research in India: Recent contributions (2012–2013)

Ashok K. Ganguli,*[a,b,c] Aparna Ganguly[c] and Mrinmoyee Basu[b]
DOI: 10.1039/9781849737623-00139

There has been remarkable progress in the field of nanoscience and technology during the last couple of years across the world. Indian scientists have made significant impact, which is being reflected, in the number of publications in high impact factor journals from the country (Fig. 1: histogram). Nanoscience and nanotechnology has been in the forefront of research in India due to the initiatives of the Department of Science and Technology (DST), Government of India (especially the NanoMission Council of the DST), Department of Biotechnology (DBT), Council of Scientific and Industrial Research (CSIR), Department of electronics and information Technology(DeiTy) and Defence Research and Development organization (DRDO) and several other institutions of the Govt. of India which have also played a major role in encouraging research in nanoscience and nanotechnology. In this direction, several centres of nanoscience and technology have been started in the institutes of technology (IIT's) and Central Universities and national laboratories. Recently, a new institute "Institute of Nanoscience and Technology" supported by DST has started functioning at Mohali, Punjab.

Many of the earlier contributions from India were focussed on synthesis and properties of nanomaterials. In the last few years, the emphasis has shifted to deliver processes/devices in the area of sensors, nanomedicine, environmental and energy – based applications. There has been enormous progress in the field of photocatalysis and electrocatalysis, photovoltaics, nanophotonics, drug delivery, sensors and water purification. (Fig. 2: pie chart). The future is to design nanoscience based solutions for problems specific to India. It is hoped to couple available resources, especially skilled manpower with nanoscience and nanotechnology to apply to challenges being faced by India. One such example would be in the area of medical diagnostics which requires human intervention (skilled) and nanotechnology (imaging or drug delivery). In this article, we have highlighted the major contributions by scientists working in India towards the progress in **nanoscience** in the recent past (2012–2013). In addition, some high quality work in engineering and technology of nanostructured materials have also been published which has not been covered here.

1 Design of nanomaterials

Nanomaterials have at least one dimension between 1 nm to 100 nm, which includes nanoparticles, nanocubes, nanorods, nanobelts, nanosheets, nanowires, and nanotubes. Depending on the size and shape, the properties (optical, electronic, magnetic, thermal, mechanical, and chemical) of nanomaterials vary. A significant effort has been exercised towards controlling the size and shape of nanostructures. The most popular techniques are sol-gel method, microemulsion technique, co-precipitation in presence

[a]*Institute of Nano Science and Technology, Habitat Centre, Phase-X, Sector-64 Mohali Punjab-160062, India*
[b]*Department of Chemistry, Indian Institute of Technology, Delhi New Delhi 110016, India*
[c]*Nanoscale Research Facility, Indian Institute of Technology, Delhi New Delhi 110016, India.*
**E-mail: ashokganguli@rediffmail.com*

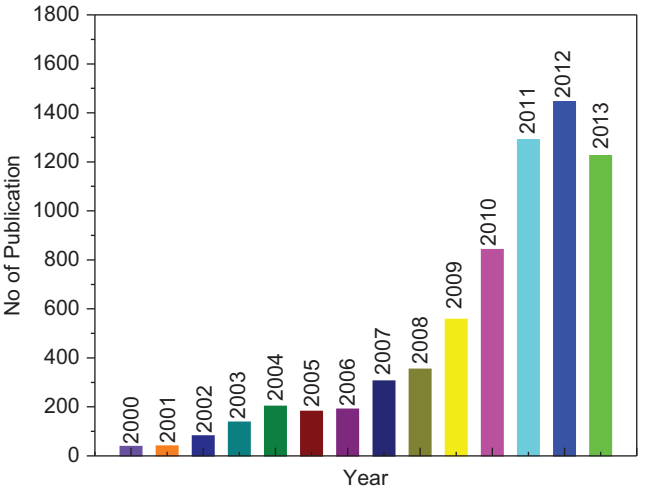

Fig. 1 Graphical representation of the yearly growth in the field of nanoscience and nanotechnology in India. (Source: Scopus Database)

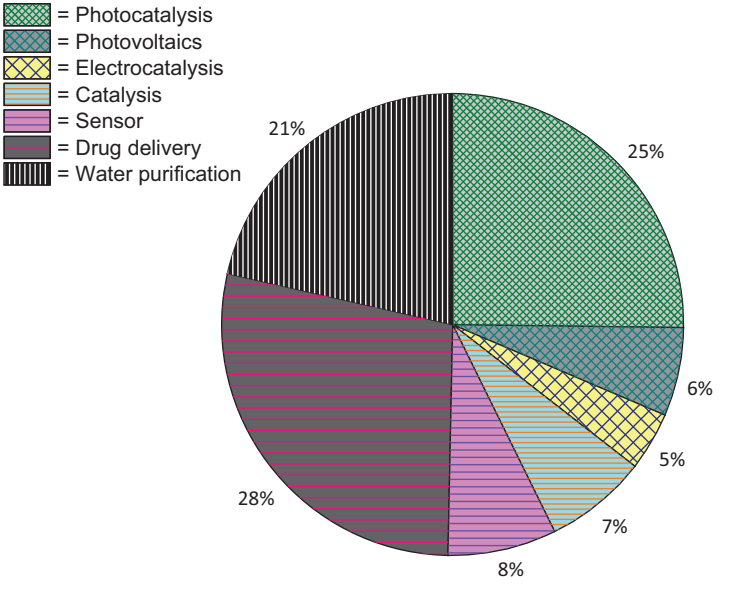

Fig. 2 Growth percent during 2012–2013 in the various sectors of nanoscience and nanotechnology in India.(Source: Scopus Database)

of stabilizers hydrothermal and solvothermal methods, template assisted methods *etc*. Applying these techniques, significant variety of materials like metal,[1,2] metal oxides,[3,4] metal chalcogenide,[5–7] alloy,[8,9] core-shell nanostructures,[10–12] organic- inorganic hybrid materials, polymers, graphene and related mimics[13,14] and nanocomposites have been documented from India in the past few years. Synthesis of nanoparticles of different sizes, shapes, chemical composition with controlled morphology is an important area of research in nanotechnology due to the relation of the above factors with the physical properties and hence on their specific applications. Some

of the key studies from India in the synthesis/design of nanomaterials in the recent past (2012–2013) are discussed below.

Shape selective synthesis of plasmonic nanoparticles is one of the intensely pursued research topics today. The effect of temperature and concentration of Br^- on the edge-length and yield of triangular nanoplates of gold by surfactant directed thermal approach has been studied.[15] The Br^- ions was varied (amount of CTAB, surfactant) and by replacing CTAB with HBr. Formation of two-dimensional plate-like structures is a kinetically controlled process. Higher nucleation results in low yields of triangles and their edge-length also became smaller. Addition of Br^- slows down the reduction of Au (III) to Au (0) impacting the yield and size of triangles. If Br^-concentration becomes very high, the reduction of Au (III) to Au (I) itself is hindered. Development of surfactant-less methods to synthesize anisotropic nanostructures is of importance and these results are encouraging to investigate the role of surfactant/bromide ions on the formation of other anisotropic structures. Ferromagnetic (hexagonal) cobalt nanostructures were synthesized by a simple and quick route using a modified polyol process in which a cobalt hydrazine complex was taken as a precursor with poly(vinylpyrrolidone)(PVP) molecules as stabilizer in ethylene glycol (solvent).[16] The growth mechanism of Co nanorods was observed through SEM images at different time intervals. The nanorod formation process shows that initially the product consists of nearly spherical nanoparticles (with an average size of 38 nm), whereas that of the end product consists of tiny nanorods.

Monodispersed gold nanoparticles of 2.2 nm (AuNPs) has been synthesized and stabilized on a unique polydentate disulfide ligand, poly(DSDMA).[17] Poly (DSDMA) has been synthesized by selective polymerization of bis (methacryloyl hydroxyethyl) disulfide (DSDMA) compound. The AuNPs ($2.2–3.2 \pm 0.1$ nm) exhibit Coulomb blockade at room temperature and are stable in DMF for one year and against 100 mM DTT for 72 h. Crosslinking of the pendent vinyl unsaturation during thermal treatment results in thermal stability at 140 °C for 4 h. In contrast, the AuNP synthesized in the presence of DSDMA using the conventional approach were stable in DMF for 15 days, against 100 mM DTT for 24 h and did not exhibit Coulomb blockade. AuNPs stabilized on poly (DSDMA) shows enhanced performance due to the graft density of 1.8 chains nm^{-2} resulting from the polydentate nature. Extension of this concept to hydrophilic monomers such as cysteine diacrylamide would lead to tunable nanocavities for newer applications in drug delivery and bioimaging.

Noble metal quantum clusters belong to a new class of materials with well-defined optical absorption and intense luminescence. Different Au clusters like Au_{25}, Au_{38}, Au_{102} have been synthesized and studied previously, but such clusters based on Ag were synthesized only recently. As most of the clusters are metastable, thus nucleation at low temperature and rapid protection by covalent chemistry are the desired steps used in the synthesis of metal clusters. Reducing agents such as $NaBH_4$ are used at very low temperature in a solution containing high concentration of the protecting agent. However, direct high temperature synthetic routes for obtaining clusters in solution, (starting from ions) was not known which has now been

reported using glutathione (SG) protected atomically precise silver clusters, $Ag_{75}(SG)_{40}$.[18] This study suggests that such clusters are likely to be stable even at elevated temperatures, which expand the possibility of cluster research.

For the synthesis of metal (Ag, Au) nanostructures a variety of **natural sources** have been employed to investigate their capping ability, reducing ability and also to develop a greener way for nanomaterial synthesis. Gold nanoparticles of spherical, triangular and square plate shape were synthesized from $HAuCl_4 \cdot 3H_2O$ solution using aqueous leaf extracts of Cocculus hirsutus.[19] Gold nanostructures are mostly stabilized by the carbonyl and amide groups present in the active component of C. hirsutus leaf extract. Slow reduction of gold ions by the mild reducing agent (ascorbic acid) present within the extract leads to the formation of gold nanostructures of variable morphologies. Gold nanoparticles (Au-NPs) were synthesized at room temperature using Prunus domestica (plum) fruit extract as reducing agent.[20] Water-soluble polyols and amino acids of plum fruit extract successfully reduce and stabilize Au-NPs. An eco-friendly method was developed using aqueous extract of Macrotyloma uniflorum for the synthesis of spherical gold nanoparticles.[21] The different functional groups present in the bio-molecules play an active role as capping agent on the nanoparticles. A simple, environmentally friendly, and naturally available protein based bio template, *viz*. the chicken eggshell membrane has been used for preparing highly fluorescent gold nanoparticles in a single step process.[22] This is a green method to prepare gold nanoparticles both in solution and on the membrane for various applications. The novelty of this technique lies in the unique properties of this membrane, such as high resistance to pH and safety in handling. The most important feature of this method is the easy abundance of the source material, which enables cost-effective preparation of gold nanoparticles. This method could be used as a very simple route to recover precious metals from chemical and industrial waste. Chiral core-shell nanostructures containing raspberry-like gold cores and well-defined dense organic shells were synthesized by an *in situ* method using a natural antioxidant (catechin) as the reducing agent.[23] This method is flexible and enables control over the shell thickness by adjusting the molar ratio of catechin to $HAuCl_4$. Here, catechin reduces Au^{3+} to gold nanostructures and gets oxidized to different oligomeric products which are adsorbed *in situ* and assembled through H-bonding and to form a thick organic shell around the generated gold nanostructures.

Apart from Au, Ag nanostructures have also been synthesized in the presence of natural sources. Silver nanoparticles (AgNPs) were prepared under mild conditions by exploiting a combination of naturally abundant polymer starch and trisodium citrate as reducing and stabilizing agent.[24] The shape-directing role of cetyltrimethylammonium bromide, CTAB has been investigated for Ag-nanoparticles synthesis in presence of Neem (Azadirachta indica) leaf extract.[25] These nanoparticles were obtained with different morphology (spherical, quantum dots, hexagonal and polyhedra).

Silver halide nanoparticles were synthesized by the direct reaction of silver nitrate ($AgNO_3$) with cetyl trimethyl ammonium bromide (CTAB)/ chloride (CTAC) and sodium salicylate (NaSal) using worm-like micelles in aqueous solution.[26] For the formation of anisotropic nanoparticles,

worm-like micellar phase has an important role. Formation of spherical particles occurs only in absence of NaSal. Interestingly, when pre-formed spherical nanoparticles are added to a worm-like micellar system, nanorods are observed. This technique may be used to synthesize anisotropic nanoparticles of various inorganic materials even if they do not have an inherent tendency (crystal habit) to form anisotropic structures.

Crystalline inorganic-organic hybrid nanoparticles (NPs) of the core shell type have been achieved by the formation of a crystalline layer of p-hydroxyacetanilide (pHA) on metallic Ag NPs.[27] The crystalline shell could be melted using electron beam in a TEM. Initially, smaller particles were deposited on the Ag NP, followed by growth of the complete crystalline shell. The change in the optical property of the Ag NPs upon the formation of crystalline pHA shell makes an interesting approach for modification of optical properties of NPs by organic crystals. This is the first report on the growth of an organic molecule as a crystalline shell over a metallic NP and it may lead to newer avenues of organic-inorganic hybrid materials with tunable properties.

Gold and silver based nanostructures can be used as plasmonic materials for the rapid detection, characterization, and quantification of analytes of importance in biomedical applications, environmental research.[28] Controlled design of dimeric plasmonic nanostructures has been possible (avoiding aggregation) by precise tuning of the distance between the two Ag surfaces by varying the thickness of the silica shell. Enhancement of Raman signals of the test species (pyrene) due to the enhanced electric fields on the surface of silver nanoparticles has been investigated by controlling the thickness of the silica shell. Theoretical studies showed the presence of an amplified electric field at the junctions of two Ag nanostructures when the separation distance was less than 15 nm, which can substantially enhance the Raman signals of molecules. In a related study, colloidal gold nanorods were aligned end-to-end *via* dithiol coupling.[29] The longitudinal surface plasmon resonance of end-to-end coupled Au nanorods exhibited a red-shift as the number of rods in the chain increased. Due to selective excitation of collective bonding and anti-bonding modes, nanostructures exhibited polarization-dependent optical properties. The surface plasmon peak energy was not strongly dependent on the angle of rod-sphere-rod trimers. The experimental scattering spectra were compared with the results obtained from theoretical calculations using the Finite Element Method (FEM) and found to be in good agreement.

The strong inhibitory and bactericidal effect as well as broad spectrum of antimicrobial activity of silver has been known for a long time. Silver nanoparticles (Ag NPs) have low toxicity toward mammalian cells and do not easily provoke microbial resistance. Use of Ag ions or silver nanoparticles are well known however very little is known of using combination of Ag NPs and Ag^+ in the form of core@shell structure. Recently it has been reported that hybrid nanostructures of Ag (Ag Nps) and AgI can be formed in agarose matrix (Ag@AgI/agarose).[30] The main advantages of such a combination are given below: (i) if the shell consists of a silver compound which has very low solubility in water, it would prevent leaching out of Ag or Ag^+ from the matrix and is less toxic to mammalian cell; (ii) synergic

effect of both Ag and Ag^+ toward the killing of microbes; (iii) by embedding such a system in a matrix, bactericide and reuse can be recovered. The water insoluble Ag@AgI in agarose matrix can be coated as thin film on quartz plates, having good mechanical strength. Good antibacterial activity against Gram-negative Escherichia coli (E. coli) and Gram-positive Staphylococcus aureus (S. aureus) bacteria was observed in saline water (both in dark and on exposure to visible light).

One pot synthesis of TOP capped nanoparticles of composition Pd_4Se (38-43 nm) and Pd_7Se_4 (62–104 nm) in good yield by thermolysis of selenated primary and secondary amines has been reported.[31] Pd_4Se (38–43 nm) has been obtained from $[PdCl_2(PhSe\text{-}CH_2CH_2CH_2\text{-}NH_2)]$ precursor and Pd_7Se_4 (62–104 nm) from $[PdCl\{C_6H_4CH(C_6H_4\text{-}2\text{-}OH)\text{-}NHCH_2CH_2CH_2\text{-}SePh\}]$ in TOP. This is the first report on the synthesis of of Pd_xSe_y material from metal organo selenium precursor.

Chemically ordered face-centred tetragonal (fct) Fe-Pt alloy nanoparticles (NPs) embedded SiO_2 films were developed on glass substrate by *in situ* hybrid sol-gel approach followed by heating at 450–900 °C in air and reducing (10% H_2–90% Ar) atmospheres.[32] At the early stage of heat treatment, Pt nanoparticles are produced and Fe remained in ionic state covalently bonded with silica network. Further heat treatment at 800–900 °C in reducing atmosphere facilitated the formation of uniformly dispersed fct Fe-Pt alloy NPs in amorphous SiO_2 film matrix. The SiO_2 matrix of the resulting fct Fe-Pt alloy NPs embedded film remained amorphous due to the absence of Fe ions. The fct Fe–Pt alloy NPs embedded SiO_2 films can find potential applications in magnetic storage devices and catalysis.

Electrodeposition technique has been used to grow crystalline fcc Co NWs within a polycarbonate template over a large diameter range using a two-electrode configuration at room temperature.[33] The face centered cubic crystalline structure of the NWs having diameter in the range of 10 to 200 nm could be maintained. Magnetization measurements with an applied field show that the nature of the *M–H* loop changes from square to linear as the diameter of the NWs increases. The coercivity was found to be 1700 Oe and 480 Oe at 5 K (1000 Oe and 250 Oe at 300 K) for 10 nm and 100 nm wires, respectively. The observed changes in the nature of the *M–H* loop and in coercivity could be explained using the fact that the domain size reduces as the diameter of the wire increases.

Cadmium deoxycholate, a Cd-salt, leads to high quality CdSe nanocrystals with dot and rod-like morphologies with photoluminescence (PL) in the blue to red region of the visible spectrum, with reproducible quantum yields as high as 47%.[34] For larger sized CdSe nanocrystals, which can emit in the red region (625–650 nm), bile acid based cadmium precursor was used. CdSe nanocrystals synthesized from cadmium deoxycholate represent a series of highly efficient emitters with pure colours and controllable sizes, shapes and structures. This leads to a new approach of synthesizing other semiconductor nanocrystals, as well as core–shell nanocrystals applying metal deoxycholate precursors.

A facile low temperature, aqueous solution-based chemical method was developed to fabricate Fe doped ZnO nanorods (ZnO : Fe).[35] With the help of structural analysis it was observed that the Fe replaces Zn atoms and is

incorporated into the crystal lattice. Substitution of Fe ions significantly influences the optical property of the ZnO nanorods. The undoped ZnO nanorods exhibit a pure excitonic emission centered at 382 nm, whereas the ZnO:Fe nanorods showed a blue shift in UV emission. High quality ultrathin 2D single crystalline sheets of PbS with well-defined rectangular morphology was obtained using a bottom up approach to initiate collective coalescence of PbS nanowires.[36] The ultrathin sheets were rectangular in shape with 1.8 nm thicknesses, 200–250 nm width and 3–20 μm length. Density functional theory (DFT) calculations shows that a single row of delocalized orbitals of one nanowire is converted into several parallel conduction channels upon sheet formation.

Thin films of Ag and Au have been obtained with the help of ion beam sputter deposition.[37] The motivation of the work was to investigate the use of discontinuous and nanostructured thin films for plasmonic applications. It is demonstrated that the films grown on different substrates exhibit a range of tenability that depends entirely on the film-substrate interface. Ag films were deposited using Ar ion energy of 150 eV while the Au films were deposited with Ar ion energies of 250–450 eV. Three types of interfaces were investigated. The first set of film-substrate interfaces consisted of Ag and Au films grown on borosilicate glass and carbon coated Cu grids. The second set of films consisted of metallic bilayers in which one of the metals (Ag or Au) was grown on a continuous film of the other metal (Au or Ag). The third set of interfaces comprised of discontinuous Ag and Au films deposited on different dielectrics such as SiO_2, TiO_2 and ZrO_2. In each case, a rich variety of nanostructures including self-organized arrays of nanoparticles, nanoclusters and nanoneedles were achieved. It is demonstrated that interfacial nanostructuring is a simple approach to achieve a variety of nanostructures such as nanoclusters, nanoparticle arrays and nanoneedles.

Like metal nanoparticles, new methods have been developed for the synthesis of nanoparticles of various metal oxides. Different morphologies (polyhedra, spherical particles) of Cu_2O have been obtained *via* solution grown reduction route using anhydrous dextrose and ascorbic acid as reducing agent and polyvinyl pyrrolidone (PVP) and sodium dodecyl sulfate (SDS) as surfactants.[38] Cu_2O nanoparticles and polyhedra were used as a photocatalyst and Azure-II as model dye, which is the main cause of pollution in industrial wastewater. It was observed that the polyhedra show higher photocatalytic activity and lower adsorption capacity compared to Cu_2O nanoparticles. In other words, the photocorrosion rate of Cu_2O polyhedra is very slow which makes it an efficient photocatalystfor the degradation of harmful and toxic dissolved waste products mainly from textile industries. Recently, CuO NPs have gained significant attention for their utility as thermal conductivity enhancers in nanofluids. Among the significant challenges that remain in developing methodologies for such nanoparticles are: i) the facile fabrication of desired shapes, ii) correlating the shapes in terms of their utility for specific applications. Various nanoscale structures of CuO have been synthesized by a chemical route where $Cu(OH)_2$ nanostructures were first synthesized by the alkaline hydrolysis of $Cu(NO_3)_2 \cdot 3H_2O$ (using NaOH as a base) and the precipitate was subsequently annealed at a temperature of 130 °C.[39] The alkaline

content (pH) of the solution during the hydrolysis was varied to tailor the morphology and dimensions of the nanostructures, (*e.g.* seeds, ellipsoids, rods and leaves). The CuO samples showed excellent response when used as nanofluids and the thermal conductivity could be raised as high as 48%. The particles with seed-like shape were found to be most effective in enhancing the thermal conductivity of the base fluid. NiO is one of the materials suitable for pseudocapacitor electrode applications owing to its high specific capacitance, low cost, and high chemical and thermal stability. The electrochemical performance of NiO nanostructures is strongly influenced by its morphology and surfactant assisted microwave method has been used for the synthesis of NiO nanoparticles.[40] Iron oxide nanoparticles with prismatic hexagonal morphology were synthesized using a low temperature approach.[41] Thermal decomposition of $[Fe(CON_2H_4)_6](NO_3)_3]$ in diphenyl ether at about 200 °C for 70 min leads to the formation of prismatic iron oxide nanoparticles without need of any capping agent or any special conditions. Shape-selective synthesis of CoO nanoparticles has been carried out with the help of a simple one-step microwave (MW) heating method.[42] The above NPs were synthesized from $CoCl_2 \cdot 6H_2O$ solution in presence of polyvinylalcohol (PVA) and sodium hydroxide (NaOH). The beauty of this methodology is that by tuning the molar ratio of Co(II) to PVA, different shapes like nanosphere, nanosheet, and nanodendrite structures of CoO were produced. Microemulsion based methods have been reported[43–46] to control the size and shape of various nanomaterials, however due to lack of *in situ* growth studies of nanoparticles in microemulsion, the growth mechanism is not clear. To get a deeper insight into the kinetic steps, a study has been carried out following slow growth of the nanoparticle (extending over eight days) to explain the crucial role of droplet interactions in the reaction kinetics.[47] Formation of iron oxalate nanorods inside the polar core of water-in-oil microemulsion droplets (cetyltrimethylammonium bromide/1 butanol/isooctane) was chosen as a model reaction and a schematic digram depicting the same has been shown in Fig. 3a. Fluorescence correlation spectroscopy (FCS), dynamic light scattering (DLS), and transmission electron microscopy (TEM) have been employed to monitor the nanostructure growth at (near) the single-droplet level and in an ensemble. Fig. 3b shows the correlation curves measured in the mixture of MDs containing SRhB and reactants for eight consecutive days.

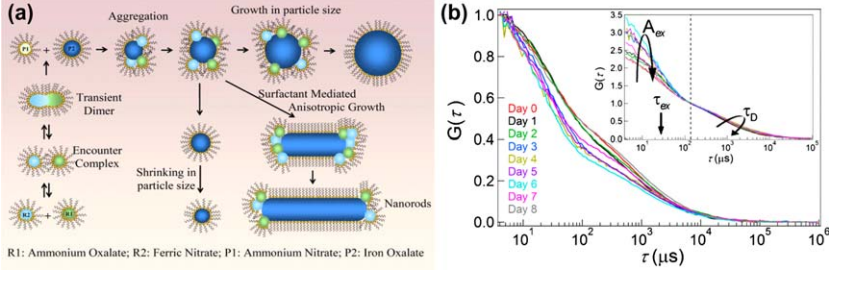

Fig. 3 (a) Growth mechanism of iron oxalate nanoparticles and nanorods inside the polar core of MDs. (b) Raw fluorescence correlation curves measured in the reaction mixture for eight consecutive days. Inset shows same raw curves when normalized at 150 μs. Adapted from reference 47.

With the help of FCS, transient dimer lifetime (28 μs) and the droplet fusion rates (and fusion tendency) on each day were monitored as the reaction progressed. The droplet fusion rate is found to directly control the nanorod growth in microemulsion solution and attain its maximum value ($3.55 \times 10^4\ s^{-1}$) on day 6, when long nanorods were found in TEM data, implying that more and more reactants are fed into the growing system at this stage. Combining FCS, DLS, and TEM results, it was observed that there are three distinct periods in the entire growth process: a long nucleation-dominant nanoparticle growth period which forms nanoparticles of critical (average) size of 53 nm, followed by a short period where isotropic nanoparticles switch to anisotropic growth to form nanorods, and finally elongation of nanorods and growth (and shrinking) of nanoparticles. The detailed analysis of FCS and DLS data of the nanostructural growth (within reverse micelles) is first of its kind and may be extended to understand the growth of other nanostructures.

Oriented nanostructures of inorganic semiconductors are desirable for many applications and, in the case of zinc oxide, its distinctive features at the nanoscale are of particular interest for potential applications in optical devices, piezo electric devices, solar cells, transparent UV-protection films, anti bacterial agents, chemical sensors, and as photocatalysts. Hence, a great deal of effort has been devoted to the development of new methodologies for the synthesis of ZnO nanostructures with tailored sizes and morphologies under mild conditions. In most of the cases, structure-directing agents, such as ethanolamine, hexamethyltetramine, and zinc complexes have been used. But these methods require strong alkaline media, hydrothermal conditions, or further heating at high temperatures. Therefore, the direct fabrication of oriented crystalline structures with controlled morphologies from water-soluble zinc salts under environmentally benign conditions still remains a challenge. A bottom up approach has been devised to synthesize ZnO nanostructured materials using long-chain polyamines which simultaneously mineralizes and assembles ZnO nanoparticles directly from water-soluble zinc salts.[48] By changing the ratio of polyamine/Zn^{2+} ions, different morphologies of ZnO (spherical shape, oval, dumbbell, and hexagonal-rod shaped structures) were obtained including the unique hollow rod structures. These chains facilitate the condensation process to form ZnO nanoparticles and their assembly in aqueous medium at neutral pH. Recently, solid-state pyrolysis of metal-organic frameworks has emerged as an alternative route to synthesize ZnO with diverse morphologies. Metal-organic frameworks (MOFs) are crystalline solids composed of single or multi nuclear metal ions as building units. Advantage of MOFs over other precursors for solid state synthesis of ZnO is its porosity and long-range ordering that offers a unique opportunity to synthesize unusual ZnO morphologies. ZnO nanostructure with different morphologies like rod, hexagonal column, and elliptical aggregates were also synthesized by one-step thermolysis of Zn-based homochiral metal organic frameworks (MOFs).[49] Two chiral 3D MOF isomers were synthesized from $Zn(CH_3COO)_2 \cdot 2H_2O$ and naturally available amino acid (valine) derived ligand, with different halogen substitutions (Cl, Br). When MOF 1 and 2 were calcined in air, elliptical aggregates of ZnO microparticles were obtained. On

the contrary, when the same MOF 1 was calcined in N_2 environment, rod-like microparticles were obtained, whereas when MOF 2 was calcined under similar conditions, hexagonal columns of ZnO microparticles were obtained. Both MOFs (MOF 1 and 2) possesses similar architecture and the only difference lies in halogen substitution (-Cl, -Br) in the crystal structure. This study leads to the understanding of the role of the anions as the structure directing agent and effect of environment on the ZnO morphologies. This solid-state transformation of ZnO microparticles with tunable morphologies using different Zn (II) based MOFs provides an important route for facile synthesis of various metal oxide functional materials.

Study on oxidation behavior of metals at nanometre scale is comparatively new. Zn-ZnO (core-shell) nanostructure was synthesized by depositing Zn nanoclusters (NCs) by the low-energy cluster beam deposition technique.[50] Core-shell nanostructure formation proceeds in two steps. In the first step, the shell of ZnO forms over Zn NCs rapidly up to certain limiting thickness; and in the next step, the shell swells gradually in a very slow rate by incorporating ZnO monomers inside it without increasing the thickness, which leads to instability and breakage. In the initial step of oxidation, the final morphology and composition depend on the initial size of Zn NCs (big size NCs could retain their original shape). But, in the next step of oxidation Zn NCs of all sizes and shapes are converted to hollow ZnO NCs.

CdS nanotips with size of 5–8 nm were synthesized by hydrothermal process using polyacrylamide (PAM) as surfactant.[51] The shape of nanocrystals (NCs) changes from particles to nanorods or nanotips depending upon the amount of PAM used. On the other hand,single source precursor like $[Cd(thqdtc)_2]$, $[Cd(thqdtc)_2(py)]$ and $[Cd(thqdtc)_2(2,20\text{-bipy})]$(thqdtc = 1,2,3,4-tetrahydroquinolinecarbodithioate; py = pyridine; 2,20-bipy = 2,20-bipyridine) has been used for the preparation of diethylenetriamine capped CdS nanoparticles.[52] The influence of pyridine on controlling the morphology of CdS nanoparticles was investigated. Flower-like and rod-like CdS nanoparticles were prepared at a relatively low temperature by thermolysis of the precursors using chelating solvent diethylenetriamine. Use of $[Cd(thqdtc)_2]$ and $[Cd(thqdtc)_2(2,20\text{-bipy})]$ afforded rod-shaped nanoparticles and flower-like nanoparticles obtained from $[Cd(thqdtc)_2(py)]$. A facile hydrothermal/solvothermal route to fabricate elegant Bi_2S_3 nanoflowers has been described.[53] Under hydrothermal conditions (for 12 h), Bi_2S_3 flowers on nickel foil composed of self-assembled nanorods were obtained. Whereas prolonged reaction (24 h) leads to ultra long micro belts. Interestingly, the architecture of Bi_2S_3 flowers obtained by solvothermal route are seen to be composed with self assembled nanorods and the synthesis duration influences their shape, size, and areal density.

Significant development has been reported in the area of nanostructured metal borides and their synthesis at low temperatures (generally borides are prepared at very high temperatures). Vertically aligned nanorods of lanthanum hexaboride were synthesized using a hydrothermal route.[54] The effect of charge of the capping agent (surfactant) strongly affects the shape and size of the precursor (neutral surfactants lead to the formation of nanorods while a cationic surfactant results in the formation of particles). This precursor mediated route leads to lanthanum hexaboride nanostructures

at much lower temperatures and allows for variation of morphology of nanostructured films. Nanostructured hydroxide precursors ($La_{1-x}Ce_x(OH)_3$, $x = 0.1$, 0.2, 0.3 and 0.5) were synthesized *via* hydrothermal route in the presence of Tergitol (surfactant, nonylphenolethoxylate) as a capping agent.[55] The precursors on heating with boron at 1300 °C lead to the formation of nanostructures (cubes, rods and pyramids) of lanthanum cerium hexaboride. Thin films using spin coating techniques have synthesized and studied for field emission behavior. The pyramidal shaped nanostructures of $La_{0.5}Ce_{0.5}B_6$ show excellent field emission characteristics with high field enhancement factor of 4502.

Owing to the high electrical conductivity and hardness of borides, chromium diboride films (100–300 nm thickness) have been deposited on to various substrates (Cu, borosilicate glass and fused silica) by thermal evaporation process.[56] The films were nanocrystalline with crystallite sizes of the order of 15–20 nm. The films on borosilicate glass and fused silica were optically transparent and insulating at thickness of $\sim$100 nm. Deposited films are nanocrystalline and show thickness dependent physical behavior. The low thickness films are transparent and insulating whilethe high thickness films are opaque and conducting. The hardnessof the films are of the order of 10 GPa. An enhancement in reflectance of Cu substrates from 25 to 50% in the near IR wavelength region was observed due to thechromium boride coatings. The hardness of the films was 10 GPa on Cu while it was 8 GPa on glass substrates. Like transition metal borides, rare-earth hexaborides also have promising scientific applications in the field of field emission, anticorrosive coatings *etc*.

Synthesis of inorganic layered nanostructures has also been of interest in the wake of the immense properties associated with graphene. In this regard, MoS_2 being a layered material has been explored as a material which can be obtained as composed of few layers of MoS_2. There are reports on Raman scattering of MoS_2 layers comprising of single, bi, four and seven layers, showing a strong dependence on the layer thickness.[57] MoS_2 is an indirect band gap semiconductor in bulk and becomes a direct band gap semiconductor in the monolayer form. New Raman modes are seen in the spectra of single- and few-layer MoS_2 samples which are absent in the bulk. The Raman mode at $\sim 230\,cm^{-1}$ appears for two, four and seven layers. This mode has been attributed to the longitudinal acoustic phonon branch at the M point (LA(M)) of the Brillouin zone. The mode at $\sim 179\,cm^{-1}$ shows asymmetric character for a few-layer sample. The most intense spectral region near $455\,cm^{-1}$ shows a layer-dependent variation of peak positions and relative intensities. The high energy region between 510 and $645\,cm^{-1}$ is marked by the appearance of prominent new Raman bands, varying in intensity with layer numbers. Resonant Raman spectroscopy thus serves as a promising non invasive technique to accurately estimate the thickness of MoS_2 layers down to a few atoms thick.

2 Photocatalysis

In India, large numbers of research groups are working in a focused manner on this topic. Photocatalytic materials have been used in variety of

applications such as air purification, water purification and anti-pollutant. Photocatalytic reaction proceeds owing to holes and electrons generated in materials by absorbing light energy. The key design component in these materials is suitable band gap for absorbing light (UV and visible) and stability of electrons and holes (recombination should be delayed). The photo-generated holes have oxidation ability and the photo-generated electrons have reduction ability. Due to wide applicability various types of materials like metal oxides, metal doped metal oxide and different composite materials have been fabricated for photocatalysis and its activity studied in detail. Here we discuss the contribution from India in the last two years in this area.

ZnO has been extensively studied for its potential applicability in photocatalysis and various methods have been developed. Zinc oxide nanoparticles were synthesized using zinc acetate solution in different alcoholic solution like methanol, ethanol and iso-propanol *etc*., with the help of sonochemical method.[58] ZnO nanoparticles were used for the photocatalytic reduction of hexavalent chromium in aqueous medium under solar radiation. ZnO particles of different morphologies were also synthesized by hydrothermal route at 95 °C by varying ratio of ethylammonium nitrate (EAN) and volume of water.[59] Morphology could be changed from cylindrical to spindle-shape and finally to spherical with increasing concentration of EAN. It was noticed that spherical ZnO superstructures showed enhanced photocatalytic activity compared to that of the commercially available ZnO. Nanoflakes, nanorods and spherical nanoparticles of ZnO have also been synthesized with the help of a simple low temperature co-precipitation method.[60] The influence of morphology of ZnO in terms of particle size, surface area, crystal growth habits and oxygen defects was studied on the photocatalytic degradation (PCD) of resorcinol.

Free-standing mats of mesoporous ZnO nanofibers been developed by electrospinning a blend of zinc acetate with a carrier polymer, polyacrylonitrile (PAN) in N, Ndimethyl-formamide (DMF) solvent. By varying the electrospinning condition, electric field strength and solution flow rate, porous ZnO fibers can be obtained with variable diameter. Mats of ZnO nanofibers with diameter of 60 nm shows effective degradation of the PAH dyes–naphthalene and anthracene. The band gap was reduced by introducing silver nanoparticles in the solution.[61]

To improve the efficiency of bare ZnO, various modifications have been attempted. Light-harvesting nanohybrids (LHNs) composed of an inorganic nanostructure along with an organic pigment has been exploited to improve the light-harvesting performance over individual components.[62] Functionalization of dense arrays of ZnO nanorods (NRs) has been achieved with biologically important organic pigment, hematoporphyrin (HP). HP-ZnO nanohybrid shows efficient electron migration from photoexcited HP to the host ZnO NRs. This essential photoinduced event activates the LHN under sunlight, which ultimately leads to the realization of visible-light photocatalysis (VLP) of a model contaminant like methylene blue (MB) in aqueous solution. Rare earth metal ions like Ce have also been co-doped in Ag-ZnO (Ce-Ag-ZnO) by a solvothermal method.[63] The photocatalytic activity of Ce-Ag-ZnO was investigated for the degradation

of Napthol Blue Black (NBB) dye in aqueous solution under solar light irradiation. Co-dopants shift the absorbance of ZnO to the visible region. The efficiency of Ce-Ag-ZnO was found to be higher than Ag-ZnO, Ce-ZnO, commercial ZnO, synthetic ZnO, TiO_2-P25 and TiO_2 (Merck) at pH 9 for the mineralization of NBB dye under solar light irradiation.

Nano crystalline powders of pure ZnO, and co-doped with Al and Li (*i.e.*, LDZ and LADZ) powders have been prepared by pyro-hydrolysis route. The Al and Li co-doped ZnO (LADZ) powders exhibit excellent photo-catalytic activity towards MB degradation under the irradiation of simulated solar light. The activity of these photo-catalysts increase with the increase of Li concentration up to 10 wt.% in LADZ nano-powder.[64]

Core shell nanostructures with ZnO forming the core and In_2S_3 as the shell were synthesized in an efficient and environmental friendly way.[65] In_2S_3 nanoparticles were successfully grown on the ZnO nanorods by the surface functionalization method using citric acid as a surface functionalizing agent. The photocatalytic activity under visible light to degrade Rhodamine B (RhB) was enhanced by these core/shell nanostructures due to the formation of heterojunctions, which prolong the separation of photogenerated electrons and holes. The photocatalytic degradation of RhB dye was found to be 83.7, 2.7, and 35.0% for the ZnO/In_2S_3 core/shell nanorod arrays, ZnO nanorods, and In_2S_3 nanoparticles, respectively, under visible light irradiation. Similarly core/shell nanorodsof ZnO/CdS with varying shell thickness were synthesized and their shell thickness dependent photocatalytic properties have been investigated.[66] The average lifetime ($\langle T \rangle$) of the core/shell nanorod arrays is larger than that of the uncoated ZnO nanorods due to charge separation. The photocatalytic studies confirmed that the ZnO/CdS core/shell nanorod arrays exhibit improved degradation efficiency compared to bare ZnO and CdS under simulated solar radiation. The core/shell nanorods show that increase in shell (CdS) thickness increases the photocatalytic efficiency, indicating efficient separation of electron-hole pairs. Bi_2O_3-ZnO heterostructures were synthesized by a simple hydrothermal-thermal decomposition method.[67] These nanostructures exhibited higher photocatalytic activity for the degradation of Acid Black 1 (AB 1) under UV light than pure ZnO, Bi_2O_3, and commercial TiO_2 (Degussa P25). The enhanced photocatalytic activity of Bi_2O_3-ZnO is attributed to the low recombination rates of photoinduced electron-hole pairs, caused by the transfer of electrons and holes between ZnO and Bi_2O_3. Ag/AgCl/ZnO nanostructures were synthesized with the help of an environmentally benign methodology applying polyamine as a mineralizing agent for ZnO nanoparticles, which facilitate the formation ofAg/AgCl within ZnO.[68] These Ag/AgCl/ZnO nanostructures represent a multi-heterojunction system in which the nanocomponents lead in a synergistic way to enhance the photocatalytic activity under visible-light irradiation.

Monodisperse porous tin dioxide nanospheres were synthesized applying a facile, low-temperature, glucose reduction pathway.[69] These SnO_2 nanospheres (average diameter of 50 nm possesses BET surface area of about 160 m^2/g) exhibit increased photocatalytic activity towards methyl orange with good recyclability and thus are suitable for applications in

environmental remediation. Oleic acid capped monodispersed SnO_2 quantum dots (QDs) of size 2.7 nm were synthesized by thermal decomposition method.[70] The surface functionalization diminishes the photocatalytic activity which is attributed to absence of surface oxygen and adsorbed hydroxyl group on the surface of the capped QDs. Type-II semiconductor based heterostructures of SnO_2/CdS were designed as efficient catalysts.[71] The schematic representation for the functionalization of SnO_2 nanorod and formation of type II semiconductor has been shown in Fig. 4a. Using time resolved spectroscopy; the effective charge separation in this heterostructure was examined and found to be more efficient compared to bare SnO_2 nanorods. Lower conductivity was observed in the heterostructure compared to uncoated SnO_2 nanorods. The efficient charge separation in the SnO_2/CdS heterostructure results in higher photocatalytic activity as the degradation of Congo red dye was found to be 97% and 20% using SnO_2/CdS heterostructure and SnO_2 respectively under UV light irradiation (Fig. 4b and 4c). Spherical Sn-SnO_2 nanoparticles ($\sim$50 nm) were synthesized from SnO microplates ($\sim$2.0 μm) using focused solar irradiation.[72] The presence of Sn(0) nanoparticles along with spherical SnO_2 nanoparticles improves the charge (electrons and holes) separation efficiency. The above nanoparticles selectively attract cationic dye molecules on the particle surface (due to negative surface charge) and degrade the dyes at a faster rate under UV light.

Though TiO_2 is a very well studied photocatalytic material it continues to be of interest. Control over the size and facets of anatase TiO_2 nanocrystals (NCs) were reported recently.[73] The microscopic images shown in Fig. 5 (a–h) clearly depict the presence of different facets obtained by varying the reaction temperature. The exposed facets play a crucial role in the photocatalytic activity of TiO_2 NCs, which is due to the preferential flow of photogenerated carriers to the specific facets. The presence of both the high-energy {001} oxidative and low-energy {101} reductive facets reduce the charge recombination thereby enhancing the photocatalytic activity of TiO_2 NCs. Fig. 5(i) shows the extent of photodegradation of methyl orange (MO) by TiO2 NCs obtained at different hydrothermal reaction durations.

In another study, photocatalytic activity of mesoporous TiO_2 nanostructures of spindle shape (diameter $\sim$6 nm and length of 30 nm) has also been carried out.[74]

Metal-ions like Ag, Co, Ni, and Pd have been doped in TiO_2 nanocatalysts on carbon-covered alumina (CCA) supports to improve performance.[75] The CCA-embedded catalysts were crystalline and had a high surface area compared to the metal-ion doped titania nanocatalysts while retaining the anatase structure of the core TiO_2. The reaction rate of the CCA-supported catalysts was in the order Pd > Ag > Co > Ni.

Co-doped (0–10%) TiO_2 powders and thin films have also been reported *via* co-precipitation and sol-gel dip coating technique, respectively. The photocatalytic effficiency of the powders was evaluated by studying the degradation of methylene blue (MB). Co-doped TiO_2 powder consists mainly of anatase phase and possesses reasonably high specific surface area, low band gap energy and flat band potentials amenable to water oxidation in photoelectrochemical (PEC) cells. The photocatalytic degradation of MB

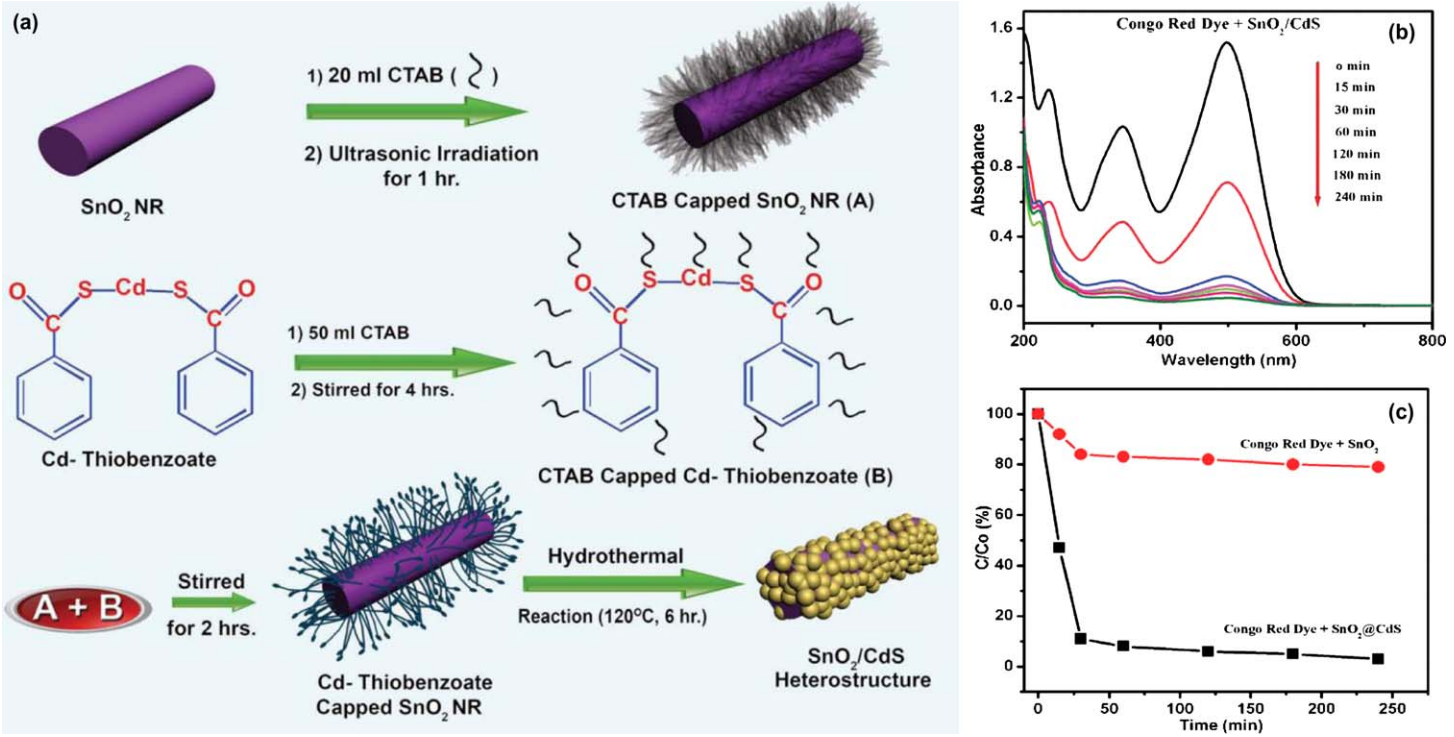

Fig. 4 (a) Schematic representation for the preparation of the SnO_2/CdS heterostructure. (b) absorbance spectral changes of Congo red solution in the presence SnO_2/CdS heterostructure (c) Photodegradation rate of Congo red by different photocatalysts (SnO_2 and SnO_2/CdS) under UV light irradiation for 4 h. Adapted from reference 71.

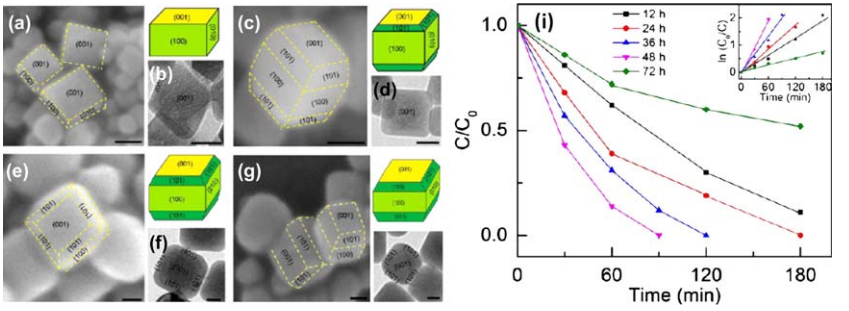

Fig. 5 Magnified FE-SEM images, TEM images, and schematics of respective TiO_2 NCs are shown with different facets hydrothermally synthesized in (a, b) 12 h, (c, d) 24 h, (e, f) 36 h, and (g, h) 48 h. The length of scale bar in all the images is 25 nm. (i) UV-light-assisted photodegradation of MO by TiO_2 NCs prepared with different reaction durations as a function of irradiation time. Inset graph shows the linear fitting curve of MO degradation. Adapted from reference 73.

by Co-doped TiO_2 powders was observed to follow the Langmuir-Hinshelwood first order reaction kinetics. It was observed that 0.1 wt.% Co-doped TiO_2 composition exhibited n-type semi-conducting behavior, higher photocurrent and photocatalytic activity compared to pure TiO_2 and among various Co-doped TiO_2 compositions.[76]

Core@shell nanostructures like Ag@TiO_2 (10–40 nm core; 15 nm shell) and CdS@TiO_2 (3 nm core; 1 nm shell) has been synthesized by applying titanium hydroxyacylate as a shell forming agent using the reverse micellar route.[77] The low rate of hydrolysis of titanium hydroxyacylate appears to be responsible for the formation of TiO_2 shell (faster rate would probability lead to TiO_2 particles). A red shift of 25 nm was observed in the surface plasmon band of silver for Ag@TiO_2 core-shell structures (compared with that of silver nanoparticles) while blue shift of the absorption band was observed for CdS@TiO_2 core-shell nanostructures (compared to bare CdS nanoparticles). CdS@TiO_2 shows a strong quantum confinement effect. No quenching was observed of the emission band of CdS for the CdS@TiO_2core-shell nanostructures.

Ag-TiO_2 microwires were synthesized with high sensitivity and photocatalytic activity.[78] The superior performance of the Ag-TiO_2 composite microwires is attributed to improved surface reactivity, mass transport and catalytic property as a result of wiring the TiO_2 surface with Ag nanoparticles. Compared to bare TiO_2 microwires, Ag-TiO_2 microwires exhibited three times higher sensitivity towards the decomposition of cationic dye such as methylene blue. Apart from being a effective photocatalytic material, Ag-TiO_2, exhibits excellent photocatalytic inactivation of Escherichia coli in the presence of visible light.[79] Photolysis alone had a small effect on inactivation while the dark experiment resulted in no inactivation whereas in the presence of Ag/TiO_2 it showed the maximum inactivation. Catalyst loading of 0.25 g/L, showed better inactivation of E. coli compared to commercial [DegussaP-25 (DP-25)] TiO_2 catalyst. An improved inactivation was observed with increasing lamp intensity and addition of H_2O_2. Addition of inorganic ions such as HCO_3^-, SO_4^{2-}, Cl^-, NO_3^-, Na^+, K^+, and Ca^{2+} leads to a negative effect towards inactivation.

The photocatalytic inactivation of E. coli followed first order kinetics and remained unaltered on varying the pH of the solution. Apart from the metal doped TiO_2, the photocatalytic efficiency of commercial titanium dioxide can be improved by using different composites of TiO_2 with metal oxide likeTiO_2/WO_3.[80] The photocatalytic activity varies with the WO_3 loading in the composites and the optimum loading of WO_3 in the composites was found to be 15 wt%. This composite showed faster dye degradation rate than commercial TiO_2 or by WO_3.

In addition to ZnO, TiO_2 or SnO_2 mixed metal oxides-doped metal chalcogenides have been investigated for photocatalysis. Au/CdSe pentapod heterostructures withAu core and CdSe arms have been synthesized.[81] Microscopic studies suggest that pentapod arms of CdSe are nucleated on the (111) facets of Au and grow only along the [001] direction. Electron transfer from photoexcited CdSe to Au, with a rate of 3.58×10^8 s^{-1} was observed from steady state and time resolved spectroscopic studies. It is interesting to note that 87.2% of R6G dye is degraded by the Au/CdSe heterostructures after 150 min of UV irradiation and the apparent rate constant for Au/CdSe heterostructures was 0.013 min^{-1}. These classes of metal-semiconductor heterostructures open up new possibilities in photocatalytic and photovoltaic applications. Metal oxides of tantalum and cerium have been fabricated to achieve better photocatalytic activity. Visible light photocatalytic property of $Sr_2Ta_2O_7$ was investigated.[82] The electronic structure of $Sr_2Ta_2O_7$ was tuned by co-doping the anionic (N)/cationic (Mo, W) species. Such doping creates impurity states within the band gap, reducing the apparent band gap significantly and hence increasing the photocatalytic efficiency. A facile solution combustion method was developed to synthesize $Bi_2Ce_2O_7$ with particle size $\sim$5 to 6 nm.[83] As $Bi_2Ce_2O_7$ has a band gap of 2.34 eV, the photocatalytic efficiency was determined with the help of degradation of malachite green (MG), a cationic dye, under solar radiation. Bi substituted $Sr_3V_2O_8$ was synthesized which exhibited photocatalytic activity towards various classes of anionic dyes under UV radiation.[84] A new series of photocatalysts (Bi_2O_3/Bi–$NaTaO_3$) were fabricated by a modified solid-state reaction.[85] The band gaps of Bi_2O_3/Bi-$NaTaO_3$ composites were tuned with varying Bi concentration to effectively absorb visible light and induced visible light photocatalytic activity. Photoluminescence studies show that the (optimum molar ratio is 0.3) Bi_2O_3/Bi-$NaTaO_3$ effectively suppresses there combination rate of photogenerated charge carriers. Further increase in bismuth concentration ($>$0.3 molar ratio) leads to impurity formation and creates defect states, which inhibit the photocatalytic activity of the above composite. The photocatalytic activity of these composites can be explained on the basis of the photosensitizing effect of Bi_2O_3. A series of Cu-Co/Cr ternary-layered double hydroxides (LDHs) containing CO_3^{2-} in the interlayer was studied to understand the role of divalent metal ions (Cu/Co ratio) on the catalytic activity.[86] The hydroxyl radicals ($OH^{\bullet}$) formed on the surface of visible-light illuminated LDHs (detected by the luminescence technique using terephthalic acid as probe molecule) was highest for LDH-4 with Cu/Co ratio of 1 : 3. The degradation of MG followed pseudo-first-order kinetics. Micro-/nanostructured copper oxides (CuO) having good catalytic activity

towards oxidation of methylene blue in the presence of hydrogen peroxide (H_2O_2) was reported.[87]

3 Photovoltaics

Significant efforts have been carried out to develop efficient solar cells using various semiconductor nanomaterials. Initially dye-sensitized solar cells were thought to be a good choice, but surface aggregation limited its applicability. To improve the efficiency, semiconductor-sensitized solar cells are drawing keen interest. The degree of charge separation has been the key factor in determining the conversion efficiency of the solar cell.

High surface area mesoporous SnO_2 agglomerates with hierarchical structures demonstrated high photoelectric conversionefficiencies of 3.05% and 6.23% (with $TiCl_4$ treatment) in dye-sensitized solar cells, which are attributed to its dual functionalityof providing high dye-loading and efficient light scattering.[88] Like SnO_2, heterostructures with NiO nanoparticles and graphene were synthesized by depositing NiO homogeneously over few-layer graphene plates (GPs).[89] The above material was used as an electrocatalyst for the counter electrode (CE) of a dye-sensitized solar cell and this yielded 3.06% power conversion efficiency, which is comparable to that using a conventional platinum thin film based counter electrode (3.57%). Low temperature single step route has been reported for the synthesis of ZnO nanostructures by varying zinc to ammonia ratio.[90] These materials when used as photo anodes in dye sensitized solar cells exhibit maximum conversion efficiency of 0.123. A green approach was developed for the synthesis of CdS nanoparticles network in poly(3-hexylthiophene-2,5-diyl)(P3HT) polymerfilm.[91] There is a significant decrease in the band gap from 2.2 eV to 1.85 eV in P3HT: CdS composite. It has been observed that the *in-situ* synthesized CdS nanoparticles are evenly distributed in the P3HT network and a significant photoluminescence quenching of P3HT with CdS suggests its potential application for photovoltaic devices. Single crystalline, oriented one-dimensional nanorods of TiO_2 have been directly grown on transparent conducting oxide (TCO) substrates which can find a lot of interest in solar photovoltaics and several other optoelectronic devices due to enhanced electron transport and lower exciton recombination rates.[92] The kinetically controlled growth of the (310) facet of TiO_2 nanorods on fluorine-doped tin oxide (FTO) coated glass substrate has been reported for the first time, which is in contrast to the previously reported (002) faceted TiO_2 nanorods. In addition to this, the growth of (110) faceted TiO_2 nanorods using amorphous fluorine doped silicon oxide (FSO) as a substrate is also demonstrated. Two different faceted TiO_2nanorods can be synthesized following same synthetic condition by varying the substrate. It has been assumed that there is a role of OH^- and water groups, which are responsible for the growth of (110) facets, which has less surface energy. The observation of (310) facet is quite surprising and can be explained based on crystallinity of FTO. Light to electricity conversion efficiency of 2.5% could be achieved by using vertically grown titania nanorods on FTO (used as photoanode) in a dye sensitized solar cell (DSSC). Microspheres of TiO_2(rutile) have been synthesized by hydrothermal reaction and used for

dye-sensitized solar cell (DSSCs) fabricated FTO coated glass substrate.[93] TiO_2-based cells exhibit a noticeable improvement in the overall efficiency: maximum 3.81% versus 0.67% for the reference cell made of a rutile TiO_2. This is attributed to the effective light trapping and dye loading capacity.

Conductive nano-fiber mats TiO_2-graphene composite nanofibers have been developed by electrospinning using polyvinylpyrrolidone as a carrier solution. Mean specific conductance values obtained for TiO_2-graphene composites are about two times higher than that of TiO_2 fibers. An efficiency of 7.6% was attained by assembling these TiO_2-graphene fiber composites as photoanodes in dye sensitized solar cells.[94]

Vertically aligned ZnO nanorod arrays were synthesized from an aqueous chemical route on soda lime and transparent conducting oxide coated glass substrates.[95] By varying the deposition time, the length and the aspect ratio of ZnO nanorods could be varied. Cadmium sulfide (CdS) nanoparticles were allowed to self-assemble onto these ZnO nanorods using chemical bath deposition method. The length of ZnO nanorods was found to be an effective parameter to improve the photoelectrochemical performance of CdS nanoparticles sensitized ZnO solar cells. Light-to-electricity power conversion efficiency of 1.2% was observed for relatively larger area (1 cm^2) solar cells. Similarly, TiO_2 microspheres were synthesized by hydrothermal method and after that these were sensitized with CdS NPs by successive ionic layer adsorption and reaction (SILAR) technique.[96] The above material exhibits improved photoelectrochemical (PEC) performance with maximum short circuit current of (J_{SC}) of 2.75 mA/cm^2. The highest power conversion efficiency of these semiconductor-sensitized solar cells (SSSCs) was 2.34%, which is much higher than the bare CdS sample (1.8%). Titania-nanoparticle-based solarpaint on FTO/glasssubstrates has been reported with a conversion efficiency of 3.6%.[97] A facile room temperature (27 °C) chemical route (SILAR) has been applied to deposit antimony sulphide (Sb_2S_3) nanoparticles on mesoporous titanium dioxide (TiO_2).[98] The method facilitates linker free approach to deposit the size tuned nanoparticles. The synthesized TiO_2/Sb_2S_3 structure on a FTO (fluorine doped tin oxide coated glass substrate) was used as a photoanode with polysulphide as liquid electrolyte and platinum coated FTO as back contact to construct the photovoltaic device. The photovoltaic performances have been tested under light illumination with standard solar simulator condition (AM 1.5G, 10 mW/cm^2). Hybrid photovoltaic devices have been fabricated with CdS modified and bare ZnO nanorods blended separately with regioregular poly(3-hexylthiophene) (P3HT) polymer as the active layer.[99] The surface modification of ZnO nanorods with CdS leads to an increase in the open circuit voltage and short circuit current, with enhanced efficiency of 300% over the unmodified ZnO: P3HT device, because of the typical band structure favoring charge transfer to the external circuit. With increase in ZnO concentration up to an optimum amount, efficiency of the cell increases. Further increase lowers the polymer content in the film, so the pathway for hole transport gets affected, which in turn decreases the efficiency of the cell. The casting solvent also plays an important role in governing the efficiency of the cell. In chloroform-cast films, more excitons dissociate into electrons and holes, which in turn increases the

efficiency of the cells as compared to that of chlorobenzene and toluene-cast films.

Ternary and quaternary metal chalcogenides ($CuInS_2$, $AgInS_2$, Cu_2ZnSnS_4) and their derivatives are mostly used for solar cell applications due to their high absorption coefficient and suitable band gap. A simple method has been developed for the synthesis of heterojunctions between a layer of Cu_2ZnSnS_4 nanoparticles and fullerene derivatives to form a p-n junction for solar cell applications.[100] $CuInGaS_2$ based solar cells were synthesized on drop-casted films of $CuInGaS_2$ (CIGS), which acts as the absorber material for the solar cells.[101] In another method, $CuInS_2$ (CIS) nanoparticles were synthesized by microwave irradiation and CIS films were obtained.[102] The CIS films were prepared by Doctor's blade method. CdS film was directly deposited on top of the CIS film through chemical bath deposition to fabricate the solar cell.

4 Catalysis

In the current era of sustainable energy, catalysis using nanoparticles has drawn considerable attention globally. Reactions in which metal and metal oxide nanoparticles show catalytic activity for a variety of important reactions like selective oxidation of alcohols to carbonyl compounds, different coupling reactions (C-N, C-S and C-C coupling), selective reduction reaction of aromatic nitro compounds and C-H activation reaction.

Nanoparticles as catalyst for coupling reaction has been well-studied and we discuss the key developments in the last few years. A simple method was developed for Matsuda-Heck arylation of olefins.[103] This olefination reaction is catalyzed by *in situ* formed Pd nanoparticles in water operable at ambient temperature. A variety of arene diazonium salts were coupled with olefins under ligand-free and aerobic conditions in high yields and stereoselectivity. *In situ* generated palladium nanoparticles also can act as a catalyst for C-C and C-O bond formation for the synthesis of benzochromene derivatives *via* ligand-free aerobic domino Suzuki coupling and Michael addition reaction.[104] Dendrimer encapsulated 2–4 nm Pd nanoparticles has been synthesized by the simultaneous reduction of different generation diazo dendrons and Pd(II) in an organic medium.[105] Dendrimer encapsulated Pd nanoparticles can efficiently catalyze the cross-coupling of arylboronic acids, aryl stannanes and organosilicon compounds with differently substituted aryl halides in addition to efficiently catalyse hydrogenation reactions. Palladium nanoparticles were synthesized in PEG which catalyze the reaction of bis(pinacolato)diboron with various aryl/benzyl halides to afford aryl/benzyl boronates in high yield.[106] For the synthesis of Pd (0) nanoparticles, a new air stable compound with selenium ligand $[PdCl_2(n\text{-}C_{22}H_{45}\text{–}Se\text{–}n\text{-}C_{22}H_{45})_2]$ has been used. Selenium ligand stabilized Pd (0) nanoparticles ($\sim$3–5 nm) efficiently catalyze Suzuki-Miyaura C-C coupling in short time and are recyclable (up to 94% yield after 5 reuses). It shows high catalytic efficiency for this coupling as 3×10^{-5} mol% is sufficient for activating ArBr.[107] Arylboronates thus prepared, have been directly used in the Suzuki-Miyaura coupling reaction with different aryl halides and benzyl halides in a convenient one-pot, two-step solvent free

green synthesis of unsymmetrical biaryls and diaryl methanes. CuO can act as a good coupling catalyst for C–O/C–S cross coupling of aryl halides with phenol or thiophenol at room temperature.[108] The scope of the reaction was extended to various arylhalides and substituted phenols under optimized condition. In general, efficient, selective, and reusable nano CuO catalysts have been developed for room temperature C-O and C-S, Ullmann type cross coupling reactions. Nanocrystalline CuO can also act as catalyst in C-N cross-coupling reaction with various aryl halides in the presenceof, Cs_2CO_3 as a base in DMSO at 80 °C.[109] 1-substituted indoles were obtained in good to excellent yields and the catalytic system can be recycled up four cycles withoutloss of catalytic activity.Condensation reaction between 3-substituted isocoumarins and 1,7-heptadiamine involves C-bond formationin the presence of 10 mol% zinc oxide nanoparticles (ZnO NPs) (< 150 nm) afforded the desired bis-isoquinolinonesin high yield and purity.[110] Zinc oxide nanostructures were explored as a reusable catalyst for the enamination of 1,3-dicarbonyls using diverse amines.[111]

Nanoparticles have also been used for reduction of aromatic compounds. A simple chemical reduction method was developed for the synthesis of spherical Ag nanoparticles (average size ~7 nm) within mesoporous alumina matrix which exhibits catalytic activity for the reduction of 4-nitrophenol to 4-aminophenol with good efficiency.[112] Like Ag nanoparticles, Au nanoparticles embedded in cubic alumina film exhibited excellent catalytic property for the reduction of 4-nitrophenol.[113] Palladium nanoparticles also catalyze the reduction of 4-nitrophenol to 4-aminophenol in aqueous medium in presence of sodium borohydride.[114] Copper nanoparticles synthesized using PEG and PVP as stabilizers act as a catalyst for the reduction of fourteen different aromatic ring substituted nitrobenzenes with $NaBH_4$ solution.[115] Self assembled thin films of nanoparticles has been embedded in polymer membrane through covalent bond mediated layer by layer (LBL) method.[116] The composite thin film is used for the catalysis of an electron transfer reactionof p-nitrophenol to p-aminophenol by sodium borohydride. Hydrotalcite (HT) supported Pt-nanoparticles of 2–5 nm size were used as catalyst for the selective hydrogenolysis of glycerol to produce 1,2-propanediol by aqueous phase reforming in the absence of any added hydrogen.[117] It was observed that the support plays an important role in the hydrogenolysis. The hydrogen required for the hydrogenolysis is derived from the reforming of H_2O over the Pt-HT catalyst. A glycerol conversion of 98% was achieved over 3 wt% Pt supported on HT. Similarly, Ni-nanoparticle supported on mesoporous ZSM-5 was synthesized which is thermally stable even at 900 °C and had uniform pore diameter of around 5 nm.[118] Reforming of methane with CO_2 with the above catalyst (at atmospheric pressure) shows 96.2% methane conversion at 800 °C with the production of synthetic gas in the H_2/CO mole ratio of 1 : 1. Cu-nanocluster was synthesized on nanocrystalline Cr_2O_3 support by hydrothermal method in the presence of a surfactant, CTAB. It was found that the catalyst is highly active for the selective oxidation of cyclohexane with H_2O_2 at room temperature.[119] Conversion of 86% was achieved over 4.3 wt% Cu loaded on nanocrystalline Cr_2O_3. Alumina supported cobalt (Co), iron(Fe), and Co-Fe bimetallic catalysts have been synthesized and investigated for their

catalytic activity towards carbon dioxide hydrogenation reaction.[120] Optimal amounts of Fe promote the catalytic reactivity of alumina supported cobalt catalysts for the CO_2 hydrogenation reaction. The hydrogenation of CO_2 revealed the presence of formate species on the catalyst during the reaction where iron promotes the supported cobalt catalyst by (i) protecting cobalt from strongly interacting with the alumina support and (ii) forming a Co-Fe alloy.

Metal oxide supports play an important role for the catalytic reaction by metal nanoparticles embedded in them. Cu catalysts on different reducible (SnO_2, CeO_2) and non-reducible supports (Al_2O_3, ZrO_2) were synthesized by a single step solution combustion method.[121] The catalytic activity of these compounds was investigated by performing the hydrogen combustion reaction. Cu-substituted SnO_2 catalyst showed the highest activity with 98% conversion at 320 °C whereas Cu-substituted ZrO_2 was the least active with similar conversion at 480 °C. The activity of bimetallic Cu-Ni and Cu-Fe-modified ceria catalysts was investigated for low-temperature water gas shift (WGS) reaction.[122] In the absence of CO_2 and H_2, 100% conversion of CO with 100% H_2 selectivity was observed at 320 °C and 380 °C, for Cu-Ni and Cu-Fe-modified ceria catalysts. Notably, in the presence of H_2O, a reverse WGS reaction does not occur over these catalysts. Nanostructured Pd-modified Ni/CeO_2 catalyst (synthesized by solution combustion method) was investigated for the water gas shift (WGS) reaction and catalytic hydrogen combustion (CHC) reaction[123] where high activity and selectivity (100%) toward H_2 production was observed.

Other than simple metal and binary metal oxides, ternary metal oxides and composites can also act as good catalysts. A general and efficient procedure was developed for the synthesis of organochalcogenides (selenides and tellurides) by reactions of organoboronic acids and dichalcogenides catalysed by $CuFe_2O_4$ nanoparticles.[124] Imidazo [1,2-*a*] pyridines have been synthesized by using nano-Fe_3O_4-$KHSO_4 \cdot SiO_2$ nanocomposite as catalyst.[125] Highly ordered two-dimensional (2D) hexagonal TiO_2-Fe_2O_3 mixed-oxide was used as catalyst in de-halogenation of aromatic chloride-, bromide-, and iodide –F, –CN, $–CH_3$, $–OCH_3$ and $–NO_2$ functional groups in the aromatic ring using 2-propanol as the dispersion medium.[126] Gold nanoparticles deposited on ceria (Au/CeO_2) show good catalytic activity for benzyl alcohol oxidation reactions using molecular O_2.[127] Series of platinum based nanoparticles have been synthesized in presence of one hydrophobic and one hydrophilic ligand containing terminal sulfonic acid group.[128] The metallic core of the nanocomposite has a great influence in the catalytic efficiency leaving aside the ligand composition. Significant conversion of benzyl alcohol to benzylacetate (with >99% selectivity) was observed when acetic acid was used as the acetylating reagent at 80 °C.

Sensors

Nanostructured materials have been widely used as sensors owing to the large surface area, small particle size and high reactivity. Incorporation of nanomaterials and nanostructures lead to significant improvement in the performance of devices in terms of sensitivity, selectivity, detection limit, response time, and multiplexing capability. Here we discuss some of the

recent developments in this field in India. The growth of sensors based on nanomaterials has been remarkable both in terms of sensitivity as well as in applicability to a wide range of materials, from gas sensors to glucose sensors and as effective probes for cellular imaging.

Owing to its chemical inertness and biocompatibility, gold nanoparticles exhibit promising results in biomedicine. Fluorescent gold clusters (FGCs) with tunable emission in the visible to NIR range are emerging as promising imaging probes.[129] Most conventional fluorescence microscopy techniques use continuous excitation and require stable fluorescence of FGCs under such conditions. Thus, by modifying the synthetic conditions, fluorescent gold clusters (FGCs) with tunable emission from blue to red and quantum yields in the range of 6–17% has been synthesized. The results indicate that FGCs composed of Au(0) are more stable imaging probes than the commonly reported red/NIR-emitting FGCs with a composition of Au(0)/Au(I), as this combination rapidly transforms into nonfluorescent large clusters on exposure to light. Small sized gold clusters with hydrodynamic diameter of 5–12 nm have been used as cell labels and are a powerful alternative to conventional quantum dot based probes with low cytotoxicity. Synthesis of water soluble and colloidally stable functionalized nanoparticles is very challenging since the harsh conjugation chemistry destabilizes the nanoparticle structure thereby limiting its application.[130] To overcome this problem, cyanoborohydride based mild conjugation chemistry has been exploited for the covalent linkage between the reducing end of carbohydrates and primary amine terminated nanoparticles such as quantum dots (QDs), iron oxide or doped semiconductor nanoparticles and different carbohydrates like maltose, lactose or dextran. Fig. 6a shows the absorption and emission spectra of different carbohydrate (glucose, galactose and fluorescein) functionalized nanoparticles. (b) Digital images of solutions of carbohydrate functionalized nanoparticles in phosphate buffer solutions of different pH and in cell culture media under day light and UV light.

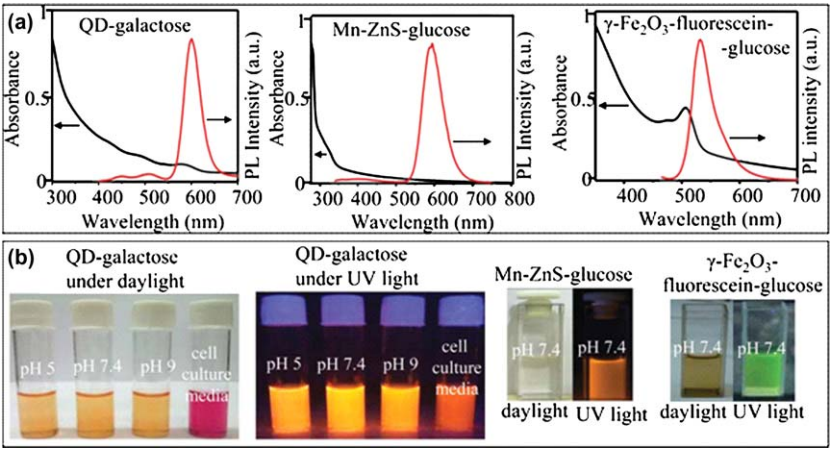

Fig. 6 (a) Absorption and emission spectra of different carbohydrate functionalized nanoparticles. (b) Digital images of solutions of carbohydrate functionalized nanoparticles in phosphate buffer solutions of different pH and in cell culture media. Adapted from reference 130.

The functionalized nanoparticles have been successfully used as nanoprobes for glycoprotein sensing and cellular targeting/imaging applications. Functionalization does not destroy the carbohydrates and produces robust functional nanoprobes with enhanced labeling specificity and reduces the non-specific binding of nanoparticles. Apart from this, gold NPs-based colorimetric sensors have also received significant consideration for the detection of analytes by the naked eye without any sample pretreatment.[131] Water-dispersible dopamine dithiocarbamate decorated gold nanoparticles (DDTC-Au NPs) have been used as sensors for the colorimetric detection of Cu^{2+} ions in water samples. Dopamine dithiocarbamate (DDTC) molecules were successfully attached on the surfaces of Au NPs. The color of DDTC-Au NPs changed from purple to blue by the addition of Cu^{2+} ions at of pH 9.0 by using Tris-tricine buffer. These changes were measured by UV-visible spectroscopy and dynamic light scattering (DLS). The present approach allows the detection of Cu^{2+} ions at 14.9×10^{-6} M. DDTC-Au NPs were effectively used as colorimetric sensors for the detection of Cu^{2+} ions in tap water.

Nanomaterials have also been extensively used as gas sensing materials for ammonia, LPG *etc*. Current–voltage (I–V) characteristics of the nanostructured organic–inorganic heterojunction devices ITO/ZnS/ZnPc(Zinc Pthalocyanine)/Al, using films of ZnS and ZnPc, have shown diode-like characteristics under different environments.[132] The fabricated ITO/ZnS/ZnPc/Al heterostructures exhibited diode-like behavior whereas for the single layer devices ITO/ZnS/Al and ITO/ZnPc/Al such a behavior was not observed. Gas sensing properties for the single layer devices ITO/ZnS/Al, ITO/ZnPc/Al and ITO/ZnS/ZnPc/Al heterojunctions were also reported. An increase in current in the n-type ZnS single layer device was observed when the device was exposed to NH_3 (donor gas), whereas a decrease in current was noticed when the device was exposed to air (acceptor gas O_2). This increase in forward current (diode current) in the presence of gases has been explained by the creation of charge carriers inside the ZnPc layer. The threshold voltage of the junction diodes has been found to depend on the temperature and the presence of donor and acceptor gases. The change in current and threshold voltages in the presence of gases suggests that this heterojunction device could be a useful gas sensor, especially for sensing NH_3 gas. Chemical vapor deposition method has been used to synthesize tree like ZnO nanostructures with large number of intersecting branches.[133] The sample shows the lowest UV/VIS PL peak intensity ratio and highest LPG response owing to its high surface-to-volume ratio and large number of junctions in the nanorods. Porous tin oxide nanoparticles which exhibited enhanced photocatalytic activity (discussed earlier under catalysis)[69] has also been used for gas sensing capabilities toward hydrogen. Surface modification of the nanospheres with Pd transforms this material into a highly sensitive and selective room-temperature hydrogen sensor. The material is able to respond to even 50 ppm H_2 in N_2 at room temperature with a response time of 10 s.

An electrochemical NO_x sensor was fabricated based on the incorporation of hemin on a ZnO–PPy nanocomposite modified Pt electrode.[134] The electrocatalytic behavior of the sensor was investigated by cyclic

voltammetry. The hemin–ZnO–PPy–Pt electrode exhibited characteristic hemin reversible redox peaks at 0.035 V and −0.11 V *vs.* Ag/AgCl respectively. The above electrode exhibited 3-fold enhanced electrocatalytic activity towards NOx compared to the hemin–PPy–Pt electrode. The electrocatalytic response of the sensor was proportional to the NOx concentration in the range of 0.8 to 2000 μM ($r^2 = 0.9974$) with a sensitivity of 0.04 μA μM^{-1} cm^{-2} and detection limit of 0.8 μM for the hemin–ZnO–PPy–Pt electrode. The low detection limit, wide linear range and enhanced sensitivity of the present sensor make it valuable for potential applications. In addition, this sensor exhibited good reproducibility and stability.

A highly sensitive mediator-free microfluidics-based sensor comprising of PDMS microchannels and patterned electrodes has been fabricated for the rapid detection of urea.[135] Urease (Urs) and glutamate dehydrogenase (GLDH) have been successfully co-immobilized onto TiO_2–ZrO_2 nanocomposite microelectrodes surface. A schematic representation for the modification of the working electrode is shown in Fig. 7a. The PDMS microchannels have been sealed with a glass substrate comprising of reference (Ag/AgCl), counter (ITO) and working (Urs-GLDH/TiO_2-ZrO_2/ITO) electrodes. This mediator-free microfluidics sensor offers improved sensitivity, detection limit and fast response time owing to its good electrocatalytic behavior of the nanocomposite as well as smaller geometry of the sensor. The sensor shows linearity as 5–100 mg/dL with improved sensitivity as 2.74 μA $[Log\ mM]^{-1}$ cm^{-2} and detection limit of 0.07 mg/dl (0.44 mM) using $3\sigma_b/m$ criteria. The Reynolds number has been found to be 0.166, indicating that fluid flow is completely laminar, controllable and the pressure drop across the microchannels is found to be 3.5×10^3 Pa. By comparing the magnitude of current response with individual normal concentration of interferents such as glucose (5 mM), ascorbic acid (0.05 mM), uric acid (0.1 mM) and lactic acid (5 mM) along with urea (1 mM) in PBS, the selectivity of the Urs-GLDH/TiO_2–ZrO_2/ITO bioelectrode (El) has been determined and shown in Fig 7b. This TiO_2–ZrO_2 nanocomposite based microfluidic device may also prove useful for the estimation of other important analytes including cholesterol and low density lipoprotein.

Diabetes mellitus is a serious metabolic disorder caused by insulin deficiency resulting in hyperglycemia, and about 200 million people worldwide are being affected by diabetes mellitus. Regular monitoring of physiological glucose level is necessary. The rising demand for glucose sensors with high sensitivity, good reliability, and excellent selectivity has compelled researchers to develop new materials for the same. Amino acids-/citric acid-/tartaric acid have been used in conjunction with hydrothermal route for the morphologically controlled synthesis of micro-/nanostructured crystalline copper oxides (CuO).[87] The surface area of metal oxides depends on the amino acid used in the synthesis. It was concluded that amino acid/citric acid/tartaric acid and time (for the hydrothermal reaction) both play an important role in tuning the morphology and structure of CuO. Electrodes modified with such CuO were used for the construction of nonenzymatic sensors, which displayed excellent electrocatalytic response

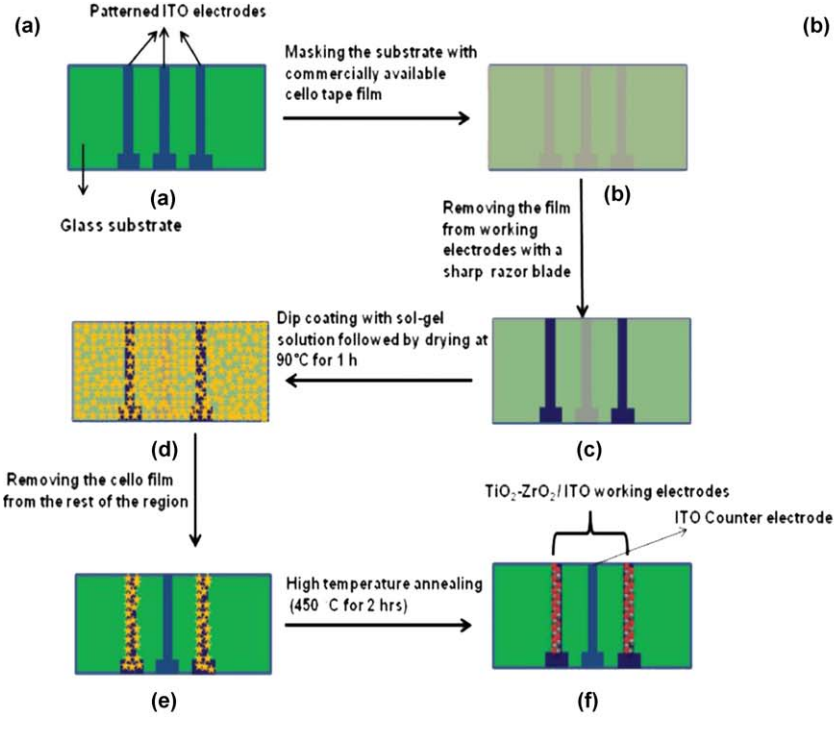

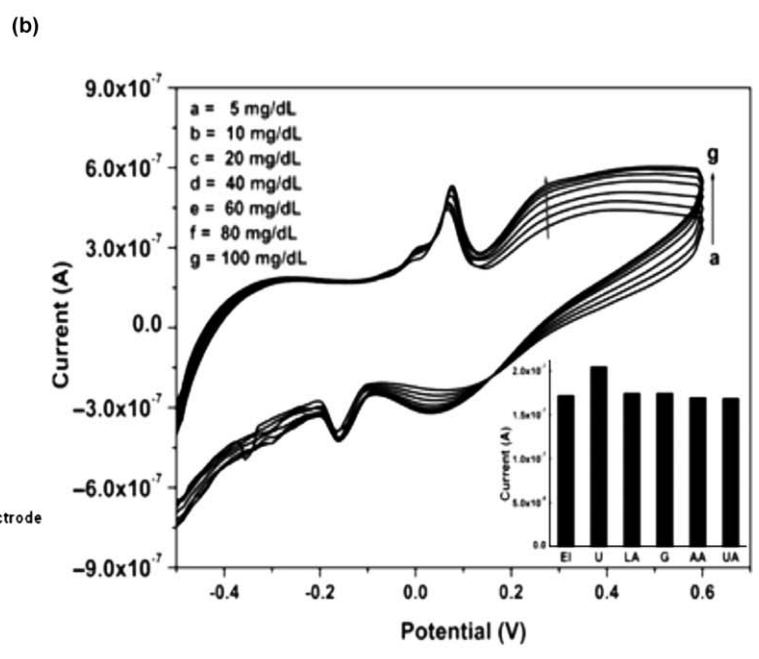

Fig. 7 (a)The process of modifying only the working ITO electrode (WE1 and WE2) with TiO_2–ZrO_2 nanocomposite using the dip coating method is shown (b) CV response of Urs-GLDH/TiO_2–ZrO_2/ITO bioelectrode as a function of urea concentration in PBS. Inset shows the effect of interferents (glucose, ascorbic acid, uric acid and lactic acid) on the current response of the Urs-GLDH/TiO_2–ZrO_2/ITO bioelectrode in PBS. Adapted from reference 135.

for the detection of H_2O_2 and glucose compared to conventional CuO. CuO–Tyr exhibited higher sensitivity (2.72 lA/mM) when compared with conventional CuO (0.87 lA/mM) in H_2O_2 sensing. This is attributed to its large surface area which enhances the accessibility of H_2O_2/glucose molecule to the active site and in turn results in high observed current. This material has also been studied for its photocatalytic activity (described in the previous section).

Cholesterol concentration in human serum is responsible for the risk of cardiovascular diseases. Therefore, it is essential to develop a cheap, simple and sensitive cholesterol biosensor to monitor the concentration of cholesterol in human serum. ZnO microtubes with $\sim$30 μm length, 2 to7 μm width and 400 to 500 nm wall thicknesses have been synthesized for this purpose. They have been obtained by a hierarchical assembly of ZnO flowers which are made of 3D assembled porous ZnO flakes.[136] They exhibit excellent microstructure-based sensing and catalytic properties. It was found that porous tubular ZnO exhibited high sensitivity (54.5 mA M^{-1} cm^{-2}) and low LOD (limit of detection, 0.2 mM) of cholesterol at room temperature and is superior in comparison to a nano gold modified sensor. Phase transformation was observed for Fe_3O_4 nanoparticles (NPs) to α-Fe_2O_3 NPs obtained during electrophoretic film deposition onto indium-tin oxide coated glass plates.[137] The *in situ* oxidation of NPs during electrophoretic deposition can be circumvented using surface passivation of the Fe_3O_4 NPs with an organic shell (carbon) as well as an inorganic shell (silica), while retaining the biocompatibility of the Fe_3O_4 NPs. The cholesterol biosensors employing Fe_3O_4@C and α-Fe_2O_3 nanocrystalline films show sensitivities of 193 nA mg^{-1} dl cm^{-2} and 218 nA mg^{-1} dl cm^{-2}, respectively, from cyclic voltammetric studies. The sensitivities achieved were of 0.42 Ω mg^{-1} dl cm^{-2} and 0.90 Ω mg^{-1} dl cm^{-2}, respectively, as calculated from electrochemical impedance spectroscopic studies. The low values of the Michaelis–Menten constant reveal the enhanced enzymatic activity of cholesterol oxidase (ChOx) on nanostructured iron oxide films. The comparable sensitivities for biosensors obtained using Fe_3O_4@C and α-Fe_2O_3 NPs suggests that encapsulation of NPs with carbon does not significantly affect the electrocatalytic activity of Fe_3O_4 NPs, while it adds to the stability of the NPs.

Interference from ascorbic acid limits the use of electrochemical sensors for detection of dopamine. Several approaches have been devised to overcome this difficulty. The interference from ascorbic acid was reduced by fabricating a negatively charged electrode surface using PEGylated arginine functionalized magnetic nanoparticles (PA-MNPs).[138] The electrochemical behavior was investigated by cyclic voltammetry and the sensor showed high sensitivity and selectivity for dopamine. The interface properties of modified electrodes were studied using Electrochemical Impedance Spectroscopy (EIS). The value of the polarization resistance (Rp) increases linearly with dopamine concentration in the range of 10μM to 1 mM and the limit of detection (LOD) was calculated to be 14.1 μM. With high sensitivity and selectivity, micromolar detection limit, high reproducibility, along with ease of preparation, this system is suitable for the determination of DA in pharmaceutical and clinical preparations.

A sensor based on $LaFeO_3$ nanostructures has also been developed for dopamine. Surfactant assisted hydrothermal process has been used to synthesize single-crystalline novel $LaFeO_3$ dendritic nanostructures.[139] The overall length of the dendrite is about 3–4 μm with the average trunk diameter ~ 80 nm, and the branches are 1–1.5 μm in length with a diameter of 85 nm. The electrochemical measurements performed on $LaFeO_3$ dendritic nanostructures deposited on the surface of a glassy carbon electrode exhibit a strong promoting effect. The oxidation current is proportional to concentration in the linear range of 8.2×10^{-8} to 1.6×10^{-7} M with a detection limit of 62 nM at S/N = 3. The sensor effectively avoids the interference of ascorbic acid and uric acid, and has been successfully applied to determine the dopamine formulations with high selectivity and sensitivity.

ZnO/CTAB and ZnO/TX-100 modified carbon paste electrodes were used as electrochemical sensors for dopamine.[140] The Triton-X 100 (TX-100) modified carbon paste electrode shows electrocatalytic properties and an enhancement in the peak current for dopamine. CTAB modified carbon paste electrodes are less sensitive for the determination of dopamine.

Plasmon enhanced fluorescence immunoassay (PEFI) format has been reported in developing a sensitive heterogeneous fluoroimmunoassay for monitoring phenylurea herbicide diuron.[141] The conformational and electrostatic effect of synthesized hapten for producing highly specific egg yolk antibody against a phenyl urea herbicide diuron was studied using molecular modelling. The generated antibodies were labeled with fluorescein isothiocyanate at different molar ratios and used as tracer in the developed fluorescence based immunoassay. The sensitivity of the assay format was enhanced by using silver nanoparticles tagged with bovine serum albumin. A significant improvement of ~10 fold increase was observed in assay sensitivity. The immunoassay has a detection limit of 0.01 ng mL^{-1} with good signal precision (~2%) in the optimum working concentration range between 1 pg mL^{-1} to 10 μg mL^{-1} of diuron. The developed heterogeneous immunoassay using IgY type antibodies can, therefore, be used as a convenient quantitative tool for the ultra-sensitive detection of pesticides in samples, and also has potential for application to the protein or DNA based biochips with improved sensitivity.

A new highly fluorescent graphene oxide (GO)/poly(vinyl alcohol) (PVA) hybrid (GOPVA) in an acidic medium (pH 4) has been developed.[142] The hybrid is highly fluorescent, because of passivation by hydrogen bonding, as evident from IR and Raman spectra. The quantum yields of GO-PVA hybrids are higher than that of GO. The highly fluorescent GO-PVA1 hybrid fibres has been used as an effective tool for selective sensing of Au^{3+} ions in aqueous media with a detectable limit of ~275 ppb. The sensitivity of Au^{3+} ion (300 μM) in the presence of 600 μM concentrations of each ion (Cu^{2+},Ag^{+}, Mg^{2+}, Ca^{2+}, Zn^{2+},K^{+}, Pb^{2+}, Co^{2+}, Ni^{2+}, Pd^{2+}, Fe^{2+}, Fe^{3+}, and Cr^{3+}), taken together, is unique, exhibiting a quenching efficiency of 76%. The quenching efficiency in the presence of a biologically analogous mixture (D-glucose, D-lysine, BSA, Na^{+}, K^{+},Ca^{2+}, Mg^{2+}, Zn^{2+}) (600 μM each) is 73%, which suggests that the GO-PVA hybrid is an efficient sensor of Au^{3+} ions. The selectivity of sensing Au^{3+} is attributed to its reduction

potential being higher than that of other metal ions. The XPS data of GO-PVA hybrid with 300 μM Au^{3+}confirm the reduction of Au^{3+} to Au^0, because of the transfer of excitons from the hybrid facilitating the selective photoluminescence (PL).

Microwave assisted fabrication of two dimensional carbon nitride from formamide ($HCONH_2$) has also been reported.[143] Microwave irradiation of $HCONH_2$ produces carbon nitride dots (CNDs) which are used as precursors for synthesis of carbon nitride (C_3N_4). The two dimensional (2D) carbon nitride sheets are formed by evaporation induced self-assembly and condensation of CNDs on a solid substrate. The drying of CND solution generates different morphologies corresponding on the concentration of CNDs such as 0D carbon nitride quantum dots, 2D carbon nitride sheets and 3D carbon nitride. The C_3N_4 modified glassy carbon electrode can be used as a highly sensitive electrochemical sensor for mercuric ions in aqueous solution. The lower detection limit of Hg^{2+} is found to be 9.1×10^{-11} M, which is far below the WHO guideline for drinking water (10^{-8} M). The simultaneous electrochemical detection of Pb^{2+}, Cu^{2+} and Hg^{2+} using a C_3N_4 modified GC electrode is also possible.

The excited state intramolecular charge transfer (ICT) property of fluorophores has been used for the design of fluorescent chemosensors. Three donor–π-acceptor–π-donor (D–π-A–π-D) based molecular probes BP, BT and BA has been developed and studied for zinc ion sensing.[144] Two heteroaromatic rings, pyrrole (BP), and thiophene (BT) and a non-heteroaromatic ring N-alkoxy aniline (BA) were selected as donor moieties linked to a bipyridine binding site through a vinylic linkage. The heteroaromatic systems BP and BT perform selective and ratiometric emission signalling for zinc ions *in vitro* in MCF-7 cell lines and thus highlights the use of BP and BT as excellent zinc ion detection probes.

Highly fluorescent blue graphitic carbon nitride quantum dots (g-CNQDs) were synthesized by a simple microwave mediated method from formamide ($HCONH_2$).[145] The fluorescence emission of g-CNQDs is found to be strongly dependent on solvent, pH as well as on excitation wavelengths; the life time of the emission decreases with increasing polarity of the solvent. These quantum dots are highly sensitive and selective fluorescent probes for mercuric ions in aqueous media due to the ''superquenching'' of fluorescence. The complex formation of Hg^{2+} ions with the CN_x sheet involving delocalized electron moieties of the latter are responsible for the quenching of fluorescence. The addition of iodide ions abstracts the bound Hg^{2+} forming HgI_2 and gives back the fluorescence characteristic of g-CNQDs. These QDs can play a dual role for selective and sensitive detection of mercuric ions as well as iodide ions in aqueous media *via* ''ON–OFF–ON'' fluorescence response with the lower limit of its detection being $\sim 10^{-9}$ M.

Nanocomposites (NCs) of silver vanadium oxide (SVO) nanospheres dispersed in ultrathin layers of polyaniline (PANI–b-$AgVO_3$) were synthesized at two different temperatures (60 and 80 °C) by *in situ* chemical oxidative polymerization.[146] The NCs synthesized at temperatures of 60 and 80 °C show approximately 4 and 2 nm ultrathin layers of PANI grown on SVO nanospheres, respectively. The size of the SVO nanospheres dispersed

in the ultrathin PANI layers are in the range of 10–40 nm. The presence of SVO in the PANI layer has been confirmed by Fourier Transform Infra Red (FTIR) and energy dispersive X-ray (EDAX) spectroscopic investigations. The electrochemical study of (PANI–b-$AgVO_3$) shows an enhancement in the capacitance (1365.6 F $g^{-}1$) compared to $V_2O_5 \cdot nH_2O$–PANI NCs (217.5 F g^{-1}) and PANI (33 F g^{-1}). The SVO dispersed in a layer of PANI NC exhibits excellent humidity sensing characteristics. The response and recovery times are found to be 4 and 8 seconds, respectively. The NCs have good potential as supercapacitors as well as humidity sensors with a fast response.

Field effect transistors using ultrathin molybdenum disulfide (MoS_2) have recently been studied for humidity sensing.[147] The observed hysteresis in atomically thin MoS_2 FET is primarily due to the presence of trap states induced by absorbed water molecules on MoS_2 surface; and also due to the photosensitivity of MoS_2 which can significantly increase the hysteresis when MoS_2 FET is exposed to white light illumination.

Surface plasmon resonance based pH sensor has been developed using coatings of silver, ITO ($In_2O_3 : SnO_2$), aluminium and smart hydrogel layers over the core of an optical fiber.[148] Different coating techniques have been used for example, silver, aluminium and ITO layers were coated using a thermal evaporation technique, while the hydrogel layer was prepared using a dip-coating method. The hydrogel layer swells and shrinks by changes in the pH of the fluid surrounding the layer. The sensor, thus, works on the principle of detecting the changes in the refractive index as the pH changes. The sensor utilizes a wavelength interrogation technique and operates in a particular window of low and high pH values. Increasing the pH value of the fluid causes swelling of the hydrogel layer, which decreases its refractive index and results in a shift of the resonance wavelength towards blue in the transmitted spectra. The ITO layer increases the sensitivity while the aluminium layer increases the detection accuracy of the sensor. The additional advantages of the sensor are short response time, low cost, probe miniaturization, probe re-usability and the capability of remote sensing.

In an interesting study for evaluating band gap, Cu has been successfully used as a sensor. Charge transfer at the interface followed by the relative alignment of the energy levels between materials affect the efficiency of the quantum dots based solar cells. And thus there exists a high demand to obtain size specific band offsets. Semiconductor charging during measurements could result in indirect and possibly inaccurate measurements due to shift in valence and conduction band position. A novel method has been developed to study the band offsets by associating an atomic like state with the conduction band and hence obtaining an internal standard.[149] This has been achieved by doping copper in semiconductor nanocrystals, leading to the development of a characteristic intra gap Cu-related emission feature assigned to the transition from the conduction band to the atomic-like Cu d state. Using this transition, the relative band alignment of II-VI semiconductor nanocrystals as a function of size (below 10 nm) was determined. QY and PL decay kinetics of the Cu related emission was also used to study the surface of the nanocrystal. Thus, by appropriately studying the mechanism of the Cu related emission, it is possible to dope Cu in any

nanocrystal and study the bulk and surface electronic structure of the nanocrystal using Cu d level as an internal standard or a nanosensor.

The configuration of hemoglobin in solution and confined inside silica nanotubes has been studied using synchrotron small angle X-ray scattering and electrochemical activity.[150] Confinement inside submicron tubes of silica help in preventing protein aggregation, which is vividly observed for unconfined protein in solution. The radius of gyration (Rg) and size polydispersity (p) of confined hemoglobin was found to be lower than that in solution. The confined hemoglobin displayed a higher thermal stability with Rg and p showing negligible changes in the temperature range 25–75 °C. A change in the electrochemical activity was observed with change in configuration between the confined and unconfined protein. Reversible electrochemical response (from cyclic voltammograms) obtained in case of the confined hemoglobin, in contrary to the observance of only a cathodic response for the unconfined protein, gave direct indication of the differences between the surrounding of the electroactive heme center in a different orientation compared to that in solution. The confined Hb showed loss of reversibility only at higher temperatures. The electron transfer coefficient (α) and electron transfer rate constant (k_s) were also different, providing additional evidence regarding structural differences between the unconfined and confined states of hemoglobin. Thus, absence of any adverse effects due to confinement of proteins inside the inorganic matrices such as silica nanotubes opens up new prospects for utilizing inorganic matrices as protein "encapsulators", as well as sensors at varying temperatures.

A new NIR emitting nanosensor for the direct detection of urea in whole blood has been developed.[151] Fig. 8a shows the schematic representations for the preparation of Au cluster from AuNP and (b) preparation of AuC@Urease and a mechanism for fluorescence quenching. The blood urea level estimated in whole blood and blood serum using this method was comparable and the data were validated against a currently used clinical method for blood serum. This is a better protocol since the proposed sensing mechanism works directly on the blood whereas the clinical methods require serum separation for the detection of urea, as many of

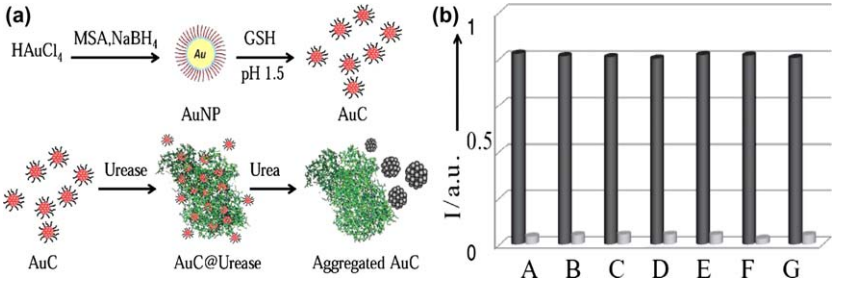

Fig. 8 (a) Schematic representations of the preparation of AuC from AuNP and Preparation of AuC@Urease. (b) Fluorescence intensity of AuC@Urease in the presence of different analytes; (A) Sensor alone (black) and after addition of urea (grey); (B-G) Sensor in presence of creatinine, albumin, glucose, uric acid, cysteine, and NaCl (black) and after addition of urea (grey). (b) Validation of AuC@Urease method with the currently practiced clinical method. (A-G) serum samples spiked with different concentrations of urea. Adapted from reference 151.

them work on colorimetric assay which is often hindered by the color of blood. Fig. 8c shows the fluorescence intensity of AuC@Urease in the presence of different analytes; (A) Sensor alone (black) and after addition of urea (grey); (B-G) Sensor in presence of creatinine, albumin, glucose, uric acid, cysteine, and NaCl (black) and after addition of urea (grey). The generality of the nanosensor is demonstrated by detecting urea in adulterated milk samples.

5 Electrocatalysis

Electrocatalysis is an inter-disciplinary area, which attracts the interest of chemists, biochemists, physicists; surface and materials scientists and chemical engineers.There are various applications of electrocatalysis for technological electrochemical reactions, organic electrosynthesis, electrode sensors, fuel cells and batteries. Due to the wide applicability, creating a high performance electrocatalyst is a major quest.

A significant emphasis in electrocatalysis is in the oxidation of methanol and ethanol for fuel cell. Platinum and palladium nanoparticles synthesized on multiwall carbon nanotubes in microwave induced reactions were used as catalysts for direct methanol, ethanol and formic acid oxidation in acidic as well as alkaline media.[152] A stable dendritic film of Pd was fabricated by depositing Pd on conducting polymer poly(3,4-ethylenedioxythiophene) (PEDOT) coated carbon paper electrode.[153] The electrochemical properties of both Pd–PEDOT/C and Pd/C electrodes were checked for electro-oxidation of 1,2-propanediol (PD) in an alkaline electrolyte. Owing to enhanced surface area and surface defects on dendritic Pd, the Pd–PEDOT/C electrode exhibits greater catalytic activity than the Pd/C electrode. Cyclic voltammetry studies suggest that peak current density increases with an increase in Pd and NaOH in the electrolyte. Mesoporous carbon supported active platinum catalysts with narrow size distribution were synthesized which show excellent electrocatalytic activity for methanol oxidation reaction in comparison with platinum supported activated carbon (Pt/AC) as well as commercial carbon (Pt/E-TEK) catalysts.[154] Poly(o-phenylenediamine) (PoPD) microrods supported Pt nanocatalyst was synthesized by the reduction of chloroplatinic acid with sodium borohydride on the PoPD support. The nanocomposite (Pt/PoPD) microrods were explored for their electro-catalytic performance towards oxidation of methanol.[155] The electro-catalytic activity of Pt/PoPD was found to be much higher (current density 1.96 mA/cm^2 at 0.70 V). Like Pt and Pd, Rh was found to be a good electrocatalyst. With the help of galvanic displacement approach shape-selective synthesis of Rh nanoparticle was carried out by using polyvinylpyrrolidone (PVP) as a shape-inducing agent.[156] A comparative study was carried out on the electrocatalytic activity of the different morphologies of Rh towards fuel cell reactions like HCHO oxidation. The peak current densities are 0.52, 0.41 and 0.25 mA cm^2 for the reaction on Rh nanospheres, Rh nanorods and bulk Rh as electrocatalysts, respectively. It was observed that Rh nanospheres are more efficient in comparison to nanorods.

Gold nanoparticles synthesized at high pH exhibited good electrocatalytic activity towards oxidation of nicotinamide adenine dinucleotide

(NADH).[157] Metal oxides also show good electrocatalytic activity in alcohol oxidation reaction. A simple polymer (P123)-assisted homogeneous precipitation method was applied to synthesize shuttle-shaped CeO_2[158] which shows higher oxidation current and lower oxidation overpotential compared with bulk CeO_2 for methanol oxidation in acidic medium. This is due to a higher number of triple-phase interfacial active centers on the shuttle-shaped CeO_2 surface, which provide additional OH_{ads} species for oxidation of the poisoning carbonaceous species at lower overpotential. Using chronopotentiometry and chronoamperometry techniques it was observed that nanostructured shuttle-shaped CeO_2 provides significant antipoisoning activity to Pt/C during the methanol electro-oxidation reaction.

Green synthetic methods were developed for preparation of platinum-graphene catalysts for proton exchange membrane fuel cell (PEMFC) applications.[159] In another report, the chemical and electrical synergies between graphite oxide and multiwalled carbon nanotubes (MWNT) were dicussed.[160] The potential hybrid composites have been demonstrated by employing them as electrocatalyst supports in proton exchange membrane fuel cells. Nitrogen-doping in hydrogen-exfoliated graphene (HEG) sheets was achieved by the pyrolysis of graphene coated with polypyrrole in an inert environment leading to the incorporation of nitrogen atoms in the graphene network with simultaneous removal of the polymer.[161] These nitrogen-doped graphene (N-HEG) sheets were used as catalyst support for dispersing platinum and platinum–cobalt alloy nanoparticles synthesized by the modified-polyol reduction method, yielding a uniform dispersion of the catalyst nanoparticles. Compared to commercial Pt/C electrocatalyst, Pt–Co/N-HEG cathode electrocatalyst exhibits four times higher power density in proton exchange membrane fuel cells. The electrocatalytic activity of binary and ternary combinations of Ni and Au with Pd for use as the anode component of a direct ethanol fuel cell (DEFC) was investigated.[162] The catalysts were grown on a carbon support by reduction of the respective precursors and the electro-oxidation of ethanol was investigated in alkaline pH. The presence of the eg^1 electron in Mn and Co oxides is considered to play a crucial role in the photocatalytic properties of the oxides. High turn over frequencies of the order of 5×10^{-4} s^{-1}, 4.8×10^{-4} s^{-1}, and 0.8×10^{-4} s^{-1} has been observed for Mn_2O_3, $LaMnO_3$, and $MgMn_2O_4$ respectively. Among the cobalt oxides, $Li_2Co_2O_4$ and $LaCoO_3$ exhibit excellent catalytic activity, with the turnover frequencies being 9×10^{-4} s^{-1} and 1.4×10^{-3} s^{-1}, respectively. Amount of O_2 evolved (A) per mol of transition metal managanites has been given in Fig. 9a which shows the overall order of activity is Co > Ni > Cr > Mn > Fe. Fig. 9b shows the amount of O_2 evolved (A) per mol of transition metal cobaltites.[163]

Anisotropic Co_3O_4 nanostructures with controlled aspect ratio (1 : 5 to 1 : 13) (made of aligned nanoparticles) were synthesized from a single nanostructured precursor (cobalt oxalate), obtained by a microemulsion method under controlled kinetic parameters and temperature of decomposition.[164] With decrease in calcination temperature from 600 to 300 °C, there was an increase in the aspect ratio of the nanorods and the individual particle size decreased. On the other hand decreasing the heating rate, the

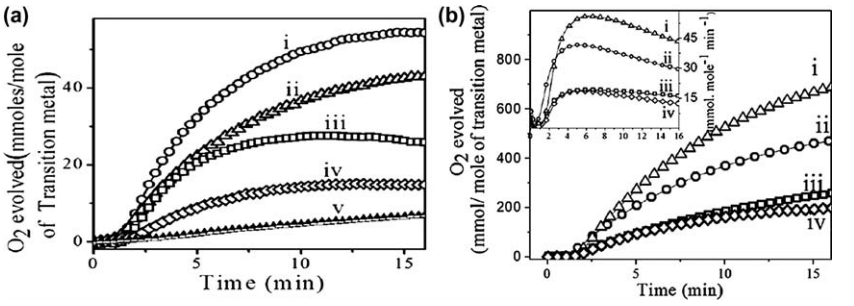

Fig. 9 (a) Amount of O_2 evolved (A) per mol of transition metal and (B) per mol of transition metal per unit surface area by (i) $LiCoMnO_4$, (ii) $LiNi_{0.5}Mn_{1.5}O_4$, (iii) $LiCrMnO_4$, (iv) $LiMn_2O_4$, and (v) $LiFeMnO_4$. (b) Amount of O_2 evolved (A) per mol of transition metal and (B) per mol of transition metal per unit surface area by (i) $LaCoO_3$, (ii) $Li_2Co_2O_4$, (iii) Mn_2O_3, and (iv) $LaMnO_3$. Adapted from reference 163.

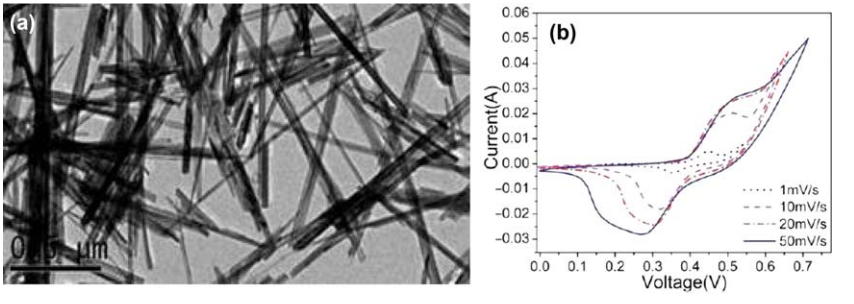

Fig. 10 (a) TEM images displaying the morphology of a-MnO_2 synthesized hydrothermally for 24 h (b) CV curves recorded for nanowire-based MnO_2 in 0.1 M KOH electrolyte at different scan rates. Adapted from reference 165.

particles become more loosely bound in the anisotropic structures and at high rate of heating robust nanorods were produced.These nanostructures of Co_3O_4were found to be excellent electrocatalysts for oxygen evolution reaction (OER), with a high current density of 104 mA/cm^2. Tetravalent Mn based ternary oxides like di-magnesium manganate (Mg_2MnO_4) were synthesized from the decomposition of nanostructured metal oxalate precursor at 500 °C and a current density of 14mA/cm^2 was obtained for oxygen evolution reaction.[141] High aspect ratio MnO_2 nanowire has been synthesized through hydrothermal method (Fig 10a). These nanowires have been used as an electrode material for rechargeable energy storage device. The introduction of this wire layer over titanium substrate helps in improving the redox reaction with the electrolyte and enhancing cycling performance. Owing to the high surface area of these nanowires in the electrode system, the specific capacitance values can rise to as high as 1050 F g^{-1} and 750 F g^{-1} as recorded in CV tests and constant current discharge studies, respectively.[165] Fig. 10b shows the CV curves recorded for nanowire-based MnO_2 in 0.1 M KOH electrolyte at different scan rates.

Fe doped $Cr_2(MoO_4)_3$\{$Fe_xCr_{2-x}(MoO_4)_3$ (x = 0, 0.25, 0.50 and 0.75)\} improved the electrocatalytic activity towards O_2 evolution reaction

(OER).[166] Substitution of Cr by Fe in the $Cr_2(MoO_4)_3$ matrix increases the electrocatalytic activity (more than 80 times) of the catalyst toward the OER. Thus, the presence of Fe in the $Cr_2(MoO_4)_3$ matrix greatly influences the electrocatalytic activity as well as the mechanism of the OER. The electrocatalytic activity of layer-by-layer self-assembled copper tetrasulfonated phthalocyanine (CuPcTS) on carbon nanotube (CNT)-modified glassy carbon (GC) electrode was reported.[167] CuPcTS was immobilized on the negatively charged CNT surface by alternatively assembling a cationic poly (diallyldimethylammoniumchloride) (PDDA) layer and a CuPcTS layer. The CuPcTS/PDDA/CNT modified GC electrode act as a redox mediator for the anodic oxidation of 2-mercaptoethanol (2-ME) in alkaline conditions.

Pt@Pd/C electro-catalyst was synthesized with the help of galvanic displacement reaction between Pt and Pd which exhibit good electrocatalytic activity toward oxygen reduction reaction.[168] A novel method for the synthesis of triangular shaped palladium nanoparticles

(Pd NPs) decorated nitrogen doped graphene was reported.[169] Nitrogen doped graphene (N-G) was synthesized by uniform coating of polyelectrolyte modified graphene surface with a nitrogen containing polymer followed by its pyrolysis. Electrocatalytic study of Pd/N-G showed that it is a good electrocatalyst for oxygen reduction reaction and highly stable in acidic media due to the strong binding between Pd NPs and graphene support. Cobalt phthalocyanine (CoPc) on multi-walled carbon nanotubes (CNTs) was synthesized and used as an electrocatalyst for oxygen reduction reaction (ORR).[170]

Pt nanoparticle (Pt NP) embedded aminoclay/Nafion (Pt/AC/ N) nanocomposite catalyst film was prepared for oxygen reduction reaction with the help of sol–gel method.[171] The prepared film has firmly bound Pt NP and could exhibit an improved electro-reduction activity compared to Vulcan carbon/Nafion supported Pt NP (Pt/VC/N). Moreover, the Pt/AC/N films have good stability in the acidic environment. The limiting current density of the Pt/AC/N film with 35.4 $\mu g/cm^2$ of Pt loading was found to be 4.2 mA/cm^2, which is 30% higher than that of the Pt/VC/N. The reaction was found to follow a four electron transfer mechanism. Accelerated durability test for 2000 potential cycles showed that *ca.* 78% of initial limiting current was retained. The results show the possible usefulness of the Pt/AC/N as the free-standing electrocatalyst layer for polymer electrolyte membrane fuel cells.

Highly efficient and stable copper nanoparticles (4–6 nm) have been obtained by thermal decomposition of aligned copper oxalate nanorods in an argon atmosphere.[172] In the case of HER, the current densities were found to be 12 mA cm^{-2} (glassy carbon electrode) and 46 mA cm^{-2} (Pt electrode) which are significantly higher than reported values (maximum 1 mA cm^{-2}). In the case of OER, the current density was found to be 1.6 mA cm^{-2} (which is slightly higher) for the glassy carbon electrode and 15 mA cm^{-2} for Pt as the working electrode which is 4–30 times higher than earlier reports. The high efficiency is attributed to the high surface area (34 $m^2\ g^{-1}$) of these tiny well-crystalline copper nanoparticles. These nanoparticles show excellent stability as electrocatalysts and retain their activity even after 50 cycles.

Another novel route was developed for the preparation of mercaptopropyl functionalized mesoporous silica supported cobalt phthalocyanine (MPS-CoPc) through co-condensation of 3-mercaptopropyltriethoxysilane and tetraethyl orthosilicate in the presence of cetyltrimethylammonium bromide as a templating agent followed by incorporation of cobalt phthalocyanine (CoPc).[173] Further, gold nanoparticles (Au NPs) were introduced into MPS-CoPc to obtain (*i.e.* Au-MPS-CoPc). The MPS-CoPc and Au-MPS-CoPc modified electrodes are highly active towards oxygen reduction. With the incorporation of Au NPs, significant increase in current and considerable decrease in oxygen reduction potential (-0.23V) was achieved. The electro-catalytic properties of Ni-doped titania hollow spheres was determined for hydrogen and oxygen evolution during water electrolysis from acidic media.[174] The anodic peak current density value (which represents the oxygen evolution phenomenon) was observed to be 13 mA cm^{-2} for 25 wt% Ni-loaded sample; whereas, the hydrogen evolution peak was most intense for 30 wt% Ni/TiO_2 material with cathodic peak current density of 32 mA cm^{-2}. Multiwalled carbon nanotubes (MCNTs) supported Pt–Pd alloy was synthesized for their electrocatalytic property towards the oxygen-reduction reaction (ORR).[175] $Pt_{46}Pd_{54}$(close to 1 : 1 ratio) shows pronounced electrocatalytic activity towards ORR. Moreover, the $Pt_{46}Pd_{54}$ nanoelectrocatalyst is highly durable and it retains its initial catalytic activity even after 1000 cycles. The electrocatalytic activity of the alloy electrocatalyst is compared with commercially available Pt black and MCNT-supported spherical Pt nanoparticles. The synergistic catalytic effect of Fe_2O_3 along with TiO_2 was investigated for electrochemical reactions.[176] After synthesis of the composite of Fe_2O_3 and TiO_2, it was added to NiP to increase the catalytic efficiency of NiP electrodes, which is well known as a catalyst electrode for hydrogen evolution reaction in alkaline medium. The incorporation of $Fe_2O_3 \cdot TiO_2$ into NiP matrix substantially reduced the overpotential during hydrogen evolution reaction (HER) in 32% NaOH solution and also improved the metallurgical properties. The electrodes exhibited high stability under dynamic experimental conditions.

6 Carbon based nanomaterials

Graphene has created great excitement owing to its novel properties and has been extensively studied. Magnetism studies in graphene and graphene nanoribbons are attributed to defects and edge states, the latter being an essential feature of these materials. The presence of zigzag edges affect the amount of the adsorbed electron donor and acceptor molecules and this is turn alters the magnetic properties of graphene.[177] The strength of materials can be improved by making composite with carbon nanotubes and has been of interest. The strength and delayed fracture of tantalum carbide (TaC) composites reinforced with long and short carbon nanotubes (CNTs) has been reported recently.[178] The TaC composite with short carbon nanotubes shows highest specific rupture strength. Shorter CNTs transform into multi-layered graphene sheets between TaC grains, whereas long ones retain the tubular structure. It is known that graphene sheets can be synthesized by chemical reduction of graphite oxide. But the as-synthesized graphene

sheets usually show low conductivity due to the presence of oxygen functional groups and large agglomeration due to van der Waals forces. For this reason, Li ions experience difficulty in intercalating between restacked graphene sheets, which limits the Li storage capacityof graphene sheets despite a high theoretical surface area and thus lower specific capacity values are observed. In this regard, the incorporation of multiwalled carbon nanotubes (MWNTs) along with the graphene sheets prevents the restacking of graphene sheets, while it also enhances the conductivity of the nanocomposite. A novel way of synthesizing graphene-carbon nanotube hybrid nanostructure as an anode for lithium (Li) ion batteries has been reported.[179] This hybrid nanostructure exhibits higher specific capacity and cyclic stability (the higher electrical conductivity of MWNTs promotes an easier movement of the electrons within the electrode).

A hybrid structure from an assembly of amorphous carbon nanotubes (a-CNTs)–reduced graphene oxide (RGO) was prepared for enhanced edge effect assisted flexible field emission device application.[180]

Carbon nanostructures prepared by chemical processes were deposited one over the other by a simple electrophoretic deposition (EPD) method on carbon cloth (CC). The hybrid carbon nanostructure showed exceptional field emission properties with significantly low turn-on and threshold field. Graphene has been used as a halogen storage material.[181] Few-layer graphene was chlorinated up to 56 weight % by irradiation with UV light in a liquid chlorine medium. However, the chlorine could be removed on heating to around 500 °C or by laser irradiation. Chlorination of graphene is a reversible process. Few layergraphene can be used to store chlorine and bromine.

7 Graphene-based nanocomposites

Nanocomposites of metal nanoparticles with dichalcogenides might find use in applications such as catalysis. In particular, cobalt and nickel particles deposited on few-layer MoS_2 are good catalysts in hydro de-sulfurization. By addition of the few-layered dichalcogenides to reduced graphene oxide resistivity can be progressively increased. Graphene-like sheets of MoS_2, WS_2, $MoSe_2$ and WSe_2 were developed employing two different methods.[182] The first method uses microwave synthesis in ethylene glycol or water medium and the second method involves laser irradiation of the bulk samples dispersed in dimethyl formamide (DMF). These grapheme-like sheets of MoS_2 exhibit room-temperature ferromagnetism and exchange bias, besides magneto-resistance. Different metal nanoparticles like gold, silver, and platinum were deposited on few-layer of metal dichalcogenide (MS_2).[183] The resistivity of the nanocomposite is found to increase with increase in the amount of MS_2. Single-sheet based transistors of GaS and GaSe have been fabricated by mechanical exfoliation from bulk crystal.[184] This has opportunities for potential applications as photodetectors, gas sensors, and optoelectronicdevices due to the large bandgap in these layered materials.Room temperature studies of bottom-gated transistor characteristics based on single-sheets of GaS and GaSe show typical n-type and p-type conductance respectively.

Very small CdSe quantum dots have been decorated on grapheme nanoribbons (GNRs) through electrochemical unzipping of single walled carbon nanotubes.[185] CdSe Q-dots have been grown on graphene nanoribbons by an *in situ* electrochemical unzipping of SWCNTs followed by a second reduction step of the oxidatively unzipped SWCNTs. This methodology gives better distribution of uniform CdSe decoration on graphene surface with accurate size control. These hybrid materials will find their applications in quantum dot sensitized solar cells, photoelectrochemical water splitting cells, photocatalysis *etc*.

One of the wide-ranging applications for semiconductor quantum dots (QD) is in the field of photovoltaics, where tunability of optoelectronicproperties helps in covering different regions of the solar spectrum thereby enabling significant absorption and use of solar energy. However several independent studies have shown that therealization of efficient photovoltaic devices out of QD materialsdepends on the ability to extract the photoexcited charge carriers (either electron or hole) from the QD before trapping or recombination of the charge carriers. In most of the QD, both the trapping and charge recombination events take place on an ultrafast time scale. To prevent fast trapping and charge recombination and extract the charge carriers, conducting polymers and carbon nanotubes (CNT) have been of interest. A new method has been devised for the synthesis and study of ultrafast charge transfer dynamics of photoexcited CdTe quantum dots (QDs)of size 2.2 nm decorated on graphene.[186] It was observed that the emission from CdTe QD-graphene gets quenched drastically which indicates the charge transfer from photoexcited CdTe to graphene. With the help of femtosecond transient absorption studies by exciting the CdTe QD particles and monitoring the transients in the visible to near-IR region, it was observed that the exciton recombination time (as monitored by the exciton bleach) of pure CdTe QD takes place within 50 ps. However, on graphene the surface exciton recombination time was found to be much longer (>1 ns) which indicates theimproved charge separation of G-CdTe composite materials as compared to that CdTe QD. The efficiency of QDSSCs is limited by several factors, including a non-uniform surface coverage and weak anchoring of QDs to the transition metal oxide, broad size distribution of QDs, sluggish photo exciton generation, and little control over recombination; all maximizing photocurrent losses. One approach to alleviate poor electron transport and transfer from the photoanode to the external circuit involves the binding of carbon nanotubes (CNTs) or graphene based nanostructures to the photosensitizer-semiconducting oxide couple. The electron accepting ability of the carbon nano-object facilitates both electron transport and transfer, thus minimizing losses and improving photocurrent generation. The electron transfer dynamics in a photoactive coating made of CdSe quantum dots (QDs) and Au nanoparticles (NPs) to a framework of ionic liquid functionalized graphene oxide (FGO) nanosheets and mesoporous titania (TiO_2).[187] A six-fold enhancement in photocurrent and an increment in photovoltage combined with an incident photon to current conversion efficiency of 27%, achieved in the composite, compared to the inferior performance of the TiO_2/CdSe/Au composite imply that FGO nanosheets and Au NPs work in tandem to

promote charge separation and furnish less impeded pathways for electron transfer and transport. Such a hierarchical rapid electron transfer model can be adapted to other nanostructures as well, as they can favorably impact photoelectrochemical performance. The role of each nano moiety in the composite, *i.e.* CdSe as the exciton generator, Au nanoparticles as an electron sink, functionalized graphene oxide for promoting electron transport and TiO_2 as the robust support, all cumulatively leading to enhanced photocurrent and photovoltage has been rationally analyzed by comparing the performance and properties of individual/twin/ternary components with that of the composite.

To increase electrocatalytic activity of monometallic and bimetallic nanomaterials, they have been incorporated into graphene to create metal-graphene composites. Reduction of Pt and Sn precursors in presence of low frequency ultrasound (20 kHz) helps in the loading of Pt and Sn monometallic and Pt–Sn bimetallic nanoparticles on the surface of reduced graphene oxide (rGO).[188] The reduced monometallic and bimetallic nanoparticles were spherical in shape with diameters around 2–6 nm, uniformly embedded on rGO sheets of few layers thickness. The electrocatalytic activity of the synthesized materials was evaluated by cyclic voltammetric studies. A novel synthetic methodology was developed for synthesizing hybrid nanostructures consisting of multiwalled carbon nanotubes (MWNT), hydrogen exfoliated graphene (HEG) and silver nanoparticles to utilize the best heat transfer properties of Ag nanoparticles, MWNT and graphene together.[189] The hybrid structure of MWNT and HEG (MWNT-HEG) has been synthesized by a simple mixing of MWNT and graphite oxide (GO) followed by exfoliation of this mixture in hydrogen atmosphere. After surface functionalization, this hybrid material was decorated with silver nanoparticles (Ag/(MWNT-HEG)) and dispersed in ethylene glycol (EG). An enhancement of about 8% in thermal conductivity was obtained for a volume fraction of 0.04% at 25 °C. A supercapacitor electrode material, cobalt doped PANI on graphene, (Gr/Co/PANI) was prepared by the *in situ* oxidative polymerization of aniline in presence of graphene and transition metal.[190] Conducting polymers are excellent candidates to fabricate hybrid materials since they have extensive π-bonding capabilities due to conjugation, which would strongly interact with the planar graphene *via* π–π stacking. The uniform structure together with high conductivity afforded high specific capacitance and good cycling stability during the charge-discharge process employing the supercapacitor electrodes. A much larger specific capacitance has been achieved for these composites in comparison with HCl doped PANI on graphene composites.

Generally Li-ion battery anodes (especially based on tin) exhibit large volume expansion leading to poor cyclic stability during charge-discharge event. To overcome this problem, composite of graphene with anode materials is useful to buffer the volume expansion. The synergestic effect of this composite material enhances the capacity of the anode material. Graphene nanosheet-SnO_2 (GNS–SnO_2) composite have been obtained using N-methylpyrrolidone as a solvent to exfoliate graphene from graphite bar with the aid of CTAB by single-phase co-precipitation method.[191] The

capacitance retention at the end of the first 10 cycles is 57%, the second 10 cycles is 77.83%, and the final 10 cycles is 81.5%. GNS–SnO_2 composite is a promising material for lithium-ion battery anode. The capacity loss in the case of graphene samples is also quite high. Some chemical modifications on the graphene substrate have already been carried out. Recently, there have been few reports about the different synthesis procedures of SnO_2-graphene based anode materials for Li ion battery applications. These SnO_2-graphene based anode materials fail to give superior charge-discharge capacities after many cycles due to the weak bonding of SnO_2 nanoparticles to the graphene support. Nitrogen doping of graphene samples shows an enhancement in specific capacity and cyclic stability due to the change in electronic structure and the creation of defects. A facile strategy was reported to synthesize SnO_2 nanoparticles dispersed nitrogen doped graphene (SnO_2/NG).[192] Nitrogen doping of graphene was carried out by the pyrolysis of polypyrrole coated poly (sodium 4-styrene sulfonate) functionalized graphene. The SnO_2 nanoparticles of 2–3 nm size are dispersed over nitrogen doped graphene by a modified polyol reduction method. The SnO_2/NG as an anode material in Li ion batteries displays superior reversible capacity, very good rate capability and excellent cyclic performance. Nitrogen doping significantly reduces the charge transfer resistance of graphene based electrodes. Nitrogen doping provided (i) high dispersion and small particle size for metal oxide nanoparticles, (ii) strong bonding of metal oxide nanoparticles with the support, which leads to a high cyclic stability for LIBs and (iii) high electrical conductivity of the graphene support. To avoid restacking of graphene layers, multiwalled carbon nanotubes (MWNTs) have been assembled along with graphene to form the supercapacitor electrode.[193] Further, RuO_2 and PANI were coated over the surface of graphene/MWNTs assemblage to attain high capacitance and energy density. Composites based on both unmodified and amine-modified graphene *via in situ* oxidative polymerization of pyrrole in presence of $SrTiO_3$has been reported.[194] The composite with unmodified graphene showed better specific capacitance but a little lower cyclability compared to that of modified graphene composite. The presence of $SrTiO_3$ ensures better thermal stability of the composites compared to that of simple graphene-polypyrrole composite. To improve the electrical and optical propertiesof chitosan-ZnO composite, hybrid composites have been synthesized with graphene oxide (GO)/mixed GO-ZnO filler using chitin or a chitosan matrix.[195] The electrical conductivity of the chitin-based GO-ZnO hybrid composites was estimated to be greater than that of the chitosan-based GO-ZnO hybrid. The chitin-based GO-ZnO hybrid composite had a higher optical band gap (3.4 eV) than the chitosan-based GO-ZnO hybrid composite (3.0 eV). The current-voltage measurement showed that electrical sheet resistance of the chitosan-based composites decreased with formation of ZnO. Previously, ZnO nanoparticles in combination with carbon nanotubes, showed improved electron accepting and storing capacity. Hence, it is reasonable; to expect that graphene sheets may play similar role of providing unique 2-D architecture to support semiconductor catalyst nanoparticle. The graphene-ZnO composites possess unusual properties as compared to their individual counterparts, and present some special

features, such as high electrical and electrochemical properties, good optical transmittance, improved field emission and capacitive properties. Graphene-based composites are emerging as a new class of materials that hold promise for many applications in different areas. Formation of graphene sheet (GSs) -ZnO composites through two-step processes has been reported.[196] Initially, graphene nanosheets were synthesized by solvothermal method and in the second-stage GSs-ZnO composite was obtained by hydrothermal method. It was observed that ZnO multipods were randomly dispersed on the surfaces of graphene sheets (GSs). In addition, a photoluminescence spectrum of GSs-ZnO multipod nanocomposites displayed fluorescence quenching. Among other composites, Mn_3O_4-GO has been investigated in detail. Mn_3O_4 is one of the most stable oxides of manganese and has a large potential for pseudocapacitor application due to its excellent electrochemical performance, environmental compatibility, relative abundance and low production cost. To improve, the capacitance of graphene oxide (GO), manganese oxide (Mn_3O_4) based thin films, GO/Mn_3O_4 composite thin films were designed using successive ionic layer adsorption and reaction (SILAR) method.[197] GO sheet has more functional groups on its basal plane and edges, which results into enhancing the loading amount of Mn_3O_4, porosity and surface area. As a result, GO/Mn_3O_4 composite exhibits higher specific capacitance and energy density as compared to GO, while larger specific capacitance and power density compared with Mn_3O_4 in neutral aqueous electrolyte. The electrochemical properties of these materials were evaluated by cyclic voltammetry, charge-discharge cyclingand impedance techniques. The results demonstrated that hybrid GO/Mn_3O_4 composite is a promising candidate for supercapacitors. MoO_2/Graphene composite for high performance anode for Li ion batteries has been synthesized by a one pot *in-situ* solution phase method.[198] 2D graphene layers entrap MoO_2 nanoparticles homogeneously within the composite. Presence of oxygen functionalities on graphene allows intimate contact between MoO_2 nanoparticles and graphene. MoO_2/Graphene is highly conducting (greater by 8 orders of magnitude) in comparison to bulk MoO_2. The layered nanostructure and the conducting matrix provide conducting pathways for charge transfer and transport between the oxide nanoparticles and graphene which are responsible for the high rate capability, a large lithium-ion capacity, and an excellent cycling stability. Impedance analyses demonstrate a lowered interfacial resistance for the composite in comparison to neat MoO_2. A novel approach has been applied to fabricate metal oxide supported conducting polypyrrole (PPy) nanocomposites, sandwiched by graphene layers.[199] This method is based on the electrostatic interactions of positively charged surfactant micelles and negatively charged graphene oxide sheets followed by reduction. Enhanced thermal stability of this hybrid composite is ascribed to the more compact structure of PPy reinforced by metal oxide nanoparticles inserted between thermally stable graphene layers. These composites exhibit significant increase in electrical conductivity which can be tuned by varing the amount of Mn doped Fe (III) oxide nanoparticles. The hybrid composites behave like semiconductors and follow 3D variable range hopping model through a range of temperatures (50–300 K).

8 Drug delivery

There has been a recent surge towards the development of new technologies in the field of drug delivery in terms of efficiency and cost effectiveness. A general *in situ* synthesis approach has been reported to prepare primary-amine-terminated mesoporous silica particles.[200] These porous particles have been incorporated with a wide range of nanoparticles such as quantum dots, iron oxide nanoparticles, doped semiconductor nanocrystals, and gold nanorods. Owing to the presence of surface functionalities on these mesoporous particles, they can be transformed for diverse applications such as drug delivery, bioimaging, and water purification. Quantum dot incorporated mesoporous particles have been used as multifunctional drug delivery carriers with simultaneous use as imaging probes. Mesoporous particles decorated with quantum dot/gold nanorod have also been used as cellular imaging probes. Post-functionalization with oleyl or TAT peptide, leads to an enhancement in their cellular interaction/uptake. The poor solubility and biocompatibility along with the disposal issues make fluorescent quantum dots such as CdSe, CdS, ZnS, InP, InAs, *etc*. impractical for imaging tissues or intercellular structures. Since calcium phosphate is the main inorganic component of human bone and teeth, hydroxyapatite ($Ca_{10}(PO_4)_6(OH)_2$,HAp) is a highly biocompatible and bioactive material.[201] Since HAp nanoparticles are not luminescent, a novel inorganic biocompatible fluorescent probe was prepared by doping HAp with lanthanides. Liquid phase pulsed laser ablation using third harmonics (355 nm) of Nd-YAG laser was used for the synthesis of fluorescent HAp nanoparticles. Europium doped HAp nanoparticles show emission with prominent peaks at 531 nm, 572 nm, 601 nm and 627 nm upon excitation at a wavelength of 325 nm. The red luminescence could also be observed under visible excitation at 459 nm and is suitable for imaging of tumor cells. Sub-nanometer sized silver clusters have also been attached to graphene *via* a covalent linker.[202] The water dispersible hybrid retains the luminescence of the cluster along with characteristics of graphene. Owing to its high adsorption property and biocompatibility, it can act as a carrier. The presence of luminescent silver clusters can be used for in-built tracking system useful for locating the drug within the blood stream. Hybrid materials of such kind also have potential as sensors and as a catalyst.

Apart from imaging, significant work has been done on encapsulation of drug molecules within various substrates in order to prevent its degradation. Several types of polymers have been used as drug delivery vehicle. Nanocarrier made of a norbornene derived isoniazid copolymer has been developed that contains well-shielded drug moieties and is soluble in both water and biological medium.[203] The biocompatibility of these drug delivery carriers have been indicated by the *in vitro* cytotoxicity assay and renal clearance analysis. Hydrazone linker chemistry has been used for covalently linked isoniazid drug for TB therapy to deliver the drug under acidic conditions. In another study by the same group[204] amphiphilic, norbornene-derived thiobarbiturate homopolymers (NDTH) loaded with doxorubicin (DOXY), a model drug has been used as nanocarrier for cancer therapy. These have a high loading capacity of about 70% w/w and can be

easily internalized by living cells as shown by Confocal Laser Scanning Microscopy (CLSM). The possibility of using poly-D-lysine (PDL)-coated CdSe copolymers as scaffolds for neuronal growth and differentiation has also been evaluated.[205] Norbornene derived phosphonate, poly-D-lysine, and phospholipid monomers were synthesized and characterized. This study elucidates the ability to synthesize and organize functionalized QDs with biologically interacting molecules and presents new opportunities in self-directed assembly that might be exploited in cell isolation, imaging, biosensors, and other applications.

Biopolymers like chitosan, derived from chitin by partial deacetylation have also been used for drug delivery. Chitin is a natural bio-polymer generally found in crustacean (crabs, shrimps and lobsters) shell and in some fungi or yeast. It is biodegradable, biocompatible, non-toxic and non-immunogenic mucoadhesive polymer. Self-assembled chitosan/insulin nanoparticles have been developed for oral insulin delivery.[206] An average of $\sim$85% insulin was encapsulated in the chitosan nanoparticles. *In vitro* release study under simulated gastric condition showed that the nanoparticles were efficient in retaining good amount of insulin, while significant amount of insulin release was noticed in simulated intestinal condition. The oral administration of chitosan/insulin nanoparticles was effective in lowering the blood glucose level of alloxan-induced diabetic mice. Another such polymer, starch acetate has been used for pharmaceutical applications because of their biocompatibility and biodegradability. Starch acetate is one of the hydrophobic biodegradable polymers currently being used or studied for controlled drug delivery.[207] Polyethylene glycol was conjugated with starch acetate to obtain an amphiphilic polymeric derivative. On its incubation with insulin solution at the critical micelle concentration, self-aggregated nanoparticles with mean particle size of 32 nm are formed. These self-aggregated nanoparticles with associated insulin have enhanced encapsulation efficiency. The mean particle size of these nanoparticles increased with the increase in the molecular weight of PEG. The above study indicated that PEGylated starch acetate nanoparticles are good bioadhesives and can be utilized as a carrier system for controlled delivery of insulin or other proteins for various therapeutic applications. Poly (3-caprolactone) (PCL) is another important biomaterial majorly used in bone repair and has wide applications in drug delivery systems, resorbable sutures *etc*. Various types of nanostructures of poly(ε-caprolactone) (PCL) were synthesized using surface modified layered silicate followed by the incorporation of drug into those nanohybrids.[208] The scaffolds of PCL and its nanohybrids with and without drugs have been prepared through electrospinning to control the dimensions of the nanofibers. The biodegradation of pure PCL and its nanohybrid scaffolds have been investigated in two different enzyme media, *e.g*. Pseudomonas cepacia lipase and Aspergillus fumigatus lipase. The enzymatic activity of Pseudomonas cepacia lipase is much higher as compared to Aspergillus fumigatus lipase indicating the specificity of the enzyme and tuned degradation. The blood compatibilities of the pure PCL and its nanohybrids were studied by platelet aggregation, platelet adhesion, and *in vitro* hemolysis assay, elucidating the excellent hemocompatibility of the novel nanohybrids. These nanohybrids have been

testified for drug delivery and show sustained and controlled release of anti-cancer drugs (dexamethasone) in the presence of two dimensional disc-like nanoparticles.

The *in vitro* cytotoxicity tests conducted for the prepared Activated Carbon Microfibres (ACF)/carbon micronanofibres (CNF) materials dispersed with Cu or Ag NPs had comparable or less toxicity compared to commercial carbon-based nanomaterials, such as CNTs and GAC. The presence of metals on the surface of fibres allowed the generation of reacting oxygen species. Cytotoxicity was found to depend on metal type and the surface charge. Larger positive surface charge caused less cytotoxicity and is attributed to the ability of the material to generate free radicals which leads to cell injury. The fluorescence microscopy images confirmed that the extent of the cell death caused by the swelling of the mitochondrial membrane was less in the ACF/CNFs as compared to CNTs.[209]

Polymeric and biodegradable nanoparticles are frequently used in drug delivery systems. Silk fibroin–albumin blended nanoparticles prepared using the desolvation method without any surfactant have been used as drug delivery vehicles.[210] These nanoparticles are easily internalized by the cells, reside within perinuclear spaces and act as carriers for delivery of the model drug methotrexate. Methotrexate loaded nanoparticles have better encapsulation efficiency, drug loading ability and less toxicity. The *in vitro* release behavior of methotrexate from the nanoparticles suggests that about 85% of the drug gets released after 12 days. The encapsulation and loading of a drug would depend on factors such as size, charge and hydrophobicity, which affect drug release. MTT assay and conjugation of particles with FITC demonstrate that the silk fibroin–albumin nanoparticles do not affect the viability and biocompatibility of cells. This blended nanoparticle, therefore, could be a promising nanocarrier for the delivery of drugs and other bioactive molecules. Dextran vesicles based on renewable resource starting materials were designed as a delivery vehicle for encapsulation of both hydrophobic anticancer drug camptothecin (CPT) as well as water-soluble Rh-B molecules (or drugs).[211] These newly synthesized dextran-PDP (DEX-PDP) amphiphilic polymers self-assembled to form vesicles of size of $\sim$120 nm under physiological conditions. The vesicular structures were found to efficiently encapsulate CPT in the unilamellar pocket and also retained the active lactone pharmacophore in CPT (more than 10 times) better compared to CPT alone in PBS. The hydrophilic and hydrophobic segments in dextran vesicles are made up of aliphatic ester-linkage which is cleaved by esterase (as stimuli) for the large drug release under physiological conditions. *In vitro* drug release studies confirmed that the vesicular scaffolds with water-soluble dye (or drug) showed enhanced stability against esterase for more than 12 h. The efficiency of the drug in killing the cells was found to be better (2.5 times) when encapsulated in the vesicles compared to CPT alone. The dual loading capability of these vesicles for both hydrophilic and hydrophobic guest molecules (and drugs) provides a new opportunity to study the combination of two drug loadings in a single nanoscaffold.Since polymers have been extensively studied as drug delivery vehicle, information about their interaction with the guest *i.e.* the drug molecule becomes essential. Sarkar *et al.*[212] have investigated these

kind of interactions existing between two polymers poly (acrylamide) (PAAm) and poly (vinyl alcohol) forming an interpolymer complex. The variation in the properties of the interpolymer complex with varying molecular weights of PVA has been looked into. Higher the molecular weight of PVA, higher the hydrophobicity imparted and greater is the interaction. Furthermore, the host-guest interaction between the interpolymer complexes and β-cyclodextrin (β-CD) has also been studied. The results indicate the occurrence of a competitive interaction between the hydrogen bonding of the interpolymer complexes and the host-guest interaction with β-CD, whereby the latter predominates. It is probable that the hydrophobic cavity of β-CD is threaded with linear polymers, thus forming a macromolecular supra-assembly. Also, there exists a preferential interaction of PAAm with β-CD by compromising its interaction with PVA. The enhanced deposition and retention of actives with this system was studied with a single species regrowth assay, antibacterial efficacy and the cell viability were studied using the live-dead staining protocol. This therefore opens new avenues in the targeted delivery of active molecules. Biocompatible Rhodamine B[213] loaded gelatin nanoparticles have been synthesized with the aim to use them as drug delivery systems exhibiting controlled release rates. To decrease the release rate of the dye, fatty acid has been polymerized on the surface of the gelatin capsules or coacervates forming protective shells. The nature of fatty acid loading and chain length affects the release from nanocapsules and it has been shown that the chain length and the hydrophobicity of the precursor fatty acid plays a governing role in the efficacy and the delayed release ability of the synthesized nanoparticles. Oleic acid based RhB-GNPs showed a slower release and a better loading efficacy compared to myristoleic acid based RhB-GNPs owing to a longer alkyl chain length of the former. The results clearly indicate the superiority of the encapsulated nanoparticles over bare organic fluorescent dye molecules which are useful for probe-labelling for sensitive target detection. Core-shell nanostructures have been used for the targeted and efficient delivery of therapeutics to tumor cells.[214] Temperature and pH responsive core–shell nanoparticles have been synthesized by comprising smart polymer shell coated on magnetic nanoparticles as an anticancer drug carrier and cancer cell-specific targeting agent. Amine groups have been introduced on magnetite nanoparticles (MNPs). Using EDC/NHS chemistry, dual-responsive poly (N-isopropylacrylamide)-block-poly-(acrylic acid) copolymer was attached to the amine-functionalized MNPs. To accomplish cancer-specific targeting properties, folic acid was tethered to the surface of the nanoparticles. Rhodamine B isothiocyanate was also conjugated to endow fluorescent property to the MNPs for cellular imaging applications. Doxorubicin (DOX), an anticancer drug was loaded into the nanoparticles and its release behavior was subsequently studied. A sustained release of DOX was observed at the desired lysosomal pH and temperature condition. Intracellular-uptake studies revealed preferential uptake of these nanoparticles into cancer cells (HeLa cells) compared to normal fibroblast cells (L929 cells). The *in vitro* apoptosis study revealed that the DOX-loaded nanoparticles caused significant death to the HeLa cells. Nanotechnology has been closely associated with pharmacy and provides intelligent systems,

devices and materials for better pharmaceutical applications. Solid lipid nanoparticles (SLN) are a new pharmaceutical delivery system. They are typically spherical with an average diameter between 10 to 1000 nanometers and possess a solid lipid core matrix that can solubilize lipophilic molecules. The lipid core is stabilized by surfactants (emulsifiers). The term lipid is used in a broader sense and includes triglycerides (*e.g.* tristearin), diglycerides (*e.g.* glycerol bahenate), monoglycerides (*e.g.* glycerol monostearate), fatty acids (*e.g.* stearic acid), steroids (*e.g.* cholesterol), and waxes (*e.g.* cetyl palmitate). Here, we report some of the important development in the field of pharmacy using solid lipid nanoparticles (SLN). Pentacyclic triterpenediol (TPD) from Boswellia serrata has shown significant cytotoxic and apoptotic potential in a large number of human cancer cell lines. To enhance the efficiency of this drug towards cancer treatment, these molecules have been encapsulated in solid lipid nanoparticles. Microemulsion method was used for the synthesis of TPD loaded SLNs.[215] TPD loaded SLNs showed significantly higher cytotoxic/antitumor potential than the parent drug. TPD-SLNs have 40–60% higher cytotoxic and apoptotic potential than the parent drug in terms of IC50, extent of apoptosis, DNA damage, and expression of pro-apoptotic proteins like TNF-R1, cytochrome-c, and PARP cleavage in HL-60 cells. Blank SLNs did not have any cytotoxic effect on the cancer as well as in normal mouse peritoneal macrophages. The *in vivo* antitumor potential of TPDSLNs was significantly higher than that of TPD alone in Sarcoma-180 solid tumor bearing mice. Therefore, SLNs of TPD successfully increased the apoptotic and anticancer potential of TPD at comparable doses (both *in vitro* and *in vivo*). Thus by using the solid lipid nanoparticles, therapeutic efficacy can be improved. Oral administration of isoniazid leads to low levels of isoniazid into plasma due to its high aqueous solubility, poor permeability and rapid and extensive hepatic metabolism. Further, a small $t_{1/2}$ of 1–4 h indicates a shorter stay in plasma and thus the need for repetitive or high doses. This may result in hepatotoxicity and neurotoxicity. To increase the bioavailability of the drug and prolonged effect, isoniazid-solid lipid nanoparticles (SLNs) were prepared.[216] Developed SLNs showed high entrapment efficiency (69%) and small size (<50 nm) such that they can bypass reticulo-endothelial system (RES) pickup resulting in prolonged circulation times. Since liver is the major site of metabolism of isoniazid, RES avoidance will reduce its elimination from the body. Single dose (25 mg/kg BW) oral pharmacokinetic studies were performed in plasma and various tissues of rats. A significant improvement ($p<0.001$) in relative bioavailability in plasma (6 times) and brain (4 times) was observed after administration of isoniazid-SLNs with respect to the free drug solution at a dose of 25 mg/kg BW. Isoniazid-SLNs showed a 3 times higher LD50. Thus solid lipid nanoparticles are beneficial for improving the life time of the drug.Rifampicin (RIF) is a vital constituent of antitubercular therapy, thus it is essential that the chemical activity remains intact under physiological conditions. However, it is observed that the drug undergoes hydrolysis at the acidic pH of the stomach. The degradation is further enhanced by its interaction with Isoniazid (INH). It was observed that both the drugs *i.e.* 26.5% of RIF and 1.43% of INH was decomposed at gastric pH.[217] Solid lipid nanoparticles (SLNs) are observed to avoid drug–drug

interaction and protect the drug against degradation. Thus, RIF has been incorporated into SLNs. As a result, the degradation got reduced to ~9% (from 26.50% when present alone) and to ~20% (from 48.81% when INH was also present). INH was also incorporated into SLNs and the percent degradation of RIF in this combination (RIF SLNs + INH SLNs) further reduced to12.35%. Thus, SLNs, besides limiting the interaction, also constitute a potential drug delivery system for antitubercular therapy.

Nanoparticles have also been used for the treatment of acne, a common skin disease in teenagers.[218] It is caused by Propionibacterium acnes (P. acnes) and Isotretinoin (ITR) is reported to have immense antiacne potential. The effect of its encasement in nanocarriers on its minimum inhibitory concentration (MIC) has been evaluated. MICs of pure drug and entrapped drug in nanolipid carriers (ITR-NLCs) and in solid lipid nanoparticles (ITRSLNs) were determined and it was found that these lipid-based nanocarriers decreased the MIC of ITR and also helped to retain the drug at the desired sites like various skin layers. Nanocarriers loaded with ITR, which is, SLNs and NLCs, enhanced the antimicrobial activity even at lower concentrations vis-à-vis the drug alone and improved drug transport potential vis-à-vis the commercial gel.

Encapsulation of natural drugs to provide protection against degradation has also been studied. Curcumin is reported to show *in vitro* anticancer effects in human cancer cell lines and majorly in the carcinogenesis of gastrointestinal tract (GIT), in animals. Its poor pharmacokinetics and stability limit its vivo clinical efficacy for other systemic cancers. A huge enhancement in the bioavailability (32-155) of curcumin was observed when it was incorporated in solid lipid nanoparticles (C-SLNs).[219] A reduction (~ by 54–85%) in IC50 values was observed with developed C-SLNs in comparison to free curcumin against a panel of human cancer cell lines (HL-60, A549, and PC3). Similar mechanisms were observed to those claimed for free curcumin, including induction of cellular apoptosis by activation of caspases, release of cyctochrome c, loss of membrane potential, blockade of nuclear factor kappa B (NF-κB) activation, and upregulation of TNF-R for C-SLNs. The extent of cell death provided by C-SLNs in all these tests was significantly higher ($p < 0.001$) which is attributed to the presence of curcumin in a dispersible/soluble form which increased the permeability across the cell surface. The display of significantly better *in vitro* anticancer effect coupled with high *in vivo* bioavailability points toward a great potential of using CSLNs for cancer therapeutics. Silica gel has also been used as a suitable host for herbal components like Terminalia chebula (Haritoki).[220] The release kinetics of the extract was observed in both 0.1 N HCl, pH of 1.2, and phosphate-buffer saline (PBS), pH of 7.2. Different dissolution models were applied to evaluate the release mechanisms and kinetics. Biphasic release patterns were found in every formulation for both the buffer systems. The kinetics followed a zero-order equation for first 4 h and a Higuchi expression in a subsequent timeline in the case of 0.1 N HCl. In the case of PBS, the formulations showed best linearity with a first-order equation followed by Higuchi's model.[221] The sustained release of the extract predominantly followed diffusion and super case II transport mechanism. The release value was always above the

minimum inhibitory concentration. Hydrophobic enkephalin analogue has been reported to self-assemble to form diverse nanostructures like organogel, nanotubes and nanovesicles.[222] *In vitro* encapsulation of curcumin by the peptide nanovesicles was studied and controlled release through pore formation was observed. Drug entrapped in opioid nanovesicles ensures protection against degradation and also leads to a longer shelf life. The special design *i.e.* two-in-one combination of curcumin-encapsulated opioid nanovesicles is helpful in increased brain entry and potential in recovering from Central Nervous System-mediated diseases and pain. In a similar effort to curb cancer[223] a near-infrared (NIR)-light controlled release of drugs has been demonstrated using graphene oxide(GO) composite microcapsules. On irradiation, local heating causes the rupture of the microcapsules and in turn triggers the light-controlled release of the encapsulated anticancer drug doxorubicin (Dox) from these capsules. Apart from graphene, its derivatives are being used for several important biomedical applications including drug delivery, gene delivery, contrast imaging, and anticancer therapy. Detailed studies on the interaction of both pristine and functionalized graphene with macrophage cells and human blood components have been carried out. Macrophages showed relatively high intracellular uptake of functionalized, hydrophilic graphene compared to the hydrophobic *p*-G, which was found to be mainly retained on the cell surface.[224]

An antithrombotic stent surface has been developed by appropriate surface modification of biocompatible metallic titanium (Ti) to address the stent restenosis issues.[225] An array of unique, intregrated TiO_2 nanostructures were developed on a metallic Ti surface using simple aqueous chemistry. All nanostructured samples showed significantly enhanced cellular viability and proliferation of endothelial cells, with raised levels of nitric oxide and substantially decreased smooth muscle cell proliferation and platelet adhesion in comparison to unmodified Ti. The benefits of such nanomodifications on metallic Ti are a solution to reduce the probability of late stent thrombosis that is associated with bare metallic stents.

Gold nanoparticles are increasingly being used in drug delivery and diagnostics. The stability and toxicity (*in vitro* and *in vivo*) has been evaluated for water soluble and surface functionalised GNPs.[226] Three different capping materials aspartic acid (GNPA), trisodium citrate dihydrate (GNPC) or bovine serum albumin (GNPB) has been used to conduct the study. Depending on the nature of surface groups, they behave differently. GNPB was found to be extremely stable, where the capped protein molecule (on the nanoparticles) successfully maintained its secondary structure and helicity, whereas colloidal stability of GNPA was most susceptible to altered conditions. Slight hepatotoxic and nephrotoxic response was observed for citrate and aspartic acid coated GNPs. The BSA coated GNP was found to be the best in terms of biocompatibility indicating that surface functional groups have a direct role in the toxicity. Green chemical routes have been developed for the synthesis of gold nanoparticles. Azadirachta indica mediated GNPs have been used as nano-vehicles for the efficient delivery of doxorubicin (DOX).[227] The stability of GNPs due to the biological capping agents was scrutinized by measuring the flocculation

parameter which was found to be in the range of 0–0.65. Doxorubicin was attached on the surface of these capped GNPs along with activated folic acid (FA) as navigational molecules for targeted drug delivery. The GNPs-FA-DOX complex was found to be non-toxic for normal cells and considerably toxic for HeLa cells. The drug loading capacity of the GNPs was found to be 93%. Doxorubicin release kinetics using GNPs followed 1st order kinetics at pH 5.3 and is ideal for solid tumor targeting. In a similar type of study, AuNPs-based drug delivery system (DDS) (Au-DOX) containing doxorubicin (DOX), a FDA approved anticancer drug has been developed *via* a low-cost and eco-friendly green chemistry approach.[228] A water extract of Eclipta Alba leaves was used to synthesize gold nanoparticles at room temperature. The presence of phenolic and protein molecules present in eclipta extract offers extra stabilization to AuNPs. As compared to pristine doxorubicin, a significant inhibition in the proliferation of breast cancer cells was observed when the gold based drug delivery was administered to breast cancer cells (MCF-7 and MDA-MB-231). Even though gold nanorods (Au NRs) are popular for biomedical applications, there are certain factors like surfactant toxicity, biological stability and controlled drug release kinetics, which limit its application. Premkumar *et al.*[229] have developed Au NR–doxorubicin conjugates (DOX@PSS-Au NR) with improved drug loading efficiency (55–56%) and minimum CTAB toxicity, by employing Au NRs (0.5–4.4 aspect ratio) coated with poly(sodium 4-styrenesulfonate) (PSS). DOX@PSS-Au NR conjugates exhibited higher biological stability with sustained drug release kinetics at pH 5. The anti-cancer potential and apoptosis inducing efficiency of DOX@PSS-Au NR conjugates in MCF-7 cells revealed higher therapeutic efficiency when compared to free DOX, as corroborated with *in vitro* cytotoxicity assay.

It is observed that the "space" in the vicinity of enzymes plays a crucial role in regulating their activity. The microstructural parameters, including surfactant head group, tail length, counter ion *etc*. has a pronounced effect.[230] Also, enzymes present at an augmented domain in reverse micelles exhibit superior activity due to increased substrate concentration and conformational flexibility of biocatalysts. The interfacial area could possibly be increased if gold nanoparticles (GNPs) are localized at the interface instead of solubilizing within the water pool. In this regard, with an aim to enhance the interfacial area which directly affects the efficiency of the enzyme, thiol-assisted confinement of gold nanoparticles has been used. With the help of bidentate dithiol ligands, higher number of GNPs were localised at the interfacial domain which enhanced the total space in vicinity of enzyme. As a result, the hydrolytic efficiency of lipase in 1,6-hexanedithiol included GNP ($\sim$20–25 nm)-doped CTAB reverse micelles by $\sim$3.4 fold as compared to that in only CTAB. In addition to the traditional drug delivery methods, new class of materials like perylene-3-ylmethanol fluorescent organic nanoparticles have also been used as a drug delivery system.[231] It is a single-component photoresponsive nanocarrier based on fluorescent organic nanoparticles consisting of perylene-3-ylmethanol that can act both as the nanocarrier for the drug and the phototrigger for the drug release. The presence of fluorescent chromophores can be used for cell

imaging; and as detectors for real time-monitoring of drug release. *In vitro* biological studies revealed that the newly developed perylene-3-ylmethanol nanoparticles exhibit good biocompatibility and cellular uptake as well as efficient photoregulated anticancer drug release ability.

Smart materials (with multiple functionalities each serving a specific purpose) have also been developed so that the efficiency of the targeted delivery can be enhanced. Magnetic mesoporous amorphous calcium phosphate nanoparticles *i.e.* porous amorphous calcium phosphate/$CoFe_2O_4$ integrated composite nanoparticles with a size $\sim$62 nm and –COOH groups on the surface have been prepared by a simple method.[232] The particles show excellent aqueous dispersion stability in physiological pH without any deterioration in hydrodynamic size and zeta potential. Owing to the presence of the carboxylate groups on the surface, the platinum pharmacophore cis-diaquadiamine platinum (II), folic acid and rhodamine isothiocyanate were conjugated on these magnetic calcium phosphate nanoparticles. The cytotoxicity and internalization efficiency of these nanocarriers have been evaluated on folate receptor over expressed HeLa cells. These drug loaded nanoagents exhibit elevated cytotoxicity and induce apoptosis in HeLa cells. Water soluble mesoporous (magnetic and luminescent) Fe_3O_4@mSiO_2@YPO_4:Tb nanoparticles with core–shell structures have been prepared.[233] The mesoporous silica coating makes the hydrophobic iron oxide water soluble and reduces the probability of fluorescence quenching. These hybrid nanospheres were functionalized with cyclodextrin and folic acid using glutathione as a coupling agent. The cyclodextrin functionalized particles show high loading capacity and pH sensitive sustained release behavior for the anticancer drug 5-FU. The presence of folic acid on the surface makes it a site specific drug carrier for 5-FU.

Green chemical routes have been used to synthesize magnetite/gold (Fe_3O_4/Au) hybrid nanoparticles from a single iron precursor (ferric chloride) and grape seed proanthocyanidin as the reducing agent.[234] These nanohybrids displayed superparamagnetism with high magnetic saturation and relaxivity (124.2 ± 3.02 $mM^{-1}s^{-1}$). The combination of gold with magnetite resulted in efficient CT contrast, which was found to be superior to the conventional iodine-contrast agents. Cytotoxicity and oxidative stress analysis revealed the biocompatibility of this material even at high doses and long incubation periods.

9 Water purification

Water, as we all know, is an essential companion of life on earth. It is vital to us, both as a universal solvent as well as being an important component of metabolic processes within the body. With the growth of various industries, environmental pollution has also gone up drastically and lack of clean water affects millions across the world. Nanotechnology based concepts, processes and devices are expected to offer effective, efficient, durable, environmentally friendly approaches that can lead to more cost-effective, less time and energy consuming and less waste generation technologies. Different classes of materials have been used for purification

process starting from silica to graphene oxide. Here we discuss some of the recent measures being undertaken in order to control water pollution.

Hybrid soft materials which promote significant enhancement in the material properties have recently gained a lot of importance. Magnetite–silica nanocomposites of ~ 30 nm size have been synthesized and utilized for different applications such as tagging (attachment of fluorophores Rhodamine, Rh B), entrapment matrix (zinc loading) and removal of arsenic for water purification.[235] Maximum sorption capacity of 170 mmol g^{-1} towards arsenic ions has been observed for these magnetite–silica nanocomposites. Nandi *et al.*[236] have developed one such new functional hybrid system that is composed of a LMWG and a polymer, the latter acting as a binding/branching agent of the small molecular gel fibers. Folic acid (F, vitamin B9), based small molecular gel in water–DMSO forms a nano-fibrous network morphology with chitosan. The fibrillar diameter of the FC hybrid gel (10.5 nm) is much lower than that of F gel (17.3 nm). The fluorescence intensity of the FC hybrid gel is enhanced by 2.75 times than that of F gel. As a result of composite formation, the shear viscosity of FC hybrid gel is 3 orders higher than that of the F gel. This newly developed FC hybrid gel has also been explored for the contaminant extraction from aqueous medium. Three dyes, Eosin Yellow (EY), Methyl Orange (MO) and Methylene Blue (MB), and some metal salts like chromium(III), cobalt(II) and copper(II) chlorides were chosen for absorption into the FC hybrid gel matrix.The dye absorption by the hybrid gel material is maximum for Eosin Yellow, (83.5%), while the either two are observed to a lesser extent. The FC hybrid gel absorbs 55% of Cu^{2+}, 67.2% of Cr^{3+} and 49% of Co^{2+} from their respective solutions.

To study the matrix-nanoparticle interaction, a polyacrylamide grafted carboxymethyl tamarind (CMTg-PAM) and a SiO_2 nanoparticle are used to synthesize a nanocomposite, CMT-g-PAM/SiO_2.[237] Because of their higher hydrodynamic radius as well as hydrodynamic volume, these nanocomposites show significantly high absorption of methylene blue (MB) dye. CMT-g-PAM/SiO_2 exhibited a maximum adsorption capacity (Qmax) of $43.859\,mg \cdot g^{-1}$. The efficiency of the adsorption process from an aqueous solution of the dye, has been improved by changing various factors like pH, temperature of the solution, time of adsorption, agitation speed, concentration of dye in the aqueous solution, and amount of adsorbent.The adsorption behavior of the nanocomposite shows that adsorption kinetics and isotherms are in good agreement with pseudo-second-order and Langmuir equations respectively. Negative values of ΔG° confirmed the spontaneous nature of adsorption.

Eco-friendly strategies have been developed to prepare sulfur/reduced graphene oxide nanohybrid (SRGO) (sulfur nanoparticles of average size ~ 20 nm) using the combined effect of the polyphenolic compounds and acids present in citrus lemon juice.[238] This nanohybrid demonstrates a fast and efficient Hg^{2+} removal at around pH 6–8. It was observed that the adsorption kinetics follows pseudosecond-order kinetics and the isotherm is well described by the Langmuir model. The thermodynamic parameters suggest that the adsorption process is endothermic and spontaneous. The nanohybrid also has excellent reusability and high selectivity of Hg^{2+}owing

to strong interaction between Hg^{2+} ions and the sulfur nanoparticles present on the surface of graphene sheets and an electrostatic attraction between the free exposed surface of the adsorbent and the metal ions. About 90% of Hg^{2+} removal is observed within 15 mins.

A green method for the synthesis of graphenic material from cane sugar, a common disaccharide has been reported. Graphene sand composite (GSC) was synthesized by combining graphene and sand for the effective removal of contaminants from water.[239] Fig. 11 a shows the FESEM image of the as synthesized GSC. Rhodamine 6G (R6G) as a model dye and chloropyrifos (CP) as a model pesticide were used to demonstrate this application. The spectroscopic and microscopic analyses coupled with adsorption experiments have revealed that physical adsorption plays a dominant role in the adsorption process. Isotherm data in batch experiments show an adsorption capacity of 55 mg/g for R6G and 48 mg/g for CP, which are superior to that of activated carbon as shown in Fig. 11b. The adsorbent can be easily regenerated using a suitable eluent.

In another report by the same group, graphene-sand composite (GSC) was synthesized using a cheap and abundant material, asphalt as the carbon precursor.[240] It was observed that the adsorption is highly dependent on the particle size, and carbon loading on sand particles. The adsorption capacity of GSC is 75.4 mg/g while it is 44.7 mg/g for activated carbon (AC) in the case of R6G. Since the carbon source used for the synthesis is cheap, large quantity of graphenic materials can be prepared in a cost effective manner and can be used for water purification.

A green chemical approach has been used to synthesize nano-silver bioconjugate (NSBC) on the surface of *R. Oryzae* which exhibits strong antimicrobial activity and adsorption affinity for organophosphorus pesticides.[241] The NSBC exhibits strong antibacterial activity against *Escherichia coli* and *Bacillus subtilis* and high adsorption capacity towards different organophosphorous pesticides. This has also been exploited to obtain potable water free from pathogens and pesticides in one step process.

Design of newer materials bearing gold nanoparticles (AuNPs) in ordered assemblies of controlled shape, size distribution, and surface functionality has been on the surge. This feature has been achieved using the technique

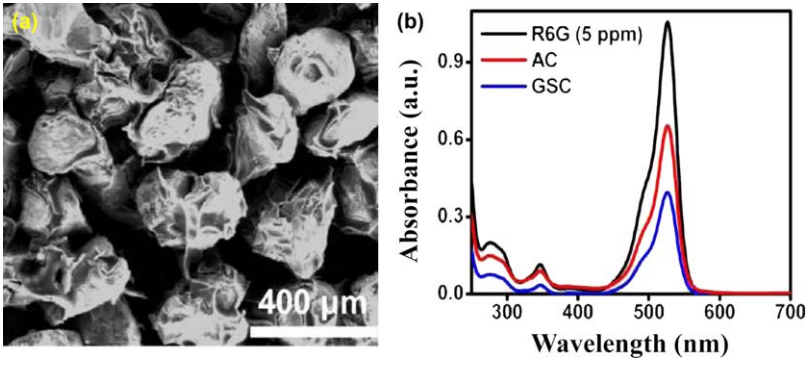

Fig. 11 (a) SEM images of graphene sand composite, (b) comparison of removal capacity among Graphene sand composite and Activated carbon. Adapted from reference 239.

called layer-by-layer (LbL) assembly.[242] Multilayers of poly(diallyldimethylammonium chloride) (PDDA) and citrate capped Au nanoparticles (AuNPs) anchored on sodium 3-mercapto-1-propanesulfonate modified gold electrode by electrostatic layer-by-layer assembly (LbL) technique have shown promising results for the direct electrochemical oxidation of As(III) species. The analytical utility of the architecture with five bilayers is exploited for arsenic sensing *via* the direct electrocatalytic oxidation of As (III), and the detection limit for As (III) species is found to be 4.36 ppb, well below the WHO guidelines of 10 ppb in drinking water. When the non-redox active PDDA is replaced by the redox active Os(2,20-bipyridine)2Cl-poly(4-vinylpyridine) polyelectrolyte (PVPOs) in the LbL assembly, the performance is found to be inferior, demonstrating that the redox activity of the polyelectrolyte is futile as far as the direct electro-oxidation of As(III) is concerned.

Stable nanocolloids of monoclinic sulfur (b-SNPs) were prepared through 'water-in-oil microemulsion technique.[243] β-SNPs-colloids expressed excellent antimicrobial activities against a series of fungal and bacterial isolates with prominent deformities at their surface. In contrast, insignificant cytotoxicity was achieved against the human derived hepatoma (HepG2) cell line upon treatment with b-SNPs. A simultaneous study was performed to determine the stock concentration of b-SNP-colloids using a novel high phase liquid chromatographic method. Cumulative results of this study hence, elucidate the stabilization of nanosized monoclinic sulfur at room temperature and their potential antimicrobial efficacy over micron-sized sulfur.γ-Fe_2O_3 incorporated mesoporous silica particles of 50–100 nm size have been synthesized which are easily separable and exhibit high efficiency in removal of toxic ions.[244] Chelating agents like EDTA have been tethered on the surface of particles. These particles are water dispersible but aggregate in response to the external magnetic field and have been used for high performance and selective removal of Cd, Pb, Hg and As. It was found that $\sim$one gram of functional magnetic mesoporous silica (MMS) can purify one liter of contaminated water with efficiency $>90\%$ and can be reused without compromising on efficiency.

Mesoporous aluminophosphate has been used as efficient adsorbent for the removal of toxic metal ions like Fe^{3+}, As(III/V), Cd(II), and Hg(II) from their respective aqueous solutions.[245] Tiny nanoparticles of mesoporous aluminophosphate have been synthesized through solvothermal method in presence of a long chain fatty acid as template. The mesophase material showed excellent adsorption capacity for the pollutant heavy metal cations and can be utilized as a potential candidate for the remediation of contaminated ground water. The cation removal efficiency in percent (%) and distribution co-efficient for As (III) are 83.75 and 5.15×10^3(mL/g), respectively whereas for As(IV) these respective values are 90.08 and 9.08×10^3 (mL/g). whereas the respective cation removal efficiency of the Fe, Hg, and Cd are89.89, 94.76, and 74.48 and respective distribution co-efficient of the corresponding metal cations are 8.84×10^{3}, $1.8 \times 10^4$and 2.92×10^3.

Nanoparticles (NPs) have been extensively used for environmental remediation and thus require a detailed understanding of the mechanistic aspects of the interaction between the species involved.[246] A model

pesticide, chlorpyrifos (CP), belonging to the organophosphorothioate group, has been chosen and studied using different concentration of silver and gold NPs insupported (on neutral alumina) and unsupported forms. It is shown to decompose to 3, 5, 6-trichloro-2-pyridinol (TCP) and diethyl thiophosphate at room temperature over Ag and Au NPs, in supported and unsupported forms. With support from various instrumental techniques like absorption spectroscopy and electrospray ionization mass spectrometry (ESI MS), transmission electron microscopy, energy dispersive analysis of X-rays, Raman spectroscopy, and X-ray photoelectron spectroscopy (XPS), it is proposed that the degradation of CP proceeds through the formation of AgNP – S surface complex. In this complex, the P–O bond cleaves to yield a stable aromatic species, 3, 5, 6-trichloro-2-pyridinol (TCP). Degradation rate was found to be affected by temperature and pH. The rate of degradation of CP by Ag NPs is greater than that of Au NPs. The results have implications that noble metal NPs can be employed for drinking water purification, as pesticide contamination is prevalent in many parts of the world.

A methodology for easy sensing and removal of heavy metal ions such as Hg^{2+}, Ag^{+}, and Pb^{2+} in water has been developed. The cation-exchange of CdS Q-dots is followed by the characteristic color development, with Hg^{2+}-exchange showing the most vivid transformation due to the bright yellow color formation, while brown coloration was observed in other metal ions. This methodology can also be used for the synthesis of stable colloidal HgS, Ag_2S, and PbS Q-dots (which are difficult to synthesize in the aqueous phase) from biopolymer-stabilized CdS Q.dots through a cation exchange process.[247] Further, ZnS Q-dot impregnated chitosan film was used to remove heavy metal ions from contaminated water as measured using atomic absorption spectroscopy (AAS). Instead of particles, films can be used as catalysts to degrade azo dyes in aqueous solution. Cu_2O NPs embedded films showed excellent stability and reusability which can find application for treatment of waste water. Synthesis of Cu_2O NPs in alumina followed by controlled reduction allows the outer surface of Cu_2O to be transformed to Cu to generate Cu_2O@CuNPs with tunable core/shell structure.[248]

Though we have not dealt with devices or technologies and kept the theme of this article around ''nanoscience'', we would like to mention one or two devices –based research published in the last two years. Fabrication of Resistor-Capacitor (RC) filters and field effect transistors (FETs) has been reported based on pencil drawings on paper, which contain turbostratic graphite crystallites as evidenced from Raman analysis.[249] Pencil drawings have been employed as resistor and an ion gel, 1-butyl-3-methylimidazolium octyl sulfate mixed with polydimethylsiloxane (PDMS) as dielectric, for the fabrication of RC filters with a cut-off frequency of 9 kHz. Fig. 12a shows the two probe current–voltage characteristics of a pencil-trace on paper substrate. Fig. 12b shows the normalized resistance of the pencil-trace on paper (width, 3 mm; thickness, 50 mm) over different lengths. The carrier mobilities were found to be $\sim$106 and 59 $cm^2\ V^{-1}\ s^{-1}$ for holes and electrons, respectively. This offers a simple, solvent-free, low-cost method of fabricating filters and transistors on paper substrate, in use-and-throw away applications not involving critical performance criteria. Fig. 12 (c) shows

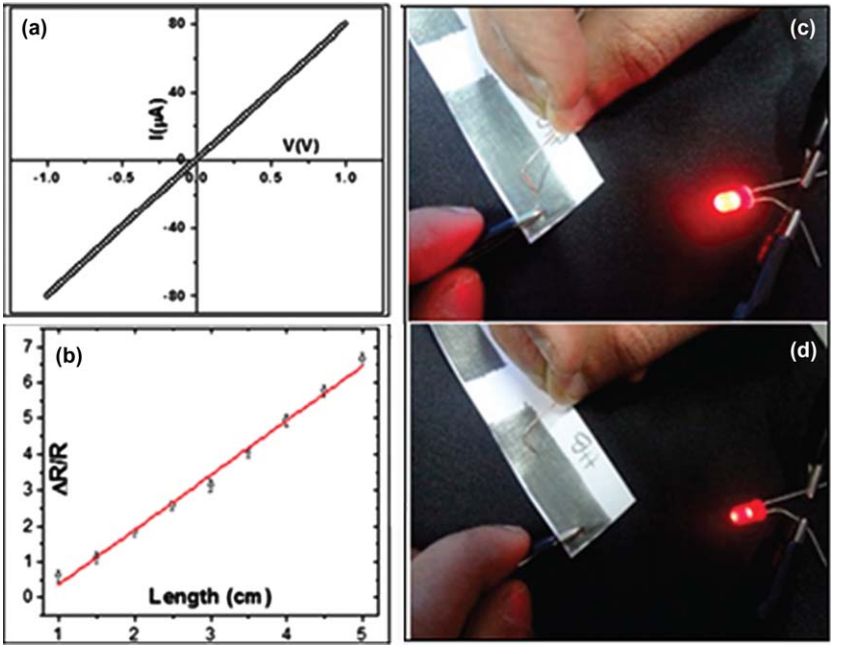

Fig. 12 (a) Two probe current–voltage characteristics of a pencil-trace on paper substrate. (b) Normalized resistance of the pencil-trace on paper (width, 3 mm; thickness, 50 mm) over different lengths. (c, d) Photographs showing the varying brightness of an LED based on the resistance of the pencil-trace. Adopted from reference 249.

the change in the brightness of an LED with the resistance of the pencil-trace. Fabrication of pencil-on-paper devices does not require any sophisticated facilities (clean room) and high end fabrication equipment. Future work may include the fabrication of large area pencil-trace based devices created using pencil plotters which may pave way to affordable, use and-recycle electronics.

An innovative large area metal–molecule–metal electrode system has been proposed for the electrical analysis of molecules.[250] The molecular top contact is essentially a single crystalline, atomically smooth, (111) oriented Au microplate glued to the end of a carbon microfibre. The device works in capacitor geometry with the chosen SAM in between the top and bottom metal electrodes, the latter being a physically deposited Au film. Polymer encapsulation of the device greatly enhanced the stability of the device. This device promises new ways of analysis, particularly involving dynamic studies such as of thermal phase transitions and the behavior of molecules under loading. Advantage of the device is its ability to be stored after fabrication for off-the-peg self-assembly. This is truly a stand-alone device not relying on sophisticated instrumentation such as STM.

Embedding ZnO nanoparticles into a SU-8 matrix, photo-curable nanocomposite material has been formulated and their piezoelectric properties were studied for low cost fabrication of self-powered nanodevices.[251] Photopatternabilty of nanocomposite was optimized for various filler concentrations. The piezoelectric coefficient of ZnO nanoparticles was

observed to be ranging between 15 and 23 pm/V, which is the highest reported. An increase in the Young's modulus of SU8 was observed with the increasing ZnO content. An SU-8/ZnO polymer composite cantilever structure was fabricated in order to demonstrate the photo-patternability of these composite structures with a 15 wt.% ZnO. The photo-curable property of these polymer composite films is exploited to demonstrate fabrication of a micro-cantilever test structure.

Aluminium-doped zinc oxide (AZO) thin film transistor, embedded in a polymer microcantilever has been developed for nano-mechanical sensing applications.[252] Due to a change in the carrier mobility of the semiconducting layer, the device senses the surface stress. Due to the low Young's modulus and high strain sensitivity of the AZO layer, this microcantilever shows a deflection sensitivity of 116 ppm per nanometer of deflection. Also, mechanical characterization of these devices shows that the resonance frequency to be 50 kHz which is suitable for sensor applications while the spring constant of these devices is 0.9 N/m.

10 Conclusions

The above perspective shows that during the past year and half (2012–2013) research in nanoscience have brought out significant contributions from India especially in the areas of carbon nanostructure-based technologies, photocatalysis, sensors and nanobiotechnology.

We find that as earlier a great amount of research is still focused on the synthesis and characterization of nanostructures. However a qualitative change is that the work is focused on nanomaterials with a specific application. This is a very important change. In addition, the proportion of research showing the specific application along with synthesis has increased. In this direction, research on catalysis (photo catalysis and electrocatalysis included) and sensors have been very productive. Research of nanocomposites with biopolymers and more importantly drug delivery and related work based on nanostructures has also been at the forefront of nanoscience research in India during 2012–2013.

There have been large numbers of publications in Royal Society of Chemistry, American Chemical Society, APS and VCH journals with *Chem Commun., J. Mater. Chem., RSC Advances, PCCP, J. Phys. Chem., Soft Matter, ACS Nano, Langmuir, Appl. Phys. Letts., Angewandte Chemie, Chem. Eur. J., Chem. Asian J.* and *Advanced Functional Materials* being among the popular high impact factor journals. There have also been some contributions to journals like *Nature* and its sister publications in the past (*Nature Nanotech, Nature Materials etc.*) or *Science, PNAS* and *Nano Letters* though the number is still insignificant from a large country like India. There is a sincere attempt among all of us to push our research to one step above to meet the expectations of the funding agencies and policy makers to do high quality research and to publish in the best journals or to apply our minds to solving problems of utmost importance to our country, namely food, water, medicine and sanitation. It is also a matter of concern that a very large number of publications of routine synthesis and characterization is also coming out from India in the name of nano-, which does

not add much to the existing knowledge and understanding. It is to be seen how research funding is channelled into future projects which demands creative high quality research or/and interdisciplinary application –oriented research. A good point is both person – specific research and large group research is both encouraged in India, unlike some (developed) countries where funds for individual projects have nearly dried up.

Apart from scientific publications, it is also noteworthy that the number of patents has also increased in the field of nanotechnology from India, but is not covered in this perspective and hopefully will be looked at another place. The advances in technology and devices in this field is yet to flood markets but they are certainly there in developed economies. The industries are waiting to understand the toxicological impact, if any, and use technologies which come up with solutions which provide ample checks and balances. The market should then take off in an exponential fashion. It is a matter of time that India will have to bear enormous foreign exchange pressure (for importing such technology), unless it comes up with indigenous technologies based on nanoscience and a sustained emphasis on academia-industry partnership, setting up of incubators and pilot plants in campuses and giving tax break to industries putting up more emphasis on in-house RandD or setting aside industrial research grants for academia in Nanoscience and Technology. Understanding of the environmental and toxicological effects of nanoparticles needs to be followed up for the development of nanoscience and its applications to industrial products and processes. We have tried to include most of the research published from India in nanoscience during 2012–2013. However it is possible that we may have overlooked some of the research inadvertently. Hence this article may be considered be a nearly complete description but not the total research in nanoscience from India during this period.

References

1 T. K. Sau and A. L. Rogach, *Adv. Mater.*, 2010, **22**, 1781.
2 S. B. Kalidindi, U. Sanyal and B. R. Jagirdar, *Inorg. Chem.*, 2010, **49**, 3965.
3 S. Kumar, C. Ravikumar and R. Bandyopadhyaya, *Langmuir*, 2010, **26**, 18320.
4 M. Ghosh, E. V. Sampathkumaran and C. N. R. Rao, *Chem. Mater.*, 2005, **17**, 2348.
5 R. Voggu, A. Shireen and C. N. R. Rao, *Dalton Trans.*, 2010, **39**, 6021.
6 S. Praharaj, S. Nath, S. Panigrahi, S. Basu, S. K. Ghosh, S. Pande, S. Jana and T. Pal, *Chem. Commun.*, 2006, 3836.
7 K. Biswas and C. N. R. Rao, *Chem. Eur. J.*, 2007, **13**, 6123.
8 J. Ahmed, B. Kumar, A. M. Mugweru, P. Trinh, K. V. Ramanujachary, S. E. Lofland and A. K. Ganguli, *J. Phys. Chem. C*, 2010, **114**, 18779.
9 D. Jana, A. Dandapat and G. De, *J. Phys.Chem. C*, 2009, **113**, 9101.
10 A. Kar, A. Datta and A. Patra, *J. Mater. Chem.*, 2010, **20**, 916.
11 A. Sarkar, S. K. Biswas and P. Pramanik, *J. Mater. Chem.*, 2010, **20**, 4417.
12 S. Kaniyankandy, S. Rawalekar, S. Verma and H. N. Ghosh, *J. Phys. Chem. C*, 2011, **115**, 1428.
13 K. S. Subrahmanyam, H. S. S. R. Matte and C. N. R. Rao, *Acc. Chem. Res.*, 2013, **46**, 149.
14 D. B. Shinde and V. K. Pillai, *Angew. Chem. Int. Ed.*, 2013, **52**, 2482.

15 D. V. R. Kumar, A. A. Kulkarni and B. L. V. Prasad, *Colloids and Surfaces A*, 2013, **422**, 181.
16 S. S. K. Kamal, P. K. Sahoo, J. Vimala, M. M. Raja, L. Durai and S. Ram, *J. Exp. Nanosci.*, 2013, **8**, 621.
17 S. C. Biradar, D. B. Shinde, V. K. Pillai and M. G. Kulkarni, *J. Mater. Chem.*, 2012, **22**, 10000.
18 I. Chakraborty, T. Udayabhaskararao and T. Pradeep, *Chem. Commun.*, 2012, **48**, 6788.
19 H. Bar, D. K. Bhui, G. P. Sahoo, S. Pyne, D. Chattopadhyay and A. Misra, *J. Exp. Nanosci.*, 2012, **7**, 109.
20 P. Dauthal and M. Mukhopadhyay, *Ind. Eng. Chem. Res.*, 2012, **51**, 13014.
21 S. A. Aromal, V. K. Vidhu and D. Philip, *Spectrochim. Acta. A*, 2012, **85**, 99.
22 P. S. Devi, S. Banerjee, S. R. Chowdhury and G. S. Kumar, *RSC Adv.*, 2012, **2**, 11578.
23 M. Raula, D. Maity, M. H. Rashid and T. K. Mandal, *J. Mater. Chem.*, 2012, **22**, 18335.
24 R. Kakkar, E. D. Sherly, K. Madgula, D. K. Devi and B. Sreedhar, *J. Appl. Polym. Sci.*, 2012, **126**, E154.
25 Z. Khan, J. I. Hussain and A. A. Hashmi, *Colloid Surface B*, 2012, **95**, 229.
26 V. K. N. Gupta, A. Mehra and R. Thaokar, *Colloid Surfaces A*, 2012, **393**, 73.
27 S. Das and A. Chattopadhyay, *RSC Adv.*, 2012, **2**, 10245.
28 A. Sio, C. Shell, N. D. Plasmon, M. Shanthil, R. Thomas, R. S. Swathi and K. G. Thomas, *J. Phys. Chem. Lett.*, 2012, **3**, 1459.
29 J. Kumar, X. Wei, S. Barrow, A. M. Funston, K. G. Thomas and P. Mulvaney, *Phys. Chem. Chem.Phys.*, 2013, **15**, 4258.
30 S. Ghosh, A. Saraswathi, S. S. Indi, S. L. Hoti and H. N. Vasan, *Langmuir*, 2012, **28**, 8550.
31 V. V. Singh, G. K. Rao, A. Kumar and A. K. Singh, *Dalton Trans.*, 2012, **41**, 1142.
32 S. Pramanik and G. De, *Bull. Mater. Sci.*, 2012, **35**, 1079.
33 S. Gayen, M. K. Sanyal, B. Satpati and A. Rahman, *Appl. Phys A*, 2013.
34 A. Chakrabarty, S. Chatterjee and U. Maitra, *J. Mater. Chem.*, 2013, **1**, 2136.
35 B. Panigrahy, M. Aslam and D. Bahadur, *Nanotechnology*, 2012, **23**, 115601.
36 S. Acharya, B. Das, U. Thupakula, K. Ariga, D. D. Sarma, J. Israelachvili and Y. Golan, *Nano Lett.*, 2013, **13**, 409.
37 R. Brahma and M. G. Krishna, *Bull. Mater. Sci.*, 2012, **35**, 551.
38 P. Sharma and S. K. Sharma, *Water Resour Manag.*, 2012, **26**, 4525.
39 K. K. Dey, A. Kumar, R. Shanker, A. Dhawan, M. Wan, R. R. Yadav and A. K. Srivastava, *RSC Adv.*, 2012, **2**, 1387.
40 S. Vijayakumar, S. Nagamuthu and G. Muralidharan, *ACS Appl. Mater. Interfaces*, 2013, **5**, 2188.
41 G. Sharma and P. Jeevanandam, *RSC Adv.*, 2013, **3**, 189.
42 S. Kundu and M. Jayachandran, *J. Nanopart. Res.*, 2013, **15**, 1543.
43 A. Ganguly, T. Ahmad and A. K. Ganguli, *Dalton Trans.*, 2009, 3536.
44 A. K. Ganguli, A. Ganguly and S. Vaidya, *Chem. Soc. Rev.*, 2010, **39**, 474.
45 S. Vaidya, P. Rastogi, S. Agarwal, S. K. Gupta, T. Ahmad, A. M. Antonelli, K. V Ramanujachary, S. E. Lofland and A. K. Ganguli, *J. Phys. Chem. C*, 2008, **112**, 12610.
46 N. M. Correa, J. J. Silber, R. E. Riter and N. E. Levinger, *Chem. Rev.*, 2012, **112**, 4569.
47 S. Sharma, N. Pal, P. K. Chowdhury, S. Sen and A. K. Ganguli, *J. Am. Chem. Soc.*, 2012, **134**, 19677.
48 J. Manna and R. Kumar, *Chem. Eur. J.*, 2012, **18**, 498.

49 T. Kundu, S. C. Sahoo and R. Banerjee, *Cryst.Growth Des*., 2012, **12**, 2572.
50 A. K. Mahapatra, U. M. Bhatta and T. Som, *J Phys. D*, 2012, **45**, 415303.
51 B. Mondal and S. K. Saha, *J. Nanopart. Res*., 2012, **14**, 1049.
52 N. Srinivasan and S. Thirumaran, *Superlattice Microst*., 2012, **51**, 912.
53 S. S. Warule, R. V. Kashid, D. R. Shinde, N. S. Chaudhari, B. B. Kale and M. A. More, *J. Nanopart. Res*., 2012, **14**, 889.
54 R. Menaka, S. Patra, Ghosh and A. K. Ganguli, *RSC Adv*., 2012, **2**, 7875.
55 R. Menaka, S. Patra, Ghosh and A. K. Ganguli, *J. Solid State Chem*., 2012, **194**, 173.
56 S. Menaka, M. G. Marka, Krishna and A. K. Ganguli, *Mater.Lett*., 2012, **73**, 220.
57 B. Chakraborty, H. S. S. R. Matte, A. K. Sood and C. N. R. Rao, *J. Raman Spectrosc*., 2013, **44**, 92.
58 P. Banerjee, S. Chakrabarti, S. Maitra and B. K. Dutta, *Ultrason. Sonochem*., 2012, **19**, 85.
59 S. Das and S. Ghosh, *Dalton Trans*., 2013, **42**, 1645.
60 N. Clament Sagaya Selvam, J. J. Vijaya and L. J. Kennedy, *Ind. Eng. Chem. Res*., 2012, **51**, 16333.
61 P. Singh, K. Mondal and A. Sharma, *J. Colloid Inter. Sci*., 2013, **394**, 208.
62 S. Sarkar, A. Makhal, T. Bora, K. Lakhsman, A. Singha, J. Dutta and S. K. Pal, *ACS Appl. Mater. Interfaces*, 2012, **4**, 7027.
63 B. Subash, B. Krishnakumar, R. Velmurugan, M. Swaminathan and M. Shanthi, *Catal. Sci. Technol*., 2012, **2**, 2319.
64 I. Ganesh, P. S. C. Sekhar, G. Padmanabham and G. Sundararajan, *Appl. Surf. Sci*., 2012, **259**, 524.
65 S. Khanchandani, S. Kundu, A. Patra and A. K. Ganguli, *J. Phys. Chem. C*, 2013, **117**, 5558.
66 S. Khanchandani, S. Kundu, A. Patra and A. K. Ganguli, *J. Phys. Chem. C*, 2012, **116**, 23653.
67 S. Balachandran and M. Swaminathan, *J. Phys. Chem. C*, 2012, **116**, 26306.
68 G. Begum, J. Manna and R. K. Rana, *Chem. Eur. J*., 2012, **18**, 6847.
69 P. Manjula, R. Boppella and S. V Manorama, *ACS Appl. Mater. Interfaces*, 2012, **4**, 6252.
70 S. Ghosh, K. Das, K. Chakrabarti and S. K. De, *Dalton Trans*., 2013, **42**, 3434.
71 A. Kar, S. Kundu and A. Patra, *RSC Adv*., 2012, **2**, 10222.
72 A. K. Sinha, M. Pradhan, S. Sarkar and T. Pal, *Environ. Sci. Tech*., 2013, xxxx.
73 N. Roy, Y. Sohn and D. Pradhan, *ACS Nano*, 2013, **7**, 2532.
74 D. Das, A. Shivhare, S. Saha and A. K. Ganguli, *Mater. Res. Bull*., 2012, **47**, 3780.
75 M. M. Mahlambi, A. K. Mishra, S. B. Mishra, R. W. Krause, B. B. Mamba and A. M. Raichur, *Ind. Eng. Chem. Res*, 2013, **52**, 1783.
76 I. Ganesh, A. K. Gupta, P. P. Kumar, P. S. Chandra Sekhar, K. Radha, G. Padmanabham and G. Sundararajan, *Mater. Chem. Phys*., 2012, **135**, 220.
77 S. Vaidya, A. Patra and A. K. Ganguli, *Sci. Adv.Mater*., 2012, **4**, 631.
78 S. S. Mandal and A. J. Bhattacharyya, *J. Chem. Sci*., 2012, **124**, 969.
79 S. Sontakke, C. Mohan, J. Modak and G. Madras, *Chem. Eng. J*., 2012, **189–190**, 101.
80 S. A. Singh and G. Madras, *Sep. Purif. Technol*., 2013, **105**, 79.
81 K. K. Haldar, G. Sinha, J. Lahtinen and A. Patra, *ACS Appl. Mater. Interfaces*, 2012, **4**, 6266.
82 P. Liu, J. Nisar, R. Ahuja and B. Pathak, *J. Phys. Chem. C*, 2013, **117**, 5043.
83 D. Saha, G. Madras and T. N. Guru Row, *Dalton Trans*., 2012, **41**, 9598.

84 D. Saha, P. Parimita Sahoo, G. Madras and T. N. Guru Row, *RSC Adv*., 2012, **2**, 10505.
85 K. H. Reddy, S. Martha and K. M. Parida, *RSC Adv*., 2012, **2**, 9423.
86 K. Parida, L. Mohapatra and N. Baliarsingh, *J Phys.Chem. C*, 2012, **116**, 22417.
87 M. U. A. Prathap, B. Kaur and R. Srivastava, *J. Colloid Inter. Sci*., 2012, **370**, 144.
88 P. Zhu, M. V Reddy, Y. Wu, S. Peng, S. Yang, a S. Nair, K. P. Loh, B. V. R. Chowdari and S. Ramakrishna, *Chem. Commun*., 2012, **48**, 10865.
89 R. Bajpai, S. Roy, N. Koratkar and D. S. Misra, *Carbon*, 2013, **56**, 56–63.
90 S. S. Kanmani and K. Ramachandran, *J. Mater. Sci*., 2012, **48**, 2076.
91 R. K. Bhardwaj, H. . Kushwaha, J. Gaur, T. Upreti, V. Bharti, V. Gupta, N. Chaudhary, G. D. Sharma, K. Banerjee and S. Chand, *Mater. Lett*., 2012, **89**, 195.
92 S. Sadhu, A. Jaiswal, S. Adyanthaya and P. Poddar, *RSC Adv*., 2013, **3**, 2313.
93 S. S. Mali, C. A. Betty, P. N. Bhosale, P. S. Shinde, P. M. R., S. R. Jadkar and P. S. Patil, *CrystEngComm*, 2012, **14**, 8156.
94 A. Anish Madhavan, S. Kalluri, D. K Chacko, T. A. Arun, S. Nagarajan, K. R. V. Subramanian, A. Sreekumaran Nair, S. V. Nair and A. Balakrishnan, *RSC Adv*., 2012, **2**, 13032.
95 S. A. Vanalakar, S. S. Mali, R. C. Pawar, N. L. Tarwal, A. V. Moholkar, J. H. Kim and P. S. Patil, *J. Appl. Phys*., 2012, **112**, 044302.
96 S. S. Mali, R. S. Devan, Y.-R. Ma, C. A. Betty, P. N. Bhosale, R. P. Panmand, B. B. Kale, S. R. Jadkar, P. S. Patil, J.-H. Kim and C. K. Hong, *Electrochim. Acta*, 2013, **90**, 666.
97 S. A. Agarkar, V. V. Dhas, S. Muduli and S. B. Ogale, *RSC Adv*., 2012, **2**, 11645.
98 D. B. Salunkhe, S. S. Gargote, D. P. Dubal, W. B. Kim and B. R. Sankapal, *Chem. Phys. Lett*., 2012, **554**, 150.
99 T. Rakshit, S. P. Mondal, I. Manna and S. K. Ray, *ACS Appl. Mater. Interfaces*, 2012, **4**, 6085.
100 S. K. Saha, A. Guchhait and A. J. Pal, *Phys. Chem. Chem. Phys*., 2012, **14**, 8090.
101 S. Singh, S. K. Samji and M. S. R. Rao, *J. Exp. Nanosci*., 2013, **8**, 320–325.
102 S. M. Hosseinpour-Mashkani, M. Salavati-Niasari, F. Mohandes and K. Venkateswara-Rao, *Mater. Sci. Semiconductor Process*., 2013, **16**, 390.
103 D. Gaikwad and D. Pore, *Synlett*, 2012, **23**, 2631.
104 A. Ahmed, Y. Nuree and J. K. Ray, *Tetrahedron Lett*., 2013, **54**, 665.
105 V. K. R. Kumar, S. Krishnakumar and K. R. Gopidas, *Eur. J. Org. Chem*., 2012, **18**, 3447.
106 A. Bej, D. Srimani and A. Sarkar, *Green Chem*., 2012, **14**, 661.
107 G. K. Rao, A. Kumar, B. Kumar and A. K. Singh, *Dalton Trans*., 2012, **41**, 4306.
108 S. G. Babu and R. Karvembu, *Tetrahedron Lett*., 2013, **54**, 1677.
109 K. H. V. Reddy, G. Satish, K. Ramesh, K. Karnakar and Y. V. D. Nageswar, *Tetrahedron Lett*., 2012, **53**, 3061.
110 V. Krishnakumar, K. M. Kumar, B. K. Mandal and F.-R. N. Khan, *ScientificWorldJournal*, 2012, **2012**, 619080.
111 U. U. Indulkar, S. R. Kale, M. B. Gawande and R. V. Jayaram, *Tetrahedron Lett*., 2012, **53**, 3857.
112 B. Naik, V. S. Prasad and N. N. Ghosh, *Powder Technol*., 2012, **232**, 1.
113 A. Mitra, D. Jana and G. De, *Chem. Commun*., 2012, **48**, 3333.
114 V. Bhalla, A. Gupta and M. Kumar, *Chem. Commun*., 2012, **48**, 11862.

115 J. Santhanalakshmi and L. Parimala, *J. Nanopart. Res.*, 2012, **14**, 1090.
116 J. Dhar and S. Patil, *ACS Appl. Mater. Interfaces*, 2012, **4**, 1803.
117 C. Pendem, P. Gupta, N. Chaudhary, S. Singh, J. Kumar, T. Sasaki, A. Datta and R. Bal, *Green Chem.*, 2012, **14**, 3107.
118 B. Sarkar, R. Tiwari, R. K. Singha, S. Suman, S. Ghosh, S. S. Acharyya, K. Mantri, L. N. S. Konathala, C. Pendem and R. Bal, *Catal. Today*, 2012, **198**, 209.
119 B. Sarkar, P. Prajapati, R. Tiwari, R. Tiwari, S. Ghosh, S. S. Acharyya, C. Pendem, R. K. Singha, L. N. S. Konathala, J. Kumar, T. Sasaki and R. Bal, *Green Chem.*, 2012, **14**, 2600.
120 T. Das and G. Deo, *J. Phys. Chem. C*, 2012, **116**, 20812.
121 V. M. Shinde and G. Madras, *Catal. Today*, 2012, **198**, 270.
122 V. M. Shinde and G. Madras, *Appl. Catal B: Environ.*, 2012, **123–124**, 367.
123 V. M. Shinde and G. Madras, *Appl. Catal B: Environ.*, 2013, **132–133**, 28.
124 D. Kundu, N. Mukherjee and B. C. Ranu, *RSC Adv.*, 2013, **3**, 117.
125 T. Guntreddi, B. Allam and K. Singh, *Synlett*, 2012, **23**, 2635.
126 A. K. Patra, A. Dutta and A. Bhaumik, *ACS Appl. Mater. Interfaces*, 2012, **4**, 5022.
127 C. Santra, S. Rahman, S. Bojja, O. O. James, D. Sen, S. Maity, A. K. Mohanty, S. Mazumder and B. Chowdhury, *Catal. Sci. Technol.*, 2013, **3**, 360.
128 A. Ghosh, F. Stellacci and R. Kumar, *Catal. Today*, 2012, **198**, 77.
129 S. Palmal, S. K. Basiruddin, A. R. Maity, S. C. Ray and N. R. Jana, *Chem. Eur. J*, 2013, **19**, 943.
130 S. Basiruddin, A. Ranjan Maity and N. R. Jana, *RSC Adv.*, 2012, **2**, 11915.
131 V. N. Mehta, M. A. Kumar and S. K. Kailasa, *Ind. Eng. Chem. Res.*, 2013, **52**, 4414.
132 A. Chowdhury, B. Biswas, R. N. Bera and B. Mallik, *RSC Adv.*, 2012, **2**, 10968.
133 S. Sarkar and D. Basak, *Sensor Actuat. B: Chem*, 2013, **176**, 374.
134 S. Prakash, S. Rajesh, S. R. Singh, C. Karunakaran and V. Vasu, *Analyst*, 2012, **137**, 5874.
135 S. Srivastava, M. A. Ali, P. R. Solanki, P. M. Chavhan, M. K. Pandey, A. Mulchandani, A. Srivastava and B. D. Malhotra, *RSC Adv.*, 2013, **3**, 228.
136 A. K. Giri, A. Sinhamahapatra, S. Prakash, J. Chaudhari, V. K. Shahi and A. B. Panda, *J. Mater. Chem.*, 2013, **1**, 814.
137 R. Sharma, V. V. Agrawal, A. K. Srivastava, L. Nain, M. Imran, S. R. Kabi, R. K. Sinha and B. D. Malhotra, *J. Mater. Chem.*, 2013, **1**, 464.
138 S. Chandra, K. Arora and D. Bahadur, *Mater. Sci. Eng: B*, 2012, **177**, 1531.
139 S. Thirumalairajan, K. Girija, V. Ganesh, D. Mangalaraj, C. Viswanathan and N. Ponpandian, *Cryst. Growth Des.*, 2013, **13**, 291.
140 M. Kumar, B. E. K. Swamy, S. Reddy, T. V. S. And and J. Maharajanna, *Anal. Methods*, 2013, **5**, 735.
141 P. Sharma, M. Kukkar, A. K. Ganguli and C. R. Suri, *Analyst*, 2013, **138**, 4312.
142 A. Kundu, R. K. Layek, A. Kuila and A. K. Nandi, *ACS Appl. Mater. Interfaces*, 2012, **4**, 5576.
143 M. Sadhukhan and S. Barman, *J. Mater. Chem.*, 2013, **1**, 2752.
144 S. Sreejith, K. P. Divya, P. Jayamurthy, J. Mathew, V. N. Anupama, D. S. Philips, P. Anees and A. Ajayaghosh, *Photochem. Photobiol. Sci.*, 2012, **11**, 1715.
145 S. Barman and M. Sadhukhan, *J. Mater. Chem.*, 2012, **22**, 21832.
146 R. S. Diggikar, M. V. Kulkarni, G. M. Kale and B. B. Kale, *J. Mater. Chem.*, 2013, **1**, 3992.
147 J. Dattatray, B. Liu, H. S. S. R. Matte, V. P. Dravid and C. N. R. Rao, *ACS Nano*, 2012, **6**, 5635.

148 S. K. Mishra and B. D. Gupta, *Analyst*, 2013, 2640.
149 G. K. Grandhi, R. Tomar and R. Viswanatha, *ACS Nano*, 2012, **6**, 9751.
150 S. S. Mandal, B. Nagarajan, H. Amenitsch and A. J. Bhattacharyya, *Eur. Biophys. J.*, 2013, **42**, 371.
151 L. V. Nair, D. S. Philips, R. S. Jayasree and A. Ajayaghosh, *Small*, 2013, **xx**, 1.
152 L. K. V, S. A. Ntim, O. Sae-Khow, C. Janardhana, V. Lakshminarayanan and S. Mitra, *Electrochim. Acta*, 2012, **83**, 40.
153 S. Dash and N. Munichandraiah, *Electrochim. Acta*, 2012, **80**, 68.
154 P. Selvam and B. Kuppan, *Catal. Today*, 2012, **198**, 85.
155 T. Maiyalagan, C. Mahendiran, K. Chaitanya, R. Tyagi and F. Nawaz Khan, *Res. Chem. Intermed.*, 2011, **38**, 383.
156 B. R. Sathe, *RSC Adv.*, 2012, **2**, 3735.
157 P. R. Chandran, M. Naseer, N. Udupa and N. Sandhyarani, *Nanotechnology*, 2012, **23**, 015602.
158 S. K. Meher and G. R. Rao, *ACS Catal.*, 2012, **2**, 2795.
159 B. P. Vinayan, R. Nagar and S. Ramaprabhu, *J. Mater. Chem.*, 2012, **22**, 25325.
160 S. S. J. Aravind and S. Ramaprabhu, *ACS Appl. Mater. Interfaces.*, 2012, **4**, 3805.
161 B. P. Vinayan, R. Nagar, N. Rajalakshmi and S. Ramaprabhu, *Adv. Funct. Mat.*, 2012, **22**, 3519.
162 A. Dutta and J. Datta, *J. Phys. Chem. C*, 2012, **116**, 25677.
163 U. Maitra, B. S. Naidu, A. Govindaraj and C. N. R. Rao, *PNA*, 2013, **110**, 11704.
164 S. Sharma, N. Garg, K. V. Ramanujachary, S. E. Lofland and A. K. Ganguli, *Cryst. Growth Des.*, 2012, **12**, 4202.
165 A. S. Nair, S. Ramakrishna, K. R. V. Subramanian, T. N. Kim, S. V. Nair and A. Balakrishnan, *J. Mater. Chem.*, 2012, **22**, 20465.
166 R. N. Singh, M. Kumar and A. S. K. Sinha, *Int. J. Hydrogen Energ.*, 2012, **37**, 15117.
167 M. Shaik, V. K. Rao, M. Gupta and P. Pandey, *Thin Solid Films*, 2012, **526**, 256.
168 K. G. Nishanth, P. Sridhar and S. Pitchumani, *Int. J. Hydrogen Energ.*, 2013, **38**, 612.
169 B. P. Vinayan, K. Sethupathi and S. Ramaprabhu, *Int. J. Hydrogen Energ.*, 2013, **38**, 2240.
170 L. N. Ramavathu, K. K. Maniam, K. Gopalram and R. Chetty, *J. Appl. Electrochem.*, 2012, **42**, 945.
171 B. Narayanamoorthy, K. K. R. Datta, M. Eswaramoorthy and S. Balaji, *Appl. Mater. Interface*, 2012, **4**, 3620.
172 B. Kumar, S. Saha, M. Basu and A. K. Ganguli, *J. Mater. Chem. A*, 2013, **1**, 4728.
173 M. Pal and V. Ganesan, *J. Electroanal. Chem.*, 2012, **672**, 7.
174 J. Chattopadhyay, R. Srivastava and P. K. Srivastava, *J. Appl. Electrochem.*, 2012, **43**, 279.
175 S. Ghosh, R. K. Sahu and C. R. Raj, *Nanotechnology*, 2012, **23**, 385602.
176 S. M. A. Shibli and J. N. Sebeelamol, *Int. J. Hydrogen Energ.*, 2013, **38**, 2271.
177 C. N. R. Rao, H. S. S. R. Matte, K. S. Subrahmanyam and U. Maitra, *Chemi. Sci.*, 2012, **3**, 45.
178 D. Lahiri, E. Khaleghi, S. R. Bakshi, W. Li, E. A. Olevsky and A. Agarwal, *Scripta Mater.*, 2013, **68**, 285.
179 B. P. Vinayan, R. Nagar, V. Raman, N. Rajalakshmi, K. S. Dhathathreyan and S. Ramaprabhu, *J. Mater. Chem.*, 2012, **22**, 9949.

180 R. Roy, A. Jha, D. Banerjee, N. Sankar, Das and K. K. Chattopadhyay, *AIP Advances*, 2013, **3**, 012115.
181 K. Gopalakrishnan, K. S. Subrahmanyam, P. Kumar, A. Govindaraj and C. N. R. Rao, *RSC Adv.*, 2012, **2**, 1605.
182 H. S. S. R. Matte, U. Maitra, P. Kumar, B. Govinda Rao, K. Pramoda and C. N. R. Rao, *Z. Anorg. Allg. Chem.*, 2012, **638**, 2617.
183 B. Govinda Rao, H. S. S. R. Matte and C. N. R. Rao, *J. Clust. Sci.*, 2012, **23**, 929.
184 D. J. Late, B. Liu, J. Luo, A. Yan, H. S. S. R. Matte, M. Grayson, C. N. R. Rao and V. P. Dravid, *Adv. Mater.*, 2012, **24**, 3549.
185 J. Debgupta, D. B. Shinde and V. K. Pillai, *Chem. Commun.*, 2012, **48**, 3088.
186 S. Kaniyankandy, S. Rawalekar and H. N. Ghosh, *J. Phys. Chem. C*, 2012, **116**, 16271.
187 R. Narayanan, M. Deepa and A. K. Srivastava, *Phys. Chem. Chem. Phys.*, 2012, **14**, 767.
188 S. Anandan, A. Manivel and M. Ashok Kumar, *Fuel Cells*, 2012, **12**, 956.
189 T. Theres Baby and R. Sundara, *AIP Adv.*, 2013, **3**, 012111.
190 S. Giri, D. Ghosh and C. K. Das, *J. Electroanal. Chem.*, 2013, **697**, 32.
191 R. Ravikumar and S. Gopukumar, *Phys. Chem. Chem. Phys.*, 2013, **15**, 3712.
192 B. P. Vinayan and S. Ramaprabhu, *J. Mater. Chem.*, 2013, **1**, 3865.
193 A. K. Mishra and S. Ramaprabhu, *AIP Adv.*, 2012, **2**, 022121.
194 D. Ghosh, S. Giri, S. Sahoo and C. K. Das, *Polym-Plast Technol.*, 2013, **52**, 213.
195 S. Anandhavelu and S. Thambidurai, *Electrochim. Acta*, 2013, **90**, 194.
196 R. Kumar, R. K. Singh, J. Singh, R. S. Tiwari and O. N. Srivastava, *J. Alloy. Compd.*, 2012, **526**, 129.
197 G. S. Gund, D. P. Dubal, B. H. Patil, S. S. Shinde and C. D. Lokhande, *Electrochim. Acta*, 2013, **92**, 205.
198 A. Bhaskar, M. Deepa, T. N. Rao and U. V. Varadaraju, *J. Power Sources*, 2012, **216**, 169.
199 D. Nandi, K. Gupta, A. K. Ghosh, A. De, N. R. Ray and U. C. Ghosh, *Chem. Eng. J.*, 2013, **220**, 107.
200 A. Sinha and N. R. Jana, *Eur. J. Inorg. Chem.*, 2012, **2012**, 4470.
201 K. Hasna, S. S. Kumar, M. Komath, M. R. Varma, M. K. Jayaraj and K. R. Kumar, *Phys. Chem. Chem. Phys.*, 2013, **15**, 8106.
202 A. Chandrasekar and T. Pradeep, *J. Phys. Chem. C*, 2012, **116**, 14057.
203 S. R. Mane, V. Rao, N, K. Chatterjee, H. Dinda, S. Nag, A. Kishore, J. Das Sarma and R. Shunmugam, *J. Mater. Chem.*, 2012, **22**, 19639.
204 S. R. Mane, V. Rao, N, K. Chaterjee, H. Dinda, S. Nag, A. Kishore, J. Das Sarma and R. Shunmugam, *Macromolecules*, 2012, **45**, 8037.
205 N. V. Rao, A. Kishore, S. Sarkar, J. Das Sarma and R. Shunmugam, *Biomacromolecules*, 2012, **13**, 2933.
206 P. Mukhopadhyay, K. Sarkar, M. Chakraborty, S. Bhattacharya, R. Mishra and P. P. Kundu, *Mater. Sci. Eng. C*, 2013, **33**, 376.
207 P. F. Minimol, W. Paul and C. P. Sharma, *Carbohyd. Polym.*, 2013, **95**, 1.
208 N. K. Singh, S. K. Singh, D. Dash, B. P. Das Purkayastha, J. K. Roy and P. Maiti, *J. Mater. Chem.*, 2012, **22**, 17853.
209 M. Ashfaq, S. Singh, A. Sharma and N. Verma, *Ind. Eng. Chem. Res.*, 2013, **52**, 4672.
210 B. Subia and S. C. Kundu, *Nanotechnology*, 2013, **24**, 035103.
211 P. S. Pramod, K. Takamura, S. Chaphekar, N. Balasubramanian and M. Jayakannan, *Biomacromolecules*, 2012, **13**, 3627.
212 S. Das, M. T. Joseph and D. Sarkar, *Langmuir*, 2013, **29**, 1818.

213 D. Sarkar, *J. Photochem. Photobiol A*, 2013, **252**, 194.
214 B. Sahoo, K. S. P. Devi, R. Banerjee, T. K. Maiti, P. Pramanik and D. Dhara, *ACS Appl. Mater. Interfaces*, 2013, **5**, 3884.
215 S. Bhushan, V. Kakkar, H. C. Pal, S. K. Guru, A. Kumar, D. M. Mondhe, P. R. Sharma, S. C. Taneja, I. P. Kaur, J. Singh and A. K. Saxena, *Mol. Pharm*., 2013, **10**, 225.
216 R. Bhandari and I. P. Kaur, *Int. J. Pharm*., 2013, **441**, 202.
217 H. Singh, R. Bhandari and I. P. Kaur, *Int. J. Pharm*., 2013, **446**, 106.
218 K. Raza, B. Singh, S. Singla, S. Wadhwa, B. Garg, S. Chhibber and O. P. Katare, *Mol. Pharm*., 10, 1958, **2013**.
219 K. Vandita, B. Shashi, K. G. Santosh and K. I. Pal, *Mol. Pharm*., 2012, **9**, 3411.
220 S. Chakraborty, M. K. Mitra, M. G. Chaudhuri, B. Sa, S. Das and R. Dey, *Appl. Biochem. Biotech*., 2012, **168**, 2043.
221 S. C. Wagh, J. S. Kumar and S. Banerjee, *J. Pharma. Res*., 2012, **5**, 2184.
222 P. Koley, A. Gayen, M. G. B. Drew, C. Mukhopadhyay and A. Pramanik, *Small*, 2012, **8**, 984.
223 R. Kurapati and A. M. Raichur, *Chem. Commun*., 2013, **49**, 734.
224 A. Sasidharan, L. S. Panchakarla, A. R. Sadanandan, A. Ashokan, P. Chandran, C. M. Girish, D. Menon, S. V Nair, C. N. R. Rao and M. Koyakutty, *Small*, 2012, **8**, 1251.
225 C. C. Mohan, P. R. Sreerekha, V. V. Divyarani, S. Nair, K. Chennazhi and D. Menon, *J. Mater. Chem*., 2012, **22**, 1326.
226 S. Das, N. Debnath, S. Mitra, A. Datta and A. Goswami, *Biometals*, 2012, **25**, 1009.
227 S. Pandey, G. Oza, A. Mewada, R. Shah, M. Thakur and M. Sharon, *J. Mater. Chem. B*, 2013, **1**, 1361.
228 S. Mukherjee, V. Sushma, S. Patra, A. K. Barui, M. P. Bhadra, B. Sreedhar and C. R. Patra, *Nanotechnology*, 2012, **23**, 455103.
229 R. Venkatesan, A. Pichaimani, K. Hari, P. K. Balasubramanian, J. Kulandaivel and K. Premkumar, *J. Mater. Chem*., 2013, **1**, 1010.
230 M. Ghosh, S. Maiti, S. Brahmachari and P. K. Das, *RSC Adv*., 2012, **2**, 9042.
231 A. Jana, K. S. P. Devi, T. K. Maiti and N. D. P. Singh, *J. Am. Chem. Soc*., 2012, **134**, 7656.
232 S. R. Rout, B. Behera, T. K. Maiti and S. Mohapatra, *Dalton Trans*., 2012, **41**, 10777.
233 S. Sahu and S. Mohapatra, *Dalton Trans*., 2013, **42**, 2224.
234 S. Narayanan, B. N. Sathy, U. Mony, M. Koyakutty, S. V. Nair and D. Menon, *ACS Appl. Mater. Interfaces*, 2012, **4**, 251.
235 M. Kokate, K. Garadkar and A. Gole, *J. Mater. Chem*., 2013, **1**, 2022.
236 P. Chakraborty, B. Roy, P. Bairi and A. K. Nandi, *J. Mater. Chem*., 2012, **22**, 20291.
237 S. Pal, S. Ghorai, C. Das, S. Samrat, A. Ghosh and A. B. Panda, *Ind. Eng. Chem. Res*., 2012, **51**, 15546.
238 S. Thakur, G. Das, P. K. Raul and N. Karak, *J. Phys. Chem. C*, 2013, **117**, 7636.
239 S. Sen Gupta, T. S. Sreeprasad, S. M. Maliyekkal, S. K. Das and T. Pradeep, *ACS Appl. Mater. Interfaces*, 2012, **4**, 4156.
240 T. S. Sreeprasad, S. Sen Gupta, S. M. Maliyekkal and T. Pradeep, *J. Hazard. Mater*, 2013, **246–247**, 213.
241 S. K. Das, M. R. Khan, A. K. Guha, A. R. Das and A. Baran, *Bioresour. Technol*., 2012, **124**, 495.

242 M. M. Ottakam Thotiyl, H. Basit, J. a Sánchez, C. Goyer, L. Coche-Guerente, P. Dumy, S. Sampath, P. Labbé and J.-C. Moutet, *J. Colloid Inter. Sci.*, 2012, **383**, 130.
243 S. Roy Choudhury, A. Mandal, D. Chakravorty, M. Gopal and A. Goswami, *J. Nanopart. Res.*, 2013, **15**, 1491.
244 A. Sinha and N. R. Jana, *Chem. Commun.*, 2012, **48**, 9272.
245 S. K. Das, M. K. Bhunia and A. Bhaumik, *Micropor. Mesopor. Mat.*, 2012, **155**, 258.
246 M. S. Bootharaju and T. Pradeep, *Langmuir*, 2012, **28**, 2671.
247 A. Jaiswal, S. S. Ghosh and A. Chattopadhyay, *Langmuir*, 2012, **28**, 15687.
248 D. Jana and G. De, *RSC Adv.*, 2012, **2**, 9606.
249 N. Kurra, D. Dutta and G. U. Kulkarni, *Phys.Chem.Chem.Phys.*, 2013, **15**, 8367.
250 R. Boya, D. Jayaraj and G. U. Kulkarni, *Chemi. Sci.*, 2013, **4**, 2530.
251 M. Kandpal, C. Sharan, P. Poddar, K. Prashanthi, P. R. Apte and V. Ramgopal Rao, *Appl.Phys. Letts.*, 2012, **101**, 104102.
252 P. Ray and V. Ramgopal Rao, *Appl.Phys. Letts.*, 2013, **102**, 064101.

Metal oxide nanoparticles

Serena A. Corr
DOI: 10.1039/9781849737623-00204

In the previous volume,[1] we considered a full range of synthetic developments for the preparation of metal oxide nanoparticles from high temperature methods to microwave assisted synthesis to low temperature routes. A more general overview of each preparative route was given. In the current chapter, we will continue our examination of recent reports of traditional and emerging synthetic approaches to nanostructured metal oxides and metal oxide nanocomposites. We will look in detail at a number of examples of composite materials, as well as examine how these materials can be characterised in order to more extensively probe the structure-property relationship. Given the number of potential applications for metal oxide nanomaterials, we will also look at specific examples of composite materials which are under investigation for electronic, energy and catalytic applications. Recent findings have demonstrated that in some cases, carefully constructed hybrid nanostructures can promote a synergetic relationship between the composite constituents.

1 Introduction

Metal oxide nanomaterials continue to be intensively studied, with their extensively reported potential applications spanning the fields of electronics, energy, catalysis, sensors, and biomedical research. These areas continue to garner intense interest, with a number of detailed reviews appearing recently.[2–7] The size, morphology and crystal structure dependence of the properties of metal oxide nanoparticles continues to drive further research into developing new synthetic routes to these important materials. In addition to synthetic approaches for phase pure materials, over which there is a high degree of control over resulting particle shape and size, there has also been much recent work on how the doping of colloidal nanocrystals can bestow on them new properties.[8] Recently, there has also been a focus on combining several entities into a single nanocomposite and investigating any concerted improved functionality which may arise as a result of some synergetic partnership between the components.

In the current volume, we will again discuss the most recent reports of synthetic approaches for metal oxide nanostructures. We will pay particular attention to the developments in high temperature methods, where a great deal of control over particle size and shape is possible. There have also been advances in hydro- and solvo-thermal approaches, where hybrid nanocomposites have shown considerable enhancement in properties when compared to the individual constituents. There have been a number of recent reports on traditional approaches to nanomaterials, including aerosol methods, template synthesis, precipitation and sol-gel, with further developments in low temperature, environmentally-benign routes to

School of Chemistry, University of Glasgow, Glasgow G12 8QQ, United Kingdom. Tel: +44 141 3302274. E-mail: serena.corr@glasgow.ac.uk

nanoparticles. With the wealth of detailed reviews and books on traditional routes to solid-state materials,[9–14] this review will focus mainly on developments over the past year.

2 Developments in the preparation of metal oxide nanoparticles

2.1 High temperature methods

2.1.1 Decomposition of precursors. In a recent review, Sun and co-workers have considered advances made in the high temperature solution-based synthesis of metal oxide nanoparticles.[15] This precursor decomposition route has allowed for the preparation of metal oxide nanoparticles with desired crystal structure and monodispersity, affording great control over their magnetic, electronic and optical properties. For example, monodisperse Co/CoO/graphene nanocomposites have been reported by this group, where the nature of the cobalt nanoparticles can be tuned through controlled oxidation.[16] These hybrids are of interest because of their potential to act as catalysts for oxygen reduction reactions (ORR). Cobalt nanoparticles (10 ± 0.7 nm) are obtained through the thermal decomposition of $[Co(CO)_8]$ in tetralin with oleic acid and dioctylamine. On exposure to the air, these particles form a 1 nm shell of CoO, whose thickness can be controlled if heated above 70 °C. Complete oxidation (*e.g.* increased heating) will produce hollow CoO nanoparticles. Dispersions of these cobalt nanoparticles in hexane can be assembled onto graphene in DMF by sonication. Figure 1 shows TEM images of the resulting nanoparticles.

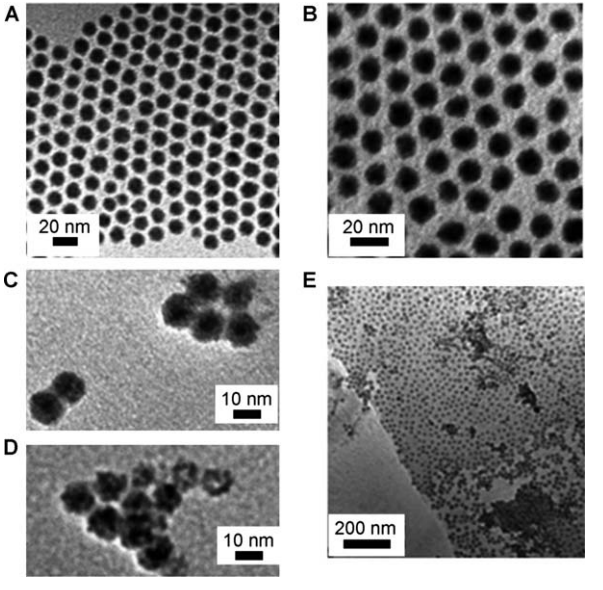

Fig. 1 TEM images of (A) 10 nm Co nanoparticles, (B) Co/CoO nanoparticles, (C) Co/CoO nanoparticles after 17 h in air, (D) Co/CoO nanoparticles after 96 h in air and (E) Co/CoO/graphene nanocomposite. Reprinted from Ref. 16 with permission from Wiley and Sons.[16]

Using a high temperature approach, Lee *et al*. have reported the synthesis of rutile RuO_2 and rutile IrO_2 nanoparticles of 6 nm in size, for use as oxygen evolution reaction (OER) catalysts.[18] Firstly, metal nanoparticles were prepared at high temperature from chloride precursors in a solution of tetralin and oleylamine, to which tetrabutylammonium borohydride reducing agent was added. The corresponding oxides were obtained after a thermal annealing step at 500 °C for 20 h in pure oxygen. The resulting single crystal nanoparticles are shown in Fig. 2.

Recently, a facile approach which gives control over the particle size, shape and structure of CoO or Co nanoparticles has been reported by Tang and co-workers.[17] Using the inexpensive starting material, cobalt acetate, in controlled ratios with oleylamine and oleic acid, ferromagnetic CoO nanoparticles of different sizes (from 75 nm to 625 nm) and 30 nm Co nanoparticles have been prepared. The thermal decomposition takes place at 300 °C and reactions may be scaled up. In this method, the oleylamine plays the role of a reducing ligand and capping agent, while the oleic acid acts only as a capping ligand. To obtain octahedral or spherical

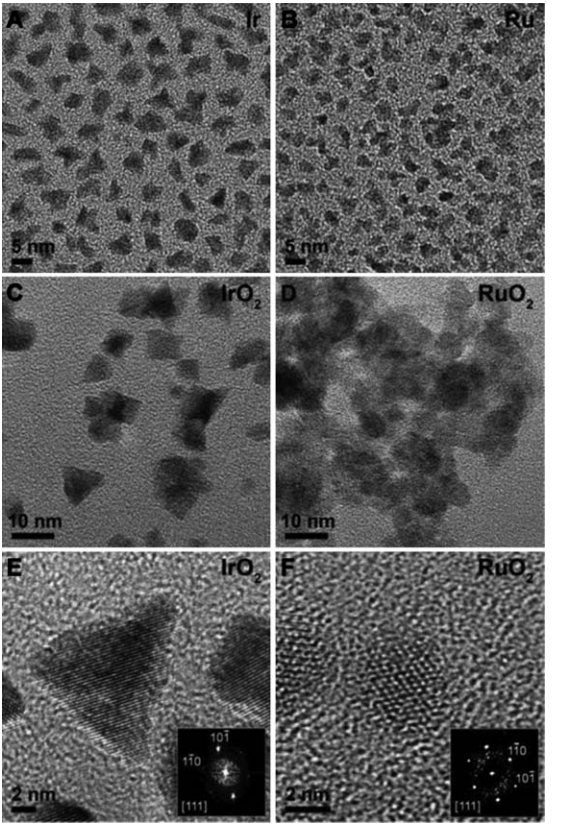

Fig. 2 TEM images of (A) Ir nanoparticles, (B) Ru nanoparticles, (C) rutile IrO_2 nanoparticles and (D) rutile RuO_2 nanoparticles from a high temperature solution route. HRTEM and FFTs reveal crystalline (E) IrO_2 particles 7 nm in size and (F) RuO_2 nanoparticles 6 nm in size after annealing in O_2. Reprinted from Ref. 18 with permission from the American Chemical Society.[18]

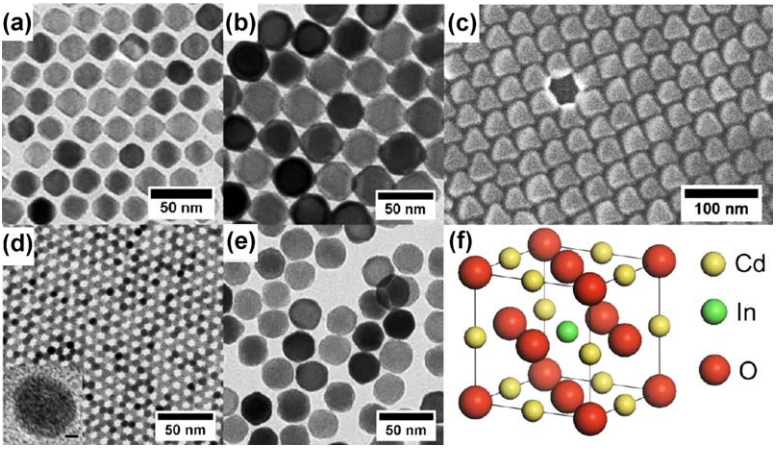

Fig. 3 TEM images of octahedral indium-doped cadmium oxide nanocrystals prepared at 300 °C with (a) 4 mmol and (b) 3 mmol oleic acid. (c) SEM of sample (b). Spherical nanoparticles produced at 315 °C using (d) 5 mmol and (e) 3 mmol oleic acid. (f) Rock salt crystal structure of indium-doped cadmium oxide. Reprinted from Ref. 19 with permission from the American Chemical Society.[19]

CoO nanoparticles of differing sizes, the ratio of cobalt:oleylamine:oleic acid is key, while an excess of oleylamine drives the formation of Co nanoparticles.

Indium-doped cadmium oxide nanocrystals have been reported for the first time by Murray and coworkers.[19] A high temperature decomposition route is employed, whereby indium (III) acetate and cadmium (II) acetylacetonate are mixed with oleic acid and 1-octadecene. By manipulating the reaction temperature and concentration of oleic acid used, the particle morphology can be tuned from octahedral crystals to small spherical particles, as shown in Fig. 3. These particle shape differences have large effects on their optical response. The negative permittivity in the near-IR observed for thin films of these materials makes them possible candidates for use as building blocks for 3-D optical metamaterials.

In an effort to tune the magnetic properties of a series of nanostructures, Heiss and co-workers have developed a post-synthetic cation exchange process using a trioctylphosphine hot injection method.[20] By cooling down the reaction, the cation exchange can be stopped. The current procedure is applied to Co^{2+} exchanging in magnetic ferrite nanomaterials and the cobalt content can be determined experimentally using EDX, Rutherford backscattering spectroscopy and atomic absorption spectroscopy. Three ferrite systems have been studied: magnetite nanoparticles, gold/magnetite core/shell nanoparticles and core/shell nanocrystals of $FeO/CoFe_2O_4$. Each is shown in Fig. 4. In the case of magnetite and Au/magnetite, the magnetocrystalline anisotropy is enhanced by the introduction of the Co^{2+} species to the surface, leading to an increase in superparamagnetic blocking temperature, coercive field and remanence magnetisation. For the $FeO/CoFe_2O_4$ core/shell particles, it is the core itself which changes and significant changes in the exchange bias are noted at low temperatures. This tuneable effect on magnetic behaviour makes this exchange process of great

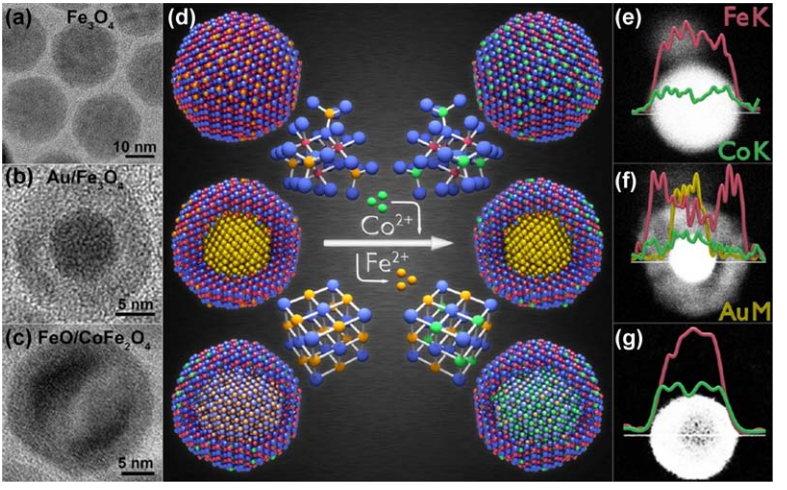

Fig. 4 TEM images of (a) magnetite nanoparticles, (b) Au/magnetite core/shell nanoparticles and (c) core/shell nanocrystals of $FeO/CoFe_2O_4$ before subjection to cation exchange procedure. (d) Schematic of cation exchange process showing the three different nanocrystal types. (e)–(f) High annular dark field STEM images of nanocrystals after cation exchange process, with EDX line scans also providing evidence of Co doping after exchange. Reprinted from Ref. 20 with permission from the American Chemical Society.[20]

interest for designing new heterostructures with desired magnetic properties.

Hierarchically structured Fe_2O_3 microboxes have been recently reported by Lou and coworkers.[21] By taking the coordination compound Prussian blue in the form of microcubes, iron oxide structures can be obtained by differing heat treatments. These are shown in Fig. 5. For example, Prussian blue microcubes annealed in air at 350 °C gave a mixture of cubic bixbyite β-Fe_2O_3 and cubic spinel γ-Fe_2O_3. Treatments at 550 °C and 650 °C yielded Fe_2O_3, but with differing morphologies. For the lower reaction temperature, the microboxes appear porous, while a hierarchical structure consisting of sheet-like particles is found for the higher temperatures. These structures display good potential for use as anode materials for Li-ion batteries and this technique could potentially be used to fabricate a range of materials.

Mathur and co-workers have reported the controlled synthesis over a range of phase compositions of iron oxides through careful consideration of the reaction parameters, including temperature, time, and the presence of oxidants and ligands.[22] The decomposition of iron oxalates is depicted in Fig. 6 and shows that the decomposition process depends on whether it is the M–O or C–O bond which is cleaved.

2.1.2 Combustion methods. Combustion methods can present an ultra-fast route for metal oxide synthesis. The fast nucleation step at the beginning is combined with a suppressed growth phase which ensures that highly crystalline, uniform, small particles are obtained. Highly crystalline nanoparticles have been prepared using a polyol-assisted pyro-synthesis route, which takes only a few seconds, by Gim *et al.*[23] Figure 7 illustrates the procedure for $LiFePO_4$ nanoparticles, which find applications as positive electrodes in Li-ion batteries.[24] Metal salts are first dissolved in polyol

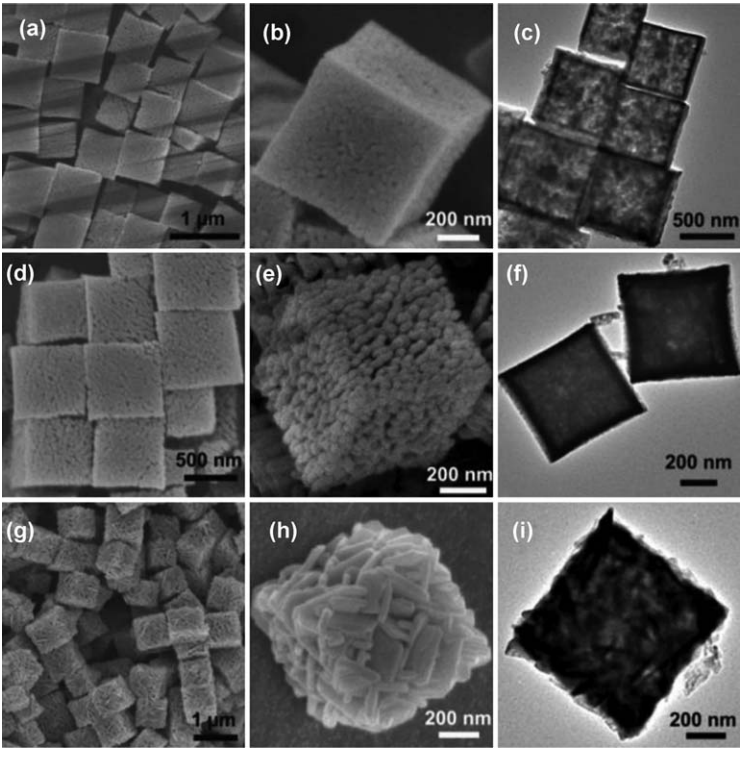

Fig. 5 TEM and SEM images of hollow iron oxide microboxes obtained from annealed Prussian blue at (a–c) 350 °C, (d–e) 550 °C and (g–i) 650 °C. Reprinted from Ref. 21 with permission from the American Chemical Society.[21]

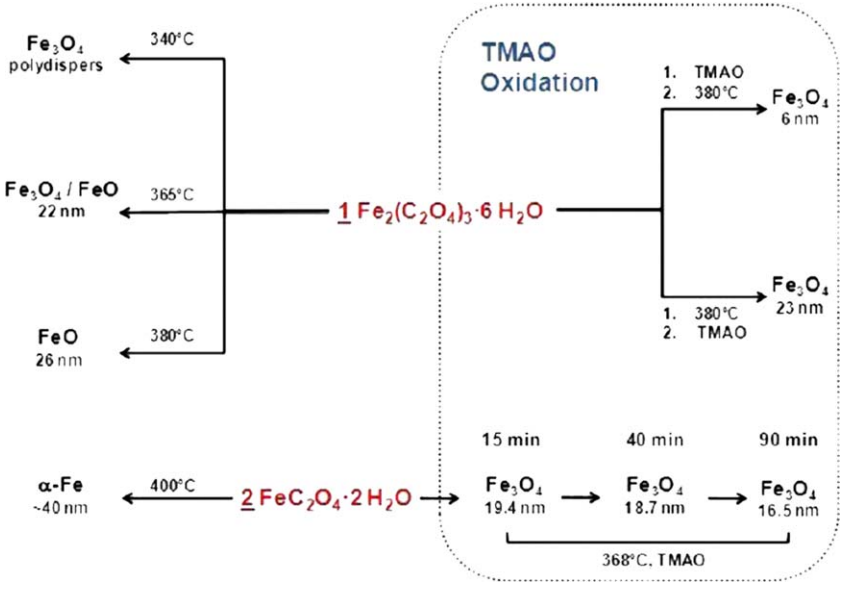

Fig. 6 Schematic of the decomposition of iron (II) and iron (III) oxalates, showing the resultant phases obtained depend on the cleavage of the M–O (for metallic phases) or C–O (for metal oxides) bonds. Reprinted from Ref. 22 with permission from the American Chemical Society.[22]

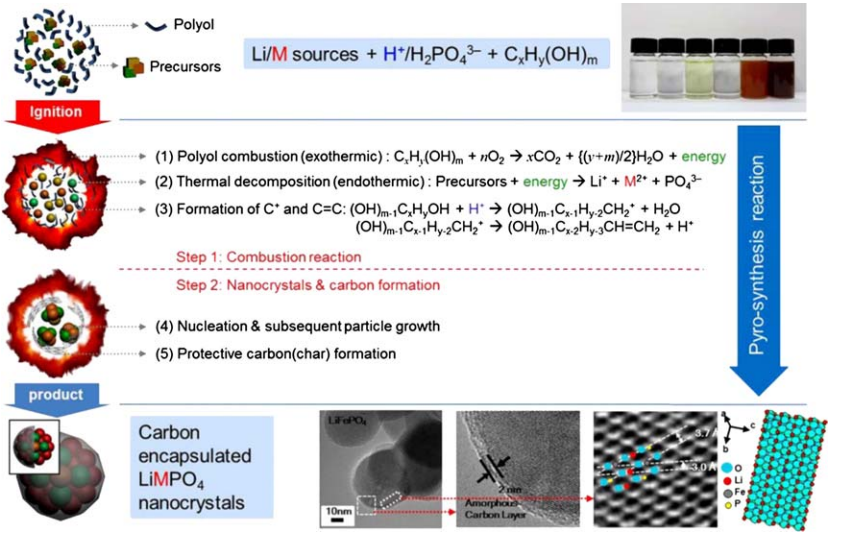

Fig. 7 Schematic for the polyol-assisted pyro-synthesis of carbon-coated $LiFePO_4$ nanoparticles. Reprinted from Ref. 23 with permission from the Nature Publishing Group.[23]

before ignition. The ultrafast process precipitates highly crystalline nanoparticles, due to a rapid nucleation step. In the case of $LiFePO_4$, the presence of phosphoric acid in the starting solution promotes the formation of carbonized structures and the resulting nanoparticles have a thin layer of conductive carbon coating which is of great benefit for electrochemical cycling.[25] The method has also been extended to prepare nanoparticles of pure metal oxides, sulfides and noble metals.

Zheng and co-workers have established a sol-flame method for the preparation of hybrid nanostructures of nanoparticle-decorated nanowires.[26] Target nanowires are grown on a substrate and a precursor solution of the desired nanoparticles is prepared by sol-gel. Dip-coating allows for uniform coating of the underlying nanowires with the nanoparticle precursor solution which, when dried in air, leaves a shell of nanoparticle precursor on the nanowire surface. A rapid combustion step follows, whereby the coated nanowires are annealed in a flame and nanoparticle formation occurs. Figure 8 shows electron microscopy images of a number of structures obtained, from metal oxide nanowires coated with metal oxide nanoparticles (*e.g.* Co_3O_4@CuO, TiO_2@CuO and ZnO@CuO) to single crystal nanoparticles coating a metal oxide nanowire (*e.g.* $ZnWO_4$@WO_3), attesting to the potential versatility of this method for highly crystalline, monodisperse nanostructure preparation.

2.1.3 Aerosol methods. In order to obtain high yields of metal oxide microspheres loaded with noble metal nanoparticles as catalysts, Wang and co-workers have established an aerosol-assisted self-assembly (AASA) process.[27] The metal oxide microspheres have been obtained through a combination of a sol-gel method, using metal alkoxide precursors, and an AASA approach. Examples of materials obtained are shown in X-ray diffraction patterns and SEM images in Fig. 9.

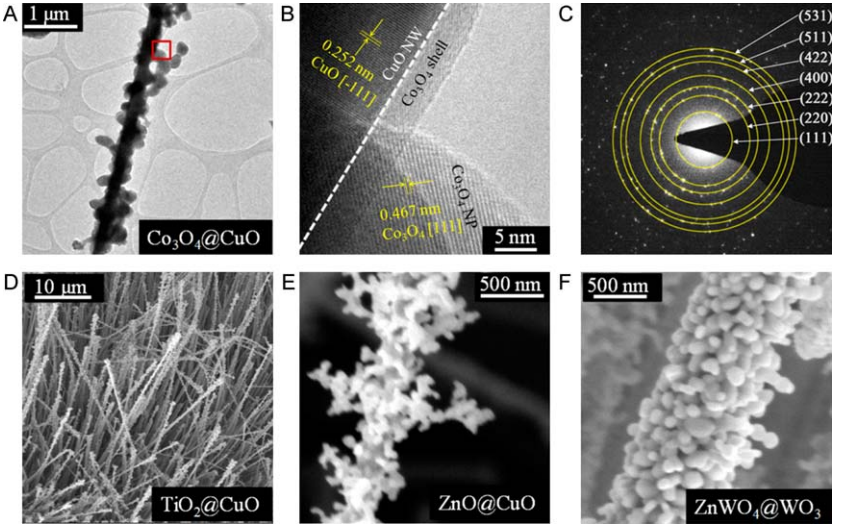

Fig. 8 (A) TEM image and (B) HRTEM image with accompanying selected area electron diffraction (SAED) pattern of Co_3O_4@CuO. (D)–(F) show SEM images of TiO_2@CuO, ZnO@CuO and $ZnWO_4$@WO_3 respectively. Reprinted from Ref. 26 with permission from the American Chemical Society.[26]

To obtain a nanocomposite including the noble metal catalysts, appropriate metal salts are dissolved in the precursor solution. Subsequent calcination or H_2 treatment affords the final composite. In this manner, a one-pot method has been developed where a uniform distribution of metal nanoparticles on the mesoporous oxide microspheres is possible. The catalytic properties of these nanocomposites have also been evaluated. This AASA technique has also been extended to prepare noble metal nanocrystals embedded in a hollow mesoporous oxide, by simultaneously utilising polystyrene nanospheres.[28] These act both as templates for the formation of the hollow metal oxide interiors and as carriers for the metal nanoparticles allowing adsorption on the inner oxide surface.

Hollow metal nanostructures have been studied by Zachariah and co-workers for their applications as nanoenergetic materials.[29] These typically consist of a metallic fuel, such as Al, and a metal oxide as an oxidiser. In the present study, the ultimate aim is the preparation of an Al/CuO nanocomposite capable of delivering a high energy density and rapid gas release. To this end, a new approach to hollow CuO spheres has been developed where precursor solutions of $Cu(NO_3)_2.3H_2O$ are atomized and thermally decomposed to particles. Hydrogen peroxide and sucrose are added to the nitrate solution as an *in situ* 'blowing' agent, facilitating the formation of hollow spheres according to:

$$2Cu(NO_3)_2 \rightarrow 2CuO + 4NO_2 + O_2$$

2.2 Template synthesis

Using a mesoporous silica template, Namai *et al*. have prepared rhodium-substituted ε-iron oxide (ε-$Rh_xFe_{2-x}O_3$) nanoparticles.[30] These particles

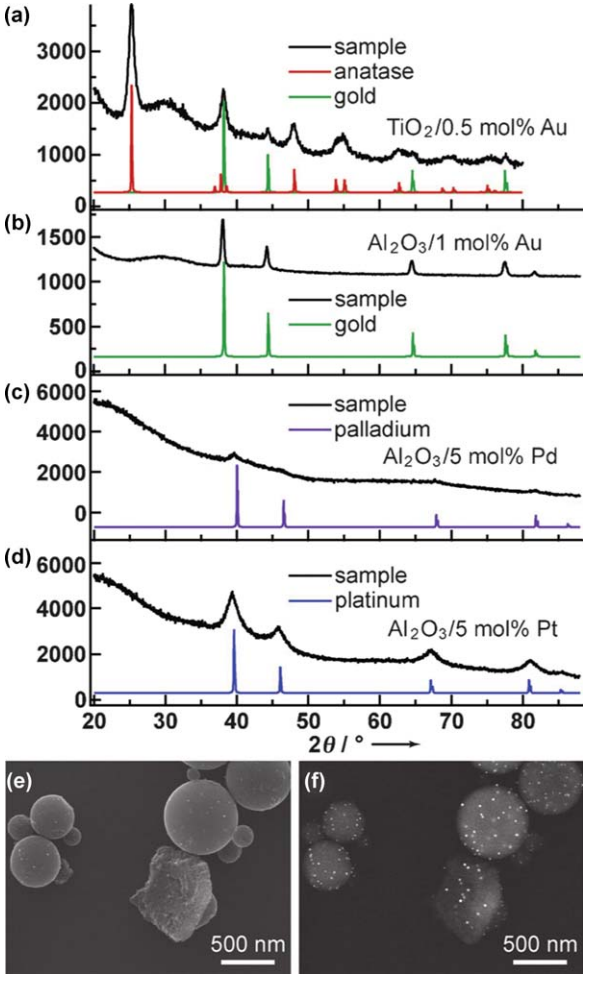

Fig. 9 X-ray diffraction patterns of AASA composites (a) TiO_2/0.5 mol% Au, (b) Al_2O_3/1 mol% Au, (c) Al_2O_3/5 mol% Pd, (d) Al_2O_3/5 mol% Pt. SEM images of the TiO_2/1 mol% Au sample in (e) secondary electron and (f) backscattered electron modes. Reprinted with permission from Ref. 26 with permission from John Wiley and Sons.[27]

display a gigantic coercive field (H_C), comparable to rare-earth magnets and high frequency millimetre wave absorption. The reaction scheme is shown in Fig. 10. The metal nitrate precursor salts in aqueous methanol are introduced to the silica template and heated in air at 1200 °C. Removal of the template is achieved using NaOH solution. The ε-phase is stabilised due to nanosized effects and the large H_C is attributed to the particles being single domain and the magnetic anisotropy of the ε-phase.

A nanocasting template approach has been used by Pellicer *et al.* to prepare Co-, Fe, and Mn-doped In_2O_3 mesoporous oxides.[31] The porous silica templates SBA-15 and KIT-6 have been employed as sacrificial templates. In the case of the iron and cobalt samples, typical mesoporous structures associated with SBA-15 and KIT-6 have been obtained, while for the manganese sample, a less ordered, mesophase is seen in TEM.

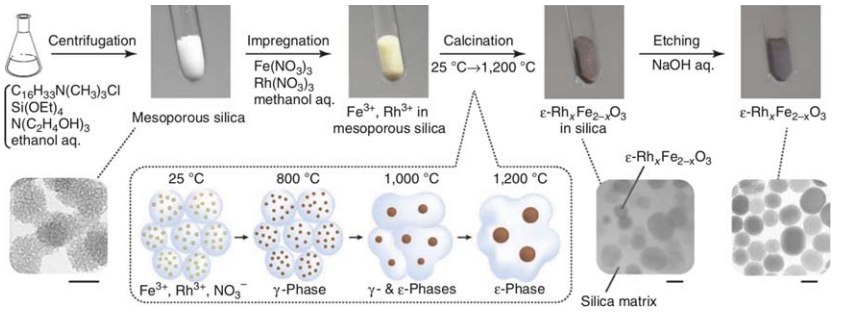

Fig. 10 Schematic for the template synthesis of ε-$Rh_xFe_{2-x}O_3$ nanoparticles using a mesoporous silica template. The resulting particle sizes from TEM are 35 nm. Reprinted from Ref. 30 with permission from the Nature Publishing Group.[30]

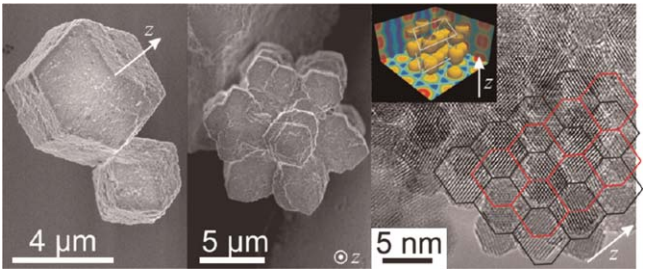

Fig. 11 TEM images of 10% Tb-doped zirconia supercrystals prepared at (a) 325 °C and (b) 350 °C. (c) HRTEM image of superlattice comprised of 6%Y-doped zirconia prepared at 350 °C. Reprinted from Ref. 33 with permission from the American Chemical Society.[33]

2.3 Hydrothermal and solvothermal synthesis

Choice of solvent in solvothermal reactions can lead to single-step reactions, whereby the solvent itself behaves not only as the reaction medium but also as a capping agent. Pinna and co-workers have taken advantage of this to develop a non-aqueous route to benzoate- and biphenolate-capped ZrO_2 nanoparticles.[32] Reaction temperatures of between 250 and 300 °C are employed and lead to absorption of organic molecules on the surface of the particles. These absorbed species not only affect the nanoparticle size, but also play a role in determining the luminescence properties of the material. Benzoate-capped ZrO_2 for reactions taking place at 325 °C or 350 °C with Tb or Y as dopants have been found to self-assemble into large heterostructures, with flower-like or bipyramid type morphologies which are highly ordered, as shown in Fig. 11.[33] The formation of benzoate species on the particle surface during the reaction leads to π-π-stacking between phenol groups on neighbouring particles, directing the formation of such assemblies. The underpinning role of solvent in the autoclave synthesis of iron oxide nanoparticles has also been extensively addressed by Douglas *et al.* to generate monodisperse particles of varying morphologies (spheres, platelets and cubes).[34]

Using an ultrasonic-assisted hydrothermal synthesis, Yang *et al.* have prepared SnO nanostructures which display excellent cycling stability for

use as supercapacitors.[35] The dissolution of $SnCl_2$ in ethanolamine is aided by ultrasonication treatment (600W, 1 h). This results in the formation of a Sn^{2+}-ethanolamine complex, which is then hydrolysed to form an intermediate $Sn_6O_4(OH)_4$ complex. Upon further sonication, SnO nanoparticles are formed but with the intermediate complex still detected in X-ray diffraction. An additional hydrothermal treatment affords pure phase SnO nanoclusters, which assemble into microplates. Nanostructured tin oxides have also been studied by Gao and co-workers as high capacity anodes for Li-ion batteries.[36] In this work, a one-step hydrothermal processing method has allowed for the growth of SnO_2 nanorods on the surface of graphene sheets which have been obtained through the *in situ* reduction of graphene oxide. The electrochemical properties of this hybrid material are found to surpass those of the SnO_2 nanorods alone. A recent paper has also reported the hydrothermal synthesis of ultra-long α-MoO_3 for use as a Li-ion battery electrode.[37] Hydrothermal treatment of molybdenum acetylacetonate in aqueous nitric acid at 200 °C for 20–25 h afforded uniform nanobelts with aspect ratios of up to 500.

Chen *et al*. have used polyethylene glycol as a solvent to prepare hollow microspheres made up of ZnO nanoparticles.[38] Zinc acetate and urea were dissolved in PEG 400, before hydrothermal treatment at 180 °C for 10 h. The presence of the PEG is crucial for the formation of the hollow spheres – without it, the particles appear irregular and polydisperse. The formation of such nanostructures follows the route of (i) self-assembly of the nanoparticles, (ii) Ostwald ripening followed by (iii) a crystal growth phase, during which the sphere cavity diameter decreases with reaction time. Electron microscopy images of the hollow spheres are shown in Fig. 12.

Recently, hydro- and solvothermal methods have been employed to generate hybrid materials, where the combination of two or more materials in a single nanocomposite provides for a synergy between the component

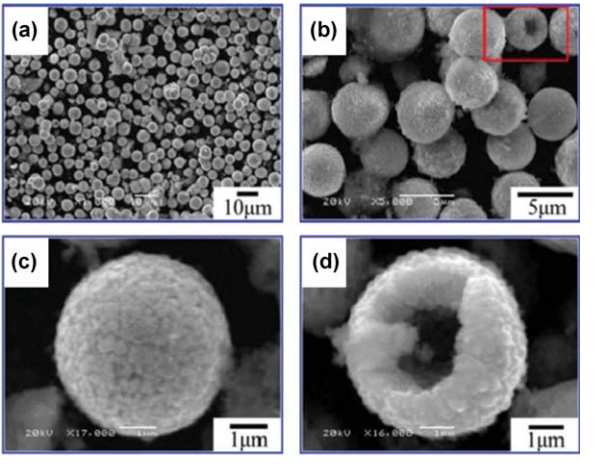

Fig. 12 SEM images of ZnO hollow spheres prepared by hydrothermal treatment (a) shows an overview of the sample, while (b) and (c) show the roughness of the surface due to the aggregation of nanoparticles. (d) shows a cracked hollow sphere. Reprinted from Ref. 38 with permission from the Royal Society of Chemistry.[38]

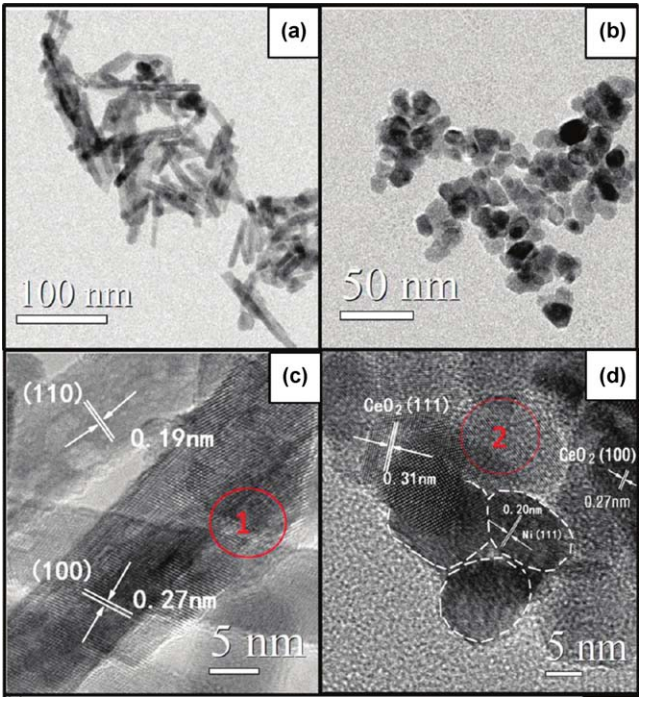

Fig. 13 TEM images of Ni/CeO_2 nanorod (a, c) and nanoparticle (b, d) catalysts prepared from Ni impregnation of the hydrothermally obtained nanostructures. Reprinted from Ref. 39 with permission the American Chemical Society.[39]

parts to enhance the overall composite properties. Du *et al.* have investigated the role of morphology in the CO_2 reforming of methane using Ni/CeO_2 catalysts.[39] By employing a hydrothermal method, ceria nanorods and nanoparticles were prepared by varying the amount of nitrate starting material. To prepare the final catalysts with a nickel content of 5 wt%, an impregnation method was used where the nanomaterials were immersed in a solution of nickel nitrate before a series of heat treatments. The resulting nanostructures of Ni/CeO_2 nanorods (a, c) and nanoparticles (b, d) are shown in Fig. 13. The presence of Ni can be verified using EDS, with evidence for Ni particles from TEM also apparent in the case of the ceria nanoparticle sample.

In order to probe the interplay between photocatalytic performance, crystal chemistry and electronic structure, Liu and co-workers have prepared the orthorhombic and tetragonal phases of $KNbO_3$ and compared their photocatalytic behaviour, together with that of the cubic $KNbO_3$ phase.[40] High-resolution TEM images of the $KNbO_3$ samples are shown in Fig. 14. The order of photocatalytic activity of each crystal phase, with a 1.5 wt% Pt co-catalyst, follows the order cubic > orthorhombic > tetragonal. Predictions from DFT calculations, in combination with careful consideration of the spatial distributions of the lowest unoccupied wave functions, point to the importance of exposed facets and electronic structure for determining catalytic performance. The resulting electron excitation and transfer afforded the cubic phase as a result of it having the highest crystal

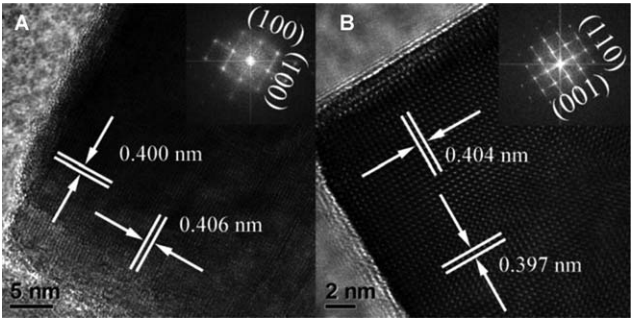

Fig. 14 HRTEM images of (A) tetragonal $KNbO_3$, with inset FFT pattern and (B) orthorhombic $KNbO_3$ with inset FFT pattern. Reproduced from Ref. 40 with permission from The Royal Society of Chemistry.[40]

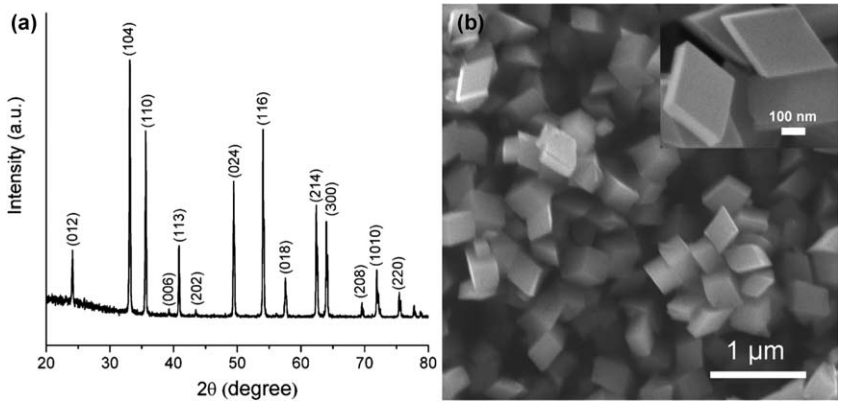

Fig. 15 (a) X-ray diffraction pattern and (b) SEM image of α-Fe_2O_3 particles obtained through hydrothermal synthesis. Reproduced from Ref. 41 with permission from The Royal Society of Chemistry.[41]

symmetry is the cause for its better performance. In the case of the orthorhombic phase, the photoreactivity is governed by the availability of exposed facets and its electronic structure, when compared to the case of the higher symmetry tetragonal phase. This combination of approaches allows for a detailed probing of the parameters which control photocatalytic activity in such catalysts.

Single-crystalline α-Fe_2O_3 with six exposed high-index facets has recently been reported through a hydrothermal approach, as shown in Fig. 15.[41] Here, $FeCl_3 \cdot 4H_2O$ and urea were dispersed in aqueous formamide solution before treatment at 120 °C for 12 h. The concentration of the formamide has an enormous effect on the growth of the particles as, without it, irregular shaped particles are obtained. The reaction time too must be considered, with shorter reaction times yielding small particles. The authors suggest that it is the selective adsorption of formamide on the β-FeOOH particle {104} plane that leads to the directed aggregation and phase transformation to α-Fe_2O_3 with such high index crystal facets.

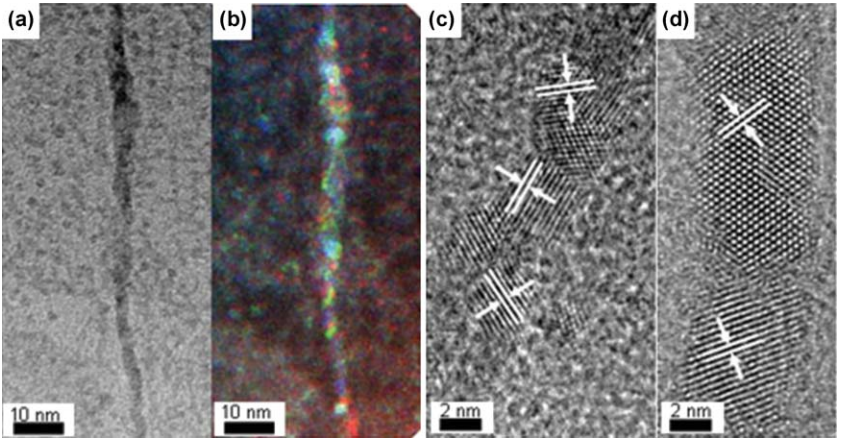

Fig. 16 TEM images of shorter CeO_2 nanowires from 4 h solvothermal reaction times. (a) Bright field TEM image and (b) false-colored image show individual crystallographic orientations. Crystallite size and orientation of CeO_2 nanowires after (c) 4 h and (d) 24 h reveal longer, more uniform materials for increased reaction times. Reproduced from Ref. 42 with permission from The Royal Society of Chemistry.[42]

Murrie and coworkers have established a solvothermal decomposition route to high aspect ratio LnO_x nanowires and have proposed a mechanism for their formation.[42] For the formation of nanowires, the presence of water (*e.g.* from water of crystallisation) and the elevation of pressure are essential. Detailed electron microscopy studies reveal that the wires are made up of regions of single crystals whose lengths vary depending on the lanthanide in question. The nanowire width also appears to decrease with increasing Ln atomic number (the exception is Dy_2O_3, where ribbons are formed). To probe this in greater detail, shorter reaction times were used and the shorter wires obtained are shown in Fig. 16.

These shorter wires appear to comprise of 3 nm particles, randomly orientated and are not as smooth as their 24 h reacted counterparts. A three-stage, imperfect orientated attachment growth mechanism has been suggested, where individual nanoparticles initially form then self-assemble into a polycrystalline chain before a recrystallisation renders the nanowire crystallographically aligned. This explains the observation of nanowire width changes across the series: heavier Ln oleates are less reactive and form smaller initial particles and given the width of a single wire is one particle across, this would account for a reduction in wire width with increasing atomic number. The self-assembly process occurs as a result of surfactant-assisted templating, where the reaction constituents organise into an organic superstructure.

By growing TiO_2 nanoparticles on a scaffold of a layered MoS_2/graphene (MG) hybrid, Jaroniec and co-workers have demonstrated that this two-step hydrothermal route employed yields an inexpensive photocatalytic material with enhanced properties.[43] The MG hybrid behaves as a co-catalyst, effectively promoting an improvement in the photocatalytic H_2 production of TiO_2 with a rate of 165.3 μmol h^{-1} for a 0.5% MG hybrid containing 95% MoS_2 and 5% graphene. In an effort to explain the

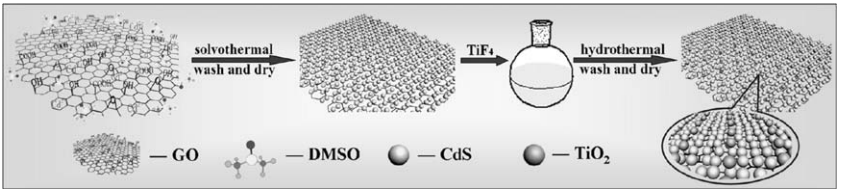

Fig. 17 Schematic showing the preparation of a multicomponent hybrid material CdS-graphene-TiO_2. Reproduced from Ref. 44 with permission from the American Chemical Society.[44]

mechanism for this enhanced behaviour, the authors propose that a co-operative partnership between the MoS_2, the graphene and the TiO_2 drives the high H_2 production. The photoexcited electrons in the conduction band of TiO_2 can transfer to the MoS_2 *via* the graphene, where electron mobility is high. A multicomponent hybrid material, encompassing CdS, graphene and TiO_2, has been prepared using an *in situ* method by Xu and coworkers.[44] A previous report by the same authors showed a one-step hydrothermal method to prepare a CdS-graphene nanocomposite, which demonstrated selective oxidation of alcohols.[45] By adding an additional hydrothermal step to introduce various amounts of TiO_2, a ternary hybrid with even better photoactivity has been achieved. The reaction scheme is shown in Fig. 17 and could be expanded to incorporate a range of graphene-based nanocomposite materials with enhanced photocatalytic behaviour.

The combination of metal particles with semiconductor nanostructures can lead to composites with enhanced catalytic or sensing properties. Xi *et al.* have reported the preparation of noble-metal particles on WO_3 nanostructures by taking advantage of the reductive nature of the WO_x starting material.[46] Briefly, $WO_{2.72}$ urchin-like structures can be prepared hydrothermally and then introduced to the desired noble metal salts in aqueous solution at room temperature. The metal ions are reduced by the $WO_{2.72}$, leading to the formation of metal nanoparticles on the surface of the nanostructure. The conversion to WO_3 occurs through the redox reaction with the metal ions and is completed on exposure to air. Enhanced photocatalytic activity for the degradation of Rhodamine B has been reported for Rh/WO_3, Au/WO_3, Pt/WO_3 and Ag/WO_3, when compared to bare WO_3 and N-doped TiO_2, making this a facile approach for metal/WO_3 hybrid nanocomposites.

As an alternative to Pt-based electrocatalysts for ORR, Zheng *et al.* have studied the synergetic effects of combining MnO_x and N–doped carbons in a single material.[47] A one-pot hydrothermal procedure yields a Mn_3O_4@polyaniline nanocomposite, which electron microscopy shows is made up of nanoparticles with a typical size of 20 nm, with an approximate 2 nm polymer coating. With subsequent heat treatment and an acid leaching step, a MnO-m-N-C nanocomposite is obtained as depicted in Fig. 18. The mesoporous structure manifests a large surface area which, combined with the incorporation of up to 5% nitrogen, accounts for an enhanced stability and comparable catalytic response with commercial Pt/C catalysts *via* a

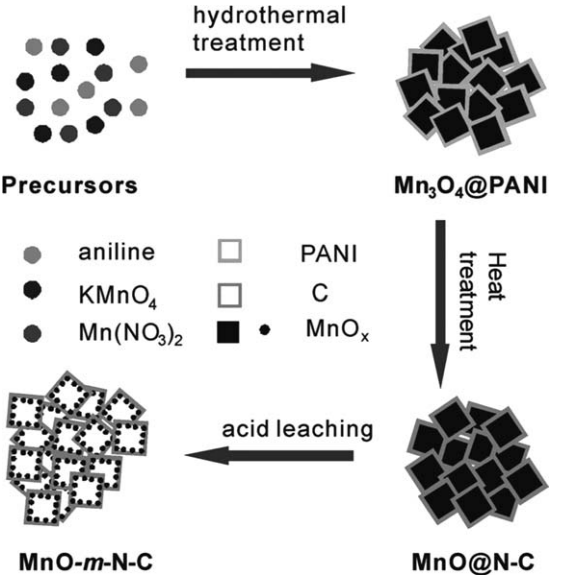

Fig. 18 Schematic of the synthetic procedure for the preparation of MnO-m-N-C nanocomposites. Reproduced from Ref. 47 with permission from Wiley and Sons.[47]

four-electron reduction pathway. Cu- and Ni-doped α-MnO_2 nanowires have also been recently prepared using a hydrothermal method for ORR catalysis.[48] For ORR applications, these nanowires were blended with conductive carbon, where graphene-like carbon was found to provide a catalyst blend with steady state currents that were approaching those of commercially available Pt/C.

A $MnCo_2O_4$-graphene hybrid has been prepared using solvothermal methods by Dai and co-workers for use as a cathode catalyst for Li-O_2 batteries.[49,50] In these cells, the Li metal anode is oxidised, while O_2 is reduced at the cathode during discharge.[51] In order to tackle the problems associated with overpotential and short life cycles, the metal oxide-graphene composite was developed to act as a cathode catalyst for the oxygen reduction reaction (ORR) and oxygen evolution reaction (OER). The metal precursors, $Co(OAc)_2$ and $Mn(OAc)_2$, are first hydrolysed in an $EtOH/H_2O$ ammonia solution and introduced to graphene oxide. This allows for uniform nucleation of the metal species on the surface of the N-doped reduced graphene oxide. A solvothermal treatment then affords the hybrid material. Electrochemical testing reveals this hybrid material displays lower overpotential and longer life cycles than other metal oxide and Pt/C-based catalysts.

2.4 Co-precipitation and sol-gel methods

In an effort to improve photocatalytic behaviour, Yu *et al*. have employed an Ag_2O co-catalyst in conjunction with Bi_2WO_3 nanoparticles for the decomposition of organic materials.[52] The Bi_2WO_3 nanoparticles were synthesised using a precipitation reaction between bismuth nitrate and sodium tungstate. The final composite was prepared *via* an impregnation method using silver nitrate solution where, after calcination, the Ag_2O

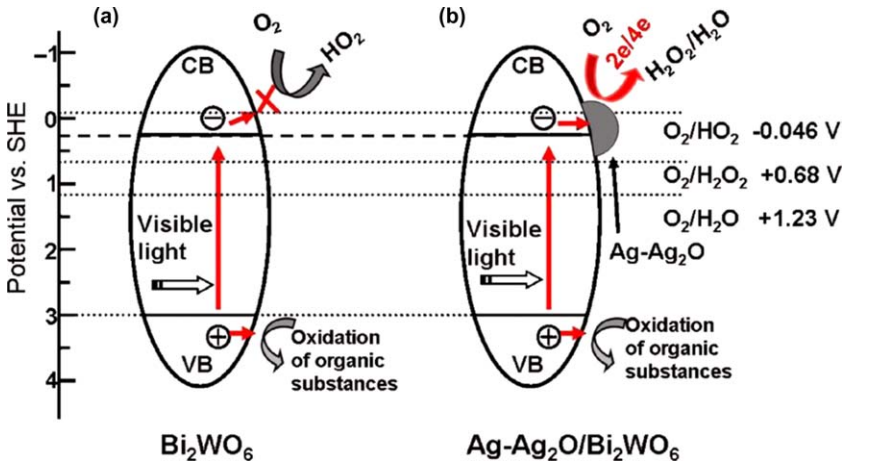

Fig. 19 Schematic illustration showing the possible photocatalytic mechanism of (a) Bi_2WO_6 and (b) Ag-Ag_2O/Bi_2WO_6. Reproduced from Ref. 52 with permission from Elsevier.[52]

co-catalyst phase is found on the surface of the particles. The photocatalytic degradation of methyl orange shows bare Bi_2WO_3 nanoparticles, even when coated with Ag nanoparticles, have no effect. Interestingly, the introduction of Ag_2O to the surface brings with it an enhanced photocatalytic activity. The proposed mechanism is illustrated in Fig. 19.

On decoloration of the organic species, XPS analysis reveals the formation of metallic Ag nanoparticles in conjuction with Ag_2O. The authors suggest that the Ag-Ag_2O co-catalyst essentially transfers the photogenerated electrons from the Bi_2WO_3 conduction band to the oxygen *via* a multi-electron transfer process.

Bifunctional catalysts comprised of $Sr_{0:95}Ce_{0:05}CoO_{3-\delta}$ loaded with copper nanoparticles have recently been prepared using a sol-gel method.[53] By mixing stoichiometric amounts of strontium nitrate, cobalt nitrate and cerium nitrate in water, ethylene glycol and citric acid, a gel was formed after heating at 80 °C for 10 h which was dried and sintered to obtain the perovskite phase. A polyol synthesis allowed for the formation of copper nanoparticles on the perovskite sample. Again, the combination of both structures in a single nanocomposite provides a material which demonstrates better performance than for the individual components alone.

2.5 Low-temperature synthetic developments

In their continued development of low temperature routes to nanostructured materials, the Brutchey group at USC have extended their vapor-diffusion sol-gel (VDSG) method for the benign production of nanocrystals to include scheelite-structured $AMoO_4$ nanocrystals.[54] Sub 30 nm, single crystal nanoparticles of $CaMoO_4$, $SrMoO_4$ and $BaMnO_4$ have been obtained after thermal aging at 80 °C and are shown in Fig. 20. This demonstrates the flexibility of such a method, which could allow for the controlled preparation of a range of metal oxide materials.

By careful consideration of pH, reaction time and $TiCl_3$ concentration, Sen and co-workers have established a room temperature route to

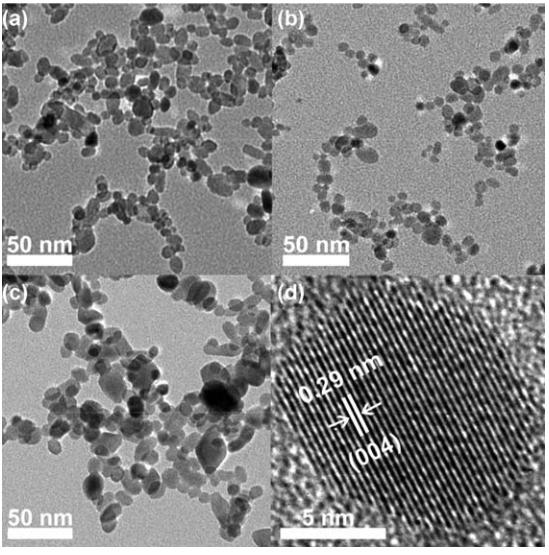

Fig. 20 TEM images of (a, d) $CaMoO_4$, (b) $SrMoO_4$ and (c) $BaMnO_4$ nanocrystals prepared *via* low-temperature VDSG method. Reprinted from Ref. 54 with permission from the American Chemical Society.[54]

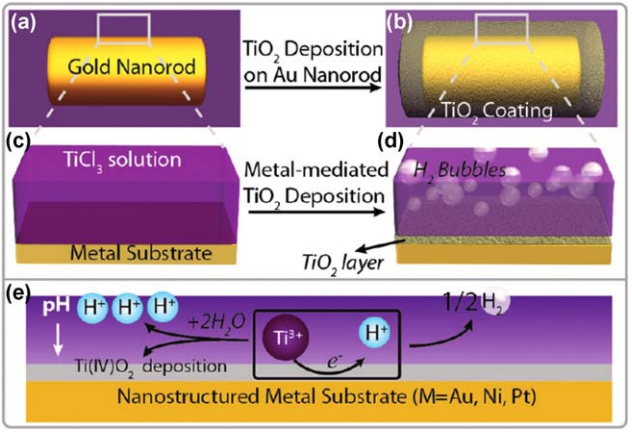

Fig. 21 Reaction scheme for the preparation of TiO_2-metal heterogeneous nanostructures. Reprinted from Ref. 55 with permission from the American Chemical Society.[55]

TiO_2-metal heterogeneous nanostructures.[55] The reaction scheme for this method is illustrated in Fig. 21. Anaerobic conditions are employed and the pH of a $TiCl_3$ solution is adjusted to 2.5, to prevent uncontrolled precipitation. Metal surfaces of Pt, Au and Ni are exposed to the solution and H_2 bubbling is noted, given the lower overpotential for H^+ reduction to hydrogen on these surfaces. To arrive at the anatase form, the material can be annealed at between 400 and 500 °C. Fine-tuning of the reaction conditions can yield TiO_2 on the ends of metal nanowires, core-shell nanostructures or composite nanotubes.

Hydrolysis at room temperature of a series of bismuth oxido clusters has found that for the $Bi_{22}O_{26}(OSiMe_2{}^tBu)_{14}$ cluster, full hydrolysis led to phase pure, metastable β-Bi_2O_3.[56] In the case of the $[Bi_{38}O_{45}(OMc)_{24}(DMSO)_9] \cdot 2DMSO \cdot 7H_2O$ cluster, (where $OMc = O_2CC_3H_5$) NaOH was required for full hydrolysis. These nanoparticles show a very high photocatalytic activity for the degradation of Rhodamine B.

3 Concluding remarks

Over the past year, there has been a number of exciting developments in the synthesis and characterisation of metal oxide nanostructures. With developments in synthetic approaches comes the need for complete and detailed characterisation in order to establish what governs the underlying mechanisms in these materials. Of increasing importance has been the combination of several nanostructures into a single composite materials and probing the nature of synergetic relationships between these constituent nanocomposite parts, which have been shown to lead to enhanced or even new properties not displayed by any single entity. This represents endless possibilities for composite design through the combination of nanoscale materials, which could lead to a wealth of unexpected properties. Through developing a deeper understanding of the structure-property relationships in these materials, the degree of control over particle size, morphology and crystal chemistry is also increasing.

There has also been a great focus on developing single-step, one-pot routes to nanomaterials, which are not only time and cost effective, but also environmentally sound. Through careful consideration of the properties of starting materials, it is possible to design experiments where all reaction steps can take place *in situ*, without the requirement of additional work-up or purification.

References

1 S. A. Corr, *Nanoscience*, Royal Society of Chemistry, Cambridge, 2013, pp. 180–207.
2 J. Meyer, S. Hamwi, M. Kroger, W. Kowalsky, T. Riedl and A. Kahn, *Adv. Mater.*, 2012, **40**, 5408–5427.
3 S. Rawalekar and T. Mokari, *Adv. Energy Mater.*, 2013, **3**, 12–27.
4 M. Zhi, C. Xiang, J. Li, M. Li and N. Wu, *Nanoscale*, 2013, **5**, 72–88.
5 Y.-F. Sun, S.-B. Liu, F.-L. Meng, J.-Y. Liu, Z. Jin, L.-T. Kong and J.-H. Liu, *Sensors*, 2012, **12**, 2610–2631.
6 M. J. Williams and S. A. Corr, *Frontiers of Nanoscience*, Elsevier, UK, 2013, pp. 29–63.
7 Z. Wang, L. Zhou and X. W. Lou, *Adv. Mater.*, 2012, **24**, 1903–1911.
8 R. Buonsanti and D. J. Milliron, *Chem. Mater.*, 2013, **25**, 1305–1317.
9 S. A. Corr and R. Seshadri, *Comprehensive Inorganic Chemistry*, Elsevier, UK, 2013, vol. 2, pp. 1–15.
10 Y. Ren, Z. Ma and P. G. Bruce, *Chem. Soc. Rev.*, 2012, **41**, 4909–4927.
11 M. Niederberger and G. Garnweitner, *Chem. Eur. J.*, 2006, **12**, 7282–7302.
12 M. Grzelczak and L. M. Liz-Marzán, *Chem. Soc. Rev.*, 2014, DOI: 10.1039/C3CS60256G, in press.
13 M. Niederberger, *Acc. Chem. Res.*, 2007, **40**, 793–800.

14 R. Sui and P. Charpentier, *Chem. Rev.*, 2012, **112**, 3057–3082.
15 J. Lee, S. Zhang and S. Sun, *Chem. Mater.*, 2013, **25**, 1293–1304.
16 S. Guo, S. Zhang, L. Wu and S. Sun, *Angew. Chem. Int. Ed.*, 2012, **51**, 11770–11773.
17 Q. Dai and J. Tang, *Nanoscale*, 2013, **5**, 7512–7519.
18 Y. Lee, J. Suntivich, K. J. May, E. E. Perry and Y. Shao-Horn, *J. Phys. Chem. Lett.*, 2012, **3**, 399–404.
19 T. R. Gordon, T. Paik, D. R. Klein, G. V. Naik, H. Caglayan, A. Boltasseva and C. B. Murray, *Nano Lett.*, 2013, **13**, 2857–2863.
20 M. Sytnyk, R. Kirchschlager, M. I. Bodnarchuk, D. Primetzhofer, D. Kriegner, H. Enser, J. Stangl, P. Bauer, M. Voith, A. W. Hassel, F. Krumeich, F. Ludwig, A. Meingast, G. Kothleitner, M. V. Kovalenko and W. Heiss, *Nano Letters*, 2013, **13**, 586–593.
21 L. Zhang, H. W. Wu, S. Madhavi, H. H. Hng and X. W. Lou, *J. Am. Chem. Soc.*, 2012, **134**, 17388–17391.
22 C. Cavelius, K. Moh and S. Mathur, *Cryst. Growth Des.*, 2012, **12**, 5948–5955.
23 J. Gim, V. Mathew, J. Lim, J. Song, S. Baek, J. Kang, D. Ahn, S.-J. Song, H. Yoon and J. Kim, *Sci. Rep.*, 2012, **2**, 946–1–6.
24 A. Manthiram, *J. Phys. Chem. Lett.*, 2011, **2**, 176–184.
25 J. Wang and X. Sun, *Energy Env. Sci.*, 2012, **5**, 5163–5185.
26 Y. Feng, I. S. Cho, P. M. Rao, L. Cai and X. Zheng, *Nano Lett.*, 2013, **13**, 855–860.
27 Z. Jin, M. Xiao, Z. Bao, P. Wang and J. Wang, *Angew. Chem. Int. Ed.*, 2012, **51**, 6406–6410.
28 Z. Jin, F. Wang, F. Wang, J. Wang, J. C. Yu and J. Wang, *Adv. Funct. Mater.*, 2013, **23**, 2137–2144.
29 G. Jian, L. Liu and M. R. Zachariah, *Adv. Funct. Mater.*, 2013, **23**, 1341–1346.
30 A. Namai, M. Yoshikiyo, K. Yamada, S. Sakurai, T. Goto, T. Yoshida, T. Miyazaki, M. Nakajima, T. Suemoto, H. Tokoro and S. Ohkoshi, *Nature Comm.*, 2012, **3**, 1035–1–6.
31 E. Pellicer, M. Cabo, E. Rossinyol, P. Solsona, S. Suriñach, M. D. Baró and J. Sort, *Adv. Funct. Mater.*, 2012, **23**, 900–911.
32 X. Bai, A. Pucci, V. T. Freitas, R. A. S. Ferreira and N. Pinna, *Adv. Func. Mater.*, 2012, **22**, 4275–4283.
33 A. Pucci, M.-G. Willinger, F. Liu, X. Zeng, V. Rebuttini, G. Clavel, X. Bai, G. Ungar and N. Pinna, *ACS Nano*, 2012, **6**, 4382–4391.
34 F. J. Douglas, D. A. MacLaren and M. Murrie, *RSC Adv.*, 2012, **2**, 8027–8035.
35 L. Wang, H. Ji, F. Zhu, Z. Chen, Y. Yang, X. Jiang, J. Pinto and G. Yang, *Nanoscale*, 2013, **5**, 7613–7621.
36 C. Xu, J. Sun and L. Gao, *J. Mater. Chem.*, 2012, **22**, 975–979.
37 Z. Wang, S. Madhavi and X. W. Lou, *J. Phys. Chem. C*, 2012, **116**, 12508–12513.
38 X. Chen, X. Jing, J. Wang, J. Liu, D. Song and L. Liu, *CrystEngComm*, 2013, **15**, 7243–7249.
39 X. Du, D. Zhang, L. Shi, R. Gao and J. Zhang, *J. Phys. Chem. C*, 2012, **116**, 10009–10016.
40 T. Zhang, K. Zhao, J. Yu, J. Jin, Y. Qi, H. Li, X. Hou and G. Liu, *Nanoscale*, 2013, **5**, 8375–8383.
41 X. Liu, J. Zhang, S. Wu, D. Yang, P. Liu, H. Zhang, S. Wang, X. Yao, G. Zhu and H. Zhao, *RSC Adv.*, 2012, **2**, 6178–6184.
42 F. J. Douglas, D. A. MacLaren, C. Renero-Lecuna, R. D. Peacock, R. Valiente and M. Murrie, *CrystEngComm*, 2012, **14**, 7110–7114.
43 Q. Xiang, J. Yu and M. Jaroniec, *J. Am. Chem. Soc.*, 2012, **134**, 6575–6578.

44 N. Zhang, Y. Zhang, X. Pan, M.-Q. Yang and Y.-J. Xu, *J. Phys. Chem. C*, 2012, **116**, 18023–18031.
45 N. Zhang, Y. Zhang, X. Pan, X. Fu and Y.-J. Xu, *J. Phys. Chem. C*, 2011, **115**, 23501–23511.
46 G. Xi, J. Ye, Q. Ma, N. Su, H. Bai and C. Wang, *J. Am. Chem. Soc.*, 2012, **134**, 6508–6511.
47 Y. Tan, C. Xu, G. Chen, X. Fang, N. Zheng and Q. Xie, *Adv. Funct. Mater.*, 2012, **22**, 4584–4591.
48 T. N. Lambert, D. J. Davis, W. Lu, S. J. Limmer, P. G. Kotula, A. Thuli, M. Hungate, G. Ruan, Z. Jin and J. M. Tour, *Chem. Commun.*, 2012, **48**, 7931–7933.
49 H. Wang, Y. Yang, Y. Liang, G. Zheng, Y. Li, Y. Cui and H. Dai, *Energy Environ. Sci.*, 2012, **5**, 7931–7935.
50 Y. Liang, H. Wang, J. Zhou, Y. Li, J. Wang, T. Regier and H. Dai, *J. Am. Chem. Soc.*, 2012, **134**, 3517–3523.
51 F. Cheng and J. Chen, *Chem. Soc. Rev.*, 2012, **41**, 2172–2192.
52 H. Yu, R. Liu, X. Wang, P. Wang and J. Yu, *Appl. Catal., B*, 2012, **111–112**, 326–333.
53 W. Yang, J. Salim, S. Li, C. Sun, L. Chen, J. B. Goodenough and Y. Kim, *J. Mater. Chem.*, 2012, **22**, 18902–18907.
54 S. P. Culver, F. A. Rabuffetti, S. Zhao, M. Mecklenburg, Y. Song, B. C. Melot and R. L. Brutchey, *Chem. Mater.*, 2013, **25**, 4129–4134.
55 R. Liu and A. Sen, *J. Am. Chem. Soc.*, 2012, **134**, 17505–17512.
56 M. Schlesinger, S. Schulze, M. Hietschold and M. Mehring, *Dalton Trans.*, 2013, **42**, 1047–1056.

Recent developments in the design of nanomaterials for photothermal and magnetic hyperthermia induced controllable drug delivery

Alexander E. Dunn,[a] Douglas J. Dunn,[a] May Lim,*[a] Cyrille Boyer[b] and Nguyễn Thi Kim Thanh[c]
DOI: 10.1039/9781849737623-00225

Recent developments in anti-cancer drugs are focused on minimising side effects and improving treatment efficacy. This can be achieved by using a carrier that releases the drug in response to a stimulus. In recent years, research has been directed towards the use of light or alternating magnetic fields as remote stimuli in what is called photothermal and magnetic hyperthermia induced controllable drug delivery, respectively. Much progress has also been made in the use of nanoparticles and polymeric macromolecules as drug carriers. By combining polymers with inorganic nanoparticles into a single entity, it becomes possible to harness the light or magnetic field responsive properties of nanoparticles with the drug storage and release properties of polymers for drug delivery. In this review, we explore recent developments of polymer-nanoparticle hybrids drug carriers for photothermal and magnetic hyperthermia controllable drug delivery.

1 Introduction

Recent improvements in cancer treatment have resulted in an increase in post-diagnosis life expectancy. These improvements were enabled by the development of potent therapeutic agents with novel modes of action. Nonetheless, due to their inherent toxicity, many of these therapeutic agents are limited by the dose that can be safely delivered without causing debilitating side effects. In addition, a systemic route of administration often results in a narrow therapeutic window such that prolonged exposure to the therapeutic agent is required in order to achieve sufficient treatment efficacy. This may lead to indiscriminate cytotoxicity of the therapeutic agent toward normal and cancer cells throughout the body, resulting in severe side effects such as immunosuppression and organ failure in the patient.

A nanomaterial based controllable drug delivery platform would overcome many of the major drawbacks in cancer therapy. These nanocarriers store the therapeutic agent in an inert and protected state during transportation and subsequently provide concentrated and on-demand release of

[a]*ARC Centre of Excellence for Functional Nanomaterials, School of Chemical Engineering, The University of New South Wales, Sydney NSW 2052, Australia*
[b]*Australian Centre for NanoMedicine and Centre for Advanced Macromolecular Design, School of Chemical Engineering, The University of New South Wales, Sydney NSW 2052, Australia*
[c]*Department of Physics and Astronomy, University College London, Gower Street, WC1E 6BT, London, United Kingdom and UCL Healthcare Biomagnetic and Nanomaterials Laboratories, 21 Albemarle Street, London, W1S 4BS, United Kingdom.*
**E-mail: m.lim@unsw.edu.au*

the agent at the site of the cancer.[1–5] In particular, the ability to control the timing, dosage and release profile of the agent as well as being able to carry out repeated on-demand dosing from a single administration would greatly increase the efficacy of the therapeutic agents. The short and long-term damage to healthy tissue will also be minimised. This approach may also help address the importance of timing on therapeutic effects, such as chrono-administration, a new concept that is receiving increasing recognition.[6]

Controlled release of drugs from a nanocarrier can be facilitated by either a local or remote stimulus. A local stimulus is one that relies on changes in conditions within the body, often taking advantage of physical and/or chemical characteristics that are unique to diseased tissue to release the drug from the carrier. A remote stimulus is one that exists outside the body, and ideally, should be non-invasive, non-irradiative, and yet able to penetrate the body for localised drug release. Remote stimuli are of particular significance because they can provide both temporal and spatial control over the drug release.

The use of light or an alternating magnetic field as remote stimuli for the controllable release of drugs, in what is known respectively as photothermal and magnetic hyperthermia induced controllable drug release, has gained much interest recently. In magnetic hyperthermia induced drug release, the drug carrier would consist of a magnetic nanomaterial that interacts specifically with an oscillating magnetic field.[7] Photothermal induced drug release relies on the interaction between a plasmonic nanomaterial and visible or infrared light.[8] Typically these interactions result in the generation of heat within the nanocarriers, which in turn initiates release of the drug. Herein, we will review recent developments in the design of nanomaterials for magnetic hyperthermia and photothermal induced controllable drug delivery, focusing on organic-inorganic hybrid systems. We will provide an overview of different ways in which metallic or oxide nanomaterials can be conjugated with polymeric macromolecules to facilitate photothermal and magnetic hyperthermia induced controllable drug delivery. Thereafter, we will review recent developments in photothermal and magnetic hyperthermia induced drug release.

1.1 Organic-inorganic hybrid nanomaterials for photothermal or magnetic hyperthermia induced controllable drug delivery

1.1.1 Design of nanomaterials for photothermal and magnetic hyperthermia induced controllable drug delivery. Stimulus responsive nano drug carrier platforms can be broadly categorized as organic-based, inorganic-based or a hybrid combination of the aforementioned. Inorganic nano-platforms include metallic nanoparticles (*e.g.* gold, silver), oxides (*e.g.* iron oxides, silica), and quantum dots. Organic nano-platforms include polymeric nanoparticles, micelles, liposomes, polymersomes and dendrimers. The use of carbon-based nanomaterials (*e.g.*, fullerenes, carbon nanotubes and graphene) has also been explored recently, although questions have been raised regarding the biocompatibility of these materials. Examples of hybrid platforms include colloidal gold encapsulated in liposomes and superparamagnetic iron oxide particles with polymer-grafted surfaces.

The most commonly reported structures for photothermal and magnetic hyperthermia induced controllable drug delivery are outlined in Fig. 1. Most of these structures are derived from earlier designs of nanomaterials based drug carriers. Perhaps the most significant of these developments was the combination of organic and inorganic materials; specifically, the light or magnetic field responsive properties of the inorganic nanomaterials were combined with the drug loading and release properties of the organic macromolecules to yield composites with controllable drug delivery capabilities.

Inorganic nanostructures for the purpose of photothermal and hyperthermia induced drug delivery almost exclusively incorporate two or more nanomaterials, whereby each provides specific functionality. The simplest designs involve the encapsulation of light or magnetic responsive materials (*e.g.* plasmonic gold nanorods for photothermal heating and magnetite nanoparticles for magnetic) within a mesoporous shell structure (see Fig. 1a), or decoration of the mesoporous structure's surface with the stimuli responsive nanoparticles (see Fig. 1b). The most commonly used mesoporous compound is silica, due to the facile synthesis methods (usually

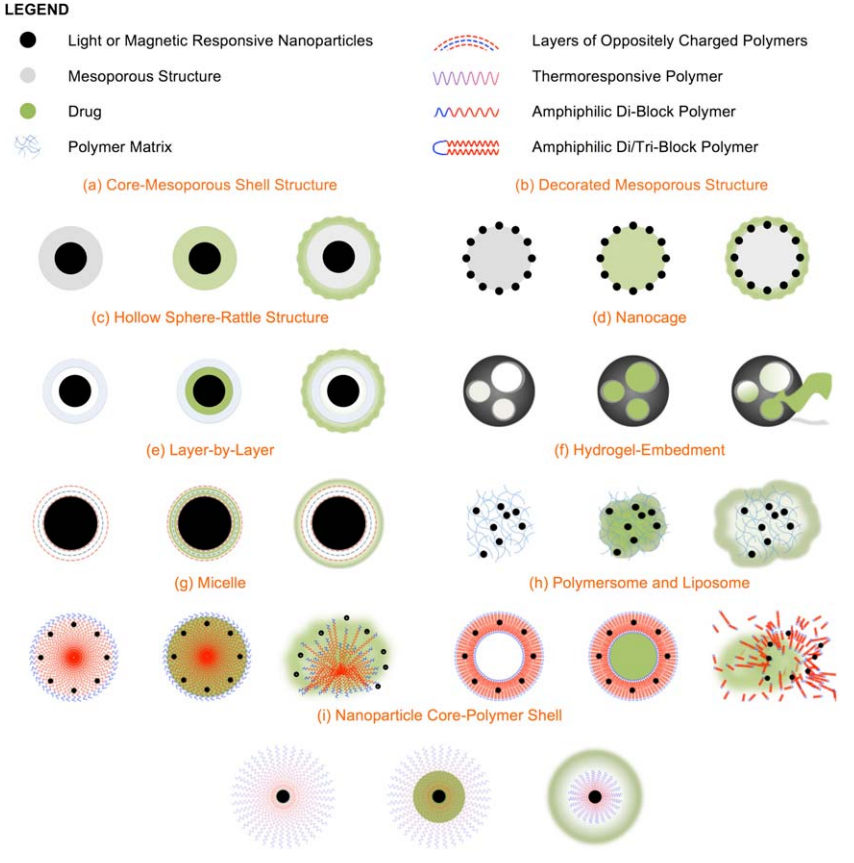

Fig. 1 Visual representation of the structure (left), loading of drug (centre) and release of drug (right) for the commonly used nanostructures in photothermal and magnetic hyperthermia induced controllable drug delivery.

via the well-established Stöber method).[9] In these carriers, the drug is stored within the pores of the mesoporous material[10–12] and released upon thermal expansion; this heat is generated by the interactions between the light and plasmonic nanomaterials, or between the alternating magnetic field and magnetic nanomaterials. Whilst simple to fabricate, the functionality of these carriers is usually limited by a low storage capacity. That is, it is usually not possible to deliver a meaningful quantity of the drug due to the small storage volume of the pores in the mesoporous material and the poor absorptivity of some drugs onto the carrier.

To address this issue, some groups have investigated the use of hollow spheres-rattle structures, in which the 'rattle' is a light responsive or magnetic material (see Fig. 1c).[13,14] These structures improve drug-loading capacity by integrating additional storage space through means of a hollow interior, and the mesoporous shells provide a pathway for diffusion of the drug from the interior of the carrier. It is noted here that most methods for synthesising inorganic hollow sphere with rattle structures are not trivial. It is only with the development of facile synthesis methods in 2008 and 2009 (for instance the work of Yin and co-workers) that the use of hollow spheres with rattles structure has become feasible for controllable drug delivery.[15–18]

Another recent development is the use of nanocages for photothermal induced drug delivery. Nanocages are hollowed out nanoparticles with a cage-like surface structure, in which the porous material and the stimulus responsive material are one and the same (see Fig. 1d). The storage and release of drug from the nanocage is facilitated through the inclusion of a phase change material that traps the drug within the nanocage until release is initiated by a temperature change. Gold nanocages have been constructed by first forming a gold-silver alloy nanoparticle, followed by etching of the silver to obtain the cage-like structure.[19,20]

Each of the aforementioned inorganic nanostructures has a number of significant design limitations. Firstly, most of them rely on diffusion as the main mechanism for drug release. Diffusion of the drug is driven by concentration gradients between the interior and exterior of the drug delivery agent. While the rate of diffusion may be modified to some extent by introducing a physical barrier or altering the environment of the drug carrier, a driving force for diffusion will always be present. This results in premature release of the drug from the carrier, as well as a lack of control over the drug release rate and profile. Secondly, some of these inorganic nanostructures lack *in vivo* stability and biocompatibility; for *in vivo* applications, aggregates of nanoparticles that are larger than 4 μm can disrupt blood flow through veins or capillaries.[21] Large nanoparticles are also more likely to be captured and removed by the reticuloendothelial system (RES); this is reflected by a short retention time of the drug carrier in the body. This is generally a suboptimal phenomenon because sufficient retention time of the drug carrier is required if meaningful quantities of drug are to be released.

To address these three issues, researchers have considered the use of polymeric macromolecules. Polymers have been shown to improve size stability, increase residence time, and enhance the permeability and retention of nanoparticles in cancer cells through provision of charge and

steric repulsions. In addition, polymeric compounds have also been shown to facilitate drug storage by providing a chemical or physical adhesion mechanism. Some of the earliest demonstrations of photothermal and magnetic hyperthermia induced drug delivery are from organic-inorganic nanocomposites prepared *via* the Layer-by-Layer (LbL) and hydrogel-embedment approaches.[22,23] In the LbL method, the drug carrier consists of a nanoparticle core that is coated in alternating layers of positively and negatively charged polymers, with the drug trapped between each layer (see Fig. 1e). The polymer layers are held in place by electrostatic forces from the oppositely charged layers before and after it. In the embedment structure, the drug carrier consists of a network of cross-linked polymer networks, sometimes referred to as a hydrogel, with the drug adsorbed within the gel matrix (see Fig. 1f). In both cases, the drug is weakly associated with the drug carrier and can be released in response to changes in pH, ionic strength, or in the case of photothermal and magnetic hyperthermia induced drug release, a change in temperature. For photothermal and magnetic hyperthermia induced drug release from the LbL and hydrogel/embedment constructs, heat is generated by plasmonic or magnetic nanoparticle cores that respond to light and alternating magnetic fields, respectively.

These electrostatic interaction based methods for modifying inorganic materials with polymers also suffer from low drug storage capacity and limitations associated with the type of drug that can be stored. To address this, researchers have developed a family of organic vesicle structures that can be broadly categorised as micelles, liposomes and polymersomes. These structures are composed of amphiphilic macromolecules: phospholipids in the case of liposomes, and amphiphilic di- or tri-block copolymers in the case of micelles and polymersomes. Micelles are formed when the amphiphilic polymers align to form a spheroid with a hydrophobic core (see Fig. 1g). Liposomes and their synthetic counter-part, polymersomes, are formed when the polymers self-assemble to form a hydrophobic bilayer membrane that encapsulates a hydrophilic core (see Fig. 1g).[24,25] The key advantages of these vesicle structures are their large drug storage capacity and the capability to load hydrophobic drugs. Moreover, for liposomes and polymersomes, hydrophobic and hydrophilic drugs can be dissolved into the bilayer membrane and central cavity, respectively, thus enabling drugs with different polarities to be delivered within a single nanostructure. The stability of these vesicle structures is dependent on the conditions of the surroundings such as pH, ionic strength and temperature. Thus, by incorporating stimuli responsive nanoparticles that are able to induce a change in the local surroundings, it is possible to induce drug release at a desired time and location in response to the stimulus applied by the administering clinicians.

Carriers that are based on electrostatic interactions between the polymer and inorganic particles also rely on the fact that the polymer can adsorb onto the particle core; these designs further assume that the polymer layers do not detach with changes to the environment pre-drug delivery and release. Where these conditions cannot be met, a better method for conjugating polymer to nanoparticle would be one where the polymer is chemically bonded to the particle to form a nanoparticle core-polymer shell

structure (see Fig. 1i). For applications in photothermal and magnetic hyperthermia induced drug release, the design typically incorporates a temperature responsive polymer that is conjugated to a light or magnetic responsive nanoparticle core, respectively. When heat is generated by the photothermal or magnetic hyperthermia effects, the polymer will contract in a manner that results in the release of drug from the drug carrier.

Evidence outlined herein seems to indicate that organic-inorganic hybrid nanomaterials are currently the most promising carrier for controllable drug delivery. The strength of these nanocarriers lies in their ability to improve functionality by harnessing the beneficial properties of both the inorganic and organic components. Typically, the inorganic component provides a stimulus response mechanism, while the organic component improves *in vivo* stability, biocompatibility and provides a drug storage/release mechanism. In the following section we will examine the key considerations for the design of these polymers and the various methods for organic-inorganic nanomaterial conjugation. We will also look at the ways in which the properties of the polymer may be tailored to suit the desired drug storage properties of the nanocomposite.

1.1.2 Strategies for polymer design and organic-inorganic nanomaterial conjugation. As outlined in the previous section, polymers play a key role in improving the size stability, biocompatibility, uptake, retention and drug storage capacity of most nanomaterial based drug delivery platform.[26–29] The main designs of interest are nanoparticle core-polymer shell and polymeric vesicles. Herein, we outline the ways in which the polymer is designed, and subsequently conjugated to the inorganic nanomaterials to form an efficient interdependent mechanism that can be used for controllable drug delivery.

Design of polymers

The key considerations in the design of a nanoparticle based drug delivery platforms for *in-vivo* applications are:

(i) The nanoparticles should be present in a size range between 10 nm to 200 nm, to take advantage of the enhanced permeability and retention (EPR) effect[30–32] that is caused by an increased permeability of the vascular system and inefficient lymphatic drainage close to tumour sites;

(ii) The surface of these nanoparticles should be anti-fouling to avoid rapid absorption of proteins, and therefore limit their clearance by the reticuloendothelial system; and[33]

(iii) The colloidal stability of the nanoparticles should be maintained in biological fluid to avoid aggregation and precipitation.

Each of these objectives may be achieved by coating the inorganic nanoparticles with a polymer. A polymer coating provides colloidal stability in water through steric stabilisation, and can provide surface functionality allowing the possibility of designing hybrid particles with capacity for multimodal targeting. In addition, the polymer shell can be employed to encapsulate therapeutic compounds thus providing the possibility of controlled release.[27]

The first generations of polymers used for the stabilisation of inorganic nanomaterials were based on natural polymers, such as dextran or carbohydrate derivatives. These biopolymers were adopted for their ability to interact with iron oxide nanoparticle surfaces whilst simultaneously conferring stability in blood plasma. Since then, a number of more advanced polymer designs have since been considered; polyvinylpyrrolidone (PVP), polyvinyl alcohol (PVA), polyethylene glycol (PEG) and its meth(acrylate) derivatives, poly(hydroxypropyl methacrylamide), and poly(*N*-acryloylmorpholine)[33] are among the most widely investigated.[34–37] These polymers are generally deemed 'biocompatible', although it is important to note that both PVA and PVP can adversely adsorb proteins because of H-bonding interactions.[38]

Further advancements in polymer synthesis techniques (using controlled radical polymerisation) have enabled the design of highly customisable polymers with well-controlled properties. For instance, an alternative to the generic linear polymer chains is the use of brush polymers (and copolymers) of poly(oligoethylene oxide (meth)acrylate).[33,39–42] These brush-like polymers (short PEG chains grafted onto an acrylic backbone) offer comparable anti-fouling properties and blood compatibility to linear PEG.[39]

In addition, polymers may be designed to be responsive to a change in their environment, such as pH, temperature and light.[43–48] These physical changes can be exploited in drug delivery to control the release profile of therapeutic agents. Temperature responsive polymers are the most relevant for photothermal and magnetic hyperthermia induced drug delivery. Of the thermoresponsive polymers, poly(*N*-isopropylacrylamide) (PNIPAM) is the most widely used due to its easily tuneable thermoresponsive properties.[49,50] The lower critical solution temperature (LCST) of PNIPAM is typically around 32 °C, and through copolymerisation with appropriate monomers, such as *N,N'*-dimethylacrylamids and *N*-hydroxymethylacrylamide, this LCST may be manipulated.[47,51,52] The other major advantage of PNIPAM is its affinity to a large range of therapeutic drugs. PNIPAM has been proven to be effective for storage and delivery of several different kinds of model drugs, including heteropolyacids (HPAs),[12] vitamin B_{12},[53] and doxorubicin.[48]

Polymer grafting onto inorganic nanoparticles

In the simplest case, physical attractions between the polymer and nanoparticles can be achieved *via* van der Waals and acid–base interactions, and/or attractive electrostatic interaction between oppositely charged nanoparticles and polymers. This can be achieved through the use of block or random copolymers; these polymers may be enhanced with several functional groups that provide multiple attachment points between the polymer and particle surface.

A more reliable way to conjugate the polymer chains with the nanoparticles is *via* chemical bonds, in what is termed 'grafting'. This is usually achieved through one of two alternative approaches: grafting "onto" and "from".[27] In the grafting "onto" approach, a functional, pre-formed polymer is grafted *in-situ* onto the nanoparticle surface using functionality capable of binding to the inorganic nanoparticles surface. For oxide

nanoparticles such as iron oxide, titanium oxide, cerium oxide, many different types of anchoring groups (dopamine,[54] carboxylic acid,[55] thiol, amine and trimethyl silane[56]) can be used.[57–59] The stability of these hybrid organic-inorganic nanoparticles depends on the strength of the affinity between the anchoring group and the oxide surface. Thiol and amine groups do not provide strong interaction with oxide inorganic materials, thus limiting their feasibility for bio-application, whilst carboxylic acid groups can be displaced by small organic carboxylic acid compounds present in biologic fluid and are limited to a specific range of pH. Multi-carboxylic acid groups have also been introduced to anchor polymers on inorganic nanomaterials.[60] A sturdier alternative is the use of silane groups that can be covalently attached onto the oxide surface by reaction of the oxide layer (*e.g.* Metal-OH) with the silane group. De Palma and co-workers[61] shows that the silane approach allows stable hybrid iron oxide nanoparticles in a large pH range, to be routinely synthesized. Phosphonic acid groups are also commonly exploited to anchor polymers onto different oxides; this often yields stability in a large range of pH and salt media. For metallic nanoparticles such as gold or silver, thiol or disulphide bonds can be employed to covalently attach polymers to the surface. For example, Haddleton[62,63] and other groups[33,64] have demonstrated that thiol presents a very strong affinity to gold surfaces, which in turn allows us to produce gold nanoparticles that are stable in biologic fluid.

In the case of grafting ''from'', an initiator molecule is fixed to the surface of the nanoparticle and the polymer is grown from the surface.[41] Different polymerisation techniques have been employed to achieve this: initially living anionic/cationic polymerisations, and more recently, controlled radical polymerisation, such as reversible addition fragmentation transfer polymerisation,[65] atom transfer radical polymerisation,[41,66,67] and nitroxide mediated polymerisation.[68] The use of these recent controlled radical polymerisation techniques has allowed us to tailor the polymer structures and to control a large range of functional monomers.[69]

As to whether grafting ''from'' or grafting ''onto'' is the better approach, the general consensus is grafting ''from'' yields a higher grafting density than the grafting ''onto'' approach.[41,70] However, grafting ''onto'' allows better control of polymer architecture and functionality, and is therefore more versatile than the grafting ''from'' method. In addition, grafting ''from'' can present difficulties in maintaining the colloidal stability of the hybrid nanoparticles in organic solvents. Nonetheless, the use of living radical polymerisation, with a carefully designed protocol, has been achieved for the modification of nanoparticles using the grafting ''from'' approach. For example, Hatton *et al.*[71] grafted several polymers from iron oxide nanoparticles coated with ATRP initiator. Ring opening polymerisation has also employed to obtain iron oxide nanoparticles coated with linear biodegradable poly(esters)[72] or by hyper-branched polymers.[73]

An alternative approach to grafting ''onto'' or ''from'' has been proposed using the recent development of high yield ''click chemistries'' (*e.g.* azide-alkyne[74,75]). These reactions provide further alternative routes to functionalising nanoparticles with polymers. For example, Turro *et al.*[76] described the stabilisation of maghemite nanoparticles using alkyne

terminated organophosphate or carboxylic acid groups to exchange with oleic acid on the iron oxide's surface. The maghemite particles were subsequently covalently attached to poly(*tert*-butyl acrylate) *via* click reactions using $CuSO_4$ as the catalyst.

Drug loading

A number of recent studies have shown that it is also possible to utilise polymers to encapsulate drugs *via* hydrophobic/electrostatic interactions or covalent bonds. Initial studies employed the use of electrostatic or hydrophobic interactions to trap drugs in a polymer matrix, or within the vesicles of micelles and polysomes/liposomes. It is important to note that in these structures, the slow diffusion of the therapeutic compounds from the polymer into the surrounding area may still occur, resulting in unspecific delivery. As an alternative approach, researchers developed labile linkers to connect therapeutic drugs to the polymer, providing a more sturdy bond and greater control over the delivery mechanism.[77–79] The breakage of these bonds can be triggered by an internal or external stimulus. For example, Yamashita *et al*. (2011) examined the use of a heat-labile, double stranded oligonucleotide as a linking agent between a gold nanorod and a PEG chain. Yamashita suggested that heat induced by the photothermal effect could be harnessed to sever this covalent bond by a retro Diels-alder reaction.[80,81]

2 Photothermal induced drug release

Light is used in photothermal induced drug release to cause a plasmonic nanomaterial to heat up, which in turn activates a heat-responsive drug release mechanism. This concept originated, in part, from photothermal therapy (also known as photoablation therapy) and photodynamic therapy, where light is used to generate heat and activate a photo-sensitive drug, respectively, in diseased cells. By itself, photothermal therapy rarely has the ability to completely destroy diseased cells and is thus never used as the sole mode of treatment.[82] Instead it is used in conjunction with other techniques such as chemotherapy, in which the heat that is released causes the pores of the diseased cells to expand, thereby improving the uptake of therapeutic drugs. Thus, applying the photothermal effect to controllable drug delivery, where the drug that is conjugated to plasmonic nanomaterial by a heat-responsive polymer, and released in response to heat from the photothermal effect, is a logical extension.

Gold nanoparticles form the basis of recent research into photothermal induced controllable drug delivery due to their established method of production, well-understood chemistry and low toxicity towards biological cells as seen in many *in vivo* and *in vitro* studies.[83] When irradiated with light, electrons in the conduction band of the gold nanoparticle are excited, followed by intraband decay of the electrons. This results in a conversion of light energy to thermal energy in what is referred to as localized surface plasmon resonance.[84–86] The ease with which gold nanoparticles can be modified to have specific peak absorbance in the visible to near-infrared region (400 nm to 1100 nm) is another reason why they are attractive for photothermal drug release applications. For *in vivo* applications, light in the

visible to infrared wavelength range is favoured due to the fact that they are less energetic and therefore less harmful to cells and tissues. Infrared light is also less attenuated by human tissue, thus enabling penetration of up to 1 cm for subcutaneous treatment.[87]

2.1 Recent developments in the application of nanomaterials for photothermal induced drug release

2.1.1 Design and synthesis of nanomaterials for photothermal applications. Gold nanospheres and gold nanorods are the most widely investigated gold nanostructures for photothermal induced drug release; this is due to their well-established methods of production and well-understood chemistry. Recent investigations have shifted focus to conjugates of gold nanospheres and nanorods with polymers, as well as other gold nanostructures. More complex morphologies such as gold vesicles (a spherical, densely packed, monolayer gold nanoparticle shell tethered using amphiphilic block copolymers),[88] nanoshells and half-shells,[1,94] nanocages[19] and nanostars[95] have been proposed for photothermal applications due to their increased surface area or loading capacity (see Fig. 3). Some investigators have also explored the use of material other than gold as photothermal agents.

An *et al*. developed 150 nm to 200 nm size thermo-sensitive liposomes with hydrophobic gold nanoparticles embedded within the liposome bilayer and the drug berberine encapsulated within the liposome's compartment (see Fig. 2).[89] This agent was prepared using the film build method in combination with supercritical CO_2 incubation, which permits the size and stability of the liposomes to be controlled by adjusting the preparation pressure. Ultraviolet light (250 nm) was used to induce the photothermal effect, and release of over 50% of the berberine within 5 min was demonstrated. This drug release rate is unprecedented, and correlates with the amount of embedded gold nanoparticles. Commutative irradiation using ultraviolet and visible light further shows that the photothermal effect induces phase transition in the liposomes without destroying the bilayer structure. The stability and the drug encapsulation efficiency of the liposome was found to decrease with increasing amounts of gold nanoparticles

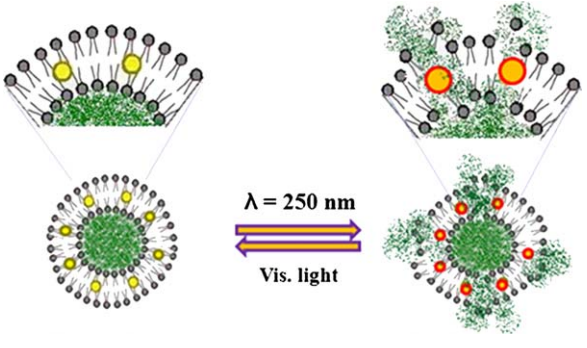

Fig. 2 Gold nanoparticle-liposomes conjugate drug release *via* light irradiation.[142] Reprinted with permission from X. An, F. Zhan and Y. Zhu, *Langmuir*, 2013, **29**, 1061–1068. Copyright 2013 American Chemical Society.

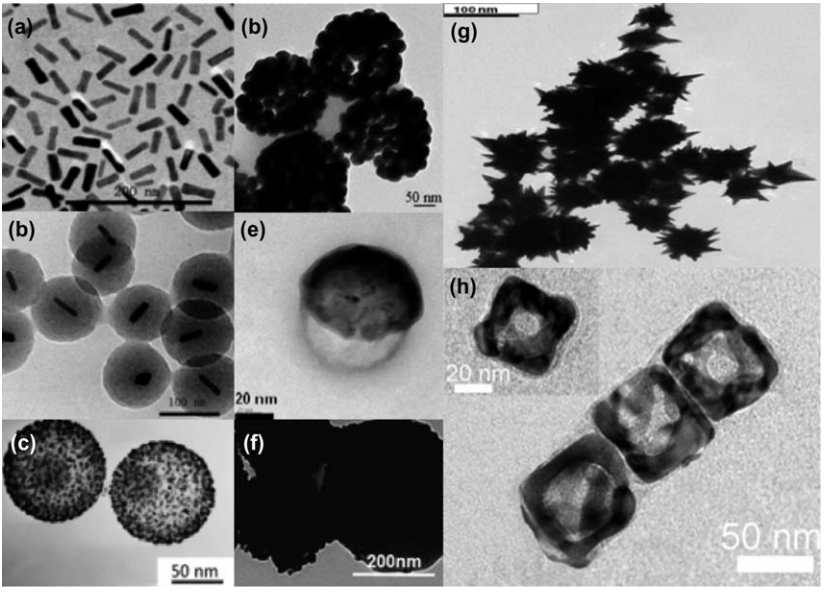

Fig. 3 TEM images of (a) gold nanorods,[100] (b) silica encapsulated gold nanorods,[100] (c) gold decorated silica rattle structure,[99] (d) gold vesicles,[88] (e) gold nano half-shell,[105] (f) gold nano shells,[1] (g) nanostars[92] and (h) nanocages.[143] Reprinted with permission from Z. Jiang, B. Dong, B. Chen, J. Wang, L. Xu, S. Zhang and H. Song, *Small*, 2013, **9**, 604–612. Copyright (2013) John Wiley and Sons. H. Liu, D. Chen, L. Li, T. Liu, L. Tan, X. Wu and F. Tang, *Angewandte Chemie International Edition*, 2011, **50**, 891–895. Copyright (2010) John Wiley and Sons. J. Lin, S. Wang, P. Huang, Z. Wang, S. Chen, G. Niu, W. Li, J. He, D. Cui, G. Lu, X. Chen and Z. Nie, *ACS Nano*, 2013, **7**, 5320–5329. Copyright (2013) American Chemical Society. S.-M. Lee, H. J. Kim, Y.-J. Ha, Y. N. Park, S.-K. Lee, Y.-B. Park and K.-H. Yoo, *ACS Nano*, 2012, **7**, 50–57. Copyright (2012) American Chemical Society. Y. Ma, X. Liang, S. Tong, G. Bao, Q. Ren and Z. Dai, *Advanced Functional Materials*, 2013, **23**, 815–822. Copyright (2013) John Wiley and Sons. Z. Fan, D. Senapati, A. K. Singh and P. C. Ray, *Molecular Pharmaceutics*, 2012, **10**, 857–866. Copyright (2012) American Chemical Society. L. Gao, J. Fei, J. Zhao, H. Li, Y. Cui and J. Li, *ACS Nano*, 2012, **6**, 8030–8040. Copyright (2012) American Chemical Society.

introduced in the preparation step; this was attributed to disruption of the bilayer microstructure of liposomes.

Huang *et al*. shows the photothermal effect can be used to trigger the controlled release of rhodamine 6G (R6G) dye that was incorporated into layer-by-layer assembly of negatively charged poly(acrylic acid, sodium salt) (PAA) and positively charged poly(allylamine hydrochloride) (PAH) polymers on gold nanorods.[90] The drug release was induced *via* heating from a laser that caused the dye to escape through the trapping layers. An increase in the number of trapping layers was shown to decrease the amount of dye released. More interestingly, the release rate is highly dependent on the thermodynamic properties of PAA and PAH, with PAA-only systems showing greater amount of dye molecules bound and a higher release rate. Isothermal titration calorimetry analysis suggested that R6G and PAA have interactions that would favour disassociation of the dye from the polymer upon heating, whereas R6G and PAH showed zero complex formation within the limit of measurement. A capping PAH layer was also shown to bind more tightly to the underlying PAA/R6G layers, thus preventing the dye from being released.

Passive tumour targeting of gold nanocages was assessed by Xia *et al.* [91] and it was found that they are preferentially absorbed by tumour tissue as opposed to normal tissue. These gold nanocages were synthesised *via* a galvanic silver-gold replacement technique where silver nanocubes were initially produced *via* polyol reduction with CF_3OOAg as the silver precursor.[19,20] The silver nanocubes were then mixed in hydrogen tetrachloroaurate which initiated a spontaneous galvanic reaction where the silver underwent dissolution whilst the gold was deposited, eventually forming a nanobox or nanocage with Au-Ag alloying.

Lin *et al.* developed gold vesicles that were loaded with Chlorin e6 (Ce6), a multifunctional photosensitizer.[88] The gold vesicles were obtained *via* the self-assembly of gold nanoparticles tethered with thiol-terminated amphiphilic block copolymers of polyethylene oxide-b-polystyrene in a film rehydration method. The gold vesicles show strong absorbance in the near-infrared range of 650–800 nm due to plasmonic coupling between neighbouring gold nanoparticles in the vesicular membranes. Notably, the gold vesicles showed higher levels of Ce6 loading compared to gold nanorods, as well as excellent biocompatibility, solubility and stability in solution.

Fan *et al.* obtained star shaped gold nanoparticles with a magnetic iron oxide core by dispersing iron oxide nanoparticles in sodium citrate, followed by reduction of hydrogen tetrachloroaurate in the presence of cetyltrimethylammonium bromide and silver nitrate.[92] The nanoparticles were then functionalised with thiolated polyethylene glycol and thiol-modified Cy3-bound S6 aptamers to minimise blood cell interaction, and to enable targeted capture of SK-BR-3 breast cancer cells with a magnet. Controllable drug release was not demonstrated, although photothermal heating was shown to result in cell death. Jing *et al.*[93] worked with polypyrrole coated 'urchinlike' gold nanoparticles. Their study found that the polypyrrole coating improved structural stability of the gold nanoparticles when exposed to heat, pH and laser irradiation and more than doubled their photothermal transduction efficiency.

Zhang *et al.* developed single wall carbon nanotubes that were modified with AS1411 aptamer and loaded with doxorubicin.[94] Carbon nanotubes have previously been shown to have strong optical absorbance in the near infra-red range.[95] In the work of Zhang *et al.*, carbon nanotubes were used to deliver doxorubicin to EC-109 cells due to the AS1411 affinity for nucleolin on the surface of EC-109 cells. While photothermal induced release of drugs was not demonstrated explicitly in Zhang *et al.*'s work, they did demonstrate that photothermal hyperthermia with carbon nanotubes can inhibit the G2-M cell cycle. Similarly, Estrada *et al.*[96] have developed multi-walled carbon nanotubes (MWCNT) functionalised with k-carrageenan hydrogels. In this case, the MWCNTs were employed as a reinforcing agent improving the mechanical properties of the hydrogel as well as a photosensitive material that enabled photothermal delivery.

Another material that has shown potential for photothermal induced drug delivery is graphene. Sahu *et al.* functionalised graphene oxide with poly(ethylene oxide)-poly(propylene oxide)-poly(ethylene oxide) triblock copolymers.[97] The release of methylene blue graphene-polymer conjugate was shown to be pH sensitive and the photothermal effect was shown to

induce cell death. Wang *et al*. developed silica coated graphene nano-sheets functionalised with hydrophilic polyethylene glycol and a targeting peptide (IP) for the delivery of doxorubicin.[98] They showed drug release can be initiated by both pH and temperature.

2.1.2 Photothermal induced controllable drug release. Liu *et al*. developed an all-in-one (photothermal therapy, drug delivery and cell imaging) system based upon silica nano-rattle sphere coated with a gold shell and functionalised with polyethylene glycol for stability.[99] An initial rapid release of Docetaxel (52% loading, approximately 1.08 μg per μg particles) in the first 20 h of drug delivery, followed by sustained release for a period of up to 7 days was observed. *In vivo* and *in vitro* studies showed the combination of photothermal therapy and Docetaxel based chemotherapy has a synergistic effect, which the authors attributed to the altered kinetics, permeability and increase uptake of the drug due to the photothermal process. Interestingly, irradiation by a near infra-red laser light did not result in additional cumulative release of the drug; this was attributed to the good thermal and mechanical stability of the nanocarrier.

Jiang *et al*. have developed mesoporous silica encapsulated gold nanocomposites for use in fluorescence imaging and photothermal controlled drug delivery.[100] Excellent biocompatibility with low toxicity was demonstrated. Additionally photothermal cancer ablation and photothermal drug delivery with doxorubicin were successfully demonstrated *in vitro*.

Gold nanocages have also been used for photothermal induced drug delivery by a phase-change material (PCM) that changes phase from solid to liquid over a very small temperature range. Xia *et al*. demonstrated this drug delivery technology by creating a mixture of doxorubicin immersed in 1-tetradecanol (melting point between 38 and 39 °C), and load the mixture into gold nanocages, whereby the mixture then solidified.[91,101] The photothermal effect could then be used to heat the nanocages and melt the PCM, releasing the drugs. It was found that, for breast cancer cells, this simultaneous drug delivery and photothermal ablation therapy significantly reduced cancer cell viability.

Ma *et al*. developed cholesteryl succinyl silane nanomicelles (CSS) loaded with doxorubicin and magnetite nanoparticles, and coated with a gold shell (see Fig. 4).[1] Using this particle system, they demonstrated this "all-in-one" drug delivery agent allows for photothermal drug release, photothermal therapy, magnetic targeted drug delivery and MR imaging. Irradiation with near-infrared laser was shown to increase the drug release by two-fold and a unique feature of the work is they are able to trigger stepwise release by controlling laser exposure (see Fig. 4). Drug release in the absence of laser irradiation was attributed to the incomplete gold shells. *In vitro* HeLa cell viability tests showed a significant decrease in cell viability only in tests that utilised nanocarriers in conjunction with near infra-red irradiation, thus the effects were attributed to the photothermal release of drug.

Yamashita *et al*.[80,102] demonstrated the *in vivo* release of single strand DNA from double strand DNA-modified gold nanorods that was triggered by the photothermal effect. This work follows their previous *in vitro* studies that showed DNA can be used as a heat-labile linker in photothermal

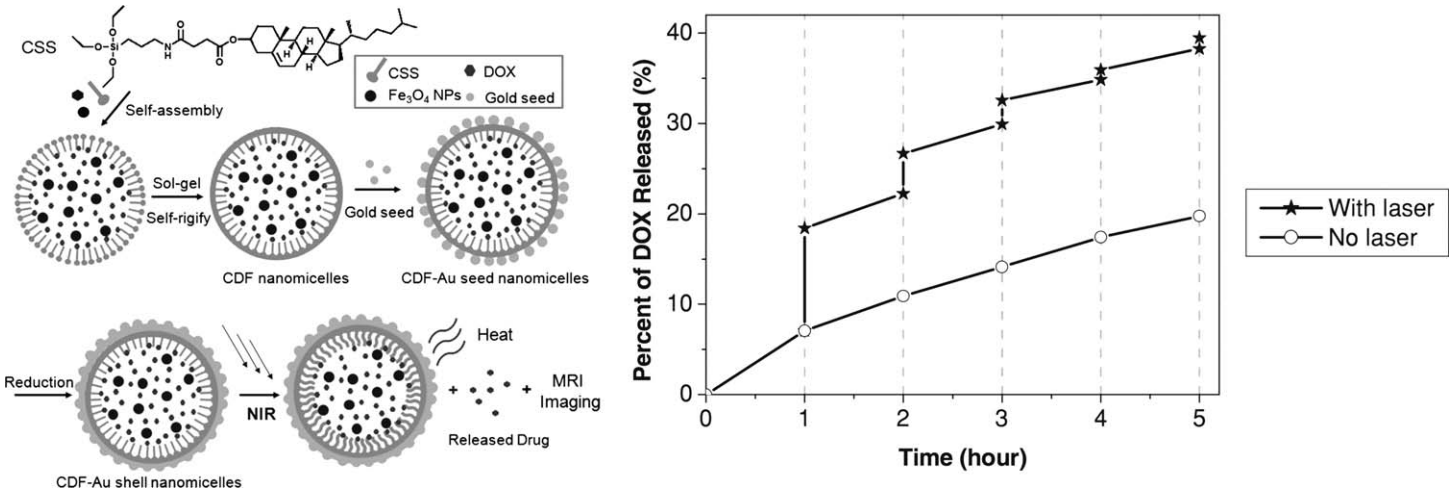

Fig. 4 Schematic showing the fabrication of cholesteryl succinyl silane (CSS) nanomicelles loaded with doxorubicin and magnetite nanoparticles (Fe_3O_4 NPs) and coated with a gold shell (left) and doxorubicin release profile from the nanomicelles in the presence and absence of laser irradiation (right).[1] Reprinted with permission from Y. Ma, X. Liang, S. Tong, G. Bao, Q. Ren and Z. Dai, *Advanced Functional Materials*, 2013, **23**, 815–822. Copyright 2013 John Wiley and Sons.

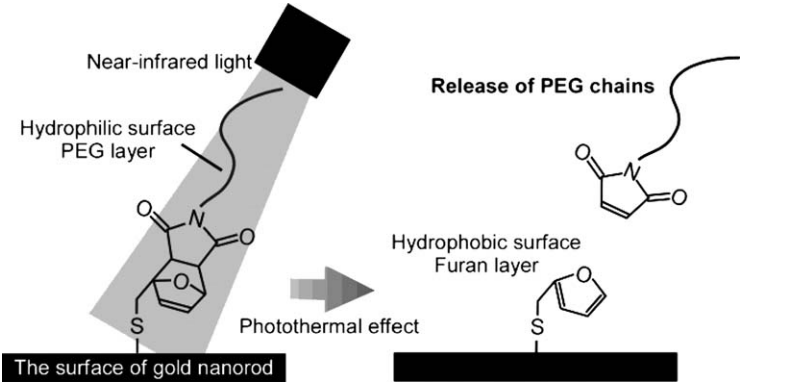

Fig. 5 PEG chain release from gold nanorods due to photothermal effect triggered retro Diels-Alder reaction.[102] Reprinted with permission from S. Yamashita, H. Fukushima, Y. Niidome, T. Mori, Y. Katayama and T. Niidome, *Langmuir*, 2011, **27**, 14621–14626. Copyright 2011 American Chemical Society.

induced release of therapeutics. The same group also showed the controlled-release system of polyethylene glycol polymer from the surface of the gold nanorods triggered by a retro Diels-Alder reaction induced by the photothermal effect (see Fig. 5).

Zanberg *et al*. demonstrated the release of smaller fluorescent dye molecules from 16 nm gold or 200 nm silica-gold core-shell nanoparticles.[103] The dye molecules were tethered to the nanoparticles' surface using a linker containing alkanethiol and oxabicycloheptene moieties. Pulsed laser irradiation of the nanoparticles led to the photothermolysis of the oxabicycloheptene motif *via* a retro Diels-Alder reaction when the temperature was raised to about 60 °C. The heating was confined to the surfaces of the nanoparticles without measurably increasing the temperature of the surroundings; photo-release of fluorescein in live oocytes and tissue cell cultures was demonstrated without killing the cells.

Several other investigators have shown that the conventional photothermal effect can modify the tumour microenvironment. For instance, increased blood flow to the tumour, causing vascular dilation that augmented the enhanced penetration and retention effect (passive targeting), can cause the cell to over express heat shock proteins (HSPs) such as glucose-regulated protein-78 (GRP78).[82,104] These changes could then be exploited for specific targeting of the drug using antibodies or peptides, and to increase vascular permeability and uptake of drugs. Lee *et al*. have developed poly(DL-lactic-co-glycolic acid) gold half-shell nanoparticles loaded with the drug methotrexate for use in rheumatoid arthritis treatment.[105] The drug carrier was conjugated with arginine-glycine-aspartic acid peptides that act as the targeting moiety for inflammation. When exposed to near-infrared irradiation, generation of heat that is due to the photothermal effect caused the drug to be released. Testing in mice found the dual treatment enabled by these nanoparticles has better efficacy than standard methotrexate treatment, which the author attributed to release at above the therapeutic dose. They also showed that higher therapeutic efficacy could be obtained when the chemo-photothermal treatment was combined with

targeted delivery. Similarly, You *et al.*[106] conjugated cyclic peptide c(TNYL-RAW), a second-generation Eph-binding antagonist with improved plasma stability and high-receptor binding affinity, to doxorubicin loaded hollow gold nanoparticles. They showed that the particles were selectively targeted to EphB4-positive tumours, and that concerted chemo-photothermal therapy mediated by the particles resulted in remarkable antitumor efficacy with reduced systemic toxicity, both *in vivo* and *in vitro*.

2.1.3 Other related developments. A key to understanding the drug release mechanisms in photothermal drug release, as well as the implications of *in vivo* use of these nanoparticles, is understanding how the surface temperature of the heated particles vary with particle and laser properties. Bendix *et al.* traps gold nanoparticles in a lipid bilayer which contains a fluorescent dye; the melted footprint around the nanoparticle was used to determine the temperatures reached during laser irradiation.[107] Bendix *et al.* showed that both particle size and laser power were important in determining the temperatures reached during irradiation (See Fig. 6). Kyrsting *et al.* similarly explored the heating profile of gold nanoparticles by placing them in the vicinity of lipid vesicles with temperature sensitive permeability.[108] They found that gold nanoparticles could be heated by several hundred degrees Celsius using laser irradiation. Honda *et al.* monitored the heating of 40 nm gold nanoparticles coated with a thermoresponsive polymer in response to laser light irradiation.[109] The plasmon peak shift that arose from changes in the refractive index of the polymer in response to temperature was monitored. Temperature increases of around 10 °C were noted when the nanoparticles were irradiated with a 1 mW laser at 532 nm.

3 Magnetic hyperthermia induced drug release

Conventional magnetic hyperthermia is a form of cancer therapy that relies on the use of an alternating magnetic field and magnetic nanomaterial to generate heat that induces apoptosis in cancerous tissue.[7] Recently, Kumar and Mohammad suggested broadening the definition of 'hyperthermia' to include magnetically modulated controllable drug delivery.[110] In this context, the heat generated by magnetic hyperthermia is used to induce a change in the therapeutic drug directly, or an agent such as a thermo-responsive polymer or liposome that is conjugated to the drug, resulting in the release of the drug.[111] There is also the possibility of combining both effects of hyperthermia, *i.e.* thermal ablation and drug delivery, as it provides the possibility of further maximising the treatment efficacy. In addition to providing a means for localised heat generation, magnetic nanomaterials have also proven to be beneficial for drug uptake by cancerous cells. The magnetic nanoparticles can be directed and concentrated in the region of interest using a magnet. Moreover, significant increase in cellular uptake of doxorubicin (a model cancer drug) has been demonstrated *in vitro*, when the drug was adsorbed onto tetraheptylammonium capped magnetite and nickel nanoparticles, as compared to standard drug administration.[112] This was attributed to interactions between the magnetic nanoparticles and the drug resistant protein, which in turn reduces the reflux of the doxorubicin, that is, the adsorption of doxorubicin onto the

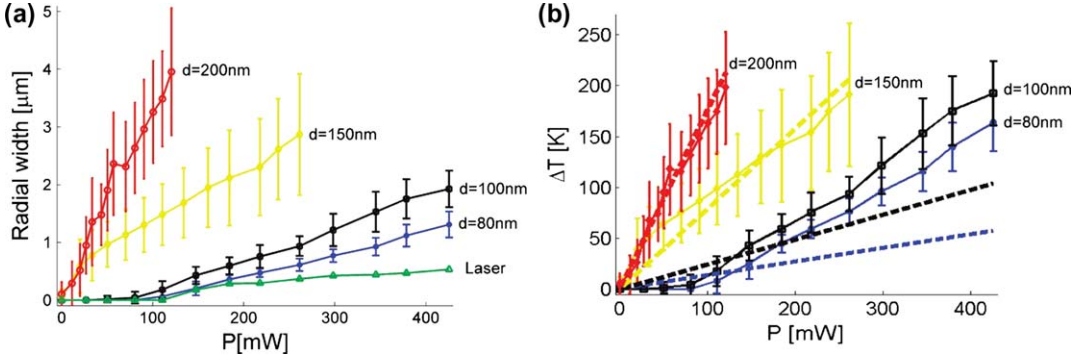

Fig. 6 Bendix *et al.*[107] measurements of surface temperatures of gold nanoparticles. (a) Melted bilayer diameter against laser power: top grey (red online): d = 200 nm; light grey (yellow online): d = 150 nm; black: d = 100 nm; dark grey (blue online): d = 80 nm; bottom grey (green online): laser alone); (b) Temperature of the surface of the gold nanoparticles against laser power (dashed lines given temperature increases as per Mie calculation). Reprinted with permission from P. M. Bendix, S. N. S. Reihani and L. B. Oddershede, *ACS Nano*, 2010, **4**, 2256–2262. Copyright (2010) American Chemical Society.

magnetic nanoparticle surface prevents it from being pumped out of the cell by the drug resistant protein.[58]

3.1 Recent developments in the application of nanomaterials for magnetic hyperthermia induced drug release

3.1.1 Design and synthesis of nanomaterials for magnetic hyperthermia applications. A number of materials can be used as magnetic responsive nanoparticles in magnetic hyperthermia induced drug release. The majority of studies focus on the use of iron oxide, primarily magnetite (Fe_3O_4) and maghemite (γ-Fe_2O_3). This is due to their well-understood and facile synthesis methods, as well as the relative ease with which biocompatibility can be achieved. The method of choice for producing magnetite is the co-precipitation of Fe^{2+} and Fe^{3+} at elevated temperatures (70–100 °C) in the presence of a base.[113] The magnetite particles can be oxidised to maghemite by peptizing in nitric acid. It is a challenge to obtain tailored morphologies (*i.e.* non-spheroid) and/or particles with high magnetisation using contemporary co-precipitation methods. Alternative synthesis methodologies for magnetite nanoparticles have thus been developed; these include co-precipitation of Fe^{2+} and Fe^{3+} in the presence of sodium carbonate,[114] forced hydrolysis of iron (II) hydroxide in a nitrogen atmosphere,[115] electro-oxidation in the presence of a stabilising surfactant,[116] and hydrogen reduction of other iron oxide crystals (*e.g.* hematite)[117] at elevated temperatures.

The use of metallic nanomaterials for magnetic hyperthermia has also attracted much interest recently due to their superior magnetic properties and ease of manipulating the size and morphology, when compared to iron oxide based nanoparticles.[118] Some recent developments in this area include the synthesis of Fe-Pt, Fe-Pd and Fe-Pt-Pd alloys with a range of shapes and sizes.[119] Lu *et al.* outlined the synthesis of magnetic cobalt nanomaterials by the reduction of Co^{2+} in the presence of a polymer ligand.[120] It is important to note that the chemical composition of many magnetic alloys renders them inherently toxic.[121] For these nanomaterials to be accepted as feasible drug carriers, the toxicity issues must be addressed. Other related developments include the use of laser ablation of iron foil to synthesise superparamagnetic Fe_3C,[122] and the synthesis of $MnFe_2O_4$ and $Mn_{1-x}Zn_xFe_2O_4$ by wet chemical co-precipitation,[45,123] and the synthesis of mesoporous $MgFe_2O_3$ from the reduction of iron (III) chloride[124] in the presence of magnesium chloride.

Investigations were also directed towards increasing the drug loading capacity of magnetic nanoparticles. Chen *et al.* synthesised magnetic silica nanotubes by first depositing hematite (α-Fe_2O_3), followed by silica, onto a carbon nanotube template.[11] The carbon template was removed and the hematite reduced to magnetite by heating the nanoparticles to 800 °C under argon. The magnetite was then oxidized to maghemite (γ-Fe_2O_3) by heating at 600 °C. Chen *et al.* claimed the open-ended tubular structure renders the magnetic silica tubes potentially applicable in hyperthermia induced drug delivery, particularly of high molecular weight therapeutic agents such as DNA or RNA.

Nanocarriers that respond to more than one stimulus have also been developed. Sahoo *et al.* developed a dual pH and temperature responsive system by tethering magnetite nanoparticles with poly(N-ispropylacrylamide)-block-poly(acrylic acid) copolymers.[48] Doxorubicin was electrostatically attached to the negatively charged poly(acrylic acid) segment of the polymer chain. The pH-responsive drug release was attributed to protonation of the carboxylic groups on the polymer chain, resulting in weaker drug-polymer interactions. The temperature-responsive nature of the agent was conferred by the thermo-responsive PNIPAM polymer block (LCST = 31 °C). The cytotoxicity, uptake and therapeutic effects of the nanocarrier was demonstrated *in vitro*, although magnetic hyperthermia induced release of the drug was not demonstrated. By combining the pH and temperature stimuli, it was found that drug release rate could be significantly increased from approximately 11% at pH 7.4 and 25 °C, to 75% at pH 5.0 and 37 °C after a period of 5 h.

Bilalis *et al.* fabricated polymeric 'microcontainers' that responded to pH, redox and magnetic induction.[125] As outlined in Fig. 7, these 'microcontainers' were synthesised by a two-stage distillation precipitation polymerisation procedure followed by sacrificial core dissolution, resulting in a poly(methacrylic acid) shell with disulfide (S–S) bonds ($PMAA_{S\text{-}S}$). These microcontainers were then decorated with magnetic nanoparticles and loaded with daunorubicin hydrochloride (a model drug). Bilalis *et al.* showed increased release of the drug from 15% to 40% when pH was

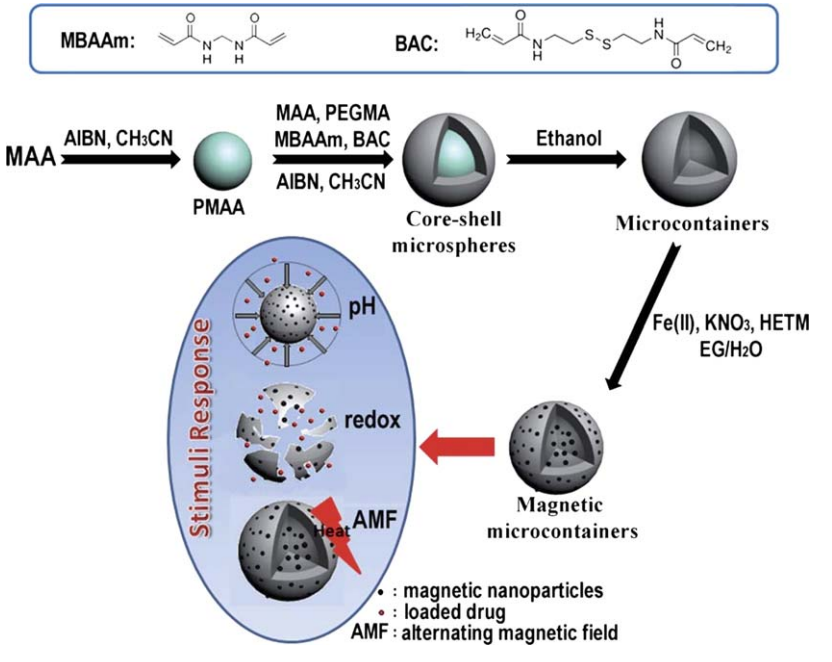

Fig. 7 Schematic illustration of the synthesis procedure for the preparation of magnetic microcontainers. Chemical structures of crosslinkers are also illustrated.[125] Reproduced from P. Bilalis, A. Chatzipavlidis, L.-A. Tziveleka, N. Boukos and G. Kordas, *Journal of Materials Chemistry*, 2012, **22**, 13451–13454 with permission from The Royal Society of Chemistry.

decreased from 5 to 7.4, and to 94% when glutathione concentration was increased from 0 to 20 mM. They further showed that the microcontainers can be used to generate heat in an alternating magnetic field, but did not demonstrate magnetic hyperthermia induced drug release for their microcontainers.

3.1.2 Magnetic hyperthermia induced controllable drug release. Kumar *et al*. prepared polyethylene glycol coated, carboxyl-enriched, mesoporous $MgFe_2O_4$ by a polyol method.[46] They showed that an 80% loading efficiency of doxorubicin could be achieved due to the highly negative surface charge and mesoporous nature of the particles. Magnetic hyperthermia in combination with drug therapy was shown to lead to the death of approximately 90% of cells *in vitro*, as compared to 40–45% cell death when only magnetic hyperthermia was applied. It is important to note here that polyethylene glycol confers size stability and biocompatibility properties to the particles, but it is not expected to play a role in the heat induced release of the drug in this work. Instead, pH enhanced release of doxorubicin was observed in a mild acidic environment; this was attributed to the dissolution of the polyethylene glycol and weakening of electrostatic bonding by excessive deprotonation of the daunosamine group of the doxorubicin molecule.

Sivakumar *et al*. incorporated superparamagnetic fluorescent nanoparticles and 5-fluorouracil (a chemotherapeutic anticancer drug) into a biopolymer matrix formed by carboxymethyl cellulose, a water-soluble cellulose with carboxymethyl groups bonded to some of the hydroxyl groups on the cellulose backbone.[126] Folate conjugated to the carboxymethyl cellulose backbone enabled the drug carrier to be targeted to folate-receptor tumour markers that are over expressed in cancer cells. Similarly, Brulé *et al*. and Arias *et al*. incorporated maghemite cores into alginate and polyalkylcyanoacrylates matrices, respectively.[127,128] In the work of Arias *et al*., the presence of the polyalkylcyanoacrylates matrix was shown to increase the amount of drugs loaded, with both the drug loading and entrapment efficiency increasing with increased drug concentration during the loading step. The amount of methotrexate that is loaded can also be increased by introducing a surfactant (Pluronic® F-68) and by increasing the rate of polymerisation; nonetheless, a polymerisation rate that is too rapid can produce undesirable precipitates. Sivakumar *et al*. and Arias *et al*. did not explicitly study the hyperthermia induced drug release properties of the drug carrier. Nonetheless, Sivakumar *et al*. did show that combined treatment of cancer cells with the drug and magnetic hyperthermia synergistically killed almost 95% of cancer cells. Brulé *et al*. showed hyperthermia significantly enhanced the effect of doxorubicin, with MCF-7 cells exhibiting viable cell coverage of $5.7\% \pm 4.2\%$ when exposed to the combined therapy, as opposed to $>50\%$ when treated with only doxorubicin-loaded microbeads or application of hyperthermia.

Mi *et al*. co-encapsulated magnetite nanoparticles and docetaxel (a model anticancer agent) within a matrix consisting of mixed copolymers of poly(lactide)-D-alpha-tocopheryl polyethylene glycol succinate and carboxyl group terminated tocopheryl polyethylene glycol succinate.[129] The carboxyl group terminated tocopheryl polyethylene glycol succinate

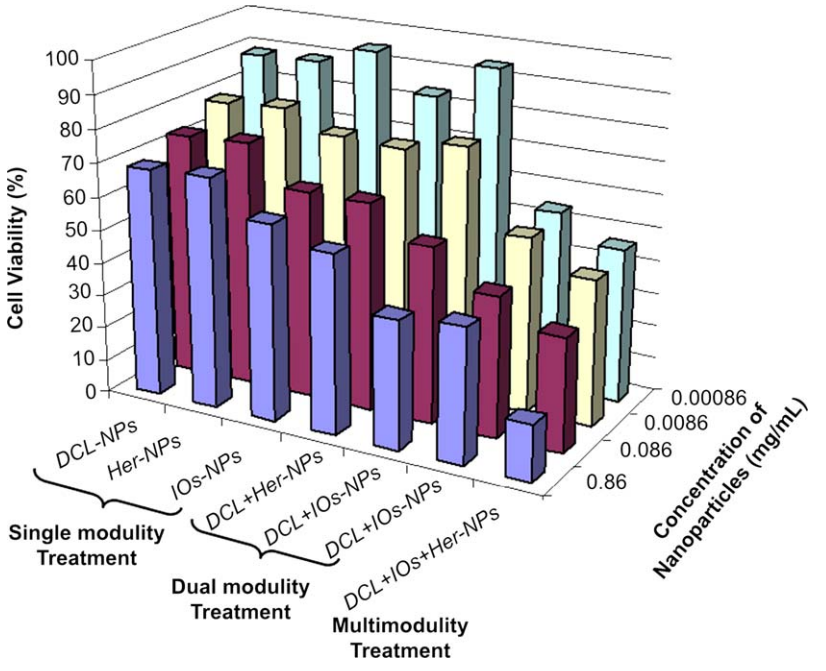

Fig. 8 Analysis of SK-BR-3 cell viability as a result of exposure to multimodal treatment herception vonjugated, thermomagnetic iron oxides and docetaxel loaded nanoparticles after 24 h incubation and 12 h recovery.[129] Reprinted from Y. Mi, X. Liu, J. Zhao, J. Ding and S.-S. Feng, Multimodality treatment of cancer with herceptin conjugated, thermomagnetic iron oxides and docetaxel loaded nanoparticles of biodegradable polymers Biomaterials, *Biomaterials*, **33**, 7519–7529, Copyright (2012), with Permission from Elsevier.

enabled herceptin to be conjugated *via* carbodiimide chemistry for biotherapy and cell targeting; the polymer was also purported to have anti-cancer and neuroprotective properties. Using this platform, Mi *et al.* demonstrated that multimodal treatment of cancer (where cell-targeting, chemotherapy, hyperthermic therapy and biological therapy are combined) shows superior *in vitro* therapeutic efficacy than single modality or dual modality treatment under all the nanoparticle concentrations tested (see Fig. 8).[129]

Recent studies have also examined the use of PNIPAM in dual responsive drug delivery systems; that is, the drug is released in response to more than one stimulus, most commonly temperature and pH. This would be highly advantageous as it would potentially improve the accuracy and control of the drug delivery mechanism. Chiang *et al.* developed superparamagnetic iron oxide nanoparticles loaded hybrid nanogels for both pH and temperature responsive delivery of doxorubicin.[130] The hybrid nanogels were co-assembled with acrylic acid/2-methacryloylethyl acrylate/ $mPEG_{2000}/PNIPA_{3000}$ copolymer SPIONs. Over 24 h at 37 °C, 17% release was observed at pH 7.4, and 55% release at pH 5.0. Release rates were notably increased through exposure to an alternating magnetic field.

Other recent studies have investigated the integration of nanoparticles into polymersomes to yield heat responsive drug delivery agents. Sanson *et al.* developed polymeric vesicles (polymersomes) which consist of

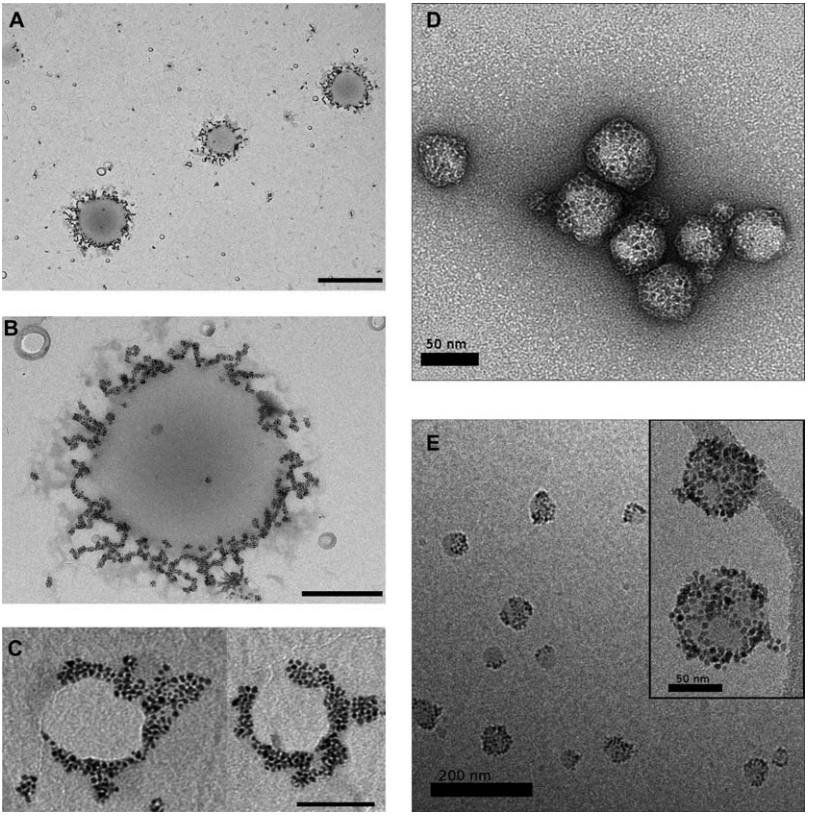

Fig. 9 TEM images of USPIO-loaded vesicles prepared by nanoprecipitation. (A) Low magnification picture of WD15–50 vesicles (scale bar 1 μm). (B) Close-up view of a WD15–50 vesicle containing ~1500 USPIOs as measured by image analysis (scale bar 300 nm). (C) WDi-70 vesicles spreading on the substrate, which enables counting ~190 USPIOs on the left and ~220 USPIOs on the right (scale bar 100 nm). (D) Image of negatively stained WDi-50 vesicles, showing a group of vesicles laying intact on the carbon substrate (scale bar 50 nm). (E) Cryo-TEM image showing homogeneously dispersed WDi-50 vesicles (scale bar 200 nm). (Inset) Close-up view of two vesicles showing a mantle of respectively ~80 and ~110 close-packed USPIOs with some uncovered areas (scale bar 50 nm).[24] Reprinted with permission from C. Sanson, O. Diou, J. Thévenot, E. Ibarboure, A. Soum, A. Brûlet, S. Miraux, E. Thiaudière, S. Tan, A. Brisson, V. Dupuis, O. Sandre and S. Lecommandoux, *ACS Nano*, 2011, **5**, 1122–1140. Copyright (2011) American Chemical Society.

hydrophobically modified maghemite (γ-Fe_2O_3) nanoparticles that were encapsulated within the membrane of poly(trimethylene carbonate)-b-poly(L-glutamic acid) (PTMC-b-PGA) block copolymer vesicles using a nanoprecipitation process (See Fig. 9). In a subsequent study, they showed that when a high frequency alternating magnetic field was applied to the polymersomes loaded with 6% (w/w) of doxorubicin and 30% (w/w) of superparamagnetic iron oxide nanoparticles, an 18% increase in cell toxicity was observed for HeLa cells that had internalised the polymersome.[24,131] Moreover, they were able to show that the cytotoxicity effects arose from the increased doxorubicin release and not from a pure magnetic hyperthermia effect. That is, when polymersomes loaded with magnetic nanoparticles only were tested, no cytotoxicity effect was observed. Their results

indicate that the applied magnetic field induces a localised hyperthermia effect that leads to increased drug release, but not cell death as would have occurred in conventional hyperthermia treatment.

Hu *et al.* prepared core-shell, double-emulsion multi-drug carriers in a facile one step emulsifying process where poly(vinyl alcohol) and magnetic iron oxide nanoparticles are use as surfactants and stabilisers, respectively.[132] They were able to incorporate a hydrophilic drug (doxorubicin) into the core and a hydrophobic drug (paclitaxel) into the shell of the emulsion, and release them upon the application of an alternating magnetic field. The hydrophilic-lipophilic balance value of poly(vinyl alcohol) was shown to be an important factor in determining the construct of the emulsion, with intermediate molecular weight poly(vinyl alcohol) (47 kDa) favouring the formation of water-in-oil-in-water (W/O/W) double emulsion. Moreover, the inclusion of iron oxide nanoparticles was shown to be critical to the formation of a stable and robust W/O/W emulsion. The magnetic hyperthermia induced drug release was also shown to be dependent on the molecular weight of poly(vinyl alcohol), with faster drug release observed for lower molecular weight polymers due to the differences in the chain flexibility and mobility. It was observed that the initial release of doxorubicin was slower than that of paclitaxel; this was explained by the more rapid heating of the magnetic iron oxide nanoparticles impregnated within the hydrophobic shell in which the paclitaxel resided. As the temperature rose then spread to the emulsion core, a faster release of doxorubicin, further aided by its affinity to water, was realized. Using a peptide (IVO24) as the targeting agent, Hu *et al.* demonstrated that the double emulsions have good biocompatibility and can achieve better treatment efficacy both *in vivo* and *in vitro*.

3.1.3 Other related developments. One of the major issues faced by researchers in the field of magnetic induction hyperthermia is measurement of the temperature profile and heat released by the nanocomposite in response to an alternating magnetic field. This information would assist in the design and refinement of the nanoparticle-polymer systems in order to achieve more efficient release mechanisms. Recently, however, Riedinger *et al.* have developed a clever solution to this problem. Fluoresceinamine (a doxorubicin substitute) was bound to an azobis[N-(2-carboxyethyl)-2-methylpropionamidine] molecule which was in turn bonded to a polyethylene glycol spacer molecules (differing in length) on the surface of magnetite nanoparticles.[44] By varying the lengths of the PEG spacers, they were able to hold the drug at varying distances from the surface of the nanoparticle. By measuring whether the drug was release when the nanoparticles were heated up by magnetic induction, they could determine whether the heat of the nanoparticle was sufficient to break the azo bond. Whilst this agent could feasibly be used for drug delivery, the primary purpose of this study was to conduct sub-nanometer temperature probing.

4 Concluding remarks

Recent studies on the use of nanomaterial mediated photothermal and magnetic hyperthermia induced drug release highlight the potential of these

platforms for cancer therapy. Potent drugs are sequestered within a nanocarrier until it is delivered to the site of diseased tissue, where it is released in a time and site-specific manner in response to heat generated by the photothermal or magnetic hyperthermia effects. The benefits of these controllable drug delivery platforms are numerous. Chiefly, drug dosage can be increased without amplifying the negative side effects of chemotherapy leading to an improvement in the treatment efficacy. The *in vitro* and *in vivo* studies outlined herein further showed that composites of polymer and plasmonic or magnetic nanomaterials are ideal drug carriers for these platforms. Inorganic nanomaterials such as gold and magnetite act as heat generators in response to the light or alternating magnetic field stimuli, while the polymer provides a drug storage/release mechanism and improves the *in vivo* stability and biocompatibility of the drug carrier.

Before photothermal and magnetic hyperthermia induced drug delivery can proceed to clinical trials and applications, some questions and limitations have to be addressed. It would be of interest to see to what extent dosage and drug delivery can be fine-tuned by using these platforms. The delivery of a wider range of drugs, and stability of these drugs when exposed to heat should also be considered. Issues with low drug loading capacity and premature release of the drug from the carrier must also be addressed; the former by selecting nanostructures with high drug loading capacity, and the latter *via* strategies such as polymersomes with improved structural integrity or heat labile bonds to chemically bind the drug to the carrier.[82,83,133] Studies in cultured cells and mice models have been promising, nonetheless, large animal studies are still required to confirm the platforms' biocompatibility, biodistribution, uptake into diseased cells and overall efficacy. Issues related to the application of light and alternating magnetic fields in a clinical setting should also be considered. For instance, the use of fiber-optic micro-needles to deliver light directly to deeper tissue has been proposed.[134]

The mechanism behind the increased efficacy is also not fully elucidated in some studies. For instance, it is not always clear if the increased efficacy is due to the action of the drug alone, or the photothermal or magnetic hyperthermia heating has induced physiological change to the diseased tissue, thereby increasing the uptake of the drug. Recent advancement in cellular biology and drug carriers can also expand the opportunities and methodologies to be considered in photothermal and magnetic hyperthermia induced drug delivery. Newly identified endothelial cell surface receptors and the release of heat shock proteins when cells are exposed to heat can be used to improved recognition and targeting of diseased cells. Thermoresponsive polypeptide drug-conjugates raise the potential for pH responsive drug delivery, and if gold or magnetic nanoparticles can be incorporated into the design, there would be potential for pH-temperature dual responsive drug delivery.[135–137]

The combination of photothermal and magnetic hyperthermia drug delivery with biomedical imaging, in a parallel area of research called 'theranostics', is also of interest. The metallic and magnetic nanoparticles used in the design of the drug carriers also have potential application as contrast agents in medical imaging. Notably, magnetic iron oxide nanoparticles have been shown to improve the image obtained in magnetic

resonance imaging.[138] Laboratory studies have also shown gold and silica to be ideal contrast agents in X-ray computed tomography,[139] photo-acoustic[140] and ultrasound imaging.[141] With the ability to correlate imaging with drug therapy, the effects of each component of the drug carrier (materials selection and design, targeting, drug loading) on each step in the delivery cascade may be assessed and quantified in an absolute manner; this should lead to a better understanding of how drug design and administration protocol affects the pharmacokinetics of the drug carrier, as well as the treatment efficacy.

References

1 Y. Ma, X. Liang, S. Tong, G. Bao, Q. Ren and Z. Dai, *Advanced Functional Materials*, 2013, **23**, 815–822.
2 S. Ramishetti and L. Huang, *Therapeutic Delivery*, 2012, **3**, 1429–1445.
3 Y. Shao, W. Huang, C. Shi, S. T. Atkinson and J. Luo, *Therapeutic Delivery*, 2012, **3**, 1409–1427.
4 O. C. Steinbach, *Therapeutic Delivery*, 2012, **3**, 1373–1377.
5 R. Petros and J. DeSimone, *Nature Reviews*, 2010, **9**, 615–627.
6 R. K. Jain, *Nat Med.*, 2001, **7**, 987–989.
7 D. Ortega and Q. A. Pankhurst, In *Nanoscience: Volume 1: Nanostructures through Chemistry*, The Royal Society of Chemistry, Cambridge, 2013, vol. 1, pp. 60–88.
8 A. O. Govorov and H. H. Richardson, *Nano Today*, 2007, **2**, 30–38.
9 S.-H. Wu, C.-Y. Mou and H.-P. Lin, *Chem. Soc. Rev.*, 2013, **42**, 3862–3875.
10 P.-J. Chen, S.-H. Hu, C.-S. Hsiao, Y.-Y. Chen, D.-M. Liu and S.-Y. Chen, *J. Mat. Chem.*, 2011, **21**, 2535–2543.
11 X. Chen, R. Klingeler, M. Kath, A. A. El Gendy, K. Cendrowski, R. J. Kalenczuk and E. Borowiak-Palen, *ACS Applied Materials & Interfaces*, 2012, **4**, 2303–2309.
12 J. Jaber and E. Mohsen, *Colloids and Surfaces B: Biointerfaces*, 2013, **102**, 265–272.
13 J. Liu, S. Z. Qiao, S. Budi Hartono and G. Q. Lu, *Angewandte Chemie International Edition*, 2010, **49**, 4981–4985.
14 Q. Mu, L. Yang, J. C. Davis, R. Vankayala, K. C. Hwang, J. Zhao and B. Yan, *Biomaterials*, 2010, **31**, 5083–5090.
15 Q. Zhang, W. Wang, J. Goebl and Y. Yin, *Nano Today*, 2009, **4**, 494–507.
16 T. Zhang, Q. Zhang, J. Ge, J. Goebl, M. Sun, Y. Yan, Y.-s. Liu, C. Chang, J. Guo and Y. Yin, *J. Phys. Chem. C*, 2009, **113**, 3168–3175.
17 Y. Zhao and L. Jiang, *Advanced Materials*, 2009, **21**, 3621–3638.
18 T. Zhang, J. Ge, Y. Hu, Q. Zhang, S. Aloni and Y. Yin, *Angewandte Chemie International Edition*, 2008, **47**, 5806–5811.
19 Y. Sun, B. T. Mayers and Y. Xia, *Nano Letters*, 2002, **2**, 481–485.
20 Y. Sun and Y. Xia, *Science*, 2002, **298**, 2176–2179.
21 J. Champion, A. Walker and S. Mitragotri, *Pharm Res.*, 2008, **25**, 1815–1821.
22 H. Zhang, D. Pan, K. Zou, J. He and X. Duan, *J. Mat. Chem.*, 2009, **19**, 3069–3077.
23 H. Ai, *Advanced Drug Delivery Reviews*, 2011, **63**, 772–788.
24 C. Sanson, O. Diou, J. Thévenot, E. Ibarboure, A. Soum, A. Brûlet, S. Miraux, E. Thiaudière, S. Tan, A. Brisson, V. Dupuis, O. Sandre and S. Lecommandoux, *ACS Nano*, 2011, **5**, 1122–1140.
25 H. Oliveira, E. Pérez-Andrés, J. Thevenot, O. Sandre, E. Berra and S. Lecommandoux, *Journal of Controlled Release*, 2013, **169**, 165–170.

26 W. B. Liechty, D. R. Kryscio, B. V. Slaughter and N. A. Peppas, *Annual Review of Chemical and Biomolecular Engineering*, 2010, **1**, 149–173.
27 C. Boyer, M. R. Whittaker, V. Bulmus, J. Liu and T. P. Davis, *NPG Asia Mater*, 2010, **2**, 23–30.
28 O. Pillai and R. Panchagnula, *Current Opinion in Chemical Biology*, 2001, **5**, 447–451.
29 R. B. Grubbs, *Polymer Reviews*, 2007, **47**, 197–215.
30 A. K. Iyer, G. Khaled, J. Fang and H. Maeda, *Drug Discovery Today*, 2006, **11**, 812–818.
31 U. Prabhakar, H. Maeda, R. K. Jain, E. M. Sevick-Muraca, W. Zamboni, O. C. Farokhzad, S. T. Barry, A. Gabizon, P. Grodzinski and D. C. Blakey, *Cancer Research*, 2013, **73**, 2412–2417.
32 K. Greish, *Drug Discovery Today: Technologies*, 2012, **9**, e161–e166.
33 C. Boyer, M. R. Whittaker, M. Luzon and T. P. Davis, *Macromolecules*, 2009, **42**, 6917–6926.
34 R. Gref, M. Luck, P. Quellec, M. Marchand, E. Dellacherie, S. Harnisch, T. Blunk and R. H. Muller, *Colloids Surf., B Biointerfaces*, 2000, **18**, 301–313.
35 C. Flesch, Y. Unterfinger, E. Bourgeat-Lami, E. Duguet, C. Delaite and P. Dumas, *Macromol. Rapid Commun.*, 2005, **26**, 1494–1498.
36 S. Laurent, D. Forge, M. Port, A. Roch, C. Robic, L. Vander Elst and R. N. Muller, *Chemical Reviews*, 2008, **108**, 2064–2110.
37 I. Banerjee, R. C. Pangule and R. S. Kane, *Advanced Materials*, 2011, **23**, 690–718.
38 P. Aggarwala, J. B. Halla, C. B. McLelanda, M. A. Dobrovolskaia and S. E. McNeil, *Advanced Drug Delivery Reviews*, 2009, **61**, 428–437.
39 G. Prencipe, S. M. Tabakman, K. Welsher, Z. Liu, A. P. Goodwin, L. Zhang, J. Henry and H. Dai, *J. Am. Chem. Soc.*, 2009, **131**, 4783–4787.
40 C. Boyer, V. Bulmus, T. P. Davis, V. Ladmiral, J. Liu and S. b. Perrier, *Chemical Reviews*, 2009, **109**, 5402–5436.
41 J. S. Basuki, L. Esser, P. B. Zetterlund, M. R. Whittaker, C. Boyer and T. P. Davis, *Macromolecules*, 2013, **46**, 6038–6047.
42 R. Tedja, A. H. Soeriyadi, M. R. Whittaker, M. Lim, C. Marquis, C. Boyer, T. P. Davis and R. Amal, *Polymer Chemistry*, 2012, **3**, 2743–2751.
43 W. Wu, J. Shen, Z. Gai, K. Hong, P. Banerjee and S. Zhou, *Biomaterials*, 2011, **32**, 9876–9887.
44 A. Riedinger, P. Guardia, A. Curcio, M. A. Garcia, R. Cingolani, L. Manna and T. Pellegrino, *Nano Letters*, 2013, **13**, 2399–2406.
45 S. A. Shah, M. H. Asdi, M. U. Hashmi, M. F. Umar and S.-U. Awan, *Materials Chemistry and Physics*, 2012, **137**, 365–371.
46 S. Kumar, A. Daverey, N. K. Sahu and D. Bahadur, *J. Mat. Chem. B*, 2013, **1**, 3652–3660.
47 L. Jianbo, Q. Yang, R. Jie, Y. Weizhong and S. Donglu, *Nanotechnology*, 2012, **23**, 505706.
48 B. Sahoo, K. S. P. Devi, R. Banerjee, T. K. Maiti, P. Pramanik and D. Dhara, *ACS Applied Materials & Interfaces*, 2013, **5**, 3884–3893.
49 C. Weber, R. Hoogenboom and U. S. Schubert, *Progress in Polymer Science*, 2012, **37**, 686–714.
50 R. Cheng, F. Meng, C. Deng, H.-A. Klok and Z. Zhong, *Biomaterials*, 2013, **34**, 3647–3657.
51 S. R. Deka, A. Quarta, R. Di Corato, A. Riedinger, R. Cingolani and T. Pellegrino, *Nanoscale*, 2011, **3**, 619–629.
52 H. G. Schild, *Progress in Polymer Science*, 1992, **17**, 163–249.
53 A. Yao, Q. Chen, F. Ai, D. Wang and W. Huang, *J. Mater. Sci.: Mater Med.*, 2011, **22**, 2239–2247.

54 M. I. Shukoor, F. Natalio, H. A. Therese, M. N. Tahir, V. Ksenofontov, M. Panthfer, M. Eberhardt, P. Theato, H. C. Schrder, W. E. G. Mller and W. Tremel, *Chem. Mater.*, 2008, **20**, 3567–3573.
55 F. Zhang and C.-C. Wang, *Langmuir*, 2009, **25**, 8255–8262.
56 H. Lee, E. Lee, D. K. Kim, N. K. Jang, Y. Y. Jeong and S. Jon, *J. Am. Chem. Soc.*, 2006, **128**, 7383–7389.
57 R. Narain, M. Gonzales, A. S. Hoffman, P. S. Stayton and K. M. Krishnan, *Langmuir*, 2007, **23**, 6299–6304.
58 G. Huang, C. Zhang, S. Li, C. Khemtong, S.-G. Yang, R. Tian, J. D. Minna, K. C. Brown and J. Gao, *J. Mat. Chem.*, 2009, **19**, 6367–6372.
59 E. Amstad, S. Zurcher, A. Mashaghi, J. Y. Wong, M. Textor and E. Reimhult, *Small*, 2009, **5**, 1334–1342.
60 X. He, X. Wu, X. Cai, S. Lin, M. Xie, X. Zhu and D. Yan, *Langmuir*, 2012, **28**, 11929–11938.
61 R. D. Palma, S. Peeters, M. J. V. Bael, H. V. d. Rul, K. Bonroy, W. Laureyn, J. Mullens, G. Borghs and G. Maes, *Chem. Mater.*, 2007, **19**, 1821–1831.
62 S. Slavin and D. M. Haddleton, *Soft Matter*, 2012, **8**, 10388–10393.
63 S. Slavin, A. H. Soeriyadi, L. Voorhaar, M. R. Whittaker, C. R. Becer, C. Boyer, T. P. Davis and D. M. Haddleton, *Soft Matter*, 2012, **8**, 118–128.
64 Y.-C. Yeh, B. Creran and V. M. Rotello, *Nanoscale*, 2012, **4**, 1871–1880.
65 C. Boyer, M. H. Stenzel and T. P. Davis, *J. Polymer Science Part A: Polymer Chemistry*, 2011, **49**, 551–595.
66 K. Matyjaszewski, *Macromolecules*, 2012, **45**, 4015–4039.
67 N. H. Nguyen, M. E. Levere and V. Percec, *J. of Polymer Science Part A: Polymer Chemistry*, 2012, **50**, 860–873.
68 J. Nicolas, Y. Guillaneuf, C. Lefay, D. Bertin, D. Gigmes and B. Charleux, *Progress in Polymer Science*, 2013, **38**, 63–235.
69 K. Matyjaszewski and J. Spanswick, *Materials Today*, 2005, **8**, 26–33.
70 S. Hansson, V. Trouillet, T. Tischer, A. S. Goldmann, A. Carlmark, C. Barner-Kowollik and E. Malmström, *Biomacromolecules*, 2012, **14**, 64–74.
71 M. Lattuada and T. A. Hatton, *Langmuir*, 2007, **23**, 2158–2168.
72 J. Tian, Y. K. Feng and Y. S. Xu, *Macromol. Res.*, 2006, **14**, 209–213.
73 L. Wang, K. G. Neoh, E. T. Kang, B. Shuter and S.-C. Wang, *Advanced Functional Materials*, 2009, **19**, 2615–2622.
74 J. E. Moses and A. D. Moorhouse, *Chem. Soc. Rev.*, 2007, **36**, 1249 –1262.
75 C. D. Hein, X.-M. Liu and D. Wang, *Pharm. Res.*, 2008, **25**, 2216–2230.
76 M. A. White, J. A. Johnson, J. T. Koberstein and N. J. Turro, *J. Am. Chem. Soc.*, 2006, **128**, 11356–11357.
77 L. Castaneda, A. Maruani, F. F. Schumacher, E. Miranda, V. Chudasama, K. A. Chester, J. R. Baker, M. E. B. Smith and S. Caddick, *Chem. Comm.*, 2013, **49**, 8187–8189.
78 S. R. MacEwan, D. J. Callahan and A. Chilkoti, *Nanomedicine*, 2010, **5**, 793–806.
79 J. Liu, H. Duong, M. R. Whittaker, T. P. Davis and C. Boyer, *Macromolecular Rapid Communications*, 2012, **33**, 760–766.
80 S. Yamashita, H. Fukushima, Y. Akiyama, Y. Niidome, T. Mori, Y. Katayama and T. Niidome, *Bioorganic & Medicinal Chemistry*, 2011, **19**, 2130–2135.
81 Z. Erno, A. M. Asadirad, V. Lemieux and N. R. Branda, *Organic & Biomolecular Chemistry*, 2012, **10**, 2787–2792.
82 M. P. Melancon, A. M. Elliott, A. Shetty, Q. Huang, R. J. Stafford and C. Li, *Journal of Controlled Release*, 2011, **156**, 265–272.
83 S. Vijayakumar and S. Paulsi, *International Journal of Pharmaceutical Sciences Review and Research*, 2013, **20**, 80–88.

84 A. M. Alkilany, L. B. Thompson, S. P. Boulos, P. N. Sisco and C. J. Murphy, *Advanced Drug Delivery Reviews*, 2012, **64**, 190–199.
85 A. Mandelis, *Opt. Photon. News*, 2002, **13**, 32–37.
86 A. Mandelis and Y. Riopel, *Journal of Vacuum Science & Technology A*, 2000, **18**, 705–708.
87 J. Robinson, K. Welsher, S. Tabakman, S. Sherlock, H. Wang, R. Luong and H. Dai, *Nano Res*, 2010, **3**, 779–793.
88 J. Lin, S. Wang, P. Huang, Z. Wang, S. Chen, G. Niu, W. Li, J. He, D. Cui, G. Lu, X. Chen and Z. Nie, *ACS Nano*, 2013, **7**, 5320–5329.
89 M. Zheng, C. Yue, Y. Ma, P. Gong, P. Zhao, C. Zheng, Z. Sheng, P. Zhang, Z. Wang and L. Cai, *ACS Nano*, 2013, **7**, 2056–2067.
90 J. Huang, K. S. Jackson and C. J. Murphy, *Nano Letters*, 2012, **12**, 2982–2987.
91 D. Liu, X. Wang, S. Han and X. Zhao, *Gaofenzi Cailiao Kexue Yu Gongcheng*, 2011, **27**, 172–175.
92 Z. Fan, D. Senapati, A. K. Singh and P. C. Ray, *Molecular Pharmaceutics*, 2012, **10**, 857–866.
93 J. Li, J. Han, T. Xu, C. Guo, X. Bu, H. Zhang, L. Wang, H. Sun and B. Yang, *Langmuir*, 2013, **29**, 7102–7110.
94 H. Zhang, C. Chen, L. Hou, N. Jin, J. Shi, Z. Wang, Y. Liu, Q. Feng and Z. Zhang, *Journal of Drug Targeting*, 2013, **21**, 312–319.
95 M. J. O'Connell, S. M. Bachilo, C. B. Huffman, V. C. Moore, M. S. Strano, E. H. Haroz, K. L. Rialon, P. J. Boul, W. H. Noon, C. Kittrell, J. Ma, R. H. Hauge, R. B. Weisman and R. E. Smalley, *Science*, 2002, **297**, 593–596.
96 A. C. Estrada, A. L. Daniel-da-Silva and T. Trindade, *RSC Advances*, 2013, **3**, 10828–10836.
97 A. Sahu, W. I. Choi, J. H. Lee and G. Tae, *Biomaterials*, 2013, **34**, 6239–6248.
98 Y. Wang, K. Wang, J. Zhao, X. Liu, J. Bu, X. Yan and R. Huang, *Journal of the American Chemical Society*, 2013, **135**, 4799–4804.
99 H. Liu, D. Chen, L. Li, T. Liu, L. Tan, X. Wu and F. Tang, *Angewandte Chemie International Edition*, 2011, **50**, 891–895.
100 Z. Jiang, B. Dong, B. Chen, J. Wang, L. Xu, S. Zhang and H. Song, *Small*, 2013, **9**, 604–612.
101 G. D. Moon, S.-W. Choi, X. Cai, W. Li, E. C. Cho, U. Jeong, L. V. Wang and Y. Xia, *Journal of the American Chemical Society*, 2011, **133**, 4762–4765.
102 S. Yamashita, H. Fukushima, Y. Niidome, T. Mori, Y. Katayama and T. Niidome, *Langmuir*, 2011, **27**, 14621–14626.
103 W. F. Zandberg, A. B. S. Bakhtiari, Z. Erno, D. Hsiao, B. D. Gates, T. Claydon and N. R. Branda, *Nanomedicine: Nanotechnology, Biology and Medicine*, 2012, **8**, 908–915.
104 A. J. Gormley, N. Larson, S. Sadekar, R. Robinson, A. Ray and H. Ghandehari, *Nano today*, 2012, **7**, 158–167.
105 S.-M. Lee, H. J. Kim, Y.-J. Ha, Y. N. Park, S.-K. Lee, Y.-B. Park and K.-H. Yoo, *ACS Nano*, 2012, **7**, 50–57.
106 J. You, R. Zhang, C. Xiong, M. Zhong, M. Melancon, S. Gupta, A. M. Nick, A. K. Sood and C. Li, *Cancer Research*, 2012, **72**, 4777–4786.
107 P. M. Bendix, S. N. S. Reihani and L. B. Oddershede, *ACS Nano*, 2010, **4**, 2256–2262.
108 A. Kyrsting, P. M. Bendix, D. G. Stamou and L. B. Oddershede, *Nano Letters*, 2010, **11**, 888–892.
109 M. Honda, Y. Saito, N. I. Smith, K. Fujita and S. Kawata, *Opt. Express*, 2011, **19**, 12375–12383.
110 C. S. S. R. Kumar and F. Mohammad, *Advanced Drug Delivery Reviews*, 2011, **63**, 789–808.

111 J. Zhang and R. D. K. Misra, *Acta Biomaterialia*, 2007, **3**, 838–850.
112 R. Zhang, C. Wu, X. Wang, Q. Sun, B. Chen, X. Li, S. Gutmann and G. Lv, *Materials Science and Engineering: C*, 2009, **29**, 1697–1701.
113 R. Massart, *Magnetics, IEEE Transactions on*, 1981, **17**, 1247–1248.
114 C. Blanco-Andujar, D. Ortega, Q. A. Pankhurst and N. T. K. Thanh, *Journal of Materials Chemistry*, 2012, **22**, 12498–12506.
115 T. Sugimoto and E. Matijević, *Journal of Colloid and Interface Science*, 1980, **74**, 227–243.
116 L. Cabrera, S. Gutierrez, N. Menendez, M. P. Morales and P. Herrasti, *Electrochimica Acta*, 2008, **53**, 3436–3441.
117 Y. Piao, J. Kim, H. Na, D. Kim, J. Baek, M. Ko, J. Lee, M. Shokouhimehr and T. Hyeon, *Nature Materials*, 2008, **7**, 242–247.
118 I. Robinson and N. T. K. Thanh, *AIP Conference Proceedings*, 2010, **1275**, 3–12.
119 D. Ung, L. D. Tung, G. Caruntu, D. Delaportas, I. Alexandrou, I. A. Prior and N. T. K. Thanh, *CrystEngComm*, 2009, **11**, 1309–1316.
120 L. T. Lu, L. D. Tung, I. Robinson, D. Ung, B. Tan, J. Long, A. I. Cooper, D. G. Fernig and N. T. K. Thanh, *Journal of Materials Chemistry*, 2008, **18**, 2453–2458.
121 A. Dhawan and V. Sharma, *Anal Bioanal Chem*, 2010, **398**, 589–605.
122 L. Franzel, M. F. Bertino, Z. J. Huba and E. E. Carpenter, *Applied Surface Science*, 2012, **261**, 332–336.
123 C. Yang, R. Jie, L. Jianbo and L. Yan, *Journal of Biomaterials Science, Polymer Edition*, 2011, **22**, 1473–1486.
124 V. M. Khot, A. B. Salunkhe, N. D. Thorat, R. S. Ningthoujam and S. H. Pawar, *Dalton Transactions*, 2013, **42**, 1249–1258.
125 P. Bilalis, A. Chatzipavlidis, L.-A. Tziveleka, N. Boukos and G. Kordas, *Journal of Materials Chemistry*, 2012, **22**, 13451–13454.
126 B. Sivakumar, R. G. Aswathy, Y. Nagaoka, M. Suzuki, T. Fukuda, Y. Yoshida, T. Maekawa and D. N. Sakthikumar, *Langmuir*, 2013, **29**, 3453–3466.
127 S. Brulé, M. Levy, C. Wilhelm, D. Letourneur, F. Gazeau, C. Ménager and C. Le Visage, *Advanced Materials*, 2011, **23**, 787–790.
128 J. L. Arias, V. Gallardo and M. A. Ruiz, In *Methods in Enzymology*, D. Nejat (Ed.), Academic Press, 2012, vol. 508, pp. 61–88.
129 Y. Mi, X. Liu, J. Zhao, J. Ding and S.-S. Feng, *Biomaterials*, 2012, **33**, 7519–7529.
130 W.-H. Chiang, V. T. Ho, H.-H. Chen, W.-C. Huang, Y.-F. Huang, S.-C. Lin, C.-S. Chern and H.-C. Chiu, *Langmuir*, 2013, **29**, 6434–6443.
131 C. Sanson, C. Schatz, J.-F. Le Meins, A. Soum, J. Thévenot, E. Garanger and S. Lecommandoux, *Journal of Controlled Release*, 2010, **147**, 428–435.
132 S.-H. Hu, B.-J. Liao, C.-S. Chiang, P.-J. Chen, I. W. Chen and S.-Y. Chen, *Advanced Materials*, 2012, **24**, 3627–3632.
133 A. E. Smith, X. Xu, D. A. Savin and C. L. McCormick, *Polymer Chemistry*, 2010, **1**, 628–630.
134 M. A. Kosoglu, R. L. Hood, J. H. Rossmeisl, D. C. Grant, Y. Xu, J. L. Robertson, M. N. Rylander and C. G. Rylander, *Lasers in Surgery and Medicine*, 2011, **43**, 914–920.
135 J. McDaniel, M. Dewhirst and A. Chilkoti, *International Journal of Hyperthermia*, 2013, **29**, 501–510.
136 J. R. McDaniel, J. Bhattacharyya, K. B. Vargo, W. Hassouneh, D. A. Hammer and A. Chilkoti, *Angewandte Chemie International Edition*, 2013, **52**, 1683–1687.

137 J. R. McDaniel, S. R. MacEwan, M. Dewhirst and A. Chilkoti, *Journal of Controlled Release*, 2012, **159**, 362–367.
138 Y.-X. J. Wang, *Quantitative Imaging in Medicine and Surgery*, 2011, **1**, 35–40.
139 D. Kim, S. Park, J. H. Lee, Y. Y. Jeong and S. Jon, *Journal of the American Chemical Society*, 2007, **129**, 7661–7665.
140 P.-H. Wang, H.-L. Liu, P.-H. Hsu, C.-Y. Lin, C.-R. Chris Wang, P.-Y. Chen, K.-C. Wei, T.-C. Yen and M.-L. Li, *BIOMEDO*, 2012, **17**, 612221–612225.
141 S. Casciaro, F. Conversano, A. Ragusa, M. Ada Malvindi, R. Franchini, A. Greco, T. Pellegrino and G. Gigli, *Investigative Radiology*, 2010, **45**, 715–724.
142 X. An, F. Zhan and Y. Zhu, *Langmuir*, 2013, **29**, 1061–1068.
143 L. Gao, J. Fei, J. Zhao, H. Li, Y. Cui and J. Li, *ACS Nano*, 2012, **6**, 8030–8040.

Nano dimensional ZnO: new chemical insights from an old material

Angela S. Pereira and Tito Trindade*
DOI: 10.1039/9781849737623-00255

Zinc oxide is a semiconductor whose technological applications are widespread in areas such as optoelectronics, sensors, transducers and biomedical sciences. This material can be prepared at the nanoscale in a variety of shapes and sizes, can be obtained as a metal doped host and also used as a functionalized filler in polymer composites. These characteristics, among many others, make this material suitable to understand nanoscale phenomena conceptually common to other nanocrystalline semiconductors. In this chapter, special focus will be made on recent research of diverse chemical routes for ZnO nanostructures and relevant size and shape dependent optical properties. Also general guidelines on fabrication parameters that affect the properties of ZnO based nanomaterials and their novel applications will be reviewed.

1 Introduction

This chapter gives an overview of recent research on chemically prepared nanosized ZnO. The chapter is organized in three main sections. The first section will present chemical methods for the synthesis of ZnO nanostructures, including methods for ZnO quantum dots. The second section highlights the relevance of structural and morphological features on defining the properties of ZnO quantum dots, with focus on the optical behavior. The closing section presents outlook for future research on this material.

This chapter will introduce concepts and methodologies that although applied to ZnO nanostructures can be conceptually extended to other semiconductor materials, such as for example nanocrystals of metal chalcogenides. In this context, the definition of ZnO as a prototype material is probably excessive, but important chemistry applied to quantum dots can be understood from the research performed on this material. It is therefore useful to present first some well-known characteristics of ZnO that make it a material of choice for many academic studies and technological applications.

Macrocrystalline ZnO crystallizes with the wurtzite type structure. It is a II-VI semiconductor with a wide band-gap of 3.37 eV, it has a direct gap band structure at room temperature, and has the largest exciton binding energy (60 meV) among the II-VI semiconductors. The high exciton binding energy gives it a high potential for room temperature light emission. This also gives ZnO strong resistance to high temperature electronic degradation during operation (*e.g.* laser diodes). The combination of high excitonic and biexcitonic oscillator strength and the ability of supporting high

Chemistry Department, CICECO, Aveiro Institute of Nanotechnology, University of Aveiro, 3810-193 Aveiro Portugal. E-mail: tito@ua.pt

temperature makes ZnO a promising material for optical applications. Hence, ZnO has been used as a visible and ultraviolet photoconductor and as a fluorescent material.[1] It has a high piezoelectric effect ($e_{33} = 1.2$ C/m^2, the highest among all the semiconductors) and acousto-optic properties have also been exploited in the past.[2] An on-going interest in ZnO has increased as a result of its crystallographic properties that could make it a suitable substrate for wide band-gap nitride semiconductor devices[3] and possibly for ultraviolet/blue/ green lasers and detectors as well.[4] Finally, ZnO is the hardest of the II-VI semiconductors, meaning its performance will not be degraded as easily as the other compounds through the appearance of defects. With all these characteristics, ZnO is an eye-catching semiconductor for numerous applications. Additionally nanocrystalline ZnO has been widely studied due to potential applications in optoelectronic fields and fabricating nanodevices,[5] especially in varistors, piezoelectric devices, surface acoustics wave devices, solar cells, transparent conductors, transparent UV-protection films, gas-detecting chemical sensors and antibacterial activity.[6–9] Researchers have been able to develop a zinc-based coating capable of resisting a great range of temperatures, and the attack of ultraviolet exposure equivalent to 19,000 solar hours. ZnO coatings are now routinely used to protect components of spacecraft, which are some of the most technically advanced and complex machines ever made. Zinc oxide is an old material that despite a long history is still regarded as a modern material, namely due to their relevance as a nanomaterial for a number of applications.

2 Optical and structural properties of ZnO quantum dots

2.1 Electronic and crystalline structure

Over the past decades many advances have been made in the area of nanomaterials science. One of the most important findings has been the existence of scalable size-dependent properties. Which brings us to the question: how do the electronic, optical, and magnetic properties of nanoscopic particles differ from those of a bulk sample of the same material? This matter is of great importance because the properties of a material change as the particle size approaches molecular dimensions and therefore new technologies can be developed based on nanomaterials.

Nanocrystals exhibiting quantum size effects (quantum dots-QDs) are also called mesoscopic atoms or artificial atoms to indicate that the scale of electron states in QDs is larger than the lattice constant of a crystal.[10] These quantum size effects observed in nanosize crystals lead to dramatic changes in transport and optical properties of the semiconductor. The electronic structure in semiconductors can be analyzed in terms of the density of electronic states (DOS). The prominent transformation from bands of continuum of states in a bulk crystal to the set of discrete electronic levels in quantum semiconductor structures is depicted in Fig 1. In a bulk semiconductor [Fig. 1(a)], the DOS is proportional to the square root of the electron energy. In quantum wells (QWs) [see Fig. 1(b)], the electrons are restricted into a layer of a few nanometers thick. The QWs DOS consists of a staircase, and the edge of the band (lowest electron states) is shifted to

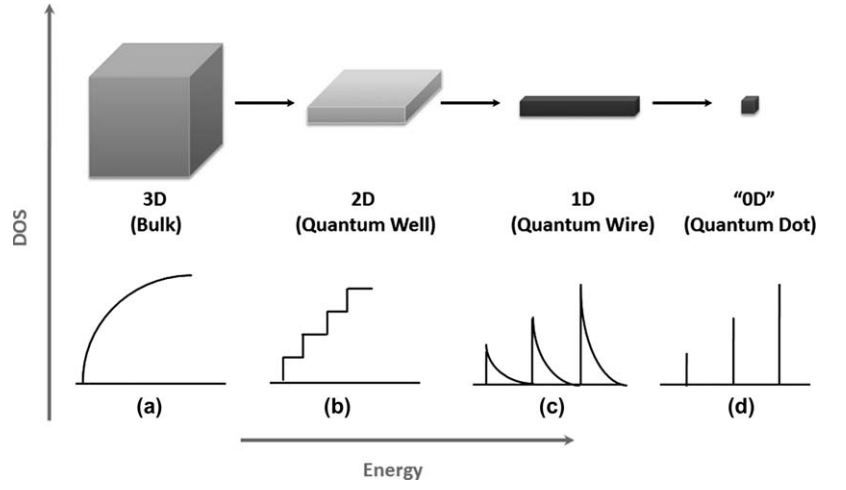

Fig. 1 Evolution of the density of states as the structural dimensionality of the semiconductor is reduced from 3D (bulk) to 0D (quantum dot). The density of states of an ideal quantum dot is discrete.

higher energies. Considering now a structure that shrinks along a second dimension, electrons can freely move only along one direction because they are confined in two dimensions and such a system is called a quantum wire [Fig. 1 (c)]. The DOS of one-dimensional systems is inversely proportional to the square root of the electron energy and thus exhibits singularities near the band edges.[11] In ideal QDs the energy levels are discrete [Fig. 1(d)] and the DOS consists of a series of sharp peaks corresponding to discrete electronic energies. In real samples not all the QDs are of the same size and therefore the peaks in the DOS are distributed around average energies corresponding to average QD sizes. In many applications, the active device material contains a large ensemble of QDs. Their joint density of states then includes a statistical broadening characterized by a Gaussian function. This broadening is often labeled inhomogeneous in distinction to the lifetime broadening, often called homogeneous broadening.

Quantum dots exhibit unique properties that have been investigated in the manufacture of new semiconductor devices. In fact, these semiconductor nanostructures are so small as compared to submicrometric powders that their electronic and optical properties diverge significantly from those of the bulk analogues. Still in a number of cases, X-ray diffraction and electron diffraction techniques have shown that quantum dots can be understood as nanometric fragments of the crystalline lattice of the bulk semiconductor. Some solids are known to exist with different structural phases (polymorphs) depending on their temperature and pressure conditions. Semiconductors of the group II-VI are more covalent as compared to other crystalline solids, thus preferring a tetrahedral coordination of the ions, originating phases such as the cubic-type (*blende*) or the hexagonal-type (*wurtzite*) structures that can be derived from close packing arrangements.

For ZnO nanocrystals the most important crystalline phase is the *wurtzite* type structure. This has been confirmed by a series of studies in which the

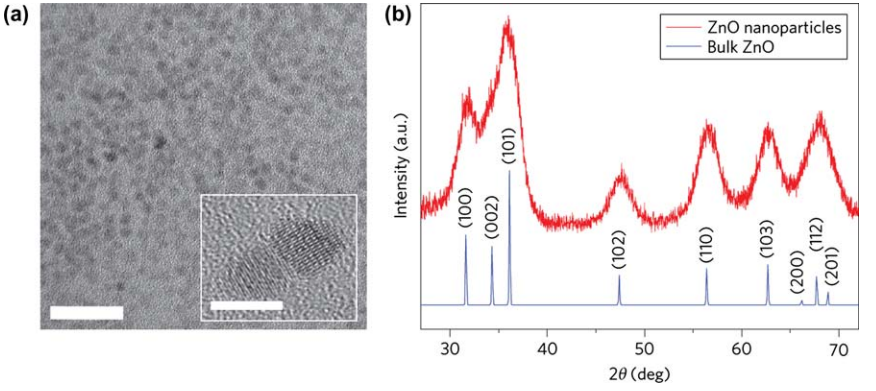

Fig. 2 a) TEM image of ZnO NPs (scale bar, 20 nm). Inset: High-resolution TEM images of same ZnO NPs (scale bar, 3 nm). b) XRD pattern from ZnO NPs (top) together with that from bulk wurtzite ZnO (bottom). Adapted by permission from Macmillan Publishers Ltd: Nature Photonics,[12] copyright 2011.

experimental XRD patterns of nanosized powders can be assigned to the hexagonal ZnO phase, though peak broadening is also observed in many cases.[12] Quian and coworkers prepared ZnO quantum dots and their XRD patterns, together with that of bulk phase ZnO, are compared and a significant broadening of the characteristic diffraction peaks when reduced to the nanoscale is presented in Fig. 2.[12] Raoufi synthesized ZnO nanoparticles by annealing a precursor, prepared by precipitation method from zinc nitrate and ammonium carbonate in aqueous solutions, at different temperatures.[13] The XRD results indicated that the ZnO NPs had wurtzite structure and that with increasing annealing temperature the crystallinity and particle size increased along with lattice parameters that approached those of the XRD bulk counterpart.

The law of Bragg dictates the condition for a sharp diffraction peak of an infinite crystalline lattice with a perfect tridimensional order. In fact, a diffraction peak has a finite width, which is associated to the imperfection of some Bragg parameters. These imperfections are associated with beam divergence, a polychromatic source, and/or tridimensional order imperfections in the crystals.[14] The shifts of this last demand may be originated by three terms: crystallite size (Scherrer equation); distortions coming from the movement of atoms inside the crystalline pattern (Debye widening) or other type of distortions that disturb the repetition of the crystalline pattern (*e.g.* micro-tensions) Excluding instrumental effects that may contribute for the broadening of the diffraction peaks, broadening due to small crystallite size can be the basis for quantitative estimates of nanocrystal size. This can be performed by taking into account the Scherrer equation:[15]

$$D_{hkl} = k\lambda/\beta_{1/2}\cos\theta \tag{1}$$

where D_{hkl} is the average diameter of a particle, k is the shape factor which is 0.9 for spherical particles, λ is the X-ray wavelength and $\beta_{1/2}$, expressed in radians, is defined as:

$$\beta_{1/2} = \left(B^2 - b^2\right)^{1/2} \tag{2}$$

B is the half width of the diffraction peak and b is the natural width of the peak from the instrument. A diffraction peak broadening is expected to reflect large scale characteristic of a crystal because small angular differences are associated with large spatial distances. This is a practical method to estimate average particle sizes though assuming that all particles are crystalline.

2.2 Quantum size effects

It was mainly during the 80's that after systematic studies on nanocrystalline semiconductors, scientists have suggested that the band gap of a direct semiconductor would be dependent on their size when their dimensions are below the Bohr's exciton radius. In fact, several experiments have confirmed that by reducing the semiconductor particle size to the nanoscale, there is a blue shift of the respective optical band gap observed in the experimental spectra.[16] The size of the nanostructure limits the radius of bound electron-hole pair that forms the exciton, leading to altered electronic and optical properties, and causes high surface energy, which alters the physical properties. Material properties change considerably due to quantum size effects arising from confinement of electrons and holes in the crystalline lattice as size is reduced. In this case, the nanocrystal is essentially smaller than the natural exciton-Bohr radius, defined to be:

$$a_B = \frac{\varepsilon_0 h^2}{m_r e^2} \tag{3}$$

where ε_0 is the dielectric constant of the quantum dot (at low frequencies), h is Planck's constant, and m_r is the reduced electron-hole mass.[17] The equations relating the electron energy levels in spherical quantum dots with infinite potential are of great importance because they indicate the size dependence of quantum confinement effects. Therefore, the electron and the whole wave functions vanish at and beyond the surface of the nanocrystal, without the possibility of any tunnelling. In the strong confinement regime, where R, the nanocrystal radius, is much smaller than a_B, the following equations have been used to express the band gap energy in function of particle size in quantum dots:

$$E(R) = E_g + \frac{\hbar^2 \pi^2}{2R^2}\left(\frac{1}{m_e^*} + \frac{1}{m_{\hbar}^*}\right) - 1.8\frac{e^2}{\epsilon \mathrm{R}} \tag{4}$$

where E_g is the bulk band gap. The second term is the kinetic energy term containing the effective masses, m^*_e and m^*_h, of the electron and the hole, respectively. The third term arises due to the Coulomb attraction between the electron and the hole.[16,18] Equation 4 shows that the semiconductor band gap increases as the particle size decreases as illustrated in Fig. 3 for ZnO quantum dots. The smaller the dot, the higher the photon energy absorbed that is observed as a blue shift in the experimental absorbance spectrum, and the higher is the energy of the emitted light due to electron-hole annihilation (excitonic emission). This makes optical spectroscopy a very effective technique to evaluate quantum size confinement

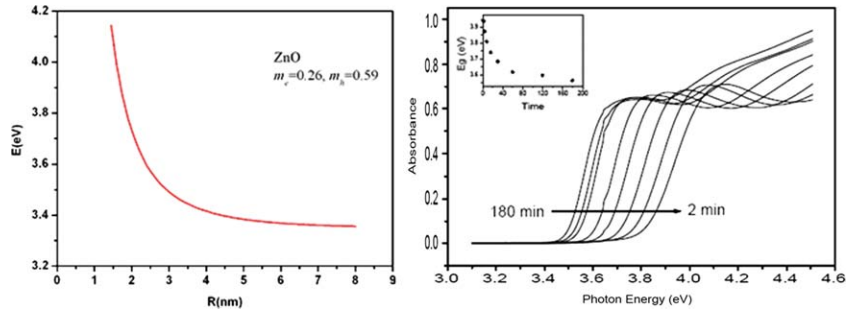

Fig. 3 Left: Estimated change in the band gap energy as a function of the size of the ZnO nanocrystals. Right: RT absorbance spectra of colloidal suspensions of ZnO as a function of aging time. Inset: band gap dependence as a function of time.

behavior in quantum dots as a first step to a vast assortment of possible applications and new technologies.

ZnO is one of the few metal oxides that present quantum confinement in experimentally obtainable range of sizes (< 7 nm). From the known electron and hole effective masses of bulk ZnO, the bulk exciton Bohr radius (a_B) for this semiconductor is approximately 23.4 Å, which is considerably small. Hence, regions of intermediate confinement ($a_B < R < 3a_B$) and weak confinement ($R > a_B$) have been recognized in ZnO nanocrystals.[19] Fig. 3 shows the dependence of the band gap energy as a function of the size of the particles for the weak confinement region, using equation 2. For values of $R > 3a_B$ (~ 40 Å), there is a plausibly correct assessment of the quantum-size shift with the theoretical curve. Nonetheless, below this value the curve undervalues the shift. The traditional undoped ZnO nanocrystals would not show large changes in the absorption for particle size larger than 50 Å, as observed by Bahnemann *et al.*[20]

Distinct size distributions of ZnO nanocrystals have been estimated from optical absorption measurements.[21] A blue shift is observed for the optical band edge in the experimental spectra as particle size decreases, hence increasing the band gap energy (Fig. 3-right). The absorbance spectra in Fig. 3-right also show well-defined excitonic peaks, characteristic of ZnO quantum dots with narrow particle size distributions. The absorption onset reallocates with the colloid aging time confirming that the average particle size is in the quantum size region. The average particle size for ZnO colloids with optical features as shown in Fig. 3, vary from 3.5 to 7 nm. Because for ZnO the effective masses of electrons and holes are relatively small ($m_e = 0.26$, $m_h = 0.59$), a band gap enlargement can also be seen for particle diameters less than about 8 nm.[22] Further growth of the particle causes a decrease in the band gap and hence a red shift of the absorption onset is observed. For particle sizes larger than about 8 nm, the absorption onset would be about 3.37 eV, corresponding to the bulk band gap for ZnO.

2.3 Photoluminescence of ZnO quantum dots

Room-temperature photoluminescence (PL) band for bulk ZnO is at 364 nm (3.4 eV), corresponding to band gap emission, though some variation of the position of the PL peak may occur for different nanostructures.

Different morphologies can originate distinct UV peak positions (Fig. 4), for example: 387 nm for tetrapods, 381 nm for needles, 397 nm for nanorods, 377 nm for shells, 379 nm for faceted rods, and 385.5 nm for ribbons/combs).[23] ZnO nanostructures large enough to not exhibit quantum confinement effects, such as nanobelts, exhibit UV emission in a range between 384 and 391 nm.[24] These differences in the peak wavelength indicate that there is a different reason for the deviation in the band-edge emission in ZnO nanostructures, as reported in diverse studies. Although quantum confinement effects have been proposed as a possible cause of the blue shift of the band-edge emission with decreasing size,[25] nanocrystals with large diameters are not likely to originate any shift considering that the Bohr radius of ZnO is 2.34 nm. A possible reason for this deviation may be due to the presence of native defects. For nanocrystals, defect density is higher at the surface, thus spectral shifts are expected to occur in nanostructures with different sizes due to different surface-to-volume ratios.

Green and/or yellow luminescence bands are the most commonly observed and widely studied, but the luminescence mechanism remains unclear. Green emission is often attributed to singly ionized oxygen vacancies, although this assignment is controversial. Zhang *et al*. described recently the nature of size tunable visible emission in ZnO nanoparticles, which showed that both the defect energy state and the quantum confinement effect are the main features contributing to tunable visible emission.[26]

The emission peaks for defect related transitions are wide and the justification for emission band broadening is not clear; some explanations might be either size polydispersity or closely spaced transitions within the nanocrystal.[27] Nonetheless, the correlation amongst the role of surface defects in the luminescence intensity and the broadening observed in the visible emission is not yet entirely comprehended.

The unique optical properties of ZnO make commercial utility a reality in photonics, spintronics, energy applications, catalysis, sensors, UV

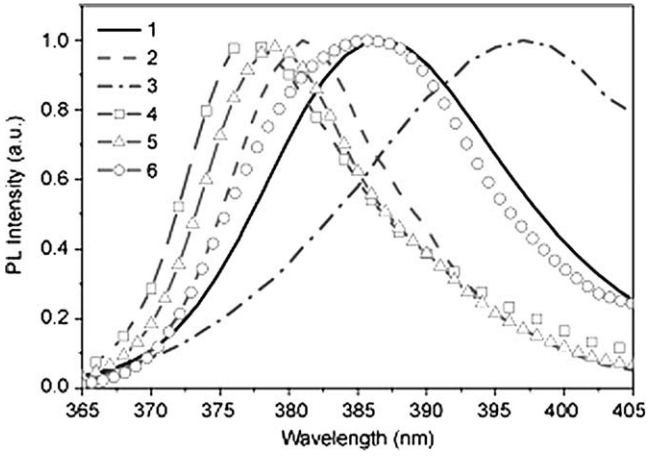

Fig. 4 Room-temperature PL spectra of various nanostructures in the UV range: 1) tetrapods, 2) needles, 3) nanorods, 4) shells, 5) highly faceted rods, 6) ribbons/combs. Reprinted with permission of John Wiley and Sons from Ref. 23. Copyright 2006.

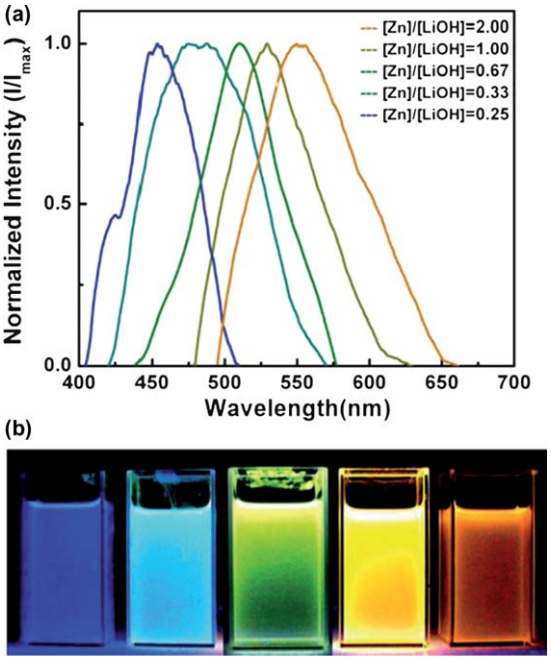

Fig. 5 (a) Photoluminescence emission spectra and (b) Photographs of ZnO QDs for different [Zn]/[LiOH] molar ratios, under irradiation by a 365 nm handheld UV lamp. Reproduced from Ref. 28.

protection films, biocidal coating, *in vitro* and *in vivo* diagnostics and therapeutic applications. Various groups have attempted to tune the photoluminescence of ZnO nanoparticles to achieve undoped multi-colour emitting ZnO QDs.[28–32] Recently Asok *et al*. have reported the synthesis for defect rich ZnO QDs.[28] An oxygen deficient environment was created by ultrasonic degasification of the precursor solutions and purging nitrogen into the reaction vessel during synthesis. The size tunability was accomplished by varying the [Zn]/[LiOH] molar ratio. This synthesis resulted in defect rich ZnO QDs with size tunable visible emission (Fig. 5).

3 Chemical synthesis of ZnO nanocrystals

Research on ZnO nanocrystals synthesis is beneficial to comprehend fundamental nucleation and growth processes occurring during the synthesis of quantum dots, in general. Various ZnO nanostructures, such as nanorods,[33–35] nanowires,[36] nanoribbons[37,38] and nanoflowers,[39] have been fabricated during the last decade, and the growth mechanisms of ZnO crystallites with different shapes have also been discussed.[40–42] On the other hand, fundamental understanding of the formation mechanism of so many diverse shapes of ZnO is far from complete. It is believed that the inconsistencies of the formation mechanism under different growing environments is significantly responsible for shape variations of ZnO, and thus research for comprehending the crystallization process of such nanostructures is attracting more and more attention. In this section, various solution chemical synthesis methods will be mentioned. Nonetheless there

are other means of production of ZnO that will not be reviewed here, namely solid-state reactions [43–46] and chemical vapour deposition.[47–50]

3.1 Colloidal procedures

Spanhel and Anderson[51] proposed a sol-gel technique that allowed the production of relatively high concentrated ZnO colloids in a short period of time. Basically the synthesis of colloidal ZnO by this route involves: (1) preparation of a zinc precursor; (2) preparation of ZnO colloids and (3) solvent removal to concentration levels resulting in desired products such as syrups and alcogels. The reaction can be represented by:

$$Zn(CH_3COO)_2 + 2LiOH \xrightarrow{EtOH} ZnO + 2Li(CH_3COO) + H_2O$$

The colloid remains in a dispersed state for weeks or even months. The Spanhel and Anderson's method was the basis for many studies on ZnO colloids. Meulenkamp[52] proved that particle growth could be governed by temperature and, the presence of water and acetate. Removal of these species could practically stop growth. Oxides can be formed by (a) hydrolysis and (b) condensation of the dissolved species. The ZnO nanoparticles continue to grow even when stored at 0 °C and it was found that solution composition and temperature have marked influence on particle growth rate. The growth rate was suggested to be governed by the product of the concentrations of the dissolved species and by the surface reactivity of the ZnO particles.[52]

Raula and coworkers have developed a solution-based method to prepare flower-like ZnO nanostructures using ascorbate ion as a shape-directing/capping agent.[53] Distinct morphologies of ZnO nanostructures such as flowerlike, spindlelike, and spherical could be achieved by increasing the reaction temperature from 60 to 90 °C.

Hu *et al* have synthesized ZnO nanoparticles using the Spanhel and Anderson's method but replacing the solvent by alcohols such as ethanol and 1-hexanol.[54] The absorbance spectra of the ZnO particles obtained in these solvents exhibited a well-defined excitonic peak characteristic of bulk ZnO. The influence of the solvent on the ZnO formation was clearly observed after mixing the zinc acetate and sodium hydroxide solutions. Thus for the longer chain alcohols, the spectra showed a well-defined absorbance onset immediately after mixing, indicating that nucleation was fast. On the contrary, for the shorter chain length alcohols (ethanol and 1-propanol), the absorbance spectra evolved with time, indicating that nucleation and growth was slower.

Colloidal particle growth results into a decrease of the total surface free energy per volume. Two possible paths have been suggested to describe ZnO nanocrystals growth in the method of Spanhel and Anderson (Fig. 6).[51] These are aggregation and Ostwald ripening, *i.e*. the larger particles grow at the expense of smaller particles. Whether the consolidation of the 3.5 or 5.5 nm clusters into the compact gel network and crystal state, necessitates Ostwald ripening as a previous step is a relevant question. Indeed, as soon as the smallest stable molecular clusters are formed, they might combine to produce other stable aggregates. The primary aggregates would further rapidly combine to give the next most stable secondary aggregates and so

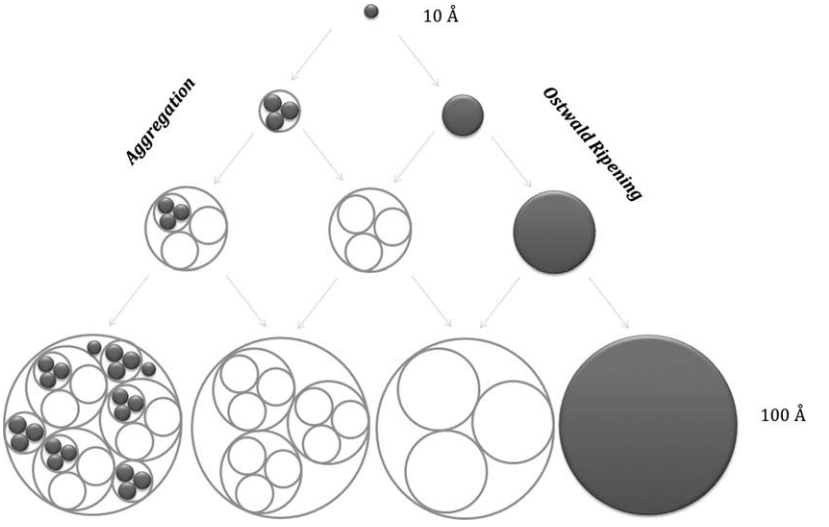

Fig. 6 Aggregation and Ostwald ripening in growth of colloidal ZnO nanocrystals. Adapted with permission from Ref. 51. Copyright 1991 American Chemical Society.

on. More so, the primary 3.5- and 5.5-nm clusters, with which they started the study, actually might be stable aggregates (fragments of the resulting large ZnO crystals). They would be a result of rapid aggregation rather than a result of Ostwald growth. To what extent aggregation-based crystal growth or Ostwald crystal growth occurs (or both overlap) remains to be further worked out. Their experimental data suggests that the Ostwald mechanism should be considered as only one possible approach to the formation of bulk materials.

A disadvantage of the sol-gel method for preparing ZnO NPs is that means to prevent particle growth while in colloidal state are limited. Nevertheless, this method has been widely used to prepare high quality ZnO nanostructures for applications such as photocatalysts,[55] solar cells[56] and as biosensors.[57]

3.2 Molecular precursors

While colloidal nanoparticles can be synthesized by a diversity of means, the most thriving has been the reaction at high-temperature of molecular precursors in a coordinating solvent.[58] This method allows good control on size, size-dispersion and crystallinity of colloidal nanocrystals. In a modality very often employed, this technique involves the direct injection of molecular precursors into a hot coordinating solvent in order to produce a single event nucleation. Slow growth and annealing in the coordinating solvent result in a regular derivatized surface and homogeneous core structure. Size selective fractionation methods allow further improvements to obtain nearly monodisperse nanocrystals, which can be then dispersed in an assortment of solvents. The quality of the nanocrystalline products is related to their crystallinity which in turn is favoured by synthesis at high temperature.[59] In a typical synthesis, a high boiling point solvent, for example TOPO, is heated under N_2 flow, until a desired temperature (usually

between 150–300 °C). When the desired temperature is reached, the Zn^{II} precursor, which was separately dissolved in another high-boiling point solvent (such as TOP) is promptly injected into the hot Zn^{II} solution and further growth of nanoparticles takes place at a given temperature. UV-vis absorption spectra confirm the size dependence with reaction time for ZnO nanostructures. Upon heating, the onset of the band-gap absorption is red-shifted to higher wavelength. Growth proceeded to completion in a few minutes after which virtually ceased. A considerable change in the absorption onset could be detected only after a long period of heating.

Progress in the synthesis of II-VI semiconductor nanoparticles has confirmed the potential of thermal decomposition to prepare high quality metal oxide nanocrystals. Hence single-source precursors have been used to obtain ZnO nanocrystals. Shim *et al* have reported ZnO nanocrystals capped with trioctylphosphine oxide and alkylamines by decomposing diethylzinc.[60] More recently this method was simplified by using less hazardous and more common precursors, such as $Zn(CH_3CO_2)_2$.[61]

Andelman *et al*. have employed $Zn(CH_3CO_2)_2$ as the precursor in a variety of solvents, such as oleic acid (OA), trioctylamine (TOA), 1-hexadecanol (HD) and 1-octadecene (OD).[62] In a standard synthesis, the precursor and capping agent were mixed in a 1 : 1 ratio in the solvent of choice TOA, HD or OD. It was found that TOA yielded nanorods (Fig. 7a), HD yielded nanotriangles (Fig. 7b), and OD yielded spherical nanoparticles (Fig. 7c). This is an illustrative example of the influence of the capping agent in defining particle morphology as consequence of selective ligand stabilization of certain crystallographic planes.[62,63] For example, a common synthetic method for nanorod formation is the use of distinct capping ligands that selectively bind to different planes, thus creating a difference in surface energies between planes and encouraging growth along one specific direction.[63] By using different capping agents there is the ability to stabilize different crystallographic planes, thus leading to different shaped particles. Hence, Andelman and coworkers have observed that for ZnO synthesis, the use of TOA originated rod growth but spherical particles when the solvent was switched from TOA to OD, a non-coordinating solvent, because in the

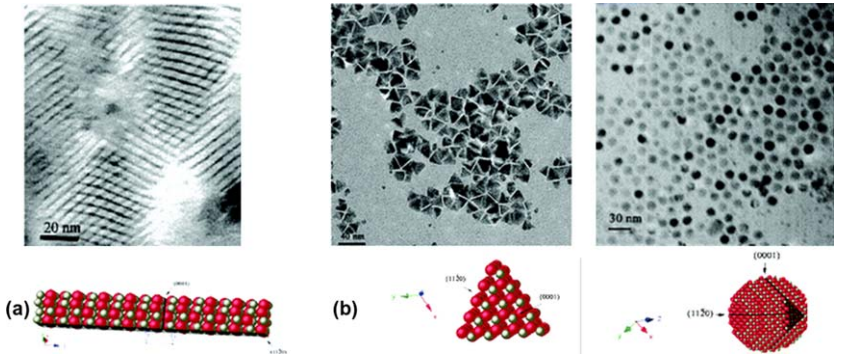

Fig. 7 TEM images of ZnO nanocrystals with a corresponding representative model (a) nanorods (b) nanotriangles (triangular prisms), and (c) spherical nanoparticles. Reprinted with permission from Ref. 62. Copyright 2005 American Chemical Society.

latter no specific crystallographic planes have been capped. The formation of nanotriangles when using HD as a solvent, is possible due to its moderate coordinating capacity. It should be noted that the nanocrystals' surfaces maintain the organic capping and as such are easily dispersed in hydrocarbon solvents, with predisposition to self-assemble upon solvent evaporation onto substrates.

The role of the capping agent (*e.g.* trioctylphosphine oxide – TOPO) in directing the growth of ZnO nanocrystals into different morphologies have been investigated.[64] The relative amount of TOPO at the particles' surface depends on the reaction temperature with consequence in the growth of ZnO nucleus in different directions of the crystallographic plane. Preferred growth orientation along the *c*-axis in ZnO anisotropic nanostructures has been recognized by powder XRD patterns in which the (101) peak intensity tends to increase. [62–64] According to Shahroosvand and Ghorbani-asl, the synthesis of ZnO nanocrystals in the presence of TOPO follows the steps indicated in Fig. 8.[64] Firstly, surface defects at the ZnO surface (Zn or O vacancies) are capped by TOPO molecules. An increase of the thermal decomposition temperature results into loss of TOPO molecules from the ZnO surface. Secondly, ZnO nanocrystals with partial coverage by TOPO eventually aggregate due to the interaction of TOPO in different crystallographic orientations. Nevertheless, two contiguous capped ZnO particles may happen to be crystallographically oriented with respect to each other; in which case, they might combine to form a single particle that is randomly oriented with respect to its neighbors. In this case, the particles grow on the surface of two connecting particles that might result in the formation of different ZnO morphologies, such as tetrapods. Finally, during the fusion of

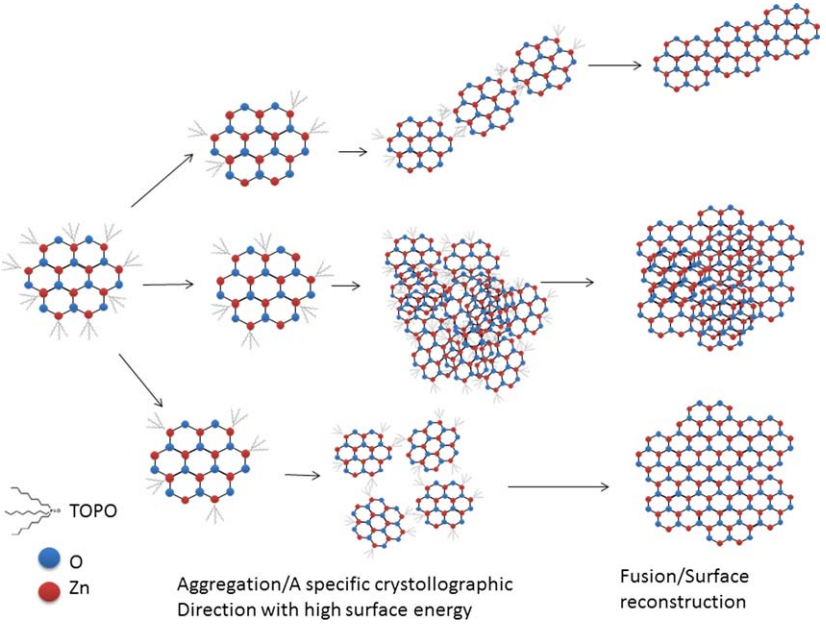

Fig. 8 Scheme of mechanism for ZnO nanoparticles growth. Adapted from Ref. 64.

the smaller particles and the growth of larger particles, larger ZnO nanoparticles with different morphologies have been obtained (Ostwald ripening).

3.3 Solvothermal routes

An alternative approach to the synthesis of nanosized ZnO by employing high-boiling temperature solvents has been the use of common solvents that although limited by lower boiling points, at normal pressure, can be heated in a sealed vessel such as an autoclave. This solvothermal route has been extensively used in the preparation of a number of conventional inorganic solids.[65] In recent times, solvothermal techniques have become progressively more frequent for the synthesis of semiconductor nanoparticles. For chalcogenide nanoparticles, two main routes can be identified; one uses as starting sources the elemental forms of the semiconductor compound and the other route uses a metal salt as precursor reagent. In a typical synthesis, powders of the metal and chalcogenide may be ground together, inserted into an autoclave filled with the solvent up to 70% of the capacity, and then heated at a constant temperature for a period of time. Similarly, this procedure can be applied by using a metal salt or precursor depending on the compound envisaged for the synthesis. Thus for ZnO the second approach has been used and it has been reported that the size and morphology of ZnO particles are altered depending on the solvent, precursor, reaction time and temperature and solution basicity.[39] Some examples of precursors may be simple zinc(II) salts, such as zinc acetate, zinc nitrate or zinc chloride.

Zhang and coworkers[39] have synthesized a diversity of well-defined morphologies such as flower-, snowflake-, prism-, prickly sphere-, and rod like samples. The polarity and saturated vapour pressure of the solvent play an important role in defining the morphology of ZnO nanocrystals. The reasons for the precursors affecting the morphology of ZnO can be attributed to different reaction path and distinguished basicities of the reacting solutions, which may influence the crystal nucleation and growth processes. In addition, the size and morphological development of ZnO is also dependent on the reaction temperature and time. Rezapoura and Talebianb have used a solvothermal synthesis to prepare ZnO in different solvents. The solvents include ethanol, ethyleneglycol, 1,4-butanediol and polyethylene glycol 600 (PEG 600) with varying viscosities, polarities and vapor pressures, that allowed the study of effects coming from solid interface-solvent interactions.[66] The result was alterations in morphologies in which the particles showed different crystal growth habits including well-faceted, smooth-plane hexagonal (ethanol), spherical (ethylene glycol), agglomerated particles (PEG 600) and nearly hexagonal rods (1,4-butanediol), as depicted in Fig. 9. The authors maintained external factors such as the zinc source, precursor concentration, pH and reaction conditions, and varied just the solvent used in the synthesis. Hence, the differences in the morphologies of the various synthesized ZnO nanostructures have been attributed to the effect of the different solvents.

Mou and coworkers prepared ZnO nanobullets and nanoflakes by using a mixture of water/ethylene glycol as the solvent, and $Zn(CH_3CO_2)_2$ as the Zn source, in closed vessel at 130 °C or 150 °C. These nanostructures were used

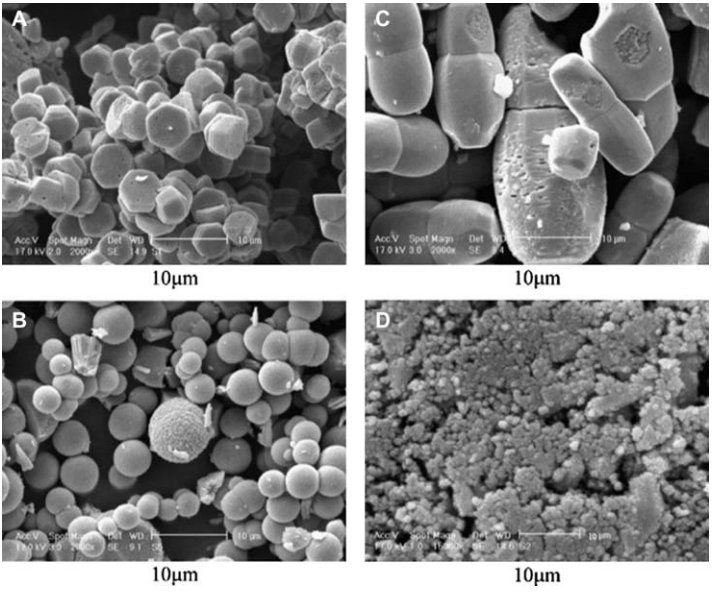

Fig. 9 SEM images of ZnO by a solvothermal route using (A) ethanol, (B) ethylene glycol, (C) 1,4-butanediol and (D) PEG 600 as solvent. Reprinted from Ref. 66. Copyright 2011, with permission from Elsevier.

as active photoanodes in a dye-sensitized solar cell system, and achieved an overall light-to-energy conversion efficiency of 1.93% and 3.64%, respectively.[67] Wang *et al.*,[68] have used ethylene glycol as the solvent and a similar method to prepare ZnO porous nanoplates, whose high specific surface area was demonstrated as valuable for strong and selective adsorption of cationic species. This work not only demonstrated the prospect of using this material as promising adsorbents for contaminant-removal and environmental remediation, but also gives insight into understanding the adsorption behaviour of porous ZnO materials.

Wang *et al.* have prepared a Zn^{II} coordination polymer employing a mixed-ligand tuned solvothermal route. Calcination of the coordination polymer originated octahedral superstructures constructed by ZnO nanoparticles with a mean diameter of 50 nm. Reaction conditions, such as temperature, reaction time, and reagent dosage, significantly affected the final morphology of the nanostructures.[69] This work is an example of a wide field still to be fully explored, in which metal coordination polymers can be regarded as precursors for chemically more simple nanostructures though with complex morphologies.

3.4 Growth in confined spaces

There are various methods for the chemical synthesis of nanocrystals in arrested particle growth conditions. The nanocrystals' colloidal stability against agglomeration can be accomplished using protective agents, either with mobile interfaces (*e.g.* surfactants, polymers) or using more rigid structures (*e.g.* zeolites, mesoporous materials). For example, surfactants may be used as capping agents for nanocrystals formed within reverse micelles (water-in-oil microemulsions).[70–72] In this case, water-in-oil

microemulsions or reverse micelles have been used as nanoreactors for the formation of nanoparticles of uniform size, through the necessary chemical reactions, in which nucleation and growth occur within the water droplets medium. The surfactant layer acts as steric stabilizer to inhibit the aggregation of the nanoparticles formed. Sarkar and co-workers have reported the direct synthesis of ZnO (*wurtzite*) nanoparticles bearing different morphologies *via* alkaline hydrolysis of $Zn(NO_3)_2$ by judicious control of the reactant concentrations in water-in-oil microemulsions of Triton X-100/hexanol/cyclohexane. Spherical nanoparticles were formed using a weak base, whereas reaction using strong bases forms nanorods at lower reactant concentration and larger rectangular nanoparticles at higher concentration.[73] Inoguchi and coworkers have prepared monodispersed and spherically shaped ZnO NPs with a diameter of less than 5 nm. These NPs were synthesized at room temperature by hydrolysis reaction of zinc diethoxide in reverse micelles.[71] Mao *et al.* have prepared ZnO nanostructures with controllable morphology by hot mixing of reverse micelles containing $Zn(NO_3)_2$ and monoethanolamine aqueous solutions (Fig. 10). It was found that the ratio of water-to-surfactant concentration played an important role in determining the final morphology, namely, nanotetrahedrons formed at lower concentrations and nanorods formed at a higher value. Homogeneous sized and morphological well-defined ZnO nanostructures exhibiting strong fluorescence emission have been reported; nanotetrahedrons exhibit a blue emission arising from interface states and a green emission related to donor defects was observed for the nanorods.[74]

Lizandara-Pueyo *et al.* have used a versatile method for the preparation of colloidal ZnO anisotropic nanoparticles.[75] This method combines the benefits of a water-in-oil emulsion with an organometallic precursor system for ZnO. The ZnO particles have a prismatic morphology and the authors have managed to control their aspect ratio. The reaction of the tetrameric precursor with heterocubane structure, methyl-zincalkoxide $[MeZnOR]_4$ (R = isopropyl, t-butyl, EtOMe, *etc.*), at the interface of a water-in-oil emulsion enabled the synthesis of prismatic ZnO nanocrystallites. The advantage of this precursor is that can be applied for the synthesis of zinc oxide in almost any aprotic organic solvent due to its good solubility. The precursor was dissolved in the organic phase of the emulsion. Over time, the precursor diffuses into the oil–water interface and reacts with water forming ZnO (Fig. 11).

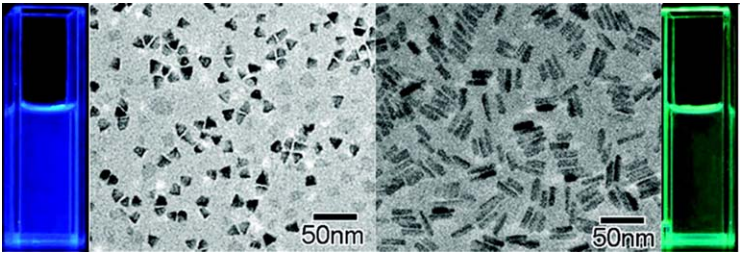

Fig. 10 TEM images and direct photographs of the ZnO tetrahedron (left, blue online) and ZnO nanorods (right, green online) under the irradiation of a 365 nm UV lamp. Reprinted with permission from Ref. 74. Copyright 2010 American Chemical Society.

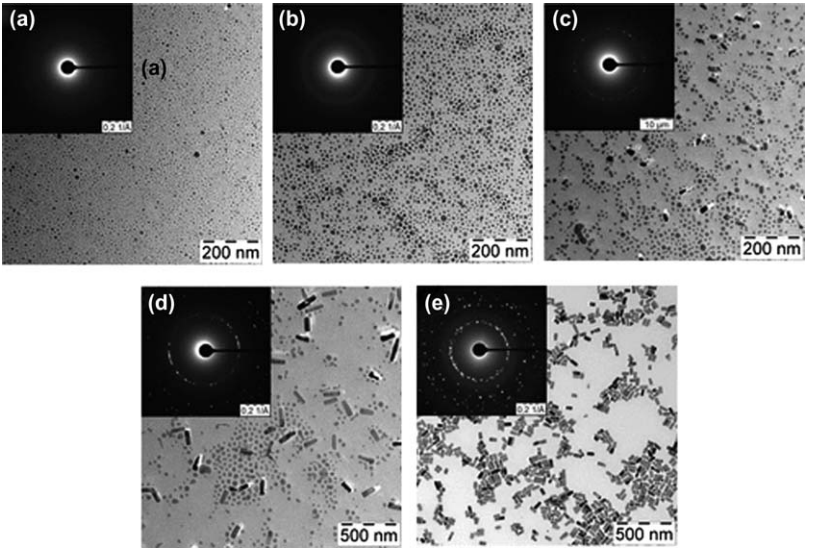

Fig. 11 TEM and electron diffraction of ZnO at different times after addition of the precursor: a) t = 15 min, b) t = 30 min, c) t = 75 min, d) t = 115 min, and e) t = 10 h. Reprinted with permission of John Wiley and Sons from Ref. 75. Copyright 2011.

Other syntheses in structured media have been reported. Thus Zhang *et al.*[76] have reported the synthesis of ZnO nanocrystals by using mesoporous silica MCM-41 as host material. This method involved a pre-functionalization step of MCM-41 mesoporous silica with ethylenediamine (ED-MCM-41), and then its use as sorbent for Zn^{2+} (Zn-ED-MCM-41). The ZnO nanocrystals were obtained after calcination in air of the Zn-ED-MCM-41 precursor. The ZnO particles were predominantly confined in the pores of MCM-41 and size quantization effects were observed.[77] The predominance of ZnO within the pores of the mesoporous matrix is consequence of extensive functionalization in the internal surfaces of MCM-41. Other similar approaches have been reported.[77–79] Mihai and coworkers have prepared ZnO nanoparticles supported on MCM-41 and SBA-15. The influence of nanoparticle loading onto the mesoporous material was studied and the photocatalytic activity toward degradation of methylene blue in water under ultraviolet irradiation was investigated. Also, a small influence on the porosity of SBA-15 as compared to MCM-41 was observed by impregnation of the hosts with ethanolic zinc salt solution.[77] Cheng *et al*. have incorporated ZnO into ZSM-5 using a wet impregnation method (Fig. 12).[78] The authors have reported that the mesopores can load more than 15% of 20 nm-sized ZnO, which can only reduce the mesopore surface area and volume, whereas micropores remained and cannot be blocked by loading ZnO particles.

Luo *et al*. have reported the synthesis of mesoporous ZnO nanowires prepared in the presence of surfactants confined in porous membranes, *via* a sol-gel or electrodeposition approach.[80] More specifically, the overall diameter of nanowires was defined by the cylindrical AAO pore channels. Surfactant nanoconfined in AAO was used to generate mesoporosity and to

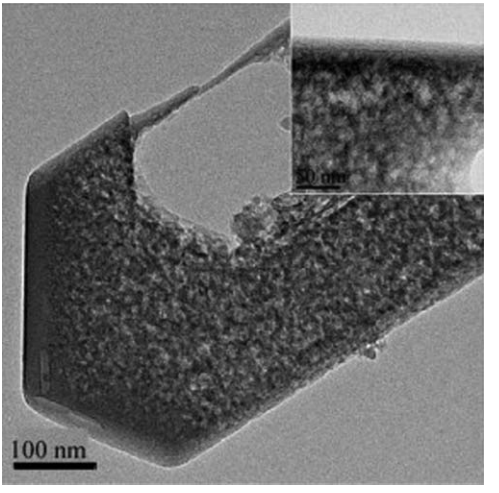

Fig. 12 TEM image of zeolite/ZnO nanohybrid showing the interior of the zeolite crystal. The dark spots are attributed to the incorporated ZnO NPs with 10–20 nm size range. Reprinted from 78, Copyright 2012, with permission from Elsevier.

control the texture of nanowires. Baber *et al*. have prepared mesoporous ZnO nanowires from the self-assembly of SDS confined within cylindrical pore channels *via* electrodeposition.[81]

Nanostructures can be also grown in confined spaces templated by polymers[82] and dendrons.[83] Braun *et al*. have used block copolymer micelles for stabilizing and structuring ZnO nanoparticles. Preformed particles could be selectively incorporated in poly(2-vinylpyridine) (P2VP) of polystyrene-block-poly(vinylpyridine) micelles and deposited as monolayer thin films on various substrates. The authors managed to synthesize the ZnO nanoparticles directly inside the P2VP phase using an organometallic precursor, being the first demonstration of such small (2–4 nm) NP synthesis showing a quantum-size effect *via* block copolymer stabilization using a one pot method.[82] Gnichwitz and coworkers made advances in the formation of advanced inorganic nanostructures *via* stable attachment of cationic monolayers onto ZnO nanoparticles originating solid-state mesoporous ZnO. The key for this approach was the synthesis of a dendron structure with cationic functionality, as well as a catechol anchoring group, which forms strong covalent bonds to ZnO nanostructures. In this case the catechol molecules were attached to the surface, and a chemical post-treatment was not necessary to achieve high homogeneity of the mono molecular surface layer. Changes in the colloidal stability of ZnO nanoparticles grafted with cationic dendric molecules were observed and directly linked to the size and charge of the attached molecules, leading to greatly enhanced stability of the ZnO quantum dots.[83]

3.5 Growth of nanorod arrays in aqueous solution

Highly oriented nanorod arrays of ZnO are emerging nanostructures for the production of novel devices. Tak and Yong[84] have developed an ammonia aqueous solution method for growing well-aligned ZnO nanorod arrays on

a silicon substrate. For ZnO nanorod growth, a thin zinc metal seed layer was deposited on a silicon substrate by thermal evaporation. Uniform ZnO nanorods were grown on the zinc-coated silicon substrate in aqueous solution containing zinc nitrate and ammonia water. The growth temperature was as low as 60–90 °C. A high density of ZnO nanorods grew vertically on the substrate. The diameter and length of nanorods were dependent on growth parameters such as Zn^{II} salt concentration, growth temperature, pH and zinc seed layer morphology. The initial zinc seed layer plays a crucial role for well-aligned ZnO nanorod growth. The ZnO nanorod's length was controlled by the number of repetitive reactions employed. The average diameter and length of the nanorods discretely increased by $\sim$15 nm and $\sim$1 μm, respectively, for each repeat reaction. Suresh *et al.*[85] have reported a simple hydrothermal approach that involved the *in situ* introduction of a polyelectrolyte. A protonated polyelectrolyte such as polyethylenimine added to the aqueous growth medium, resulted in that part of the positively charged species binding themselves around the lateral facets of the ZnO nanorods. This offers possibility to control the lateral dimensions of the ZnO nanorods quenching defect levels and with enhancement of the UV band edge emission. Vertically aligned single crystalline ZnO nanorod arrays were grown by a simple one-step solution-based approach on a Zn foil substrate (Fig. 13).[86] The ZnO nanorod synthetic approach is improved by employing pure water without the use of additives such as previously used ammonia or hydrogen peroxide. This approach relies on the fact that water has the ability to oxidize Zn, in the presence of oxygen, to form ZnO nanorods.

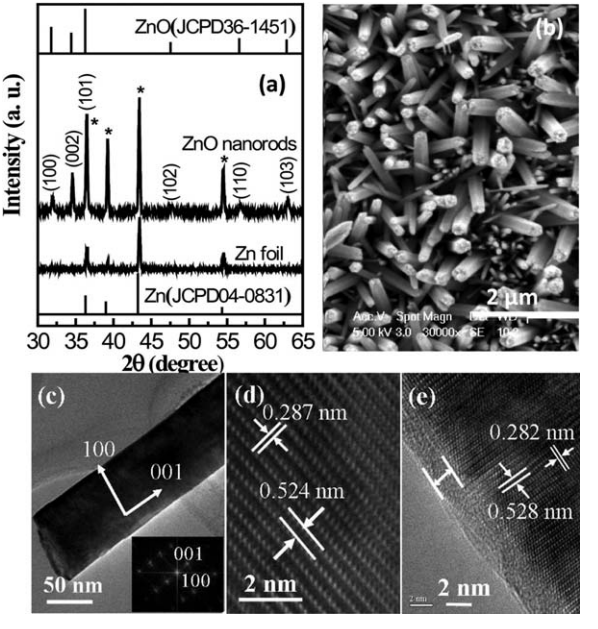

Fig. 13 Structural and morphological characterization of ZnO nanorods by a)XRD, b) SEM, c) TEM. Inset-electron diffraction, d) and e) HRTEM.[86]

Wang and coworkers have developed an hydrothermal method for the synthesis of well-defined ZnO nanostructured films prepared directly on Zn foil.[87] Thus the Zn foil acted simultaneously as the Zn source and also as the growth substrate. Porous ZnO films based on nanosheets, nanotubes and nanoflowers have been prepared by adjusting the alkali type, reaction time and temperature. The high ratio of exposed *c*-axis [001] facet in the ZnO film plays an important role in enhancing the photocatalytic activity of ZnO. In addition, the hierarchically self-assembled porous nanosheet ZnO film has a large specific surface area, leading to the increased contact area of ZnO with rhodamine B and UV light adsorption.

4 Chemistry on the surface of ZnO nanocrystals

An important aspect on the science of nanocrystals is the development of a surface chemistry that allows their interaction with specific surroundings. This is a field of research that merges chemical knowledge traditionally found in distinct specialities such as coordination chemistry, solid state chemistry and organic chemistry. For example an active area of research has been the functionalization of nanocrystals with biomolecules without changing their optical properties and morphological characteristics. Thus biological molecules have been immobilized on coatings made of polymer matrices and inorganic supports by a variety of techniques.[88–90] A number of these immobilization techniques have been previously developed for the functionalization of macro-sized supports, but more recently have been applied to bring together biomolecules and nanoparticles.[91–93]

Many research groups have explored the emitting properties of nanocomposites made by dispersing quantum-sized particles into a polymeric matrix.[94–97] The hybrid nanocomposites not only inherit the high luminescence of the quantum dots but also possess the advantages recognized in polymers such as flexibility, film integrity, and conformity. The control of particle size, size distribution and dispersion homogeneity over the entire matrix is the critical prerequisite to assure the optical and electrical properties of the composites for nanodevice applications. In a number of situations the chemistry of the particles surfaces' has been adjusted to the polymer characteristics. Thus to hybridize inherently hydrophilic inorganic nanocrystals into a polymer matrix *via* bulk polymerization of an hydrophobic monomer, the nanocrystals can be first submitted to surface modification. A common method makes use of appropriate capping agents such as long chain aliphatic thiols, amines or trioctylphosphine oxide (TOPO), which have the ability to coordinate to the solid surfaces leaving hydrophobic chains outwards and thus enhancing the compatibility of the inorganic nanocrystals with the organic matrix. On the other hand, and as described before, organically passivated nanocrystals can be obtained by straightforward synthetic methods.

Methods for the surface modification of ZnO nanocrystals have been developed in which special care is required to avoid changes on particle size and hence on the size dependent optical properties. A few essential rules can be collected from the application of these surface modification methods. It is important to avoid excessively high temperatures because particle sintering

can occur with detrimental consequences on the size dependent ZnO properties. The capping should be selected in order to prevent further growth of a selected particle size distribution and to provide stability through the coordinative saturation of dangling bonds on the particle surface.

Although the size of nanoparticles can be manipulated by capping agents, the nanoparticles under ambient conditions still gradually and irreversibly aggregate, namely during solvent evaporation. More importantly, the aggregated nanoparticles cause serious drawbacks in the photoluminescence, in terms of wavelength shift and intensity decay.[51] Surface modification is an interesting technique to control the size of the ZnO nanoparticles and is also believed to be an efficient approach to adjust the luminescent colour and uniformity of nanocomposites for novel electro-optical applications and also for biomedical applications.

Surface modification of nanosized ZnO allows further functionalities and ZnO coupled with others types of materials have been explored, such as in the form of metal/ZnO,[98–102] carbon-based material/ZnO[103–109] or polymer-based materials/ZnO nanocomposites.[110–113] The preparation of metal/ZnO nanocomposites may have a widespread range in applications, such as the enhancement of gas sensing properties,[114] photocatalytic and photoelectrochemical applications[102] or as an antimicrobial agent in packaging.[98] Another example is its use as a cholesterol biosensor described by Wang *et al*.[101] The authors created a novel scheme for the fabrication of Pt-Au functionalized ZnO nanorods (Pt–Au@ZnO NRs) and multi-walled carbon nanotubes (MWCNTs) modified electrodes and subsequently develop these hybrid structures for cholesterol biosensing. The ZnO nanorods decorated with Pt-Au were prepared by a chemical synthesis method. A suspension of the nanocomposites was deposited onto the MWCNTs modified glass carbon electrode, and followed with cholesterol oxidase (ChOx) immobilization. The combination of MWCNTs and Pt–Au@ZnO NRs provided a favorable environment for cholesterol oxidase and resulted in an enhanced analytical response of the biosensor. Alternatively, low density polyethylene film nanocomposites containing both Ag and ZnO nanoparticles were synthesized and used in the preparation of packages filled with orange juice and stored at 4 °C.[98] The microbial stability of the juice was evaluated and showed a significant reduction of the growth rate of *L. plantarum* when using the nanocomposite packaging material. Carbon based materials are an important subject in materials science. The conjugation of carbon-based materials with other materials, such as semiconductors or, more specifically, ZnO nanostructures can open new avenues to a widespread of applications.[103–109] These nanocomposites can range from vertically aligned ZnO nanorod/graphene hybrid architectures for gas sensors[103] to high performance photocatalysts[104] or as emissive ZnO-graphene quantum dots for white-light-emitting diodes.[105] The production of polymer nanocomposites is of great industrial importance as these multi-phase systems consume a large percentage of plastics production. As many other ZnO-based materials, polymer/ZnO nanocomposites have applications as bulk heterojunction photovoltaic devices.[112] In this particular case the authors based their studies on blends of a conjugated

polymer poly[2-methoxy-5-(3′,7′-dimethyloctyloxy)-1,4-phenylenevinylene] as electron donors and ZnO nanocrystals as electron acceptors. The authors provide a deeper understanding of the photovoltaic properties of these composite blends and demonstrate that reasonably efficient photovoltaic devices can be obtained with different size and morphology ZnO nanoparticles. Devi and coworkers devised an amperometric xanthine biosensor based on polypyrrole/ZnO nanoparticles composite film[111] and Olad and Nosrati prepared a nanostructured PVC/ZnO–polyaniline hybrid coating with enhanced corrosion resistance.[115]

Biofunctionalization is important, and very much used, surface modification procedure. Long term stability and ability for molecular recognition is a feature necessary for using nanostructures as active components in biosensing devices and as bioimaging probes.[116,117] Numerous functionalization approaches for nanocrystalline ZnO specifically focusing on luminescence properties can be explored for example by using different capping agents.[118–120] Cao *et al.* have probed the morphology effect of nanostructured ZnO films on a stepwise surface functionalization methodology that allowed them to hybridize DNA selectively on the films.[121] The authors tested three morphologies of ZnO nanorod film with comparable thickness: nanorods, rough surfaces and planar films. Selegård and coworkers have prepared biotinylated ZnO by a surface modification process that involved the coupling of silanes and biotin to both the ZnO nanoparticles and ZnO thin films.[122] This two-step functionalization approach was developed by the authors as having potential for specific targeting in bioimaging probes and for recognition studies in biosensing applications.

5 Doping of ZnO quantum dots with metal ions

The modification of the electronic and optical properties of semiconductors by intentional inclusion of dopants into nanosized host lattices has been a great endeavour pursued by several researchers. While doping in bulk semiconductors form the basis of a number of products coming from current semiconductor technology, the doping of semiconductor nanocrystals has revealed a great challenge in nanoparticle science. The small dimensions of colloidal quantum dots guide the way to new difficulties not stumbled upon in bulk materials. A practical challenge in the synthesis of doped quantum dots is the effective inclusion of the dopant in the crystalline lattice. Prior investigational studies have verified the predisposition for dopant ions to not be included in the nanocrystals during synthesis.[123] The dopant may be likely to diffuse to the surface or into the solution due to thermodynamic driving forces because the dopant is only a few lattice constants from the particles' surface.[123,124] A closely related challenge is that of determining experimentally the exact environment of the dopants in the quantum dots. Some research has focused on specifically looking at the doping of II–VI semiconductor nanocrystals with transition metals [125–128] and rare-earth elements.[129–131] In general, these dopants influence the quantum dots not by introducing extra carriers, but rather by providing an impurity core that can interact with the quantum-confined electron-hole pair. Consequently, these dopants do not affect the absorption spectrum,

but sturdily alter the luminescence properties. Additionally, since these dopants can be paramagnetic, they may also introduce a localized spin into the nanoparticle. Nonetheless, introducing the dopant in the core (*i.e.*, not at the surface or interface) of the nanoparticle without compromising their quality (*i.e.*, high crystallinity, well-controlled size, and a small size dispersion nanoparticles) still remains the main challenge.

Transition d-metal ions or lanthanide-doped ZnO has been used as an effective phosphor material.[125,126,130–133] Pure ZnO exhibits green emission when excited in the UV wavelength range. This emission has been assigned to oxygen vacancies or to interstitial zinc in excess, leading to intra gap electronic levels.[134]

A strategy for the preparation of doped colloidal ZnO nanocrystals uses solutions of zinc salts in which dopant ions have been added. The impurities introduced into nanosized ZnO alter the local structure and cause a remarkable change of its properties due to quantum confinement effects (Fig. 14). Radovanovic *et al.* have reported the preparation of colloidal transition metal doped ZnO quantum dots.[133] This method yielded highly crystalline and relatively monodispersed doped ZnO nanocrystals with a variety of colours (Fig. 14). Ligand-field electronic absorption spectroscopy was used as a dopant-specific optical probe to monitor incorporation during nanocrystal growth and to verify internal substitutional doping in ZnO:Co and ZnO:Ni QDs.[132] Pereira, Ankiewicz and coworkers used electron paramagnetic resonance spectroscopy (EPR) to probe the localization of the transition metal dopant in ZnO:Co and ZnO:Mn QDs.[125,126]

A similar method was used for doping ZnO nanocrystals with lanthanide ions, such as Tb^{3+} or Eu^{3+}.[129–131, 133] Pereira *et al.* have prepared Tb^{III} doped ZnO QDs showing the characteristic emission lines of Tb^{III}. These authors have employed a chemical surface modification of the doped ZnO nanocrystals using TOPSe to produce ZnSe shells, that along with photoluminescence studies, allowed to conclude the localization of the dopant cations to be inside the ZnO core.[131]

Other methods for preparing doped ZnO quantum dots are based on solid state reactions,[135] chemical vapour deposition[136] and solvothermal routes.[127] The sol-gel method[137,138] as proposed by Spanhel and Anderson has been frequently used.[51] In this approach an ethanolic medium has been used to promote the dehydration of $Zn(OH)_2$, which is formed when Zn^{2+} ions are precipitated by OH^- ions, leading to nanosized ZnO. Radovanovic

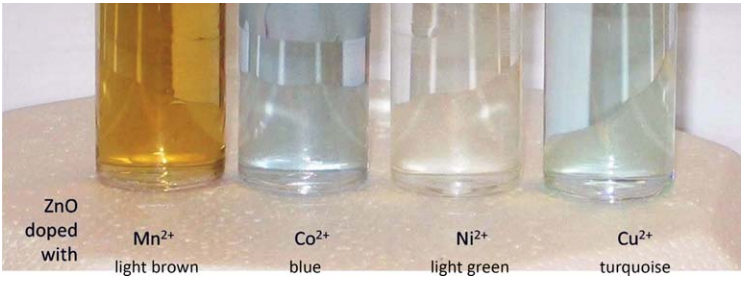

Fig. 14 Photograph of transition metal doped ZnO quantum dots in colloidal samples.

et al. have reported the hydrolysis of $Zn(CH_3CO_2)_2$ in the presence of d-metal ions following modifications of techniques known to yield highly crystalline and relatively monodispersed nanocrystals of pure ZnO.[133] The above chemical methods generally result in spheroidal doped ZnO nanoparticles.[57,125,131,139] Other particle morphologies are also known, such as nanoflowers,[140] nanotetrapods[141] and nanowires.[127,128] For example, Wu and coworkers were able to prepare Cr-doped ZnO nanowires using a solvothermal method.[127] Cr-doped ZnO had optical capability in the whole range of visible light spectrum and can greatly enhance the photocatalytic efficiency of ZnO. While still in early application developments, there is interest to control doping levels in ZnO to nanoengineer materials for targeted applications, UV LEDs,[142] laser diodes,[143] photodetectors,[144] and conductive materials.[145]

6 Technological applications of ZnO nanocrystals

Nanotechnology is a suite of techniques used to manipulate matter at the nanoscale and down to the atomic and molecular level. A possible way to understand the potential of this technology when using nanosized solids is that at this scale the material's properties change dramatically and scale with size. In fact, by reduction in particle size without change in substance, new properties can emerge in terms of electrical conductivity, elasticity, mechanical strength, optical features and chemical reactivity. An illustrative example is the change on the opacity of conventional ZnO pigments (*Chinese White*) formed by sub-micrometric particles but that as nanosized powders can be used as transparent pigments in sunscreens. Nanoscale technologies are poised to become a strategic platform with global implications in manufacturing, food, agriculture and health in the immediate years ahead.

ZnO has a long history of usage for pigments and protective coatings on metals.[146–148] The electrical, optoelectronic and photochemical properties of ZnO has resulted in its use for solar cells, transparent electrodes and blue/UV light emitting devices. ZnO-based semiconductor and nanowire devices are also promising for the integration on a single chip. So far, the various applications of ZnO nanomaterials such as biosensors and UV detectors are under way.[101,111,142,149,150] Nanobelts and relevant nanostructures are a unique group that is likely to have important applications in nanoelectronics. Piezoelectric ZnO based nanobelts and nanorings for applications such as sensors, transducers and actuators in micro- and nanoelectromechanical systems have been developed by Kong *et al.*[151] Owing to the positive and negative ionic charges on the zinc- and oxygen-terminated ZnO basal planes, respectively, a spontaneous polarization normal to the nanobelt surface is induced. Researchers have made single-crystal ZnO nanobelts that spontaneously rolled into helical structures. The nanohelixes or nanosprings have piezoelectric properties and show great promise for biomedical applications and in microsystems. Piezoelectric semiconductors are natural resonators and therefore do not need all the conventional circuitry for signal and emission processing. Physical stimulation causes piezoelectric materials to naturally oscillate at a known frequency. It might

therefore be possible to treat the material to attract a protein from a cancer cell and then even a single molecule of that protein could be detected with just one nanospring.

The medical area of nanoscience application is potentially most valuable, with many projected benefits to humanity. For example, cells themselves are very complex and can be regarded as composed of efficient nanomachines. Some areas of nanoscience aim to learn from biological nanosystems, while others are focusing on the integration of organic and inorganic objects at the nanoscale. The huge surface area on nanoparticles systems present diverse opportunities to place functional groups at the surface. Particles can be created that can expand/contract with changes in pH,[152] or interact with anti-bodies in special ways to provide rapid *ex vivo* medical diagnostic tests.[153,154] Muhammad and coworkers have developed a pH-sensitive drug delivery system that minimizes drug toxicity by preparing acid-decomposable, luminescent ZnO QDs which are used to seal the nanopores of mesoporous silica nanoparticles in order to inhibit premature drug release.[152] After cell internalization, the ZnO QDs are rapidly dissolved in the acidic intracellular compartments, and the loaded drug is released from the silica NPs. The authors believe that in this case, ZnO QDs have a dual-purpose by not only acting as a lid but also as a synergistic antitumor agent. Developments in both genomics and nanotechnology are likely to enable sensors that can determine genetic make-up quickly and precisely, enhancing knowledge of people's predisposition to genetic diseases. The second area is drug delivery, which is likely to benefit from the development of nanotechnology.[152,155,156] For example, drugs may be contained within a molecular carrier, either to protect them from stomach acids or to control the release of the drug to a specific targeted area, reducing potential side effects. The ultimate combination of advanced drug delivery technologies would be a device that once implanted in the body will monitor continuously the level of various biochemicals in the bloodstream and will release the required drug. For example, an insulin-dependent diabetic could use such a device to continuously monitor and adjust insulin levels autonomously. There is no doubt that this is a direction that current advances in which microfluidics and drug delivery are heading.

Nanosized ZnO has been used in sunscreens,[157] such as in sunscreen lotions that screen both UVB (290–320 nm) and UVA (320–400 nm) sunlight radiation and as high sun protection factor makers. New sunscreen formulations based on nanoparticles of ZnO are smooth and clear without unpleasant residues. The small particle size enables highly transparent, UV blocking coating systems. These applications have been involved in some controversy due to limited knowledge about the toxicity of these nanoparticles in a variety of contexts.[158,159]

Dye photodegradation is an application for many morphologies of ZnO nanostructures, ranging from particles[160] to sheets[161] and rods.[162,163] Becker revealed the influence of individual effect of particle size on the photocatalytic activity of ZnO, when maintaining morphology and crystallinity. Smaller particle size ZnO and crystallinity (when preparing ZnO with the same solvent) showed improved photocatalytic activity.[160] Lai took advantage hollow 3D structures and, consequently higher surface area of

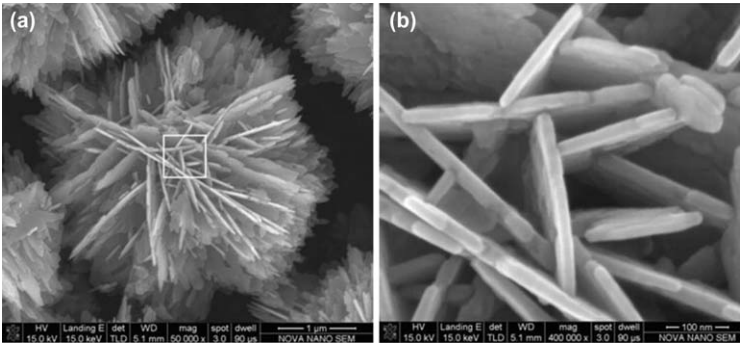

Fig. 15 (a) low- and (b) high-magnification image of the fluffy ZnO sphere. Reprinted from Ref. 161. Copyright 2010, with permission from Elsevier.

''fluffy'' ZnO nanosheets (Fig. 15) to increase the photodegradation of rhodamine B, when compared to other morphologies. The active sites exposed during the reaction, facilitated the migration of reactants and products and increased the photoreaction rate.[161]

Pencil-like ZnO microrods were prepared by Liu *et al*. in the presence of aqueous ethylenediamine/ethanolamine[162] and showed high photocatalytic activity for the degradation of methylene blue. The authors have proposed a single-nucleus growth process for the formation mechanism of the pencil-like ZnO when using those solvents. Tang and coworkers also grew ZnO microrods on a Si substrate using mild hydrothermal conditions and aqueous solutions of methenamine. The morphology and size was controlled by alteration of the reaction conditions, such as temperature, concentration, and ionic strength, ranging from nanoparticles to nanorods and consequently microrods.

A series of binary semiconducting oxide nanobelts (or nanoribbons), such as ZnO, Ga_2O_3, CdO and PbO_2 have been successfully synthesized[164] by evaporation of the source compounds. Pure, structurally uniform and single crystalline ZnO nanobelts were obtained free from defects, with a rectangular-like cross-section with typical widths of 30–300 nm. The belt-like morphology appears to be a unique and common structural characteristic for the family of semiconducting oxides with cations of different valence states and materials of distinct crystallographic structures. The nanobelts are an ideal system for fully understanding dimensionally confined transport phenomena in functional oxides and building functional devices along individual nanobelts. Arnold *et al*. have applied nanobelt materials to make a field effect transistor and single wire sensors.[165] The above examples unambiguously demonstrate that nanosized ZnO has a diversity of properties that are size and shape dependent with great implications in emerging technologies.

7 Conclusions

In closing, the preceding review has shown recent advances on fundamental studies and applications of nanosized ZnO prepared by chemical routes. Although this material may be considered to be ''old'' due to the vast

literature available, it has emerged in the last decades as subject of renewed interest mainly due to its relevance in nanoscience and nanotechnology. Many current challenges found in nanoscience can be approached by using this semiconductor in a myriad of particle morphologies and on the basis of established knowledge for quantum-sized matter. Indeed, ZnO can be synthesized in a variety of nanoscopic systems exhibiting properties scalable with size and dependent on shape and surface characteristics. In this context, recent advances on the synthesis of ZnO nanostructures have shown the role of chemistry in opening new avenues for applications of this material in future technologies.

References

1 M. Sofos, J. Goldberger, D. A. Stone, J. E. Allen, Q. Ma, D. J. Herman, W. W. Tsai, L. J. Lauhon and S. I. Stupp, *Nat. Mater.*, 2009, **8**, 68–75.
2 C. R. Gorla, N. W. Emanetoglu, S. Liang, W. E. Mayo, Y. Lu, M. Wraback and H. Shen, *J. Appl Phys.*, 1999, **85**, 2595–2602.
3 W. I. Park and G. C. Yi, *Adv. Mater.*, 2004, **16**, 87–90.
4 Y. Yang, Y.-Q. Li, S.-Y. Fu and H.-M. Xiao, *J. Phys. Chem. C*, 2008, **112**, 10553–10558.
5 H. Kind, H. Yan, B. Messer, M. Law and P. Yang, *Adv. Mater.*, 2002, **14**, 158–160.
6 V. Noack, H. Weller and A. Eychmüller, *J. Phys. Chem. B*, 2002, **106**, 8514–8523.
7 J. A. Rodriguez, T. Jirsak, J. Dvorak, S. Sambasivan and D. Fischer, *J. Phys. Chem. B*, 1999, **104**, 319–328.
8 K. Westermark, H. Rensmo, A. C. Lees, J. G. Vos and H. Siegbahn, *J. Phys. Chem. B*, 2002, **106**, 10108–10113.
9 C. X. Xu, X. W. Sun, B. J. Chen, P. Shum, S. Li and X. Hu, *J. Appl Phys.*, 2004, **95**, 661–666.
10 F. Boxberg and J. Tulkki, in *Handbook of Nanotechnology, Nanometer Structures - Theory, Modeling, and Simulation*, ed. A. Lakhtakia, SPIE, 2004.
11 G. Schmid, *Nanoparticles*, Wiley-VCH, Weinheim, 2004.
12 L. Qian, Y. Zheng, J. G. Xue and P. H. Holloway, *Nat. Photonics*, 2011, **5**, 543–548.
13 D. Raoufi, *Renew. Energ.*, 2013, **50**, 932–937.
14 C. Oprea, V. Ciupina and G. Prodan, *Romanian J. Phys.*, 2008, **53**, 223–230.
15 A. L. Patterson, *Phys. Rev.*, 1939, **56**, 978–982.
16 L. E. Brus, *J. Chem. Phys.*, 1984, **80**, 4403–4409.
17 N. Peyghambarian, S. W. Koch and A. Mysyrowicz, *Introduction to semiconductor optics*, Prentice Hall, Englewood Cliffs, NJ, 1993.
18 M. L. Steigerwald and L. E. Brus, *Accounts Chem. Res.*, 1990, **23**, 183–188.
19 R. N. Bhargava, V. Chhabra, T. Som, A. Ekimov and N. Taskar, *10th International Conference on II-VI Compounds*, Bremen, Germany, 2001.
20 D. W. Bahnemann, C. Kormann and M. R. Hoffmann, *J. Phys. Chem.*, 1987, **91**, 3789–3798.
21 N. S. Pesika, Z. S. Hu, K. J. Stebe and P. C. Searson, *J. Phys. Chem. B*, 2002, **106**, 6985–6990.
22 A. Pereira, unpublished work
23 A. B. Djurišić and Y. H. Leung, *Small*, 2006, **2**, 944–961.
24 D. X. Zhao, C. Andreazza, P. Andreazza, J. G. Ma, Y. C. Liu and D. Z. Shen, *Chem. Phys. Lett.*, 2004, **399**, 522–526.

25 T. B. Hur, Y. H. Hwang and H. K. Kim, *Appl. Phys. Lett.*, 2005, 86.
26 L. Zhang, L. Yin, C. Wang, N. Lun, Y. Qi and D. Xiang, *J. Phys. Chem. C*, 2010, **114**, 9651–9658.
27 A. Layek, S. De, R. Thorat and A. Chowdhury, *J. Phys. Chem. Lett.*, 2011, **2**, 1241–1247.
28 A. Asok, M. N. Gandhi and A. R. Kulkarni, *Nanoscale*, 2012, **4**, 4943–4946.
29 H.-M. Xiong, R.-Z. Ma, S.-F. Wang and Y.-Y. Xia, *J. Mater. Chem.*, 2011, **21**, 3178–3182.
30 H.-P. Wang, H. Jiang and X.-M. Wang, *Chem. Commun.*, 2010, **46**, 6900–6902.
31 X. Tang, E. S. G. Choo, L. Li, J. Ding and J. Xue, *Chem. Mater.*, 2010, **22**, 3383–3388.
32 D.-P. Liu, G.-D. Li, Y. Su and J.-S. Chen, *Angew. Chem. Int. Ed.*, 2006, **45**, 7370–7373.
33 L. Guo, Y. L. Ji, H. B. Xu, P. Simon and Z. Y. Wu, *J. Am. Chem. Soc.*, 2002, **124**, 14864–14865.
34 J. Zhang, L. D. Sun, X. C. Jiang, C. S. Liao and C. H. Yan, *Cryst. Growth Des.*, 2004, **4**, 309–313.
35 B. Weintraub, Z. Zhou, Y. Li and Y. Deng, *Nanoscale*, 2010, **2**, 1573–1587.
36 Y. J. Zhang, N. L. Wang, S. P. Gao, R. R. He, S. Miao, J. Liu, J. Zhu and X. Zhang, *Chem. Mater.*, 2002, **14**, 3564–3568.
37 L. Wang, K. Chen and L. Dong, *J. Phys. Chem. C*, 2010, **114**, 17358–17361.
38 P. Gao and Z. L. Wang, *J. Phys. Chem. B*, 2002, **106**, 12653–12658.
39 J. Zhang, L. D. Sun, J. L. Yin, H. L. Su, C. S. Liao and C. H. Yan, *Chem. Mater.*, 2002, **14**, 4172–4177.
40 S. Barth, F. Hernandez-Ramirez, J. D. Holmes and A. Romano-Rodriguez, *Prog. Mater. Sci.*, 2010, **55**, 563–627.
41 S. L. Ji and C. H. Ye, *J. Mater. Sci. Technol.*, 2008, **24**, 457–472.
42 W. Lu and C. M. Lieber, *J. Phys. D Appl. Phys.*, 2006, **39**, R387–R406.
43 P. C. Si, X. F. Bian, H. Li and Y. X. Liu, *Mater. Lett.*, 2003, **57**, 4079–4082.
44 L. M. Shen, L. C. Guo, N. Z. Bao and K. Yanagisawa, *Chem. Lett.*, 2003, **32**, 826–827.
45 K. Li, H. Luo and T. Ying, *Mater. Sci. Semicond. Process.*, 2011, **14**, 184–187.
46 X. Yin, B. Wang, M. He and T. He, *Nano Res.*, 2012, **5**, 1–10.
47 H. B. Zeng, G. T. Duan, Y. Li, S. K. Yang, X. X. Xu and W. P. Cai, *Adv. Funct. Mater.*, 2010, **20**, 561–572.
48 H. F. Greer, W. Z. Zhou, M. H. Liu, Y. H. Tseng and C. Y. Mou, *Cryst. Eng. Comm.*, 2012, **14**, 1247–1255.
49 M. I. B. Utama, J. Zhang, R. Chen, X. L. Xu, D. H. Li, H. D. Sun and Q. H. Xiong, *Nanoscale*, 2012, **4**, 1422–1435.
50 J. J. Wu and S. C. Liu, *Adv. Mater.*, 2002, **14**, 215–218.
51 L. Spanhel and M. A. Anderson, *J. Am. Chem. Soc.*, 1991, **113**, 2826–2833.
52 E. A. Meulenkamp, *J. Phys. Chem. B*, 1998, **102**, 5566–5572.
53 M. Raula, M. H. Rashid, T. K. Paira, E. Dinda and T. K. Mandal, *Langmuir*, 2010, **26**, 8769–8782.
54 Z. S. Hu, G. Oskam and P. C. Searson, *J. Colloid Interface Sci.*, 2003, **263**, 454–460.
55 L. Zhang, L. Yin, C. Wang, N. Lun and Y. Qi, *ACS Appl. Mater. Interfaces*, 2010, **2**, 1769–1773.
56 P. V. Kamat, K. Tvrdy, D. R. Baker and J. G. Radich, *Chem. Rev.*, 2010, **110**, 6664–6688.
57 Y. Liu, K. Ai, Q. Yuan and L. Lu, *Biomaterials*, 2011, **32**, 1185–1192.

58 C. B. Murray, D. J. Norris and M. G. Bawendi, *J. Am. Chem. Soc.*, 1993, **115**, 8706–8715.
59 S. Sapra, A. L. Rogach and J. Feldmann, *J. Mater. Chem.*, 2006, **16**, 3391–3395.
60 M. Shim and P. Guyot-Sionnest, *J. Am. Chem. Soc.*, 2001, **123**, 11651–11654.
61 C.-C. Lin and Y.-Y. Li, *Mater. Chem. Phys.*, 2009, **113**, 334–337.
62 T. Andelman, Y. Y. Gong, M. Polking, M. Yin, I. Kuskovsky, G. Neumark and S. O'Brien, *J. Phys. Chem. B*, 2005, **109**, 14314–14318.
63 G. Munoz-Hernandez, A. Escobedo-Morales and U. Pal, *Cryst. Growth Des.*, 2009, **9**, 297–300.
64 H. Shahroosvand and M. Ghorbani-asl, *Cryst. Eng. Comm*, 2012, **14**, 8199–8207.
65 K. A. Littau, P. J. Szajowski, A. J. Muller, A. R. Kortan and L. E. Brus, *J. Phys. Chem.*, 1993, **97**, 1224–1230.
66 M. Rezapour and N. Talebian, *Mater. Chem. Phys.*, 2011, **129**, 249–255.
67 J. X. Mou, W. G. Zhang, J. Fan, H. Deng and W. Chen, *J. Alloy. Compd.*, 2011, **509**, 961–965.
68 X. B. Wang, W. P. Cai, Y. X. Lin, G. Z. Wang and C. H. Liang, *J. Mater. Chem.*, 2010, **20**, 8582–8590.
69 L. Wang, D. Zhao, S. L. Zhong and A. W. Xu, *Cryst. Eng. Comm.*, 2012, **14**, 6875–6880.
70 S. Hingorani, V. Pillai, P. Kumar, M. S. Multani and D. O. Shah, *Mater. Res. Bull.*, 1993, **28**, 1303–1310.
71 M. Inoguchi, K. Suzuki, K. Kageyama, H. Takagi and Y. Sakabe, *J. Am. Ceram. Soc.*, 2008, **91**, 3850–3855.
72 D. Sarkar, S. Tikku, V. Thapar, R. S. Srinivasa and K. C. Khilar, *Colloid. Surf., A*, 2011, **381**, 123–129.
73 D. Sarkar, S. Tikku, V. Thapar, R. S. Srinivasa and K. C. Khilar, *Colloid. Surf., A*, 2011, **381**, 123–129.
74 J. Mao, X.-L. Li, W.-J. Qin, K.-Y. Niu, J. Yang, T. Ling and X.-W. Du, *Langmuir*, 2010, **26**, 13755–13759.
75 C. Lizandara-Pueyo, S. Siroky, M. R. Wagner, A. Hoffmann, J. S. Reparaz, M. Lehmann and S. Polarz, *Adv. Funct. Mater.*, 2011, **21**, 295–304.
76 W. H. Zhang, J. L. Shi, L. Z. Wang and D. S. Yan, *Chem. Mater.*, 2000, **12**, 1408–1413.
77 G. D. Mihai, V. Meynen, M. Mertens, N. Bilba, P. Cool and E. F. Vansant, *J. Mater. Sci.*, 2010, **45**, 5786–5794.
78 X.-W. Cheng, Q.-Y. Meng, J.-Y. Chen and Y.-C. Long, *Micropor. Mesopor. Mater.*, 2012, **153**, 198–203.
79 N. Khaorapapong, N. Khumchoo and M. Ogawa, *Mater. Lett.*, 2011, **65**, 657–660.
80 H. M. Luo, Q. L. Lin, S. Baber and A. Naalla, *J. Nanomater.*, 2010.
81 S. Baber, M. Zhou, Q. L. Lin, M. Naalla, Q. X. Jia, Y. Lu and H. M. Luo, *Nanotechnology*, 2010, **21**, 165603.
82 C. H. Braun, T. V. Richter, F. Schacher, A. H. E. Mueller, E. J. W. Crossland and S. Ludwigs, *Macromol. Rapid Comm.*, 2010, **31**, 729–734.
83 J.-F. Gnichwitz, R. Marczak, F. Werner, N. Lang, N. Jux, D. M. Guldi, W. Peukert and A. Hirsch, *J. Am. Chem. Soc.*, 2010, **132**, 17910–17920.
84 Y. Tak and K. J. Yong, *J. Phys. Chem. B*, 2005, **109**, 19263–19269.
85 V. Suresh, S. Jayaraman, M. I. b. Muhamad Jailani and M. P. Srinivasan, *J. Colloid Interface Sci.*, 2013, **394**, 13–19.
86 C. Luan, A. Vaneski, A. Susha, X. Xu, H.-E. Wang, X. Chen, J. Xu, W. Zhang, C.-S. Lee, A. Rogach and J. Zapien, *Nanoscale Res. Lett.*, 2011, **6**, 340.

87 L. Wang, Y. Zheng, X. Li, W. Dong, W. Tang, B. Chen, C. Li, X. Li, T. Zhang and W. Xu, *Thin Solid Films*, 2011, **519**, 5673–5678.
88 H. Gai, I. Stayton, X. Liu, B. Lin and Y. Ma, *TrAC, Trends Anal. Chem.*, 2007, **26**, 980–992.
89 L. Jiang, H. Dong and W. Hu, *Soft Matter*, 2011, **7**, 1615–1630.
90 C. Monico, M. Capitanio, G. Belcastro, F. Vanzi and F. S. Pavone, *Int. J. Mol. Sci.*, 2013, **14**, 3961–3992.
91 P. Tiwari, K. Vig, V. Dennis and S. Singh, *Nanomaterials*, 2011, **1**, 31–63.
92 R. Matsuno and K. Ishihara, *Macromol. Symp.*, 2009, **279**, 125–131.
93 Y. Jiang, C. Guo, H. Xia, I. Mahmood, C. Liu and H. Liu, *J. Mol. Catal: B*, 2009, **58**, 103–109.
94 W. J. E. Beek, M. M. Wienk, M. Kemerink, X. N. Yang and R. A. J. Janssen, *J. Phys. Chem. B*, 2005, **109**, 9505–9516.
95 A. J. Moule, L. Chang, C. Thambidurai, R. Vidu and P. Stroeve, *J. Mater. Chem.*, 2012, **22**, 2351–2368.
96 T. Xu and Q. Qiao, *Energy Environ. Sci.*, 2011, **4**, 2700–2720.
97 L. Zhao and Z. Lin, *Adv. Mater.*, 2012, **24**, 4353–4368.
98 A. Emamifar, M. Kadivar, M. Shahedi and S. Soleimanian-Zad, *Food Control*, 2011, **22**, 408–413.
99 P.-K. Chen, G.-J. Lee, S. Anandan and J. J. Wu, *Mater. Sci. Eng. B*, 2012, **177**, 190–196.
100 H. Tang, G. Meng, Q. Huang, Z. Zhang, Z. Huang and C. Zhu, *Adv. Funct. Mater.*, 2012, **22**, 218–224.
101 C. Wang, X. Tan, S. Chen, R. Yuan, F. Hu, D. Yuan and Y. Xiang, *Talanta*, 2012, **94**, 263–270.
102 F. Xiao, F. Wang, X. Fu and Y. Zheng, *J. Mater. Chem.*, 2012, **22**, 2868–2877.
103 J. Yi, J. M. Lee and W. Il Park, *Sensor Actuators, B*, 2011, **155**, 264–269.
104 B. Li and H. Cao, *J. Mater. Chem.*, 2011, **21**, 3346–3349.
105 D. I. Son, B. W. Kwon, D. H. Park, W.-S. Seo, Y. Yi, B. Angadi, C.-L. Lee and W. K. Choi, *Nat. Nanotechnol.*, 2012, **7**, 465–471.
106 T. Lu, L. Pan, H. Li, G. Zhu, T. Lv, X. Liu, Z. Sun, T. Chen and D. H. C. Chua, *J. Alloy. Compd.*, 2011, **509**, 5488–5492.
107 H. Chang, Z. Sun, K. Y.-F. Ho, X. Tao, F. Yan, W.-M. Kwok and Z. Zheng, *Nanoscale*, 2011, **3**, 258–264.
108 J. O. Hwang, D. H. Lee, J. Y. Kim, T. H. Han, B. H. Kim, M. Park, K. No and S. O. Kim, *J. Mater. Chem.*, 2011, **21**, 3432–3437.
109 Q.-P. Luo, X.-Y. Yu, B.-X. Lei, H.-Y. Chen, D.-B. Kuang and C.-Y. Su, *J. Phys. Chem. C*, 2012, **116**, 8111–8117.
110 B. Ramezanzadeh, M. M. Attar and M. Farzam, *J. Therm. Anal. Calorim.*, 2011, **103**, 731–739.
111 R. Devi, M. Thakur and C. S. Pundir, *Biosens. Bioelectron.*, 2011, **26**, 3420–3426.
112 W. J. E. Beek, M. M. Wienk, M. Kemerink, X. Yang and R. A. J. Janssen, *J. Phys. Chem. B*, 2005, **109**, 9505–9516.
113 K. Segala, R. L. Dutra, C. V. Franco, A. S. Pereira and T. Trindade, *J. Braz. Chem. Soc.*, 2010, **21**, 1986–1991.
114 G. Zhu, Y. Liu, H. Xu, Y. Chen, X. Shen and Z. Xu, *Cryst. Eng. Comm*, 2012, **14**, 719–725.
115 A. Olad and R. Nosrati, *Prog. Org. Coat.*, 2013, **76**, 113–118.
116 S. T. Selvan, T. T. Y. Tan, D. K. Yi and N. R. Jana, *Langmuir*, 2010, **26**, 11631–11641.
117 Y. L. Wu, C. S. Lim, S. Fu, A. I. Y. Tok, H. M. Lau, F. Y. C. Boey and X. T. Zeng, *Nanotechnology*, 2007, 18.

118 Y. Gong, T. Andelman, G. F. Neumark, S. O'Brien and I. L. Kuskovsky, *Nanoscale Res. Lett*., 2007, **2**, 297–302.
119 A. Lenz, L. Selegard, F. Soderlind, A. Larsson, P. O. Holtz, K. Uvdal, L. Ojamae and P.-O. Kall, *J. Phys. Chem. C*, 2009, **113**, 17332–17341.
120 N. S. Norberg and D. R. Gamelin, *J. Phys. Chem. B*, 2005, **109**, 20810–20816.
121 Y. Cao, E. Galoppini, P. I. Reyes, Z. Duan and Y. Lu, *Langmuir*, 2012, **28**, 7947–7951.
122 L. SelegArd, V. Khranovskyy, F. Soderlind, C. Vahlberg, M. Ahren, P.-O. Kall, R. Yakimova and K. Uvdal, *ACS Appl. Mater. Interfaces*, 2010, **2**, 2128–2135.
123 P. V. Radovanovic and D. R. Gamelin, *J. Am. Chem. Soc*., 2001, **123**, 12207–12214.
124 F. V. Mikulec, M. Kuno, M. Bennati, D. A. Hall, R. G. Griffin and M. G. Bawendi, *J. Am. Chem. Soc*., 2000, **122**, 2532–2540.
125 A. O. Ankiewicz, W. Gehlhoff, J. S. Martins, A. S. Pereira, S. Pereira, A. Hoffmann, E. M. Kaidashev, A. Rahm, M. Lorenz, M. Grundmann, M. C. Carmo, T. Trindade and N. A. Sobolev, Phys, *Status Solidi B*, 2009, **246**, 766–770.
126 A. S. Pereira, A. O. Ankiewicz, W. Gehlhoff, A. Hoffmann, S. Pereira, T. Trindade, M. Grundmann, M. C. Carmo and N. A. Sobolev, *J. Appl Phys*., 2008, 103.
127 C. L. Wu, L. Shen, Y. C. Zhang and Q. L. Huang, *Mater. Lett*., 2011, **65**, 1794–1796.
128 O. Lupan, T. Pauporte, T. Le Bahers, B. Viana and I. Ciofini, *Adv. Funct. Mater*., 2011, **21**, 3564–3572.
129 T. Monteiro, M. J. Soares, A. Neves, S. Pereira, M. R. Correia, M. Peres, E. Alves, D. Rogers, F. Teherani, V. Munoz-SanJose, T. Trindade and A. Pereira, *J. Non-Cryst. Solids*, 2006, **352**, 1453–1456.
130 M. Peres, A. Cruz, S. Pereira, M. R. Correia, M. J. Soares, A. Neves, M. C. Carmo, T. Monteiro, A. S. Pereira, M. A. Martins, T. Trindade, E. Alves, S. S. Nobre and R. A. S. Ferreira, *Appl. Phys. A*, 2007, **88**, 129–133.
131 A. S. Pereira, M. Peres, M. J. Soares, E. Alves, A. Neves, T. Monteiro and T. Trindade, *Nanotechnology*, 2006, **17**, 834–839.
132 D. A. Schwartz, N. S. Norberg, Q. P. Nguyen, J. M. Parker and D. R. Gamelin, *J. Am. Chem. Soc*., 2003, **125**, 13205–13218.
133 P. V. Radovanovic, N. S. Norberg, K. E. McNally and D. R. Gamelin, *J. Am. Chem. Soc*., 2002, **124**, 15192–15193.
134 K. Vanheusden, C. H. Seager, W. L. Warren, D. R. Tallant and J. A. Voigt, *Appl. Phys. Lett*., 1996, **68**, 403–405.
135 B. Y. Geng, G. Z. Wang, Z. Jiang, T. Xie, S. H. Sun, G. W. Meng and L. D. Zhang, *Appl. Phys. Lett*., 2003, **82**, 4791–4793.
136 S. Y. Bae, H. W. Seo and J. H. Park, *J. Phys. Chem. B*, 2004, **108**, 5206–5210.
137 R. Viswanatha, S. Sapra, S. Sen Gupta, B. Satpati, P. V. Satyam, B. N. Dev and D. D. Sarma, *J. Phys. Chem. B*, 2004, **108**, 6303–6310.
138 X. Wang, X. G. Kong, G. Y. Shan, Y. Yu, Y. J. Sun, L. Y. Feng, K. F. Chao, S. Z. Lu and Y. J. Li, *J. Phys. Chem. B*, 2004, **108**, 18408–18413.
139 R. Buonsanti, A. Llordes, S. Aloni, B. A. Helms and D. J. Milliron, *Nano Lett*., 2011, **11**, 4706–4710.
140 A. A. Ibrahim, G. N. Dar, S. A. Zaidi, A. Umar, M. Abaker, H. Bouzid and S. Baskoutas, *Talanta*, 2012, **93**, 257–263.
141 Y. C. Qiu, K. Y. Yan, H. Deng and S. H. Yang, *Nano Lett*., 2012, **12**, 407–413.
142 A. Wei, X. W. Sun, J. X. Wang, Y. Lei, X. P. Cai, C. M. Li, Z. L. Dong and W. Huang, *Appl. Phys. Lett*., 2006, 89.

143 J. Bao, M. A. Zimmler, F. Capasso, X. Wang and Z. F. Ren, *Nano Lett*., 2006, **6**, 1719–1722.
144 S. S. Shinde and K. Y. Rajpure, *J. Alloy. Compd*., 2012, **522**, 118–122.
145 W.-J. Jeong and G.-C. Park, *Sol. Energ. Mat. Sol. C*., 2001, **65**, 37–45.
146 L. Veleva, J. Chin and B. del Amo, *Prog. Org. Coat*., 1999, **36**, 211–216.
147 L. H. Yang, F. C. Liu and E. H. Han, *Prog. Org. Coat*., 2005, **53**, 91–98.
148 L. Vayssieres, *Adv. Mater*., 2003, **15**, 464–466.
149 N. H. Al-Hardan, M. J. Abdullah, N. M. Ahmed, F. K. Yam and A. A. Aziz, *Superlattice Microst*., 2012, **51**, 765–771.
150 A. J. Gimenez, J. M. Yanez-Limon and J. M. Seminario, *J. Phys. Chem. C*, 2011, **115**, 282–287.
151 X. Y. Kong, Y. Ding, R. Yang and Z. L. Wang, *Science*, 2004, **303**, 1348–1351.
152 F. Muhammad, M. Y. Guo, W. X. Qi, F. X. Sun, A. F. Wang, Y. J. Guo and G. S. Zhu, *J. Am. Chem. Soc*., 2011, **133**, 8778–8781.
153 Y. F. Cheng, R. Yuan, Y. Q. Chai, H. Niu, Y. L. Cao, H. J. Liu, L. J. Bai and Y. L. Yuan, *Anal. Chim. Acta*, 2012, **745**, 137–142.
154 W. H. Hu, Z. S. Lu, Y. S. Liu, T. Chen, X. Q. Zhou and C. M. Li, *Lab. Chip*, 2013, **13**, 1797–1802.
155 K. C. Barick, S. Nigam and D. Bahadur, *J. Mater. Chem*., 2010, **20**, 6446–6452.
156 F. Muhammad, M. Y. Guo, Y. J. Guo, W. X. Qi, F. Y. Qu, F. X. Sun, H. J. Zhao and G. S. Zhu, *J. Mater. Chem*., 2011, **21**, 13406–13412.
157 N. Serpone, D. Dondi and A. Albini, *Inorg. Chim. Acta*, 2007, **360**, 794–802.
158 G. J. Nohynek, E. K. Dufour and M. S. Roberts, *Skin Pharmacol. Physiol*., 2008, **21**.
159 G. J. Nohynek, J. Lademann, C. Ribaud and M. S. Roberts, *Crit. Rev. Toxicol*., 2007, **37**, 251–277.
160 J. Becker, K. R. Raghupathi, J. St Pierre, D. Zhao and R. T. Koodali, *J. Phys. Chem. C*, 2011, **115**, 13844–13850.
161 Y. L. Lai, M. Meng and Y. F. Yu, *Appl. Catal. B*, 2010, **100**, 491–501.
162 Z. F. Liu, Q. H. Zhang, Y. G. Li and H. Z. Wang, *J. Phys. Chem. Solids*, 2012, **73**, 651–655.
163 Q. W. Tang, L. Lin, Z. P. Mao, Z. Y. Tang and J. H. Wu, *RSC Adv*., 2012, **2**, 2211–2216.
164 Z. W. Pan, Z. R. Dai and Z. L. Wang, *Science*, 2001, **291**, 1947–1949.
165 M. S. Arnold, P. Avouris, Z. W. Pan and Z. L. Wang, *J. Phys. Chem. B*, 2003, **107**, 659–663.